NASA/CP-1999-209136/PT 2

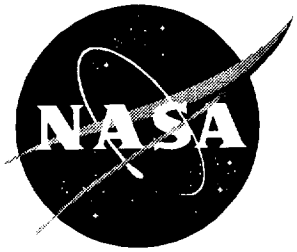

CEAS/AIAA/ICASE/NASA Langley International Forum on Aeroelasticity and Structural Dynamics 1999

Edited by

Woodrow Whitlow, Jr.
NASA John H. Glenn Research Center at Lewis Field
Cleveland, Ohio

Emily N. Todd
Institute for Computer Applications in Science and Engineering (ICASE)
Hampton, Virginia

Proceedings of a workshop sponsored by the Confederation of European Aerospace Societies (CEAS), the American Institute of Aeronautics and Astronautics (AIAA), the National Aeronautics and Space Administration (NASA), Washington, D. C., and the Institute for Computer Applications in Science and Engineering (ICASE), Hampton, Virginia, and held in Williamsburg, Virginia
June 22–25, 1999

National Aeronautics and
Space Administration

Langley Research Center
Hampton, Virginia 23681-2199

June 1999

The use of trademarks or names of manufacturers in this report is for accurate reporting and does not constitute an official endorsement, either expressed or implied, of such products or manufacturers by the National Aeronautics and Space Administration.

Available from:

NASA Center for AeroSpace Information (CASI)
7121 Standard Drive
Hanover, MD 21076-1320
(301) 621-0390

National Technical Information Service (NTIS)
5285 Port Royal Road
Springfield, VA 22161-2171
(703) 605-6000

PREFACE

Aeroelasticity is a multidisciplinary technology area that integrates steady and unsteady aerodynamics and elastic structures. Its importance has been recognized and considered since the early days of flight. It is critical in that proper aeroelastic design reduces or eliminates the need for costly fixes later in the development process. As the performance of vehicles increased, the need for control systems to control the structural responses increased and, for very high-speed vehicles, the effects of structural heating on the structural dynamic response had to be modeled. The advent of the computer led to the development of computational unsteady aerodynamics methods that are used to predict aeroelastic response across the aircraft flight envelope. The effects of aerodynamics and elastic structures must be considered and modeled accurately to predict aeroelastic responses and to provide data for designing active control systems. In recent years, smart materials and adaptive structures have been introduced as a means to control the response of flexible structures.

Even as prediction methods advanced, the role of testing maintained its importance in the design and certification processes. Models have improved, allowing for more realistic representation of aircraft. Facility capabilities have increased, measurement techniques have improved, and the prediction methods have been used to guide tests. This resulted in more efficient and effective use of test facilities.

As we strive to improve the performance of aircraft during flight, we have made significant advances in understanding their behavior during ground operations. The dynamic response during taxi, takeoff, and landing have been shown to be critical to the performance of the flight crew, to the ride comfort of the passengers, and to the safe operations of aircraft. The design of landing gear, brakes, and tires is taking on more importance in the aircraft design process.

With the importance of aeroelasticity and structural dynamics increasing in the design and operation of aircraft and spacecraft, it was with great pleasure that I accepted the responsibility of serving as Technical Chair of the International Forum on Aeroelasticity and Structural Dynamics 1999. I would like to thank the CEAS Specialists Committee on Structures and Materials for allowing me to take on this important and honorable task. This is the premier gathering of aeroelasticians and structural dynamicists anywhere. We have an outstanding program that will spark rewarding discussion and lead to many advances in the future. Because of the success of this forum, I feel honored to recognize those who worked so diligently to make this great event happen.

I would like to acknowledge Irving Abel for his efforts in bringing this outstanding forum to the United States for the first time. The Program Committee members deserve special congratulations for their efforts in selecting an outstanding series of papers to be presented. I thank the Organizing Committee members, especially Dr. Robert Moses, for their help with the organization of the forum. Mr. Lee Pollard deserves recognition for his efforts in designing the artwork that is featured on the forum program and on the website. Finally, I wish to acknowledge the outstanding support of Ms. Emily N. Todd of the Institute of Computer Applications in Science and Engineering for all of her help in addressing the administrative details necessary to make the conference a success and in preparing this document.

Woodrow Whitlow, Jr.
NASA John H. Glenn Research Center at Lewis Field

Organizing Committee:

Howard M. Adelman, NASA Langley Research Center, Hampton, VA, USA
Peretz P. Friedmann, University of Michigan, Ann Arbor, USA
Robert W. Moses, NASA Langley Research Center, Hampton, VA, USA
Thomas E. Noll, NASA Langley Research Center, Hampton, VA, USA
Boyd Perry III, NASA Langley Research Center, Hampton, VA, USA
Emily Todd, Institute for Computer Applications in Science and Engineering, Hampton, VA, USA (Administrative Chair)
Woodrow Whitlow, Jr., NASA John H. Glenn Research Center at Lewis Field, Cleveland, OH, USA (Technical Chair)

Program Committee:

H. Climent, CASA, Madrid, Spain
L. Balis Crema, University of Rome "La Sapienza", Rome, Italy
P. P. Friedmann, University of Michigan, Ann Arbor, USA
H. G. Hönlinger, DLR-Institut für Aeroelastik, Göttingen, Germany
R. Labourdette, ONERA, Chatillon, France
A. J. Morris, Cranfield University, Cranfield, UK
M. Nash, Defence Research Agency, Farnborough, UK
M. Pecora, CIRA, Capua, Italy
C. Petiau, Dassault Aviation, Saint Cloud, France
R. Pyrah, B. Ae. Military Aircraft, Warton, UK
O. Sensburg, DASA, Daimler-Benz Aerospace AG Munich-Ottbrunn, Germany
C. Stavrinidis, ESA/ESTEC, Noordwijk, The Netherlands
G. R. Tomlinson, The University of Sheffield, Sheffield, UK
W. Whitlow, Jr., NASA John H. Glenn Research Center at Lewis Field, Cleveland, OH, USA
B. Winzell, SAAB, Linkoping, Sweden
R. J. Zwaan, NLR, Amsterdam, The Netherlands

CONTENTS

PREFACE iii

PART 1*

COMPUTATIONAL FLUID DYNAMICS

A New Compendium of Unsteady Aerodynamic Test Cases for CFD: Summary of AVT WG-003 Activities 1
Luis P. Ruiz-Calavera, Robert Bennett, John H. Fox, Robert W, Galbraith, Evert Geurts, Michael J deC Henshaw, XingZhong Huang, Ian W. Kaynes, Thomas Löser, Pierre Naudin, and Masato Tamayama

FLEXIBLE AIRCRAFT

A Combined Modal/Finite Element Analysis Technique for Nonlinear Beam Dynamic Response Under Harmonic Excitation 13
Matthew I. McEwan, Jan R. Wright, Jonathan E. Cooper, and Andrew Y. T. Leung

An $H\infty$ Approach to Control Synthesis with Load Minimization for the F/A-18 Active Aeroelastic Wing 23
Rick Lind

MULTIDISCIPLINARY DESIGN OPTIMIZATION

Aeroelastic Constraints in MDO 33
F. Mastroddi, E. Ciancaleoni, and L. Morino

MDO of an Innovative Configuration – Aerodynamic Issues 43
G. Bernardini, A. Frediani, and L. Morino

LIMIT CYCLE OSCILLATION

Simulation of Nonlinear Airfoil/Control-Surface Flutter at Subsonic Speeds using Classical Unsteady Aerodynamics and an Euler Method 53
Silvio Schulze

Limit Cycle Oscillation Prediction Using Artificial Neural Networks 71
Charles M. Denegri, Jr. and Michael R. Johnson

TEST METHODS

A Procedure to Improve Convergence and Accuracy of Iterative Model Updating Methods 81
Stefan Keye

Computer-controlled Normal Mode Tuning 89
J. M. Sinapius and R. C. Lake

*Part 1 is presented under separate cover.

Vibro-Acoustics Modal Testing at NASA Langley Research Center 101
Richard S. Pappa, Jocelyn I. Pritchard, and Ralph D. Buehrle

Wind Tunnel Tests and Analysis on Flutter of Spacecraft Including Pitching Effects in Its Launching Configuration 115
Atsushi Kanda and Tetsuhiko Ueda

TILTROTOR

Aeroelastic Tailoring for Stability Augmentation and Performance Enhancements of Tiltrotor Aircraft. 121
Mark W. Nixon, David J. Piatak, Lawrence M. Corso and David A. Popelka

Analysis of Fuselage Vibrations Induced by the Proprotor in a Tiltrotor Aircraft 139
M. Gennaretti and U. Iemma

Multi-Body Analysis of an Active Control for a Tiltrotor 149
G.L. Ghiringhelli, P. Masarati, P. Mantegazza, and M. W. Nixon

Rotary Wing Test Stand Capability for the Republic of Korea 159
Jeffrey Breaks and Michael Cooper

PANEL FLUTTER

Review of Nonlinear Panel Flutter at Supersonic and Hypersonic Speeds 171
Chuh Mei, K. Abdel-Motagaly, and R. Chen

Nonlinear Response of Composite Panels under Combined Acoustic Excitation and Aerodynamic Pressure 189
K. Abdel-Motagaly, B. Duan, and C. Mei

Panel Flutter Analyses for the First Brazilian Satellite Launcher 201
J. G. Damilano, Jamil C. Said, and João L. F. Azevedo

LANDING DYNAMICS I

Self-Induced Brake Torque Oscillations of Landing Gear as an Interaction of Non-linear Tyre with Brake Control System 211
Wolfgang G. Luber

Nonlinear Transient Whirl Vibration Analysis of Aircraft Brake Systems 225
Craig F. Chang

CERTIFICATION

An Unsteady Aerodynamics Identification Procedure for Flutter Prediction 235
S. Prudhomme, C. Blondeau, M. Humbert, and A. Bucharles

Parameter Estimation in Flutter Analysis by Wavelet and Neural Network 245
Y. S. Wong, B. H. K. Lee, and T. K. S. Wong

Flutter Speed Prediction during Flight Flutter Testing Using Neural Networks 255
J. E. Cooper and W. J. Crowther

Overview of Recent Flutter Boundary Prediction Techniques Based on Testing Data Analysis 265
Pei Chengming, Qiu Zhihua, and Zhai Kun

COMPUTATIONAL FLUID DYNAMICS II

Aeroelasticity Simulations in Turbulent Flows 275
Jean-Pierre Grisval, Cédric Liauzun and Zdeňek Johan

FLUTTER CONTROL

Active Control of Flutter in Compressible Flow and Its Aeroelastic Scaling 287
E. Presente and P. P. Friedmann

New Experimental Stall Flutter Active Control of a Bridge Section 311
L. Lecce, E. Selvaggi, F. Nicolosi, M. Baruffo, and A. Abate

STRUCTURAL OPTIMIZATION

A Reduced Basis Model for Aeroelastic Optimization 325
S. Grihon and J. P. Esquerré

A Survey of Shape Parameterization Techniques 333
Jamshid A. Samareh

Reduced Order Design-Oriented Stress Analysis using Combined Direct and Adjoint Solutions 345
Eli Livne and Guillermo D. Blando

REDUCED-ORDER MODELS

Reduced-Order Models Based on Linear and Nonlinear Aerodynamic Impulse Responses 369
Walter A. Silva

NONLINEARITY

Transonic Flutter Suppression Control Law Design, Analysis, and Wind Tunnel Results 381
Vivek Mukhopadhyay

TESTING

Wavelet Applications for Flight Flutter Testing 393
Rick Lind, Marty Brenner and Lawrence C. Freudinger

LINEAR METHODS

Aerodynamic and Aeroelastic Insights using Eigenanalysis 403
Jennifer Heeg and Earl H. Dowell

Influence of Nonplanar Supersonic Interference on Aeroelastic Characteristics 415
V. Kouzmin, S. Kouzmina, V. Mosounov and F. Ishmuratov

An Application of the P-Transform Method for Transient Maneuvering Analysis 425
John R. Dykman and William P. Rodden

A Damping Perturbation Method for Flutter Solution: The g-Method 433
P. C. Chen

PART 2

AEROELASTIC APPLICATIONS I

Vortex-Lattice-Method to Analyze Aerodynamic Interference of Wing/Pylon/Store Configurations of an F-16 Wing ..... 443 -1
J. Cattarius, S. Preidikman, D. T. Mook, and D. J. Inman

Flutter Stability of Movable Control Surfaces for Aircraft Stores ..... 457 -2
Claudio Ponzi and Johannes Schweiger

STRUCTURE AND AERODYNAMICS INTEGRATION

Structural Optimization using Computational Aerodynamics ..... 469 -3
Daniella E. Raveh, Yuval Levy and Moti Karpel

Multidisciplinary Aero-Structural Modeling on Parallel Computers ..... 483 -4
Ryoichi Onishi, Toshiya Kimura, Zhihong Guo, and Toshiyuki Iwamiya

Astros: Seamless Integration of Astros with a Unified Aerodynamic Module: Applications Benchmarking and Testing ..... 491 -5
A. G. Striz and S. Y. Jung

NONLINEAR FLUTTER

Characterizing the Effects of Geometrical Nonlinearities on Aeroelastic Behavior of High-Aspect Ratio Wings 501 6
Mayuresh J. Patil, Dewey H. Hodges, and Carlos E. S. Cesnik

Simulation of Nonlinear Transonic Aeroelastic Behavior on the B-2 ..... 511 -7
D. R. Dreim, S. B. Jacobson, and R. T. Britt

Singular Perturbation Technique for Nonlinear Aeroelastic Analysis 523 8
D. Dessi and F. Mastroddi, and L. Morino

Application of The Centre Manifold Theory in Nonlinear Aeroelasticity ..... 533 -9
L. Liu, Y. S. Wong, and B. H. K. Lee

DEVICES

Flutter Suppression and Vibration Control of Plate-Wing Structures Using Self-Sensing Active Constrained Layer Damping ..... 543 -10
Jeng-Jong Ro and Ehab Elsaadawy

An Examination of Applying Shunted Piezoelectrics to Reduce Aeroelastic Response ..... 553 -11
Anna-Maria Rivas McGowan

A Comparison Study of the Performance of a Saturation Absorber and Classical Vibration Control Methods 573
Hanafy M. Omar and Donald Kunz

Creation of a Finite Element Model for F/A-18 Structural Dynamic Analyses Based on Ground Vibration Test Data 585
S. A. Dunn

Effects of Transient Hypersonic Flow Conditions on Failure Prediction of Panels 595
Radu Udrescu and Giuseppe Surace

Nonlinear Regular and Chaotic Flutter of an Airfoil with a Trailing Edge Flap in Supersonic Flow 605
Z. Dzygadlo, I. Nowotarski, and A. Olejnik

BUFFET

Correlation of Fin Buffet Pressures on an F/A-18 with Scaled Wind-Tunnel Measurements 615
Robert W. Moses and Gautam H. Shah

Twin-Tail Buffet Simulation using a Multi-Disciplinary Computing Environment (MDICE) 627
Essam F. Sheta, John M. Siegel, Jr., Freddy N. Golos and Vincent J. Harrand

Adaptive Suction and Blowing for Twin-Tail Buffet Control 639
Osama A. Kandil and Zhi Yang

LANDING DYNAMICS II

An Overview of Landing Gear Dynamics 649
Jocelyn Pritchard

Actively Controlled Landing Gear for Aircraft Vibration Reduction 665
Lucas G. Horta, Robert H. Daugherty and Veloria J. Martinson

Aircraft and Ground Vehicle Winter Runway Friction Assessment 679
Thomas J. Yager

AEROELASTIC TAILORING

Application of Direct Search Method to Aeroelastic Tailoring of an Arrow Wing Configuration 691
Koji Isogai

Ply Angle Optimization of Non-Uniform Composite Beams Subject to Aeroelastic Constraints 699
T. Evrard, R. Butler, S. W. Hughes, and J. R. Banerjee

Influence of Aeroelastic Tailoring in the Multidisciplinary Design of a New Aircraft 709
Roland Kelm, Michael Dugas, Rudolf Voit-Nitschmann, and Michael Grabietz

Synergistic Interaction of Aeroelastic Tailoring and Boundary Moment Control on Aircraft Wing Flutter 719
Frank H. Gern and Liviu Librescu

FLUID-STRUCTURE INTERACTION

Non-Linear Fluid and Structures Interaction Simulation 735
Reid B. Melville and Raymond E. Gordnier

Divergence and Flutter of Adaptive Laminated Composite Aircraft Wings Featuring Damaged Bonding Interfaces 747
L. Librescu, U. Icardi and M. Di Sciuva

AEROELASTIC APPLICATIONS II

Improving the Convergence of the Doublet-Lattice Method Through Tip Corrections 763
Myles L. Baker and William P. Rodden

Aeroelastic Analysis of a Trimmed Generic Hypersonic Vehicle 777
I. Nydick and P. P. Friedmann

Stiffness and Damping Effects of Launch Vehicle Aeroelastic Coupling 811
K. W. Dotson, R. L. Baker, and B. H. Sako

SYSTEM MODELING

Finite Element Model Updating using Experimental Vibration Data: Parameterisation and Regularisation 821
Michael I. Friswell, and John E. Mottershead

Optimal System Realization in Frequency Domain 831
Jer-Nan Juang and Peiman G. Maghami

Identification of a Non-Proportionally Damped Truss Structure 847
Steven Naylor, Jan R. Wright and Jonathan E. Cooper

Nonlinear Aeroelastic System Identification via Wavelet Analysis in the Neighbourhood of a Limit Cycle 857
F. Mastroddi and A. Bettoli

Vortex–Lattice–Method to Analyze Aerodynamic Interference of Wing/Pylon/Store Configurations of an F16 Wing

J. Cattarius[1] S. Preidikman[2] D. T. Mook[3] D. J. Inman[4]

Virginia Polytechnic Institute and State University,
Blacksburg, Virginia 24061–0261

March 26, 1999

Abstract

This paper will show initial results of a complete aeroelastic F16–like semi–span wing model, used to analyze the feasibility of piezoelectric stack actuation as a wing/store flutter suppression system. The model can identify the presence of aerodynamic interference between the store, pylon, and wing wakes and examine its significance with respect to the pressure and lift forces on the participating bodies. The wing and store data considered in this analysis, represent an F16 configuration that was identified to induce flutter in flight at subsonic speeds [9]. The pylon is based on the concept of the decoupler pylon, introduced by Reed and Foughner in 1978 and flight tested in the early 1980's, and models both yaw and pitching motion of the store.

The complete aeroelastic model is simulated in ABAQUS which has been augmented by the unsteady–vortex–lattice–method (UVLM) to calculate the aerodynamic loading. Both codes communicate through an iterative handshake procedure during which displacements and air loads are updated. For each increment in time the force/displacement equilibrium is found in this manner. At this point, the analysis is confined to a static analysis of the flexible structure. The wing is modeled as an elastic plate and pylon and store are rigid bodies. The store is connected to the pylon through an elastic joint possessing two degrees of freedom, pitch and yaw, respectively.

[1]Department of Engineering Science and Mechanics; Center for Intelligent Materials, Systems, and Structures
[2]Department of Engineering Science and Mechanics
[3]Department of Engineering Science and Mechanics
[4]Department of Mechanical Engineering, Center for Intelligent Materials, Systems, and Structures

1 Introduction

Wing/Store Flutter is an aeroelastic phenomenon for which both structural and aerodynamic entities are equally important. Throughout the years a variety of analytical control schemes have aimed at suppressing wing/store flutter through active counter–mechanisms. They have been developed analytically and tested on wind tunnel models. The most common of these procedures act on "wing–owned" control surfaces, such as ailerons, leading edge flaps, and/or trailing edge flaps. The control laws range from simple velocity feedback to optimal control including some adaptive configurations together with system identification. However, the analytical representation of the system needs to be linearized in order to take advantage of the advanced control mechanisms. Linearization forms a system that exhibits good results under certain operating conditions yet deteriorates in performance quickly when system parameters change. Aerodynamic forces exhibit highly nonlinear characteristics and are the main, but not sole, source of system changes. In the past ten years, researchers have established that structural non–linearities are an important contributor to the overall dynamics of the system, e. g. [11].

In 1978, Reed and Foughner patented the so–called decoupler pylon which mounted stores elastically to the wing, in contrast to the standard rigid connection. The idea was to decouple the store from the wing by using an elastic pylon and with that restore the performance capabilities of the wing. Simulations, wind tunnel tests and flight tests with an F16 verified the potential of the method. It offered a practical alternative to previously pursued wing-based methods.

In the past 15 years several semi–active decoupler pylon concepts, (e. g., adjustable spring stiffness, electromagnetic friction damper), aimed at increasing the system's tolerance to changing air and maneuver loads have been proposed. Cazier and Kehoe [3] headed a program in 1986 to design, build, and flight test such a modified decoupler pylon. They introduced an alignment system that maintained the store in a nominally aligned static position. Flight tests demonstrated a 37% increase in flutter speed over conventional store attachments.

In 1994, Gade and Flowers [1] first investigated the possibilities of active flutter suppression by means of a "smart" pylon. Smart materials are easy to operate and require less space than equivalent mechanical devices. The active concept is envisioned to improve flutter suppression beyond the semi–active case and to provide, in the future, a practical environment for controlled store release.

In the last three years Gade and Inman [2] fortified the smart concept and developed a series of advanced control algorithms to suppress flutter based on the concept of piezoceramic stack actuators. The analytical strategies are based on fundamental structural and aerodynamic models that fall short of the complicated physics involved in the problem. To compensate for these shortcomings, elaborate robustness studies involving uncertainty models were undertaken. Simulations provide encouraging results as to how flutter can be

suppressed by application of the active "smart" decoupler pylon.

To assess the capabilities of the "smart" pylon reliably, it is necessary to model the physics of the problem more accurately, particularly the aerodynamic aspects. Wing/store flutter is a three–dimensional phenomenon and therefore it necessitates three dimensional treatment of the structure and aerodynamics.

1.1 Aerodynamic Model

The unsteady–vortex–lattice–method (UVLM) is based on the fundamental physical observation that the flow past immersed bodies generates vorticity along surfaces in contact with the flow. For attached flow this effect is confined inside a thin boundary layer. The vorticity leaves the boundary layer to enter the free stream only at trailing edges or other sharp edges and forms the trailing vortex sheet or wake. The boundary layer itself need not be modeled explicitly but its implicit effects on the global flow mechanics are fully accounted for. Meaning, the global flow can actually be regarded as being inviscid, confining vorticity into the boundary layers and the wake. The location of the separation is not provided as part of the solution. It must be specified a–priori in the sense of an implicit Kutta condition.

The UVLM has its main restriction in the incompressibility assumption, which makes it impossible to capture shock waves and the drag associated with them. The flow speed must be kept within the subsonic range. On the other hand, the vortex–lattice method also yields the wake as part of the solution and is capable of approximating flow interference due to the shedding of vorticity. The UVLM, and its variations, has been in use for many years and has been applied to various aerodynamic configurations, including bridge flutter [6], influence of canards onto the main wing in the case of an X29 fighter airplane [7], and store separation including wake effects [8].

The mesh of the complete semi–span model can be taken from Figure A.3. The complete configuration consists of 662 panels, 30 fuselage panels, 160 wing panels, 52 pylon panels, and 420 store panels.

The fuselage is an extension of the wing from the root inboard to the plane of symmetry. All fuselage panels contribute implicitly to the lift force by inducing velocities at the control points on the wing. There is no explicit participation of the fuselage in the force calculations, i. e., the total lift force is calculated across the wing panels only.

The wing extends from span station 41 to the wing tip at span station 180. It is modeled as a camberless lifting surface in the shape of the plan form of the F16 wing, see Figure A.3. From both the trailing edge and the wing tip, vorticity is shed to form the trailing vortex sheet and the wing tip vortex, respectively.

At span station 120 the decoupler pylon is rigidly attached to the wing. The pylon is also modeled as a thin plate, which convects vorticity from its trailing edge into the wake. The shape of the pylon is modified from its original design, see Figure A.2, to accommodate the pitch motion of the attached store. The v–shaped lower edge of the pylon allows a maximum

+/- 5 degree store pitch angle.

The store itself is an axisymmetric, open body of revolution. Again, vorticity is shed from the trailing edge which produces a tube like wake.

1.2 Structural Model

ABAQUS is a commercial finite element package that has been chosen for its powerful non-linear capabilities. ABAQUS allows great freedom of model design, where anything from geometric nonlinearities, i. e., large displacement theory, to structural non–linearities, e. g., freeplay, can be implemented. The model considered in this early stage of our research employs a static non–linear solution process.

The data available to specify the structure are taken from [9]. The F16 wing is modeled as a uniform plate using 4–noded reduced order general shell elements. The wing root is connected rigidly to the rigid fuselage, which, in turn, is clamped along the plane of symmetry. The symmetric mode frequencies are displayed in Table 1. Since further structural

Quantity	True Frequency	Model Frequency
Wing Bending	4.07 Hz	4.05 Hz
GBU-8/B Pitch	5.35 Hz	5.04 Hz
GBU-8/B Yaw	8.12 Hz	8.01 Hz
Wing Torsion	-.- Hz	13.04 Hz

Table 1: Wing Natural Frequency Data

properties of the wing could not be obtained, we defined a reasonable mass for the wing (2000 kg) and tuned the stiffness as to match the natural frequencies of the measurements in [9]. Mode shapes of the first four symmetric modes are depicted in Figure A.1. The store is modeled as a rigid body with mass and inertia properties given in Table 2. The decoupler

Quantity	Value
Mass	1027.0 kg
I_{pitch}	710.5 kg·m^2
I_{yaw}	710.5 kg·m^2
I_{roll}	27.5 kg·m^2

Table 2: GBU-8/B Mass and Inertia Properties

pylon has a mass of 161 kg and was also modeled rigidly with its mass concentrated at the area centroid. It is rigidly connected to the wing at the specified forward and aft mount location. The pivot point is located forward from the forward mount and coincides with the

chord location of the C. G. of the store. The torsional spring stiffnesses for pitch and yaw are 1.15×10^6 N · m/rad and 1.85×10^6 N · m/rad, respectively.

A full scale schematic of the semi–span configuration, examined here, can be taken from Figure A.2. The structural mesh coincides with that of the aerodynamic model.

2 Results

The airspeed for this simulation is 193 m/s at an altitude of 3000 m with an angle of attack of 4.0 degrees. The simulation starts by means of an impulsive start, during which the model is accelerated from rest to its final speed in one time increment. Within 60 time increments the solution converges to its steady state values. The development of the pressures on the wing along the leading and trailing edge are depicted in Figure 1. The data clearly identifies the presence of the pylon by a pronounced dip in pressure magnitudes in its vicinity. This data is in good agreement with wind tunnel measurements published by [10].

The corresponding lift force on the wing at steady state is shown in Figure 2. The shaded area is a measure of the total lift produced by all wing panels and the numbered lines display lift force per panel along span–wise rows. Row one being the leading edge and row 10 the trailing edge. Under above conditions the wing model produces a total lift of about 6.9 kN per wing, enough to sustain stable cruise for an F16 with a maximum mass of almost 14 metric tons.

The store pressure coefficients are displayed in Figure 3 and are consistent with measurements published by [12]. The term 'row' in Figure 3 refers to panel sections along the length of the store. The store consists of twelve identical rows, where row one is adjacent to the pylon on the side of the wing tip and row twelve is adjacent to the pylon facing toward the fuselage. Near the trailing edge of the store the pressure plot exhibits numerical disturbances that are related to the singularities in the Biot–Savart Law. The UVLM code employs empirical tolerance margins to eliminate such effects. The effects shown in Figure 3 are of little consequence to the physics of the overall fluid flow.

Consulting the resultant force distributions over the length of the store, displayed in Figure 4, it is evident that the store is subjected to a significant drag force upstream from the pivot point, which results in a small pitch up. It forces the store into a slightly bigger angle of attack than the wing. We intend to add trailing edge fins to the store model, which will force alignment of the store body with the flow. Lift and Side Forces are very small and have no considerable effect on the store position.

Figure 5 displays the wake shed from the wing, pylon, and store after 60 time steps, which corresponds to 0.1284 s or a flight distance of 24 m. Aerodynamic interference is clearly noticeable in the wing wake, downstream along the location of the pylon; without a pylon the wing wake would be a smooth sheet across the span. The effects of this interference on the wing lift are, in this steady–state simulation, small, however. The model retains all wake elements of the past 40 time steps in the sense of a first–in–last–out buffer. In other words,

once every time step vorticities enter the wake from the trailing edge of the wing and stepwise shift through the wake for a total of 40 time steps. After that time, they have traveled a distance of about twice the average chord length and their influence on the airplane becomes negligible.
In light of the non–dynamic character of the current analysis, this is not unexpected. Interference is presumed to effect the wing lift, if it occurs within one chord length of distance to the trailing of the wing. In a dynamic environment, the motion of the wing, store, and pylon is almost certain to induce larger interferences which, in return, will have a more pronounced effect on the lift of the wing.

3 Conclusion

We have demonstrated a new aeroelastic modeling technique that consists of two independent building blocks: ABAQUS and UVLM. Results from the static analysis are in good agreement with experimental wind tunnel data and make the pursue of this method desirable. The method possesses the versatility of modeling non–linear structural and aerodynamic effects and offers a unique tool to examine fluid–structure interactions in the time domain. By employing the unsteady–vortex–lattice method it is possible to include wake induced effects in the aeroelastic analysis and account for aerodynamic interference phenomena. Already, steady–state simulations reveal the onset of aerodynamic interference, even though it is not significant as far as lift reduction is concerned. This is expected to change with the introduction of a dynamic solution process.

References

[1] P. Gade and G. Flowers, 1994, AIAA 94-1746, *AIAA/ASME Adaptive Structures Forum*, Hilton Head, South Carolina, "Flutter Suppression of an Airfoil with Unsteady Forces Using a Piezoelectric Active Strut"

[2] P. Gade and D. J. Inman, 1998, *Dissertation at Virginia Polytechnic Institute and State University*, "Performance enhancement and stability robustness of wing/store flutter suppression system"

[3] F. W. Cazier and M. W. Kehoe, 1986, AIAA-86-9730, *AIAA/AHS/CASI/DGLR/ IES/ISA/ITEA/SETP/SFTE 3rd Flight Testing Conference*, Las Vegas, Nevada, "Flight Test of a Decoupler Pylon for Wing/Store Flutter Suppression"

[4] A. Cenko, E. Tinoco, 1994, *AIAA 22nd Aerospace Science Meeting Proceedings*, "PanAir Applications to Mutual Interference Effects due to close Proximity"

[5] A. Cenko, 1983, *AIAA 21st Aerospace Science Meeting Proceedings*, "PanAir Applications to Complex Configurations"

[6] S. Preidikman, D. T. Mook 1997, *Journal of Wind Engineering*, Vol. **69**–71, pp. 955–974, "A new Method for Actively Suppressing Flutter of Suspension Bridges"

[7] D. T. Mook, A. H. Nayfeh, 1990, *Computing Systems in Engineering*, Vol. **1**, Nos 2–4, pp. 461–482, "Numerical Simulations of Dynamic/Aerodynamic Interactions"

[8] C. R. Kayakayoglu, 1993, *NASA Technical Report* N97–71841, "Unsteady Subsonic Aerodynamics for Maneuvering Wing/Fuselage/Pylon/Store Configurations and Store Separation Including Wake Effects"

[9] J. D. Clayton, R. L. Hailer, J. M. Hassler Jr. , 1985, *NASA Contractor Report* 172354, "Design and Fabrication of the NASA Decoupler Pylon for the F16 Aircraft"

[10] W. E. Triplett, 1984 *Journal of Aircraft*, Vol.21(**5**), pp. 329–334, "Wind Tunnel Correlation Study of Aerodynamic Modeling for F/A-18 Wing-Store/Missile Flutter"

[11] E. H. Dowell, *AIAA-90-1031-CP*, 1990, "Nonlinear Aeroelasticity"

[12] O. Özkan, M. F. Ünal, A. R. Aslan, Y. Bozkurt, and N. H. Aydin, *Journal of Aircraft*, Vol.32 (**1**), pp. 161–170, "Aerodynamic Characteristics of External Store Configurations at Low Speeds"

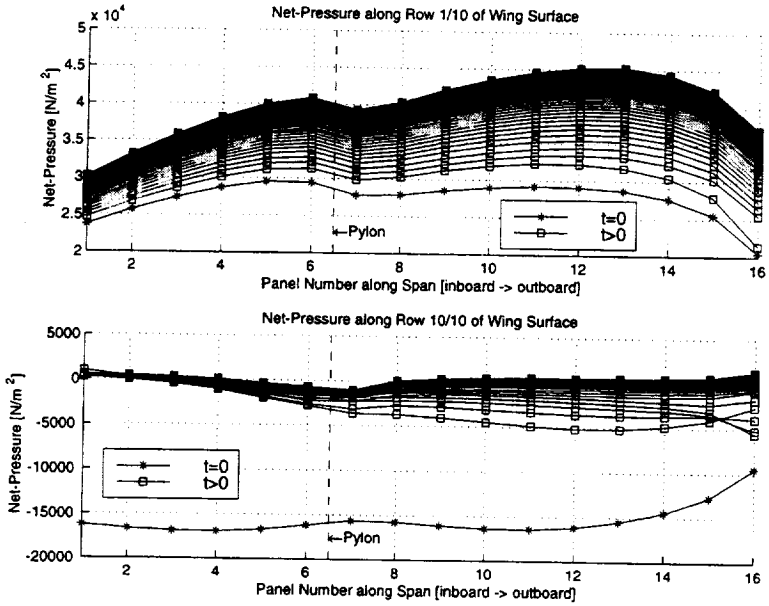

Figure 1: Pressure Distribution over Wing

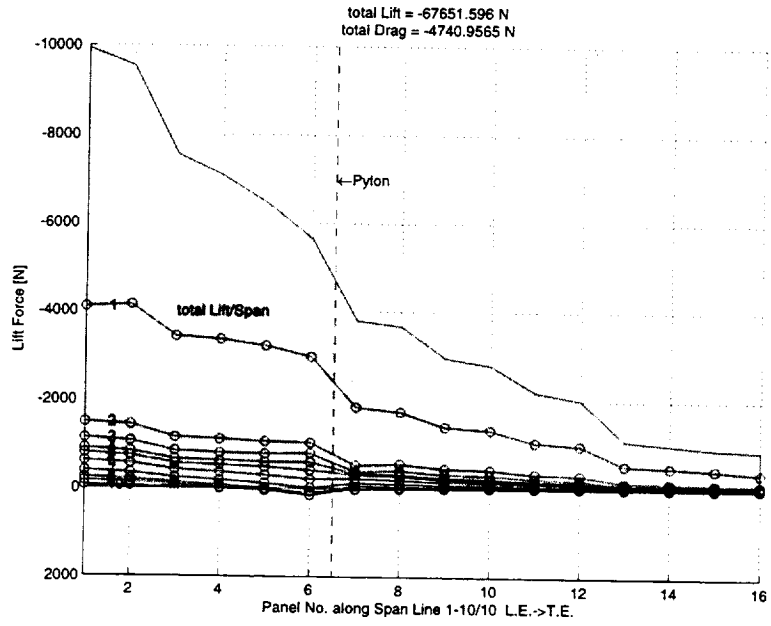

Figure 2: Total Lift Force on Wing

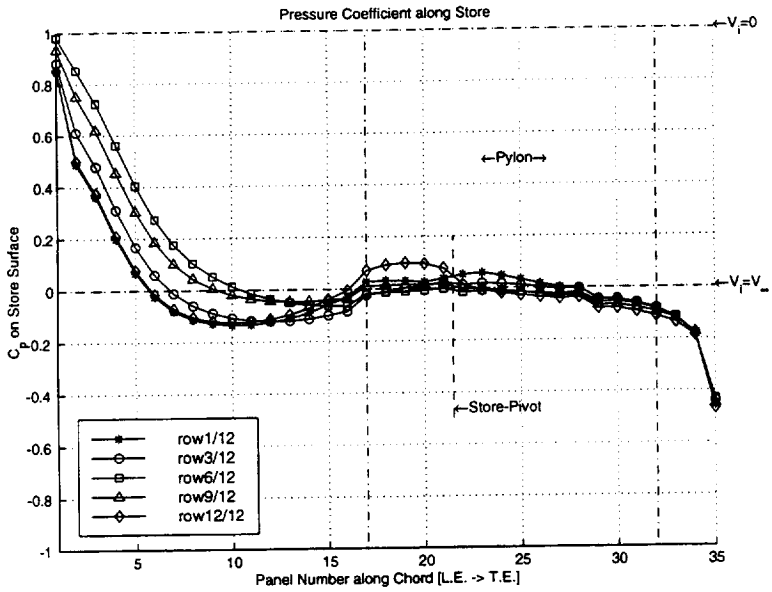

Figure 3: Pressure Coefficient on Store

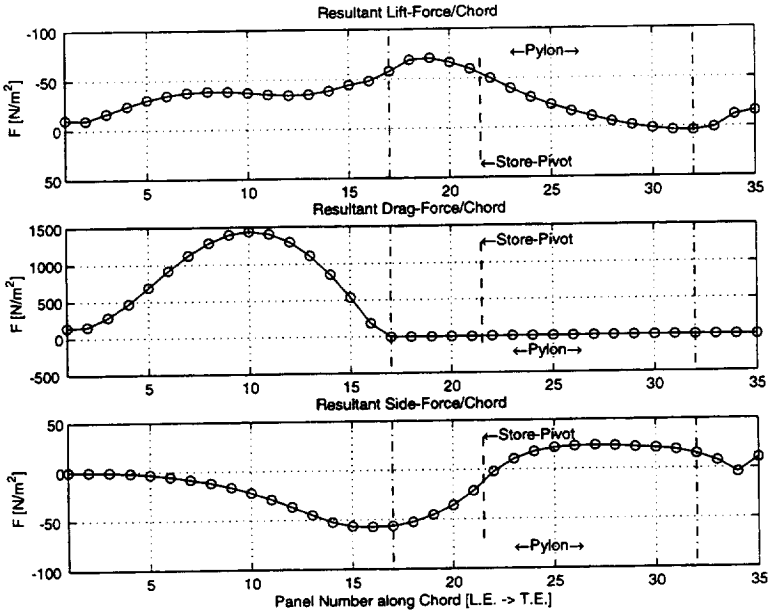

Figure 4: Resultant Forces/Chord on Store

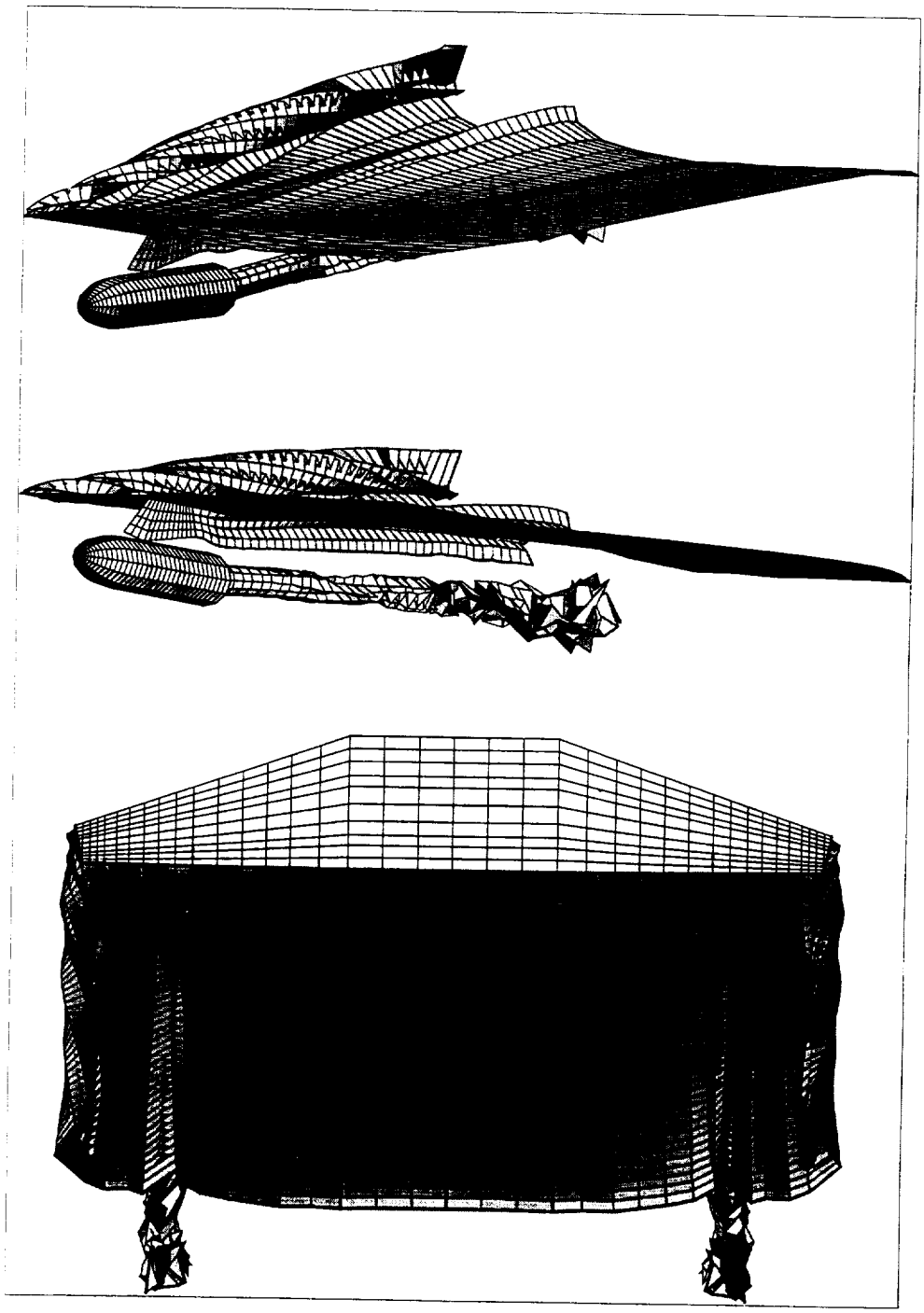

Figure 5: Wake Shedding of Wing/Pylon/Store Configuration

A Appendix

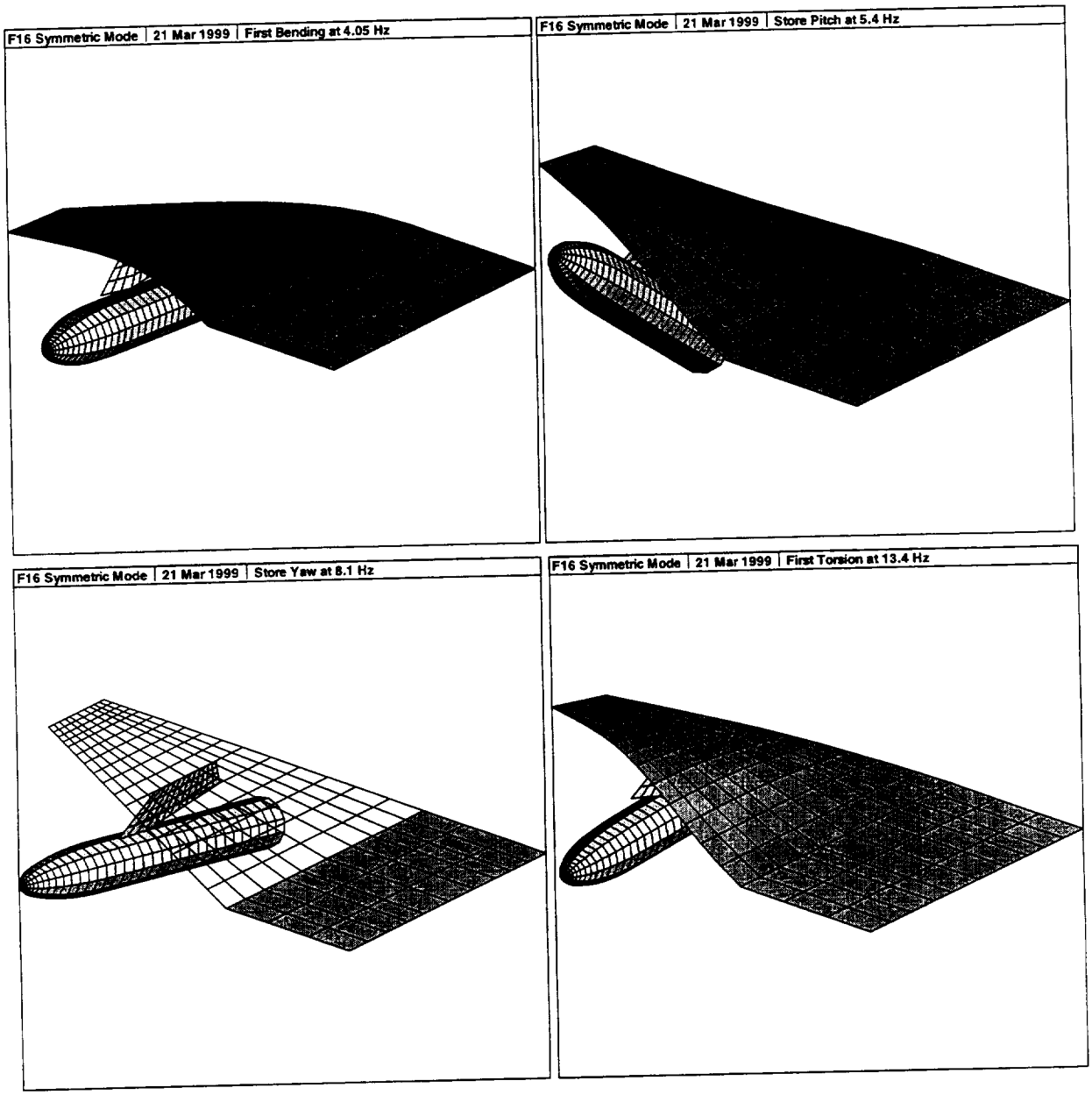

Figure A.1: Symmetric Modes of Wing/Store/Pylon Configuration

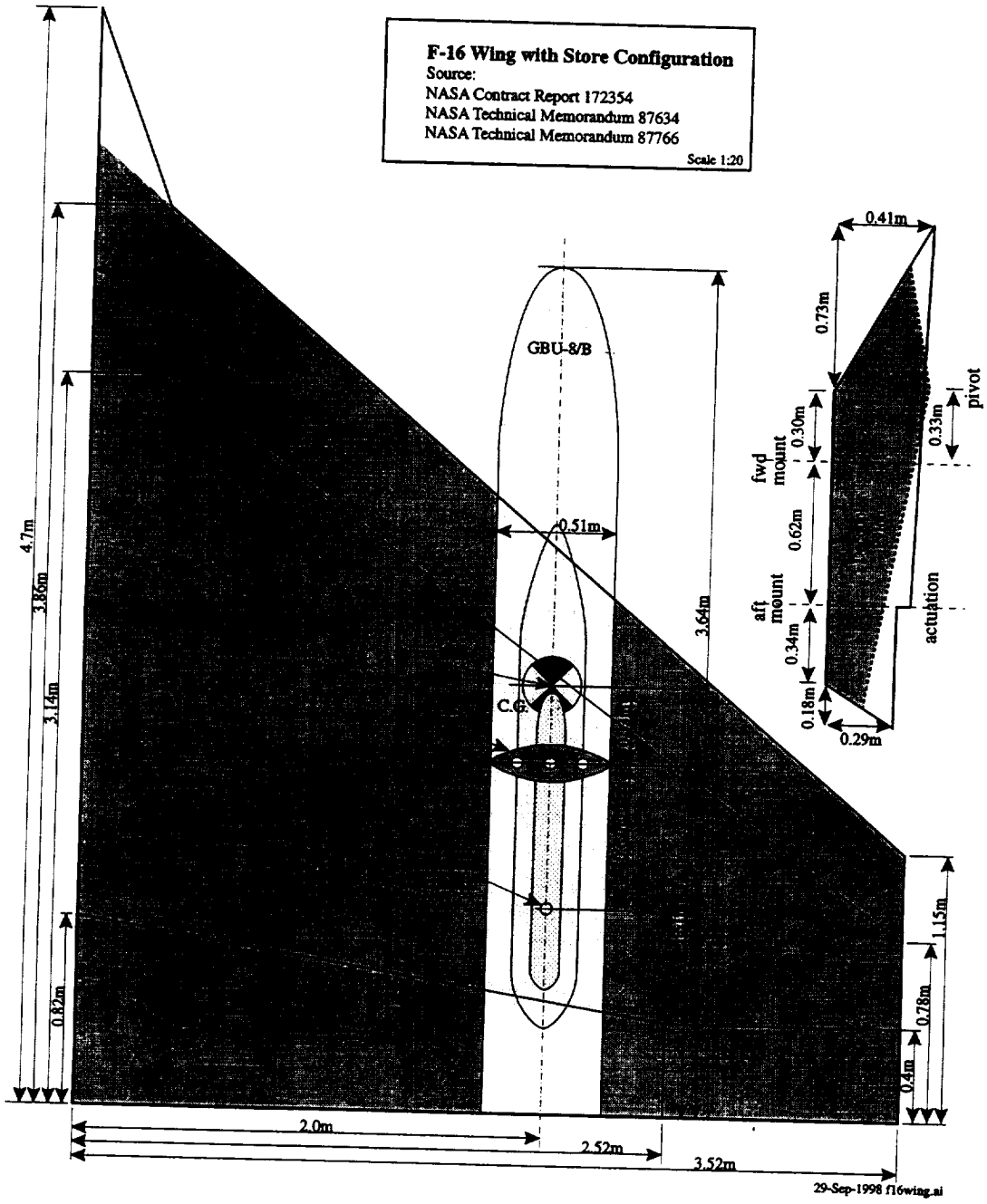

Figure A.2: Structural Schematic of Wing/Store Configuration. The shaded pylon and wing area depicts the shape used for the model representation.

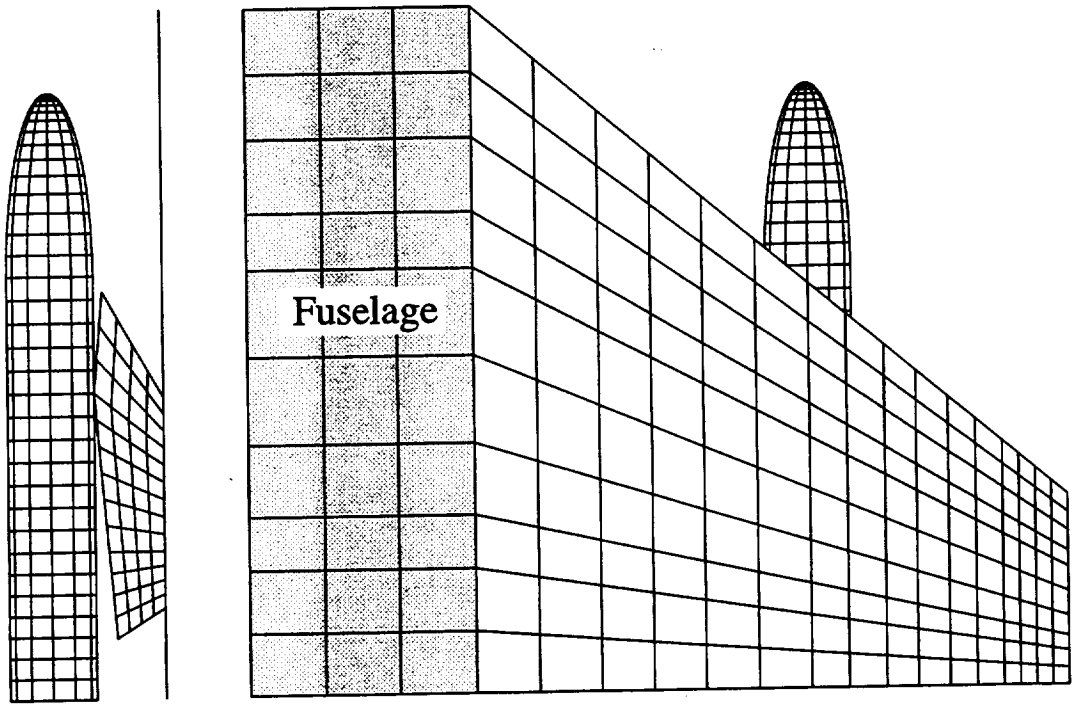

Figure A.3: Structural and Aerodynamic Mesh: 632 Panels, 748 Nodes.

FLUTTER STABILITY OF MOVABLE CONTROL SURFACES FOR AIRCRAFT STORES

Claudio Ponzi *
Alenia Marconi Systems - Missile Systems Division
Via Tiburtina km.12, 400 I-00131 Roma

Johannes Schweiger **
DaimlerChrysler Aerospace AG, Military Aircraft MT24,
P.O. Box 801160, D-81663, Muenchen, Germany

ABSTRACT

Flutter stability of movable control surfaces for aircraft stores is a rather complex topic because a large variety of different store system conditions, aircraft configurations, store to aircraft functional conditions, aircraft maneuver and environmental conditions have to be covered by analysis as well as by ground and flight tests. For this purpose, the most critical or most sensitive flutter parameters of the stores must be known and covered by analysis and tests. For stores with only fixed aerodynamic stabilizers, the verification of their flutter stability is usually quite simple because these surfaces are small and stiff. For them, it is usually sufficient to include only their mass properties and attachment stiffnesses in the aircraft flutter analysis, where the store is considered only by its rigid body motions Only in some cases it is required to include also effects from rigid aerodynamic surfaces on the store. But as soon as a surface is used to provide control forces, it usually needs to be larger and thus gets also more flexible. Additional flexibility is added by the drive system, and, in some cases by a free floating attachment mode for captive flight conditions. Detailed flutter investigations for the store itself are usually performed by the store manufacturer. On this side however, possible impacts from the different types of aircraft are not known and could also not be covered in their multitude during the development of a new store. For example, the aerodynamic flow field in the vicinity of the aircraft, especially under the fuselage, can be completely different from free flight conditions. This paper explains how to handle these aspects and depicts major advantages and drawbacks of the state of the art analysis and testing techniques. The different specifications for the development and certifications of aircraft and stores are also addressed briefly. Finally an approach will be described how the flutter stability of control surfaces can be enhanced by means of formal mathematical optimization methods.

Keywords: store flutter, aeroelasticity, store-aircraft integration, unsteady aerodynamics, structural optimization, flutter flight test, all-movable surface.

1.INTRODUCTION

In 1955, Holt Ashley gave in ref.[1] the definition of flutter as „a dynamic instability occurring in an aircraft in flight, at a speed called the flutter speed, where the elasticity of the structure plays an essential part in the instability„. This definition obviously also applies to any other kind of flying objects. Aircraft stores with movable control surfaces include air-to-air and air-to-surface missiles, guided bombs, or other stand-off weapons, with or without an own propulsion system. Depending on the specific kind of their mission,

* HARM PNU International Precision Navigation Upgrade Project Leader
e-mail: cponzi@aleniasystems.finmeccanica.it
** Head of Structural Dynamics and Aeroelasticity
e-mail: johannes.schweiger@m.dasa.de

different approaches are used for their design and qualification. Some stores are designed for a one time use only, others are carried almost constantly on the aircraft during training missions, which means that they have to be certified for several hundred flying hours. For captive flight conditions, some of them meet the aircraft flutter stability requirements quite easily because they are much faster in free flight than the airplane, but for others the captive flight is more critical for flutter.

On some stores, the control surfaces must only be capable to guide the store to an unmoving target, on others they must maximize aerodynamic forces and moments for fast, high-g maneuvers. For instance, the Aspide multirole missile developed by Selenia, represented in Fig.1 mounted under the F-104ASA, is characterized by rear body fixed wings and all movable center body wings.

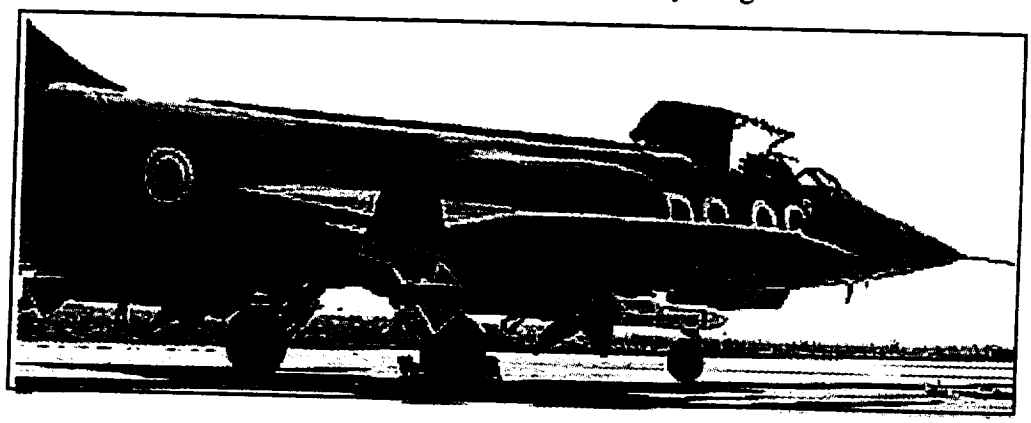

Fig.1: Aspide missile mounted on F-104 ASA.

2.FLUTTER OF ALL-MOVABLE SURFACES

2.1. Global Flutter Sensitivity of All-movable Surfaces

Some aircraft also use all-movable surfaces like fore- and tailplanes, sometimes also integrating symmetric and antisymmetric control functions like in a taileron for pitch and roll. Because these configurations are all very sensitive for flutter, they are treated in the applicable specifications for flutter separately from other control surfaces which are attached to fixed surfaces. Their criticality is also known from ground launched rockets as reported in ref.[2]. The reason for this is the spigot axis, an intrinsic, limited structural boundary, which determines the major part of the overall flexibility. Ref.[3] describes these characteristics for the foreplane of a fighter aircraft. Although specifications for the structural integrity of airplanes and stores are quite different, one thus recognizes that the aircraft and the missile communities share the same problems with respect to flutter.

General design requirements for the structural integrity for guided missiles are treated in ref.[4], depicting key parameters for flutter sensitivity in chapter 3.8: „Aeroelastic Stability„, which thoroughly treats aeroelastic stability margins, aeroservoelastic stability, all movable control surface features, mass balance, rigidity of balance weight attachment, design loads for balance weight attachments, rigidity and frequency of control surfaces, freeplay, and hydraulic dampers.

2.2. Avoidance of Flutter during Store Separation

In addition to the general design rules mentioned above, in order to prevent flutter occurrence, the spigot axis of most stores is restrained by a lock on the drive during captive flight. In the case of the Aspide missile, this lock is deactivated by sufficient hydraulic pressure in the actuator circuit. The mechanical drawing for this system is shown in Fig.2.

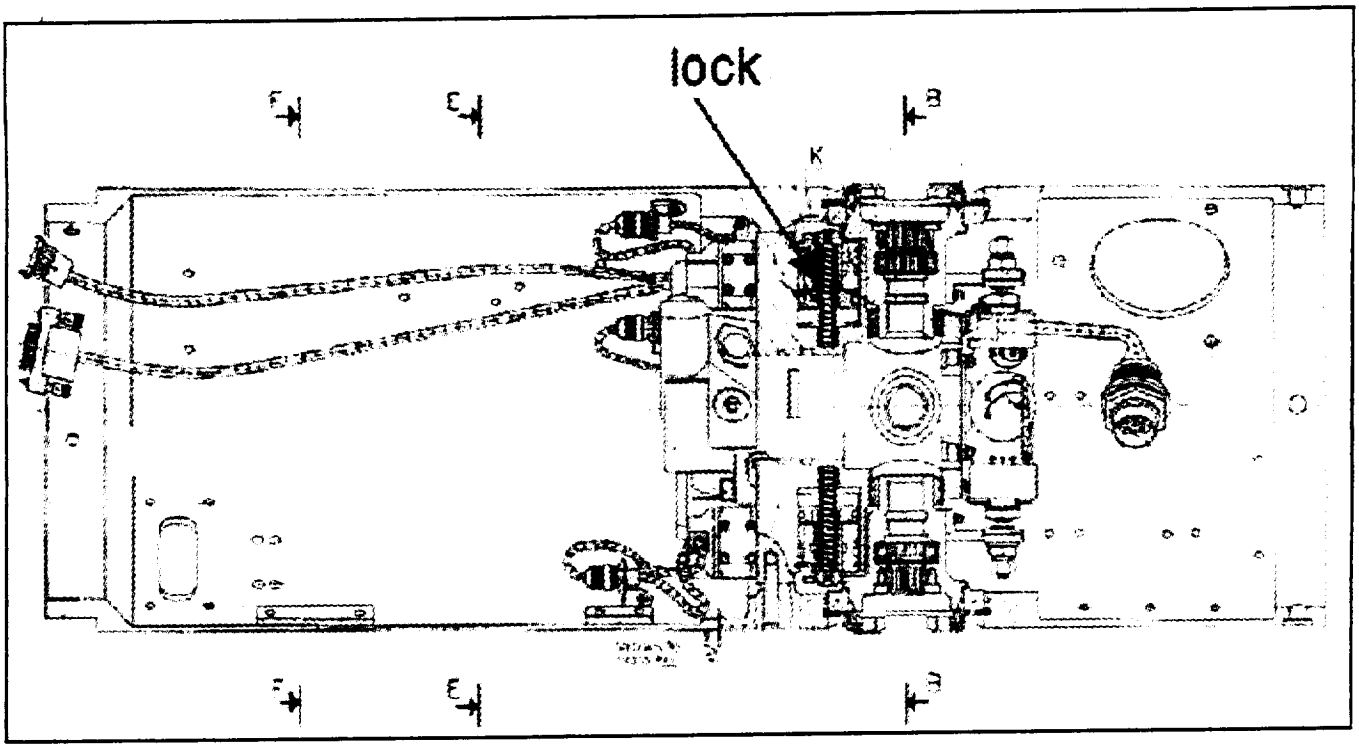

Fig2: Fin lock mechanism in Aspide actuation system.

2.3. Avoidance of Flutter during Captive Flight

In addition to the rules for meeting store separation flutter free conditions, two philosophies can be adopted. As for in the Aspide missile, the fins are locked to enhance the stability. Depending on the flight condition of the aircraft, however, such a mechanical constraint may cause high static loads on the control surfaces which lead to unfavorable effects on the overall store structure too. A free-floating control surface, which represents the second solution, can dispel the static loads but may also be unruly with respect to flutter. If it is possible or not to design a stable free-floating control surface, this strongly depends on the flow conditions with respect to Mach number and turbulence, as well as on missile systems design issues. The later solution was adopted on the HARM missile, developed by Texas Instruments Incorporated.

2.4. Provisions for Zero Freeplay

Because of store body and fin flexibilities, freeplay of the control surface attachment can be the major source for flutter for both captive and free flight. It can be assimilated to a mathematical perturbation in angle of attack which may help the instability develop. In the Aspide missile, wing axis rotation is activated by a differential hydraulic pressure torque as shown in Fig.3 which ensures zero freeplay.

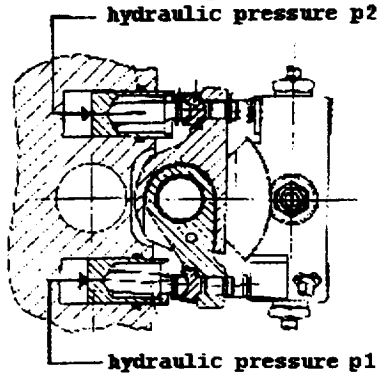

Fig.3: Differential hydraulic pressure system for Aspide missile.

Experience has shown that the common practice for removing freeplay encountered during flutter flight tests consists in modifying either hardware or software design. Hardware modifications are more expensive at a late stage of design, whereas software modifications are less expensive but have the pitfall of reducing the missile flight envelope.

3.GENERAL DIFFERENCES FOR FLUTTER OF AIRCRAFT AND MISSILES

Airplanes are in general designed for a long life time with many take-offs and soft landings. Missiles or other aircraft stores on the other hand are sometimes designed for a one time use only. Nevertheless, they must meet the safety standards of the airplane during captive flight and store separation.

Major differences with respect to specifications and mutual interference effects are represented in Table 1. Some comments arise from this table which are addressed below.

ITEM	AIRCRAFT	STORE
General Specification for the Structure	MIL-A-8860	MIL-M-8856B
Specification for Strength and Rigidity, Vibration, Flutter, Divergence	MIL-A-8870	No specific specification
General Design Criteria for Airborne Stores, Suspension Equipment and Aircraft-Store Interface (Carriage Phase)	MIL-A-8591H	MIL-A-8591H
Specification for Certification	MIL-A-8868 (Strength and Rigidity. Data and Reports) MIL-STD-1763	MIL-STD-1763 (Aircraft/Store Certification)
Vibration Environment	Maneuvers, gusts, buffet, engine noise, gunfiring, landing impacts	Same nature as for aircraft but generally lower levels
Aerodynamic Environment	Perturbed by store	Dispersion: strongly perturbed by aircraft

Table 1: Flutter Design „Environment„ Differences for Aircraft and Stores

3.1. Specifications

General specifications for the structure of aircraft and missiles are MIL-A-8860[4] and MIL-A-8856B[5]. The latter also encompasses aeroelastic stability criteria which are specified for aircraft in a dedicated document MIL-A-8870[6]. For the captive carriage flight phase, interface design criteria have been developed, such as MIL-A-8591H[7],which in chapter 3.12 „Flutter and divergence„ mentions indeed both MIL-A-8860 and MIL-A-8856B. As far as certification is concerned, the aircraft side is covered by MIL-A-8868[8], whereas MIL-STD-1763A[9] covers the case of the integrated weapon.

3.2.Vibration Environment

The dynamic environment for the store in captive conditions is generally far worse than in free flight. Stores are designed to stand captive carriage life in terms of vibration levels and frequencies referred to prescribed flying times (refs.[10,11]). Table 1 lists the sources of vibration in captive carriage which contribute to limiting service life and building up fatigue levels. It should be mentioned here that the vibration environment is also important for flutter because of its impacts on freeplay.

3.3. Aerodynamic Environment

The aerodynamic flow field for the free flying store undergoes heavy modifications when the store is in captive conditions under the wing or fuselage, during separation, and in the vicinity of other stores, altering from type to type of all parent aircraft to be considered. Such secondary flows, which also include contributions from the change of aircraft configuration in flight (landing gear out, wing trailing edge down) affect the loads onto the missile.

4. AIRCRAFT / STORE INTEGRATION RULES FOR FLUTTER CLEARANCE

4.1. General Requirements for Aircraft / Store Integration

A general statement of work which describes the activities for correctly integrating a store onto an aircraft (however specialized to the case of the Aspide) is described in ref.[12]. It consists of three phases represented in Fig.4.

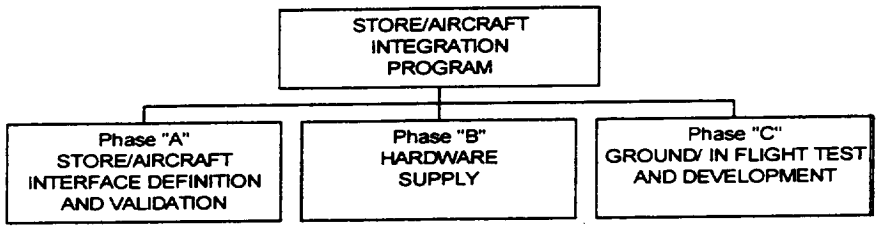

Fig.4: Integration Program Breakdown Structure

4.2. Requirements for Aircraft / Store Structural Integration

For aircraft/ store design, ref.[4] states in chapter 3.11 „Missile and launch platform compatibility„ that „the required analyses, tests, and documentation shall be consistent with the missile and launch platform(s) interface and may include, but are not limited to the following areas:

- structural captive flight loads
- missile launch dynamic response loads
- missile dynamic response loads due to separation of an adjacent store
- stress and fatigue
- aircraft/missile aeroelastic stability
- field landing, taxiing, and take-off tests
- aircraft/ missile ground vibration modal tests
- aircraft vibration and aeroacoustic environments
- catapult and arrested landing tests
- aircraft/missile ground vibration modal tests
- aircraft/missile flight flutter tests
- aircraft/missile flight loads tests.

For the airborne carried missile, the requirements of MIL-A-8591 shall be met and the aircraft/stores certification procedures of MIL-STD-1763 shall be followed„. Therefore, refs.[4, 7, 9] contain all requirements to cover the store point of view.

4.3. Requirements for Aircraft / Store Flutter Clearance

Requirements for flutter free store configurations are listed in table 2. They can be split into two groups:

- those general requirements that are specific for stores in free flight conditions,
- those additional requirements that are specific for the aircraft-store integration.

ITEM	REFERENCE
Aeroelastic Stability	MIL-M-8856B para 3.8
Structural Dynamics Tests (incl. flutter model wind tunnel test)	MIL-M-8856B para 30.7 of Appendix A (Laboratory and Ground Tests)
Aeroelastic Stability Flight Tests	MIL-M-8856B para 30.2.3 of Appendix B (Operational Tests)
Aeroelastic Stability Program Report	MIL-M-8856B para 30.4.3 of Appendix C (Analyses, Data and Reports)
Aeroelastic Stability Analysis Report	MIL-M-8856B para 30.6 of Appendix C
Flutter Model Wind Tunnel Test Report	MIL-M-8856B para 30.8.2 of Appendix C
Aeroelastic Stability, Vibration and Aeroacoustic Flight Test Planning Report	MIL-M-8856B para 30.11.1 of Appendix C
Aeroelastic Stability Flight Test Letter Reports	MIL-M-8856B para 30.11.5.1 of Appendix C
Aeroelastic Instability, Vibration or Sonic Fatigue Occurrence Report	MIL-M-8856B para 30.11.5.3 of Appendix C
Flutter and Divergence for Carriage Phase	MIL-A-8591 para 3.12 mentions both MIL-M-8856B and MIL-A-8870
Flutter Analysis	MIL-STD-1763 para 5.1.4.4.3.1
Aeroelastic Effect Tests	MIL-STD-1763 TEST 143 of Appendix I (Ground Test Procedures)
Flutter Test	MIL-STD-1763 TEST 210A of Appendix II (Flight Test Procedures)

Table 2: Flutter Requirements for Stores

From the aircraft point of view, flutter certification and qualification of combat aircraft is extensively described in ref.[13], which naturally mentions all of the items treated in table 2. Because the physics involved in aircraft and store flutter is the same, the aircraft and missile communities are recommended to closely cooperate, even with the risk of performing redundant activities, in order to optimize the complete weapon system.

5. GEOMETRIC AND STRUCTURAL FLUTTER SENSITIVITY PARAMETERS

Besides the stiffness properties of the spigot and its drive and lock mechanisms, the freeplay of all-movable surfaces must be kept within very tight tolerances. Ref.[3] describes the main geometric and structural flutter sensitivity parameters for an all-movable fighter aircraft foreplane. Because of the similarities, these results can also be applied to typical store control surfaces. The most important parameters are:

- overall planform, leading edge sweep angle, airfoil shape and thickness, which determine the basic unsteady aerodynamic characteristics,
- spigot axis sweep angle, which usually gives the highest flutter speed near 30 degrees,
- distances between spigot axis, center of gravity, and aerodynamic center,
- frequencies of fin attachment pitch and roll eigenmodes, and frequency separation between them

- frequency increase of pitch mode with airspeed, which largely depends on the mass moment of inertia about the pitch axis and on the amount of static mass unbalance,
- stiffness and eigenmodes of the fin itself.

For the last item, the designer is limited in the design space, because the static design of a missile fin usually requires already a single piece casted or machined part from high strength/high modulus metal.

6. FLUTTER ANALYSIS

The basis of flutter analysis is formed by a proper structural analysis model. Today, Finite Element Methods (FEM) are used almost exclusively for this purpose. These models must be suitable to describe the structural dynamic characteristics of the complete system with high accuracy, because the quality of the obtained unsteady aerodynamic forces directly depend on them.

For the external forces, which are produced by the vibrating structure, linear potential flow methods are common practice to calculate aircraft and store aerodynamics, including interference effects between them. The most used ingredients are potential flow approximations associated to finite element methods such as the Doublet Lattice or Mach Box methods (refs.[13, 14, 15, 16, 17, 18]). Linear transonic effects are treated with the „Transonic Small Perturbation Theory„ (ref.[13]) which is a linearized approximation of the non-linear potential equations. For high supersonic Mach numbers, the Piston Theory[19,20] gives good linear approximations.

These tools are usually sufficient for the prediction of the general flutter stability of a free flying object, but unfortunately not for a store in turbulent flow conditions under an aircraft fuselage, and in the vicinity of other stores.

One of the concerns the flutter engineer deals with is predicting how structural and aerodynamic non-linearities affect the real behavior of the structure. Typical phenomena include the onset of stable limit cycle oscillations beyond the linear flutter boundary or the existence of unstable limit cycles within the linear flutter boundary. Ref.[21] describes neutrally stable limit cycles oscillations due to aerodynamic non linearities whereas refs.[14, 15, 19, 20, 22, 23] call for structural non linearities. Analytical methods for predicting non linear flutter boundaries are time domain techniques (refs.[14, 20, 21, 23]), or, when structural linearization is performed (for instance, using the harmonic balance method of refs.[15, 22] , or the iterative procedure of ref.[18]), frequency domain techniques apply.

Referring to structural non-linearities, the flutter speed ratio (ratio of non linear flutter speed to linear flutter speed) depends on the so-called amplitude parameter (amount of freeplay divided by the amplitude of the limit cycle). Thus one realizes that prescriptions on maximum freeplay represent an attempt of limiting flutter onset. Structural non-linearities such as friction, freeplays, softening and hardening stiffnesses are addressed in refs.[14, 15, 22, 23, 24] which depict and discuss mathematical models for formulating these effects and show their influence on flutter predictions. Aerodynamic non-linearities are discussed in ref.[21] which proposes a direct CFD direct solving of the Euler (inviscid) equations to account for high incidence angles. Ref.[16] includes non linear augmentations due to fin leading and side edge flow separation. Ref.[25] discusses in Chapter VI unsteady transonic aerodynamics and aeroelasticity. Ref.[26] suggests to maintain a linear formulation relating pressure coefficients and angles of attack but accounts for local non-linear effect matching.

7. FLIGHT FLUTTER TESTING

The aim of any flight flutter test is, according to ref.[13], to establish measured structural frequency and damping trends in the critical flutter modes for the key configurations, to match to these measurements and

thus establish the basis for a flight envelope expansion to the maximum envelope. Because of the complex flow conditions for a store in the vicinity of an aircraft, flight flutter tests are still the only fully reliable method to verify stability of the weapon system. But unfortunately they can only describe the conditions at the time of the test: issues like increasing freeplay can only be covered by inspection procedures.

In order to define the proper flight test instrumentation, the flutter characteristics of the store and the aircraft must be known, and possible interference effects between them must carefully be evaluated.

As a successful example of a flutter cleared weapon, Fig.5 represents three different F-104ASA-store configurations, including the Aspide missile. The figure also depicts typical flight test points and the cleared flight envelopes for the three configurations.

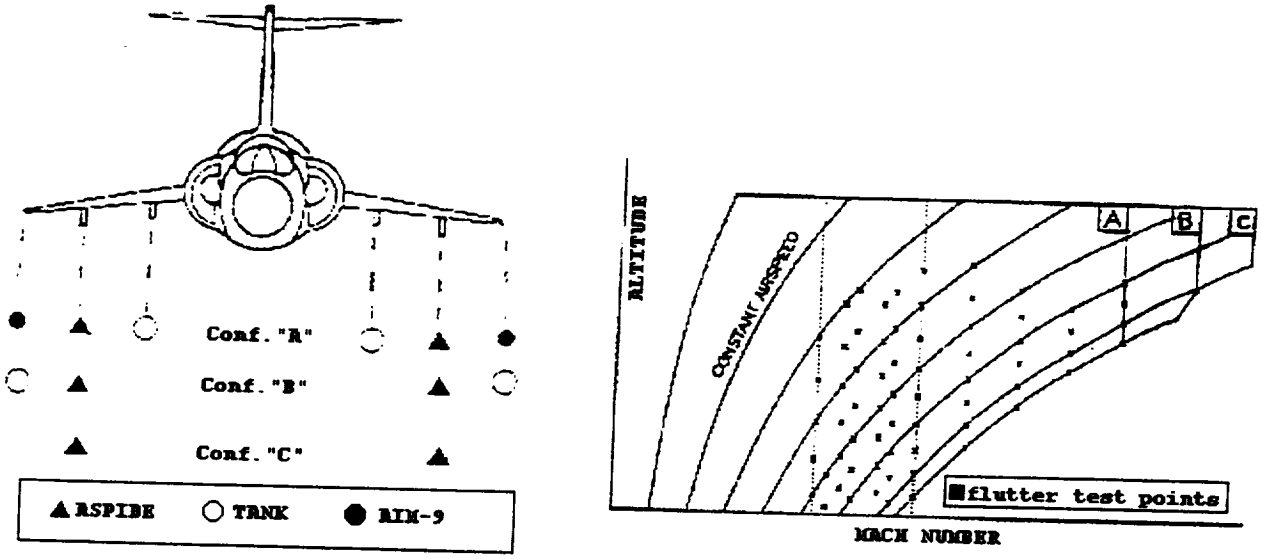

Fig.5: Key configurations, typical flight test points, and flutter flight envelope for F-104ASA.

8. FLUTTER ANALYSIS AND OPTIMIZATION OF A TYPICAL CONTROL FIN

In aircraft design it has become common practice to use formal mathematical optimization methods for structural design. These tools will not only provide the lightest possible structure automatically. It is even more valuable that these designs will at the same time also fulfill all static, structural dynamic, and aeroelastic constraints. For a sound structure with respect to static loading conditions, it is a not too difficult task for an experienced engineer to find a design which meets all requirements with respect to allowable material properties, especially, if a reliable analysis model (FEM) is available. This process can easily be turned into an optimization process, assuming that the lightest possible structure is the one where each element is sized to the minimum for at least one loading condition. This kind of optimization process is based on so-called optimality criteria, which are only indirectly substituting the real objective. For aeroelastic constraints however, it is usually much more difficult to find a design that meets the requirements at a still tolerable weight. It is almost impossible even for very experienced engineers to predict, how a design must be changed in order to meet aeroelastic requirements. Only extensive parametric studies will do this job fairly well. In the case of flutter, there are also no simple optimality criteria at hand to do this job. And even if there were any, it would not be possible to combine them with other ones like for static strength because the criteria will not be the same.

In the case of flutter, usually only direct mathematical formulations of the problem will help. This means that gradients for the stiffness and mass of all members of the structure are required with respect to the

flutter speed. In addition to the structural stiffness distribution, concentrated balance masses at dedicated positions within or even outside of the structure should be considered to obtain the best possible design with respect to minimum weight.

To demonstrate the effectiveness of these tools, the Dasa multidisciplinary optimization program LAGRANGE[27,28,29,30] was applied to the FEM model in Fig. 6 for a typical all-movable control surface of an aircraft store. It consists of plate elements, assuming that their thickness is already meeting minimum allowable margins with respect to limit strength and fatigue from vibrations. For simplicity, only one point on the beam extending forward along the fin root was considered for the location of a variable balance mass. All other sensitive design parameters, as described above, are fixed in this example. In this case, the flutter speed can be increased as depicted in Fig. 7.

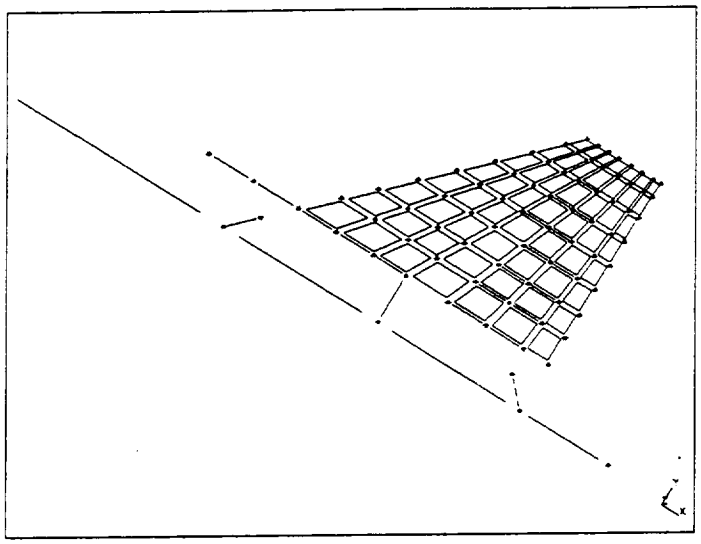

Fig. 6: Finite Element model for a typical missile fin.

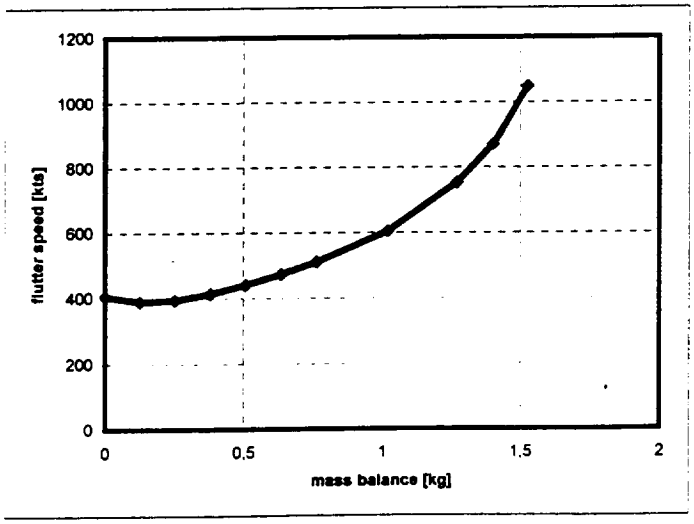

Fig. 7: Optimization results with balance mass attached on a fin root extension.

If balance masses are attached directly to the main surface, a surprise like in Fig. 8 from ref.[31] can show up: an increase in balance mass in the most favorable position will first lower the flutter speed before an improvement starts. The reason for this is that the mass not only separates the involved flutter modes but

also changes the involved mode shapes. This may have been the reason, why the flutter optimization attempts by balance masses reported in ref.[3] for a foreplane were unsuccessful.

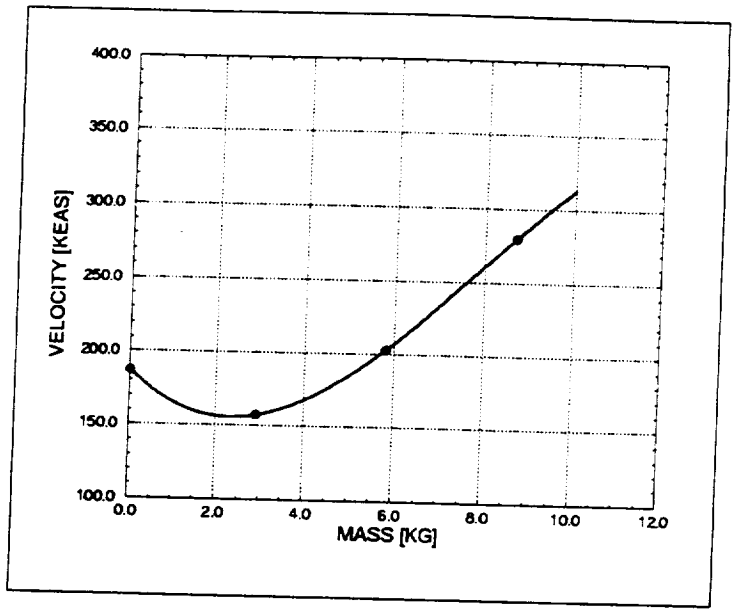

Fig. 8: Effectiveness of a balance mass in the leading edge of an aircraft wing from ref.[31].

In general, mass balance is more effective on freely movable surfaces, whereas additional stiffness helps better on fixed surfaces.

9. CONCLUSIONS

Efforts are needed in flutter analysis for filling the gap between prediction and testing results. This can be achieved in two steps. Firstly, more work is needed for gaining full confidence in structural and aerodynamic tools, and improving unsteady aerodynamic methods for the complex flow conditions of a store under an aircraft. The application of existing procedures for verification and certification represents the second step since they recommend to strictly cover all aircraft-store combinations by means of analysis, testing and correlation of results.

For the integration of a new store, it is very important that the flutter mechanisms of the store itself be fully known to the aircraft flutter engineer in order to set up a correct analysis model and to define the proper ground and flight tests, including the suitable instrumentation. For the development or modification of the store itself, the store manufacturer needs to know the possible impacts from the aircraft and the store attachment system onto the flutter stability of the store and the complete weapon system.

Aeroservoelastic aspects are often the major potential instability of a missile, as reported in ref.[32]. But these were not addressed in this paper, because they are not the primary concern for the integration of an aircraft store.

Modern structural optimization methods are offering efficient approaches for the enhancement of the flutter stability of any flying system.

Although all aspects of the flutter stability of stores, aircraft, and the combined system are covered by the applicable specifications, it may be desirable for the future to formalize a closer cooperation between store and aircraft manufacturer and the contracting agency for the verification of flutter stability for the complete weapon systems.

REFERENCES

1. Bisplinghoff R. L., Ashley H., and Halfman R. L.: "Aeroelasticity". Addison-Wesley Publishing Company, Inc., 1955.
2. Lee B. H. K., Plosenski M. J., Barrington, P. E., Markow, A. B., and Coffey, C. G. :"Aeroelastic Testing of an Unmanned Air Vehicle". AGARD-CP-566, 1995.
3. Schweiger, J. Sensburg O., and Ponzi, C. :"Aeroelastic Tailoring for Flutter Constraints". Proceedings of the ICAS Conference 86-4.7.1, London U.K., 1986.
4. MIL-A-8860:"Airplane Strength and Rigidity, General Specification for".
5. MIL-M-8856B "Missiles, Guided, Structural Integrity General Specification for", 22 July 1991
6. MIL-A-8870 "Airplane Strength and Rigidity, Vibration, Flutter and Divergence".
7. MIL-A-8591H "Airborne Stores, Suspension Equipment and Aircraft-Store Interface (Carriage Phase); General Design Criteria for", 30 June 1994.
8. MIL-A-8868 "Airplane Strength and Rigidity, Data and Reports".
9. MIL-STD-1763A "Aircraft/Store Certification Procedures", 31 December 1990.
10. AERITALIA Military Aircraft Group "„F104S Aggiornamento Sistema d'Arma - Fase Aggiuntiva di Sviluppo", doc. P.M.F104 - 850712, 29 July 1985.
11. Luber W., and Becker J. "Design and Qualification of Equipment Trays in High Dynamic Environment", CEAS 1995.
12. ALENIA Missile Systems Division :"Aspide - Aircraft Integration Phase C - Alenia Support to Test and Development", Rev.A, 15 November 1995.
13. Ramsay R. B. "Flutter Certification and Qualification of Combat Aircraft", CEAS 1995
14. Sepahy, D. „Aeroelastic Analysis of Missile Control Surfaces with Structural Non-Linearity", AGARD-CP-451, 1988.
15. Luber, W. :"Flutter Prediction on a Combat Aircraft involving Backlash and Actuator Failures on Control Surfaces", Conference Proceedings of the International Forum on Aeroelasticity and Structural Dynamics, Volume 2, Roma, Italy, June 1997.
16. Dillenius M. F. E., Mcintosh S. C. :"Aeroelastic Tailoring Procedure for Controlling Fin Hinge Moments", AGARD-CP-451, 1988.
17. Kuran B., Onen C., and Ozguven H. N. :"Effects of Aeroelasticity on the Stability of Unguided Missiles", Conference Proceedings of the International Forum on Aeroelasticity and Structural Dynamics, Volume 3, Roma, Italy, June 1997.
18. Lee C. L. :"An Iterative Procedure for Nonlinear Flutter Analysis", AIAA Journal Vol.24, No.5, 1986.
19. Kurt Elli, H., and Rodden W. P. :"Aerothermoelastic Analysis of a Typical Missile Fin Subjected to Transient Aerodynamic Heating", CEAS 1995.
20. Lewis A. P. :"A Theoretical Investigation of the Non-Linear Aeroelastic Behaviour of a Missile Control Fin", CEAS 1995.
21. Vahdati M., Kurt-Elli H., and Imregun M. :"Missile Fin Flutter Analysis using an Integrated Aeroelasticity Method", Conference Proceedings of the International Forum on Aeroelasticity and Structural Dynamics, Volume 2, Roma, Italy, June 1997.
22. Breitbach E. :"Effects of Structural Non-Linearities on Aircraft Vibration and Flutter", AGARD-R-665, 1978.
23. ONERA - Direction des Structures: "Course on Aeroelasticity", technical report 72/3064 RY 033 R, March 1993.
24. Bisplinghoff R. L., and Ashley H. :"Principles of Aeroelasticity", Dover Publications, 1962.
25. Dowell, E. H., and Ilgamov, M.:"Studies in Nonlinear Aeroelasticity", Springer Verlag, 1988.
26. Ponzi C. :"Computational Method for Matching Aerodynamic Experimental Data with Theoretical Influence Matrices", Journal of Aircraft, Volume 30, Number 1, January-February 1993.

27. Krammer, J.: Practical Architecture of Design Optimization Software for Aircraft Structures Taking the MBB-LAGRANGE Code as an Example. AGARD-Lecture Series No. 182, 1992.
28. Hörnlein, H.; Simpson, J.: Performance of Integrated Structural Design Tools and Applications. ECCOMAS conference, Paris, 1996.
29. Schweiger, J.; Krammer, J.; Hörnlein, H.: Development and Application of the Integrated Structural Design Tool LAGRANGE. 6th AIAA/NASA/ISSMO Symposium on Multidisciplinary Analysis and Optimization, CP-4169. Seattle, WA., 1996.
30. Schweiger, J.; Krammer, J.; Coetzee, E.: MDO Application for Active Flexible Aircraft Design. 7th AIAA/NASA/ISSMO Symposium on Multidisciplinary Analysis and Optimization, CP-4835. St. Louis, MO, 1998.
31. Schweiger, J.; Weiss, F. ; Dobbs, S. K. : Aeroelastic design and flight test evaluation of the Ranger 2000 training aircraft. The Aeronautical Journal of the Royal Aeronautic Society. October 1996, London, England.
32. Flomenhoft, H. I.: The Revolution in Structural Dynamics. Dynaflo Press, Palm Beach Gardens, Fl.,1997.

STRUCTURAL OPTIMIZATION USING COMPUTATIONAL AERODYNAMICS

Daniella E. Raveh*, Yuval Levy† and Moti Karpel‡
Faculty of Aerospace Engineering
Technion, Israel Institute of Technology, Haifa 32000, Israel

Abstract

A recently developed methodology for aircraft structural design, based on nonlinear airloads, is extended to include a modal-based optimization option, and an optional different computational aerodynamics code for loads analysis. Nonlinear maneuver loads are evaluated by a newly developed computational scheme that efficiently combines fluid dynamics iterations with iterations for elastic shape deformations and trim corrections. An efficient design process is obtained by performing several optimization runs during one maneuver loads analysis, where each optimization is based on the interim non-converged airloads. This method was recently presented with structural optimization based on full-size, discrete-coordinate analyses. To allow the application of the method with large finite-element models and many constraints, the discrete-coordinates optimization is replaced by a modal-based optimization where a set of low-frequency vibration modes of the baseline structure is used to represent the structure throughout the optimization, both for response analysis and for sensitivity analysis. Comparative modal-based and discrete-coordinate design cases are shown to converge to the same optimal design variable values, even though they do not follow the same path. The current study also extends the loads analysis by replacing the flow computation with a newly developed code that handles complex geometries by using the Chimera overset grid method. This method greatly simplifies the process of grid generation and therefore allows for realistic complex configurations to be considered. Moreover, the method avoids the problem of mesh discontinuities due to elastic shape deformations and control surface deflections, as the displacements of each component only affect the component's mesh. The method is demonstrated with a wing-fuselage-elevator transport aircraft model performing symmetric and antisymmetric maneuvers at Mach 0.85.

Introduction

A main issue in structural design optimization is the validity of the disciplinary analyses used, especially the structural analysis and the fluid dynamics analysis. Evidence of this can be found in structural design studies based on very detailed finite element models.[1] In contrast, aerodynamic tools of automated structural design systems (*e.g.* NASTRAN[2] and ASTROS[3]) are usually based on the relatively simple linear potential flow models (*e.g.* the Doublet-Lattice Method[4]). While linear aerodynamics provides a good approximation of the aerodynamic loads in the subsonic flow regime, it may be inadequate for the transonic regime where shock waves significantly affect the flow field. In the more advanced stages of structural design, the linear aerodynamic loads are normally replaced with more accurate maneuver loads, calculated from databases of loads from wind tunnel testing or from Computational Fluid Dynamics (CFD) analyses (*e.g.* Love[5]). These databases reflect the airloads acting on the rigid configuration, and thus have to be corrected to account for structural elasticity. The resulting design process is therefore non-automatic. The purpose of the current study is to integrate CFD-based maneuver loads into a structural design optimization scheme that accounts for stresses and static aeroelastic considerations. The study focuses on a fully automated integration of the load analysis and design steps, such that the optimization is based on the computed, nonlinear, trimmed loads, and the loads computation is automatically affected by the structural changes during the design process.

Three major obstacles prohibit the use of CFD schemes for structural design: First, regular CFD

*Graduate Student; currently Post Doctoral Fellow in the School of Aerospace Engineering, Georgia Institute of Technology.
†Lecturer
‡Professor

schemes are designed to provide the airloads on a rigid configuration, in specific flight conditions. They do not have the required mechanism to account for aircraft flexibility and required algorithms to trim the aircraft according to a prescribed maneuver. Second, the high computational costs that are associated with CFD analyses. This difficulty is amplified in structural design applications where the airloads have to be evaluated several times during the design process. Third, aeroelastic considerations require the evaluation of the derivatives of the aerodynamic loads with respect to the structural design variables. When using nonlinear CFD analyses these derivatives are not available explicitly, and their evaluations by finite-difference methods typically amounts to unreasonable computational costs.

Several studies published in recent years address the evaluation of maneuver loads using CFD schemes. Generally, these studies differ in the CFD scheme used, the structural elastic model, the way the two disciplines are integrated, and in the amount of generality and complexity of the studied test cases. The early works on computational static aeroelasticity combined CFD analyses with simple structural models and were applied to wing models only.[6-8] Tatum and Giles[9] addressed a complete aircraft configuration using a full potential aerodynamic method (SIMP), together with an equivalent plate structural model, and Vinh *et al*[10] added a trim routine to the CAP-TSD (Computational Aeroelasticity Program - Transonic Small Disturbance) code.[11] Schuster *et al*[12] addressed the problem of computing the flow field about flexible fighter aircraft operating at extreme flight conditions, using Euler/Navier-Stokes simulations for flows where the small disturbance assumption is no longer valid. Guruswamy and co-authors[13-18] performed aeroelastic computations on a wing, a wing-fuselage configuration, and complete aircraft configurations using an Euler/Navier-Stokes aerodynamic method coupled with finite-element structural models (ENSAERO).

Karpel *et al*[19] introduced an efficient computational scheme for evaluating the aerodynamic maneuver loads on flexible rockets in supersonic flight conditions, based on an Euler solver. Computational efficiency was obtained by applying relatively small number of elastic shape updates and maneuver trim corrections during the process of flow field convergence. This scheme was expanded by Raveh *et al*[20] to realistic aircraft configurations whose trimmed conditions were achieved through the use of varied incidences, control surface deflections, and rotation rates. A modal structural model was used for interfacing the CFD and structural models and for calculating elastic shape deformations and applying them to the CFD grid. A trim-corrections algorithm was used for varying the incidences and control-surface deflections for obtaining user-defined maneuvers. This maneuver loads scheme serves also in the current study.

Raveh and Karpel[21] introduced a structural design methodology, based on nonlinear maneuver loads. An affordable design process, in terms of the required computational resources, was obtained by a new approach to the integration of analysis and optimization. Several structural optimization runs, using ASTROS, were performed within one flow simulation where each optimization run is based on interim, non-converged maneuver loads, such that the flow simulation and the structural design are converged simultaneously. The necessity of computing the sensitivity of the airloads to structural design changes was circumvented since in every optimization run the airloads were applied as a fixed set of loads. The number of iterations required for convergence of the combined maneuver-optimization analysis was practically the same as that of regular CFD analysis for a rigid-shape configuration.

The above approach was based on the assumption that the computational time required for structural optimization is relatively small compared to the time required for the CFD loads analysis. For large finite element models, and for design studies that involve many constraints, this assumption may not be valid. The current study broadens the design methodology of Ref. 21 to include the modal-based option to structural optimization, as presented by Karpel and co-authors.[22-26] The modal-based structural design is based on modal representation of the structure in both the static and the dynamic disciplines. The structure is represented throughout the optimization by a set of the low-frequency vibration modes of the baseline structure. The disciplinary responses and their sensitivity derivatives to changes in the design variables are calculated with respect to the modal coordinates. The reduced-basis modal representation decreased the computational cost of typical design cases by one to two orders of magnitude.[23, 26]

The computation of maneuver loads in Refs. 20 and 21 is also generalized in this study to include a different CFD scheme that is more suitable for applications that involve moving grids. Comparison of maneuver loads analyses performed with the two different CFD schemes demonstrates the independence of the algorithms with respect to the CFD method used.

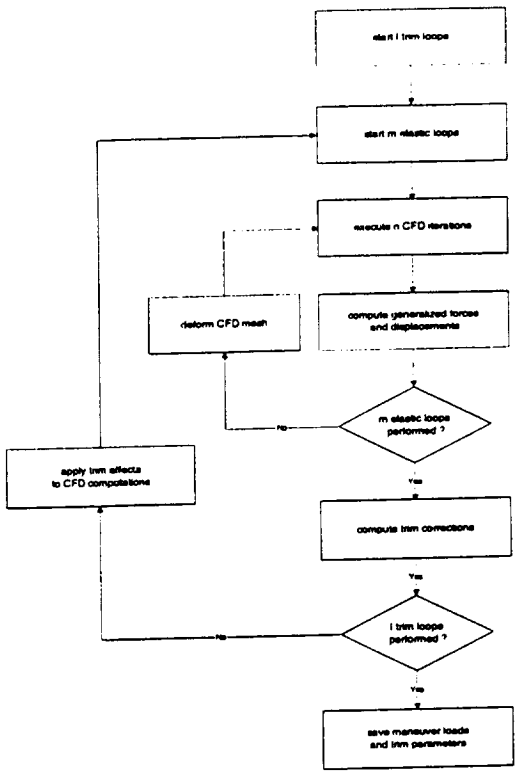

Figure 1: Phases of the maneuver analysis

Maneuver Loads Analysis

Maneuver load analysis is comprised of three levels of iterative processes. The inner-most level contains the original CFD analysis for a rigid-shape configuration which, if iterated until convergence, provides the aerodynamic load distribution on the rigid aircraft with prescribed aerodynamic incidences. The next iterative level introduces the structural elasticity which is combined with the aerodynamic loading to obtain the corresponding deformed shape. This level, if iterated until convergence, provides a load distribution that agrees with the shape distribution of the elastic aircraft. The outer-most level contains the maneuver trim loop where the incidences and control surface deflection angles are varied to obtain the total aerodynamic forces and moments implied by the maneuver. For computational efficiency, both the elastic deformations and trim corrections are introduced during the CFD solution convergence, as described in Fig. 1.

The user prescribes a number of CFD iterations after which elastic deformations are computed and applied to the CFD grid, and a number of elastic shape updates after which maneuver corrections are performed. Typically, the number of CFD iterations between two successive shape updates is 5 to 10 percent of the number of iterations required for flow field convergence. The shape and trim parameters are not updated after each CFD iteration in order to avoid excessive computations, and also in order to avoid numerical instabilities in the flow computations. The main advantages of the integrated aeroelastic computation scheme are that typical convergence rates and computational costs are very similar to those of a rigid-shape CFD run.

The core of the maneuver loads analysis is a CFD code by Yaniv[27] (FA3DMB) for solving the Euler equations. The code is based on Jameson *et al* multistage method,[28] a finite volume method using central differencing in space with explicit time-stepping. A steady state solution to the time dependent Euler equations is obtained by iterating in time using local time steps and implicit residual smoothing.

Elastic shape deformations, denoted by $\{u_E\}$, are calculated based on the modal approach to static aeroelasticity[29] which assumes that the elastic deformations of the aircraft structure, under external loads, can be described as a linear combination of a set of low-frequency elastic mode shapes $[\phi_E]$, namely,

$$\{u_E\} = [\phi_E]\{\xi_E\} \tag{1}$$

where $\{\xi_E\}$ is the generalized elastic displacement vector. The static equilibrium equation in generalized coordinates is given by

$$[K_E]\{\xi_E\} = \{F_E\} \tag{2}$$

where $[K_E]$ is the generalized stiffness matrix associated with $[\phi_E]$, and $\{F_E\}$ is the generalized aerodynamic force vector. Orthogonality of the rigid-body and elastic modes with respect to the structural mass and stiffness matrices implies that $[K_E]$ is diagonal and that inertia relief effects in the right hand side of Eq. (2) are handled automatically.[30] The generalized forces in Eq. (2) are obtained by summing the aerodynamic forces according to

$$\{F_E\} = [\phi_{EA}]^T\{F_A(a, \xi_E)\} \tag{3}$$

where $\{F_A\}$ is the aerodynamic force vector at the aerodynamic surface grid points. The vector $\{F_A\}$ depends on the aerodynamic trim parameters vector $\{a\}$ and on the elastic shape $\{\xi_E\}$. The matrix $[\phi_{EA}]$ is the elastic modes matrix, expressed at the aerodynamic interface grid points. The elastic mode shapes were mapped from the finite elements nodes, in which they are generated, onto the CFD interface grid points, by a newly developed method, based on the Infinite Plate Spline (IPS) by Harder and Desmarais[31] and Beam Spline[2] methods. The interface method is presented in details in Ref. 32.

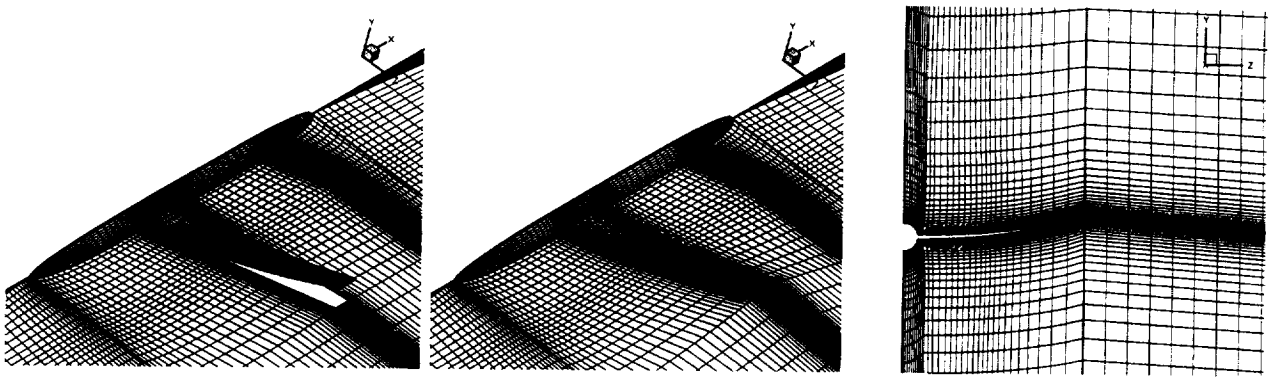

Figure 2: CFD Grid deformation

The generalized elastic deformations are transformed into displacements of the CFD interface points and applied to the whole grid using a three steps shearing method, following the method suggested by Schuster *et al.*[12] First are moved the interface points, according to the computed generalized displacements by

$$\{u_A\} = [\phi_{EA}]\{\xi_E\} \tag{4}$$

Then, the surfaces ahead, behind, and beside the deformed interface surfaces are adjusted so that they meet the displaced boundaries of the interface surfaces. Finally, internal grid points are redistributed, such that each grid point along an η grid line (normal to the surface) is moved in the same direction as the first point (point $j = 1$) by the distance

$$u_j = u_1 \left(1 - \frac{S_j}{S_{gl}}\right) \tag{5}$$

Figure 2 illustrates the above described steps of applying the elastic shape deformations to the CFD grid.

Most structural design cases are based on aerodynamic loads of prescribed aircraft steady maneuvers defined by the rigid body accelerations $\{\ddot{\xi}_R\}$. In symmetric maneuvers, the required aerodynamic lift and moment coefficients, C_L and C_M, are related to $\{\ddot{\xi}_R\}$ by

$$qS \left\{ \begin{array}{c} C_L \\ C_{M\bar{c}} \end{array} \right\}_{req} = [M_R]\{\ddot{\xi}_R\} \tag{6}$$

where $\bar{c}$ is the reference chord, S is the reference area, and q is the dynamic pressure. The mass matrix $[M_R]$ is associated with the rigid-body modes matrix $[\phi_R]$ where the first mode reflects a unit heave, and the second reflects a unit pitch about the center of gravity. Similar expressions can be written for antisymmetric or asymmetric maneuvers.

The CFD run starts with an initial estimate of the trim variables that are updated during the flow field convergence according to the differences between the required and the current values of the aerodynamic coefficients. The current values are calculated during the CFD solution by

$$\left\{ \begin{array}{c} C_L \\ C_{M\bar{c}} \end{array} \right\}_{cur} = \frac{1}{qS}[\phi_{ER}]^T\{F_A\} \tag{7}$$

where $[\phi_{ER}]$ is the matrix of rigid body modes expressed in the CFD surface interface points. The angle of attack α and elevator deflection δ are corrected in a symmetric maneuver by

$$\left\{ \begin{array}{c} \alpha \\ \delta \end{array} \right\}_{new} = \left\{ \begin{array}{c} \alpha \\ \delta \end{array} \right\} + \left\{ \begin{array}{c} \Delta\alpha \\ \Delta\delta \end{array} \right\} \tag{8}$$

where

$$\left\{ \begin{array}{c} \Delta\alpha \\ \Delta\delta \end{array} \right\} = \left[\begin{array}{cc} \tilde{C}_{L\alpha} & \tilde{C}_{L\delta} \\ \tilde{C}_{M\alpha\bar{c}} & \tilde{C}_{M\delta\bar{c}} \end{array} \right]^{-1} \times \left(\left\{ \begin{array}{c} C_L \\ C_{M\bar{c}} \end{array} \right\}_{req} - \left\{ \begin{array}{c} C_L \\ C_{M\bar{c}} \end{array} \right\}_{cur} \right) \tag{9}$$

and $\tilde{C}_{L\alpha}$, $\tilde{C}_{M\alpha}$, $\tilde{C}_{L\delta}$ and $\tilde{C}_{M\delta}$ are the derivatives of the aerodynamic coefficients with respect to the symmetric trim variables. With nonlinear CFD analysis, these derivatives are not available explicitly. They can be obtained from a computationally expensive finite-difference analysis, but this is not necessary because trim convergence is likely to occur even with rough estimates of the derivatives, such as the aerodynamic derivatives obtained from a linear analysis. Relaxation can be used to avoid large overshoots of the correcting terms, as suggested in Ref. 21.

The initial values of the aerodynamic trim parameters can be the maneuver trim parameters obtained

from trim analysis conducted with linear aerodynamics. However, as shown in Ref. 21, the algorithm is robust with respect to the initial choice of trim parameters. Therefore, initial trim parameters can be almost arbitrarily set, *e.g.*, zero angle of attack and zero control-surface deflection.

Angular rates associated with the maneuver (*e.g.* pitch rate in the symmetric maneuver case) are introduced to the aerodynamic analysis by adding terms to the fluid dynamics equations to account for the fact that they are written in a rotating frame of reference. The formulation of the flow equations in a frame of reference rotating in a steady pitch rate is presented in Ref. 32.

Following every trim iteration, the corrections to the angle of attack and control-surface deflection angle are introduced into the CFD solver. The change in the angle of attack is introduced to the CFD solver by changing the far field flow conditions.

Changing the control-surface deflection angle amounts to a change in the configuration and therefore requires regeneration of the aerodynamic grid. A difficulty that arises is the slope discontinuity that is caused by the rigid rotation of the elevator relative to the fuselage, which in turn results in discontinuities in the updated CFD mesh. To avoid grid discontinuities, that are prohibited in the FA3DMB code, elevator rotations are treated by an *elevator mode* enhanced with a *blended zone*. The elevator mode is an artificial mode that describes unit rigid elevator rotation where the elevator is rigidly rotated while the rest of the aircraft does not move. Discontinuities in the mode shape are avoided by adding a blended zone at the elevator root, ranging along a few grid lines, that are moved only by a fraction of the total elevator rotation. Figure 3 displays a part of the elevator mode, where the blended zone ranges along the first two elevator grid lines. The elevator mode is used for CFD mesh update in the same way as the elastic modes are used for CFD mesh updates for elastic corrections.

This difficulty of grid discontinuities, related to relative movements of parts of the aircraft, can be avoided by using the Chimera overset grid method instead of the multi-block, patched grid approach. In this study a similar maneuver trim procedure was introduced into a different Euler/Navier-Stokes code that employs the Chimera overset grid method.[33] The EZNSS code, developed by the second author of this paper, provides the choice between two implicit algorithms, the Beam and Warming[34] algorithm or the partially flux-vector splitting algorithm reported by Steger *et al.*[35] Finite differences in the framework of structural computational mesh are used in

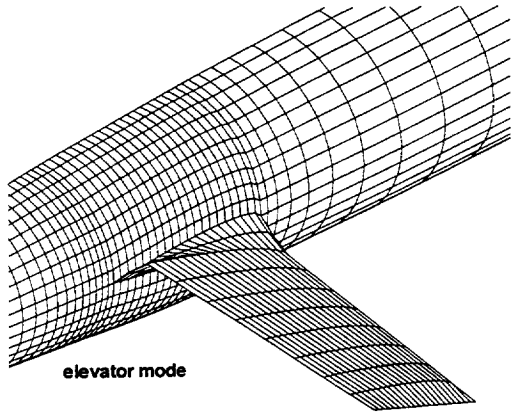

Figure 3: Elevator mode

the discretization process. Grid generation and inter grid connectivity are handled in the following manner. A separate computational mesh is generated for each component separately. An outer grid, or in the case of an aircraft, the fuselage mesh, is extended to fully include the meshes of the rest of the components. The holes that the meshes introduce into each other and the boundaries of the meshes and the holes are handled using the Chimera approach.[33] In this approach, intersecting components, such as the fuselage and the wing, create overlapping holes and therefore introduce complication in the intersection region. A convenient mean to provide proper interpolation near intersection regions is to generate collar grids.[36] In the current work, an automatic collar grid generation for intersecting geometries is employed. The collar grid is algebraically generated based on the surfaces of the geometries and is smoothed using an elliptic grid generation method. The automatic collar grid generation is embedded in the CFD code to facilitate control-surface deflections. Also embedded in the CFD code, are the hole generation and the grid connectivity procedures.

The introduction of the maneuver trim procedure into the EZNSS code allows to elegantly handle the geometry changes and removes the problems of grid discontinuities altogether. Furthermore, it demonstrates that the algorithms for elastic shape updates and trim corrections are independent of the CFD code used.

Structural Design

As mentioned in the introduction, the main difficulty in the integration of the maneuver loads computations with structural optimization arises from

the fact that the load analysis is computationally intensive and therefore extremely expansive. Typical time measures for the CFD and finite-element models of this study are 7 hours for a maneuver load analysis compared to 5 minutes for a structural optimization. Obviously it is impractical to perform a complete maneuver load analysis for every optimization step.

The new approach is based on the execution of several optimization runs during the maneuver analysis, where each optimization is based on the non-converged maneuver loads. The steps of the combined load–optimization analysis are illustrated in Fig. 4. The analysis starts with load computations for the baseline structure represented by its modal model. The analysis pauses several times during the flow field convergence for structural optimization. At each pause the interim non-converged loads are extracted and mapped onto the structural nodes. Optimization is then performed using ASTROS, while introducing the nonlinear loads as a virtually fixed set of loads. These loads do not provide the exact required maneuver loads, because they are extracted from a non-converged maneuver analysis, and because of the weight change during the optimization which changes the required maneuver lift. Therefore, at each optimization step the aircraft is trimmed using the linear rigid derivatives of the aerodynamic coefficients. These trim corrections are reduced to zero as the maneuver analysis and structural optimization converge. The nonlinear trimmed loads define some of the design cases in a structural optimization task. Other design cases in the same optimization task may include linear or nonlinear loads, possibly from other disciplines, and using different boundary conditions. A new modal database for the new structure is created at the final-analysis stage of the optimization. The new vibration frequencies and modes of the optimized structure are used as input to the CFD simulation which then resumes by applying the airloads to the new structure.

Trim corrections are computed within ASTROS, based on the linear rigid aerodynamic derivatives, according to

$$\begin{bmatrix} K_{ll} & K_{lr} & -qT_{AS_l}^T A_a \\ K_{rl} & K_{rr} & -qT_{AS_r}^T A_a \\ D^T M_{ll} + M_{rl} & D^T M_{lr} + M_{rr} & 0 \end{bmatrix} \begin{Bmatrix} u_l \\ u_r \\ \Delta a \end{Bmatrix} = \begin{Bmatrix} F_{S_l} \\ F_{S_r} \\ 0 \end{Bmatrix} + \begin{Bmatrix} M_{ll}D + M_{lr} \\ M_{rl}D + M_{rr} \\ 0 \end{Bmatrix} \{\ddot{\xi}_R\} \quad (10)$$

This equation is a modified version of the trim equation solved in ASTROS,[37] where K and M are the discrete coordinate structural stiffness and mass matrices respectively, and the subscripts r and l denote

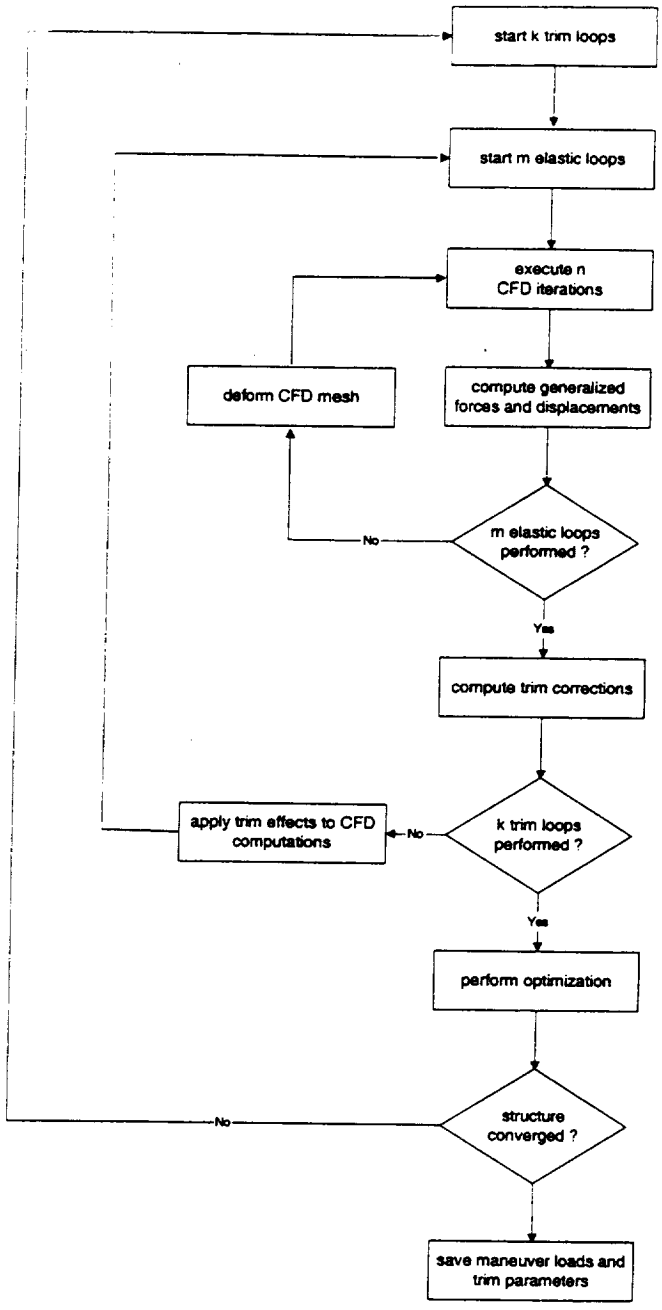

Figure 4: Phases of the load analysis–structural optimization procedure

the restrained and left-over degrees of freedom respectively. The kinematic rigid-body displacement matrix is denoted by D, q is the dynamic pressure, $[T_{AS}]$ is the structure-to-aerodynamic model transformation matrix, $[A_a]$ is the aerodynamic force coefficient matrix for a rigid aircraft, and $\{a\}$ is the aerodynamic trim parameters vector. $\{F_S\}$ is the nonlinear maneuver loads vector extracted from the non-converged CFD simulation and mapped onto the structural nodes. Equation 10 is solved for $\{\Delta a\}$ - the required corrections to the aerodynamic trim parameters that would provide the maneuver rigid-body accelerations $\{\ddot{\xi}_R\}$. The equation is also solved for the l-set and r-set maneuver displacements, u_l and u_r respectively.

ASTROS is unique in its capability to simultaneously optimize for several design cases from different disciplines with different boundary conditions. When some of the design cases require the evaluation of aerodynamic loads, the designer can choose either to perform every aerodynamic load evaluation by a separate CFD run, or to limit the use of CFD only to design cases that would benefit the most from an accurate evaluation of the aerodynamic loads. When required, several CFD runs can be performed at the same time in parallel, all paused at the same position for elastic, trim, and optimization updates.

Modal-Based Optimization

The design approach presented in the previous section was motivated by the run-time differences between an optimization run and a CFD analysis, that were obtained for the models of this study. However, it is realized that for larger finite-element models, and for design studies that involve a large number of constraints, the optimization run time may become much larger, and it would be impractical to perform several optimization runs within one design study. The computational cost of the structural optimization can be minimized, even for large finite-element models, by replacing the discrete coordinates optimization with a modal-based optimization.

The basic assumption behind the modal-based optimization is the same one that is used for maneuver loads analysis. The displacements calculated by Eq. (1) as a linear combination of a set of low-frequency vibration modes are used for aerodynamic loads calculations and for stress analysis. It was previously shown[24-26] that, with approximately 20 to 40 modes taken into account, typical application of the basic modal approach yields accurate stress results when applied to the structure for which the modes are calculated, but exhibit large errors when applied to modified structures without changing the modal basis. To allow for an efficient, fixed-basis, optimization process with analytic sensitivity expressions, the modal basis is complemented with modal perturbations that are calculated once for the baseline structure, and then used efficiently throughout the optimization process. The revised method presented several cost-effectiveness trade-off options. The fastest option was the first-order, the mode-displacement (MD) method,[24,25] which is also the least accurate (but still adequate in cases of moderate design changes). The summation-of-forces (SOF) method, with expandable modal basis,[26] was the most accurate option, but also the most time consuming. Demonstrated with optimization cases of 5 to 28 thousand degrees of freedom, the various modal-based options demonstrated CPU speed-up factors of 7 to 80.

As demonstrated below, the most simple modal-based optimization option (1st-order MD option) can be adequately used in the CFD-based optimization process. With the modal data base updated in each optimization run, the entire process should converge to the optimal solution even though the interim optimization runs might be somewhat inaccurate.

Numerical Example

The Aircraft Model

A simple transport aircraft model which has all the features necessary to verify the proposed methodology was created. The model aircraft includes a fuselage, wing, aileron and all-movable tail. The wing and elevator are similar in shape and structure - both are tapered and swept aft. The cross section profiles of the wing and elevator are scaled NACA0012 symmetric airfoils. The fuselage is axisymmetric and is $20m$ long. Table 1 summarizes the wing and tail geometrical dimensions.

	wing	tail
aspect ratio	10	6.4
half span	$10m$	$4m$
root chord	$3m$	$1.5m$
leading edge sweep angle	20°	20°
taper ratio	.333	.667

Table 1: Wing and tail geometrical dimensions

An H-type grid topology is used to generate the computational mesh for the flow simulations. Taking

advantage of the multi-zone capability of the CFD code the grid is divided into 24 zones, each describing a logical component such as wing upper/lower surface, fuselage, etc. The entire flow field contains approximately 500,000 grid points.[21]

A general view of the structural model is given in Fig. 5. It has approximately 1000 degrees of freedom. The torsion boxes of the wing and tail, and the aileron are modeled in detail with elements representing skin, ribs, spars, spar caps and stringers. Table 2 summarizes the weights of the half-aircraft model. The wing weighs 384.6kg of which 284.6kg is the weight of the torsion-box structure which is subjected to optimization. A modal analysis is performed to provide the 13 low-frequency vibration modes, and the corresponding generalized stiffness matrix required for the CFD maneuver analysis.

component		weight $[kg]$
wing		384.6
aileron		8.5
elevator		98.5
fuselage:	structure	2700.0
	fuel	2000.0
	engine	700.0
total weight		5891.6

Table 2: Weight summary - half aircraft

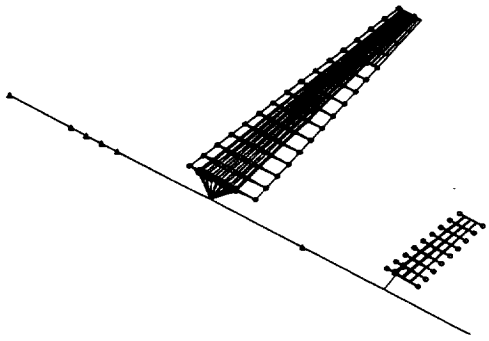

Figure 5: Finite element model

Maneuver Loads Analysis

The following description is of a $3g$ pull-up maneuver of the baseline structure, at Mach 0.85 and height of $11,000m$, which defines a pitch rate of $\dot{\theta} = (n-1)g/V = 0.066[rad/sec]$, and which corresponds to required lift and moment coefficients of $C_L = 0.84$, and $C_M = 0$.

Figure 6 presents the convergence history of the lift and moment coefficients, indicating their approach to the required values, while Fig. 7 shows the convergence history of the residual for the maneuver run case compared to that of a regular CFD run of a rigid-shape configuration. These figures indicate the good convergence properties of the scheme. Reference 21 includes more details on the maneuver loads analysis results, plus a demonstration of the robustness of the scheme with respect to initial trim parameters, and with respect to the aerodynamic derivatives that are used to trim the aircraft.

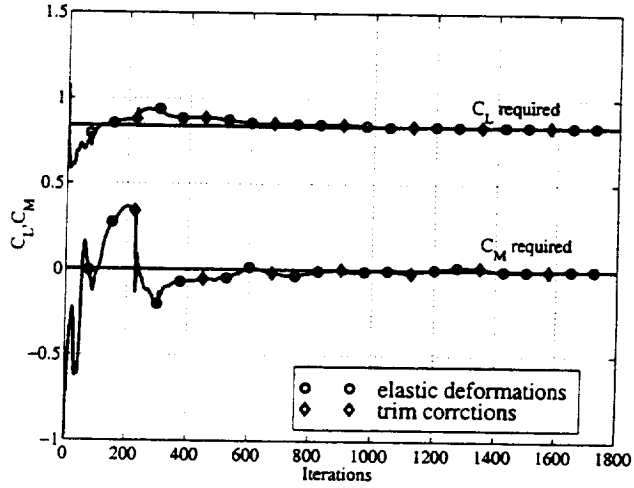

Figure 6: C_L and C_M convergence history

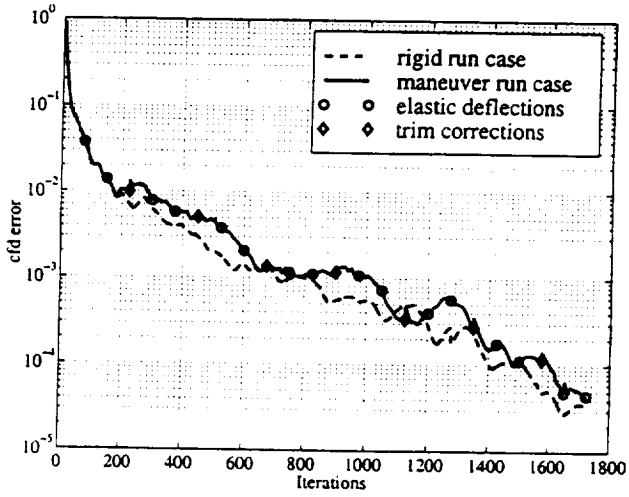

Figure 7: Residual decay history

To evaluate the effects of the nonlinear model-

ing on the loads distribution, a second maneuver loads analysis was performed, using ASTROS and its linear aerodynamic module, USSAERO.[38] Figure 8 presents the differential pressure coefficient (ΔC_p) distribution along this wing section, comparing the linear and nonlinear values. It is notable that the nonlinear and linear pressure distributions significantly differ. The nonlinear chordwise center of pressure is moved aft compared to the linear one, causing a nose-down moment and an increased sectional wash-out angle. The difference between the computed linear and nonlinear ΔC_p distributions, which is attributed to the different aerodynamic theories, has a significant effect on the structural optimization, especially on the local structural gage distribution, as seen in the following section.

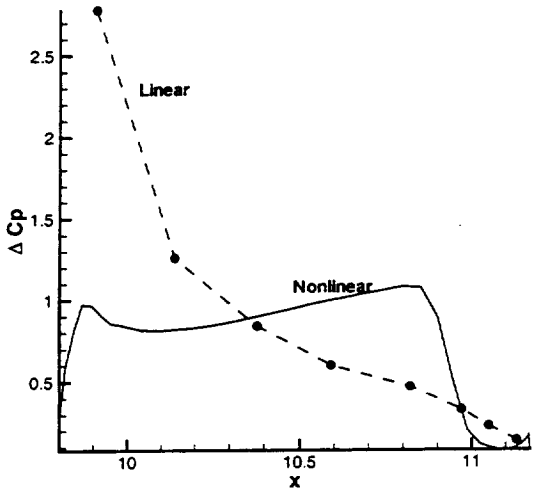

Figure 8: Differential pressure coefficient distribution at 82% of the span

Structural Design

The wing torsion box is divided into five spanwise segments. At each segment, the design variables control the thicknesses of the wing skin, the ribs, the front and rear spar webs, and the cross section area of the front and rear spar-caps, and the stringers, resulting in a total of 35 design variables. The torsion box is optimized for minimum weight under the following constraints:

(a) The Von-Mises stresses are constrained by 2/3 of the material ultimate stress ($280MPa$) in a symmetric $3g$ pull-up maneuver at Mach 0.85, $h = 11,000m$.

(b) (b) The aileron effectiveness is constrained by $\eta_{rmr} \geq 30\%$ in an antisymmetric roll maneuver at Mach 0.85, $h = 11,000m$, where η_{rmr} is the aeroelastic aileron effectiveness.

The combined loads–optimization process was executed by replacing every third trim correction in a maneuver load run by a structural optimization run. Optimization runs were carried out using the two approaches: (a) with the standard discrete-coordinate static aeroelastic module of ASTROS, modified to accommodate the CFD loads as a fixed set of loads to which a trim correction is added in every optimization step, and (b) with the modal-based option of ASTROS.

Figure 9 shows the history of convergence of the lift and moment coefficients. showing both design studies. In both cases the convergence of the aerodynamic coefficients is smooth. Until the first optimization pause, both design studies follow the same trend. Following the optimization, the plots slightly differ, where it is noted that the modal-based optimization has a bit larger fluctuations in the coefficient values.

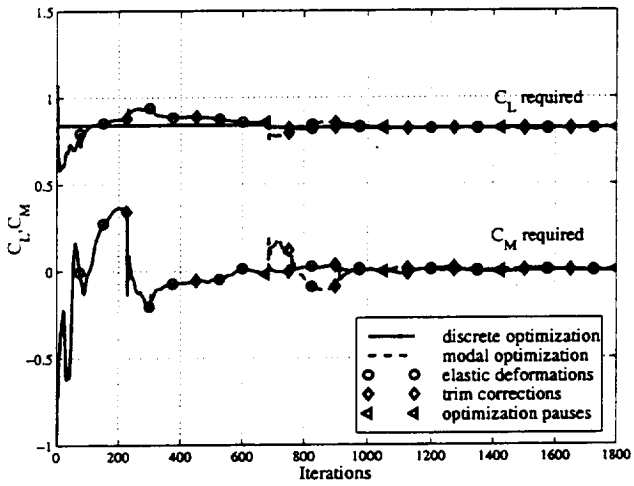

Figure 9: C_L, C_M convergence history - optimization case

Figure 10 shows the history of residual decay of the combined maneuver–optimization run case. On return from the optimization, when the airloads are applied to the optimized structure that is less stiff, new deformations are obtained. These shape change increase the CFD error which then rapidly decays. The phenomenon is further amplified in the modal-based optimization due to the larger changes in the design variable values in each optimization. The total number of iterations required for convergence of the combined loads–optimization run is almost the same as for a CFD run of a rigid-shape configuration in the discrete optimization run case, and slightly larger in the modal-based optimization run case.

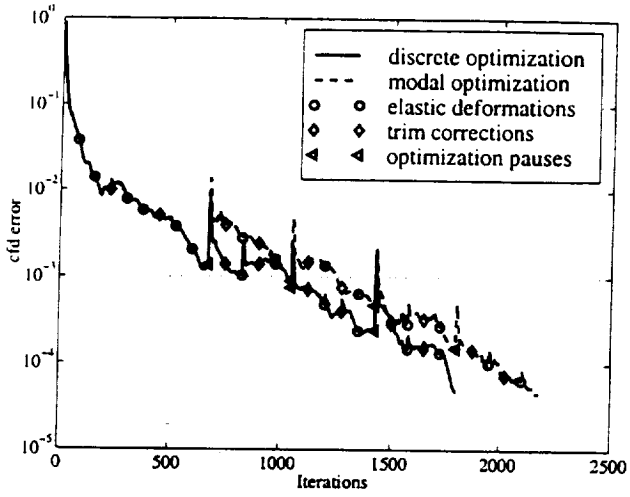

Figure 10: Residual decay history - optimization case

To evaluate the effects of nonlinear loads on the structural design, the same optimization run case was performed by the standard ASTROS, with both design cases based on linear aerodynamics. The structural optimization in ASTROS was performed by several gradient-based design steps, with each step based on a single-variable optimization using structural approximation concepts. The reference optimization performed by ASTROS with linear aerodynamics converged in 7 optimization steps, and the variable-structure weight was reduced from 284.6kg to 180.0kg. The same design task using the non-linear maneuver loads lead to a variable-structure weight of 173.9kg. Figure 11 shows the history of weight reduction during the optimization, comparing the reference ASTROS optimization with the CFD-based optimizations (discrete-coordinates and modal-based run cases). The same optimal weight was obtained by the discrete-coordinate and the modal-based optimization studies. It is noted that while in the discrete-coordinate optimization the weight was monotonically reduced, in the modal-based optimization a non-monotonic convergence was observed.

The 4% difference between the optimal weight of the linear and nonlinear wing designs is not small considering the fact that both load distributions yield the same design maneuvers, and that the optimization was not only controlled by the maneuver stresses, but also by the demand for aileron effectiveness, that was similarly analyzed in both design cases using linear aerodynamics. A distinct effect of the non-linear loads can be observed when examining the optimal values of the design variables of the linear and nonlinear designs (Fig. 12). The nonlinear design reflects the discrete optimization, similar values were obtained by the modal-based optimization. While the skin converged to almost the same values as for the linear and nonlinear designs, with small differences near the tip due to the different wash-outs, significant differences were found in the front and rear spars. Material is moved in the CFD-based optimization from the front spar to the rear spar because the centers of chordwise pressure distributions are significantly aft of those of linear aerodynamics,which also cause larger wing tip wash-out.

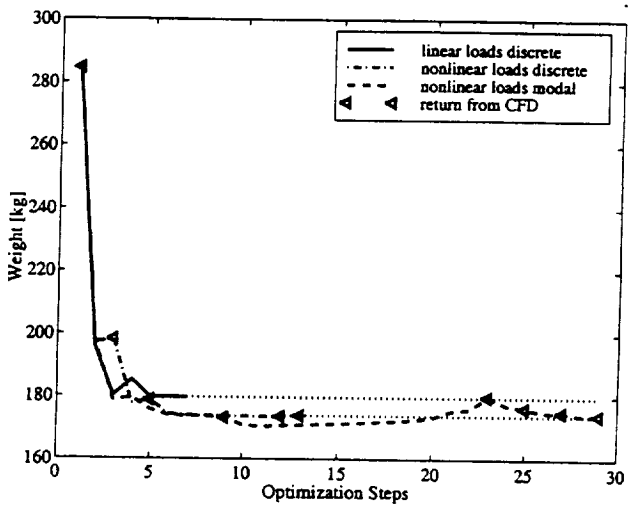

Figure 11: Wing structure weight history

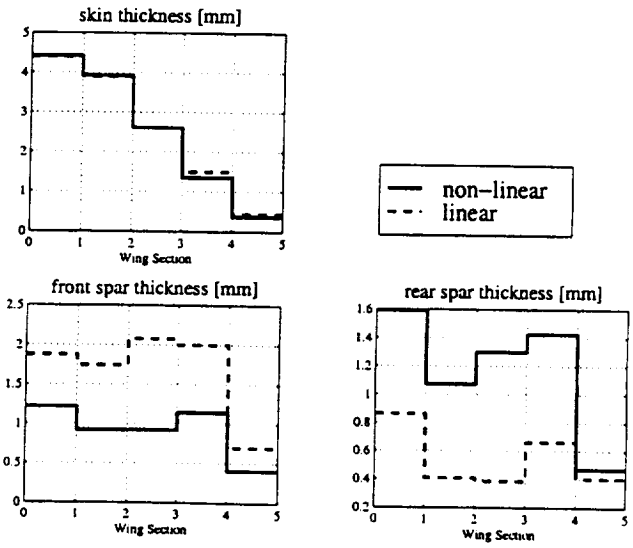

Figure 12: Optimal Design Variables

Load Analysis with EZNSS

The computational mesh used for the EZNSS simulations consisted of five zones, fuselage, wing, elevator, and two collar grids, one for the fuselage-wing intersection and one for the fuselage-elevator intersection. The fuselage grid is based on an O-type mesh. For the wing, tail, and collar grids a C-H-type grid topology is used. The entire flow field consists of approximately 600,000 grid point. Figure 13 shows the model's complete geometry and the computational mesh of the main components. Figure 14 shows a close-up of the fuselage-wing collar grid (every other grid point in each direction is shown).

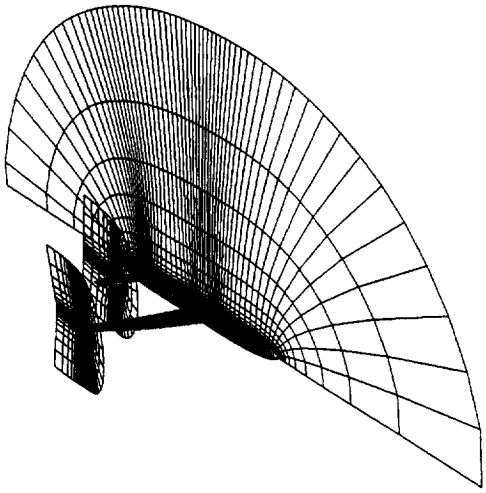

Figure 13: Overall view of the grid system

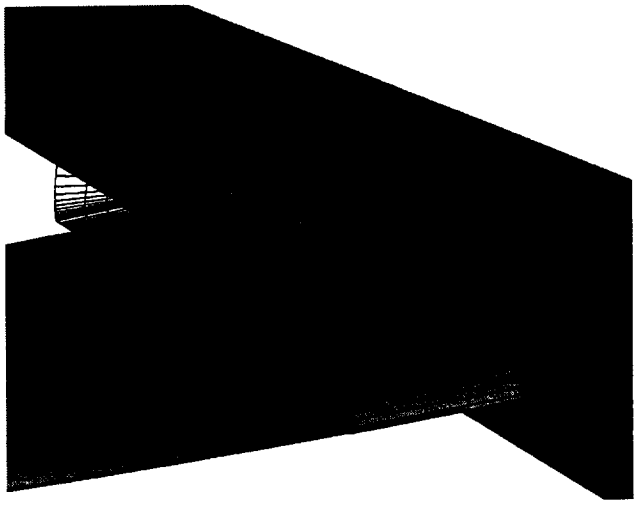

Figure 14: Close-up of the fuselage-wing collar grid

The results of the flow simulations using the EZNSS are presented in figures 15, 16 and 17. Figure 15 shows the convergence history of the lift and moment coefficients. Both coefficients converge to their required values and the convergence history follows a similar behavior to the FA3DMB simulations.

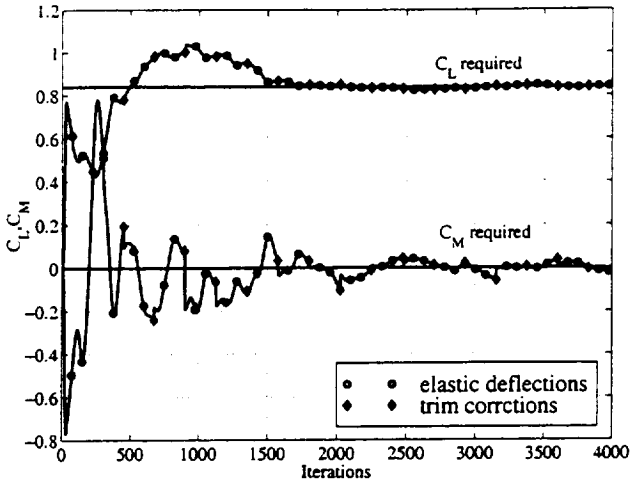

Figure 15: C_L and C_M convergence history (EZNSS)

Figure 16 shows the convergence history of the simulation. Also shown in the figure is the convergence history of a simulation of a rigid geometry. In contrast to the FA3DMB simulations, each geometry change is associated with a rather large increase of the residual. The large changes arise due to the Chimera overset method. Every control-surface deflection or elastic correction may change grid points in the fuselage mesh from being holes to become regular points. Since such points are far from convergence, their inclusion in the simulation contributes large values to the residuals. However, the number of these points is limited and the implicit algorithm has fast convergence qualities. Therefore, the residual values decrease quickly to the values of a rigid-shape simulation.

Figure 17 shows the converged aerodynamic pressure distribution on the aircraft surface in $3g$ pull-up maneuver. A shock wave can be seen at approximately 85% of the chord on the upper wing surface. Another shock exists on the lower surface of the elevator. A similar image for the flow obtained using the FA3DMB code can be found in Ref. 21.

Conclusions

The paper presented efficient methodology for structural design studies, with static aeroelastic considerations, where the aerodynamic loads are provided by a nonlinear CFD scheme. Structural optimization was performed both with the regular discrete

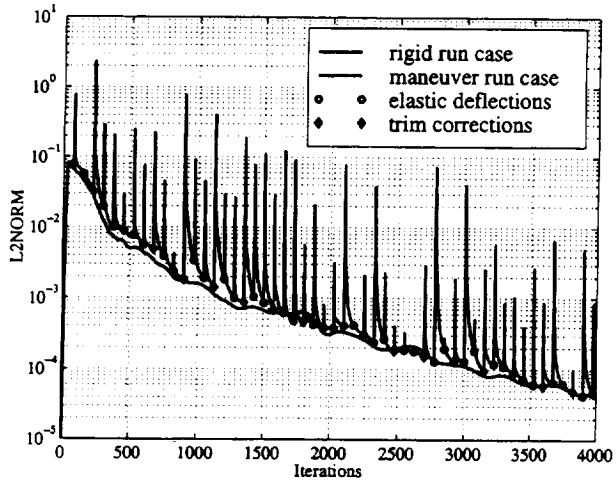

Figure 16: Residual decay history (EZNSS)

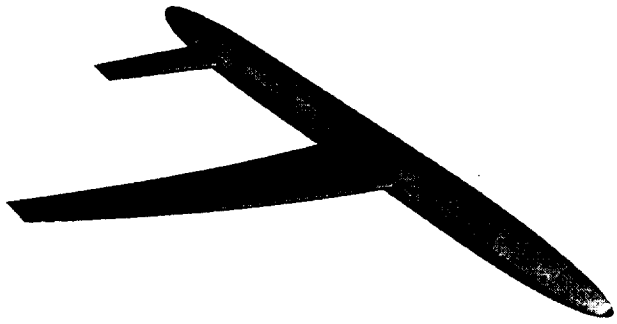

Figure 17: Surface pressure contours (EZNSS)

coordinate approach and with the modal-based option. Both cases demonstrated very good convergence properties of both the aerodynamic loads and the structural design, with the total number of CFD iterations required for convergence being almost the same as for a regular flow analysis for a rigid configuration. It was demonstrated that the use of a simplified structural modeling does not significantly affect the convergence of the combined loads-optimization process. The discrete coordinate and modal-based optimizations converged to the same optimal designs, where in the modal-based optimization, a nonmonotonic convergence was observed, which in turn slightly increased the number of iterations required for convergence. For the relatively small finite-element model of this study the use of the modal-based optimization does not provide any computational cost reduction, however, for larger models, the discrete-coordinates optimization must be replaced by the modal-based optimization to maintain a computationally affordable design process. Comparison between the linear and nonlinear designs showed significant differences in both total weight and local structural gage distribution, indicating that accurate evaluation of the maneuver loads is important even in the early design stages.

The maneuver analysis was examined using two flow simulation schemes. The first is an explicit, finite volume scheme using a multi-block patched grid approach (FA3DMB), and the second is an implicit, finite difference code using the Chimera overset grid method (EZNSS). The EZNSS code allows to perform a rigid body like rotation and therefore the whole elevator is placed at the angle of deflection providing higher efficiency. The maneuver analysis exhibited good convergence properties, for both codes, with different convergences patterns due to the different grid methods, indicating that the loads analysis methodology is independent of the flow analysis used.

The study establishes a framework for structural design, where some disciplines are based on nonlinear aerodynamic modeling while others are based on linear methods. The computational schemes presented are specifically designed for the study of realistic aircraft configurations, based on detailed finite-element modeling and involving several design disciplines.

References

1. Haftka R. T. Structural optimization with aeroelastic constraints: A survey of us applications. *International Journal of Vehicle Design*, 7(3–4):381–392, 1986.
2. Rodden W. P. and Johnson E. H. *MSC/NASTRAN Version 68 Aeroelastic Analysis User's Guide.* The Macneal-Schwendler Corporation, 1994,pp.28–32.
3. Neill D. J., Johnson E. H., and Canfield R. A. ASTROS - A Multidisciplinary Automated Structural Design Tool. *Journal of Aircraft*, 27(12):1021–1027, 1990.
4. E. Albano and Rodden W. P. A Doublet-Lattice Method for Calculating Lift Distributions on Oscillating Surfaces in Subsonic Flows. *AIAA Journal*, 7(2):279–285, 1969.
5. Love M. H. Integrated airframe design at the lockheed martin tactical devision. Technical report, Lockheed Martin Tactical Aircraft Systems, Fort Worth, TX, 1996.
6. Whitlow W. Jr. and Bennett R. M. Application of a Transonic Potential Flow Code to the Static Aeroelastic Analysis of Three-Dimensional Wings. In *Proceedings of the 23rd Structures, Structural Dynamics, and Materials Conference*, volume 2, pages 267–276, New-Orleans, Louisiana, May 1982. AIAA-82-0689.
7. Agrell N. and Hedman S. G. Calculations of Transonic Steady State Aeroelastic Effects for Canard Airplane. In *Proceedings of the 13th Congress of the International*

Council of the Aeronautical Sciences, AIAA Aircraft System and Technology Conference, pages 59–66, Seattle, Washington, 1982. ICAS-82-2.1.2.

8. Pittman J. L. and Giles G. L. Combined Nonlinear Aerodynamic and Structural Method for the Aeroelastic Design of a Three-Dimensional Wing in Supersonic Flow. In *Proceedings of the Applied Aerodynamics Conference*, pages 36–44, San Diego, CA, June 1986. AIAA-86-1769.
9. Tatum K. E. and Giles G. L. Integrating Nonlinear Aerodynamic and Structural Analysis for a Complete Fighter Configuration. *Journal of Aircraft*, 25(12):1150–1156, 1988. AIAA-87-2863.
10. Vinh L., Edwards J. W., Seidel D. A., and Batina J. T. Transonic Stability and Control of Aircraft Using CFD Methods. In *Proceedings of the AIAA Atmospheric Flight Mechanics Conference*, Minneapolis, Minnesota, August 1988. AIAA-88-4374.
11. Batina J. T., Seidel D. A., Bland S. R., and Bennet R.M. Unsteady Transonic Flow Calculations for Realistic Aircraft Configurations. In *Proceedings of the 28th Structures, Structural Dynamics, and Materials Conference*, Monterey, CA, April 1987. AIAA-87-0850.
12. Schuster D. M., Vadyak J., and Atta E. Static Aeroelastic Analysis of Fighter Aircraft Using a Three-Dimensional Navier-Stokes Algorithm. *Journal of Aircraft*, 27(5):820–825, 1990.
13. Guruswamy G. P. Coupled Finite-Difference/Finite-Element Approach for Wing-Body Aeroelasticity. In *Proceedings of the 4th Symposium on Multidisciplinary Analysis and Optimization*, Cleveland, Ohio, September 1992. AIAA-92-4680.
14. Guruswamy G. P. and Byun C. Direct Coupling of Euler Flow Equations With Plate Finite Element Structures. *AIAA Journal*, 33(2):375–377, February 1995.
15. Appa K., Argyris J., and Guruswamy G. P. Aircraft Dynamics and Loads Computations Using CFD Methods. In *Proceedings of the 37th Structures, Structural Dynamics and, Materials Conference*, pages 215–220, Salt Lake City, UT, April 1996. AIAA-96-1342.
16. Kapania R. K., Bhardwaj M. K., Reichenbach E., and Guruswamy G. P. Aeroelastic Analysis of Modern Complex Wings. In *Proceedings of the 6th Symposium on Multidisciplinary Analysis and Optimization*, pages 258–265, Bellevue, WA, September 1996. AIAA-96-4011.
17. Guruswamy G. P. and Tu E. L. Navier-Stokes Computations on Flexible Advanced Transport Wings in Transonic Regime. *Journal of Aircraft*, 33(3):576–581, July 1996.
18. Byun C. and Guruswamy G. P. A Parallel, Multi-Block, Moving Grid Method for Aeroelastic Applications on Full Aircraft. In *Proceedings of the 7th Symposium on Multidisciplinary Analysis and Optimization*, pages 570–580, St. Louis, MO, September 1998. AIAA-98-4782.
19. Karpel M., Yaniv S., and Livshits D. S. Integrated solution for Computational Static Aeroelastic Problems. *Journal of Spacecraft and Rockets*, 35(5):612–618, September 1998. AIAA-96-4012.
20. Raveh D.E., Karpel M., and Yaniv S. Non-Linear Design Loads for Maneuvering Elastic Aircraft. In *Proceedings of the 38th Israel Annual Conference on Aeroepace Sciences*, pages 150–160, Tel-Aviv,Israel, February 1998.
21. Raveh. D. E. and Karpel. M. Structural optimization of flight vehicles with non-linear aerodynamic loads. In *7th AIAA/USAF/NASA/ISSMO Symposium on Multidisciplinary Analysis and Optimization*, St. Louis, MO, September 1998. AIAA-98-4832.
22. Karpel M. Multidisciplinary Optimization of Aeroservoelastic Systems Using Reduced-Size Models. *Journal of Aircraft*, 29(5):939–946, 1992.
23. Karpel M. and Brainin L. Stress Considerations in Reduced-Size Aeroelastic Optimization. *AIAA Journal*, 33(4):722–726, 1995.
24. Karpel M., Moulin B., and Love M. H. Modal-Based Structural Optimization with Static Aeroelastic and Stress Constraints. *Journal of Aircraft*, 34(3):433–440, 1997.
25. Karpel M. Modal-Based Enhancement of Integrated Structural Design Optimization Schemes. *Journal of Aircraft*, 35(3):437–444, 1998.
26. Karpel M., Moulin B., and Love M. H. Structural optimization with stress and aeroelastic constraints using expandable modal basis. In *Proceedings of the 39th Structures, Structural Dynamics, and Materials Conference*, pages 1460–1468, Long Beach, CA, April 1998.
27. Yaniv S. Navier-Stokes Calculations for Rotating Configurations: Implementation for Rockets. *Journal of Spacecraft*, 33(5):756–758, 1996.
28. Jameson A., Schmidt W., and Turkel E. Numerical Solution of the Euler Equations by Finite Volume Methods Using Runge-Kutta Time-Stepping Schemes. In *Proceedings of the 14th Fluid and Plasma Dynamics Conference*, Palo Alto, CA, June 1981. AIAA-81-1259.
29. Sheena Z. and Karpel M. Static Aeroelastic Analysis Using Aircraft Vibration Modes. In *Proceedings of the 2nd International Symposium on Aeroelasticity and Structural Dynamics*, pages 229–232, Aachen, Germany, 1985.
30. Karpel M. and Sheena Z. Structural Optimization for Aeroelastic Control Effectiveness. *Journal of Aircraft*, 26(8):493–495, 1989.
31. Harder R. L. and Desmarais R. N. Interpolation Using Surface Splines. *Journal of Aircraft*, 9(2):189–191, February 1972.
32. Raveh D. E. *Integrated Aero-Structural Design of Maneuvering Flexible Flight Vehicles*. PhD thesis, Technion - Israel Institute of Technology, Haifa, Israel, February 1998.
33. Benek J. A. Buning P. G. and Steger J. L. a 3-d chimera grid embedding technique. In *Proceedings of the 7th Computational Fluid Dynamics Conference*, pages 322–331., Cincinnati, OH, July 1985. AIAA-85-1523.
34. Beam R. M. and Warming R. F. An implicit factored scheme for the compressible navier-stokes equations. *AIAA Journal*, 16:393–402, 1978.
35. Steger J. L. Ying S. X. and Schiff L. B. A partially flux-split algorithm for numerical simulation of unsteady viscous flows. In *Workshop on Computational Fluid Dynamics*, University of California, Davis, 1986.
36. Parks S. J. Buning P. G. Chan W. M. and Steger J. L. Collar grids for intersecting geometric components within the chimera overlapped grid scheme. In *10th AIAA Computational Fluid Dynamics Conference*, Honolulu, HI, June 1991. AIAA-91-1587.
37. Neill D. J., Herendeen D. L., and Venkayya V. B. *ASTROS Theoretical Manual*. Flight Dynamics Directorate, Wright Laboratory, Airforce Material Command, Wright-Patterson Air Force Base, OH, May 1995,pp.121–132.
38. Woodward F. A. An Improved Method for the Aerodynamic Analysis of Wing-Body-Tail Configurations in Subsonic and Supersonic Flow, Part I - Theory and Applications. In *NASA CR-2228*, May 1973.

Multidisciplinary Aero-Structural Modeling on Parallel Computers

Ryoichi Onishi*, **Toshiya Kimura**†
Center for Promotion of Computational Science and Engineering
Japan Atomic Energy Research Institute
2-2-54 Nakameguro Meguro, Tokyo 153-0061, Japan

Zhihong Guo‡
The Institute of Physical and Chemical Research
2-1 Hirosawa Wako, Saitama 351-01, Japan

Toshiyuki Iwamiya§
Computational Science Div., National Aerospace Laboratory
7-44-1 Jindaiji Higashimachi Chofu, Tokyo 182, Japan

Abstract

The system for coupled aero-structural analysis has been implemented on distributed-parallel processing environment at Japan Atomic Energy Research Institute(JAERI). The system is based on loose coupling of CFD(Computational Fluid Dynamics) and CSD(Computational Structural Dynamics), solves fluid and structural equations concurrently exchanging each solution data, and has been applied to the dynamic aeroelastics problem of a high aspect-ratio swept-back wing. The analytical model of skin, spar, and rib construction of a wing box structure was created and used for aero-structural computations. Parallel and distributed approach employed in the system is efficient for multidisciplinary applications.

Nomenclature

$[C]$	Damping matrix.
$\{f\}$	External force.
$[K]$	Stiffness matrix.
$[M]$	Mass matrix.
$\hat{Q}, \hat{E}, \hat{F}, \hat{G}$	Generalized flux vectors.
$\{u\},\{\dot{u}\},\{\ddot{u}\}$	Displacement,velocity,and acceleration vectors.
ξ, η, ζ	Generalized coordinator.

*Assistant Advisor, Parallel Processing Tools.
†Senior Scientist, Parallel Algorithms.
‡Researcher,Materials Fabrication Lab.
§Head,Software Engineering Lab.

Introduction

During the last two decades, complexities of computational models for CFD/CSD analysis have been largely increased with the computer progress. As shown in Table 1, simple models like a lumped-mass and beam were used for aeroelastic design purpose on early low performance computer[1]. The introduction of finite element method to CSD made it possible to use more sophisticated models such as aerodynamic panel or contoured surface. Most of the early researches are concerned with static analysis because of computer performance issue, and dynamic analysis or flutter prediction is becoming a major interest of current research efforts. Also CFD made a large progress in solving non-linear flow. With these advanced software tools and computers, aerospace companies are exploring multi-disciplinary engineering into aerospace research and development[2][3][4].
In our research, primary concern is the dynamic aeroelastic analysis using three-dimensional structural model[5][6]. Parallel processing technologies have been largely introduced as a key to efficient computations of fluid and structural codes. The thick line region in Table 1 designates our research coverage.

Table 1. Progress in Computational Aeroelastic Analysis

Computational Model	CFD	CSD	Analysis
Two Dimensional Wing Lumped Mass Panel	Linear Flow	Moment Coefficient FEM Modal Analysis	Static Structural Analysis
Contoured Surface Wing Box	Euler Navier-Stokes	FEM Direct Method	Dynamic Responce
Current	Turbulant Flow Algebraic LES DNS		Design Optimization

Our Research Interests

Analytical Equations

Tight or loose coupling approach is applied to solve fluid-structural interaction problems. In Tight Coupling(TC), fluid and structural equations are solved in one step. Ref.[7] shows the approach of merging stiffness matrix for fluid and structure and solving it in one equation. Ref.[8] shows other TC approach solving the Newton-Raphson equation with the tangent vector which contains fluid and structural derivatives. The derivatives are derived from fluid and structural equations. This approach allows to use different forms of the equations.

In Loose Coupling(LC), two different equations are solved in different steps. Usually the solver program for each equation is prepared and executed in different processes through the interface for exchanging each solution data. We considered LC had the advantage in larger flexibility in integrating solver programs on distributed environment. The equation(1) and (2) are the structural motion equation and Navier-Stokes fluid equation. CSD code solves the equation(1) by the finite element method and CFD code solves the equation(2) by the finite difference method. They were integrated with the interface program for moving grid generation and load transfer. (See Ref.[9] and [10] for more details of the fluid-structure interface.) As described in later section, each program is parallelized and executed on different computer.

$$[M]\{\ddot{u}\} + [C]\{\dot{u}\} + [K]\{u\} = \{f\} \tag{1}$$

$$\frac{\partial \hat{Q}}{\partial t} + \frac{\partial \hat{E}}{\partial \xi} + \frac{\partial \hat{F}}{\partial \eta} + \frac{\partial \hat{G}}{\partial \zeta} - \frac{\partial \hat{E}_v}{\partial \xi} - \frac{\partial \hat{F}_v}{\partial \eta} - \frac{\partial \hat{G}_v}{\partial \zeta} = 0 \tag{2}$$

Geometry Processing and Grid Generation

Geometry is a common data set of fluid and structural grid, and is automatically generated from parametric data defining a wing configuration. The parameters define the data relating to wing plan form, contour, and internal layout. Polygon data of the external skin is formed by wing plan form and contour. Internal structures are generated by simply connecting external polygon nodes or by cutting out external surface at rib and spar locations. Figure 1 shows the examples of simple and complex generations of a wing geometry. Finite element data with load and constraint conditions for CSD code is generated by discretizing external surface into 20 Degrees-Of-Freedom shell elements. Flowfield grid is also generated from external surface(Figure 2). Fluid and structure interface is so accomplished as to contact at same grid positions in simple generation scheme. In complex generation, grid point is completely different from the opposite. Simple generation scheme makes easy to implement a conversion program of deformation and pressure data. Deformation and pressure are converted into a movement data of fluid grid and structural load, respectively. Although requiring interpolations of deformation and pressure because of the dispositions of fluid and structural grids, complex generation scheme has an advantage in configuring flowfield and structure.

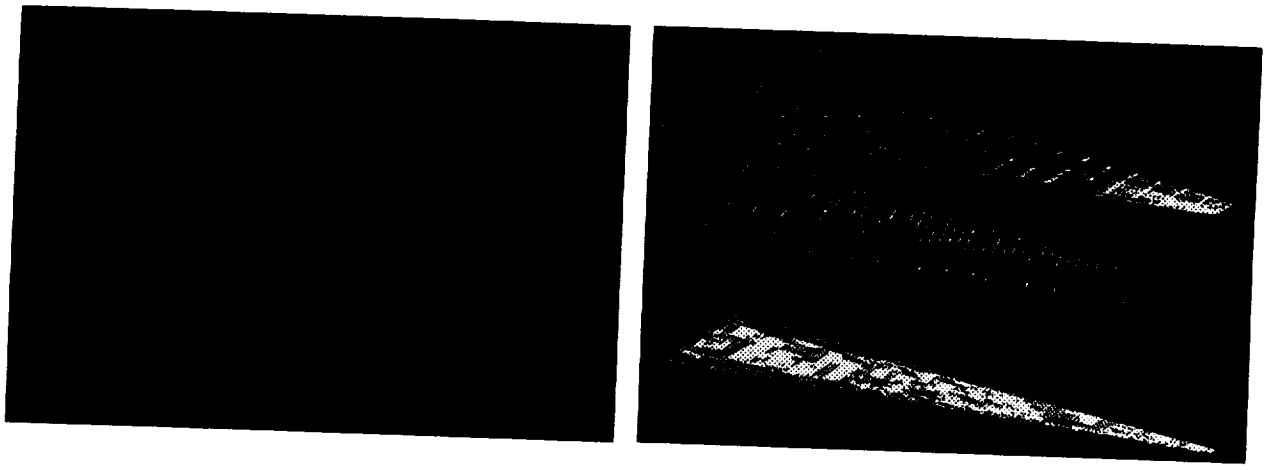

Figure 1. Simple and Complex Geometries of a Wing Box.

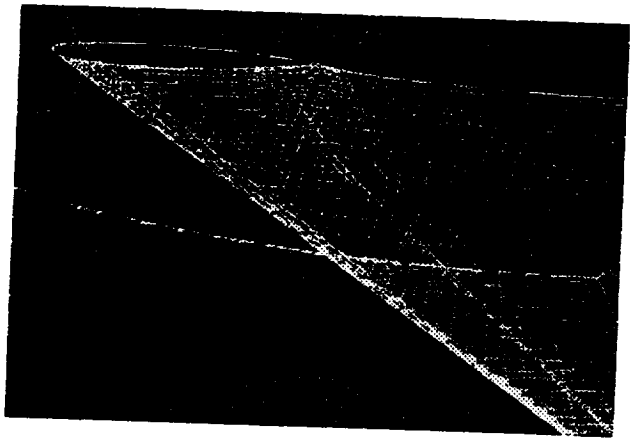

Figure 2. Fluid Grid Around Wing Surface.

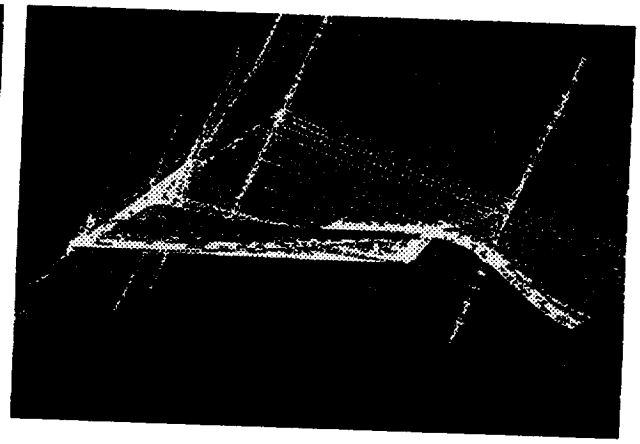

Figure 3. Moving Grid Generation. (viewed from front and upward.)

Example Run on Parallel Computers

The system was applied to the transonic analysis of a high aspect-ratio wing on distributed parallel computers. Configuration of a wing was come from the preliminary design of YXX transport aircraft[11]. A computational model have the following dimensions of NAL (National Aerospace Laboratory) flutter tunnel model with 1/45 size of a full scale aircraft.

Wing span	0.355m
Root chord length	0.125m
Aspect ratio	10
Taper ratio	0.324
Thickness ratio	16%
Kink location length	0.106m
Swept back angle of 32% chord line	17 degree
Airfoil	Super critical

Before applying a computational model to the analysis, structural characteristics was evaluated in comparison with the wind tunnel model. Figure 4 shows the result of a modal analysis of a finite element model, showing 1st bending mode. Current model was tuned to have near frequency of a physical model only for 1st bending. It is our future subject to improve the model accuracy by tuning higher frequencies.

Figure 4. Results of a Modal Analysis.(1st bending mode)

In the distributed parallel environment, 5 different types of parallel computers are connected with 800 MBPS HIPPI switch and data communications between computers are established by Stampi library. Stampi has so developed on the standard MPI(Message Passing Interface) library as to add the capabilities for the communications between different types of parallel computers[12][13]. CFD and CSD codes on different computers are executed simultaneously while each code is parallel-processed. Distributed parallel processing has greatly reduced the required time for the coupling computations as shown in Table 2. Table 2 presents a comparison of the execution times for the single and distributed processing. Single processing case shows CFD, Grid, and CSD prosecces are executed on one computer, and distributed case shows CFD and Grid process are executed on vector computers while CSD process is executed on scaler computer. The names of the computers used are IBM RS6000/SP(scalar type), Hitachi SR2201(scalar type), and Fujitsu VPP300(vector type). As shown in the table, CFD and Grid generator are more efficient when they are executed on vector computer while CSD is more efficient on scalar computer. The best performance has been observed when they are executed on the distributed computers of VPP300 and SR2201.

Table 2. Comparison of the Execution Speed in sec. of Single and Distributed Processing
Type: The type of computer.
Number:The number of processor elements for each process.

Type Number	RS6000/SP (45,1,2)	SR2201 (60,1,3)	VPP300 (8,1,6)	VPP300&SR2201 (14,1.5)
CFD	5.139	2.501	1.645	1.315
Grid	1.183	0.956	0.071	0.071
CSD	0.991	1.139	1.795	0.793
Total	9.152	4.945	2.029	1.395

Conclusion

An approach for constructing a computational platform for multidisciplinary applications of aero-structural simulations has been presented. The major advantages of distributed parallel processing approach are:

- the availability of large CPU numbers and memory spaces.
- the selection of the best suited computers for the specific codes.

Current results have been obtained from the limited runs of the computers. Future works include the flutter analysis by longer computations.

References

[1] "*Summary of Analytical Flutter Investigations for the Model 737 Airplane*," D6-17751,THE BOEING COMPANY COMMERCIAL AIRPLANE DIVISION, 1967.

[2] Schweiger,J.,Krammer,J. and Coetzee,E.,"MDO Application for Active Flexible Aircraft Design," AIAA-98-4835, presented at the 7th AIAA/USAF/NASA/ISSMO Symposium on Multidisciplinary Analysis and Optimization, St. Loius, MO, Sept. 2-4,1998.

[3] Siegel,J.M.,Parthasarathy,V.,Kingsley,G.M.,Dionne,P.J. and Harrand,V.J.,"Application of a Multi-Disciplinary Computing Environment (MDICE) for Loosely Coupled Fluid-Structural Analysis," AIAA-98-4865,presented at the 7th AIAA/USAF/NASA/ISSMO Symposium on Multidisciplinary Analysis and Optimization, St. Loius, MO, Sept. 2-4,1998.

[4] Tinoco,E.N.,"The Changing Role of Computational Fluid Dynamics in Aircraft Development," AIAA-98-2512,presented at the 16th AIAA Applied Aerodynamics Conference, Albuquerque, NM, June 15-18,1998.

[5] Kimura,T., Onishi,R., Ohta,T. and Guo,Z., "Parallel Computing for Fluid/Structure Coupled Simulation," presented at the 10th International Conference on Parallel CFD,Hsinchu, Taiwan, May 11-14,1998.

[6] Onishi,R., Kimura,T., Ohta,T. and Guo,Z., "Development of Parallel Computing Environment for Aircraft Aero-Structural Coupled Analysis," presented at the 9th International Conference on Parallel CFD,Manchester, U.K., May 19-21,1997.

[7] Loehner,R., Yang,C., Cebral,J., Baum,J.D., Luo,H., Pelessone,D. and Charman, C., "Fluid/ Structure Interaction using a Loose Coupling Algorithm and Adaptive Unstructured Grids," AIAA Paper 95-2259,presented at the 26th AIAA Fluid Dynamics Conference, San Diego, CA, June 19-22,1995.

[8] Felker,F.F.,"Direct Solution of Two-Dimensional Navier-Stokes Equations for Static Aeroelasticity Problems," AIAA Journal, Vol. 31, No. 1, January 1993.

[9] Onishi,R.,Kimura,T., Guo,Z. and Iwamiya,T., "Computational Aeroelastics by Coupling Compressible Fluid Equations with Shell Finite-Element Structure," AIAA Paper 98-2407, presented at the 16th AIAA Applied Aerodynamics Conference, Albuquerque, NM, June 15-18, 1998.

[10] Onishi,R.,Kimura,T., Guo,Z. and Iwamiya,T.,
"Coupled Aero-Structural Model: Approach and Application to High Aspect-Ratio Wing-Box Structures," AIAA Paper 98-4837, presented at the 7th AIAA/USAF/NASA/ISSMO Symposium on Multidisciplinary Analysis and Optimization, St. Louis, MO, Sept. 2-4, 1998.

[11] Kheirandish,H.R., Beppu,G. and Nakamichi,J., "Numerical Flutter Simulation of a High-Aspect-Ratio Swept-Back Wing Based on the Navier-Stokes Equations," Journal of the Japan Society for Aeronautical and Space Sciences, Vol. 45, No. 525, Oct. 1997.

[12] Kimura,T. and Takemiya,H., "Local Area Metacomputing for Multidisciplinary Problems: A Case Study for Fluid/Structure Coupled Simulation.", presented at the 12th ACM International Conference on Supercomputing, Melbourne, Australia, July 1998.

[13] Koide,H., Imamura,T., Ohta,H., Kawasaki,T., Takemiya,H., Higuchi,K., Kasahara,H. and, Aikawa,H., "Development of a Message Passing Library for Heterogeneous Parallel Computer Cluster," Proceedings of the Conference on Computational Engineering and Science, Vol. 3, No. 1, May, 1998.

ASTROS*: SEAMLESS INTEGRATION OF ASTROS WITH A UNIFIED AERODYNAMIC MODULE: APPLICATIONS BENCHMARKING AND TESTING

A.G. Striz and S.Y. Jung
The University of Oklahoma, Norman, Oklahoma 73019
Tel.: (405) 325-1730 - Fax: (405) 325-1088 - e-mail: striz@ou.edu

Abstract

This paper reports application cases to benchmark and test the analysis capabilities of the seamless integration of the Automated **STR**uctural **O**ptimization **S**ystem (ASTROS) with a unified steady/unsteady aerodynamics module (ZAERO) called ASTROS*. With these unified aerodynamics, ASTROS* can now perform analysis and design optimization for realistic wing-body configurations throughout the linear subsonic/supersonic and the nonlinear transonic/hypersonic flight regimes. Three fully-built up wing/ fuselage models were used to validate ASTROS* and to show its applicability in all Mach number ranges.

Background and Introduction

ASTROS is a finite element based optimization code tailored to the preliminary design of aerospace structures[1], but applicable to all industries involving light weight structural design coupled with other disciplines. As such, it combines generality with the flexibility of multiple discipline integration. For the design of aircraft, spacecraft, or missiles, ASTROS can save design effort and time, improve flight performance, and reduce structural weight. Specifically, ASTROS was created to allow for the effective multidisciplinary interaction between aerodynamics, structures, controls, and other modules. While an enhancement of the aeroservoelastic capabilities in ASTROS is in progress, the seamless integration of a unified aerodynamic module (ZAERO from ZONA Technology, Inc.) for all Mach numbers with ASTROS has been completed[2]. The resulting code is called ASTROS*. The new module ZAERO, which consists of four steady/unsteady aerodynamic codes, improves the capabilities of ASTROS in several ways: it allows for the modeling, analysis, and optimization of realistic wing-body configurations, and it adds the nonlinear unsteady transonic/hypersonic flow regimes to the Mach number ranges already supported in ASTROS to jointly cover all flight regimes.

Here, the objective was to present benchmarking and applications test cases for the validation of ASTROS* and to exercise some of its new capabilities in the unified flight regime of the subsonic-transonic-supersonic and hypersonic speeds for various wing planforms. The capabilities of the ZAERO module will be briefly described. Three fully built-up aircraft wing models will be introduced which were used to perform the analyses for the benchmarking and testing of ASTROS*. They are the *Generalized Advanced Fighter* (GAF) wing, the *Drones for Aeroelastic and Structural Testing* (DAST) wing, and the *ASTROS* Aeroelastic Wing* (AAW). The metal GAF wing model was generated from MSC/NASTRAN data, obtained from ZONA Technology, Inc.[3] The composite (orthotropic) DAST model was developed from a supercritical wing model used to analyze a drone, flown in a flight test facility[4]. The ASTROS* and MSC/NASTRAN data for this model were generated from Engineering Analysis Language (EAL) data, obtained from NASA Langley Research Center. The AAW model represents a derivative of a MSC/ NASTRAN model supplied by AFRL/WPAFB[5]. For verification and validation, some of the ASTROS* results were compared with those from MSC/NASTRAN and a minimum state flutter solution method.

ZAERO: UAIC Based Aerodynamic Module

The ZAERO module consists of four major steady/unsteady aerodynamic codes that jointly cover the complete flyable Mach number range. Together they enhance the purely subsonic and supersonic capabilities for lifting surface type configurations presently available in ASTROS and MSC/NASTRAN. Thus, the ZAERO module serves as a unified aerodynamic tool for general wing-body configurations throughout all Mach numbers using a AIC (Aerodynamic Influence Coefficient) approach[6]. In detail, the different codes have the following capabilities:

- *ZONA6:* Subsonic steady/unsteady aerodynamics for arbitrary wing-body configurations with or without external stores including body wake effects

- *ZTAIC:* Unsteady transonic AIC method using externally provided steady pressure input

- *ZONA7:* Supersonic steady/unsteady aerodynamics for arbitrary wing-body configurations with or without external stores

- *ZONA7U:* Unified supersonic and hypersonic steady/unsteady aerodynamics for arbitrary wing-body configurations with or without external stores.

Development of Benchmarking Models GAF, DAST, and AAW

In order to benchmark and test the aerodynamic, structural, and aeroelastic analysis as well as structural design optimization capabilities in ASTROS* for multiple disciplines, all three wing models were used. They consisted of fully built-up finite element models with skins, spars, and ribs. In the DAST EAL model, the spaces between the ribs of the original structure were rather large; therefore, many local modes were experienced in the normal modes analysis, causing problems in the flutter analyses. To prevent these local vibration modes, more ribs were added to the original structure. Also, the skins of the DAST wing consisted of composite material. The fuselage was included in the AAW model, and its structural and aerodynamic effects were considered. The GAF and AAW wing models represented fighter wings and were a good choice to test ZONA6 and ZTAIC at the transonic Mach number M = 0.85. Since the DAST model had a supercritical wing thicker than the other two wings, it was already transonic at Mach M = 0.8 and was used to test ZONA6 and ZTAIC at this Mach number. The GAF and AAW wing models were also utilized to test ZONA7 in the supersonic regime; however, the DAST wing was too thick for supersonic flow. Although none of the three models represented hypersonic wings, ZONA7U was tested on the GAF and AAW models at M = 3.0, in the high supersonic/low hypersonic regime.

Application Cases

Structural, aerodynamic, and aeroelastic analyses were performed for the three aircraft wing models (Table 1). For the steady Navier-Stokes flow calculations in the transonic regime, required for the calculation of the transonic aerodynamic influence coefficients in ZAERO, the CFD code ENSAERO[7] was used on a CRAY supercomputer. Then, static structural, normal modes, and flutter analyses were performed for the GAF wing and normal modes, static aeroelastic, and flutter analyses for the DAST and AAW wings. All ASTROS* and MSC/NASTRAN cases were run on SUN SPARC Ultra workstations.

Table 1. Summary of Aircraft Wing Model Analyses

GAF Model	DAST Model	AAW_Model
· Statics · Normal Modes · Flutter - With ZONA6 - With ZTAIC - With ZONA7 - With ZONA7U	· Static Aeroelasticity - With ZONA6 - With ZTAIC · Normal Modes · Flutter - With ZONA6 - With ZTAIC	· Static Aeroelasticity - With ZONA6 - With ZTAIC - With ZONA7 - With ZONA7U · Normal Modes · Flutter - With ZONA6 - With ZTAIC - With ZONA7 - With ZONA7U

The GAF Wing Model:

Structural Configuration, Static Analysis, and Normal Modes Analysis: The GAF wing is composed of spars, ribs, and skins. A leading edge flap and a trailing edge control surface are attached to the main wing box. The wing is cantilevered at the root. The FE model is shown in Figure 1a. Spars, ribs, and skins were modeled by QUAD4 elements, and CELS2 elements were used to connect the control surface to the wing box. The model had 288 nodal points and a total of 530 elements. A static analysis was performed for applied distributed loads. The wing showed a tip displacement under load of 27.068 in. The maximum principal stress was 64,000 psi. The natural frequencies (see Table 2), modes, and generalized stiffness and mass were also calculated. The modes were later used in the flutter calculations.

Aerodynamic Analysis: The steady aerodynamic pressure coefficients as input for ZTAIC were calculated on a CRAY supercomputer using ENSAERO, first in Euler flow, then in Navier-Stokes flow, with a Reynolds number of 10,000,000 and with spanwise and normal viscous terms. For turbulence, the Baldwin-Lomax turbulence model was used and, for vortex flow correction, Degani-Schiff modeling. Iteration indices were less than 1.0E-09 throughout, with 500 Euler flow iterations and at least another 500 Navier-Stokes flow iterations. There were 151, 44, and 34 grid points in the x-, y-, and z-directions, respectively. The number of grid points on the wing surfaces was 61 by 34. Total CPU time for these calculations was about 2 hours per case, which consisted of M = 0.85 and M = 0.90 with angles of attack $\alpha = 0.0°$ and $\alpha = 5.0°$. The higher transonic cases required more iterations to counter slower convergence rates.

Table 2. Aircraft Wing Model Free Vibration Analyses

Mode	Freq. (*Hz.*) - GAF Model	Freq. (*Hz.*) - DAST Model	Freq. (*Hz.*) - AAW Model
1	1.02243E+01	0.00000E+00	0.00000E+00
2	3.09708E+01	0.00000E+00	0.00000E+00
3	3.58906E+01	1.12884E+01	5.47166E+00
4	4.97371E+01	4.86654E+01	9.28638E+00
5	5.80406E+01	5.57209E+01	1.27116E+01
6	6.55094E+01	1.03325E+02	1.36666E+01
7	7.60945E+01	1.30824E+02	1.57567E+01
8	8.47504E+01	1.47822E+02	1.58556E+01

Flutter Analysis: Flutter analyses were performed by the k-method in ASTROS*, the p-k method in MSC/NASTRAN, and by the root-locus method. Mach numbers were M = 0.85 (using ZONA6 and ZTAIC in ASTROS*), M = 1.15 (using ZONA7), and M = 3.0 (using ZONA7U). A comparison of the results is given in Table 3. The generalized aerodynamic loads as calculated in ASTROS* were utilized in the root-locus method. The generalized unsteady aerodynamic force coefficients Q1j at M = 0.85, calculated by ZTAIC, and their approximations by the minimum state method[8] are shown in Fig. 2. The associated V-g and root-locus plots for this case are given in Figures 3 and 4, respectively.

The DAST Wing Model:

Structural Configuration and Normal Modes Analysis: The DAST model was a wing model but had free boundary conditions and could maneuver like a full airplane (Fig. 1b). It was a spar-rib-skin wing made from composite material, specifically, from AS/3501 graphite epoxy with the following lamina stiffnesses: E_1 = 1.8E+6 psi, E_2 = 0.86 E+6 psi, ν_{12} = 0.3, $G_{12} = G_{1z} = G_{2z}$ = 0.46 E+6 psi, ρ = 0.057 lbs/in^3. The strenghts were: $S_L^{(+)}$ = 210,000 psi, $S_L^{(-)}$ = 170,000 psi, $S_T^{(+)}$ = 7,000 psi, $S_T^{(-)}$ = 36,000 psi, S_{LT} = 9,000 psi. The skins were modeled by QUAD4 and TRIA3 plate elements composed of four plies. The asymmetric stacking sequence of these plies was assumed to be [90,±45,0], rather than the simple orthotropic orientations in the EAL model. The spars and ribs also utilized QUAD4 elements. The spar caps were modeled by BAR elements. The total number of nodal points was 428, with a total of 1680 elements. Fuselage weight was added to the model. The model had two trailing edge control surfaces. Again, the natural frequencies (see Table 2), modes, and generalized stiffness and mass were calculated with the first two frequencies corresponding to the rigid body modes plunge and pitch. To calculate eigenvalues, the Inverse Power method was used. Again, the modes were later used in the flutter calculations.

Aerodynamic Analysis: The aerodynamic analysis of the wing was performed by the CFD code ENSAERO as for the GAF wing model. It was shown that the DAST model was just entering the transonic regime at Mach M = 0.7 for zero degree angle of attack, and was fully transonic at Mach M = 0.8. The strength of the shock in Euler flow was larger than that in Navier-Stokes flow.

Steady Aeroelastic Analysis: Since the trailing edge was composed of two straight lines, two CAERO7

Table 3. Flutter Analysis Results of GAF Model

Mach	Method	Flutter Speed (*in/sec*)	Flutter Frequency (*Hz*)	Remarks
0.85	ZONA6	17,336	14.3	
	ZTAIC	18,172	18.1	
	MSC/NASTRAN	15,800	16.7	
	Root-locus (ZONA6)	15,888	17.3	
	Root-locus (ZTAIC)	16,581	15.6	
1.15	ZONA7	20,776	19.8	
	MSC/NASTRAN	14,500	0.0	Divergence
	Root-locus (ZONA7)	14,170	0.0	Divergence
3.0	ZONA7U	31,743	21.1	
	MSC/NASTRAN	36,100	22.0	
	Root-locus (ZONA7U)	33,536	21.3	

entries were chosen, one with 15 by 7 panels for the inboard wing section, the other with 15 by 10 panels for the outboard wing section, for a total of 255 panels. Symmetric static aeroelastic analysis was performed and the trim parameters angle of attack and control surface deflection angle were calculated under a 10g pull-up condition with zero pitching rate and zero pitching acceleration at Mach M = 0.80. The inboard control surface was assumed to be fixed. Grid point displacements and ply stresses in the plate elements were computed at the trim condition. ZONA6 was used for the aerodynamic calculations. The trim parameters for the rigid and flexible structures at this trim condition are given in Table 4. The calculated angle of attack, 4.06° for the rigid case, was reasonable and a large deflection angle, -45.98°, of the control surface was necessary to obtain trim since no horizontal tail was included. The vertical displacement at the wing tip was 5.506 in. The required CPU time was 9 minutes 25.0 seconds

Flutter Analysis: Flutter analyses were performed by the k-method in ASTROS* and by the root-locus method for a Mach number of M = 0.80 using ZONA6 and ZTAIC. The results from ASTROS* and the root-locus method were compared and are shown in Table 5. The generalized unsteady aerodynamic loads calculated in ASTROS* were also used in the root-locus method. The V-g plot for the flutter results by ZONA6 in ASTROS* is shown in Fig. 5. The required CPU time by the k-method and ZONA6 in ASTROS* was 13 minutes 13.5 seconds and that by the k-method and ZTAIC in ASTROS* 5 hours 22 minutes 31.4 seconds, respectively.

The AAW Model:

Structural Configuration and Normal Modes Analysis: The FEM representation of the skins, spars, and ribs consisted of QUAD4 plate elements while those of the horizontal tail, vertical tail, and fuselage were BAR elements. The structural FEM configuration is shown in Fig. 1c. There were nearly 800 grid points and over 2000 elements in the model. The natural frequencies (see Table 2), associated normal modes, and generalized stiffness and mass matrices were calculated as for the GAF model. The Inverse Power method was used. The translation component in the axial direction of the fuselage was fixed. The first two modes were rigid body modes, vertical translation and pitching rotation. These data were used in the subsequent flutter calculations. The required CPU time was 6 minutes 2.7 seconds.

Aerodynamic Analysis: Aerodynamic analyses of the main wing of the AAW model were performed using the CFD code ENSAERO as for the GAF and DAST wing models.

Static Aeroelastic Analysis: The aerodynamic panels of the wing, the horizontal tail, and the vertical tail

Table 4. Trim Parameters of DAST Model: 10*g* Pull-up Maneuver, $M = 0.8$, by ZONA6 of ASTROS*

DEFINITION	LABEL	FLEXIBLE	RIGID	
LOAD FACTOR	"NZ "	3.86399E+03	3.86399E+03	(Input)
PITCH ACCELERATION	"QACCEL"	0.00000E+00	0.00000E+00 *rad/s²*	(Input)
ANGLE OF ATTACK	"ALPHA"	4.03914E+00	4.06115E+00 *deg*	(Computed)
CONTROL SURFACE	"AIL1"	0.00000E+00	0.00000E+00 *deg*	(Input)
CONTROL SURFACE	"AIL2"	-4.50767E+01	-4.59823E+01 *deg*	(Computed)
PITCH RATE	"QRATE"	0.00000E+00	0.00000E+00 *deg/s*	(Input)
THICKNESS/CAMBER	"THKCAM"	1.00000E+00	1.00000E+00	(Input)

Table 5. Flutter Analysis Results of DAST Model at M = 0.80

Method	Flutter Speed (*in/sec*)	Flutter Frequency (*Hz*)
k-method (ZONA6)	14,357.3	48.67
Root-locus (ZOZA6)	13.489.5	36.30
k-method (ZTAIC)	11,800.0	56.01
Root-locus (ZTAIC)	12,892.0	49.30

Table 6. Trim Parameters of AAW Model: 7*g* Pull-up Manuever, $M = 0.85$, by ZONA6 of ASTROS*

DEFINITION	LABEL	FLEXIBLE	RIGID	
LOAD FACTOR	"NZ "	2.70479E+03	2.7047E+03	(Input)
PITCH ACCELERATION	"QACCEL"	0.00000E+00	0.0000E+00 *rad/s²*	(Input)
ANGLE OF ATTACK	"ALPHA"	6.26928E+00	6.9735E+00 *deg*	(Computed)
CONTROL SURFACE	"STBLTR"	2.34365E+00	2.5108E+00 *deg*	(Computed)
PITCH RATE	"QRATE"	0.00000E+00	0.0000E+00 *deg/s*	(Input)
THICKNESS/CAMBER	"THKCAM"	1.00000E+00	1.0000E+00	(Input)

Table 7. Trim Parameters of AAW Model: 7*g* Pull-up Maneuver, $M = 3.0$, by ZONA7U of ASTROS*

DEFINITION	LABEL	FLEXIBLE	RIGID	
LOAD FACTOR	"NZ"	2.70479E+03	2.7047E+03	(Input)
PITCH ACCELERATION	"QACCEL"	0.00000E+00	0.0000E+00 *rad/s²*	(Input)
ANGLE OF ATTACK	"ALPHA"	7.09505E+00	2.1903E+00 *deg*	(Computed)
CONTROL SURFACE	"STBLTR"	-2.32463E+00	2.8218E+00 *deg*	(Computed)
PITCH RATE	"QRATE"	0.00000E+00	0.0000E+00 *deg/s*	(Input)
THICKNESS/CAMBER	"THKCAM"	1.00000E+00	1.0000E+00	(Input)

were modeled using CAERO7 cards. Horizontal and vertical panels were generated separately for the fuselage, using over 40 CAERO7 cards, as well. Over 700 boxes and 1100 aerodynamic grid points were required to calculate the aerodynamic loads for the AAW model. Symmetric static aeroelastic analysis was performed and the trim parameters angle of attack and horizontal control surface deflection angle were calculated under a 7g pull-up trim condition with zero pitching rate and zero pitching acceleration at velocities ranging from transonic to low hypersonic. The main wing flaps were assumed to be fixed. Grid point displacements and element stresses were calculated at this trim condition. ZONA6, ZTAIC, ZONA7, and ZONA7U were used to obtain the aerodynamics at Mach numbers M = 0.85, 0.85, 1.15, and 3.0, respectively. The calculated trim parameters for both the rigid and flexible structure at this trim condition are shown in Tables 6 and 7 for M = 0.85 by ZONA6 and M = 3.0 by ZONA7U, respectively. The required CPU times were 1 hour 10 minutes 6.6 seconds, 6 hours 4 minutes 10.6 seconds, 47 minutes 47.5 seconds, and 49 minutes 59.2 seconds for ZONA7, ZTAIC, ZONA7, and ZONA7U, respectively.

Flutter Analysis: Flutter analyses were performed by the k-method in ASTROS* and by the root-locus method for three aerodynamic regimes: transonic (M = 0.85 by ZONA6 and ZTAIC), low supersonic (M = 1.15 by ZONA7), and high supersonic/low hypersonic (M = 3.0 by ZONA7U). The comparable results from ASTROS* and the root-locus method are listed in Table 8. The generalized unsteady aerodynamic loads from ASTROS* were used in the root-locus method. The V-g plots for the flutter speed determination at M = 0.85 by ZONA6 and at M = *3.0* by ZONA7U are given in Figures 6 and 7.

Table 8. Flutter Analysis Results of AAW Model

Mach Number	Aerodynamic Module	Method	Flutter Speed (*in*/sec)	Flutter Frequency (*Hz*)
0.85	ZONA6	k-method	11,281.4	14.80
		Root-locus	10,978.9	14.77
	ZTAIC	k-method	10,713.7	14.96
		Root-locus	10,537.6	14.73
1.15	ZONA7	k-method	11,087.9	14.90
		Root-locus	11,308.3	14.93
3.0	ZONA7U	k-method	58,768.0	8.55
		Root-locus	No Flutter	

There was no flutter until 50,000 in/sec by the root-locus method and ZONA7U. The required ASTROS* CPU times were 56 minutes 41.7 seconds, 6 hours 59 minutes 52.9 seconds, 39 minutes 57.2 seconds, and 29 minutes 44.4 seconds for ZONA6, ZTAIC, ZONA7, and ZONA7U, respectively.

Conclusions

The benchmarking and testing of the aeroelastic analysis capabilities in the recently modified code ASTROS* throughout the unified subsonic to hypersonic flow regime was the main characteristic of the present research. Three wing models, GAF, DAST, and AAW, were selected and modified as required. ASTROS* was then applied to the models, and the accuracy, ease of use, and applicability of the code to reasonably sized problems was tested. Some of the ASTROS* results were compared to MSC/NASTRAN results, especially in flutter analysis, where the ZAERO results in ASTROS* (k-method) were compared to results from MSC/NASTRAN (p-k-method) and the root-locus method. Acceptable results were obtained for the three models for most of the cases. Some anomalies occurred and need to be investigated further: the results for ZTAIC on the GAF wing showed a higher flutter speed than linear theory; the k-method, p-k method, and root-locus flutter results did not always agree well, especially for the GAF wing, with k-method results generally higher; the results for M = 3.0 are probably questionable as the wings did not represent high supersonic/low hypersonic configurations; the DAST model had to be more heavily modified to obtain acceptable results, most likely due to problems encountered in the EAL/ASTROS* conversion. The best intuitive results were obtained for the DAST and AAW wing models. Therefore, these wing models seem to represent the best choice for use as benchmarks. Additional cases need to be run: for non-symmetric configurations in steady aeroelasticity and flutter; to evaluate other failure modes such as buckling; with high supersonic/low hypersonic models to evaluate ZONA7U; with stores and full bodies to evaluate these respective ZAERO capabilities; modeling a control system with the newly incorporated aeroservoelastic facilities in ASTROS*.

Acknowledgments

The present work was supported in part by a USAF/STTR Phase II contract (No. F33615-96-C-3217) to ZONA Technology, Inc., the University of Oklahoma, and Professor Moti Karpel from Technion University, Israel. The authors gratefully acknowledge support from Silicon Graphics and its CRAY division which allowed them the use of their computers for the CFD computations required in the study.

References

1. Johnson, E.H., and Venkayya, V.B., "Automated Structural Optimization System (ASTROS), Theoretical Manual," AFWAL-TR-88-3028, Vol. 1, December 1988.

2. Chen, P.C., Liu, D.D., Sarhaddi, D., Striz, A.G., Neill, D.J., and Karpel, M., "Enhancement of the Aeroservoelastic Capability in ASTROS," STTR Phase I Final Report, WL-TR-96-3119, Sept. 1996.

3. Chen, P. C., Private Communication, ZONA Technology, Inc., 1997.

4. Murrow H. N., and Eckstrom C. V., "Drones for Aerodynamic and Structural Testing (DAST) - A Status Report", *Journal of Aircraft*, Vol. 16, No. 8, Aug. 1979, pp. 521-526.

5. Pendleton, E., Griffin, K., Kehoe, M., and Perry, B., "A Flight Research Program for Active Aeroelastic Wing Technology", *AIAA-96-1574, Proceedings of the 37th AIAA Structures, Structural Dynamics, and Materials Conference*, Salt Lake City, Utah, April 15-17, 1996, pp. 2263-2273.

6. Chen, P.C., Sarhaddi, D., Liu, D.D., and Karpel, M., "A Unified Aerodynamic-Influence-Coefficient Approach for Aeroelastic/Aeroservoelastic and MDO Applications," AIAA Paper No. 97-1181-CP, 38th AIAA/ASME/ ASCE/AHS/ASC Structures, Structural Dynamics, and Materials Conference, Kissimmee, Florida, April 7-10, 1997.

7. Guruswamy, G. P., "User's Guide for ENSAERO - A Multidisciplinary Program for Fluid/ Structural/ Control Interaction Studies of Aircraft (Release 1)", *NASA TM* 108853, Oct. 1994.

8. Karpel, M., "Physically Weighted Approximations of Unsteady Aerodynamic Forces using the Minimum-State Method", *NASA TP*-3025,1991.

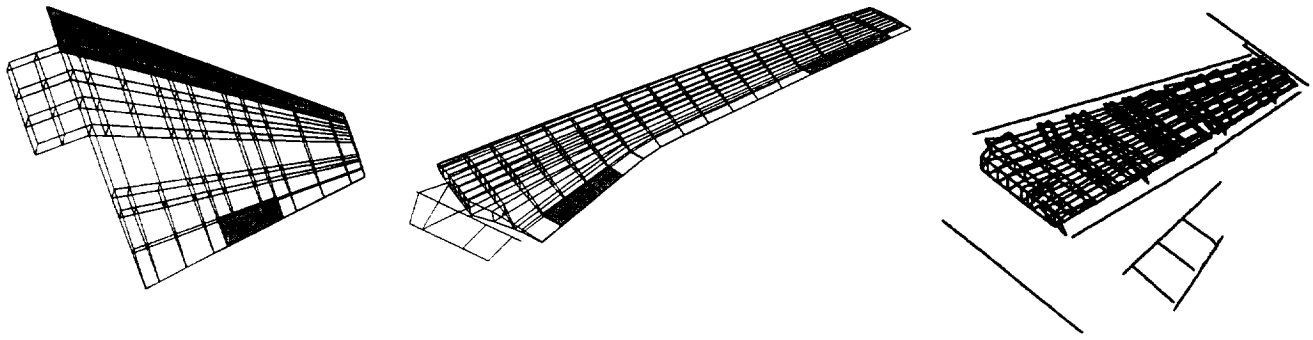

(a) (b) (c)

Figure 1. Wing Models: a) GAF b) DAST c) AAW

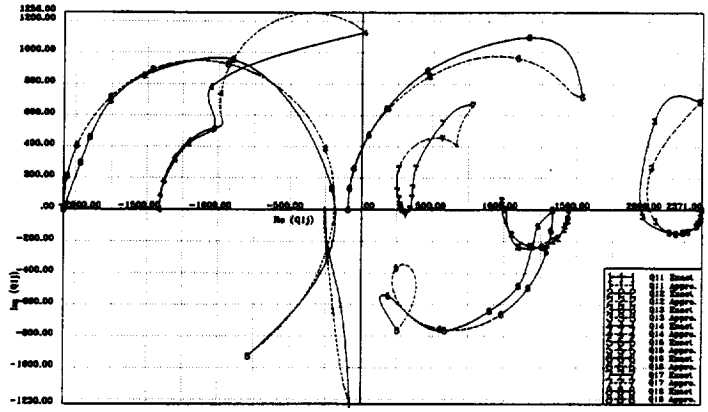

Figure 2. Generalized Unsteady Aerodynamic Coefficients Q_{1j} of GAF Model: M = 0.85, by ZTAIC of ASTROS* and Approximated by the Minimum State Method

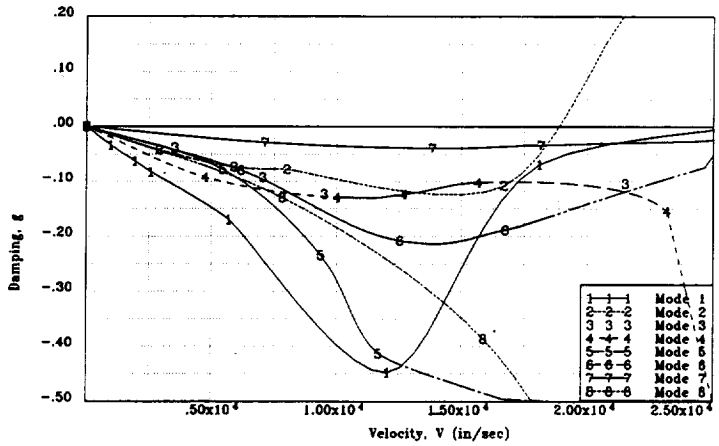

Figure 3. V-g Plot of GAF Model: M = 0.85, by ZTAIC of ASTROS* (Flutter Speed = 18,172 in/sec, Flutter Frequency = 18.1 Hz)

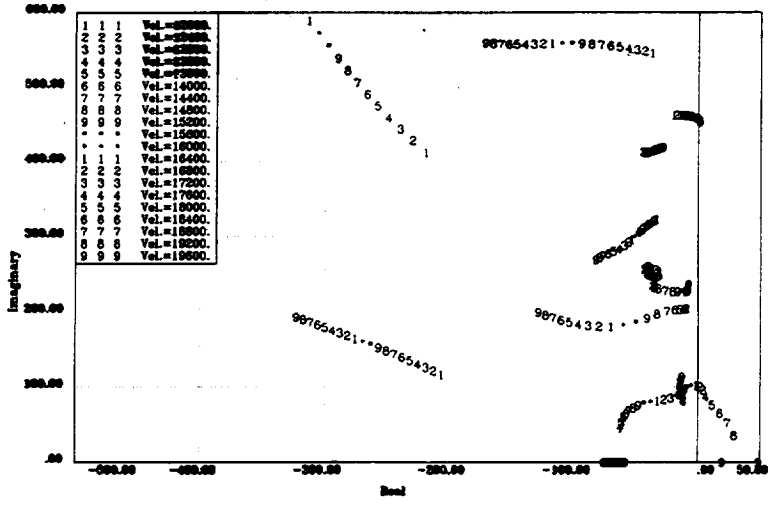

Figure 4. Root-Locus Plot of GAF Model: M = 0.85, using ZTAIC of ASTROS* (Flutter Speed = 16,581 in/sec, Flutter Frequency = 15.6 Hz)

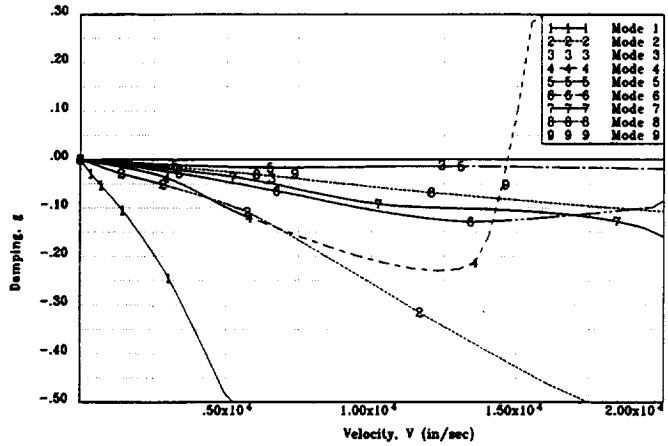

Figure 5. V-g Plot of DAST Model: M = 0.80, by ZONA6 of ASTROS*
(Flutter Speed = 14,358 in/sec, Flutter Frequency = 48.67 Hz)

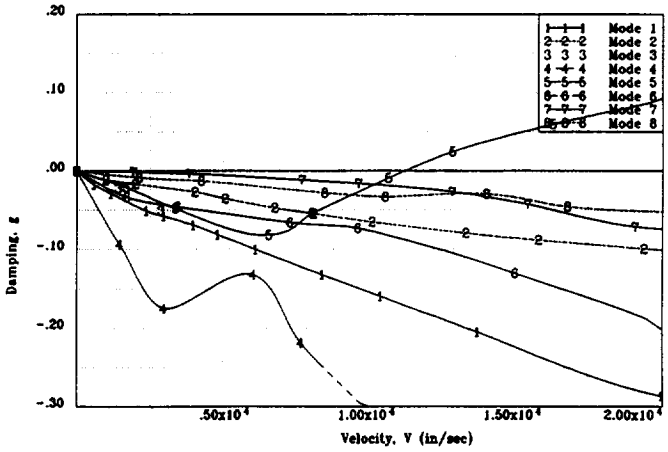

Figure 6. V-g Plot of AAW Model: M = 0.85, by ZONA6 of ASTROS*
(Flutter Speed = 14,358 in/sec, Flutter Frequency = 48.67 Hz)

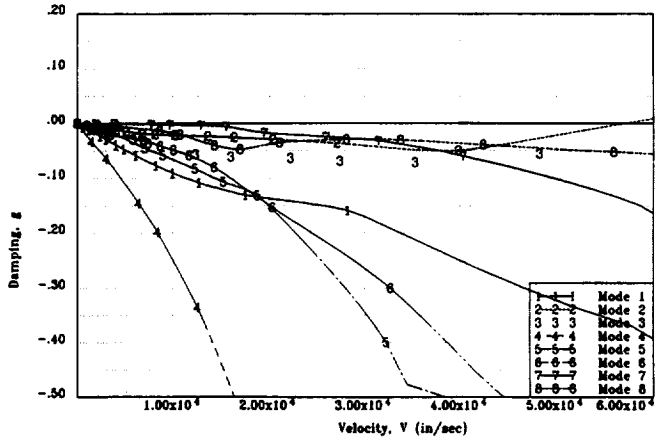

Figure 7. V-g Plot of AAW Model: M = 3.00, by ZONA7U of ASTROS*
(Flutter Speed = 58,768 in/sec, Flutter Frequency = 8.55 Hz)

Characterizing the Effects of Geometrical Nonlinearities on Aeroelastic Behavior of High-Aspect-Ratio Wings

Mayuresh J. Patil*, Dewey H. Hodges†
Georgia Institute of Technology, Atlanta, Georgia
and
Carlos E. S. Cesnik‡
Massachusetts Institute of Technology, Cambridge, Massachusetts

This paper presents the results of nonlinear aeroelastic analysis of a representative large-aspect-ratio wing. The effects of steady-state lift and drag are characterized and quantified. Certain simplifications for obtaining nonlinear results are given and a way of avoiding deleterious nonlinear effects is presented.

Introduction

There has been a growing interest in High Altitude, Long Endurance (HALE) aircraft in recent years. These aircraft are being considered for unmanned reconnaissance mission, long term surveillance, environmental sensing and also for communications relay. Such aircraft have slender wings (aspect ratio of the order of 35), which are highly flexible. Due to the high flexibility and large aspect ratios, large deflections can result, reaching about 25% of wing semispan. Linear theory fails to accurately analyze such deformation and the changes in the stiffness and dynamic characteristics of the wing (e.g., natural frequencies) accompanying such deformation. Linear theory thus fails to give accurate estimates of the speeds at which aeroelastic instabilities occur.

Aeroelastic characteristics of highly flexible aircraft has been investigated by van Schoor and von Flotow[1] The complete aircraft was modeled using a few modes of vibration, including rigid-body modes. Linear aeroelastic and flight dynamic analysis results for a HALE aircraft are presented by Pendaries[2] The results highlight the effects of wing flexibility on the aeroelastic characteristics of the wing and aircraft flight dynamic characteristics. Both analyses, though focused on the aeroelastic characteristics of high-aspect-ratio wings, are linear and do not take into account the geometrical nonlinearities induced by large deflections.

As will be shown in this paper, it is of primary importance to analyze the structure using accurate geometrically nonlinear structural models. It is necessary here to reiterate that such analyses are not only required in extreme situations but are even necessary under normal flight conditions. The wings of HALE

*Graduate Research Assistant, School of Aerospace Engineering Member, AIAA.
†Professor, School of Aerospace Engineering, Fellow, AIAA. Member, AHS.
‡Assistant Professor of Aeronautics and Astronautics. Senior Member, AIAA. Member, AHS.

aircraft are highly curved during flight. Curved beams behave very differently from straight wings. The static, dynamic and aeroelastic characteristics of curved wings are affected by curvature-induced changes in the effective bending-torsion coupling and the direction of aerodynamic loading. It is necessary to take these effects into account when analyzing a flexible and curved high-aspect-ratio wing, regardless of whether the wing is pre-curved or curved due to structural deformation.

Present Model

The present study analyzes a high-aspect-ratio wing as a beam. A complete nonlinear mixed variational formulation is used for the structural dynamics of the wing.[3] Two-dimensional (2-D) unsteady finite state aerodynamics theory is used for the loading. 2-D aerodynamics is an ideal approximation for such large aspect ratios. The formulation and analysis is given in detail in Ref. 4.

By using simple shape functions, the mixed variational formulation leads to a set of coupled nonlinear differential equations in terms of the element displacements (u) and rotations (θ), nodal internal forces (F) and moments (M), and linear and angular momenta (P and H). The equations are presented here for the i^{th} finite element,

$$\begin{gathered}
\tfrac{\Delta\ell}{2}[-C^{ab}(I-C^{bw})e_1+C^{aw}\gamma]^i+u^i+\tfrac{\Delta\ell}{2}[-C^{ab}(I-C^{bw})e_1+C^{aw}\gamma]^{i+1}-u^{i+1}=0 \\
\tfrac{\Delta\ell}{2}[(I+\tfrac{\widetilde{\theta}}{2}+\tfrac{\theta\theta^T}{4})C^{ab}\kappa]^i+\theta^i+\tfrac{\Delta\ell}{2}[(I+\tfrac{\widetilde{\theta}}{2}+\tfrac{\theta\theta^T}{4})C^{ab}\kappa]^{i+1}-\theta^{i+1}=0 \\
-\dot{P}-\widetilde{\Omega}P-mgC^{wi}e_3+f_a+\Delta\ell(\widetilde{k}_b+\widetilde{\kappa})(\tfrac{F^-+F^+}{2})+F^+-F^-=0 \\
\begin{gathered}
-\dot{H}-\widetilde{\Omega}H-\widetilde{V}P-mg\widetilde{\zeta}_{cg}C^{wi}e_3+\widetilde{\zeta}_{ac}f_a+m_a+ \\
\Delta\ell(\widetilde{e}_1+\widetilde{\gamma})(\tfrac{F^-+F^+}{2})+\Delta\ell(\widetilde{k}_b+\widetilde{\kappa})(\tfrac{M^-+M^+}{2})+M^+-M^-=0
\end{gathered} \qquad (1) \\
\dot{u}+V_0+\widetilde{\Omega}_0(r_b+u)-C^{aw}V=0 \\
\dot{\theta}+(I+\tfrac{\widetilde{\theta}}{2}+\tfrac{\theta\theta^T}{4})C^{ab}(C^{wa}\Omega_0-\Omega)=0
\end{gathered}$$

where γ and κ, the strains and curvatures, are related to F and M via a cross-sectional constitutive law, and V and Ω, the linear and angular velocities, are related to P and M using the cross-sectional inertial properties. The direction cosine matrix C^{xy} transforms the components of a vector from the y-frame to x-frame. The frames a, b, w are, respectively, at the wing root, at an arbitrary undeformed wing cross section, and at an arbitrary cross section of the deformed wing.

f_a and m_a are the aerodynamic forces and moments acting on each element, and are calculated using geometrically exact airloads model coupled with a linear finite state inflow model given briefly as,

$$\frac{1}{2\pi\rho}\{L_n\}=-b^2[M]\left\{\ddot{h}_n+\dot{v}_n\right\}-bU_0[C]\left\{\dot{h}_n+v_n-\lambda_0\right\}-{U_0}^2[K]\{h_n\}-b[G]\left\{\dot{U}_0h_n-U_0v_n+U_0\lambda_0\right\} \quad (2)$$

where the equations are in terms of coefficients of the Glauert expansion, L is the pressure distribution, U is the freestream velocity, v is the velocity perpendicular to the airfoil, h is the airfoil deformation, λ is the induced flow, and $[M]$, $[C]$, $[K]$, $[G]$ are constant matrices given in Ref. 5.

Table 1: Model data

WING	
Half span	16 m
Chord	1 m
Mass per unit length	0.75 kg/m
Mom. Inertia (50% chord)	0.1 kg m
Spanwise elastic axis	50% chord
Center of gravity	50% chord
Bending rigidity	2×10^4 N m^2
Torsional rigidity	1×10^4 N m^2
Bending rigidity (edgewise)	CaseStiff: 5×10^6 N m^2
	CaseFlex: 1×10^6 N m^2
FLIGHT CONDITION	
Altitude	20 km
Density of air	0.0889 kg/m^3

The induced flow is calculated by a finite-state induced flow model, which is expressed as a set of first-order differential equations approximating the unsteady flow over an airfoil, viz.,

$$[A]\{\dot{\lambda}_n\} + \{\lambda_n\} = \{c\}\left(\dot{v}_0 + \frac{1}{2}\dot{v}_1\right) \tag{3}$$

where $[A]$ and $\{c\}$ are constant matrices given in Ref. 6.

By coupling the aerodynamic and structural equations the complete nonlinear aeroelastic model is obtained. There are various analyses possible with such an analysis tool. Firstly, it is used to calculate the nonlinear steady state for the given flight parameters. One could then linearize the problem about this nonlinear steady state to get the instability speed. This instability speed predicts whether infinitesimal disturbances are amplified or alleviated. If they grow (e.g., there is an instability), however, then a time-marching solution is required to determine the amplitude of limit-cycle oscillations.

Results and Discussion

The objectives for this research have been to analyse the aeroelastic behavior of high-aspect-ratio wings while taking into consideration the non-trivial steady state and obtain some understanding as to the changes caused by large deflections, the nature and occurence of these effects and the nessecity and sufficiency of the theories in including the nonlinear effects. The case used for this study is a slender wing with semispan-aspect-ratio of 16.[7] The results are presented for two values of edgewise bending rigidity (denoted as CaseStiff and CaseFlex), because the aeroelastic behavior has strong dependence on the frequency distribution of various mode (including edgewise bending mode). The model data for the case is presented in Table 1.

Linear Results

Table 2 presents the natural frequencies for the wing. The two cases considered are such that in CaseFlex the first edgewise bending mode frequency is lower than the torsional mode and in CaseStiff it is

Table 2: Linear frequency results

	CaseStiff	CaseFlex
1^{st} Flatwise Bending	2.247	2.247
2^{nd} Flatwise Bending	14.61	14.61
3^{rd} Flatwise Bending	44.01	44.01
1^{st} Torsion	31.15	31.15
1^{st} Edgewise Bending	35.49	15.87

Table 3: Comparison of linear aeroelastic results

	Present Analysis	Analysis of Ref. 8	% Diff.
Flutter Speed	32.21	32.51	-0.9
Flutter Frequency	22.61	22.37	+1.1
Divergence Speed	37.29	37.15	+0.4

higher. The flatwise bending mode frequencies are an order of magnitude lower than the edgewise bending and torsional frequencies, a normal occurance in high-aspect-ratio wings.

Table 3 presents the linear flutter results for the wing at an altitude of 20 km above sea level where high-altitude long-endurance (HALE) aircrafts are expected to fly. The results are compared with those obtained by linear flutter code based on modal solution[8] and a satisfactory correlation is observed. Note that the linear flutter results are unaffected by the edgewise bending modes and thus are the same for both CaseStiff and CaseFlex cases.

Effect of Steady-State Lift

The aircraft in flight is supported by the lift produced by the wing. This lift in turn produces deflections of the wing. For low-aspect-ratio wings the steady-state deflections are small and the nonlinearities negligible. With increasing aspect ratio, there is increase in the root bending moment for the same loading, leading to increase in the curvature of the wing. Also the total deflection of the wing is magnified due to the long length. Thus large deflections are expected in a high-aspect-ratio wing, even at normal steady-state loads.

The lift and the associated deflection lead to a drastic change in the structural dynamic characteristics of the wing and consequently a possibly catastrophic change in aeroelastic stability. To investigate these effects, nonlinear aeroelastic analysis is conducted on the wing model about a steady state obtained by assuming a constant load distribution over the wing. Figs. 1 and 2 show the change in the structural dynamic frequencies with wing loading for the two cases. The maximum tip deflection (at load of 20 N/m) is less then 25% of the wing span. However, the curvature and the corresponding internal strains are still small. The high deflections are a result of the length of the beam. The flatwise frequencies seem to remain almost constant. The edgewise bending and torsion modes are the ones that are significantly affected. The deflection of the wing leads to a structural coupling between the torsion and edgewise bending modes. For CaseStiff, there is a decrease in the (originally) torsional mode frequency and increase in the (originally)

edgewise bending mode frequency, while for CaseFlex it is the opposite. Basically the higher frequency increases further and the lower frequency decreases.

Though change of frequencies in flight is a matter of concern, it is the changes in aeroelastic characteristics that are very important. Fig. 3 shows the changes in the flutter speed and frequency with wing loading for CaseStiff. There is a drastic decrease in flutter speed with increase in wing loading. This can be attributed to the decrease in frequency with wing loading. There is almost a 50% decrease in flutter speed which significantly compromises the flight envelope. Also this decrease occurs for low wing loadings, and thus this effect will occur even at normal flight conditions. Therefore, it is nessecary to include such effects – not only during the detailed analysis stage – but even during the preliminary design stage, the stage at which the avoidance of such deleterious effects could effect the largest cost reduction.

The nonlinear flutter results for CaseFlex are even more surprising. By comparing with CaseStiff, one would expect that the flutter speed for CaseFlex would increase with wing loading, since the torsional mode frequency increases; and it does as seen in Fig. 4. But unexpectedly the edgewise bending mode becomes unstable at a lower speed at the slightest wing deflection. Now such behavior is of immediate concern since it is in general practically impossible to have a straight wing even for no wing loading. The behavior can be attributed to the fact that an infinitesimal deflection induces a coupling between the torsion and edgewise bending modes. It is this torsional content in the lower frequency edgewise bending mode that leads to the instability. And since the pure edgewise mode is just neutrally stable, any small amount of coupling is enough to destabilize it, thus the jump in flutter data. Fig. 5 shows the frequency and damping versus velocity plots for various wing loading conditions. The various wing loadings leads to levels of nonlinearities and consequently levels of coupling. At very low wing loading (1 N/m), there is less coupling and the instability is quite weak. It can be expected that a small amount of structural damping as well as the neglected aerodynamic drag should be able to eliminate this weak instability. Thus, even though the flutter speed is around 22 m/s, the actual system may not exhibit catastrophic failure until about 34 m/s where there is a much stronger instability. The strength of the instability increases with increase in the wing loading. As can be seen in Fig. 5, at 10 N/m, there is sufficient coupling and the flutter is stronger and would need to be taken seriously. Another way of understanding this instability is by plotting the unstable damping at a fixed velocity with change in wing loading. Fig. 6 shows such a plot of modal frequency and damping at 25 m/s. The continous increase in the unstable damping from zero (neutral stability) to high values (strong instability) are indicative of the smooth transition in the system behavior. Whether or not the lower flutter mode is significant depends completely on the frequencies, which in turn depends on the wing loading and the coupling introduced by this nonlinearity.

Characterizing the Lift-Induced Nonlinearities

The nonlinear effects that were presented in the earlier section significantly change the aeroelastic behavior of high-aspect-ratio wings. Though it has been explained physically in the earlier section, there is a need to dig deeper into the equations and find the source of the nonlinearities and use it to effectively analyse the system.

The source of the nonlinearity comes from the fourth equation in the equation set (1). In the undiscretized form, the equation can be written as,

$$-\dot{H} - \tilde{\Omega}H - \tilde{V}P - mg\tilde{\zeta}_{cg}C^{wi}e_3 + \tilde{\zeta}_{ac}f_a + m_a + (\tilde{e}_1 + \tilde{\gamma})F + (\tilde{k}_b + \tilde{\kappa})M + M' = 0 \tag{4}$$

Here, the term $\tilde{\kappa}M$ is the dominant nonlinear term, where κ and M were introduced before. If the equation is linearized about a steady state, we get two terms, $\tilde{\bar{\kappa}}\hat{M} + \tilde{\hat{\kappa}}\bar{M}$, where $\bar{(\,)}$ is the steady state value and $\hat{(\,)}$ is the perturbation. It is obvious here that if there is a steady-state bending moment (and corresponding

Table 4: Comparison of curved beam and fully nonlinear analyses

	CaseStiff			CaseFlex		
	Fully Nonlinear	Curved Beam	% Error	Fully Nonlinear	Curved Beam	% Error
Tors. - Edge. Bend. Freq.	17.10	16.39	-4.2	35.37	35.76	+1.1
Edge. Bend. - Tors. Freq.	43.95	44.19	+0.5	12.64	12.33	-2.5
Flutter Speed	22.36	22.37	+0.1	22.25	21.98	-1.2
Flutter Freq.	15.83	15.23	-3.8	12.18	11.88	-2.5

curvature) in the flatwise direction, the above terms will affect the torsion and edgewise bending equations (due to the cross product). It is important here to note that there will be two terms affecting the torsion and edgewise bending equations. One term is due to the steady-state moment ($\bar{M}$) and the other due to steady-state curvature ($\bar{\kappa}$). Out of these two terms, it is the one due to the steady-state curvature that is more important because of the ratios of the flatwise bending rigidity to the other cross-sectional rigidities being small. This implies that one could approximate the nonlinear behavior by assuming a curved beam represented by the nonlinear steady state and not considering the internal moments that are actually present.

Linear curved beam aeroelastic analysis where the beam shape is based on the actual nonlinear deflection of the beam (which can be easily calculated using a simple nonlinear beam analysis) is much simpler to implement then is a complete nonlinear analysis as presented here. For a high-aspect-ratio wing with low wing loading, such an analysis may give sufficiently accurate results for the changes in aeroelastic behavior of a lifting wing. To test this hypothesis, aeroelastic analysis is conducted on a curved beam with the same curvature as that obtained when the wing is loaded with 10 N/m loading. The results are presented in Table 4 and compared with those obtained by using the complete nonlinear analysis. The results show that more than 95% accuracy can be obtained by simple curved wing aeroelastic analysis, and show that the nonlinearity due to steady state curvature is the most important nonlinearity for a long slender wing.

Another point of interest here is the aerodynamic nonlinearity induced due to the large deflection. Due to the large slope of the beam deflection, the lift which is perpendicular to the wing acts at an angle pointing towards the center of the aircraft. This lead to a decrease in the effective lift in the vertical direction. Such nonlinearity are more important in the static steady-state calculation and have been discussed in detail in Ref. 7

Avoiding Catastrophic Decrease in Flutter Speed

From the earlier sections it is clear that wing bending leading to large deflections in a slender wing can lead to dangerous aeroelastic repurcussions. But, it also points out the major culprit; the wing curvature due to deformation leads to torsion-edgewise bending coupled modes which can be destabilized. Thus it is important to control the curvature of the beam. One could increase the stiffness of the beam, but that would lead to an increase in the overall weight. A much simpler way would be to pre-curve the wing downwards so that at nominal flight condition the wing is as close to a straight wing as possible. One could optimize the pre-curvature to give maximum flutter clearance over all expected flight conditions.

Assuming that the nominal flight condition leads to a wing loading of 10 N/m, one could seek to minimize the wing deflection by constructing a wing with constant pre-curvature. Such a pre-curved

Table 5: Comparison of pre-curved beam and straight wing results

	CaseStiff Wing			CaseFlex Wing		
	Pre-curved (nom. load)	Straight (nom. load)	Straight (no load)	Pre-curved (nom. load)	Straight (nom. load)	Straight (no load)
Tors. - E. Bend. Freq.	26.04	17.10	31.15	30.74	35.37	31.15
E. Bend. - Tors. Freq.	39.27	43.95	35.49	15.50	12.64	15.87
Flutter Speed	30.17	22.36	32.21	22.08	22.25	32.21
Flutter Freq.	21.26	15.83	22.61	15.39	12.18	22.61

Table 6: Effect of drag for CaseFlex

	Results with Drag	Linear Results
Flat. Bending Freq.	2.257	2.247
Torsion Freq.	31.15	31.15
Flutter Speed	32.26	32.21
Flutter Freq.	22.66	22.61

model was used and aeroelastic analysis was conducted at nominal flight condition. It is neccesary here to point out that the cross-sectional coefficients change with curvature. Here, the curved beam analysis was conducted using the given cross-sectional coefficients for simplicity. For more consistent results one would need to use an appropriate cross-sectional analysis tool, *e.g.*, Ref. 9. Table 5 gives the torsion-edgewise bending frequencies and the flutter results of a pre-curved wing under nominal conditions and compares them with the straight wing results with and without the nominal load. By introducing the pre-curvature, the linear straight wing results are partly recovered. For CaseStiff, there is 35% increase in the flutter speed at nominal condition. Fig. 7 shows the damping and frequency plot with corresponding plots for the straight wing. It is again seen that precurvature leads to decrease in the detrimental nonlinear effects of lift. For CaseFlex, the flutter results are similar to those obtained for a lower wing loading, *i.e.*, the lower flutter mode is weaker and the higher flutter mode occurs at lower velocity. Thus even though there is no significant change in the flutter speed, the flutter is weaker in a pre-curved wing and thus might be overcome easily by inherent structural and aerodynamic damping (Fig. 8).

Effect of Drag

The effect of drag on the aeroelastic response has also been shown to be important in some cases. To qualitatively investigate the effect of drag, a constant wing loading in the edgewise direction is added assuming a lift-to-drag ratio of 5, which is very low and thus gives an idea as to the maximum effect of drag. At the nominal condition of drag wing loading of 2 N/m (20% of lift) the frequencies and aeroelastic damping results are calculated for CaseFlex and presented in Table 6. It clearly shows that the effect of drag is negligible even for the flexible case, much less than the large effect of lift.

Conclusion

Nonlinear aeroelastic analysis has been conducted on a representative high-aspect-ratio wing. The nonlinear effects of steady-state lift and drag have been investigated, and an effective way of avoiding catastrophic changes in aeroelastic behavior has been pointed out. From the foregoing results and discussions one can draw the following conclusions:

- There is a drastic change in the structural and aeroelastic characteristics of high-aspect-ratio wings under nominal wing loads.
- The type of nonlinear aeroelastic behavior is intimately connected with the distribution of modal frequencies relative to each other and the corresponding normal mode shapes, including flatwise bending, torsion and edgewise bending modes.
- The dominant geometrically nonlinear effect comes from the non-zero steady-state curvature, and thus the effect of nonlinear behavior on the linearized stability can be fairly accurately predicted by using a linear analysis for curved beams.
- The decrease in flutter speed due to large deflections may be essentially cancelled out by pre-curving the wing so as to get an approximately straight wing at nominal flight condition.

Acknowledgments

This work was supported by the U.S. Air Force Office of Scientific Research (Grant number F49620-98-1-0032), the technical monitor of which is Maj. Brian P. Sanders, Ph.D.

References

[1] van Schoor, M. C. and von Flotow, A. H., "Aeroelastic Characteristics of a Highly Flexible Aircraft," *Journal of Aircraft*, Vol. 27, No. 10, Oct. 1990, pp. 901 – 908.

[2] Pendaries, C., "From the HALE Gnopter to the Ornithopter - or how to take Advantage of Aircraft Flexibility," In *Proceedings of the 21st Congress of the International Council of the Aeronautical Sciences*, Melbourne, Australia, Sept. 13 – 18, 1998, A98 - 31715.

[3] Hodges, D. H., "A Mixed Variational Formulation Based on Exact Intrinsic Equations for Dynamics of Moving Beams," *International Journal of Solids and Structures*, Vol. 26, No. 11, 1990, pp. 1253 – 1273.

[4] Patil, M. J., Hodges, D. H., and Cesnik, C. E. S., "Nonlinear Aeroelastic Analysis of Aircraft with High-Aspect-Ratio Wings," In *Proceedings of the 39th Structures, Structural Dynamics, and Materials Conference*, Long Beach, California, April 20 – 23, 1998, pp. 2056 – 2068.

[5] Peters, D. A. and Johnson, M. J., "Finite-State Airloads for Deformable Airfoils on Fixed and Rotating Wings," In *Symposium on Aeroelasticity and Fluid/Structure Interaction, Proceedings of the Winter Annual Meeting*. ASME, November 6 – 11, 1994.

[6] Peters, D. A., Karunamoorthy, S., and Cao, W.-M., "Finite State Induced Flow Models; Part I: Two-Dimensional Thin Airfoil," *Journal of Aircraft*, Vol. 32, No. 2, Mar.-Apr. 1995, pp. 313 – 322.

[7] Patil, M. J., Hodges, D. H., and Cesnik, C. E. S., "Nonlinear Aeroelasticity and Flight Dynamics of High-Altitude Long-Endurance Aircraft," In *Proceedings of the 40th Structures, Structural Dynamics and Materials Conference, Saint Louis, Missouri*, April 12 – 15, 1999, pp. 1113 – 1123, AIAA Paper 99-1470.

[8] Patil, M. J., "Aeroelastic Tailoring of Composite Box Beams," In *Proceedings of the 35th Aerospace Sciences Meeting and Exhibit*, Reno, Nevada, Jan. 1997.

[9] Cesnik, C. E. S., Hodges, D. H., and Sutyrin, V. G., "Cross-Sectional Analysis of Composite Beams Including Large Initial Twist and Curvature Effects," *AIAA Journal*, Vol. 34, No. 9, Sept. 1996, pp. 1913 – 1920.

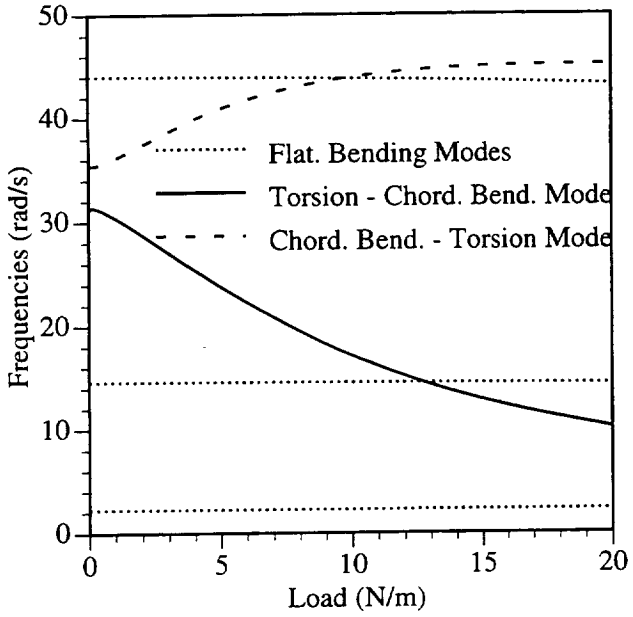

Figure 1: Variation of frequency with load for CaseStiff

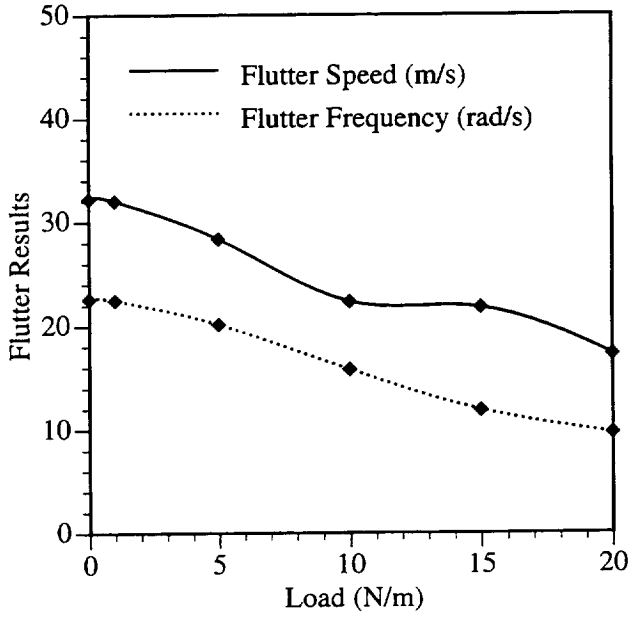

Figure 3: Variation of flutter results with load for CaseStiff

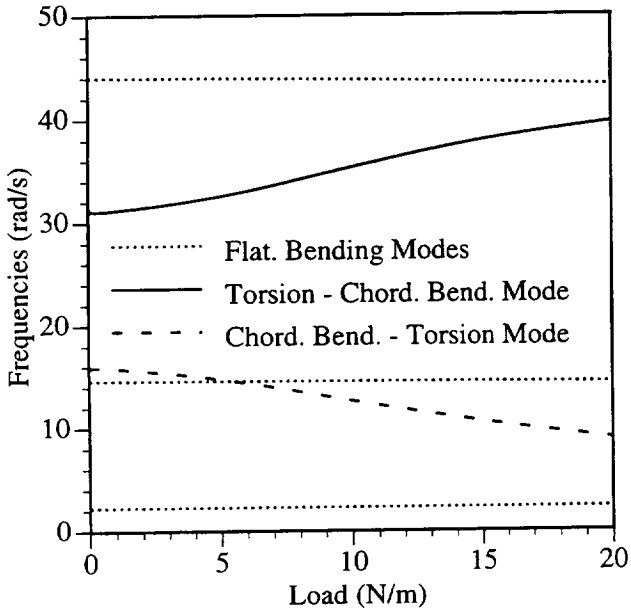

Figure 2: Variation of frequency with load for CaseFlex

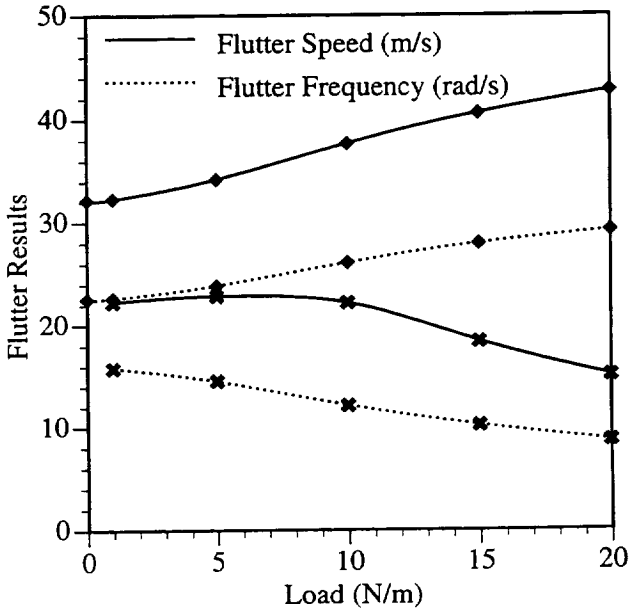

Figure 4: Variation of first two flutter modes with load for CaseFlex

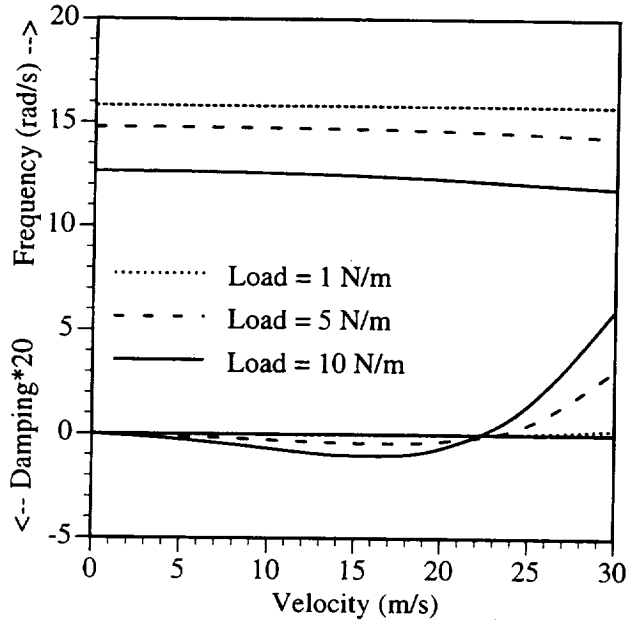

Figure 5: Variation of modal frequency and damping for various loadings (CaseFlex)

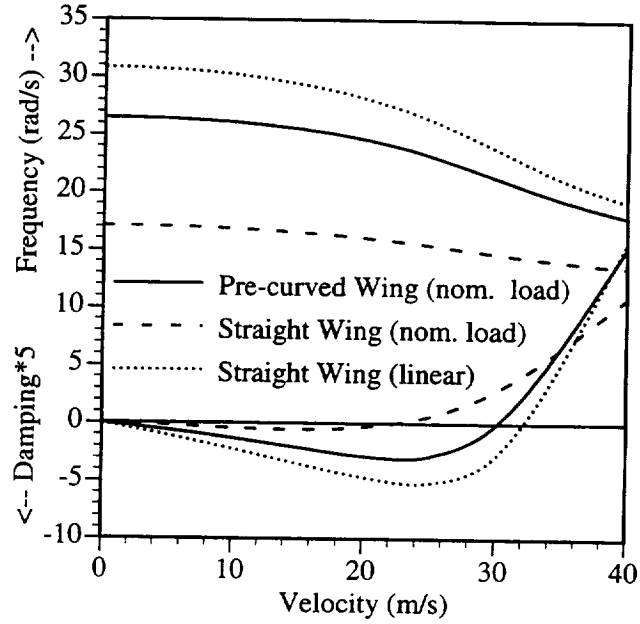

Figure 7: Effect of precurvature on the modal frequency and damping of CaseStiff

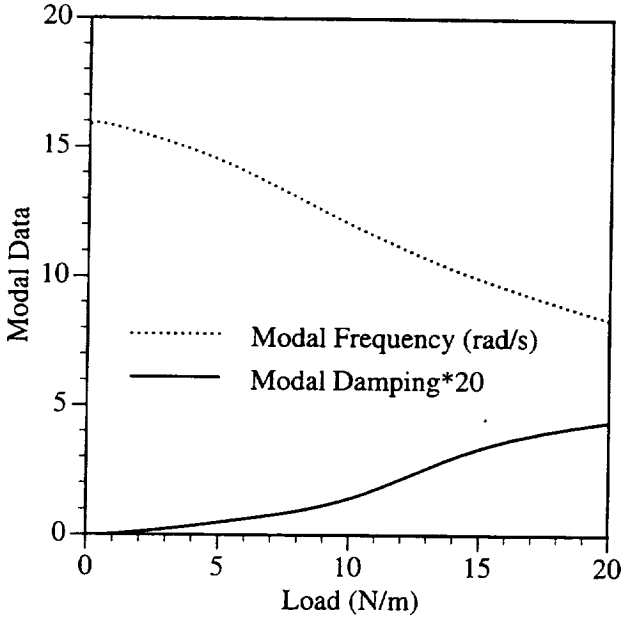

Figure 6: Variation of modal frequency and damping with loadings at velocity of 25m/s (CaseFlex)

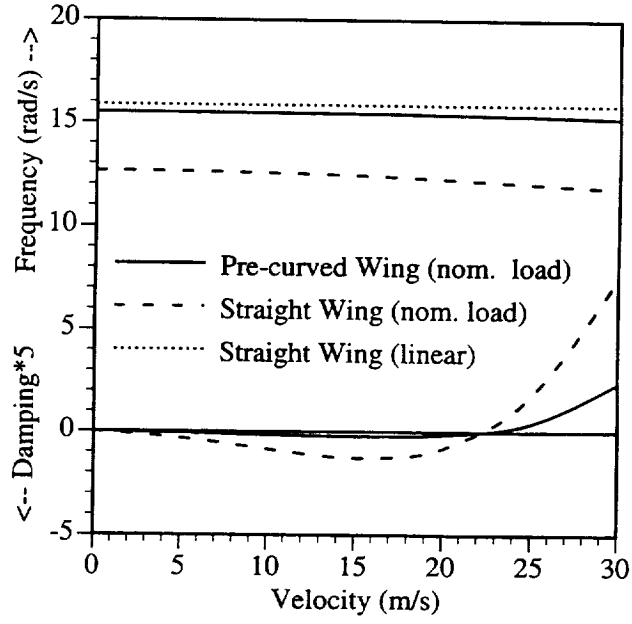

Figure 8: Effect of precurvature on the modal frequency and damping of CaseFlex

Simulation of Non-Linear Transonic Aeroelastic Behavior on the B-2

D.R. Dreim, S.B. Jacobson, and R.T. Britt
Northrop Grumman Integrated Systems and Aerostructures
Pico Rivera, California

Abstract

At high subsonic flight speeds, large flexible aircraft begin to encounter unsteady airloads which are not predicted by most currently available aerodynamic analysis and design methods. With increasing speed and the development of transonic flow and shocks, viscous effects quickly become very important, and flow separation can occur. The Northrop Grumman USAF B-2 Bomber encountered a nonlinear aeroelastic Residual Pitch Oscillation (RPO) under these conditions. Simulation studies were performed with the Computational Aeroelasticity Program-Transonic Small Disturbance, Viscous (CAPTSDv) computer program to evaluate its ability to predict these nonlinear aeroelastic responses. Open and closed loop simulations were performed to assess the participation of the flight control system. Control system actuator hysteresis characteristics were modeled and found to be a significant participant in the RPO phenomenon. Simulations were also performed for varying Mach numbers and altitudes to establish the stability boundaries and compare with flight test data. These CAPTSDv simulations compared well with flight data and revealed many potential further modeling enhancements.

Key Words

Residual pitch oscillation, Limit cycle oscillation, Shock induced oscillation, Transonic aerodynamics, Body freedom flutter, Hump mode, Computational fluid dynamics, Computational aeroelasticity.

Introduction

At high subsonic flight speeds, large flexible aircraft begin to encounter unsteady airloads which are not predicted by most currently available aerodynamic analysis and design methods. With increasing speed and the development of transonic flow and shocks, viscous effects quickly become very important, and flow separation can occur.

The Northrop Grumman USAF B-2 Bomber encountered a nonlinear aeroelastic Residual Pitch Oscillation (RPO) during low altitude high speed flight. The RPO response was observed after control surface pitch doublets were input at flight conditions outside the operational envelope[1]. The initial air vehicle response decayed in amplitude but transitioned to a small, constant amplitude, residual pitch oscillation after several cycles.

Eleven additional dedicated flights were performed to investigate the RPO phenomenon. The pitch oscillation was characterized by a rapid decrease in damping over a very narrow Mach number range. The RPO motion was dominated by an interaction of the rigid body short period mode and the 1st flexible symmetric bending mode and exhibited limit cycle characteristics. The oscillation also exhibited "hump" mode characteristics for many configurations. Altitude variations indicated the phenomenon was more severe at low altitudes, but the critical Mach number was nearly constant. Angle of attack increases produced increases in the oscillation amplitude. Configurations with heavy outboard fuel were more sensitive to RPO since the 1st flexible symmetric bending mode frequency was in close proximity to the short period mode.

Chase plane video of the B-2 during control surface excitations showed a moving shock visible in the condensation clouds over the engine nacelles. Analysis of the flight data indicated that the RPO was caused by an oscillating shock interacting with the short period and 1st flexible symmetric bending modes.

Simulation models of the B-2 were developed using the Computational Aeroelasticity Program - Transonic Small Disturbance - Viscous (CAPTSDv) computer code, and evaluations were performed to assess its ability to predict the B-2 RPO non-linear aeroelastic phenomenon. CAPTSDv performs a time marching solution, which employs the transonic small disturbance potential aerodynamic formulation. CAPTSDv includes an interactive viscous boundary layer modeling capability, which enables calculation of the aerodynamic flow field where transonic shocks and flow field separation begin to occur. The viscous effects play a key role in predicting the location and motion of oscillating shocks, which were believed to be important in modeling the B-2 RPO. The CAPTSDv structural equations utilize a modal

formulation to compute the air vehicle elastic deformations.

Applying CAPTSDv to the B-2, required adding the vehicle rigid body motions, the closed loop flight control system, and the capability to trim the free flying vehicle. Non-linear surface actuator hysteresis characteristics were also modeled.

Analytical studies were performed for two vehicle configurations where flight data were recorded. Heavy and light outboard fuel tank configurations with a forward center of gravity and a heavy payload were evaluated. Simulations for open and closed loop flight control systems were performed to assess the participation of the flight control system. Surface actuator hysteresis characteristics were varied to evaluate their contribution. Simulations were performed for various Mach numbers and altitudes to establish the stability boundaries and to compare with flight test data.

B-2 RPO Flight Testing and Results

After the RPO was encountered, 11 dedicated flights were flown to collect data to better understand the phenomenon and to define the on-set boundaries. Data were collected with the envelope expansion and flutter clearance instrumentation suites. Many flight conditions, fuel distributions, and CG configurations were tested which were operationally achievable, although not necessarily typical.

Data were gathered for both control surface pitch doublets and random excitations. Pitch doublets were input at 0.002 Mach number increments during very slow accelerations starting from 0.005 Mach number below the test point to 0.005 Mach number above the test point. Real time data analysis was performed to quantify the damping. If greater than 3% damping existed for the doublets, a symmetric pitch rudder random excitation was executed at the test point. All flight data results presented herein use both sources of data collectively.

Figure 1 shows typical Attitude Motion Sensor Set (AMSS) vertical load factor responses to pitch doublets as an RPO condition is approached. The response transitions from being highly damped to being oscillatory with a relatively small increase in Mach number. Figure 2 shows a typical AMSS pitch rate response near an RPO condition where the initial pitch response decays in amplitude with positive damping and then transitions to a zero damped small amplitude residual oscillation after several cycles. The oscillatory motion is dominated by interaction of the rigid body short period and 1st flexible symmetric bending modes.

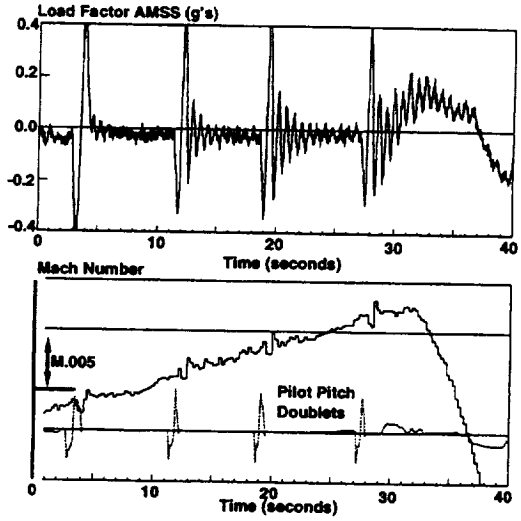

Figure 1 - Pitch Response Approaching RPO

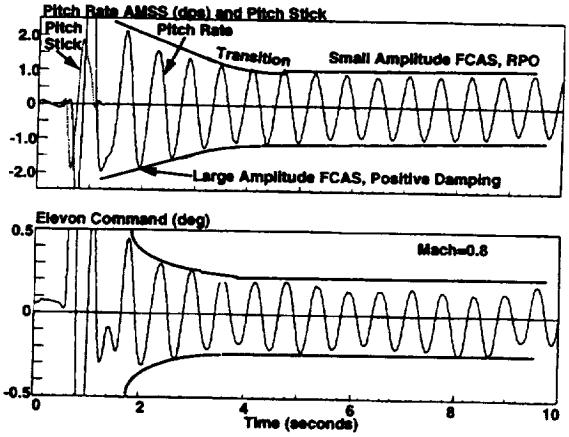

Figure 2 - Typical RPO Response To Pitch Doublet

A complete understanding of the interaction between the rigid body short period and the 1st flexible symmetric bending modes proved to be somewhat illusive during the flight test program. As the RPO Mach number was approached, the frequencies of these two modes came together, and mode identification became difficult. In most cases, only one frequency and damping result could be extracted.

Only limited data were taken at Mach numbers far away from the RPO Mach, where the two modes were not in close proximity. Flight data presented does not contain tracking of the short period and 1st flexible modes independently, but presents the interacting result. Figure 3 illustrates the rigid body

short period and 1st flexible symmetric bending mode frequency trends.

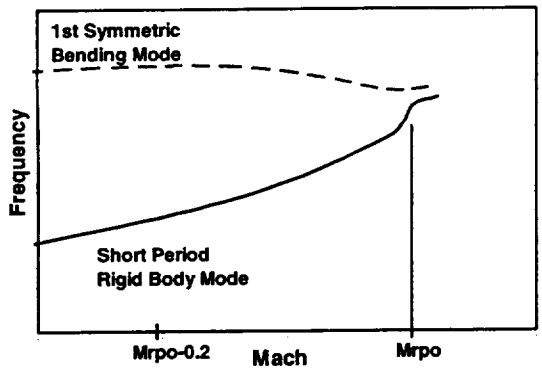

Figure 3 - Critical Mode Frequency Trends

Conditions affecting RPO sensitivity in order of decreasing importance are: Mach number, forward CG, heavy outboard fuel, elevated load factor (elevated angle of attack), heavy payload, and low altitude. In general, the closer the short period and 1st symmetric bending mode frequencies are, the more sensitive the configuration is to RPO. Forward CGs increase the short period frequency. Increased outboard fuel generally reduced the first symmetric bending mode frequency. Higher dynamic pressures at lower altitudes intensified the RPO at a given Mach number, and slightly reduced the critical RPO onset Mach number.

Analysis of the RPO flight data did not show the characteristics normally expected of a classical flutter phenomenon. An oscillating shock was visible in the condensation cloud over the engine nacelles during some of the forced response tests. The RPO occurred in a very narrow transonic Mach number range where a shock induced oscillation (SIO) is most likely to occur. Flight test data indicated that the aircraft aerodynamic center moved aft by as much as 3 feet as the RPO Mach was approached. The conclusion from the flight test program was that the RPO was most likely a shock induced oscillation (SIO).

CAPTSDv Application Results

The aeroservoelastic (ASE) models developed and used during the Engineering and Manufacturing Development phase of the B-2 program did not predict the RPO phenomenon. The RPO was discovered during flight test, and occurred in the low altitude high subsonic regime where nonlinear aerodynamic flow field effects are present. The aerodynamic representations used for the ASE models were based on linear aerodynamic prediction methods. Simulations with CAPTSDv were initiated to assess the participation of nonlinear flowfields.

Simulation of the rigid body plunging (h) and pitching (θ) motions in CAPTSDv was performed following the procedure of Reference 2. CAPTSDv was modified at Northrop Grumman with the assistance of Dr. John Edwards of NASA Langley Research Center (LaRC) to include the rigid body equations of motion. The equations implemented are:

$$\dot{\omega} = qU_\infty + (mg - \mathbf{q}_\infty SC_L)/m \qquad (1)$$

$$\dot{h} = \omega \qquad (2)$$

$$\dot{q} = \mathbf{q}_\infty S\bar{c}C_m / I_y \qquad (3)$$

$$\dot{\theta} = q \qquad (4)$$

Where:

q = Pitch rate
m = Mass
g = Gravity
U_∞ = Freestream Velocity
$\mathbf{q}_\infty$ = Freestream Dynamic Pressure
S = Reference Surface Area
$\bar{c}$ = Reference Chord
C_L = Lift Coefficient
C_m = Pitching Moment Coefficient
I_y = Moment of Inertia about C.G.

These equations are correct within a body fixed, "rotating" coordinate system. Their use in the inertial coordinate system in the CAPTSDv code is a reasonable approximation for the small pitch rates involved in this study.

The downwash boundary condition was modified to account for the rigid body motions:

$$\Phi_z^{\pm} = f_x^{\pm} + f_t - \frac{\omega}{U_\infty} - (x - x_{cg})c\frac{q}{U_\infty} \qquad (5)$$

Where:

x = Streamwise Location
x_{cg} = Streamwise Location for Center of Gravity

The first two terms are the streamwise slope and vertical velocity of the upper (+) and lower (-) vehicle surfaces, including elastic deformation. The last two terms are the additional terms necessary for the rigid body plunge and pitch motions. This work uncovered sign errors in equation 28 of Reference 2.

The B-2 aircraft configurations which were

evaluated during this study are shown in the following table:

Desc.	Wt. (Lbs)	Pitch Iner. (In-Lbs)	C.G. %MAC	Payld (Lbs)	Fuel (Lbs)
Heavy	328k	3.57E9	28	46k	64.9k
Light	266k	2.71E9	28	46k	33.7k

The Heavy configuration is representative of the most sensitive RPO flight configuration and the Light configuration is representative of the reduced outboard fuel configuration tested. While analyses were performed at 4,000, 8,000 and 16,000 altitudes, discussions contained herein will present only the 4,000 feet altitude cases.

Aerodynamic Modeling

The CAPTSDv aerodynamic grid contains 100 streamwise, 60 spanwise, and 50 vertical grid points for a total of 300,000 aerodynamic grids. Sixty of the streamwise and forty of the spanwise grid points reside on the B-2 planform. The aerodynamic grids for the first three rows and the planform geometry evaluated in CAPTSDv are compared with the actual B-2 geometry in Figure 4.

The B-2 aircraft wing tip and control surfaces edges are planform aligned and are not streamwise as on typical aircraft. Modeling of the wing tip requires that the grid lines which start at the wing root, extend beyond the wing tip to the outer boundary in a smooth fashion. Since, tightly packed grid lines are undesirable and can cause poor convergence (Ref. 7), a clipped wing tip was defined. The wing tip model possesses the same planform area as the actual. The flight control surfaces were modeled by selecting constant chord and streamwise grid lines which best approximated the actual geometry. The Middle Elevon was not modeled since it does not actively move during the RPO responses. Other modeling approaches which may represent the wing tip and control surface geometries more accurately were not investigated during this study.

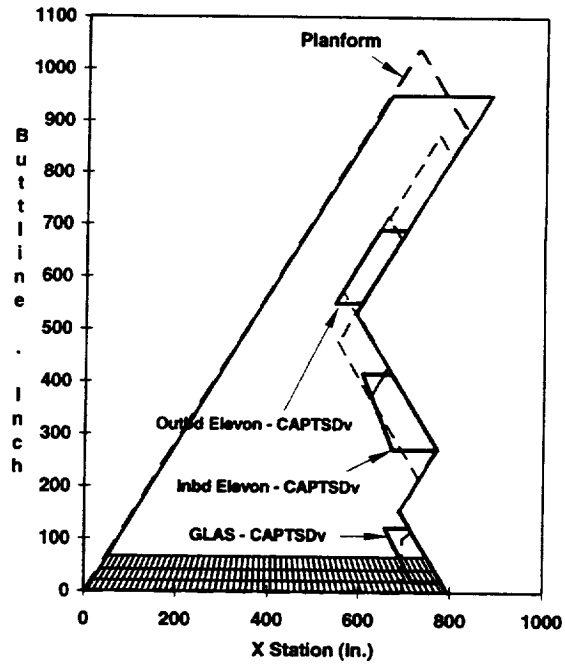

Figure 4 - B-2 Planform and CAPTSDv Aerodynamic Layout

The aerodynamic model for CAPTSDv was developed from a B-2 moldline definition referred to as the "nacelle subtracted moldlines". CAPTSDv currently does not have the capability to model the engine mass flow. The moldlines in the area of the nacelle have been modified so that the inlet mass flow is approximately represented. These moldlines were previously developed for CFD based performance analyses.

Structural Modeling

The structural model is derived from a NASTRAN finite element model of the B-2 aircraft. The model is constructed with beam elements and has been tuned to match ground vibration test results. The NASTRAN model was used extensively for B-2 analyses. NASTRAN modes, frequencies, generalized mass, and generalized stiffness quantities were generated for the desired configurations. These results were then processed by the modal preprocessor to transform them onto the CAPTSDv aerodynamic grid locations. All CAPTSDv aeroelastic simulations were performed with the first five elastic modes plus the rigid body pitch and plunge modes. The control surface mode frequencies are above those of the first five modes and were not included. The control surface commanded deflections were therefore modeled aerodynamically

but not inertially.

The primary elastic contributor to the RPO phenomenon is the 1st flexible symmetric wing bending mode. The unique flying wing configuration of the B-2 yields a design in which this lowest elastic mode and the closed loop rigid body short period mode frequencies are in close proximity at medium and high air speeds. Figure 5 shows the 1st flexible symmetric wing bending mode deflection characteristics. Figure 6 contains a listing of the modal frequencies for the Heavy and Light structural configurations.

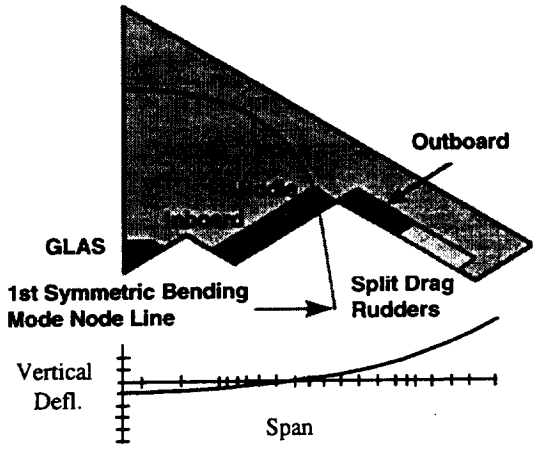

Figure 5 - 1st Flexible Symmetric Bending Mode Deflection Characteristics

Heavy Config. (Hz.)	Light Config. (Hz.)	
1.80	2.12	(1st Flexible Symmetric Bending)
4.37	5.15	
8.74	10.41	
9.58	12.31	
14.69	17.12	

Figure 6 - Modal Frequencies

Flight Control Modeling - Linear

The B-2 aircraft employs a full time active flight control stability augmentation system. Figure 7 shows the major components of this system. The B-2 flight control surfaces include three sets of elevons for pitch and roll control, a centerline gust load alleviation surface (GLAS) for pitch control, and upper and lower split drag rudders for yaw control. Since the flight control surfaces are large, surface motions as small as 1 degree can command up to 1 g incremental load factor at medium and high speeds.

Sensor feedbacks used for stability augmentation include the Air Data System (ADS) and the Attitude Motion Sensor Set (AMSS). The ADS measures the vehicle flight condition, angle of attack, and angle of sideslip. The AMSS senses the vehicle inertial attitudes and accelerations and is located on the vehicle centerline near the 1st flexible symmetric bending mode node line, forward of the center of gravity. The Flight Control Computers (FCCs) compute the surface position commands in response to pilot commands and feedback sensor inputs.

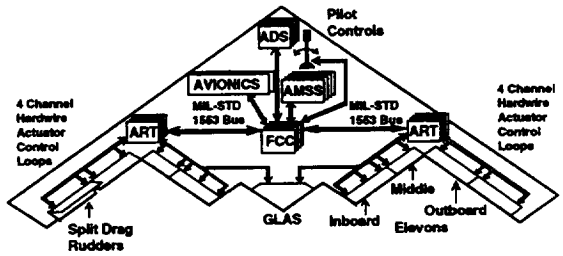

Figure 7 - Flight Control Architecture

A simplified Flight Control System (FCS) pitch control augmentation model was implemented into CAPTSDv to evaluate the FCS effects and closed loop aeroservoelastic interaction. CAPTSDv rigid body plus flexible load factor and pitch rate responses at the AMSS sensor location were used for the feedback sensor inputs to the FCS model. The simplified version of the full up FCS was valid for the RPO flight conditions, and used the same control algorithms, filter compensation, gains, and calculations as the operational flight program in the FCCs. Fifth order linear actuator position to command models were tuned to match flight data for each of the surfaces. Surface command rate and position limits were also included.

Nonlinear FCAS Model

The Flight Control Actuation System (FCAS) hydraulic actuators which position the B-2 control surfaces have nonlinear response characteristics for small amplitude motion commands. These nonlinear characteristics are caused by a small overlap in the actuator main control valve as shown in Figure 8. This overlap results, in a small deadband in the commanded fluid flow and actuator rate from the main control valve, and shows up as an effective hysteresis in the surface position to command response. Figure 9 shows the effect of the hysteresis on actuator position when a sinusoidal surface command is applied. The surface position lags the command and has flattened peaks as measured during flight testing.

The time/phase delays are dependent on the amplitude of motion and for small motions significantly degrade the closed loop FCS stability.

The flight test elevon position to command frequency responses shown in Figure 10 have over 25 degrees of additional phase lag for small and slow commanded elevon motion from a pilot pitch frequency sweep as compared with large and fast commanded motion from a random excitation. The 25 degree additional phase lag occurs across a wide frequency range and represents variable time delays of approximately 62 milliseconds at 7 radians/second, 44 milliseconds at 10 radians/second, and 29 milliseconds at 15 radians/second. Time history analysis of flight data showed the FCAS hysteresis size and resulting phase delay was inversely proportional to a combination of the commanded elevon amplitude, rate, and frequency.

The phase delay from the FCAS hysteresis effectively eliminates the gain and phase stability margins measured with large amplitude elevon motion, and can contribute to closed loop limit cycle oscillations for small amplitude elevon motion. Limit cycle oscillations will set up at an amplitude which has zero damping because of the amplitude dependant FCAS phase delays.

Figure 2 shows a large amplitude pitch doublet flight test example, where large surface motions initially provided a well damped pitch response. The vehicle approaches a zero damped limit cycle oscillation (LCO) around 4 seconds when the elevon deflections became smaller and the additional phase delays generate a zero damped condition. The small amplitude oscillation is bounded, since larger amplitude motions are stable.

A constant size actuator hysteresis was implemented into CAPTSDv to approximate the small amplitude motion effects. Flight test data showed approximately 0.13 degrees of hysteresis on the inboard elevon during small amplitude motion. The variations in hysteresis size with commanded amplitude and rate that were observed in flight, were not included in CAPTSDv. Future upgrades to include a variable hysteresis size would provide improved modeling.

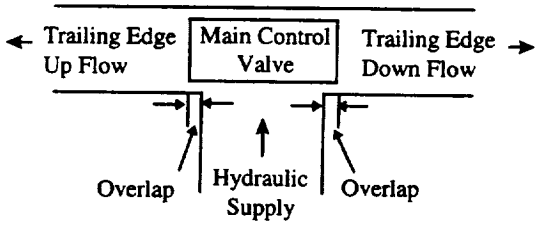

Figure 8 - Main Control Valve Overlap

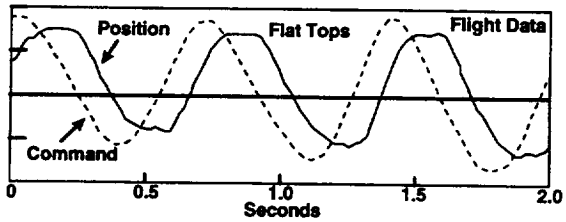

Figure 9 - Elevon Hysteresis Position Vs. Command

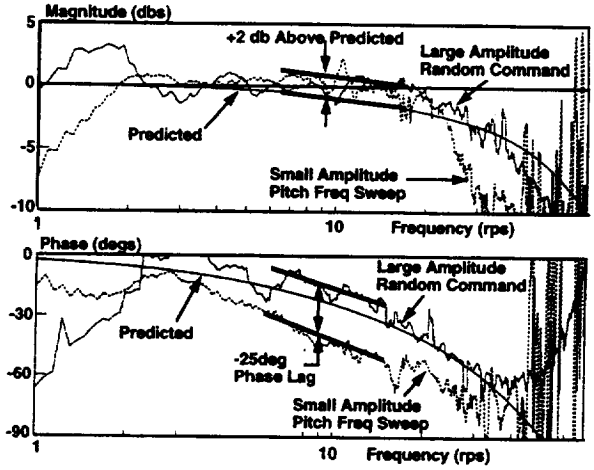

Figure 10 - FCAS Hysteresis Effects - Elevon Position / Command

Other Flight Control System and Actuator Model Limitations

Mechanical backlash and surface free play were estimated at up to ±0.3 degrees, but were not modeled in CAPTSDv. For the range of control surface motions expected during RPO, the control surfaces would not encounter a zero hinge moment condition. Therefore, for the current studies, modeling of the freeplay was considered of secondary importance. However, improved modeling of the actuator and surface inertias, mechanical backlash, freeplay, and interaction with airloads, could improve the simulation.

Static Pressures vs. Wind Tunnel Results

The chordwise static pressures of CAPTSDv were compared with wind tunnel data recorded from a 6% scale model. The configuration was representative of a 1g high altitude deflected shape and was sting mounted on the plane of symmetry. Figure 11 shows upper, lower, and delta coefficients of pressure (Cp) at spanwise station 474 (through middle of inboard elevon) for the heavy configuration at 4,000 altitude and Mach 0.8. Results for conditions of approximately zero angle of attack

are shown. Note Cp upper and Cp lower are plotted on left and right vertical axes respectively. The Cp lower results are plotted unconventionally (with negative values down) for clarity. The delta Cp lower minus upper results show good agreement with the wind tunnel data.

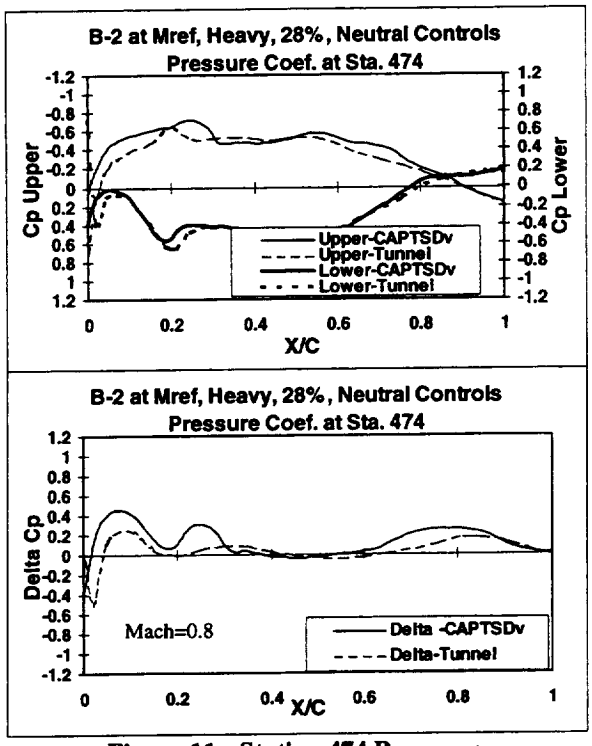

Figure 11 - Station 474 Pressures

Trim Solutions

Initial CAPTSDv solutions were performed to obtain a trimmed state at 1 g flight with a zero pitching moment. The angle of attack was varied to obtain lift equal to the air vehicle weight and the inboard elevon was deflected to trim the pitching moment. The B-2 normally trims with a combination of the inboard and middle elevons.

Dynamic Simulation Results

The dynamic simulations were started from the saved trim solutions and run for a sufficient time to evaluate the stability characteristics. Inboard elevon control surface doublet commands were used to perturb the air vehicle. Simulations for both open and closed loop control laws were generated. All closed loop solutions were run with the same 0.13 degree hysteresis (unless specifically stated otherwise) on the GLAS, inboard elevon, and outboard elevon.

Dynamic aeroelastic simulations were run at a series of Mach numbers to determine the stability characteristics. Transient responses of the vehicle angle of attack were used to extract the damping and frequency information. Large amplitude pitch doublet excitations were used and the damping properties were extracted in the first 3 seconds of the response, prior to the onset of constant amplitude residual pitch oscillations. As with the flight test data, independent identification of the rigid body short period and 1st flexible symmetric bending modes from the CAPTSDv results was difficult.

Heavy Configuration

Dynamic aeroelastic simulations were run for the heavy configuration at 4,000 feet altitude for a series of Mach numbers with 1 degree inboard elevon doublet excitations. Angle of attack transient responses for several open and closed loop control law simulations at several Mach numbers are shown in Figure 12.

The CAPTSDv open and closed loop 4,000 foot altitude stability boundary for the heavy configuration is compared to flight test results in Figure 13. The flight test results are shown with symbols, for the raw data, and a fitted curve. The damping curve fit used the minimum damping values at each Mach number. The FCS closed versus open loop simulation results tend to slightly increase the frequency of the RPO motion and raise the Mach number of the neutrally stable point. The CAPTSDv frequencies are slightly lower than the flight results. The damping for the closed loop CAPTSDv simulations compare well with flight test. The abrupt slope change at 0.785 Mach number is believed to be associated with the development of shocks.

Figure 14 shows station 345 closed loop upper and lower surface pressure coefficients (Cpu and Cpl) for several Mach numbers. Station 345 is located outboard of the engine nacelles and passes through the inboard elevon. These pressure distributions were obtained from the trimmed aeroelastic solution prior to applying the control surface doublet. The significant change in the mid chord pressure distribution as the Mach number increases is believed to be one of the prime contributors to the RPO onset. Shocks begin to develop around Mach 0.785 and become very strong by Mach 0.835.

The significant change in the pressure distributions cause large movements in the aircraft aerodynamic center. This was suspected from analysis of the flight test data.

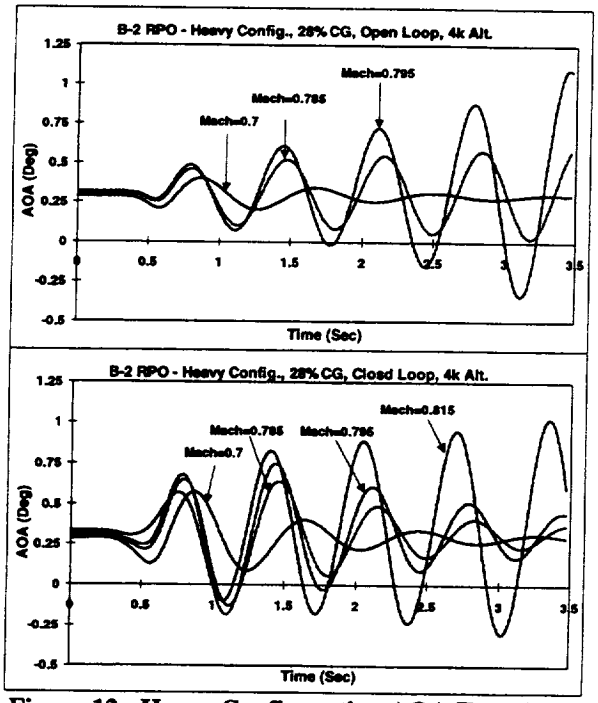

Figure 12 - Heavy Configuration AOA Transients (4,000 Alt.)

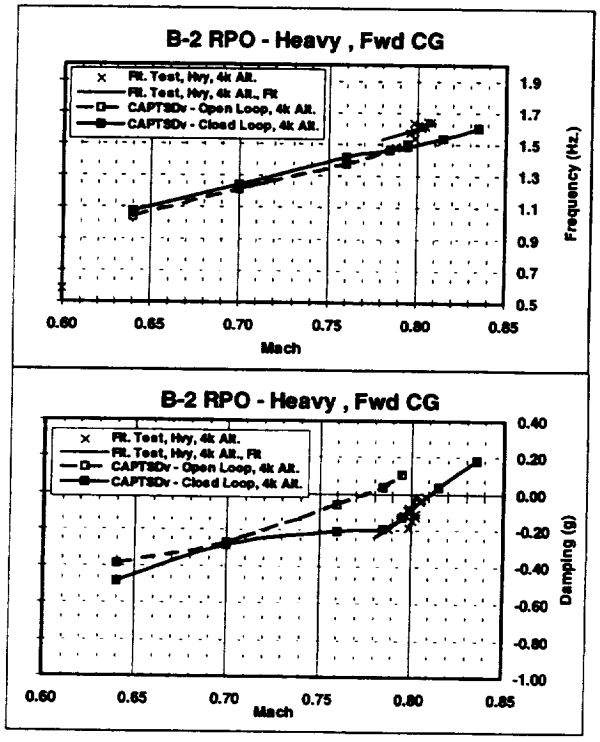

Figure 13 - Heavy Configuration Stability Boundary (4,000 Alt.)

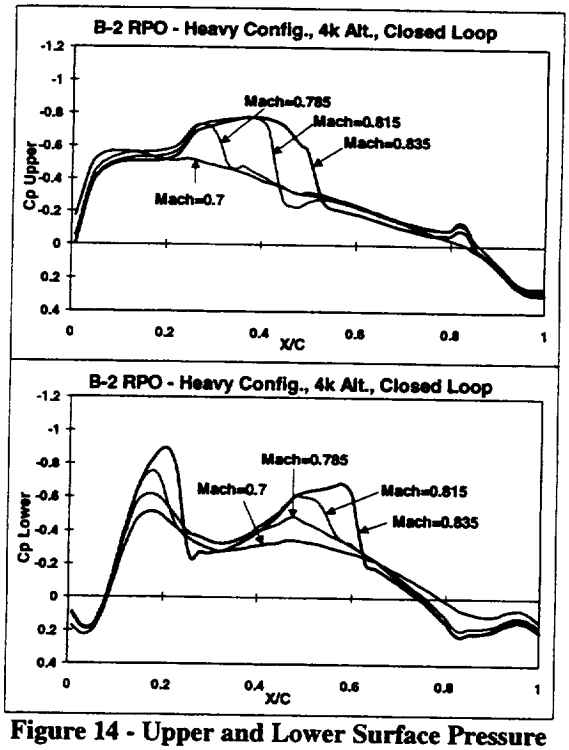

Figure 14 - Upper and Lower Surface Pressure Distribution . vs. Mach (Station 345)

Figure 15 shows a CAPTSDv simulation which predicts a divergent transient response for the closed loop heavy configuration at 4,000 feet altitude and Mach 0.835. The upper plot shows the angle of attack and control surface positions. The lower plot shows the CG vertical acceleration along with the angle of attack. Figure 16 shows how the chordwise pressures vary with angle of attack. Chordwise pressure distributions for trim, and angles of attack of -3.22 and 5.28 degrees were selected for visualization.

Figure 16 shows the upper and lower surface pressure coefficients at station 345, through the middle of the inboard elevon, for the selected time cuts. Both the upper and lower surface (near 60% chord) shock locations move forward for nose up angles and aft for nose down angles. The upper surface shock motion was contrary to the expected result as described in Reference 5. Even though this example case represents higher amplitudes of motion than observed in flight, it illustrates a ±5 percent chord variation in shock position. The inboard elevon motion during the vehicle oscillations also impact the pressure distribution. The FCS works to damp and reduce the oscillations by commanding the inboard elevon trailing edge up when the aircraft AOA is nose down.

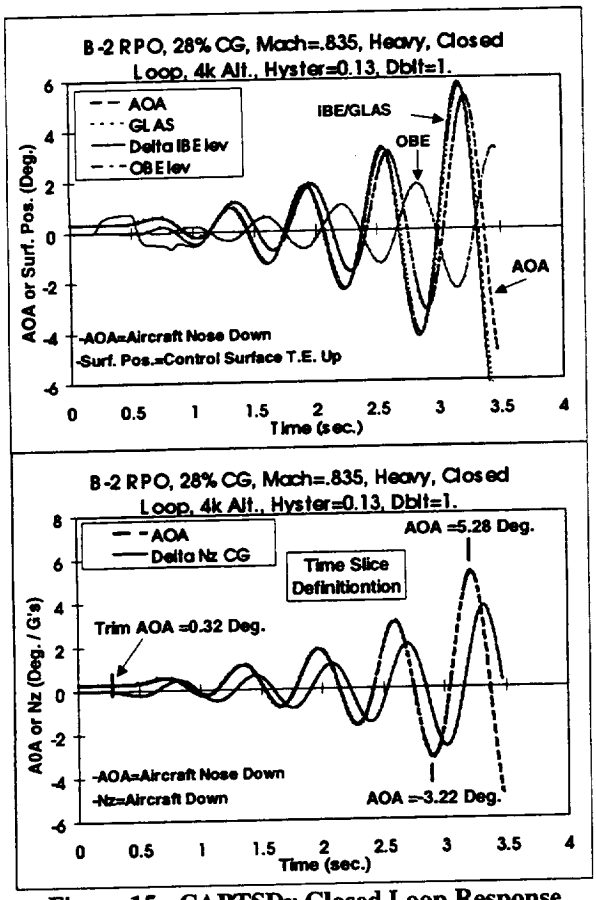

Figure 15 - CAPTSDv Closed Loop Response Above RPO Onset

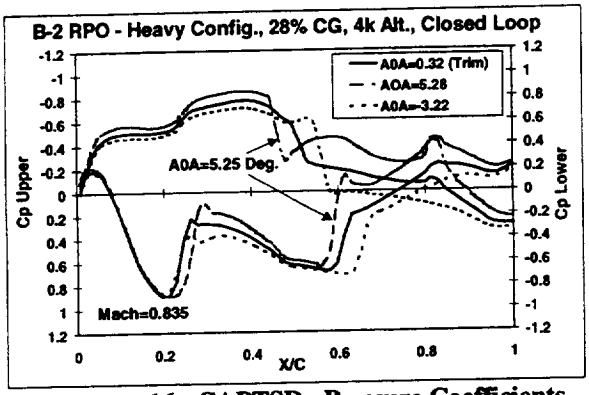

Figure 16 - CAPTSDv Pressure Coefficients .vs. AOA (Station 345)

Light Configuration

Dynamic aeroelastic simulations were also run for the light configuration at 4,000 feet altitude. Selected angle of attack transient responses for the open and closed loop control law simulations are shown in Figure 17. Extracting the frequency and damping data for the light configuration was more difficult than the heavy configuration. The lower Mach number responses were highly damped (dead beat) and did not have sufficient response to adequately extract frequency and damping values. The light weight short period damping was generally much higher than typical structural modes. Higher quality frequency and damping data could be computed in CAPTSDv in the future by making enhancements that would allow control surface frequency sweeps or random excitation inputs.

The light configuration open and closed loop 4,000 foot altitude stability boundary (for Mach numbers that weren't deadbeat) is compared to flight test results in Figure 18. The CAPTSDv closed loop frequencies appear to abruptly change near a Mach number of 0.8. The dominant aircraft frequency appears to be primarily from the short period mode below Mach 0.8, a combination of both short period and 1st flexible symmetric wing bending between Mach 0.8 and 0.85, and takes on a higher frequency normally associated with the 1st flexible symmetric bending mode above Mach 0.85.

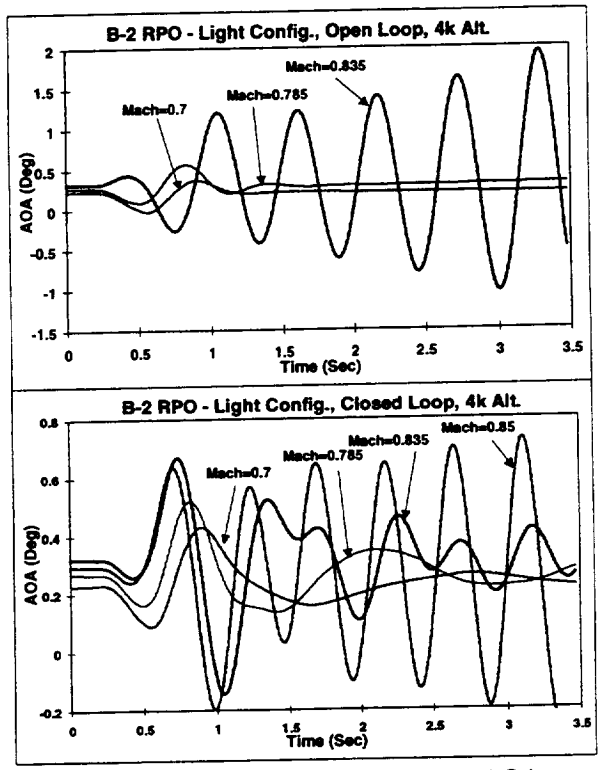

Figure 17 - Light Configuration AOA Transients (4,000 Alt.)

CAPTSDv simulation and flight results have similar damping up to Mach 0.82, where the flight results exhibit a hump mode character. The hump mode character did not appear during the simulations. The cause of this difference has not been determined and is a subject of future studies. Two hypotheses for the source of the difference are:

1) the degree of flow separation is under predicted and in flight the flow separation helps quench the oscillations, and 2) the spanwise flow in separated regions, (CAPTSDv does not predict) disrupts the shock development.

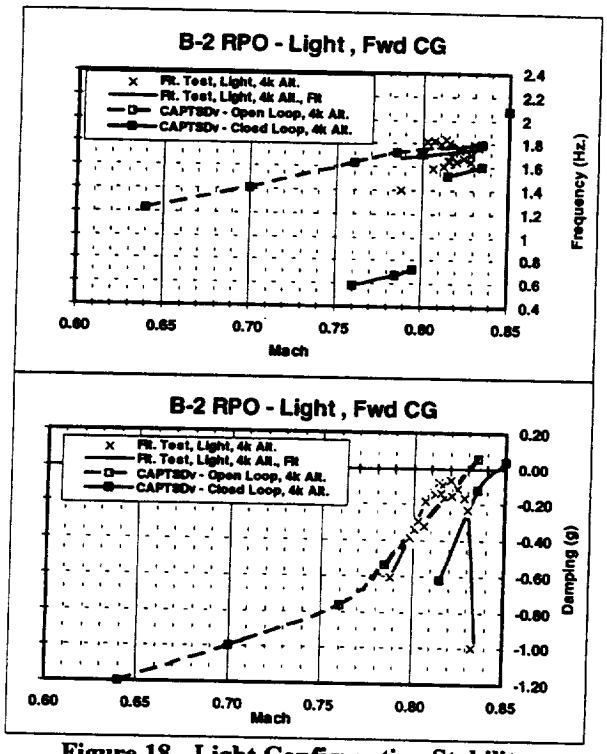

Figure 18 - Light Configuration Stability Boundary (4,000 Alt.)

Non-linear Control Results

When the actuator hysteresis was included in the CAPTSDv aeroservoelastic simulations, constant amplitude residual pitch oscillations occurred, similar to those seen in flight test. This was a major advancement in understanding the flight test results and the physics of the RPO mechanism. Constant amplitude residual pitch oscillations occurred when the actuator hysteresis was included for Mach numbers with light damping.

Figure 19 shows actuator hysteresis size variation results for the heavy configuration at 4,000 feet altitude. The initial transient responses have positive damping with decaying amplitude but transition to constant amplitude residual oscillations, similar to the flight data in Figure 2. The frequency of the residual oscillations appear to be independent of the hysteresis size, while the amplitude is approximately a linear function of the hysteresis size.

These simulation studies modeled the GLAS, inboard elevon, and outboard elevon with the same 0.13 degree hysteresis. Further modeling improvements would adjust the hysteresis for each surface using flight test data.

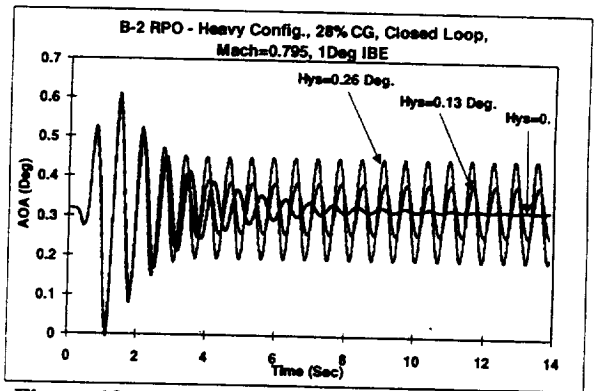

Figure 19 - Effect of Actuator Hysteresis - Heavy Configuration

Conclusions

CAPTSDv showed good success in predicting the non-linear aeroelastic RPO behavior on the B-2 Bomber. Two vehicle configurations were evaluated, where flight data were available. Open and closed loop flight control system simulations were performed to assess the participation of the flight control system. Control actuator hysteresis characteristics were modeled and found to be a key contributor in simulating the RPO. Mach number and altitude sweeps that were run to establish the stability boundaries, compared well with flight test data. The CAPTSDv results increase the understanding of the B-2 RPO and establish improved capabilities for non-linear aeroelastic and aeroservoelastic simulation.

The following conclusions can be made from the studies performed:

1. The CAPTSDv transonic small disturbance potential aerodynamic formulation was capable of predicting the B-2 RPO phenomenon where previous analysis tools could not. CAPTSDv's moderate computational requirements as compared to the large requirements of higher order methods, make it more feasible to perform multiple configuration surveys.
2. Steady flow field pressure distributions predicted by CAPTSDv matched B-2 wind tunnel data well.
3. CAPTSDv simulation results for the heavy configuration at 4,000 feet altitude configuration produced a good match to flight test results. Frequency and damping characteristics compared well with the flight test data. CAPTSDv predicted the point of neutral stability within 0.007 Mach number of the flight results. CAPTSDv showed that

as the RPO Mach number is approached, strong shocks develop on both the upper and lower surfaces.
4. CAPTSDv simulations for the light configuration showed a more severe RPO response than the flight test results. Although response characteristics were similar in many aspects, the hump mode character observed during flight testing was not simulated.
5. Identifying and extracting frequency and damping properties for highly damped transient responses and closely spaced modes were very difficult with CAPTSDv as they were with the flight data.
6. Closed loop control simulations with actuator hysteresis successfully simulated the constant amplitude residual pitch oscillations recorded during B-2 flight testing. This was a major advancement in understanding the flight test results and the physics of the RPO mechanism.
7. Results from this study are consistent with the flight test conclusions, in that the RPO phenomenon is due to a non-linear shock induced oscillation (SIO) where the air vehicle's rigid body short period and 1st flexible symmetric bending modes interact.

Recommendations

Recommendations based on the results of this study include the following:
1. Develop the capability to perform control surface frequency sweeps or random excitations within CAPTSDv. This would provide an enhanced means to identify highly damped or closely spaced modes.
2. Investigate improved geometric approaches to more accurately model the wing tip and control surfaces and evaluate their impact on the predicted RPO.
3. Model the middle elevon so it can be used in concert with the inboard elevon to trim the aircraft.
4. Model the FCAS with a variable hysteresis similar to that observed in the flight data with small and large amplitude surface commands/rates.
5. Improve modeling of the surface backlash and free play to improve the correlation with flight data.
6. Model the control surface dynamics by including the control surface modes and inertial terms in the simulation.
7. Continue flow field investigations including computing aerodynamic center movement and shock phasing relationships with the aircraft angle of attack.
8. Perform additional studies to investigate why the hump mode characteristics were not predicted. Investigate queenching mechanisms such as large flow separation or spanwise flow effects.

Acknowledgements

The authors would like to acknowledge and thank Dr. John Edwards of NASA LaRC for his help and support under Contract NAS1-19347. The authors would also like to thank Paul Kelly who performed much of the initial work contained herein prior to his retirement from Northrop Grumman.

References

1. Jacobson, S.B., Britt, R.T., Dreim, D.R., and Kelly, P.D., "Residual Pitch Oscillation (RPO) Flight Test and Analysis on the B-2 Bomber", AIAA Paper 98-1805, 39th SDM Conference, April 1998, Long Beach, CA
2. Vinh, Lam-Son, Edwards, J.W., Seidel, D.A., Batina, J.T., "Transonic Stability and Control of Aircraft Using CFD Methods", AIAA Paper 88-4374, AIAA Atmospheric Flight Mechanics Conference, Minneapolis, Minn., August 1988.
3. Edwards, J.W., "Transonic Shock Oscillations Calculated With A New Interactive Boundary Layer Coupling Method", NASA Langley Research Center, Hampton, Virginia, 23681-0001, Presented at the 31st Aerospace Sciences Meeting & Exhibit, Jan. 11-14, 1993, Reno, NV.
4. Pi, W.S, "Procedures and Guidelines For Using The CAP-TSD Code For Transonic Aeroelastic Applications On Realistic Aircraft Configurations", NOR 91-72, August 1991
5. Dowell, E.H., Crawley, E.F., Curtiss, H.C. Jr., Peters, D.A., Scanlan, R.H., Sisto, F., "A Modern Course In Aeroelasticity" , 3rd Edition, Kluwer Academic Publishers, 1995, Page 476
6. Pitt, D.M., Drouin, D.V., Fuglsang, D.F., "Applications of XTRAN3S and CAP-TSD to Fighter Aircraft", WRDC-TR-89-3048, Final Report for The Period June '97 to Dec. '98, Air Force Contract F33615-87-C-3212
7. Gibbons, M.D., Soistmann, D.L., Bennett, R.M., "Flutter Analysis of Highly Swept Delta Wings By Conventional Methods", NASA Technical Memorandum 101530, November 1988
8. Edwards, J.W., "Calculated Viscous and Scale Effects on Transonic Aeroelasticity", NASA LaRC, Hampton, Virginia, 23681-0001, Presented at the AGARD Structures and Materials Panel Workshop on Numerical Unsteady Aerodynamics / Aeroelastic Simulation, Oct. 1997, Aalborg, Denmark
9. Dreim, D.R., and Jacobson, S.B, "Computational Prediction of Non-Linear Transonic Aeroelastic Behavior of Large Flexible Aircraft", NASA LaRC, Contract NAS1-19347 Task 26, Final Report, 30 Oct. 1998

Singular Perturbation Technique for Nonlinear Aeroelastic Analysis

D. Dessi, F. Mastroddi

Dipartimento Aerospaziale - Università degli Studi di Roma "La Sapienza"

via Eudossiana, 16 - 00184 Rome - Italy - E-mail daniele@morino.ing.uniroma1.it

E-mail franco@mastroddi.ing.uniroma1.it

L. Morino

Dipartimento di Meccanica Industriale - Università di "Roma Tre"

via Della Vasca Navale, 79 - 00146 Rome - Italy - luigi@thames.dimi.uniroma3.it

Abstract

In this paper we consider an aeroelastic section with cubic free-play nonlinearities, approximating Wagner's function in the expression of aerodynamic forces with exponentials in the time domain. The mathematical model is then recast in the standard first order ordinary differential form, with $\mathbf{x}$ the global state-space vector, to which nonlinear analysis tools apply. An extensive numerical study has been performed to show the dependence of Hopf bifurcation characteristics from the structural and geometric properties of the wing section. Bifurcation and frequency vs. dynamic pressure plots are presented. In such cases the onset of flutter might happen before the linear flutter speed for certain initial conditions.

1 Introduction

It is well known that there exist two types of flutter: benign and explosive. In the first case, above the flutter speed, the system tends to limit cycle oscillations (LCO) with amplitude growing like $\sqrt{U-U_L}$ (for small values of $U-U_L$, where U_L is the linear flutter speed, obtained with classical linear stability analysis). In the second case, even below the flutter speed, the system may experience finite-amplitude oscillations, provided that the initial conditions are sufficiently high (the initial condition amplitude necessary to excite this destructive oscillations varies like $\sqrt{U_L-U}$, again for small values of U_L-U). From a mathematical point of view the two phenomena may be described in terms of stable and unstable limit cycles (see Figs. 1 and 2). The first case, stable limit cycle, is known as supercritical Hopf bifurcation, the second one as subcritical Hopf bifurcation (Guckenheimer and Holmes [1]).

There is well known experimental evidence (see Refss. [2], [3], [4], [5]) that large amplitude, stable limit cycle and small amplitude, unstable limit cycle oscillations might appear before the linear flutter boundary speed. Indeed, some theoretical papers (Refss. [6], [7], [8], [9], [10], [11]) have highlighted the possibility, under suitable initial conditions, of finite amplitude limit-cycle oscillations prior to the onset of the exponentially growing linear flutter. Such a phenomenon is well depicted by amplitude versus velocity bifurcation plots: the bifurcation curve shows a

turning point that reverses the sub-critical Hopf bifurcation into a supercritical-like shape. From a physical point of view, this may be described in terms of the dependence of the flutter boundary upon the initial conditions (the case of interest is that of an airfoil elastically costrained by a soft torsional spring). For such a phenomenon, known as 'explosive' or 'violent', an estimate of flutter boundary can be achieved by exploring the bifurcation diagram of steady-state motion amplitudes versus flow speed. This shows a sub-critical Hopf bifurcation which exhibits a turning point at a velocity lower than the flutter speed, determining a 'knee' in the bifurcation diagram. From an aeronautical point of view, this phenomenon indicates that the linear flutter speed is not at all a safe prediction - a more detailed (nonlinear) analysis must be addressed to compute this new limit. In the present case, a fifth-order method is needed to describe, at least approximately, the stability properties of the system. A methodology for analyzing fifth-order nonlinearities is presented.

2 Normal Forms Method

The objective of this section is to present an elementary introduction to the normal form method for the study of nonlinear dynamical systems (for more details about the present application of normal forms method to aeroelastic systems, see [12], where the general theory well explained in [1], [13], [14] and [15] is considered). The implementation of the method in the case of algebraic nonlinearities is examined in this section, whereas the application to fifth-order analysis of nonlinear aeroelastic systems with cubic nonlinearities is considered in Sect. 3.

The normal form method is based on the idea that a nonlinear system can be simplified by a coordinate transformation. This goal is achieved by two different steps: first, by reducing the number of equation by applying the center manifold theorem and second, by eliminating in the reduced equation the nonlinear terms that do not contribute significantly to the solution: such a selection of the nonlinear terms is performed by introducing the "resonance condition". Consider a dynamical system of the type

$$\dot{\mathbf{x}} = \mathcal{F}(\mathbf{x}, \varepsilon) = \Lambda \mathbf{x} + \mathbf{f}(\mathbf{x}, \varepsilon) \tag{1}$$

where Λ is a diagonal matrix, $\mathbf{f}(\mathbf{x}) = \varepsilon\, \mathbf{f}^{(2)}(\mathbf{x}) + \varepsilon^2\, \mathbf{f}^{(3)}(\mathbf{x}) + \ldots$ with $\mathbf{f}^{(m)}(\mathbf{x})$ denoting a generic polynomial of degree m and ε is a perturbation parameter[1]. The solution is given in terms of an asymptotic expansion of the type (near-identity)

$$\mathbf{x} = \mathcal{U}(\mathbf{y}, \varepsilon) = \mathbf{y} + \varepsilon \mathbf{u}^{(2)} + \varepsilon^2 \mathbf{u}^{(3)} + \ldots + O(\varepsilon^{M+1}) \tag{2}$$

Using Eq. 2, Eq. 1 is transformed into (see below)

$$\dot{\mathbf{y}} = \mathcal{G}(\mathbf{y}, \varepsilon) = \Lambda \mathbf{y} + \mathbf{g}(\mathbf{y}, \varepsilon) + O(\varepsilon^{M+1}) \tag{3}$$

where the vector of nonlinear terms $\mathbf{g}(\mathbf{y}, \varepsilon)$ includes the so-called resonant terms, which satisfy the associated resonance condition

$$\lambda_i - \lambda_{j_1} - \lambda_{j_2} - \ldots - \lambda_{j_m} = 0 \tag{4}$$

where $i, j_1, \ldots, j_m = 1, \ldots, N+1$ and m is the order of the nonlinear term considered. Therefore, if the resonant condition, which must be evaluated for each algebraic nonlinear term of Eq. 1, is

[1]The parameter ε may be eliminated by setting $\varepsilon \mathbf{x} = \hat{\mathbf{x}}$; it is introduced here in order to facilitate the analysis of the order of magnitude in the contest of asymptotic expansions.

satisfied, the corresponding nonlinear term must be included in the resonance equation, Eq. 3; if it is not satisfied, the nonlinear term contributes to the expression of the near-identity transformation given by Eq. 2. Substituting Eq. 2 into Eq. 1 we obtain

$$[\mathbf{I} + D\mathbf{u}(\mathbf{y},\varepsilon)]\,\dot{\mathbf{y}} = \mathcal{F}(\mathbf{y} + \mathbf{u}(\mathbf{y},\varepsilon),\varepsilon) \tag{5}$$

Taking into account the final form of transformed equations (see Eq. 3) and substituting this into Eq. 5, the resultant equation is

$$\mathcal{G}(\mathbf{y},\varepsilon) = \mathcal{F}(\mathbf{y} + \mathbf{u}(\mathbf{y},\varepsilon),\varepsilon) - D\mathbf{u}(\mathbf{y},\varepsilon)\mathcal{G}(\mathbf{y},\varepsilon) \tag{6}$$

Separating in $\mathcal{F},\mathcal{G}$ the linear parts from the nonlinear ones and rearranging the previous equation yields

$$\mathbf{g}(\mathbf{y},\varepsilon) = \mathbf{f}(\mathbf{y},\varepsilon) + \mathbf{\Lambda u}(\mathbf{y},\varepsilon) - D\mathbf{u}(\mathbf{y},\varepsilon)\mathbf{\Lambda y} - D\mathbf{u}(\mathbf{y},\varepsilon)\mathbf{g}(\mathbf{y},\varepsilon) \tag{7}$$

It is possible to re-write the previous equation as

$$D\mathbf{u}(\mathbf{y},\varepsilon)\mathbf{\Lambda y} - \mathbf{\Lambda u}(\mathbf{y},\varepsilon) = \mathbf{f}(\mathbf{y},\varepsilon) - D\mathbf{u}(\mathbf{y},\varepsilon)\mathbf{g}(\mathbf{y},\varepsilon) - \mathbf{g}(\mathbf{y},\varepsilon) \tag{8}$$

This equation is called the 'homological equation', and must be solved in the unknowns terms of near-identity transformation terms $\mathbf{u}^{(2)}, \mathbf{u}^{(3)}, \ldots$ for each order in ε. The solution of this equation is obtained immediately, by taking into account that

$$D\mathbf{u}^{(q)}(\mathbf{y},\varepsilon)\mathbf{\Lambda y} - \mathbf{\Lambda u}^{(q)}(\mathbf{y},\varepsilon) = -\mathbf{E}\mathbf{u}^{(q)}(\mathbf{y},\varepsilon) \tag{9}$$

where $\mathbf{E} = [E_{ik}] = [(\lambda_i - \lambda_{j_1} - \lambda_{j_2} - \ldots - \lambda_{j_m})\delta_{ik}]$ to yield

$$\mathbf{E}\mathbf{u}^{(q)}(\mathbf{y},\varepsilon) = \mathbf{F}^{(q)}(\mathbf{y},\varepsilon) - \mathbf{g}^{(q)}(\mathbf{y},\varepsilon) \tag{10}$$

where $\mathbf{F}^{(q)}(\mathbf{y},\varepsilon) = \mathbf{f}^{(q)}(\mathbf{y},\varepsilon) - D\mathbf{u}^{(q)}(\mathbf{y},\varepsilon)\mathbf{g}^{(q)}(\mathbf{y},\varepsilon)$. Finally, one may choose $\mathbf{g}^{(q)}$ to eliminate all the term in $\mathbf{F}^{(q)}(\mathbf{y},\varepsilon)$ for which $E_{kk} = 0$. This leaves $-\mathbf{E}\mathbf{u} = \hat{\mathbf{F}}^{(q)}(\mathbf{y},\varepsilon)$ (where $\hat{\mathbf{F}}^{(q)}(\mathbf{y},\varepsilon)$ includes the remaining terms). Hence, each element of the vector $\mathbf{u}^{(q)}$ is given by $u_k^{(q)} = -\hat{F}_k^{(q)}/E_{kk}$. Note that when the resonance condition is satisfied, the solution of the homological equation is undetermined and the simpler choice is to set $u_k^{(q)} = 0$.

3 Amplitude and Frequency of Limit-Cycle-Oscillations

In the present section, particular attention is devoted to show:

- the existence of a velocity range, less than the linear flutter speed, such that the onset of LCO (Limit Cycle Oscillations) is possible for sufficiently large initial conditions;
- the dependence of the shape of the bifurcation diagram ('knee' or 'pitchfork') from the position of the elastic center;
- the possibility to foresee analytically this dynamic behavior using a fifth-order asymptotic method.

Typical section model used is given in Appendix A. The coefficients considered in this case are

$$\mu = 100 \quad x_\alpha = 0.25 \quad \bar{\omega} = 1.2 \quad r_\alpha = 0.5 \quad a_h = \text{variable} \tag{11}$$

and the pitching moment is $M(\alpha) = \alpha + \beta_\alpha \alpha^3$. By a root-locus stability analysis, flutter speed and frequency are respectively $U_L = 4.937$ and $\omega_L = 0.255$ as shown in Fig. 3. In Fig. 4 the numerical LCO amplitudes in pitch are given in the neighborhood of U_L and for some values of a_h, with $\bar{\omega} = 1.2$, $\mu = 100$, $x_\alpha = 0.25$, $r_\alpha = 0.5$ and $\beta_\alpha = -50$. These LCO amplitudes (both stable and unstable) are computed with a modified Shooting Method routine to save time, disregarding the transient state and providing also the LCO period and the Floquet multipliers. Different values of a_h correspond to various position of the elastic center along the chord; it is apparent how the shape of the bifurcation diagram changes with a_h: for $a_h \simeq 0.48$ the 'knee' at the turning point disappears, and the bifurcation turns itself from a sub-critical one into a super-critical one. The difference between these two types of Hopf bifurcations can be explained considering the flutter boundaries that are qualitatively depicted in Fig. 2; the arrows show how the amplitudes of the LCOs increase or decrease according to different initial conditions in a more complex manner than in the 'pitchfork' case: collecting these results is possible to split the state space into different regions called basin of attraction, that are in general N-dimensional (only plane sections are usually given).

This fact may be more evident on examining a typical time series of α and ξ from numerical integration of Eq. 1 by a forth-order Runge-Kutta method for the speed value $U = 4.932$: transient state moves toward different steady state solution depending on given initial conditions (Figs. 5 and 6).

The stability of these LCO can be analyzed by means of the Floquet theory, whose results are partially shown in Fig. 7 in terms of Floquet multipliers moduli; when someone of these N multipliers gets out of the unit circle, the corresponding LCO becomes unstable. In Fig. 7, the multipliers whose modulus approaches unity are shown in the neighborhood of the linear flutter speed: the upper branch refers to the unstable limit cycle which starts in the bifurcation point (modulus larger than unity), while the lower branch refers to the stable limit cycle in which the unstable one turns in at turning point.

It is interesting also to point out the difference between linear and nonlinear stability regions in the plane of parameters U and a_h, as shown by Fig. 8. As long as the elastic center nears to the center of mass, linear and nonlinear boundaries lead to different lower flutter speed for the onset of flutter oscillations, because of the presence of the turning point whose abscissa (in the corresponding bifurcation plot) is reported in Fig. 8.

As outlined before, a nonlinear stability analysis has been developed by the normal forms method. In Fig. 9 third-order and fifth-order approximations of numerical simulation data are drawn in order to show how the third-order approximation does not succeed in describing at least qualitatively the 'knee-type' bifurcations. It is possible to note that fifth-order approximation leads to better results also for supercritical bifurcations for a_h values less than 0.48.

The poor agreement shown in Fig. 9 between the numerical and the 'analytically determined' minimum flutter speed suggests that fifth-order approximations are not sufficiently accurate in the neighborhood of the Hopf bifurcation. This is only partially true: first it is important to keep in mind that the error grows not with U but with the curvilinear abscissa along the bifurcation curve, as well pointed out by other perturbation techniques (*e.g.*, the Multiple Time Scale Method, see [12] for more details); second, the normal forms method has been applied under the center manifold hypothesis, that prescribes that only the critical modes (and the associated generalized

coordinates) worth considering. In the case of a 'knee' bifurcation, as shown in Fig. 10, this hypothesis is already violated for small values of $U - U_L$.

More informations about the system nonlinear behavior may be known by determining the frequencies of LCO. Such frequencies depend upon the velocity as well. For velocities less than the linear flutter one U_L, the modes corresponding to eigenvalues close to the imaginary axis are more effective in driving the solution than the larger damped ones, so that the frequency of oscillation is mainly given by the imaginary part of the corresponding eigenvalues. Beyond the linear flutter speed, in general the frequency of LCO depend on the velocity in a different manner than the imaginary part of the eigenvalues, as it is shown in 11. These numerical frequencies are approximated by the normal form method in Fig. 12.

A Model Equations

Consider a two-degree-of-freedom airfoil, elastically constrained by a torsional spring, oscillating in pitch and plunge. Using standard notations, the plunging deflection is denoted by h, positive in the downward direction, and α is the pitch angle about the elastic axis, positive with nose up. The elastic axis is located at a distance $a_h\, b$ from the mid-chord, while the mass center is located at a distance $x_\alpha\, b$ from the elastic axis. Both distances are positive when measured towards the trailing edge of the airfoil. The aeroelastic equations of motion for linear springs are derived by Fung [16]. For nonlinear restoring forces such as those for cubic springs in both pitch and plunge, they are given by Alighanbari *et al.* [6] as follows

$$\ddot{\xi} + x_\alpha \ddot{\alpha} + 2\zeta_\xi \frac{\bar{\omega}}{U}\dot{\xi} + \left(\frac{\bar{\omega}}{U}\right)^2 \xi = -p(\tau) \tag{12}$$

$$\frac{x_\alpha}{r_\alpha^2}\ddot{\xi} + \ddot{\alpha} + 2\zeta_\xi \frac{1}{U}\dot{\alpha} + \frac{1}{U^2} M(\alpha) = r(\tau) \tag{13}$$

where $\xi = h/b$ is the non-dimensional plunge displacement of the elastic axis, r_α is the radius of gyration about the elastic axis, ζ_ξ and ζ_α are the viscous damping coefficients in plunge and pitch, respectively; note that $M(\alpha)$ is the overall expression of the torsional spring moment, including the linear part. In Eqs. 12 and 13, U is defined as $U = V/b\omega_\alpha$ and $\bar{\omega}$ is given by $\bar{\omega} = \omega_\xi/\omega_\alpha$ where ω_ξ and ω_α are the uncoupled plunging and pitching modes natural frequencies, and the $\dot{}$ denotes differentiation with respect to the non-dimensional time τ defined as $\tau = V\,t/b$ In Eqs. 12 and 13, $p(\tau)$ and $r(\tau)$ are the lift and pitching moment, respectively. For the incompressible flow, Fung [16] gives the following expressions for $p(\tau)$ and $r(\tau)$

$$\begin{aligned} p(\tau) &= \frac{1}{\mu}\left(\ddot{\xi} - a_h\ddot{\alpha} + \dot{\alpha}\right) + \frac{2}{\mu}\int_0^\tau \phi(\tau-\sigma)\dot{\xi}_{3/4}(\sigma)\,d\sigma \\ r(\tau) &= \frac{1}{\mu r_\alpha^2}\left[a_h\left(\ddot{\xi} - a_h\ddot{\alpha}\right) - \bar{a}_h\dot{\alpha} - \frac{1}{8}\ddot{\alpha}\right] + \frac{2}{\mu r_\alpha^2}\left(\frac{1}{2} + a_h\right)\int_0^\tau \phi(\tau-\sigma)\dot{\xi}_{3/4}\,d\sigma \end{aligned}$$

with $\xi_{3/4}(\tau) = \dot{\xi}(\tau) + \bar{a}_h\dot{\alpha}(\tau) + \alpha(\tau)$ and $\bar{a}_h = 1/2(1 - a_h)$, where the Wagner function is approximated by $\phi(\tau) = 1 - a\,e^{-b\tau} - c\,e^{-d\tau}$ and the constants a, b, c and d are given by Jones [17]. Because of the existence of the integral term in the expression of aerodynamic forces, classical methods to investigate stability properties of dynamical systems do not work: for example, the system stability near equilibrium points cannot be analyzed readily since most of the available

methods for nonlinear dynamical systems are developed for ordinary differential equations. In order to eliminate the integral term, a new variable is defined as

$$u(\tau) = \int_0^\tau \phi(\tau - \sigma)\dot{\xi}_{3/4}(\sigma)d\sigma \tag{14}$$

The aim of successive algebraic manipulations in the Laplace domain (all the equations are Laplace-Transformed) is to re-write this relationship as a differential equation in the unknown function $u(t)$. In the following, transformed terms will be denoted by $\tilde{}$, while with the letter 's' is denoted the Laplace variable[2]. The Jones approximation of the Wagner function in the Laplace domain is

$$\tilde{\Phi}(s) = \frac{1}{s} - \frac{a}{s+b} - \frac{c}{s+d}$$

while the Laplace transform of u is $\tilde{u}(s) = \tilde{\Phi}(s)\, s\, \tilde{\xi}_{3/4}(s,y)$, where $\tilde{\xi}_{3/4}(s,y) = s\tilde{\xi}(s,y) + s\bar{a}_h\tilde{\alpha}(s,y) + \tilde{\alpha}(s,y)$. After some algebraic manipulation, the rational approximation of Theodorsen function is

$$\left(s^2 + e_{10}s + e_{11}\right)\tilde{u}(s) = \left(e_{13}s^2 + e_{12}s + e_{11}\right)\left(s\tilde{\xi}(s,y) + s\bar{a}_h\tilde{\alpha}(s,y) + \tilde{\alpha}(s,y)\right) \tag{15}$$

where it is possible to note the existence of third order derivatives of α and ξ, with

$$e_{10} = b + d\,; \qquad e_{11} = bd\,; \qquad e_{12} = b + d - bc - ad\,; \qquad e_{13} = 1 - a - c$$

At this point, the equation of motion are Laplace transformed and re-written as

$$\begin{aligned} &e_1\, s^2\, \tilde{\xi} + e_2\, s^2\, \tilde{\alpha} + e_3\, s\, \tilde{\xi} + e_4\, s\, \tilde{\alpha} + e_5\, \tilde{\xi} = -\tilde{u} \\ &e_6\, s^2\, \tilde{\xi} + e_7\, s^2\, \tilde{\alpha} + e_8\, s\, \tilde{\alpha} + e_9\, M(\alpha) = e_{14}\, \tilde{u} \end{aligned} \tag{16}$$

with coefficients

$$\begin{aligned} e_1 &= \frac{1}{2}(1+\mu) & e_2 &= \frac{1}{2}(-a_h + \mu x_\alpha) & e_3 &= \mu\zeta_\xi\frac{\bar{\omega}}{U} & e_4 &= \frac{1}{2} \\ e_5 &= \frac{1}{2}\mu\left(\frac{\bar{\omega}}{U}\right)^2 & e_6 &= -a_h + \mu x_\alpha & e_7 &= \frac{1}{8} + a_h^2 + \mu r_\alpha^2 & e_8 &= \bar{a}_h + 2\mu\zeta_\alpha\frac{r_\alpha^2}{U} \\ e_9 &= \mu\left(\frac{r_\alpha}{U}\right)^2 & e_{14} &= 1 + 2\,a_h \end{aligned}$$

Expliciting the higher order derivatives

$$\begin{aligned} s^2\,\tilde{\xi} &= a_{41}\tilde{\xi} + a_{43}\tilde{u} + a_{44}s\,\tilde{\xi} + a_{45}s\,\tilde{\alpha} + f_4\tilde{M}(\alpha) \\ s^2\,\tilde{\alpha} &= a_{51}\tilde{\xi} + a_{53}\tilde{u} + a_{54}s\,\tilde{\xi} + a_{55}s\,\tilde{\alpha} + f_5\tilde{M}(\alpha) \end{aligned} \tag{17}$$

where

and substituting Eq. 17 in the Eq. 15, with the aim of eliminating the second and third derivatives of α and ξ, it is possible in the end to obtain the differential equation for u explicited respect to the higher order derivative.

$$s^2\tilde{u} = a_{61}\tilde{\xi} + a_{62}\tilde{\alpha} + a_{63}u + a_{64}s\,\tilde{\xi} + a_{65}s\,\tilde{\alpha} + a_{66}s\,\tilde{u} + f_6\tilde{M}(\alpha) + f_7\tilde{M}'(\alpha)s\,\tilde{\alpha} \tag{18}$$

[2]Note that the same procedure can be developed in the time domain, but the use of differential calculus makes the things less clear

$$a_{41} = -\frac{e_5 e_7}{e_1 e_7 - e_6 e_2} \quad a_{43} = -\frac{e_7 + e_2 e_{14}}{e_1 e_7 - e_6 e_2} \quad a_{44} = -\frac{e_3 e_7}{e_1 e_7 - e_6 e_2}$$

$$a_{45} = -\frac{e_4 e_7 - e_2 e_8}{e_1 e_7 - e_6 e_2} \quad a_{51} = \frac{e_5 e_6}{e_1 e_7 - e_6 e_2} \quad a_{53} = \frac{e_6 + e_1 e_{14}}{e_1 e_7 - e_6 e_2}$$

$$a_{54} = \frac{e_3 e_6}{e_1 e_7 - e_6 e_2} \quad a_{55} = -\frac{e_1 e_8 - e_4 e_6}{e_1 e_7 - e_6 e_2} \quad f_4 = \frac{e_2 e_9}{e_1 e_7 - e_6 e_2}$$

$$f_5 = -\frac{e_1 e_9}{e_1 e_7 - e_6 e_2}$$

Denoting with M' the derivative respect to the variable α of the term $M(\alpha)$ and introducing the coefficients

$$\begin{aligned}
a_{61} &= a_{41}[e_{12} + e_{13}(a_{44} + a_{54})] + a_{51}[e_{12} + e_{13}(1 + a_{45} + a_{55})] \\
a_{62} &= e_{11} \\
a_{63} &= -e_{11} + a_{43}[e_{12} + e_{13}(a_{44} + a_{54})] + a_{53}[e_{12} + e_{13}(1 + a_{45} + a_{55})] \\
a_{64} &= e_{11} + e_{13}(a_{41} + a_{51}) + a_{44}[e_{12} + e_{13}(a_{44} + a_{54})] + a_{54}[e_{12} + e_{13}(1 + a_{45} + a_{55})] \\
a_{65} &= e_{11} + e_{12} + a_{45}[e_{12} + e_{13}(a_{44} + a_{54})] + a_{55}[e_{12} + e_{13}(1 + a_{45} + a_{55})] \\
a_{66} &= e_{13}(a_{43} + a_{53}) - e_{10} \\
f_6 &= f_4[e_{12} + e_{13}(a_{44} + a_{54})] + f_5[e_{12} + e_{13}(1 + a_{45} + a_{55})] \\
f_7 &= e_{13}(f_4 + f_5)
\end{aligned}$$

The inverse Laplace transform may be applied to Eqs. 17 and 18, yielding a system of three second-order differential equation, which may be easily re-written in the first-order linearly-diagonal form $\dot{\mathbf{x}} = \mathbf{\Lambda x} + \mathbf{f(x)}$ by using standard techniques.

References

[1] Guckenheimer, J. and Holmes, P., "Nonlinear Oscillations, Dynamical Systems, and Bifurcations of Vector Fields", *Applied Mathematical Sciences*, Springer-Verlag, New York, 1983

[2] Lacabanne, M., "An Experimental Analysis of the Aeroelastic Behaviour with a Freeplay in a Control Surface", *Proceeding of International Forum of Aeroelasticity and Structural Dynamics*, , Roma, 1997

[3] Matsushita, H, Saitoh, K. and Granasy, P., "Wind Tunnel Investigation of Transonic Limit Cycle FLutter", *AIAA Journal*, , 1998

[4] Lee, B.H.K. and Tron, A., "Effects of Structural Nonlinearities on Flutter Characteristics of the CF-18 Aircraft", *Journal of Aircraft*, **26**, pp. 781-786, 1989

[5] Chen, P.C., Sarhaddi, D. and Liu, D.D., "Limit-Cycle-Oscillations Studies of a Fighter with External Stores", *AIAA-98-1727*, pp. 258-266, 1998

[6] Alighanbari, H, and Price, S.J., "The Post-Hopf-Bifurcation Response of an Airfoil in Incompressible Two-Dimensional Flow", *Nonlinear Dynamics*, **10**, pp. 381-400, 1996

[7] Yang, Z.C. and Zhao, L.C., "Analysis of Limit Cycle Flutter of an Airfoil in Incompressible Flow", *Journal of sounds and vibration*, **123**, pp. 1-13, 1988

[8] Shen, S.F., "An Approximate Analysis of Nonlinear Flutter Problems", *Journal of Aeronautical Sciences*, **26**, pp. 25-32, 1959

[9] Lee, B.H.K., Jiang, L. and Wong, Y.S., "Flutter of an Airfoil with a Cubic Nonlinear Restoring Force", *AIAA-98-1725*, 1998

[10] Woolston, D.S., Runyan, H.L. and Andrews, R.E., "An Investigation of Certain Types of Structural Nonlinearities on Wing and Control Surface Flutter", *Journal of Aeronautical Sciences*, **24**, pp. 57-63, 1957

[11] Grzedzinski, J., "Flutter Calculation of an Aircraft with Nonlinear Structure based on Center-Manifold Reduction", *CEAS Conference*

[12] Dessi, D., "Analisi Teorica and Numerica del Fenomeno del Flutter Nonlineare", *Tesi di Dottorato di Ricerca in Ingegneria Aerospaziale*, Università di Roma 'La Sapienza', 1998

[13] Arnold, V.I., "Metodi Geometrici della Teoria delle equazioni Differenziali Ordinarie", Editori Riuniti - Edizioni Mir, Mosca, (I edizione), 1978

[14] Wiggins, S., "Introduction to Applied Nonlinear Dynamical Systems and Chaos", *Text in Applied Mathmatics*, Springer-Verlag, New York, 1990

[15] Chow, S and Hale, J. K., "Methods of Bifurcation Theory", Springer-Verlag, New York, 1982

[16] Fung, Y. C., "An Introduction to the Theory of Aeroelasticity", Dover Publications, New York, 1969

[17] Jones, R. T., "The Unsteady Lift of a Wing of Finite Aspect Ratio", NACA Rept. 681, 1940

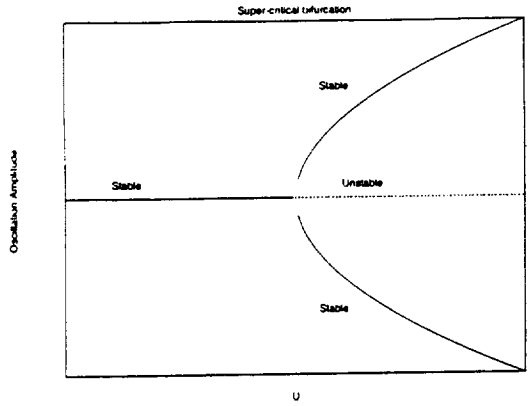

Figure 1: Super-critical Hopf Bifurcation - pitchfork-like shape

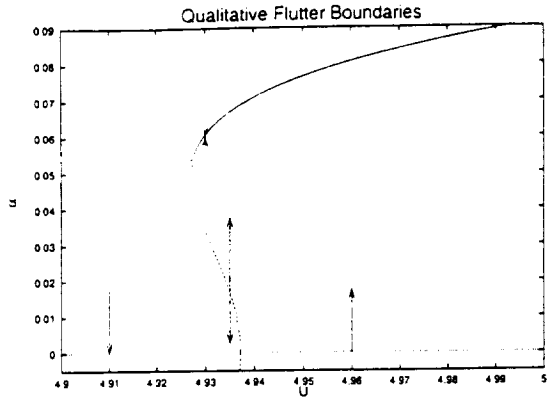

Figure 2: Sub-critical Hopf Bifurcation with turning point

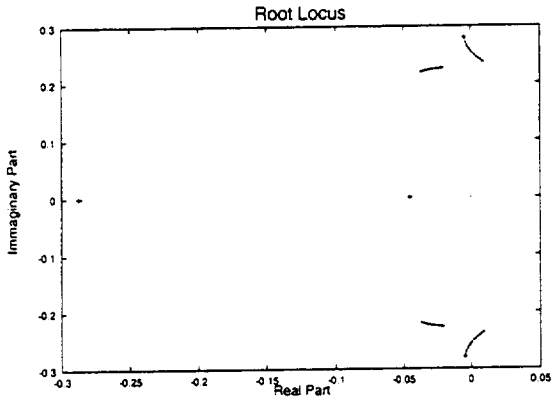

Figure 3: Root locus - eigenvalues of the linear part of equations of motion

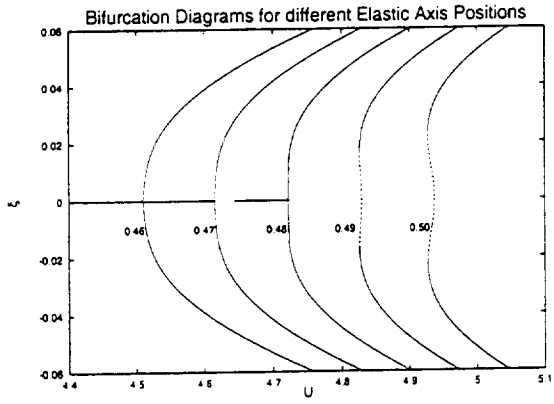

Figure 4: Numerical bifurcation diagrams (Shooting Method)

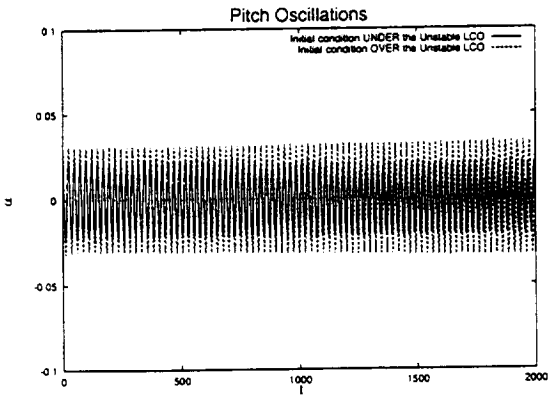

Figure 5: Time histories for plunge and pitch ($a_h = 0.5$, $U = 4.932$)

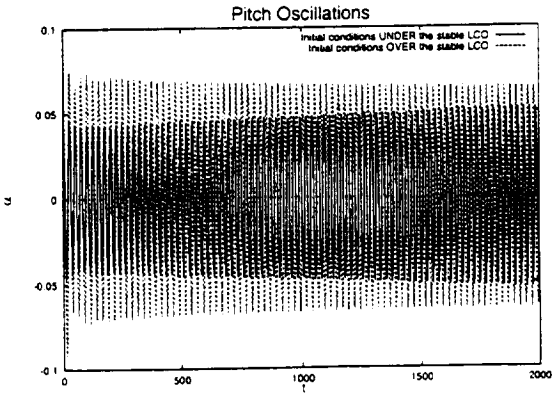

Figure 6: Time histories for plunge and pitch ($a_h = 0.5$, $U = 4.932$

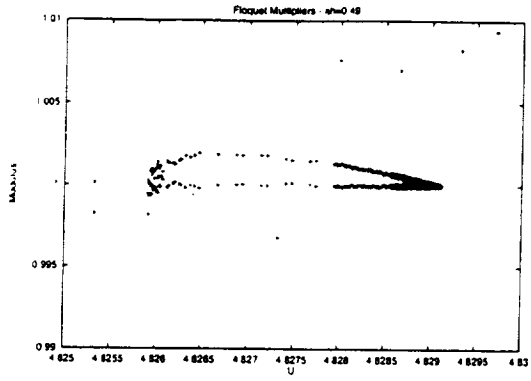

Figure 7: Floquet multipliers for stable and unstable branches of the bifurcation diagram - $a_h = 0.49$

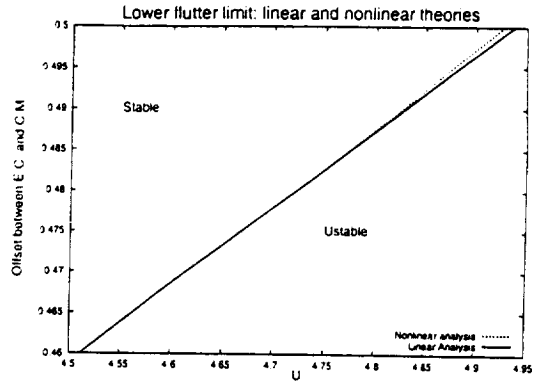

Figure 8: Stability zones in the plane (U, a_h): linear and nonlinear analysis for the lower flutter limit

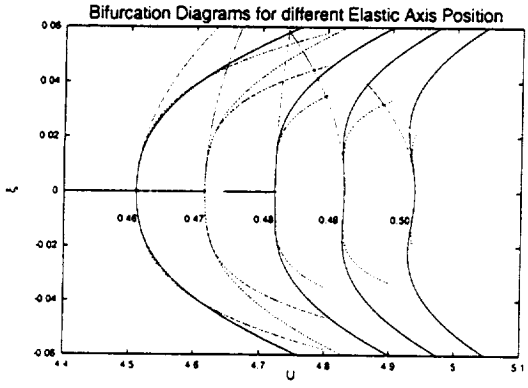

Figure 9: Bifurcation digrams and their approximation with the normal form method

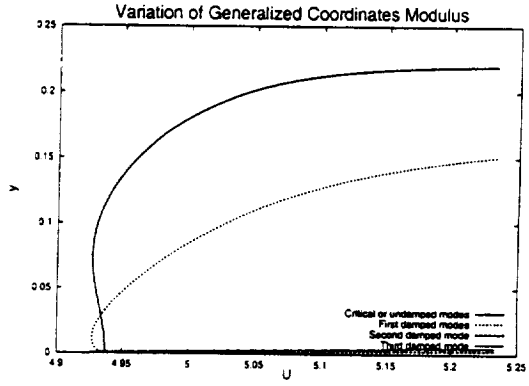

Figure 10: Generalized coordinates modulus in the neighborhood of U_L, results obtained by Shooting Method

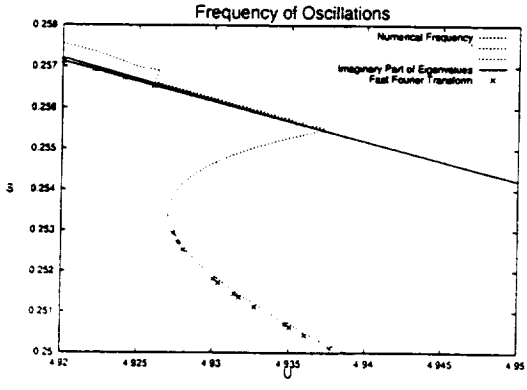

Figure 11: Numerical LCO frequencies vs. speed: comparison with imaginary part of the eigenvalues ($a_h = 0.5$)

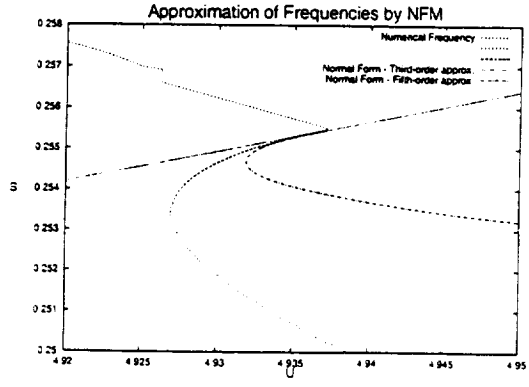

Figure 12: Numerical LCO frequencies vs. speed: comparison with normal form approximation

Application of the Centre Manifold Theory in Nonlinear Aeroelasticity*

L. Liu[1], Y. S. Wong[2]

Department of Mathematical Sciences
University of Alberta, Edmonton, Canada.

B. H. K. Lee[3]

Institute for Aerospace Research
National Research Council, Ottawa, Canada.

1. Introduction

In dynamic response investigations of aircraft structures, classical theories assume linear aerodynamics and linear structures, so that the aeroelastic equations can be reduced to a set of linear equations that can be readily solved. However, in many instances, linear aerodynamics give insufficiently accurate results. For example, when the airspeed approaches transonic Mach numbers, linear theory fails to detect the transonic dip and other phenomena associated with the presence of shock waves. Aircraft structures also can have nonlinearities that affect not only the flutter speed, but also the characteristics of the dynamical response. Hence, to obtain a better understanding of the physical and mathematical aspect of nonlinear aeroelasticity, recent research[11] has been directed towards the study of these two types of nonlinearities.

Lee et. al.[8-10] studied a two-degree-of-freedom aeroelastic system with a structural nonlinearity represented by a cubic restoring spring force. When the system is subject to an external forcing term with driving frequency ω, Lee et. al. derived analytical formulae that provide amplitude-frequency relationships for the pitch and plunge motion, respectively. However, for a self-excited system (i.e. in the absence of external forcing term), the reference frequency ω is not known, and the motion can not be determined from the amplitude-frequency relationships they derived. Several procedures were discussed in [9] to estimate the frequency value ω for the self-excited system, but the results were not satisfactory except when the velocity U^* is very close to the linear flutter speed U_L^*. To overcome this limitation in Lee et. al.[9] analysis, we apply the centre manifold theory of Carr[1] and the principal of normal form[13], to derive a frequency relation for self-excited motion of a two-degree-of-freedom nonlinear system. Using the frequency equation and the amplitude-frequency relationships, limit cycle oscillation (LCO) for self-excited system can be predicted analytically.

*This work is supported by the National Sciences and Engineering Research Council of Canada

[1]Research Student, email: lliu@vega.math.ualberta.ca

[2]Professor

[3]Principal Research Officer

2. Model formulation

The mathematical model presented in this paper is based on a coupled system of nonlinear integro-differential equations. The governing equations are derived for a two-degree-of-freedom motion of an airfoil oscillating in pitch and in plunge. The plunging deflection is denoted by h, positive in the downward direction, α is the pitch angle about the elastic axis, positive with the nose up. The elastic axis is located at a distance $a_h b$ from the midchord while the mass centre is located at a distance $x_\alpha b$ from the elastic axis. Both distances are positive when measured towards the trailing edge of the airfoil. The notations used are shown in Fig. 1. The aeroelastic equations of motion have been derived by Fung[2]. The equations which include the structure nonlinearities with subsonic aerodynamics are written as follows[8]:

$$\begin{aligned} \xi'' + x_\alpha \alpha'' + 2\zeta_\xi \frac{\bar{\omega}}{U^*}\xi' + (\frac{\bar{\omega}}{U^*})^2 G(\xi) &= -\frac{1}{\pi\mu}C_L(\tau) + \frac{P(\tau)b}{mU^2} \\ \frac{x_\alpha}{r_\alpha^2}\xi'' + \alpha'' + 2\zeta_\alpha \frac{1}{U^*}\alpha' + (\frac{1}{U^*})^2 M(\alpha) &= \frac{2}{\pi\mu r_\alpha^2}C_M(\tau) + \frac{Q(\tau)}{mU^2 r_\alpha^2} \end{aligned} \tag{1}$$

where $\xi = h/b$ is the nondimensional displacement and the $'$ denotes differentiation with respect to the nondimensional time τ defined as $\tau = Ut/b$. U^* is a nondimensional velocity defined as $U^* = U/b\omega_\alpha$, and $\bar{\omega}$ is given by $\bar{\omega} = \omega_\xi/\omega_\alpha$, where ω_ξ and ω_α are the uncoupled plunging and pitching modes natural frequencies, respectively. ζ_ξ and ζ_α are the damping ratios, r_α is the radius of gyration about the elastic axis. $G(\xi)$ and $M(\alpha)$ are the nonlinear plunge and pitch stiffness terms, respectively. $C_L(\tau)$ and $C_M(\tau)$ are the lift and pitching moment coefficients, respectively. For incompressible flow, Fung[2] gives the following expressions for $C_L(\tau)$ and $C_M(\tau)$:

$$\begin{aligned} C_L(\tau) =& \pi(\xi'' - a_h\alpha'' + \alpha') + 2\pi\{\alpha(0) + \xi'(0) + (\frac{1}{2} - a_h)\alpha'(0)\}\phi(\tau) \\ &+ 2\pi\int_0^\tau \phi(\tau-\sigma)(\alpha'(\sigma) + \xi''(\sigma) + (\frac{1}{2} - a_h)\alpha''(\sigma))d\sigma \\ C_M(\tau) =& \pi(\frac{1}{2} + a_h)\{\alpha(0) + \xi'(0) + (\frac{1}{2} - a_h)\alpha'(0)\}\phi(\tau) \\ &+ \pi(\frac{1}{2} + a_h)\int_0^\tau \phi(\tau-\sigma)\{\alpha'(\sigma) + \xi''(\sigma) + (\frac{1}{2} - a_h)\alpha''(\sigma)\}d\sigma \\ &+ \frac{\pi}{2}a_h(\xi'' - a_h\alpha'') - (\frac{1}{2} - a_h)\frac{\pi}{2}\alpha' - \frac{\pi}{16}\alpha'' \end{aligned}$$

where the Wagner function $\phi(\tau)$ is given by

$$\phi(\tau) = 1 - \psi_1 e^{-\varepsilon_1\tau} - \psi_2 e^{-\varepsilon_2\tau}$$

and the constants $\psi_1 = 0.165$, $\psi_2 = 0.335$, $\varepsilon_1 = 0.0455$, and $\varepsilon_2 = 0.3$ are obtained from Jones[5]. $P(\tau)$ and $Q(\tau)$ are the externally applied forces and moments, respectively.

To eliminate the integral terms in the integro-differential equations given in (1), Lee et. al.[8] introduced four new variables:

$$w_1 = \int_0^\tau e^{-\varepsilon_1(\tau-\sigma)}\alpha(\sigma)d\sigma, \qquad w_2 = \int_0^\tau e^{-\varepsilon_2(\tau-\sigma)}\alpha(\sigma)d\sigma,$$

$$w_3 = \int_0^\tau e^{-\varepsilon_1(\tau-\sigma)}\xi(\sigma)d\sigma, \qquad w_4 = \int_0^\tau e^{-\varepsilon_2(\tau-\sigma)}\xi(\sigma)d\sigma.$$

The system (1) can then be rewritten in a general form containing only differential operators as:

$$\begin{aligned} c_0\xi'' + c_1\alpha'' + c_2\xi' + c_3\alpha' + c_4\xi + c_5\alpha + c_6w_1 + c_7w_2 + c_8w_3 \\ + c_9w_4 + (\frac{\bar{\omega}}{U^*})^2 G(\xi) = f(\tau) \\ d_0\xi'' + d_1\alpha'' + d_2\alpha' + d_3\alpha + d_4\xi' + d_5\xi + d_6w_1 + d_7w_2 + d_8w_3 \\ + d_9w_4 + (\frac{1}{U^*})^2 M(\alpha) = g(\tau) \end{aligned} \tag{2}$$

The coefficients $c_0, c_1, ...c_9, d_0, d_1, ...d_9$ are given in appendix A of Ref[11]. $f(\tau)$ and $g(\tau)$ are functions depending on initial conditions, Wagner function and the forcing terms, namely,

$$f(\tau) = \frac{2}{\mu}((1/2 - a_h)\alpha(0) + \xi(0))(\psi_1\varepsilon_1 e^{-\varepsilon_1\tau} + \psi_2\varepsilon_2 e^{-\varepsilon_2\tau}) + \frac{P(\tau)b}{mU^2},$$

$$g(\tau) = -\frac{(1+2a_h)}{2r_\alpha^2}f(\tau) + \frac{Q(\tau)}{mU^2r_\alpha^2}.$$

By introducing a variable vector $X = (x_1, x_2, ...x_8)^T$ with $x_1 = \alpha$, $x_2 = \alpha'$, $x_3 = \xi$, $x_4 = \xi'$, $x_5 = w_1$, $x_6 = w_2$, $x_7 = w_3$, and $x_8 = w_4$, the coupled equations given in (2) can be written as a set of eight first order ordinary differential equations $X' = f(X, \tau)$. In this paper, we assume that there is no external forcing, i.e. $Q(\tau) = P(\tau) = 0$ in (1). For large values of τ when transients are damped out and steady solutions are obtained, $f(\tau) = 0$ and $g(\tau) = 0$. Thus, the system can be expressed as $X' = f(X)$, i.e.,

$$\begin{cases} x_1' = x_2 \\ x_2' = a_{21}x_1 + a_{22}x_2 + a_{23}x_3 + a_{24}x_4 + a_{25}x_5 + a_{26}x_6 + a_{27}x_7 \\ \quad +a_{28}x_8 + j(d_0(\frac{\bar{\omega}}{U^*})^2 G(x_3) - c_0(\frac{1}{U^*})^2 M(x_1)) \\ x_3' = x_4 \\ x_4' = a_{41}x_1 + a_{42}x_2 + a_{43}x_3 + a_{44}x_4 + a_{45}x_5 + a_{46}x_6 + a_{47}x_7 \\ \quad +a_{48}x_8 + j(c_1(\frac{1}{U^*})^2 M(x_1) - d_1(\frac{\bar{\omega}}{U^*})^2 G(x_3)) \\ x_5' = x_1 - \varepsilon_1 x_5 \\ x_6' = x_1 - \varepsilon_2 x_6 \\ x_7' = x_3 - \varepsilon_1 x_7 \\ x_8' = x_3 - \varepsilon_2 x_8 \end{cases} \tag{3}$$

The expressions for j, a_{21}, ..., a_{28}, a_{41}, ..., a_{48} are given in Chapter 5 of Ref[11].

In this paper, the structual nonlinearities are represented by cubic functions $M(\alpha)$ and $G(\xi)$, such that

$$M(\alpha) = \beta_1\alpha + \beta_3\alpha^3 \tag{4}$$

where β_1 and β_3 are constants. A Similar expression for $G(\xi)$ in the plunge degree of freedom can be written by replacing α with ξ.

3. Centre manifold and normal form

Following the analysis presented by Lee, Jiang & Wong[9], the bifurcation parameter is associated with U^*, and the bifurcation value is U_L^*, which is the value of the linear flutter speed. To study the dynamic response of the system, we introduce a perturbation parameter δ such that $1/U^* = (1-\delta)/U_L^*$. Introducing this expression into (3), an autonomous system with the bifurcation parameter is obtained, i.e, $X' = f(X;\delta)$. The equilibrium points are then evaluated from $f(X;\delta) = 0$. Without lose of generality, we assume the origin to be the equilibrium point. The original system (3) can now be rewritten as:

$$\begin{cases} X' = A \cdot X + \delta B \cdot X + (1-\delta)^2 F(X) \\ \delta' = 0 \end{cases} \tag{5}$$

The matrix A is an 8×8 Jacobian matrix evaluated at the equilibrium point and the bifurcation value (i.e. $\delta = 0$). A has one pair of purely imaginary eigenvalue $\lambda_1 = i\omega_0$, $\bar{\lambda}_1 = -i\omega_0$, one pair of complex eigenvalue with negative real part, $\lambda_2 = b + ic$, $\bar{\lambda}_2 = b - ic$, and four negative real eigenvalues λ_3, λ_4, λ_5, λ_6. The second and the third terms of equation (5) are nonlinear in X and δ, and the expressions for B and F are given in Ref[11].

To apply the center manifold theory, we first transform system (5) to a standard form. A transformation matrix P is obtained from the eigenspace of A, such that

$$P^{-1} \cdot A \cdot P = \begin{pmatrix} J_1 & 0 \\ 0 & J_2 \end{pmatrix} := J, \quad J_1 = \begin{pmatrix} 0 & \omega_0 \\ -\omega_0 & 0 \end{pmatrix}$$

$$J_2 = \begin{pmatrix} b & c & 0 & 0 & 0 & 0 \\ -c & b & 0 & 0 & 0 & 0 \\ 0 & 0 & \lambda_3 & 0 & 0 & 0 \\ 0 & 0 & 0 & \lambda_4 & 0 & 0 \\ 0 & 0 & 0 & 0 & \lambda_5 & 0 \\ 0 & 0 & 0 & 0 & 0 & \lambda_6 \end{pmatrix}.$$

Introducing a new variable, $Y = P^{-1} \cdot X = (y_1, y_2, \ldots, y_8)^T$, system (5) becomes:

$$\begin{cases} Y' = J \cdot Y - \delta(P^{-1} \cdot B \cdot P)Y + (1-\delta)^2 P^{-1} \cdot F(P \cdot Y) \\ \delta' = 0 \end{cases} \tag{6}$$

The dynamic response of system (6), which is in 9-dimensions, can be investigated through an invariant two-dimensional system. This is achieved by applying the centre manifold theory given by Carr[1]. Let $J_3 = \begin{pmatrix} J_1 & 0 \\ 0 & 0 \end{pmatrix}$, $Y_A = (y_1, y_2, \delta)^T$, $Y_B = (y_3, y_4, y_5, y_6, y_7, y_8)^T$, system (6) can be rewritten as

$$\begin{cases} Y_A' = J_3 \cdot Y_A + F_A(Y_A, Y_B) \\ Y_B' = J_2 \cdot Y_B + F_B(Y_A, Y_B) \end{cases} \tag{7}$$

where F_A and F_B are nonlinear functions of Y_A and Y_B starting from the second order terms while the first order terms have already been included in the first part associated with Y_A

and Y_B. From the centre manifold theorem given by Carr[1], there exists a centre manifold H for (6). The important consequence is that the solution of the second system given in (7) can be expressed as $Y_B = H(Y_A)$. Hence, the flow of (7) near the equilibrium point is governed by $Y_A' = J_3 \cdot Y_A + F_A(Y_A, H(Y_A))$, which is a 3-dimensional system.However, the exact expression of the function H is often impossible to obtain. Following another important result given by Carr[1], the centre manifold H can now be approximated to any desired degree of accuracy. Assuming the polynomial approximation of the centre manifold H is denoted by $\Phi = (\phi_3, \phi_4, \phi_5, \phi_6, \phi_7, \phi_8)^T$, in which:

$$\phi_i(y_1, y_2, \delta) = h_{i1}y_1\delta + h_{i2}y_2\delta + h_{i3}y_1^2 + h_{i4}y_2^2 + h_{i5}\delta^2 + h_{i6}y_1y_2 \tag{8}$$

$$i = 3, 4, 5, 6, 7, 8$$

where h_{31}, h_{32}, ..., h_{36}, h_{41}, ..., ..., h_{86} are constants to be determined from using the centre manifold theory. Substituting (8) into the second system of (7): $\Phi'(Y_A) \cdot Y_A' = J_2 \cdot \Phi(Y_A) + F_B(Y_A, \Phi(Y_A))$, and applying the first system of (7) to replace Y_A': $\Phi'(Y_A) \cdot (J_3 \cdot Y_A + F_A(Y_A, \Phi(Y_A))) = J_2 \cdot \Phi(Y_A) + F_B(Y_A, \Phi(Y_A))$, we equate the coefficients associated with $y_1\delta$, $y_2\delta$, y_1^2, y_2^2, δ^2, and y_1y_2 to obtain a system of 36 algebraic equations with h_{31}, h_{32}, ..., h_{86} as variables. These equations can be solved by a computer program such as Maple[4]. Extension to a higher order center manifold is straightforward, but the algebra becomes considerably much more complex.

Once the expression of the center manifold is obtained, the original system will be reduced to a three dimensional system on the center manifold. Since the solution of the reduced system will not be exactly indentical to Y_A, we denote the corresponding solutions for y_1 and y_2 by u_1 and u_2, respectively. Regarding δ as a parameter, the system is reduced to two dimensions:

$$\begin{cases} u_1' = \omega_0 u_2 + g_1(u_1, u_2, \delta) \\ u_2' = -\omega_0 u_1 + g_2(u_1, u_2, \delta) \end{cases} \tag{9}$$

where g_1 and g_2 contain the nonlinear terms as functions of u_1, u_2 and δ. An important result in the application of the centre manifold theorem is that the asymptotic behavior of the solutions near the equilibrium point and the bifurcation value of the original eight dimensional system can now be studied by analyzing the reduced two dimensional system given in (9).

To simplify equation (9) for symbolic computations, we rewrite the system as:

$$U' = B \cdot U + F(U) \tag{10}$$

with

$$B = \begin{pmatrix} b_{11}(\delta) & b_{12}(\delta) \\ b_{21}(\delta) & b_{22}(\delta) \end{pmatrix}, \qquad F(U) = \begin{pmatrix} f_1(u_1, u_2, \delta) \\ f_2(u_1, u_2, \delta) \end{pmatrix}.$$

where $U = (u_1, u_2)^T$. The first term $B \cdot U$ is the linear part for u_1, u_2, and the second term $F(U)$ is the nonlinear part for u_1, u_2.

Now let the transformation matrices:

$$NP = \frac{1}{\sqrt{b_{12}^2 + \omega^2 + (\alpha - b_{11})^2}} \begin{pmatrix} 0 & b_{12} \\ \omega & \alpha - b_{11} \end{pmatrix},$$

$$NP^{-1} = \frac{\sqrt{b_{12} + \omega^2 + (\alpha - b_{11})^2}}{b_{12}\omega} \begin{pmatrix} -\alpha + b_{11} & b_{12} \\ \omega & 0 \end{pmatrix}.$$

where $\alpha = \frac{1}{2}(b_{11} + b_{12})$, $\omega = \sqrt{b_{11}b_{22} - b_{12}b_{21} - \alpha^2}$. By introducing a new variable $Y = NP^{-1} \cdot U$, $Y = (y_1, y_2)^T$, $U = (u_1, u_2)^T$, system (10) can be transformed into the standard form:

$$Y' = J \cdot Y + NP^{-1} \cdot F(NP \cdot Y)$$

i.e.

$$\begin{cases} y_1' = \alpha y_1 - \omega y_2 + F_1(y_1, y_2, \delta) \\ y_2' = \omega y_1 + \alpha y_2 + F_2(y_1, y_2, \delta) \end{cases} \tag{11}$$

where F_1, F_2 are nonlinear terms of y_1 and y_2 , α and ω are related to the parameter δ.

The complex form of system (11) can be written as:

$$Z' = \lambda Z + h(Z, \bar{Z})$$

where $\lambda(\delta) = \alpha(\delta) + i\omega(\delta)$, $Z = y_1 + iy_2$, $h(Z, \bar{Z})$ includes nonlinearities of Z and $\bar{Z}$ starting from the second order terms.

By the principle of normal form, we now introduce the near identity transformation:

$$Z = V + g(V, \bar{V})$$

where V is a new variable , and g includes the second and the third order nonlinearities of V and $\bar{V}$. The normal form of the system (10) can be expressed as:

$$V' = \lambda V + F_{21} V^2 \bar{V}$$

where F_{21} is a complex number whose value is related to δ.

Taking $a(\delta) = Re(F_{21})$ and $b(\delta) = Im(F_{21})$, we express $V = r(\tau) * e^{\theta(\tau)}$, and write the normal form in polar coordinates as:

$$\begin{cases} r' = \alpha r + ar^3 \\ \theta' = \omega + br^2 \end{cases}$$

Expanding the coefficients α, ω a and b at $\delta = 0$, the above system becomes:

$$\begin{cases} r' = \dot{\alpha}(0)\delta r + a(0)r^3 = r(\dot{\alpha}(0)\delta + a(0)r^2) \\ \theta' = \omega(0) + \dot{\omega}(0)\delta + b(0)r^2 = (\omega(0) + \dot{\omega}(0)\delta) + b(0)r^2 \end{cases} \tag{12}$$

Note that the prime denotes derivatives with respect to τ and the dot denotes derivatives with respect to δ. The stability of the fixed point and the periodic orbit can be analyzed . Furthermore, the frequency of the limit cycle oscillations can be predicted from a frequency equation given by:

$$\omega = \omega_0 + (\dot{\omega}(0) - \frac{b(0)\dot{\alpha}(0)}{a(0)})\delta \tag{13}$$

The amplitude of the motion of the original system can be predicted from the reduced system on the center manifold. However, due to errors introduced in approximating the centre manifold, the predicted amplitude value may not be sufficiently accurate. For an autonomous system, Lee et al.[9] derived the following amplitude-frequency relationship using the standard perturbation method:

$$\begin{cases} R^2 = f_1(\omega) \pm \sqrt{f_2(\omega)} \\ r^2 = A(\omega) R^2 \end{cases} \tag{14}$$

where R and r denote the amplitude for pitch and plunge motion, respectively, f_1, f_2 and A are functions of ω and the aerodynamic parameters, and they are defined in Ref[9]. Together with the frequency equation given in (13), the amplitude of the limit cycle oscillation can be predicted.

4. Case studies and discussion

To illustrate the accuracy of the analytical formulae given in equations (13) and (14) in predicting the frequency and amplitude of limit cycle oscillations, we consider the following two examples. In both cases, the analytical predictions are compared with solutions obtained by using the Runge-Kutta fourth-order numerical time integration scheme applied to the system (3).

In the first example, we investigate the aeroelastic system with only a cubic structural nonlinearity in the pitch degree of freedom, i.e., $M(\alpha) = \alpha + 3\alpha^3$, $G(\xi) = \xi$. The elastic axis of the airfoil is placed at the 1/4 chord point (i.e. $a_h = -1/2$), the other coefficients in system (3) are given by $\mu = 100$, $x_\alpha = 1/4$, $\zeta_\xi = \zeta_\alpha = 0$, $r_\alpha = 0.5$, and $\bar{\omega}$ is varied.

Since $\zeta_\alpha = \zeta_\xi = 0$, it is more convenient to define the bifurcation parameter δ as $1/(U^*)^2 = (1-\delta)/(U_L^*)^2$. This will simplify the algebraic computations, while achieving the same result as that of using δ as $1/U^* = (1-\delta)/U_L^*$. For different $\bar{\omega}$, the bifurcation value U_L^* is different, thus results in different frequency equations.

For the system parameters used, $U_L^* = 6.28509$ for $\bar{\omega} = 0.2$. The approximate centre manifold is given by:

$$\begin{cases} \phi_3 = -2.278662600 y_1 \delta - 2.932984813 y_2 \delta \\ \phi_4 = 5.389063673 y_1 \delta - 3.395569702 y_2 \delta \\ \phi_5 = -2.576198739 y_1 \delta + 0.5470484684 y_2 \delta \\ \phi_6 = -0.03759292923 y_1 \delta + 0.05243761634 y_2 \delta \\ \phi_7 = 0.01137223245 y_1 \delta - 0.01813461435 y_2 \delta \\ \phi_8 = -7.328109745 y_1 \delta + 0.4092693894 y_2 \delta \end{cases}$$

Substituting $y_3 = \phi_3$, $y_4 = \phi_4$, $y_5 = \phi_5$, $y_6 = \phi_6$, $y_7 = \phi_7$, $y_8 = \phi_8$ into the first two equations of (7), a governing system of equations for y_1 and y_2 is obtained. Note that by replacing y_i using the above expressions given in ϕ_i, for $i = 3, 4, 5, 6, 7, 8$, the solution for system (7) can be approximated by explicit functions in terms of y_1, y_2 and δ. However, y_1, y_2 are no

longer exactly identical to those defined in the original system (6), hence we denote y_1 and y_2 by u_1 and u_2. Therefore,

$$\begin{cases} u_1' = -.08404421373u_2 - .005002186045\delta u_1 + .022980152 61\delta u_2 \\ \quad +.000001060912229u_1^3 - .00001078496711u_1^2u_2 + .07708383842\delta^2 u_1 \\ \quad +.00003654575512u_1u_2^2 - .00004127944026u_2^3 - .06508466062\delta^2 u_2 \\ u_2' = .08404421392u_1 - .1034553702\delta u_1 + .3210345363\delta u_2 \\ \quad +.00002847473453u_1^3 - .0002894669955u_1^2u_2 + .3223789845\delta^2 u_1 \\ \quad +.0009808829109u_1u_2^2 - .001107934352u_2^3 - 1.281473950\delta^2 u_2 \end{cases}$$

Transform this reduced system into a standard form, rewritting the standard form in complex form, and introducing the near identity transformation, we obtain the normal form. Applying Taylor expansion to the coefficients of the normal form expressions in polar coordinates, the coefficients in Eq.(12) are given by:

$$\begin{aligned} \omega(0) &= \omega_0 = 0.08404421382 \\ \dot{\omega}(0) &= -0.06321776140 \\ \dot{\alpha}(0) &= 0.1580161751 \\ a(0) &= -0.0002233463476 \\ b(0) &= 0.00007505815011 \end{aligned}$$

By analyzing system (12) with these results, we can verify that when $\delta < 0$, the equilibrium point is asymptotically stable, which means that for $U^* < U_L^*$, all motions will finally decay to zero amplitude. For $\delta > 0$, the equilibrium point becomes unstable. However, there is a stable periodic orbit with a frequency $\omega = 0.0840 - 0.0101\delta$ when $\bar{\omega} = 0.2$.

For different values of $\bar{\omega}$, and using the same procedure, we derived the corresponding frequency relation which depends on the bifurcation parameter δ (or the ratio $\gamma = U^*/U_L^*$) as shown in Table 1. Numerical simulations using Runge-Kutta scheme were carried out to compare with the analytical predictions.

Table 1. The frequency relationship with the bifurcation parameter $\gamma = U^*/U_L^*$.

$\bar{\omega}$	$\omega = \omega(\delta)$	$\omega = \omega(\gamma)$	U_L^*
0.2	$0.0840 - 0.0101 * \delta$	$0.0739 + 0.0101/\gamma^2$	6.28509
0.4	$0.1192 - 0.0333 * \delta$	$0.0859 + 0.0333/\gamma^2$	5.23376
0.6	$0.1730 - 0.0616 * \delta$	$0.1114 + 0.0616/\gamma^2$	4.40100
0.8	$0.2244 - 0.0823 * \delta$	$0.1421 + 0.0823/\gamma^2$	4.11454
1.0	$0.2522 - 0.0702 * \delta$	$0.1820 + 0.0702/\gamma^2$	4.33559

In Figs 2(a) and 2(b), we display the frequency and the amplitude for pitch motion that are predicted using the analytical formulae (13) and (14) when $\bar{\omega}$=0.2. These results are compared with numerical simulations, and it is shown that excellent agreement in both frequency and amplitude of the limit cycle oscillations is obtained.

In the second example, we consider an aeroelastic system with cubic structural nonlinearities in both pitch and plunge. Here, $M(\alpha) = \alpha + \beta_\alpha \alpha^3$ and $G(\xi) = \xi + \beta_\xi \xi^3$, where

$\beta_\alpha = 40$ and $\beta_\xi = 0.1$. The other coefficients are the same as defined in the previous example with $\bar{\omega}$ varying. For different $\bar{\omega}$, with the corresponding bifurcation value U_L^*, the frequency relations with the bifurcation parameter $\delta = 1 - (U_L^*/U^*)^2$ are obtained. In the derivation of the frequency equation for a fixed value of $\bar{\omega}$, we can show that when either β_α or β_ξ is zero, the nonlinear coefficients do not affect the resulting frequency. When both coefficients β_α and β_ξ are presence but $\beta_\alpha >> \beta_\xi$, then the frequency relations is not sensitive to the values of β_α and β_ξ. Hence, for the example considered here where $\beta_\alpha = 40$ and $\beta_\xi = 0.1$, the frequency equations for a given $\bar{\omega}$ are almost the same as those reported in Table 1. However, the corresponding amplitudes give by Eq.(14) are dependent upon the nonlinear coefficients β_α and β_ξ. In Figs (3a) and (3b), we display the frequency and the amplitude for the pitch motion for $\bar{\omega} = 0.2$. These results show that the agreement with numerical simulation is excellent.

References

[1] Carr,J. (1981) Application of Centre Manifold Theory, Springer-Verlag, New York.

[2] Fung,Y.C. (1993) An Introduction to the Theory of Aeroelasticity, Dover Publications Inc., New York.

[3] Guckenheimer,J. and Holmes,P. (1993) Nonlinear Oscillations, Dynamical Systems, and Bifurcation of Vector Fields, Springer-Verlag.

[4] Heck,A. (1993)Introduction to Maple, Springer-Verlag, New York.

[5] Jones,D.J. and Lee,B.H.K. (1985) Time marching numerical solution of the dynamic response of nonlinear systems, National Research Council of Canada, Aeronautical Note, NAE-AN-25, NRC No. 24131.

[6] Krylov,N. and Bogoliubov,N. (1947) Introduction to Nonlinear Mechanics, translation by Solomon Lifschitz, Princeton University Press, Princeton.

[7] Lee,B.H.K. and Desrochers,J. (1987) Flutter analysis of a two-dimensional airfoil containing structural nonlinearities, National Research Council of Canada, Aeronautical Report LR-618, NRC No. 27833.

[8] Lee,B.H.K. Gong,L. and Wong,Y.S. (1997) Analysis and computation of nonlinear dynamic response of a two-degree-of-freedom system and its application in aeroelasticity, *J. Fluids Structures* 11, 225-246.

[9] Lee,B.H.K. Jiang,L.Y. and Wong,Y.S. (1999) Flutter of an airfoil with a cubic nonlinear restoring force, *J. Fluids Structures* 13, 75–101.

[10] Lee,B.H.K. and LeBlanc,P. (1986) Flutter analysis of a two-dimensional airfoil with cubic nonlinear restoring force, National Research Council of Canada, Aeronautical Note NAE-AN-36, NRC No. 25438.

[11] Lee,B.H.K. Price,S.J. and Wong,Y.S. (1999)Nonlinear Aeroelastic Analysis of Airfoils: Bifurcation and Chaos, to appear in Progress in Aerospace Sciences.

[12] Nayfeh,A.H. and Mook,D.T. (1979)Nonlinear Oscillations, John Wiley & Sons, New York.

[13] Wiggins,S. (1996)Introduction to Applied Nonlinear Dynamical Systems and Chaos, Springer-Verlag, New York.

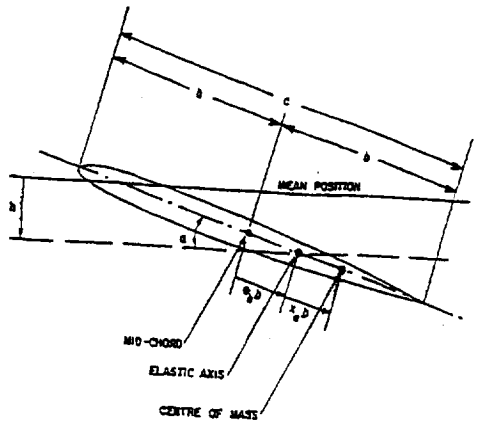

Fig. 1. Two-degree-of-freedom airfoil motion.

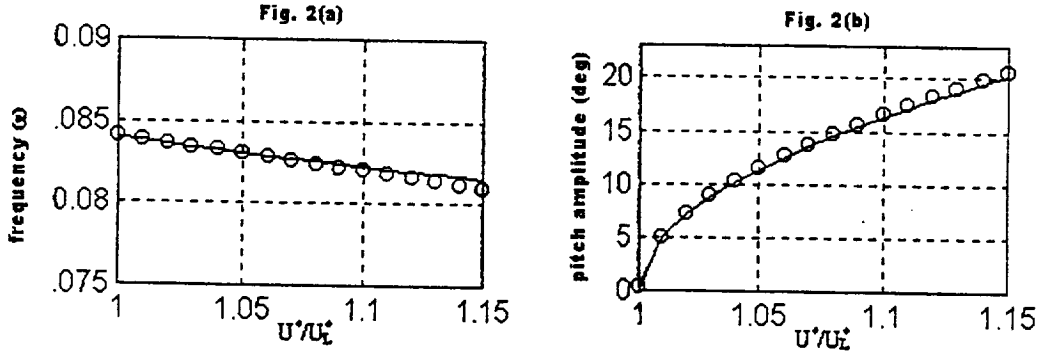

Fig. 2: Frequency and amplitude of pitch motion for ϖ=8.2.
Cubic nonlinearity in pitch degree-of-freedom.
—: prediction, O: numerical.

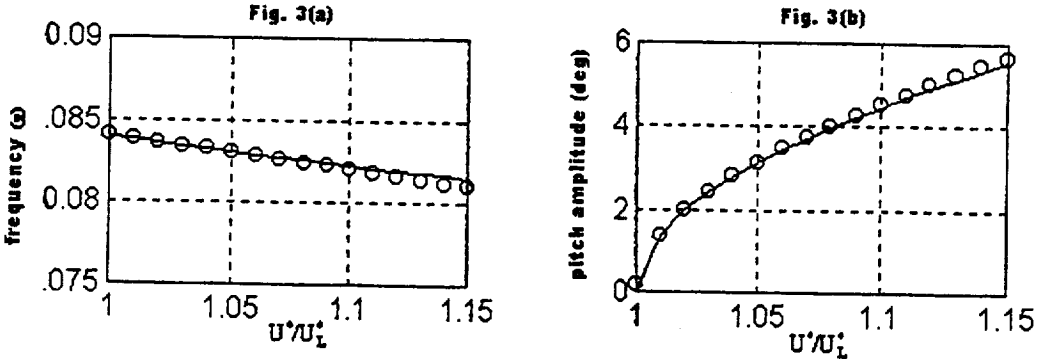

Fig. 3: Frequency and amplitude of pitch motion for ϖ=8.2.
Cubic nonlinearities both in pitch, plunge degree-of-freedom.
—: prediction, O: numerical.

FLUTTER SUPPRESSION AND VIBRATION CONTROL OF PLATE-WING STRUCTURES USING SELF-SENSING ACTIVE CONSTRAINED LAYER DAMPING

Jeng-Jong Ro and Ehab Elsaadawy

Aerospace Engineering Dept.
Old Dominion University
Norfolk, VA 23529

ABSTRACT

Active Constrained Layer Damping (ACLD) treatment has been used successfully for controlling the vibration of various flexible structures. The treatment provides an effective means for augmenting the simplicity and reliability of passive damping with the low weight and high efficiency of active controls to attain high damping characteristics over broad frequency bands. In this study, a self-sensing configuration of the ACLD treatment is utilized to simultaneously suppress the bending and torsional vibrations of plates and flutter control of a plate-wing structure. The treatment considered ensures collocation of the sensor/actuator pairs in order to guarantee stable operation.

First part of this study, a three-layer network of the Self-sensing Active Constrained Layer Damping (SACLD) treatment is used to control multi-modes of vibration of a flexible aluminum plate (0.264m x 0.127m x 4.826E-4m) which is mounted in a cantilevered arrangement. Two ACLD patches (0.264m x 0.0635m) with self-sensing polyvinylidine fluoride (PVDF) actuators oriented by (14°/-14°) configuration are treated on one side of plate. The theoretical characteristics of the multi-layer treatment are presented in this paper and compared with the experimental performance.

Secondly, the concept of vibration control using SACLD/plate is implemented to perform the flutter suppression experimentally. The experimental demonstration of flutter control of the SACLD/plate-wing structure is performed in the Low Speed wind Tunnel (LST) at Aerospace Department at ODU. Simple linear control with self-sensing strain and strain rate feedback is utilized to study the performance of the SACLD/plate in flutter control.

1. INTRODUCTION

The ACLD treatment combines the attractive attributes of both the passive and active controls to achieve optimal vibration damping. In general, the ACLD system includes several elements: a piezoelectric element as the active constraining layer, a viscoelastic element as the constrained shear layer, a sensor sensing the vibration and a feedback controller as shown in Figure (1). The effectiveness of ACLD treatments and its high rate of energy dissipation as compared to conventional constrained layer damping are attributed to the enhanced shear strain

of the viscoelastic layer which is produced by extension/contraction of the piezo-actuators[1-4]. Such characteristics make the ACLD treatment provide a practical means for controlling the vibration of massive structures with the currently available piezoelectric actuators without the need for excessively large actuation voltages.

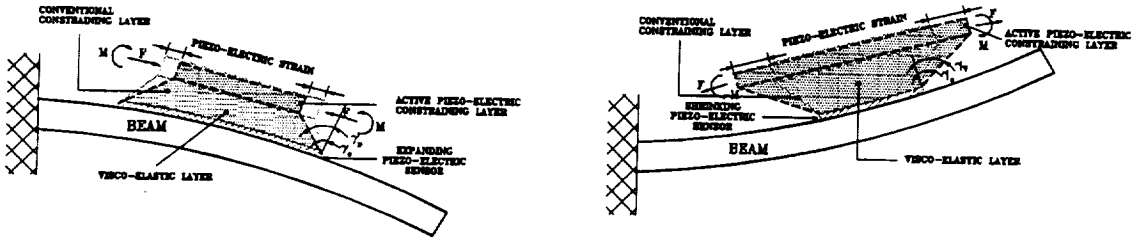

Figure (1) – Schematic drawing of Active Constrained Layer Damping (ACLD) treatment.

A new type of Self-sensing Active Constrained Layer Damping (SACLD) which combines the ACLD configurations with self-sensing polyvinylidine fluoride (PVDF) actuators was developed by Yellin and Shen[5]. The actuator and the sensor are combined into a single element called a self-sensing actuator. The self-sensing PVDF actuators have the advantage of being truly collocated compared to separated sensor and actuator in close proximity. Collocated control has been shown to have many advantages relating to the closed-loop stability. Goh and Caughey[6] demonstrated that without considering the dynamic characteristics of sensors and actuators, the collocated control structures are unconditionally stable at all frequencies.

Several researchers have studied the applications of the self-sensing piezoelectric actuators. Dosch, et al.[7] developed a self-sensing technique to actively damp the vibration in a cantilever beam with rate feedback control and positive position feedback control. In their study, a simple analog bridge circuit was developed to implement the self-sensing actuator for measuring either strain or rate of strain in the actuator. Anderson and Hagood[8] investigated several important issues related to the modeling and implementation of a self-sensing piezoelectric actuator. The study showed that small change in the bridge circuit impedance would significantly alter the open-loop zeros and degrade the closed-loop system performance. It emphasized that the critical step in designing the bridge circuit is an impedance match between the self-sensing piezoelectric element and a reference impedance. Vipperman and Clock[9] presented a LMS-based adaptive algorithm implemented on a digital signal processor. The algorithm is used to compensate for the mismatch between the self-sensing piezoelectric element and a reference impedance in the bridge circuit.

The first section of the current study, the first bending and torsional modes of a cantilevered plate are controlled with a SACLD treatment. The plate is fully treated with two patches of SACLD with (-14 /14) oriented PVDF actuators. The two self-sensing PVDF actuators act as two independent actuating units in order to control either the bending or torsional mode. A bridge circuit is setup to implement the self-sensing actuator for measuring either strain or rate of strain in the PVDF actuator. The reference capacitors are carefully tuned to match the impedance of PVDF actuators. The finite element model of the SACLD treated plate is utilized

to predict the effectiveness of the self-sensing PVDF actuators. The theoretical predictions are verified with experimental results.

Flutter can be defined as the dynamic instability of an elastic body immersed in an air-stream. The flutter of plate-wing structure is dominated by first bending and torsional modes of vibration of structures. Flutter often leads to a catastrophic structural failure; therefore, a flutter suppression system is always required to improve the flutter performance and to enhance service life of the aero-structures[10-13]. The flutter control mechanics of SACLD treated plate-wing structures can be described in the following. Firstly, a SACLD/ plate-wing structure can be utilized to suppress the flutter by actively controlling the coupling between first bending and torsional modes of vibration. Secondly, the flutter suppression is achieved by passively increasing the structural damping of plate-wing system with SACLD treatment.

This paper is organized in five sections. In Section 1, a brief introduction is given. In Section 2, a finite element model of SACLD-treated plate is developed. The performance of the SACLD-treated plates is presented in Section 3 along with comparison with the theoretical prediction. Section 4 experimentally demonstrates the effectiveness of flutter control of SACLD/ plate-wing structures. Section 5 summarizes the conclusions of the present study.

2. FINITE ELEMENT MODELING

A finite element model is presented in this section to describe the dynamics of plates treated with SACLD. Figure (2) shows a schematic drawing of the SACLD treatments of the sandwiched plate which is divided into N finite elements. It is assumed that the shear strains in the piezo-electric layers and in the base plate are negligible. The transverse displacement, w, of all points on any cross section of the sandwiched plate are considered to be the same. The damping layers are assumed to be linearly viscoelastic with their constitutive equations described by the complex shear modulus approach such that $G_2=G_2'+j\eta G_2'$. In addition, the top piezoelectric layer, the viscoelastic core and the base plate are considered to be perfectly bonded together.

The elements of treated plate are considered two-dimensional elements bounded by four nodal points. Each node has seven degrees of freedom to describe the longitudinal displacements u_1 and v_1 of the constraining layer, u_3 and v_3 of the base plate, the transverse displacement w and the slopes $w_{,x}$ and $w_{,y}$ of the deflection line. The deflection vector $\{\delta\}$ can be written as:

$$\begin{aligned}\{\delta\} &= \{u_1, v_1, u_3, v_3, w, w_{,x}, w_{,y}\}^T \\ &= \left[\{N_1\}\ \{N_2\}\ \{N_3\}\ \{N_4\}\ \{N_5\}\ \{N_5\}_{,x}\ \{N_5\}_{,y}\right]^T \{\delta^e\}\end{aligned} \tag{1}$$

where $\{\delta^e\}$ is the nodal deflection vector, $\{N_1\}$, $\{N_2\}$, $\{N_3\}$, $\{N_4\}$, $\{N_5\}$, $\{N_5\}_{,x}$, and $\{N_5\}_{,y}$ are the spatial interpolating vectors corresponding to u_1, v_1, u_3, v_3, w, $w_{,x}$, and $w_{,y}$ respectively. Subscripts ,x and ,y denote spatial derivatives with respect to x and y, respectively.

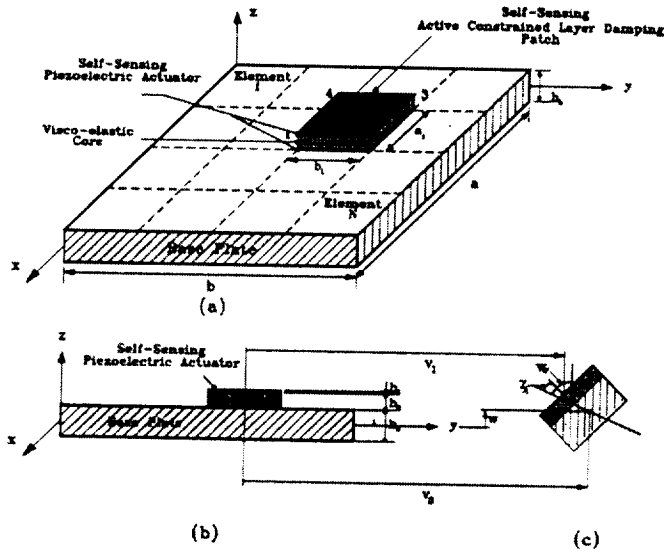

Figure (2) - Schematic drawing of a plate with SACLD patch.

Consider the following energy functional Π_p for the treated SACLD plate system:

$$\Pi_p = \int_v (U - T_K + W_e + W_c) dV , \tag{2}$$

where U is the strain energy, T_K is the kinetic energy, W_e is the work done by external forces, W_c is the work done by the control forces and moments and V is the volume of the plate. Minimizing the plate energy functional using classical variational methods such that $\{\partial \Pi_p / \partial \{\delta^e\}\} = 0$ leads to the following finite element equation:

$$[M]_i \{\ddot{\delta}^e\} + [K]_i \{\delta^e\} = \{F_c\}_i \tag{3}$$

In the above equation $[K]_i$, $[M]_i$, and $\{F_c\}_i$, are the plate stiffness matrix, mass matrix and piezo-electric forces and moments[1], respectively. Equation (3) describes the dynamics/control of a single SACLD treated plate element in a matrix form. Assembly of the corresponding stiffness and mass matrices for the different elements and applying the proper boundary conditions yields the overall stiffness and mass matrices for the entire SACLD/plate system. The resulting eigenvalue problem is then utilized as a basis for optimizing the dynamic characteristics of the open-loop system (i.e. the Passive Constrained Layer Damping treatment (PCLD)) and the closed-loop system (i.e. the Self-sensing Active Constrained Layer Damping treatment).

3. PERFORMANCE OF VIBRATION CONTROL OF THE SACLD TREATED PLATES

In this section, the experimental investigation of the performance of the SACLD/plate system is reported. Also comparisons between the predictions of the finite element model and the experimental results are presented. The theoretical predictions of the first bending and torsional modal frequencies and modal damping ratios of a cantilevered SACLD treated plate are determined when using PCLD and SACLD treatments with a proportional and derivative controller.

3.1 Experimental setup

Figure (3) shows a schematic drawing of the experimental set-up and the associated finite element mesh along with the boundary conditions used in this study. The plate is divided into 11x7 grid with 60 SACLD/plate elements having 490 active degrees of freedom. The set-up includes an aluminum rectangular plate which is fully treated with two SACLD patches. The geometry of the plate is 0.264m long, 0.127m wide and 0.4826mm thick. It is mounted in a cantilevered configuration. The material properties and thickness of piezo-electric material layer (part number:1-1003702-8NiAl, AMP Sensors Inc., Valley Forge, PA) and the viscoelastic layer (DYAD 606, Soundcoat, Dear Park, NY) are listed in Table (1). An acoustic exciter is utilized to excite the system with multi-sine sweep. The sweep frequency range is selected to be from 1 Hz to 30 Hz in order to excite both the first bending and torsional modes. A laser sensor (Model MQ, Aeromat Corp., NJ) is used to measure the bending and torsional vibrations of the treated plate at node 77 as shown in Figure (3). The signal of the laser sensor is sent to a spectrum analyzer to determine the frequency content and the amplitude of vibration. As shown in Figure (3), two surface-bounded self-sensing PVDF actuators are oriented by 14° and –14° with respect to the nodal line of first torsional vibration of the plate. The orientation angle is determined by the width-to-length ratio of the SACLD patches. With such an arrangement, the two halves of SACLD can be utilized to detect the bending and torsional modes of vibration of the plate. With two anti-symmetric sensor/actuator pairs, the sensed signals are in-phase for bending vibration and out-of-phase for torsional vibration. Thus, active control of bending vibration can be achieved by feeding back the two in-phase signals to the two PVDF actuators. Similarly, active control of torsional vibration can be accomplished by feeding back the two out-of-phase signals to the two PVDF actuators, respectively. The desired control action is then obtained by sending the output signals to two bridge circuits respectively. The bridge circuits are used to subtract the effect due to the applied control voltage from the PVDF actuator's output signal, leaving only the signal resulting from the piezoelectric strain or rate of strain. A reference capacitor is used to match the capacitance of PVDF element. The output signals from the bridge circuit are sent to high voltage amplifier as the control voltage. Design details of the bridge circuits are given by Dosch and Inman[7].

It is worth mentioning that controlling the bending and torsional modes of vibration can be achieved by two independent controllers with the two properly-oriented SACLD patches. When the plate is subjected to bending modes, the piezoelectric sensor signals are in-phase and so are the two piezoelectric control forces. Hence, the y components of control forces will be eliminated. This arrangement will significantly reduce the control spillover to the torsional modes when the bending modes are controlled. Similarly, when the plate is subjected to torsional modes of vibration, the two piezoelectric sensor signals are out-of-phase and so are the two piezoelectric control forces. Accordingly, the x components of the control forces will be eliminated reducing the control spillover to the bending modes.

3.2 Experimental Results

Figure (4-a) shows a plot of the normalized experimental amplitudes of vibration of the plate for different strain feedback control gains. According to Figure (4), amplitude attenuations of the first bending mode of 75.30%, 92.365% and 96.69% are obtained for control gains of 250,

600, and 1300, respectively. The corresponding attenuations of the first torsional mode are 21.3%, 21.12% and 35.05% for control gains of 250, 600 and 1300, respectively. Such attenuations are normalized with respect to the amplitude of vibration of uncontrolled plate, i.e. plate with PCLD treatment. The maximum control voltages are 42.7volt, 55.2volt and 93.1volt for control gains of 250, 600 and 1300, respectively.

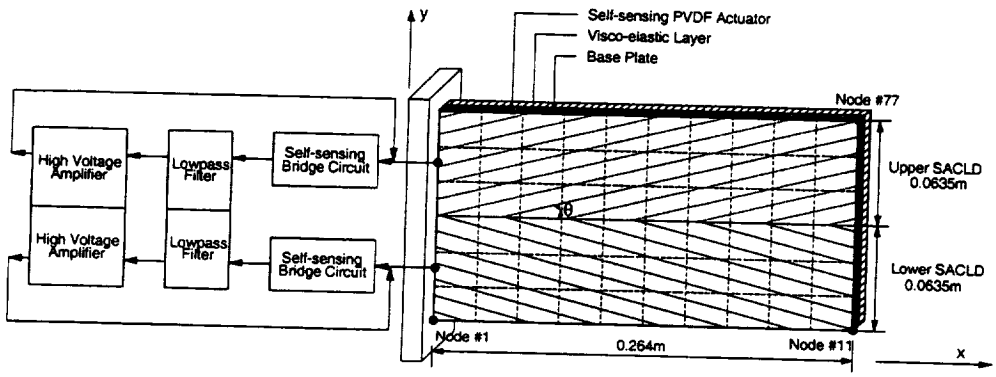

Figure (3) - Schematic drawing of the experimental set-up and associated finite element mesh

Table (1) - Physical and geometrical properties of the SACLD treatment

Layer	Thickness(m)	Density(Kg/m^3)	Modulus(MPa)
Viscoelastic	5.08×10^{-4}	1104	30**
PVDF	28×10^{-6}	1780	2500*

* Young's modulus ** Shear modulus

Figure (4-b) displays the vibration amplitudes for different strain rate feedback gains. The corresponding experimental attenuations of the vibration amplitude of fundamental bending mode obtained are 60.8%, 84.55% and 91.56% for control gains of 250, 600, and 1300, respectively. The corresponding attenuations for the torsional mode are 53.78%, 73.99% and 84.07% for the same set of control gains. The maximum control voltages are 43.7volt, 59.2volt and 82.1volt for control gains of 250, 600 and 1300, respectively.

It is clear that increasing the control gain has resulted in improving the attenuations of the plate vibration. It is evident that the SACLD treatment has produced a significant attenuation of both bending and torsional modes of vibrations simultaneously as compared to the attenuations produced by conventional PCLD treatments.

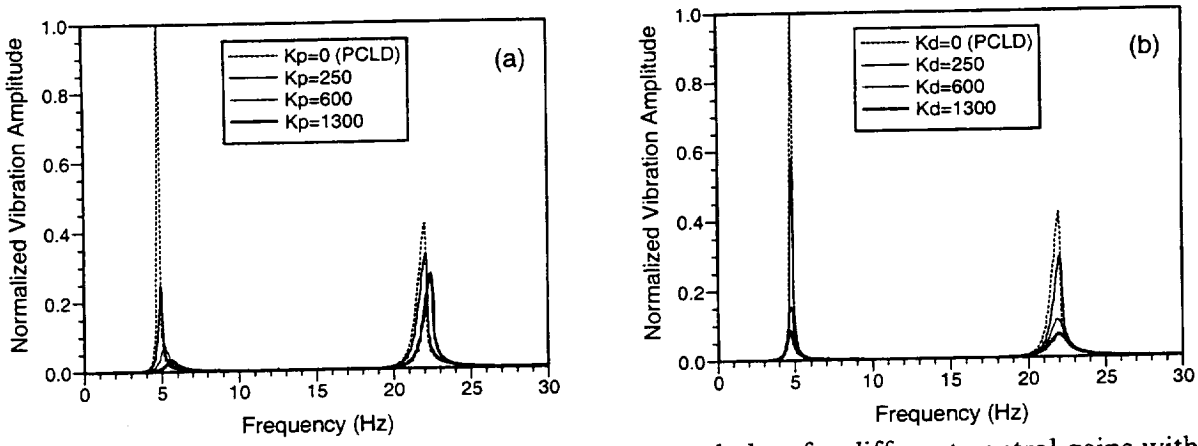

Figure (4) - Vibration amplitudes of the SACLD-treated plate for different control gains with (a) strain feedback (b) strain rate feedback.

Figures (5) and (6) present comparisons between the theoretical and experimental natural frequencies and the loss factor for different control gains. Close agreement between theory and experiment is evident. Note also that increasing the control gain has resulted in increasing the damping ratio for SACLD treatments. The comparisons emphasize the effectiveness of the SACLD treatment in acquiring the large damping ratio to simultaneously attenuate both the bending and the torsional structural vibrations.

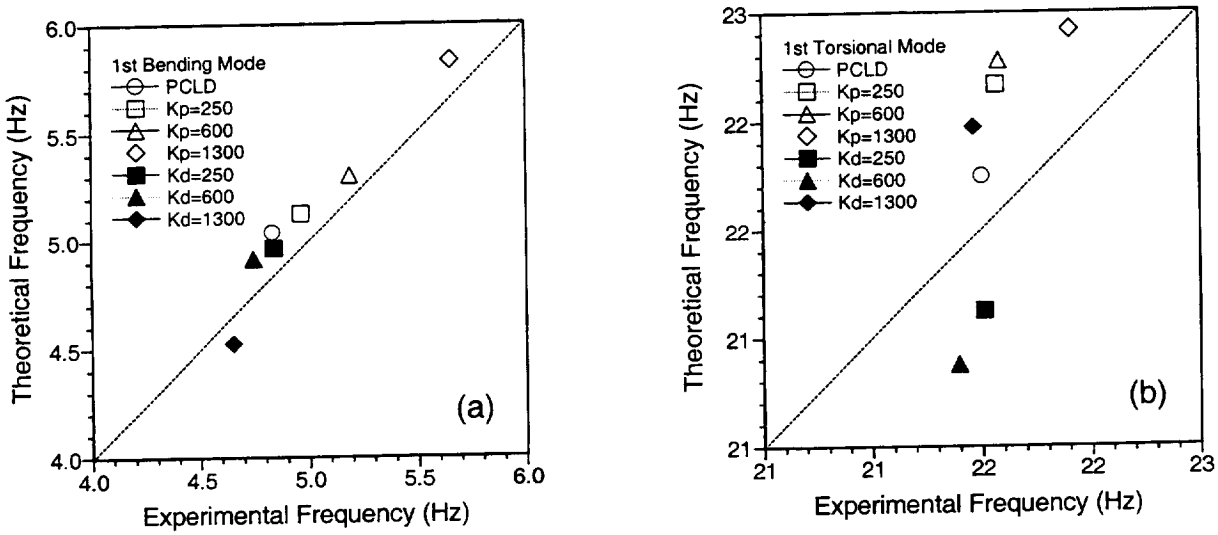

Figure (5) - Comparisons between the theoretical and experimental natural frequencies of a SACLD-treated plate (a) first bending mode and (b) first torsional mode for different control gains.

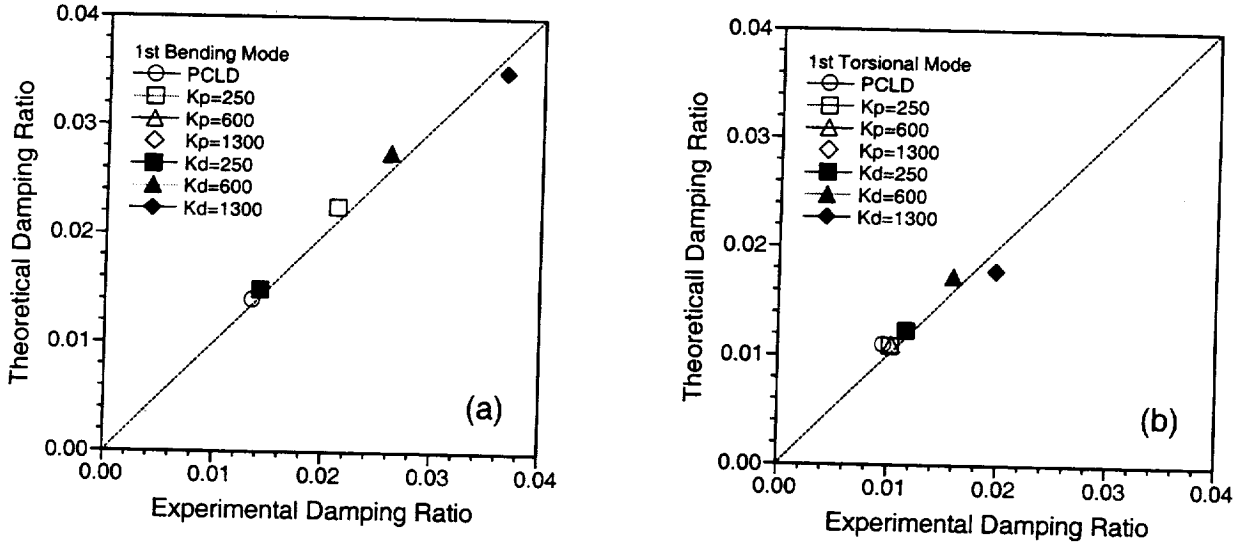

Figure (6) - Comparisons between the theoretical and experimental damping ratio of a SACLD-treated plate (a) first bending mode and (b) first torsional mode for different control gains.

4. PERFORMANCE OF FLUTTER CONTROL OF THE SACLD TREATED PLATES

The test facility used in the experimental demonstration of the effectiveness of SACLD/plate-wing structures in flutter suppression is the ODU low-speed wind tunnel. The tunnel is of the closed-return type, fan driven and has a test section of 1.2192m (wide) by 0.9144m (high) by 2.4384m (long). The lower bound of the speed range is 10 m/sec, which is set by the fan stability while the upper bound, set by the maximum driven power, is 55 m/sec. A Virtual Instrument (VI) was designed and built using LabView (National Instrument) to enable performing the measurements of the flow velocity in the test section. The experimental setup as shown in Figure (3) is installed vertically in the test section of the tunnel. The response at node 77 is measured by the B&K laser velocity transducer type 3544.

Figures (7-a, b) present the frequency response at node 77 for three different strain and strain rate feedback control gains, $K_{p,\,d}$ = 0, 75 and 300, respectively. The flow speed is aet at 22.93 m/sec which corresponds to the critical flutter speed of SACLD/plate-wing without control (PCLD). According to Figure (7-a), the flutter suppression is 93% for K_p = 75 with averaged control voltage 87V. The flutter can be completely suppressed for K_p = 300 with averaged control voltage 340V. Given that the strain rate feedback control is not effective in the low frequency range, the flutter suppressions are 23.6% and 82.23% for K_d= 75 and 300, respectively.

Figure (8) shows the critical flutter speed for untreated plate, PCLD/plate and SACLD/plate with $K_{p,\,d}$ = 75, 150 and 300, respectively. According to Figure (8), the critical flutter speed can be increased from 22.46 m/sec for untreated plate to 28.28 m/sec for SACLD/plate with K_p=300. It corresponds to 25.91% increase in flutter speed. Thus, Figures (7) and (8) clearly demonstrate the effectiveness of the flutter control of SACLD/plate-wing structures.

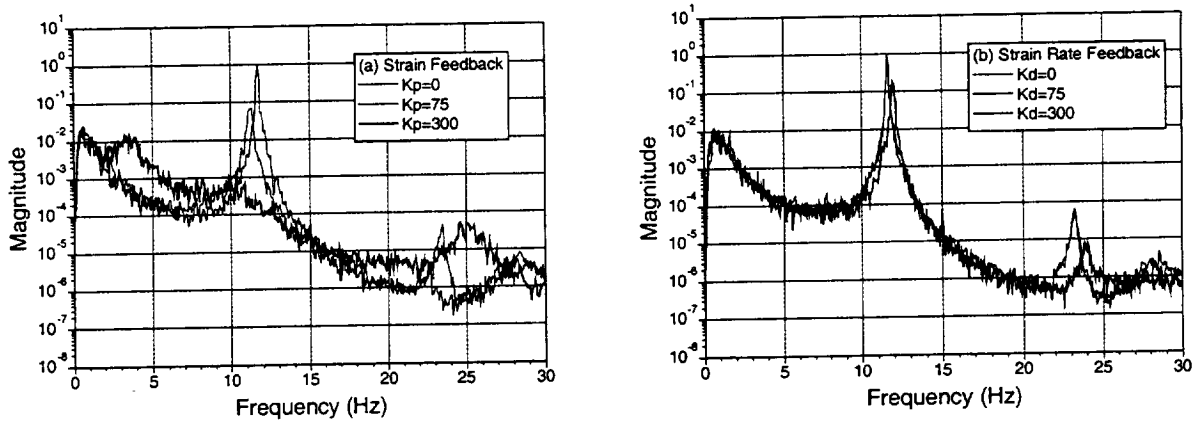

Figure (7) – magnitude flutter response of SACLD/plate–wing structures with (a) strain feedback control and (b) strain rate feedback control.

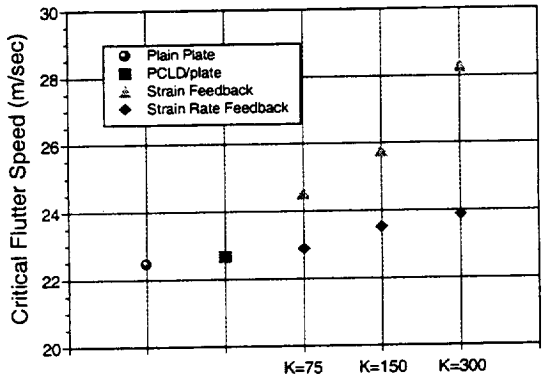

Figure (8) – critical flutter speeds of untreated plate, PCLD/plate and SACLD/plate with three different strain and strain rate feedback gains.

5. SUMMARY

This paper has presented theoretical and experimental comparisons between the frequency and damping characteristics of plates treated with SACLD in vibration control. The dynamic characteristics of the treated plates are determined for different proportional and derivative control gains. The fundamental issues governing the performance of this class of smart structures have been introduced and modeled using finite element method. The accuracy of the developed finite element model has been validated experimentally. The effectiveness of the SACLD treatment for simultaneous attenuation of both bending and torsional modes of vibration of the plates has also been clearly demonstrated. The results obtained indicate that the SACLD treatments have produced significant attenuation of the structural vibration as compared to conventional PCLD.

The developed experimental techniques with relatively simple, linear feedback control have been successfully used to suppress flutter as presented in this paper. The performance of SACLD/plate in flutter suppression is experimentally demonstrated for strain feedback and strain

rate feedback with different levels of control gains. The results show that the flutter response can be completely suppressed and the flutter speed can be significantly increased. Much higher flutter speeds might be obtained by selecting an appropriate control law and optimal gains. Although this study has focused on the control of plate-wing like structures using fully treated SACLD with a simple linear controller, optimal design, control and placement of partial SACLD treatments for more complex structures are natural extension of the present study.

ACKNOWLEDGMENTS

Part of this work is funded by The U.S. Army Research Office (Grant number DAAH-04-96-1-0317). Special thanks are due to Dr. Gary Anderson, the technical monitor, for his invaluable technical inputs.

REFERENCES

1. BAZ, A. and J. RO, "Vibration Control of Plates with Active Constrained Layer Damping", *Journal of Smart Materials and Structures*, **5**, pp. 272-280, 1996.
2. Shen, I. Y. "Hybrid Damping Through Intelligent Constrained Layer Treatments." *Transaction of ASME, Journal of Vibration and Acoustics*, **116**, pp. 341-349, 1994.
3. Azvine, B. G., R. Tomlinson and R. J. Wynne, "Use of Active Constrained-Layer Damping for Controlling Resonant Vibration", *Journal of Smart Materials and Structures*, **5**, pp. 272-280, 1996.
4. Liao, W. H. and K. W. Wang, "On the Analysis of Viscoelastic Materials for Active Constrained Layer Damping Treatments", *Journal of Sound and Vibration*, **207**(3), pp. 319-334, 1997.
5. Yellin, J. M. and I. Y. Shen "An Experimental Investigation of a self-sensing Active Constrained Layer Damping Treatment", *SPIE Proceedings*, Vol. **2720**, 196-203, 1996.
6. Goh C. J. and T. K. Caughey, "On the Stability Problem Caused by Finite Actuator Dynamics in the Control of Large Space Structures", *International Journal of Control*, **41**(3), pp. 787-802, 1985.
7. Dosch, J. J. and D. J. Inman, "A Self-Sensing Piezoelectric Actuator for Collocated *Journal of Intelligent Material Systems and Structures*, **3**, pp. 166-185, 1992.
8. Anderson E. H. and N. W. Hagood, "Simultaneous Piezoelectric Sensing/Actuation: Analysis and Application to Controlled Structures", *Journal of Sound and Vibration*, **174**(5), pp. 617-639, 1994.
9. Vipperman J. S. and R. L. Clark, "Implementation of an Adaptive Piezoelectric *AIAA Journal*, **34**(10), pp. 2102-2109, 1996.
10. Yang, Z.-C., L. C. Zhao and J. S. Jiang,"A Semi-active Flutter Control Scheme for a Two Dimensional Wing", *Journal of Sound and Vibration*, **184**(1), pp. 1-7, 1995.
11. Waszak M. R. and S. Srinathkumar, "Flutter Suppression for the active Flexible Wing:A *Journal of Aircraft*, **32**(1), pp. 61-67, 1995.
12. Nam, Changho, Youdan Kim and Terrence A. Weisshaar, "Optimal Sizing and Placement of Piezo-actuators for Active Flutter Suppression," *Smart Material and Structures*, **5**, pp. 216-224, 1996.
13. Sanda, Tomio and Kosaku Takahashi "Flutter and Vibration Control of Aluminum Plate Wing by Piezoceramic Actuators," *SPIE Proceedings*, Vol. **3329**, pp. 42-49, 1998.

An Examination of Applying Shunted Piezoelectrics to Reduce Aeroelastic Response

Anna-Maria Rivas McGowan*
NASA Langley Research Center, MS 340, Hampton, VA 23681-2199

ABSTRACT

Several analytical and experimental studies clearly demonstrate that piezoelectric materials (piezoelectrics) can be used as actuators to actively control vibratory response, including aeroelastic response. However, two important issues in using piezoelectrics as actuators for active control are: 1) the potentially large amount of power required to operate the actuators, and 2) the complexities involved with active control (added hardware, control law design, and implementation). Active or passive damping augmentation using shunted piezoelectrics may provide a viable alternative. This approach requires only simple electrical circuitry and very little or no electrical power. The current study examines the feasibility of using shunted piezoelectrics to reduce aeroelastic response using a typical-section representation of a wing and piezoelectrics shunted with a parallel resistor and inductor. The aeroelastic analysis shows that shunted piezoelectrics can effectively reduce aeroelastic response below flutter and may provide a simple, low-power method of subcritical aeroelastic control.

1. INTRODUCTION

Over the last decade, smart material-based actuation systems (or "smart devices") have been studied as potential alternatives to the use of conventional control mechanisms for controlling aeroelastic response. The use of smart devices introduces a unique facet in controlling dynamic aeroelastic response: the use of structural forces, as opposed to aerodynamic forces, for control. The ability to effectively and efficiently control structural response via internal structural forces or dampers may allow aircraft designers to take advantage of the inherent flexibility in air vehicles to create more efficient structural designs that may also improve flight performance. Ultimately, the use of smart devices can be used in combination with conventional aerodynamic control surfaces to allow for many new active and/or passive aeroelastic control approaches.

Due to their 20 KHz bandwidth and effectiveness in strain actuation, piezoelectric materials used as actuators have been the smart device of choice for aeroelastic control applications. Numerous studies have shown that piezoelectric actuators can be used to control structural and aeroelastic response. References 1 - 3 provide comprehensive overviews of work in aeroelastic control using piezoelectric and other smart materials-based actuators. In particular, the research described in references 4, 5, and 6 were instrumental not only in demonstrating the benefits of using piezoelectric actuators for active aeroelastic control, but also in addressing some of the many realistic issues associated with applying piezoelectric actuators to large and full-scale structures. Two critical issues in using piezoelectrics as actuators for active control are the potentially large amount of power required to operate the actuators and the complexities of active control. For example, reference 7 states that the power required to control a structure using piezoelectric patch actuators is a function of the voltage squared. Since high voltages (i.e., 200 volts) and a large number of piezoelectric actuators are typically required to control vibration on large structures, the amount of power required can be considerable. Secondly, active control approaches using smart or conventional actuators generally have the additional complexities of a control law, substantial additional hardware, and possible, unplanned instabilities caused by the control law.

One potential alternative is damping augmentation using shunted piezoelectrics. This approach allows for active or passive damping augmentation, yet cannot cause instability. Furthermore, shunted piezoelectrics use little to no power and are simple to apply; the only necessary hardware is the piezoelectrics themselves and simple electric circuitry using resistors and inductors. The present research examines the feasibility of using shunted piezoelectrics (shunted by a parallel resistor and inductor) to reduce aeroelastic response at speeds below flutter. A typical-section

representation of a wing is used and the shunted piezoelectrics are represented as a damped vibration absorber placed on the elastic axis of the wing. The analytical approach taken in the current work is an extrapolation of existing analytical methods, which primarily focus on application of shunted piezoelectrics to simple beams and plates. As such, following background information, this report first documents the application of shunted piezoelectrics to a simple one-dimensional structure and discusses the constraints and assumptions made in the existing analytical methods. Following this, the aeroelastic equations of motion are derived for a two degree-of-freedom typical wing section with shunted piezoelectrics placed on the elastic axis. Using this aeroelastic model, the response of the typical section to external forcing functions is shown at several airspeeds. Observations as to the response reduction are provided and the potential impact on future air vehicle designs are discussed. All derivations in the current document are summarized to save space. A more detailed analysis can be found in reference 8.

2. BACKGROUND

A number of studies have been conducted on the behavior of electric circuits used for shunting. [9-24] In particular, reference 9 presents a derivation of the effective mechanical impedance for a piezoelectric shunted by an arbitrary circuit. This work focused on resistive and series resistor, inductor, and capacitor (RLC) circuits and forms the basis for the present work. In addition, references 18 and 19 discuss the parallel RLC shunt circuit and follow the methodology of reference 9 to develop an associated analytical model; these references are also used for the current work. Furthermore, in reference 20, Wu shows experimental results using parallel RLC circuits to add damping to multiple modes.

The foregoing research efforts clearly demonstrate the effectiveness of using shunted piezoelectrics to reduce vibration amplitudes. Reference 21 presents a good discussion of the some of the practical limitations and some analytical models. In addition, reference 22 provides a comparison of the use of piezoelectrics for damping augmentation versus constrained layer damping. Application of shunted piezoelectrics to a variety of areas has been considered (although not all results have been published) including vibration suppression and acoustic damping on flight vehicles, space structures[23], and machinery. In some cases, simple scale-model experiments have been conducted. Although many researchers have demonstrated the viability of shunted piezoelectrics in laboratory experiments with much success, commercial or full-scale demonstrations are limited. As mentioned earlier, the current work seeks to analytically examine the feasibility of using piezoelectrics, shunted via a parallel resistor and inductor, to reduce aeroelastic response. The analysis allows numerous observations and conclusions; however, final application in an aircraft wing or tail will certainly require considerable additional research and, of course, experimental studies.

A parallel RLC shunt circuit was chosen for the current study because it is much more effective than a resistive shunt circuit and it is easier to tune than a series RLC shunt circuit. In practice, use of a parallel or series RLC shunt circuits usually requires a simulated inductor. Without the simulated inductor, large and heavy inductors would be required to shunt the average-sized piezoelectric.[18] Reference 12 shows that lightweight, compact, simulated inductors can be created using operational amplifiers and resistors. Furthermore, use of a simulated inductor enables active shunting wherein the shunt circuit is actively "tuned" as the host structure changes. More discussion of tuning the shunt circuit is provided subsequently. The analysis for the current feasibility study begins with the piezoelectric constitutive relations, which are augmented to include the effects of the parallel RLC shunt circuit.

2.1 Piezoelectric constitutive relations

The piezoelectric constitutive equations, assuming linearity and uniaxial loading are well documented. Addition of the shunt circuit is accomplished by augmenting the electrical impedance in the constitutive equations with that of a parallel RLC electrical circuit. For the current study, conventional, one-way electro-mechanical coupling was employed such that the coupled (open-circuit) compliance with the addition of the shunt circuit is:

$$s_{11}^{OC,SH}(\tilde{s}) = s_{11}^{OC,PZT}\left[\frac{\tilde{s}^2 RLC^S + \tilde{s}L + R}{\left(1-k_{31}^{\ 2}\right)\left(\tilde{s}L+R\right)+\tilde{s}^2 RLC^S}\right] \tag{1}$$

The electro-mechanical coupling coefficient, k_{31}, is used for simplicity where: $k_{ij} = d_{ij}/\sqrt{s_{ij}^{SC}\varepsilon_i^T}$ and ε is the dielectric constant.[25] In equation 1, the follow definitions were used: $\tilde{s}$ is the Laplace variable, C^S is capacitance at constant strain, R is resistance, and L is inductance. The compliance shown in equation 1 will be used to represent the compliance of the shunted piezoelectric in the subsequent equations of motion. Recall that uniaxial loading of the piezoelectric was assumed; as such, equation 1 only reflects the compliance in extension (the "1" direction in Figure 1).

3. SHUNTED PIEZOELECTRICS APPLIED TO A GENERIC HOST STRUCTURE

3.1 Description of the analytical model

Application of shunted piezoelectrics to a generic host structure is considered to form a basis for the more complex aeroelastic studies that will be examined next. Moreover, application to a generic structure allows for clear examination of the general characteristics of shunted piezoelectrics and examination of the implications of the assumptions and constraints employed in the current analytical methods. The analytical methods presented in references 9 and 18 were primarily followed with a few noted exceptions.

The equation of motion for a generic host structure with a surface-bonded piezoelectric, as shown in Figure 2, is developed based on the following assumptions:

1) The thickness and length of the piezoelectric are small compared to that of the host structure.
2) The inertial effects of the piezoelectric are negligible.
3) The piezoelectric is poled in the "3" direction and only displacement in the "1" direction is considered. This assumption is consistent with the assumption of uniaxial loading on the piezoelectric.
4) An external shunt circuit consisting of a resistor and inductor connected in parallel is attached to the electrodes of the piezoelectric creating a parallel resistor-inductor-capacitor electric circuit.
5) The "1" direction of the piezoelectric is perpendicular to the bending node lines of the host structure, such that the shunted piezoelectric acts primarily to reducing bending response. Thus, torsion vibration modes are largely unaffected by the damping characteristics of the shunted piezoelectric and are not represented in the equation of motion.
6) Damping in the host structure is negligible.

Considering the bending degree of freedom only, the equation of motion in terms of Laplace transforms and the mechanical impedance of the host structure with shunted piezoelectrics is:

$$Z_{SYS}^{mech}(\tilde{s}) = m_{STR}\tilde{s} + \frac{K_{STR}}{\tilde{s}} + Z_{PZT}^{mech}(\tilde{s}) \tag{2}$$

The mass of the piezoelectric can easily be included in the equations of motion by adding the term $m_{PZT}\tilde{s}$. However, as mentioned in the assumptions above, this term is normally not necessary since the inertial characteristics of the piezoelectric are negligible for most applications. The mechanical impedance of a shunted piezoelectric can be modeled as:

$$Z_{PZT}^{mech}(\tilde{s}) = \frac{K_{PZT}(\tilde{s})}{\tilde{s}} = \frac{T_1(\tilde{s})\cdot A_1}{\tilde{s}\cdot S_1(\tilde{s})\cdot L_1} = \frac{A_1}{\tilde{s}\cdot L_1 \cdot s_{11}^{OC,SH}(\tilde{s})} \tag{3}$$

where the extensional stiffness of the piezoelectric in the "1" direction is used (see Figure 1). There are a few important observations concerning the use of the extensional stiffness of the piezoelectric. Though the extensional stiffness of the piezoelectric is considerable (piezoelectric materials have a Young's Modulus on the order of aluminum), that stiffness does not significantly affect the response of the host structure primarily because the piezoelectrics are short and thin compared to the host structure. Thus, the effect of this stiffness on the response of

the host structure is negligible unless numerous piezoelectrics are used. In addition, it is important to remember that the above equations were developed assuming a simple, lumped-parameter system. To obtain the best results using this idealization, use of experimentally-measured values for the natural frequency of the host structure are required. Alternatively, a more rigorous definition of piezoelectric stiffness can be used, an example of which is derived in reference 26.

Referring again to equation 3, the open-circuit compliance of the shunted piezoelectric (from equation 1) must be incorporated. Thus, including the mechanical impedance of the shunted piezoelectric into the equation of motion (equation 2) yields:

$$Z_{SYS}^{mech}(\tilde{s}) = m_{STR}\tilde{s} + \frac{\left(K_{STR} + K_{PZT}^{SC}\right)}{\tilde{s}} + \left(\frac{K_{PZT}^{OC}}{\tilde{s}}\right)\frac{k_{31}^{\ 2}\left(\tilde{s}RLC^{S}\right)}{\left(\tilde{s}^{2}RLC^{S} + \tilde{s}L + R\right)} \tag{4}$$

where: $K_{PZT}^{SC} = A_1/\left(L_1 s_{11}^{SC}\right)$ and $K_{PZT}^{OC} = A_1/\left(L_1 s_{11}^{OC}\right)$ are the short-circuit and open-circuit stiffnesses of the piezoelectric, respectively. Note that, K_{PZT}^{SC} is the stiffness of the piezoelectric without any external electrical stimulus (i.e., shunt circuit or control law input). Then, it follows that the normalized response of the host structure response is:

$$\frac{X(\tilde{s})}{X_{st}(\tilde{s})} = \frac{-\left(G^2 - \Omega^2\right) + i2\zeta G}{-\left[\overline{K}_{31}^{\ 2}G^2 - \left(G^2 - 1\right)\left(G^2 - \Omega^2\right)\right] - i2\zeta G\left(G^2 - 1\right)} \tag{5}$$

The following dimensional and nondimensional terms are used for simplification: $X_{st}(\tilde{s}) = F(\tilde{s})/K_{STR}$; $\omega_{SC}^{\ 2} = \left(K_{STR} + K_{PZT}^{SC}\right)/m_{STR}$; $\omega_{OC}^{\ 2} = \left(K_{STR} + K_{PZT}^{OC}\right)/m_{STR}$; $\overline{K}_{31}^{\ 2} = \left(\omega_{OC}^{\ 2} - \omega_{SC}^{\ 2}\right)/\omega_{SC}^{\ 2}$ (which is the generalized electro-mechanical coupling coefficient); $\omega_E^{\ 2} = 1/\left(LC^S\right)$; $\zeta = 1/\left(2RC^S\omega_{SC}\right)$; $\Omega^2 = \omega_E^{\ 2}/\omega_{SC}^{\ 2}$; and, $G = \omega/\omega_{SC}$. Furthermore, based on the above terms, the inductance in the shunt circuit is defined as: $L = 1/\left(\omega_{SC}^{\ 2}\Omega^2 C^S\right)$. Likewise, the resistance is defined as: $R = 1/\left(2\omega_{SC}\zeta C^S\right)$.

Several important observations can be made regarding the above nondimensional parameters. First, the short-circuit natural frequency, ω_{SC}, is the natural frequency of the system without any external electric stimulus. Thus, for the model considered, ω_{SC} represents the bending natural frequency of the structure including the stiffness of the piezoelectric but not the effects of the shunt circuit. Second, the generalized electro-mechanical coupling coefficient, $\overline{K}_{31}$, is the ratio of the short-circuit modal stiffness of the piezoelectric to the total system modal stiffness. As such, $\overline{K}_{31}$ is proportional to the fraction of system modal strain energy that is converted to electric energy by the open-circuit piezoelectric, and thus, is a measure of the shunted piezoelectric's influence on the system.[9] Clearly, this influence is ultimately determined by how well the piezoelectric is bonded to the host structure. More accurate representation of the characteristics of the adhesive used to bond the piezoelectrics may require a higher fidelity representation of this coupling coefficient. However, experimental results show that the above representation is typically suitable.[19] The final nondimensional parameter to note is the damping ratio, ζ. The definition for ζ used herein differs from that currently published in the literature. The damping ratio used above is the mechanical analog of the damping ratio of a parallel RLC electric circuit. Previous references (e.g., 9, 13, 16, 18, 19, and 20) use $\zeta = RC^S\omega_{SC}$, which is appropriate for a series resistor-inductor-capacitor shunt circuit but not for a parallel circuit such as the one used in the current work. Note that Wu (in references 18 and 19) also uses a parallel circuit and obtains the same function for normalized amplitude as shown in equation 5 using different terminology. In particular, he defines damping ratio as $\zeta = RC^S\omega_{SC}$. Either definition of damping ratio (Wu's[18,19] or the one used herein) is acceptable as long as it is used consistently. Quantitative comparisons with results from previous derivations will be shown in the next section.

3.2 Failure scenarios

Equation 5 can be used to determine the response of the host structure for various values of resistance, inductance and capacitance (piezoelectrics). As will be discussed in the next section, accurately selecting the shunt circuit

parameters is critical to obtaining optimal response reduction. Before optimum conditions of the shunt circuit are examined, it is informative to examine the response of the host structure for extreme conditions of the shunt circuit. One such condition is complete failure, or a disconnection, of the shunt electric components (the resistor and inductor). In this case, the piezoelectric merely adds a small amount of stiffness to the host structure and dissipates a little strain energy. Though the piezoelectrics considered herein are assumed to be massless, inclusion of the mass of the piezoelectrics typically has negligible effects on the dynamic response of the host structure.

The other extreme condition is a shunt circuit with values of resistance and inductance that are extremely different from the values needed for optimum response reduction. This condition raises the question: Can the addition of the shunt circuit to the piezoelectric cause an increase in the response of the host structure, or even cause an instability in the structure? Two characteristics of the shunt circuit prevent this from occurring: 1) the shunt circuit has no external energy source, such as a voltage or current source; and 2) the resistor in the circuit will always dissipate energy. Thus, use of a shunted piezoelectric will be a fail-safe system for the vast majority of applications. The only way in which adding shunted piezoelectrics (that are not also being used as actuators) to a structure can worsen the dynamic response of the structure is if the weight of the piezoelectrics is considerable, and if the piezoelectrics are placed far from the structure's center of gravity. In this case, the piezoelectrics (regardless of the tuning of or the existence of the shunt circuit) will act as an unbalanced mass on the structure. Practically speaking, if the weight of the piezoelectrics used is significant enough to cause this type of complication, then piezoelectrics are most likely not to be the best choice for reducing structural response. However, as mentioned above, a condition exists, between the two extremes discussed, that yields optimal response reduction of the host structure.

3.3 Damped vibration absorber analogy

Adjusting or tuning the shunt circuit to obtain optimal response reduction is greatly simplified by using the "tuning" techniques developed for damped vibration absorbers. These techniques apply because shunted piezoelectrics can essentially be modeled as damped vibration absorbers (DVA). This analogy becomes clear by examining the nondimensional or normalized response of a lumped mass system with an attached damped vibration absorber as shown in Figure 3 and described using equation 6. The DVA is represented by mass, m_2, stiffness, k_2, and damping, c_2; the host structure is represented by mass, m_1, and stiffness, k_1.

The nondimensional response of the system shown in Figure 3 is:

$$\frac{x_1(\tilde{s})}{x_{st}(\tilde{s})} = \frac{x_1(\tilde{s})}{F_1(\tilde{s})/k_1} = \frac{-\left(G^2-\Omega^2\right)+i2\zeta G}{-\left[M\Omega^2G^2-\left(G^2-1\right)\left(G^2-\Omega^2\right)\right]-i2\zeta G\left(G^2-1+MG^2\right)} \tag{6}$$

where: $\omega_1^2 = \frac{k_1}{m_1}$, $\omega_2^2 = \frac{k_2}{m_2}$, $\Omega^2 = \frac{\omega_2^2}{\omega_1^2}$, $G^2 = \frac{\omega^2}{\omega_1^2}$, $M = \frac{m_2}{m_1}$, $c_c = 2m_2\omega_1$, $\zeta = \frac{c_2}{c_c}$. Note that Italics are used to describe the damped vibration absorber system to distinguish it from the other equations used in this report. Examination of equation 6 reveals many similarities to equation 5. The only two differences in the equations are: 1) the squared generalized electro-mechanical coupling coefficient, $\overline{K}_{31}^2$, of equation 5 is analogous to the $M\Omega^2$ term in equation 6; and 2) equation 6 contains the term $i2\zeta MG^3$, which does not exist in equation 5, and no simple analog is obvious. However, the overall behavior of the normalized amplitude in equation 6 is still maintained when the term $i2\zeta MG^3$ is removed. Thus, the normalized response of a host structure with attached shunted piezoelectrics (defined in equation 5) is very similar to the normalized response of a simple, lumped-parameter spring mass with an attached damped vibration absorber (defined in equation 6).

As with any analogy, however, there are limitations to the use of the above mentioned analogy of a damped vibration absorber to shunted piezoelectrics. For very large and very small damping ratios, ζ, the analogy between the damped vibration absorber and shunted piezoelectrics is not appropriate because neither condition can be realistically attained by the shunted piezoelectric. At these conditions, the term $i2\zeta MG^3$ becomes significant in the damped vibration

absorber. Very large damping ratios (i.e., ζ approaching infinity) simulate the two masses in Figure 3 being locked together such that their relative displacement is zero and thus, no work is done by the damping force. For the shunted piezoelectric, this condition equates to an "infinite" stiffness in the piezoelectric such there is no displacement in the piezoelectric. The above case of an "infinite" stiffness piezoelectric is not realistic. On the other hand, very small damping ratios signify that the damping force is near zero and very little, if any, energy dissipation takes place. For some conditions of m_2 and k_2 and with $\zeta_2 = 0$ in the damped vibration absorber, this means that the presence of the damped vibration absorber can further amplify the motion of the host structure, particularly if the host structure has damping. Since the piezoelectric material has inherent damping, the piezoelectric will always dissipate some energy from the motion of the host structure regardless of the existence of, or the components in, the shunt circuit. Furthermore, since the shunt circuit described herein can not supply voltage to the piezoelectric (and thus, create an actuator) and the resistor in the shunt circuit always dissipates some energy from the piezoelectric, the case of zero damping is unrealistic for a shunted piezoelectric. Moreover, cases of near zero damping ratios must be carefully examined to ensure realism. Also, note that since the shunted piezoelectrics were considered massless for the current study, the above scenario is precluded for the results herein.

3.4 Tuning the shunt circuit

As with the shunted piezoelectric circuit, appropriate tuning is required for the damped vibration absorber to reduce the response of the host structure most effectively. Tuning requires adjusting the parameters Ω and ζ for both the damped vibration absorber and the shunted piezoelectric circuit. The same methodology used to tune a damped vibration absorber can be applied to tune a shunted piezoelectric circuit since the two systems perform similarly. This tuning methodology is described in several references (see e.g., references 27, 28, and 29). An abbreviated summary (shown below) of one method to tune a damped vibration absorber (DVA) is applied to tuning the shunt circuit.

Tuning is accomplished using equation 5 in combination with Figure 4. Figure 4 depicts nondimensional response of the host structure, with shunted piezoelectrics as described in equation 5, plotted using several values of damping ratio and an untuned value of frequency ratio, Ω=0.9466. The first step in tuning is to find the optimal frequency ratio Ω_{opt}. Use of Ω_{opt} ensures the electrical natural frequency of the shunt circuit is tuned to create an electrical antiresonance (infinite electrical impedance) at the frequency of the structural mode of interest. Graphically, using Ω_{opt} equates to making the two "peaks" of the response of the host structure with shunted piezoelectrics the same height (see Figure 4).

Finding Ω_{opt} begins with identifying the nondimensional frequencies, G_1 and G_2, corresponding to points A and B in Figure 4. Note that all curves pass through points A and B regardless of the value of damping ratio. G_1 and G_2 are defined: $G_{1,2}^2 = 1 \pm \overline{K}_{31}/\sqrt{2}$. The second step is to force the nondimensional amplitudes at points A and B in Figure 4 to be equal and solve for the optimal (tuned) frequency ratio Ω_{opt}:

$$\Omega_{opt}^2 = 1 - \overline{K}_{31}^2/2 \tag{7}$$

Using the above frequency ratio, the inductance for the shunt circuit can be obtained. The optimal inductance is:

$$L_{opt} = 1/\left(\omega_{SC}^2 \Omega_{opt}^2 C^S\right) \tag{8}$$

Next, the optimal damping ratio must be found; this enables optimum energy dissipation through the resistor at the optimal frequency. Thus, optimal damping ratio is a function of optimal frequency ratio. Graphically, use of the optimal damping ratio ensures the two, level peaks of the response are at their lowest value. Thus, to find ζ_{opt}, the optimal frequency, Ω_{opt}, is used and the slope at points A or B is set to zero. Optimal damping ratio can then be written as:

$$\zeta_{opt} = \frac{1}{4\sqrt{1 \pm \frac{\overline{K}_{31}}{\sqrt{2}}}}\left[\left(2 - \frac{\overline{K}_{31}^2}{2} - 2\left(1 \pm \frac{\overline{K}_{31}}{\sqrt{2}}\right)\right) \mp \overline{K}_{31}\sqrt{2 - \tfrac{5}{4}\overline{K}_{31}^2 + 2\left(1 \pm \frac{\overline{K}_{31}}{\sqrt{2}}\right)}\right] \tag{9}$$

This expression for optimal damping ratio differs from that shown in previous references for two reasons: 1) damping ratio is defined differently in the current text, as mentioned earlier; and 2) the procedure used in the present work to find optimal damping ratio differs from previous references. For example, using $\zeta = RC^S\omega_{SC}$, Wu defines optimal damping ratio as $\zeta_{opt} = 1/\left(\sqrt{2}\overline{K}_{31}\right)$ in reference 18. A numerical example will be used to examine the accuracy of both definitions subsequently. Note that the magnitude of the damping ratio shown in equation 9 can be used to obtain the resistance value for the shunt circuit. The optimal (tuned) resistance in the shunt electric circuit is:

$$R_{opt} = 1/\left(2\omega_{SC}C^S|\zeta_{opt}|\right) \tag{10}$$

Hence, using equations 8 and 10, the inductance and resistance of the shunt circuit can be tuned for optimal response reduction for a given value of capacitance in the piezoelectric, C^S. For active control using the shunt circuit, the inductance and resistance would be actively adjusted as the host structure changes. For passive control, the shunt circuit would be tuned for the condition of interest and the resistance and inductance would not be updated as the host structure changes.

3.5 Analytical validation and limitations of the tuning methodology

The validity of the derivations for optimal frequency and damping ratio can be determined by using a simple example. First, the peak nondimensional amplitude of the host structure's response at the optimum condition is at frequencies, G_1 and G_2, which are the locations of points A and B. To find this amplitude, the simplest form of the equation for nondimensional amplitude may be used since the amplitude at these frequencies is independent of damping: $\left.\frac{X(\tilde{s})}{X_{st}(\tilde{s})}\right|_{\zeta=\infty} = \frac{1}{G^2-1}$. Thus, the peak nondimensional amplitude at optimum response reduction is:

$$\left.\frac{X(\tilde{s})}{X_{st}(\tilde{s})}\right|_{G_1} = \frac{\sqrt{2}}{\overline{K}_{31}} \tag{11}$$

Note that equation 11 was obtained without using any tuning parameters and thus can be used to check the validity of the results using the tuning parameters.

As an example, assume a host structure with shunted piezoelectrics where $\overline{K}_{31} = 0.12$, which is a typical value. The response of this host structure at untuned values is shown in Figure 4. Figure 4 shows the response of the host structure using the optimal frequency ratio, as calculated using equation 7, and using the magnitude of the optimal damping ratio, as calculated using equation 9. The peak nondimensional amplitude of the response using the calculated tuning parameters is: 11.79. Using equation 11, the peak response at optimum response reduction is: $\left(X(\tilde{s})/X_{st}(\tilde{s})\right)|_{G_1} = 11.79$ which indicates the accuracy of the derivations herein.

As a comparison, the definitions used in current literature can also be examined. The optimum frequency ratio used herein is the same as that in current literature; however, the definition of damping ratio and the derivation of optimal damping ratio differs. Using the definition for damping ratio as specified in current literature and using the corresponding optimum damping ratio defined as $\zeta_{opt} = 1/\left(\sqrt{2}\overline{K}_{31}\right)$ in reference 18, yields a peak nondimensional amplitude of 12.19 for the same example. Thus, both definitions of damping ratio can be used to obtain the optimum values; however, for the simple lumped-parameter system considered, a more accurate calculation for optimum tuning parameters is possible using the derivations developed herein.

It is crucial to recall that the preceding tuning methodology was developed following the methodology used to tune a damped vibration absorber (shown in Figure 3), where the host structure (represented by m_1 and k_1) does not have damping ($c_1 = 0$). When the host structure has damping, two important characteristics of the response become apparent. First, with damping in the host structure, it is very difficult to derive closed-form solutions for Ω_{opt} and

ζ_{opt} as was done previously, primarily because two unique points such as A and B no longer exist. However, as mentioned in reference 13, the above tuning techniques may still be used reliably for structures that have small damping. These tuning techniques can be used by either neglecting the damping in the host structure and solving the above equations or by accounting for the damping using an iterative computational procedure. Both techniques should yield similar answers for Ω_{opt} and ζ_{opt} because the tuning parameters are not highly a function of the damping that exists in the host structure. Reference 30 provides an alternative technique for tuning a system that has small damping.

The second important characteristic of the response when the host structure has damping is that the effectiveness of the shunted piezoelectric (and likewise the damped vibration absorber) is strongly dependent on the damping of the host structure. Increased damping in the host structures results in decreased effectiveness of the shunted piezoelectric because the shunted piezoelectric is primarily adding damping to the host structure. The larger the damping inherent in the system, the less the percentage of total system damping the shunted piezoelectric can add.

In the next section, a two-degree-of-freedom aeroelastic model (with aerodynamic and structural damping) will be used in place of a generic host structure. All preceding derivations are applicable to this model, as will be discussed subsequently.

4. SHUNTED PIEZOELECTRICS APPLIED TO AN AEROELASTIC WING

4.1 Description of the analytical model

In this section, a simple two degree-of-freedom aeroelastic model is used to examine the feasibility of using shunted piezoelectrics to reduce aeroelastic response (see **Figure 5**). This type of model (analogous to the typical section models described in references 31 and) is useful in explaining the fundamental mechanisms of aeroelasticity. In the typical section model used herein, the shunted piezoelectrics were modeled as a damped vibration absorber, as shown in **Figure 5**. The aeroelastic equations of motion are first developed using the characteristics of the damped vibration absorber. Then, the terms representing the shunted piezoelectric are substituted in the equations of motion in place of the damped vibration absorber terms. In the model depicted in **Figure 5**, the mass, m_2, stiffness, K_2, and damping, C_2, represent the damped vibration absorber, which is located at the elastic axis. The absorber is oriented to move in the "h" direction (wing bending or plunging of the elastic axis). Twist about the elastic axis is represented by the torsion (or pitching) degree-of-freedom, "θ".

In this simplified idealization, the piezoelectrics are oriented to reduce the wing bending response due to the vertical motion of the damped vibration absorber. Vertical motion of the damped vibration absorber results in bending forces being applied to the wing section. Orienting the shunted piezoelectrics to affect bending response corresponds to orienting the "1" direction of the piezoelectric (see Figure 1) parallel to the elastic axis of the wing and, thus, perpendicular to the nodelines of the primary bending modes. A graphical depiction of this orientation is shown in Figure 6. This figure shows a very simplified depiction of a potential application of shunted piezoelectrics to reduce wing bending response. For actual application, the shunted piezoelectrics should be placed in the regions of highest strain for the modes of interest. More discussion of issues related to applying shunted piezoelectrics is provided subsequently. To affect torsion response on an orthotropic wing, the piezoelectrics shown in Figure 6 would be rotated 90°. However, a more complex model than the one shown in Figure 6 would be required to accurately examine the effects of shunted piezoelectrics oriented in such a manner since a "rotating" damped vibration absorber, or something similar, would have to be modeled. For the current study, only the effects of shunted piezoelectrics on bending response is considered.

4.2 Aeroelastic equations of motion with a damped vibration absorber

The dimensional aeroelastic equations of motion of the typical section model used with the damped vibration absorber were reduced, for simplicity, to include only the plunging and pitching aeroelastic equations of motion. This

simplification is accomplished by substituting the characteristics of the damped vibration absorber from the absorber equation of motion into the plunging and pitching aeroelastic equations of motion. Nondimensionalization of the equations of motion is attained by multiplying through by $1/(m_w \omega_h^{\,2})$, where $\omega_h^{\,2} = K_h/m_w$ is the uncoupled plunging natural frequency of the wing. It is important to note that, in most aeroelastic derivations, the equations of motion are nondimensionalized by multiplying through by $1/(m_{air}\omega^2)$. However, in the present study, nondimensionalization using $1/(m_w \omega_h^{\,2})$ enables direct comparison between the aeroelastic equations of motion with shunted piezoelectrics and the equation of motion derived earlier for shunted piezoelectrics applied to a generic host structure. The following nondimensional parameters were used in the nondimensional aeroelastic equations of motion: $r_\alpha^{\,2} = \dfrac{I_\alpha}{m_w b^2}$; $\omega_\alpha^{\,2} = \dfrac{K_\theta}{I_\alpha}$; $\omega_2^{\,2} = \dfrac{K_2}{m_2}$; $\Omega^2 = \dfrac{\omega_2^{\,2}}{\omega_h^{\,2}}$; $G^2 = \dfrac{\omega^2}{\omega_h^{\,2}}$; $\mu = \dfrac{m_w}{m_{air}}$; $M = \dfrac{m_2}{m_w}$; $C_c = 2m_2\omega_h$; and, $\zeta = \dfrac{C_2}{C_c}$. The nondimensional aeroelastic equations of motion can thus be written:

$$\left[\frac{-\left\{M\Omega^2G^2-\left(G^2\left(1+\frac{L_h}{\mu}\right)-(1+ig_h)\right)\left(G^2-\Omega^2\right)\right\}-i2\zeta G\left(G^2\left(1+\frac{L_h}{\mu}\right)-(1+ig_h)+MG^2\right)}{-\left(G^2-\Omega^2\right)+i2\zeta G}\right]\frac{\bar{h}}{b}-\left[G^2\left(x_\alpha+\frac{L_\theta}{\mu}\right)\right]\bar{\theta}=0$$

$$\left[-G^2\left(x_\alpha+\frac{M_{\frac{h}{b}}}{\mu}\right)\right]\frac{\bar{h}}{b}-\left[G^2\left(r_\alpha^{\,2}+\frac{M_\theta}{\mu}\right)-\frac{\omega_\alpha^{\,2}}{\omega_h^{\,2}}r_\alpha^{\,2}(1+ig_\theta)\right]\bar{\theta}=0 \qquad (12)$$

Structural damping, g, is approximated assuming small damping forces that are opposite in phase to velocity and directly proportional to the elastic restoring force. In addition, simple harmonic motion is assumed thus, the degrees of freedom and aerodynamic lift and pitching moment can be written:
$h = \bar{h}e^{i\omega t}$, $\theta = \bar{\theta}e^{i\omega t}$, $x_2 = \bar{x}_2 e^{i\omega t}$, $L_A = \bar{L}_A e^{i\omega t}$, $M_A = \bar{M}_A e^{i\omega t}$ where the barred terms (i.e., $\bar{h}$) represent the amplitude and phase angle of each term.

The aerodynamic lift and pitching moment were developed using Theodorsen's exact aerodynamic solution.[31-33] Thus, the aerodynamic lift and pitching moment are defined:

$$\bar{L}_A = -\pi\rho b^3\omega^2 L_h\frac{\bar{h}}{b}-\pi\rho b^3\omega^2\left(L_\alpha-\left(\tfrac{1}{2}+a\right)L_h\right)\bar{\theta}$$

$$\bar{M}_A = -\pi\rho b^4\omega^2\left(M_h-\left(\tfrac{1}{2}+a\right)L_h\right)\frac{\bar{h}}{b}-\pi\rho b^4\omega^2\left(M_\alpha-\left(\tfrac{1}{2}+a\right)(L_\alpha+M_h)+\left(\tfrac{1}{2}+a\right)^2L_h\right)\bar{\theta} \qquad (13)$$

In the above equations, L_h, L_α, M_h, and M_α, are functions of Theodorsen's function, C(k), where k is the reduced frequency defined as: $k = \omega b/V$. Note that Theodorsen's representation of the aerodynamic forces includes aerodynamic damping. To simplify the aerodynamic lift and pitching moment equations, the following substitutions are used: $m_{air} = \pi\rho b^2$; $L_\theta = L_\alpha - \left(\tfrac{1}{2}+a\right)L_h$; $M_{\frac{h}{b}} = M_h - \left(\tfrac{1}{2}+a\right)L_h$; and, $M_\theta = M_\alpha - \left(\tfrac{1}{2}+a\right)(L_\alpha + M_h) + \left(\tfrac{1}{2}+a\right)^2 L_h$.

Equation 12 represent the pitch and plunge equations of motion of a typical wing section with a damped vibration absorber placed on the elastic axis (shown in **Figure 5**). Notice that in examining equation 13, it is apparent that the only differences between the aeroelastic equations of motion derived above and the equation describing the lumped parameter system in Figure 3 (equation 6) are the addition of the aerodynamic forces and the torsional characterisitics of the wing. As discussed earlier, the damped vibration absorber can be used to represent shunted piezoelectrics with two important modifications to the nondimensional equations of motion. These are: 1) substituting the squared generalized electro-mechanical coupling coefficient, $\bar{K}_{31}^{\,2}$, for the $M\Omega^2$ terms; and 2) removing the terms containing $i2\zeta MG^3$.

4.3 Aeroelastic equations of motion with shunted piezoelectrics

Making the aforementioned modifications to the aeroelastic equations of motion yields:

$$\left[\frac{-\left\{\overline{K}_{31}{}^2G^2-\left(G^2\left(1+\frac{L_h}{\mu}\right)-(1+ig_h)\right)\left(G^2-\Omega^2\right)\right\}-i2\zeta G\left(G^2\left(1+\frac{L_h}{\mu}\right)-(1+ig_h)\right)}{-\left(G^2-\Omega^2\right)+i2\zeta G}\right]\frac{\overline{h}}{b}-G^2\left(x_\alpha+\frac{L_\theta}{\mu}\right)\overline{\theta}=0$$

$$\left[-G^2\left(x_\alpha+\frac{M_{\frac{h}{b}}}{\mu}\right)\right]\frac{\overline{h}}{b}-\left[G^2\left(r_\alpha{}^2+\frac{M_\theta}{\mu}\right)-\frac{\omega_\alpha{}^2}{\omega_h{}^2}r_\alpha{}^2(1+ig_\theta)\right]\overline{\theta}=0 \tag{14}$$

These equations can also be simply written as:

$$\begin{bmatrix}\overline{A} & \overline{B}\\ \overline{D} & \overline{E}\end{bmatrix}\begin{Bmatrix}\frac{\overline{h}}{b}\\ \overline{\theta}\end{Bmatrix}=\begin{Bmatrix}0\\0\end{Bmatrix} \tag{15}$$

Note that the electrical properties of the shunted piezoelectric are represented by using the nondimensional terms defined previously for a generic host structure with shunted piezoelectrics (see equation 5) : $\zeta=1/(2RC^S\omega_h)$, $\Omega^2=\omega_E{}^2/\omega_h{}^2$, $\overline{K}_{31}{}^2=\left(\omega_{OC}{}^2-\omega_h{}^2\right)/\omega_h{}^2$. In these equations the identity, $\omega_{SC}=\omega_h$, has been introduced since the short circuit natural frequency, ω_{SC}, is the natural frequency of the wing including piezoelectrics without any external electrical stimulus such as a shunt circuit. In addition, it follows that the inductance and resistance are defined:

$$L=1/\left(\omega_h{}^2\Omega^2C^S\right) \qquad R=1/\left(2\omega_hC^S|\zeta|\right) \tag{16}$$

Using equation 14, the effectiveness of the shunted piezoelectrics to reduce aeroelastic response can be examined. Optimal reduction in aeroelastic response can be obtained by using the tuning methodologies discussed previously. In the next section, computer simulations of the typical model used herein is employed to examine the effectiveness of the shunted piezoelectrics to reduce aeroelastic response at subcritical speeds (speeds below flutter). Examination of the impact of shunted piezoelectrics on flutter values was beyond the scope of the current work.

5. COMPUTER SIMULATIONS

5.1 Flutter analysis to establish the stability boundary

To examine the effectiveness of the shunted piezoelectrics, analytical simulations of the typical section model described above were developed using MATLAB.[34] The following parameters were used for all of the subsequent analyses: $\mu=40$, $r_\alpha{}^2=0.6$, $x_\alpha=0.15$, $a=-0.25$, $b=3$ ft. Two aeroelastic models were examined. For each model, the aeroelastic response with and without structural damping (g_h and g_θ) was considered. Initially, a flutter analysis of each aeroelastic model without the shunted piezoelectrics was conducted to establish the stability boundary and to select the subcritical speeds for the response reduction simulations. Removing the effect of the shunted piezoelectrics in the flutter analysis was accomplished by setting: $M=\Omega=\zeta=0$. Two different flutter analysis methods were used to verify the final flutter values for each model; both methods yielded approximately the same flutter values for each model. The k method (also called American method) and the P-k (or British method) were employed. Table 1 summarizes the parameters used for the models and their calculated flutter speeds and frequencies.

Table 1 Parameters for aeroelastic models used in computer simulations and flutter values

Model name	ω_h	ω_θ	g_h	g_θ	Flutter speed (ft/sec)	Flutter frequency (rad/sec)
1a	12	40	0.0	0.0	517	28.3
1b	12	40	0.03	0.03	537	26.9
2a	20	40	0.0	0.0	446	31.3
2b	20	40	0.03	0.03	464	30.1

5.2 Forced response analysis

The effectiveness of the shunted piezoelectrics to reduce response was examined at five subcritical velocities. The velocities used for models 1a and 1b were 100, 200, 280, 330, and 380 ft/sec. The velocities used for models 2a and 2b were 70, 150, 220, 285, and 330 ft/sec. The velocities were chosen by considering that, for a typical airplane, the maximum dive speed is usually 20% less than the flutter speed and the maximum cruise speed is typically 20% less than the maximum dive speed. For example, maximum cruise speed for model 1a would be approximately 330 ft/sec. In choosing the other velocities, three values of velocity below the maximum cruise speed were considered to encompass the wide range of speeds a typical airplane might experience in its flight envelope. One velocity above the maximum cruise speed was also considered to explore response reduction at speeds outside the typical flight envelope.

Effectiveness of the shunted piezoelectrics at the aforementioned speeds was examined by studying the response of the typical section models to sinusoidal forcing functions, P (plunge force) and T (torsion moment). Assuming simple harmonic motion, P and T can be written: $P = \bar{P}_o e^{i\omega t}$ and $T = \bar{T}_o e^{i\omega t}$. These forcing functions were first nondimensionalized using the same quantities used in equation 13 to obtain: $\bar{p}_o = \bar{P}_o / \left(m_w \omega_h^{\,2}\right)$ and $\bar{t}_o = \bar{T}_o / \left(m_w \omega_h^{\,2}\right)$. To further simplify the simulation results, the plunging and pitching responses were normalized by static deflections. The static plunging and pitching deflections are given by: $\frac{\bar{h}_{st}}{b} = \frac{\bar{p}_o}{b}$ and $\bar{\theta}_{st} = \frac{\bar{t}_o}{b^2} \frac{\omega_h^{\,2}}{\omega_\alpha^{\,2} r_\alpha^{\,2}}$. The resulting normalized responses are:

$$\frac{\bar{h}}{\bar{h}_{st}} = \frac{\bar{E} - \frac{\bar{t}_o}{\bar{p}_o b}\bar{B}}{\Delta} \qquad \frac{\bar{\theta}}{\bar{\theta}_{st}} = \frac{\omega_\alpha^{\,2} r_\alpha^{\,2}}{\omega_h^{\,2}} \left(\frac{\bar{A} - \frac{\bar{p}_o b}{\bar{t}_o}\bar{D}}{\Delta} \right) \tag{17}$$

where Δ is the determinant of the matrix $\begin{bmatrix} \bar{A} & \bar{B} \\ \bar{D} & \bar{E} \end{bmatrix}$ from equation 15.

In addition, the following values for plunging and pitching deflections were used for all of the models examined: $\bar{h}_{st} = 0.75$ feet, $\therefore \bar{p}_o = 0.75$ and $\bar{\theta}_{st} = 2^\circ \therefore \bar{t}_o = 2.09$. The normalized wing responses given in equation 17 will be used throughout the remaining analyses. The subcritical response of the aeroelastic models, with and without the shunted piezoelectrics, will be examined considering a linear sweep of the frequency of the forcing functions from 9 rad/sec to 45 rad/sec. Furthermore, as discussed previously, since the shunted piezoelectrics considered herein were oriented to reduce plunging (bending) response, the model used is not sufficient for a reliable, quantitative analysis of pitching (torsion) response reduction. Thus, only the normalized plunge response will be emphasized in the computer simulations.

5.3 Tuning the shunt circuit to reduce aeroelastic response

With the typical section properties and forcing function parameters fixed, the only remaining parameters are those relating to the shunted piezoelectrics, namely $\bar{K}_{31}$, Ω, and ζ. As mentioned previously, the generalized electro-

mechanical coupling coefficient, $\overline{K}_{31}$, is primarily a function of how well the piezoelectrics are bonded to the host structure. Assuming that all piezoelectrics used in the current study were bonded using currently available bonding materials and techniques, one (typical) value of $\overline{K}_{31}$ was used for all of the analyses: $\overline{K}_{31} = 0.12$.

As shown earlier, the frequency ratio, Ω, and the damping ratio, ζ, are the two critical parameters that determine the effectiveness of the shunted piezoelectrics. These quantities determine the value of capacitance (the piezoelectrics), resistance, and inductance in the shunt circuit and can be tuned to optimize the vibration reduction of the host structure. However, the wing used herein includes both aerodynamic damping and structural damping. The methodology shown earlier for tuning the shunt circuit can be applied to systems with damping by either: 1) neglecting the damping that exists in the host structure and solving for the optimal frequency and damping ratio; or 2) using an iterative computational procedure where the damping in the host structure is included as the tuning parameters are found. As mentioned previously, both methods should yield similar results. The former method is not desirable for the aeroelastic system since excluding the aerodynamic damping to seek closed-form solutions for optimum frequency and damping ratio would lead to inaccuracies in the calculation of the aeroelastic response. Thus, the latter approach of using a simple, computer-based iterative procedure was implemented. Table 2 summarizes the optimal values found for each model using a computational, iterative procedure.

Table 2 Optimal frequency and damping ratios

Model name	Velocity (ft/sec)	Ω_{opt}	ζ_{opt}
1a	100	.9906	.0776
	200	1.0046	.0848
	280	1.0170	.0932
	330	1.0233	.0974
	380	3.0122	.0251
1b	100	.9894	.0793
	200	1.0032	.0868
	280	1.0158	.0938
	330	1.0234	.0986
	380		
2a	70	.9801	.0730
	150	.9895	.0766
	200	.9987	.0793
	285	1.0224	.0853
	330	1.0406	.0898
2b	70	.9792	.0750
	150	.9884	.0783
	200	.9977	.0809
	285	1.0219	.0868
	330	1.0414	.0914

In examining Table 2, note that except at 380 ft/sec for models 1a and 1b, the variation in optimum frequency ratio with airspeed is not significant. This is due to the small variation in the plunge natural frequency with airspeed, which is an indicator that a passive shunt circuit might be effective in reducing plunge response. In addition, an approximate verification of the values in Table 2 can be made by comparing with the values obtained using the empirical solutions for optimal frequency and damping ratio derived earlier for a generic structure. Recall that the only difference between the previous development using a generic structure and the current development using a

wing is the addition of a coupled, torsional degree-of-freedom and aerodynamics on the wing. Using equations 7 and 9, the optimal frequency ratio and the magnitude of the optimal damping ratio are 0.996 and 0.0725, respectively. These values are very close to the values in Table 2 except at 380 ft/sec for models 1a and 1b. The optimal damping ratio at this airspeed is very low, which may indicate that the damped vibration absorber analogy is no longer valid at this airspeed for this wing. More discussion on the significance of the above optimal tuning results will be given after an examination of the response reduction results in the next section.

5.4 Results of forced response analysis

The responses of the wing models were calculated with and without shunted piezoelectrics at each airspeed. Sample plots of the bending response at 200 ft/sec for model 1a is shown in Figure 7 and for model 2a in Figure 8. As expected, these plots closely resemble the plots shown in Figure 4 of the shunted piezoelectrics applied to a generic host structure. In both cases, the shunted piezoelectric creates a "double hump" in the magnitude of the response and, consequently, two 90° drop-offs in the phase. Also, note that in Figures 7 and 8 the response is plotted using the optimal tuning values as well as the non-optimal tuning values for another airspeed. Although use of the optimal tuning values clearly yields the best response reduction, use of the non-optimal tuning values yields considerable response reduction as well. Using plots such as these for each airspeed, the percent reduction in the peak plunging response using the shunted piezoelectrics can be calculated. Overall, the shunted piezoelectrics were very effective in reducing the plunge response of the typical section models considered; a 10% to 70% reduction was calculated for the range of airspeeds considered, except at 380 ft/sec for models 1a and 1b.

In general, the effectiveness of the shunted piezoelectrics is largely a function of the percent of inherent aeroelastic damping the shunted system can add using the optimum frequency and damping ratios. That is, the more damping that already exists in the aeroelastic system, the less effective the shunted piezoelectric. This characteristic is displayed in the results in several ways:

1) The overall decrease in the effectiveness of the shunted piezoelectrics with airspeed for all of the models.
2) The overall decrease in effectiveness with added inherent structural damping, g_θ and g_h. This is evident by comparing the responses of model 1a with model 1b, and comparing responses of model 2a with model 2b.
3) The general increase in effectiveness for models 2a and 2b as compared to models 1a and 1b.

In examining the first item above, note that a common characteristic of aeroelastic systems is small damping at low airspeeds and increased damping with airspeed. For the mode that goes unstable, this characteristic is followed by a reverse in the damping trend near the flutter speed, toward zero damping at flutter.[31] Thus, the overall decrease in the effectiveness of the shunted piezoelectric with increased airspeed is due to the increased inherent aerodynamic damping with airspeed. Figure 9 shows this trend clearly. In this figure, the results for the models with and without structural damping are plotted for actively shunted piezoelectrics. Thus, the only damping present for the models without structural damping (models 1a and 2a) is due to the aerodynamics and the shunted piezoelectric.

The second item in the list above addresses the impact of adding inherent structural damping, g_θ and g_h. In comparing the responses in Figure 9, note that the only difference of the "b" models over the "a" models is the addition of inherent structural damping, g_θ and g_h (see Table 1). This additional damping reduces the response for the "b" models at all airspeeds, and thus results in the shunted piezoelectrics being less effective for the "b" models. Although the reduction in effectiveness was not considerable for the models considered, the impact of inherent structural damping cannot be ignored since this quantity can vary significantly for aeroelastic structures.

The last item in the list above addresses the comparison between models 1a and 1b with models 2a and 2b. Overall, the plunge responses of models 2a and 2b were less damped than models 1a and 1b, resulting in the shunted piezoelectrics being more effective on models 2a and 2b. This is not surprising considering that models 2a and 2b are generally less stable than models 1a and 1b, as is evident by examining their flutter characteristics and comparing the responses shown in Figures 9 and 10.

Another important issue in examining the results is the impact of using non-optimum frequency and damping ratios. As mentioned previously, passive use of the shunt circuit would imply tuning the circuit for one condition and using these tuning values for the entire flight envelope. To simulate this in the current study, it was assumed that the shunt circuit would be tuned for the maximum cruise condition and these optimum (tuning) values would be used at the other speeds. The passive shunt circuit was less effective than the active shunt circuit at every airspeed except the maximum cruise speed. This characteristic is shown in Figure 10 where the response with an active shunt circuit is compared with that of a passive shunt circuit. The effectiveness of the passive shunt circuit depends primarily upon the variation of plunge natural frequency. Thus, at velocities far from the maximum cruise condition, the impact of using off-tuned values was most significant (as much as a 20% drop in effectiveness). On the other hand, considering the simplicity of a passive shunt circuit and that this circuit is still 80% as effective as the active circuit at worst conditions, the passive shunt circuit may be a desirable approach for some aeroelastic applications.

The reduction of the pitch response due to the shunted piezoelectrics was essentially negligible, as anticipated; approximately 0.2% reduction for models 1a and 1b and 1.5% reduction for models 2a and 2b. As with the reductions in plunge responses, the reductions in pitch response increased slightly as the natural frequency of the shunt circuit got closer to the natural pitch frequency.

Lastly, V=380 ft/sec for models 1a and 1b represents a unique case. At this condition only, the plunge due to pitch response (the flutter mode) dominates the overall plunge response. At this speed, the shunt circuit was tuned for the plunge due to pitch mode as opposed to the plunge natural mode (see Table 2). However, recall that the shunted piezoelectrics were oriented to reduce plunge response only. Thus, examination of the effectiveness of the shunted piezoelectrics on the plunge due to pitch response is probably beyond the realistic usability of the simple lumped parameter idealization used. Correspondingly, the response at this speed was significantly different from the responses at the other speeds where the shunt circuit was tuned for the plunge natural mode. For example, the response was uncharacteristically very sensitive to variations in frequency and damping ratios; thus, tuning at this speed was quite difficult. Recall that the responses of models 1a and 1b were calculated using the same optimal frequency and damping ratio because, structural damping typically does not significantly affect these values. However, the addition of structural damping resulted in the shunted piezoelectrics being significantly off-tuned for model 1b. Moreover, in reviewing Table 2, note that the damping ratio for V=380 ft/sec is very low. As mentioned previously, simulation of the shunted piezoelectric at very low damping ratios using a damped vibration absorber analogy may be inaccurate. Thus, further investigation of the behavior of the typical section with shunted piezoelectrics for coupled modes with low damping ratio is required before reliable conclusions can be reached for these conditions.

Overall, the shunted piezoelectrics were very effective in reducing plunge response using both a passive and active shunt circuit. At the unique condition of V=380 ft/sec for models 1a and 1b, the effect of the shunted piezoelectrics is uncertain and requires further investigation. At all other speeds, the shunted piezoelectrics reduced the response of all modes, although the impact on pitch modes was not significant due to the orientation of the shunted piezoelectrics for the current study.

6. APPLICATION ISSUES AND RECOMMENDATIONS FOR FUTURE WORK

The preceding analysis examined the application of shunted piezoelectrics to a simple two-degree-of-freedom model of an aeroelastic system. While this analysis clearly shows that shunted piezoelectrics can reduce aeroelastic response, considerable additional research is required before shunted piezoelectrics can be applied to realistic air vehicles for aeroelastic response reduction. This research includes developing improved analytical models and experimental validation. Limited (unpublished) data on the use of shunted piezoelectrics on air vehicles is available. Wind-tunnel tests are tentatively planned to further assess using shunted piezoelectrics for aeroelastic response reduction. In an actual application, shunted piezoelectrics will likely be most effective if they are designed into the

structure, as opposed to being used as a retrofit. To effectively design shunted piezoelectrics into a structure the following considerations must be addressed: maximize the strain energy transfer from the host structure to the piezoelectric and maintain structural integrity. These objectives can often have conflicting requirements. To achieve the first objective, for example, the piezoelectrics are placed in the high-strain regions of the host structure as indicated by examination of the mode shapes of interest. However, piezoelectric materials, as compared to traditional load-carrying materials, have an lesser load-carrying capability.[24] Thus, piezoelectric materials should not be relied upon as critical load-carrying structural components and thus must be carefully designed into the host structure. These design considerations are also applicable to applications where piezoelectrics are used as actuators.

Sensing equipment is also necessary to use shunted piezoelectrics. The frequency of the mode of interest on the host structure and the natural frequency of the shunt circuit must be accurately measured to tune the shunt circuit. For active shunting, sensing must be continuous. For passive shunting, sensing equipment is only needed in the initial tuning of the shunt circuit.

Another important issue that must be addressed for realistic aeroelastic application is ensuring the robustness the shunted piezoelectrics as the natural frequency of the air vehicle varies. To address the issue of varying natural frequencies on the host structure, some researchers have examined "self-tuning" shunt circuits to retune the circuits as the natural frequency of the host structure varies.[14, 15] These self-tuning circuits (or active shunting) behave like an active control system: given an input (the short circuit natural frequency, ω_{SC}), an active control law determines the optimal frequency and damping ratios needed to optimally reduce the response. Alternatively, if modal response in a specific portion of the flight envelope is of most importance, the shunt circuit can be tuned a priori for the flight condition of interest and shunted piezoelectrics can be used passively. In this application, the shunted piezoelectrics still dissipate energy at conditions other than the one of interest; however, the shunted piezoelectrics are most effective at the flight condition for which they were tuned. Another method to consider is designing the shunted piezoelectric to reduce response in more than one mode simultaneously. This method, examined in references 13, 16, and 20, may prove to be very useful for air vehicles that have multiple modes contributing to an unacceptably large response. The above approaches have the added advantage of accomodating the variation of piezoelectric capacitance with voltage.

Finally, in general, increasing the damping in a structure has the primary effect of reducing vibration amplitudes at resonances. This can lead to reduced displacements, stresses, fatigue and noise. In addition, references 9 and 35 and observe that damping can also add robustness and stability to marginally-stable active control systems which, in turn, can reduce the chance of spillover that can destabilize a system. Thus, shunting a piezoelectric and actuating it using a control law may provide a highly robust and very effective vibration control approach.

7. CONCLUSIONS

The feasibility of using shunted piezoelectrics to reduce aeroelastic response at speeds below flutter was examined via analysis. The piezoelectrics used in this study were shunted using a parallel resistor and inductor. Examination of this shunt circuit applied to a generic host structure was first studied to assess the general characteristics of this application and the limitations of the current analytical methods. These developments were used as a basis for applying shunted piezoelectrics to a typical-section aeroelastic model. Using Theodorsen aerodynamics, the response of two aeroelastic models to sinusoidal forcing functions was examined to study the effectiveness of using shunted piezoelectrics to reduce aeroelastic response. These results demonstrate that shunted piezoelectrics can significantly reduce aeroelastic response; for example, reductions of up to 70% in plunging response were realized. The effectiveness of the shunted piezoelectrics was found to be a strong function of the inherent structural and aerodynamic damping. Thus, this application may not be effective for highly damped structures. However, for lightly damped structures, shunted piezoelectrics provide a simple, low-power, fail-safe vibration suppression mechanism. Follow-on studies are planned to explore developing higher fidelity models and to validate the results via wind-tunnel testing.

ACKNOWLEDGEMENTS

The author would like to acknowledge the invaluable discussions with Drs. Chuh Mei, Donald Kunz, Ray Kvaternik, Robert Bennett, Jim Wu, and Ms. Jennifer Heeg.

REFERENCES

[1] Weisshaar, T.A., "Aeroservoelastic Control with Active Materials- Progress and Promise," CEAS International Forum on Aeroelasticity and Structural Dynamics, Manchester UK, June 1995.

[2] Crowe, C. R. and Sater, J. M., "Smart Aircraft Structures," Future Aerospace Technology in the Service of the Alliance, Vol. 1: Affordable Combat Aircraft, AGARD Conference Proceedings 600, pp. A20-1 to A20-15, Paris, France, 1997.

[3] Loewy, R.G., "Recent Developments in Smart Structures with Aeronautical Applications," Journal of Smart Materials and Structures, Vol. 5, October 1997, pp. 11-41.

[4] Hopkins, M.A., Henderson, D.A., Moses, R.W., Findlay, D., Voracek, D.F., Spangler, R.L., Ryall, T., and Zimcik, D., "Active Vibration Suppression Systems Applied to Twin Tail Buffeting," Proceedings of SPIEís 5th Annual Symposium on Smart Structures and Materials, Paper No. 3326-05, San Diego, CA, March 1-5, 1998.

[5] Moses, R.W., "Active Vertical Tail Buffeting Alleviation on a Twin-Tail Fighter Configuration in a Wind Tunnel," Proceedings of the CEAS International Forum on Aeroelasticity and Structural Dynamics 1997, Rome, Italy, 1997.

[5] Pinkerton, Jennifer L. and Moses, Robert W., "A Feasibility Study To Control Airfoil Shape Using THUNDER", NASA TM-4767, November 1997.

[6] McGowan, A. R., Heeg, J., and Lake, R.C., "Results of Wind-Tunnel Testing From the Piezoelectric Aeroelastic Response Tailoring Investigation," Proceedings of the 37th AIAA/ASME/ASCE/AHS/ASC Structures, Structural Dynamics and Materials Conference, Salt Lake City, UT, April 1996.

[7] Brennan, M. C. and McGowan, A. R., "Piezoelectric Power Requirements for Active Control," Proceedings of the SPIE's 4th Annual Symposium on Smart Structures and Materials, Mathematics and Control in Smart Structures Conference, Paper 3039-69, March 1997.

[8] McGowan, A. R., "A Feasibility Study of Using Shunted Piezoelectric Piezoelectrics to Reduce Aeroelastic," SPIE's 6th Annual Symposium on Smart Structures and Materials, Industrial and Commercial Applications Conference, Newport Beach, CA Paper number 3674-20, March1999.

[9] Agnes, G.S., "Active/Passive Piezoelectric Vibration Suppression," Proceedings of the 1994 SPIE Smart Structures and Materials, Passive Damping Conference, Orlando, FL, Vol. 2193, Feb. 14-16, 1994, pp. 24-34.

[10] Hagood, N.W., IV, and von Flotow, A.H., "Damping of Structural Vibrations with Piezoelectric Materials and Passive Electrical Networks," Journal of Sound and Vibration, Vol. 146, No. 2, 1991, pp. 243-268.

[11] Forward, R. L., "Electronic Damping of Vibrations in Optical Structures," Journal of Applied Optics, Vol. 18, No. 5, March 1979, pp. 690-697.

[12] Edberg, D.L., Bicos, A.S., and Fetcher, J.S., "On Piezoelectric Energy Conversion for Electronic Passive Damping Enhancement," Proceedings of Damping '91, San Diego, CA, Paper GBA-1, Feb. 1991.

[13] Hollkamp, J.J., "Multimodal Passive Vibration Suppression with Piezoelectrics," Proceedings of the 34th AIAA/ASME/ASCE/AHS /ASC Structures, Structural Dynamics, and Materials Conference and AIAA/ASME Adaptive Structures Forum, La Jolla, CA, Apr. 19-22, 1993, Paper number: AIAA 93-1683-CP, pp. 3227-3237.

[14] Hollkamp, J.J., and Starchville, T.F., "A Self-Tuning Piezoelectric Vibration Absorber," Proceedings of the AIAA/ASME Adaptive Structures Forum, Hilton Head, SC, Apr. 21-22, 1994, pp. 521-529.

[15] Wang, K.W., Yu, W.K., and Lai, J.S., "Parametric Control of Structural Vibrations via Piezoelectric Materials Shunted with Adaptive Circuits," Proceedings of the Conference on Smart Structures and Materials 1994: Mathematics and Control in Smart Structures," Orlando, FL, Vol. 2192, Feb. 14-16, 1994, pp. 120-131.

[16] Agnes, G. S., "Development of a modal model for simultaneous active and passive piezoelectric vibration suppression." Journal of Intelligent Material Systems and Structures, Vol. 6(4), 1995, pp. 482-487.

17 Yarlagadda, S., Lesieutre, G.A., Yoshikawa, S., and Witham, J., "Resistively Shunted Piezocomposites for Passive Vibration Damping," AIAA Paper No. A96-27071 06-39, Proceedings of the AIAA/ASME/AHS Adaptive Structures Forum, Salt Lake City, UT, Apr. 18-19, 1996, pp. 217-227.
18 Wu, S., "Piezoelectric Shunts with a Parallel R-L Circuit for Structural Damping and Vibration Control," Proceedings of SPIE's Symposium on Smart Materials and Structures, Vol 2720, March 1996, pp. 259-269.
19 Wu, S., and Bicos, A.S., "Structural Vibration Damping Experiments Using Improved Piezoelectric Shunts," Proceedings of the SPIE's 5th Annual Symposium on Smart Structures and Materials, Passive Damping and Isolation Conference, San Diego, CA, Vol. 3405, Mar. 3-4, 1997, pp. 40-50.
20 Wu, S.Y., "Method for Multiple Mode Shunt Damping of Structural Vibration Using a Single PZT Transducer," Proceedings of SPIE's 6th Annual Symposium on Smart Structures and Materials, Vol. 3327, March 1998.
21 Smith, C.A., and Anderson, E.H., "Passive Damping by Smart Materials: Analysis and Practical Limitations," Proceedings of the Smart Structures and Materials Symposium, Passive Damping and Isolation Conference, Vol. 2445, San Diego, CA, Mar 1-2, 1995, pp. 136-148.
22 Hollkamp, J.J., and Gordon, R.W., "An Experimental Comparison of Piezoelectric and Constrained Layer Damping," Proceedings of the Smart Structures and Materials Symposium, Passive Damping and Isolation Conference, Paper No. A95-37751 10-39, San Diego, CA, Vol. 2445, Mar. 1-2, 1995, pp.123-133.
23 Hagood, N.W., IV, Aldrich, J.B., and von Flotow, A.H., "Design of Passive Piezoelectric Damping for Space Structures," Final Report, NASA CR 4625, September 1994.
24 Agnes, G.S., and Inman, D.J., "Nonlinear Piezoelectric Vibration Absorbers," Journal of Smart Materials and Structures, Vol. 5, Issue 5, Oct. 1996, pp. 704-714.
25 IEEE Standard on Piezoelectricity, Standard 176-1987, 1987, New York, NY.
26 Crawley, E.F., and DeLuis, J., "Use of Piezoelectric Actuators as Elements of Intelligent Structures," AIAA Journal, Vol. 25, No. 10, 1987, pp. 1373-1385.
27 Den Hartog, J.P., Mechanical Vibrations, Fourth Edition, McGraw-Hill Book Company, Inc, New York, New York, 1956.
28 Ormondroyd, J., and Den Hartog, J.P., "The Theory of the Dynamic Vibration Absorber," May 1928, Transactions of the ASME, APM-50--7, pp. 9-22.
29 Timoshenko, S., and Young, D.H., Vibrations Problems in Engineering, Third Edition, D. Van Nostrand Company, Inc., Princeton, New Jersey, 1955.
30 Hunt, J. B., Dynamic Vibration Absorbers, Mechanical Engineering Publications, Ltd., London, England, 1979.
31 Bisplinghoff, R.L., Ashley, H., and Halfman, R.L., Aeroelasticity, Addison-Wesley Publishing Company, Inc., Reading, Massachusetts, 1955.
32 Fung, Y.C., An Introduction to the Theory of Aeroelasticity, Dover Publications, Inc., New York, 1969.
33 Theodorsen, T., "General Theory of Aerodynamic Instability and the Mechanism of Flutter," NACA Rrt 496, 1935.
34 Using MATLAB, The Mathworks, Inc., 1997.
35 Ashley, H. Edberg, D., "On the Virtues and Prospects for Passive Damping in Large Space Structures," Proceeding of Damping '86, AFWAL-TR-86-3059, Vol. 1, May 1986.

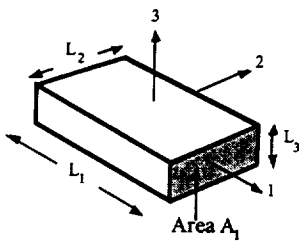

Figure 1. Typical piezoelectric element

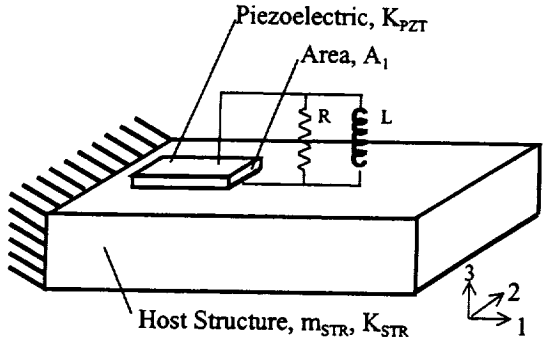

Figure 2. Generic host structure with a shunted piezoelectric

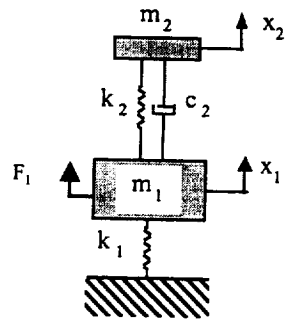

Figure 3. A damped vibration absorber attached to a host structure

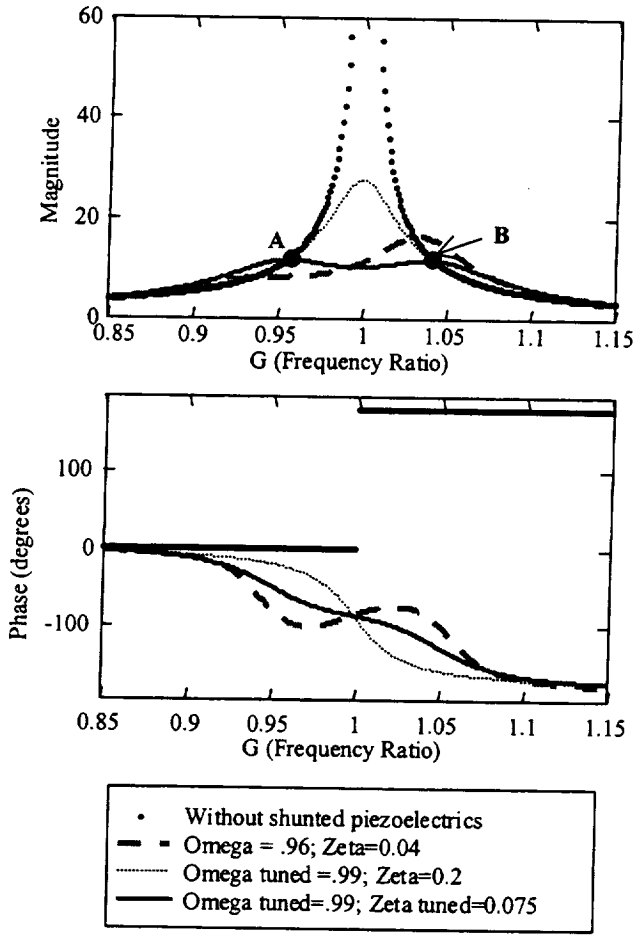

Figure 4. Response of host structure with attached shunted piezoelectrics

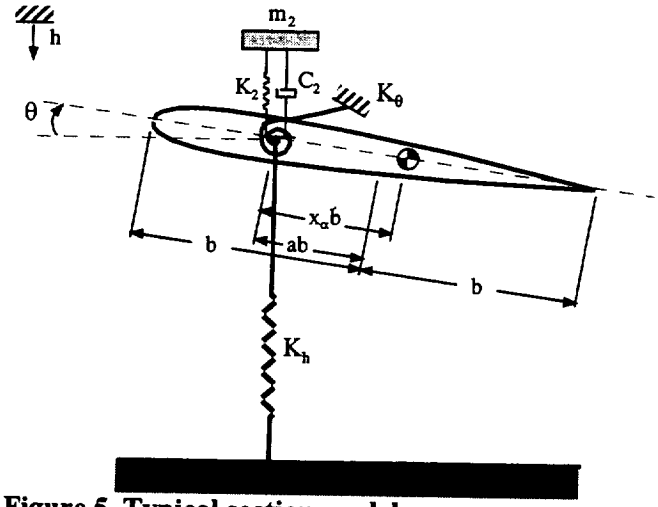

Figure 5. Typical section model

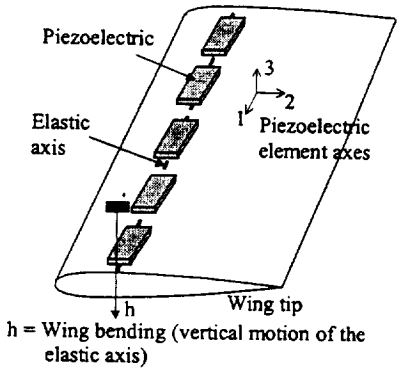

Figure 6. Example applications of shunted piezoelectrics on a wing

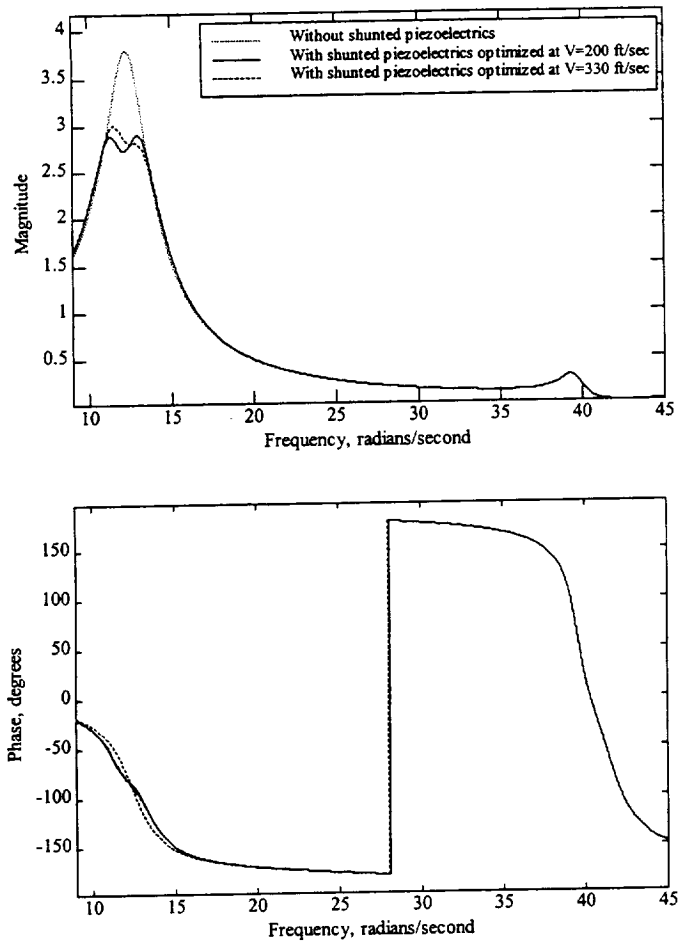

Figure 7. Nondimensional plunge response for model 1a at 200 ft/sec

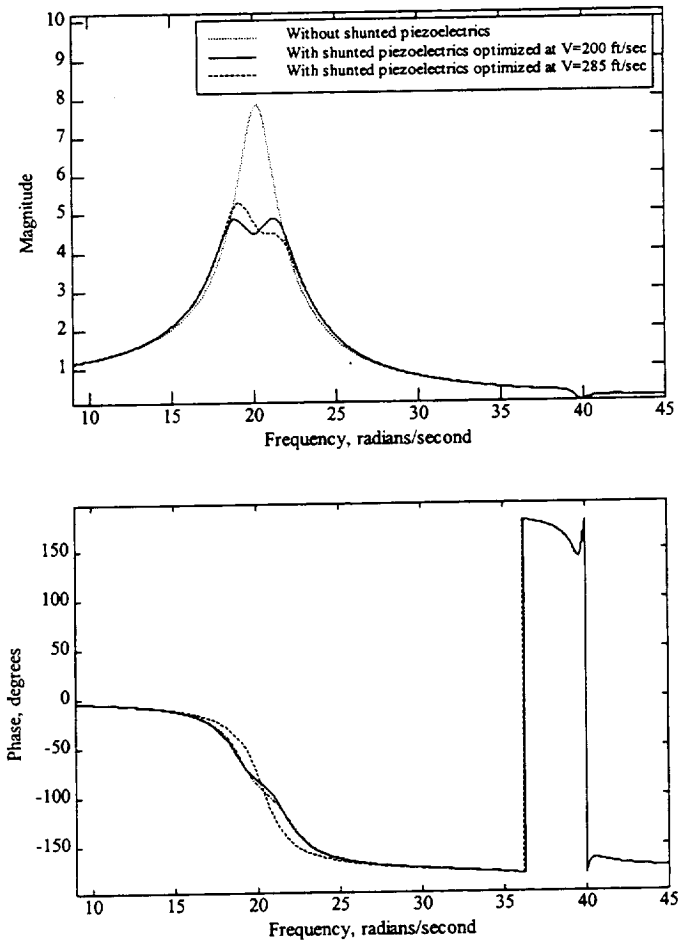

Figure 8. Nondimensional plunge response for model 2a at 200 ft/sec

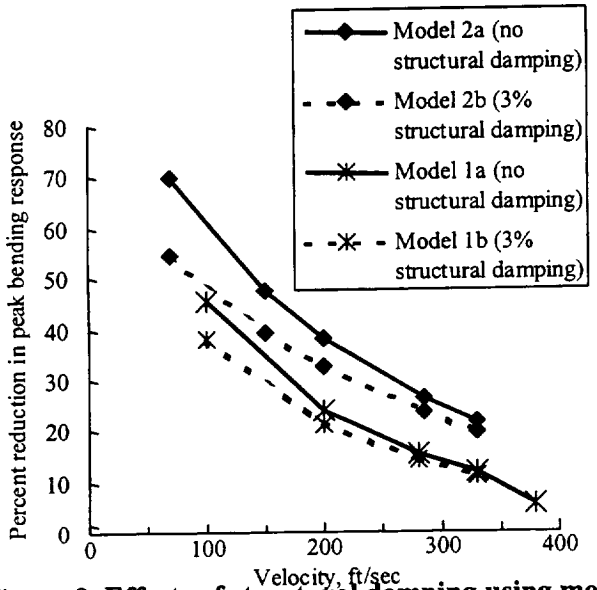

Figure 9. Effects of structural damping using models that are actively shunted

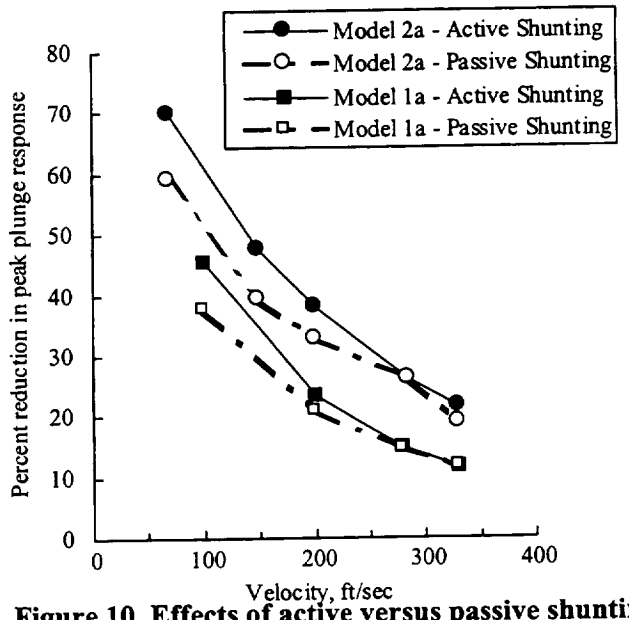

Figure 10. Effects of active versus passive shunting using models with no structural damping

A Comparison Study of the Performance of a Saturation Absorber and Classical Vibration Control Methods

Hanafy M. Omar, Graduate Research Assistant
Donald Kunz, Associate Professor
Department of Aerospace Engineering
Old Dominion University
Norfolk, VA 23529-0247

Introduction

The saturation absorber is an application of the saturation phenomenon as a vibration suppression device. The saturation phenomenon occurs in autoparametric, multi-degree-of-freedom systems, if the natural frequencies of the absorbers and the plants are commensurable ($\omega_p = 2\omega_c, 3\omega_c, \ldots$). To control the vibratory response of a plant with a single degree of freedom, a second-order absorber is introduced and coupled to the plant with quadratically nonlinear terms. When the plant is forced at its resonant frequency and the magnitude of the response reaches its saturation level, the nonlinear coupling forms an energy bridge between the plant and the absorber.

The objective of the research described in this paper is to quantify the performance of the saturation control (response, the required control authority, robustness to the plant parameter variation), as compared with the performance of classical controllers, such as velocity feedback, and nonlinear controllers like the Fuzzy Logic Controller (FLC). This comparison will serve to identify the advantages and the disadvantages of saturation control, especially regarding the control authority required to suppress the response of a vibrating system. In addition, a parametric study of the nonlinear coupling parameters will result in guidelines for obtaining the desired absorber performance. A comprehensive understanding of the role of each parameter on the response of the system is also given.

Structural Modeling

The structural model used to perform the comparison is a uniform cantilever beam actuated by two patches of piezoceramic material. The configuration is similar to that described in Refs. 1 and 2, except that the non-homogeneity due to the existence of the actuator has been taken into consideration (Fig. 1). For the purposes of this research, only the first mode of the cantilever beam is being controlled.

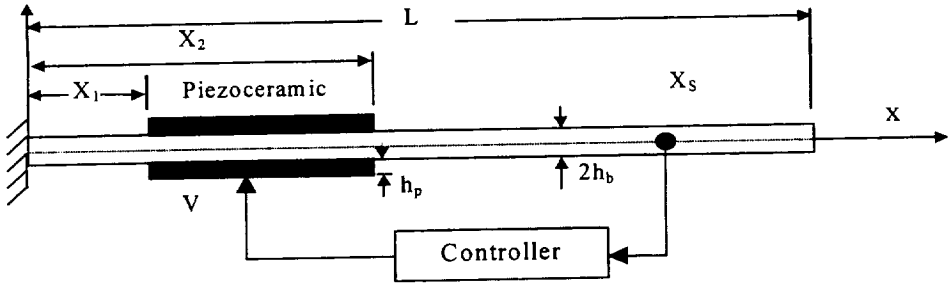

Figure 1. Beam Model

For the piezoceramic actuator, when a voltage is applied in the z direction of the piezoelectric material, the strain resulted in the x direction will be

$$\varepsilon_{pe} = \frac{d_{31}V}{h_p} \tag{1}$$

where V is the applied voltage and d_{31} is the piezoelectric material constant. However, it is assumed that the actuator is bonded to the beam, which serves as a constraint on its deformation. Assuming that the strain distribution is linear, as a result of Kirchoff's hypothesis [3], the induced moment distribution (m_x) in the beam beneath the actuator is given by

$$m_x(x) = EIC_o \tag{2}$$

where

$$C_o = \frac{3E_p d_{31}(h_p + 2h_b)(V(t)_1 - V_2(t))}{4(h_b + 3h_p)(E_p h_p^2 + E_b h_b^2)} \tag{3}$$

The equation of motion of the beam is then

$$\rho S\frac{\partial^2 W(x,t)}{\partial^2} + \bar{C}\frac{\partial W(x,t)}{\partial} + \frac{\partial^2}{\partial x^2}(EI(x)\frac{\partial^2 W(x,t)}{\partial^2 x}) = F(x,t) + EIC(\delta'(x-x_1) - \delta'(x-x_2)) \tag{4}$$

where $\delta'(x)$ is the derivative of the Dirac delta function with respect to x. To solve this equation, considering that the beam is nonhomogenous, the Rayleigh-Ritz method is used.

$$W(x,t) = \sum_{i=1}^{n} \phi_i(x) q_i(t) \tag{5}$$

Where ϕ_i are the mode shapes of the uniform cantilever beam. Then,

$$[m]\{\ddot{q}(t)\} + [c]\{\dot{q}(t)\} + [k]\{q(t)\} = [Q(t)] + [F(t)] \tag{6}$$

where

$$m_{i,j} = \int_0^L \rho_b S_b \phi_i(x)\phi_j(x)dx + \int_{x_1}^{x_2} \rho_p S_p \phi_i(x)\phi_j(x)dx$$

$$k_{i,j} = \int_0^L E_b I_b \frac{d^2\phi_i(x)}{dx^2}\frac{d^2\phi_j(x)}{dx^2}dx + \int_x^{x_2} E_p I_p \frac{d^2\phi_i(x)}{dx^2}\frac{d^2\phi_j(x)}{dx^2}dx \tag{7}$$

$$Q_i(t) = C_o(E_b I_b + E_p I_p)\frac{i\pi}{L}\left\{\cos(\frac{i\pi x_2}{L}) - \cos(\frac{i\pi x_1}{L})\right\}$$

The state-space model of the uncoupled system can be determined, and the damping matrix [c] can be obtained experimentally by measuring the damping of each mode.

The dimensions and the properties of the beam and the piezoceramic used in this research for numerical simulation are shown in Table 1.

Table 1. Beam and Piezoceramic Dimensions and Properties

	Length	Width	Thickness	Density	Young's Modulus	Piezoelectric constant
Beam	16 in	1.5 in	0.04 in	2700 kg/m^3	70 GPa	63 Gpa
Piezoceramic	1.81 in	1.31 in	0.01 in	7600 kg/m^3		$-476*10^{-12}$ m/V

Saturation Absorber

Internal Resonance (IR) has been the subject of extensive research. It began from adding physical supplementary system to the primary one. Haxton *et al.* [4] and Hatwal *et al.* [5] added a pendulum to the mass-spring-damper system, and concluded that the pendulum can work as a passive vibration absorber. Golnarghi [6] used the phenomenon as an active absorber by adding a slider, the motion of which makes nonlinear quadratic and cubic coupling with the primary system, to control the vibration of a cantilever beam. Tuer *et al.* [7] used a pendulum actuated by a dc motor to do the same task. This enables the designer to change the frequency and the damping of the absorber easily. It was found that the stronger the nonlinear coupling between the system the more energy can be transferred between them.

In Refs. 8 and 9, the supplementary, physical system was replaced by computer software to generate the oscillator and the nonlinear coupling. Oueini *et al.* [10] replaced the software by a solid state electronic circuit to emulate a second-order oscillator and the non-linear coupling needed for the IR. The plant used was a dc motor undergoing free vibration. A parametric study was performed, and two energy dissipation methods (DEM) were studied to prevent energy from returning to the plant from the absorber. This was accomplished by changing the time at which the damping was added to the absorber.

Control of forced vibration using IR on a dc motor and using an electronic oscillator was investigated by Oueini and Nayfeh [11]. The method was extended to multi-degree-of-freedom-systems, and demonstrated for the forced vibration of a cantilever beam [1,2]. The vibration modes of this system could be easily uncoupled, and it was shown that each mode could be controlled as a single-degree-of-freedom system. The absorber parameters for both applications were determined by trial and error. Pai *et al.* [12] also implemented saturation control using a digital computer and applied it to a cantilever beam.

Since analytical solutions using perturbation methods for single-degree-of-freedom systems were performed in Ref. 11 and for uncoupled multi-degree-of-freedom systems in Refs. 1, 2 and 12, there appears to be little need to develop an analytical solution herein. Thus, the focus from this point on will be on the study of the absorber parameters, and the comparison of saturation control with the other control methods.

A numerical simulation was performed by MATLAB using Simulink. The first mode is excited by applying harmonic force with a frequency equal to the first mode natural frequency. The absorber is modeled as a quadratic differential equation.

$$\ddot{u}_i + 2\xi_{ci}\lambda_i\dot{u}_i + \lambda_i^2 u_i = \alpha_i u_i W(x_s) \qquad i = 1,2....m \tag{8}$$

where m is the number of the controlled modes. ζ_{ci} and λ_i are the damping and frequency of the absorber, respectively. $W(x_s)$ is the beam modal displacement measured at location x_s. The control voltage sent to the piezoelectric material is

$$V_a = \sum_{i=1}^{m} \gamma_i u_i^2 \tag{9}$$

Only the first mode will be excited and controlled in this investigation, so let m =1. The equations of the first mode and its corresponding absorber can be written as

$$\text{Plant: } \ddot{\eta} + 2\xi\omega_n\dot{\eta} + \omega_n^2\eta = f\cos(\Omega t) + \gamma u^2 \tag{10}$$

$$\text{Absorber: } \ddot{u} + 2\xi_c\lambda_c u + \lambda_c^2 u = \alpha\eta W(x_s) \tag{11}$$

The performance of the absorber depends on the values of α and γ, and also the initial conditions of the absorber and the plant. It has been shown that the quadratic coupling creates a mechanism by which each absorber influences only the mode with which is internally resonant [1,2]. The magnitude of the steady-state response of the coupled plant and absorber can be obtained from Ref. 2.

$$\text{Beam steady-state magnitude: } A_b \approx \frac{1}{\alpha}\left[\xi_c^2 + \frac{1}{4}(\sigma+\tau)^2\right]^{\frac{1}{2}} \tag{12}$$

$$\text{Absorber steady-state magnitude: } A_c \approx \frac{1}{\alpha\gamma}\left[\Lambda \pm \left((\alpha f)^2 - \Gamma^2\right)^{\frac{1}{2}}\right]^{\frac{1}{2}} \tag{13}$$

where

$$\Lambda \approx \frac{1}{2}\tau(\sigma+\tau) - \xi\xi_c,\ \Gamma \approx \frac{1}{2}\mu(\sigma+\tau) + \xi_c\tau,\ \sigma \approx (\omega_n - 2\lambda_c),\ \tau \approx \Omega - \omega_n \tag{14}$$

and σ is a detuning parameter which measures the nearness of the absorber natural frequency to twice the natural frequency of the plant. τ is another detuning parameter, which measures the nearness of the frequency of the excitation force to the resonant frequency. It is evident that magnitude of the system response at steady-state does not depend on the magnitude of the exciting force. This magnitude can be small, if the damping of the absorber and the detuning parameters equal zero (i.e., the system is at resonance and the condition of internal resonance is satisfied).

The following sections expand on the discussion in Ref. 1 of the effect of the saturation control parameters on the transition response of the plant. Let $\bar{\alpha}$, $\bar{\gamma}$ and $\bar{f}$ be the nominal values for α, γ and f, respectively. For this discussion, the damping of the absorber is set to zero, and the absorber is activated 10 seconds after the excitation is first applied.

Effect of changing α

In Fig. 2, the response of the beam looks somewhat like a decaying response with a beat. The responses using smaller and larger values of α are shown in Figs. 3 and 4, respectively. It can be seen that decreasing α from its nominal value reduces the number and frequency of the beats, but

increases the lag between the time when the absorber is turned on and the initial change in the system response. Increasing α decreases the lag, but increases the number, frequency and the amplitude of the beats. The steady-state response and the corresponding control action are the same for all values of α.

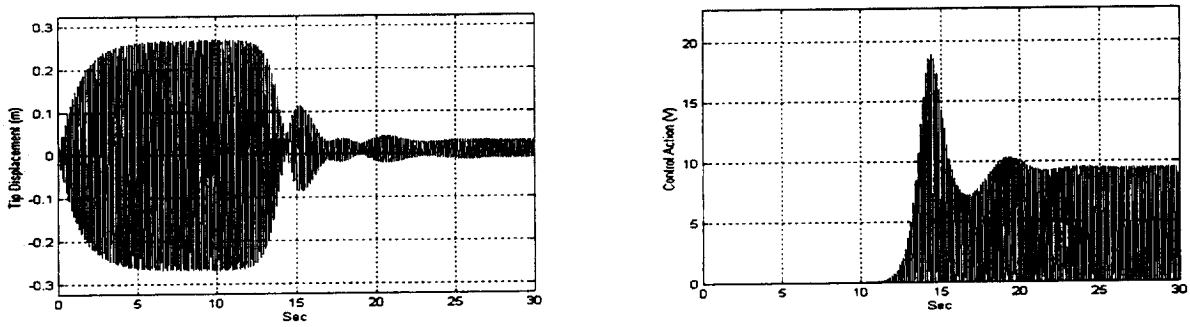

Figure 2. $\alpha = \bar{\alpha}$, $\gamma = \bar{\gamma}$, $u(0) = 1$, $f = \bar{f}$

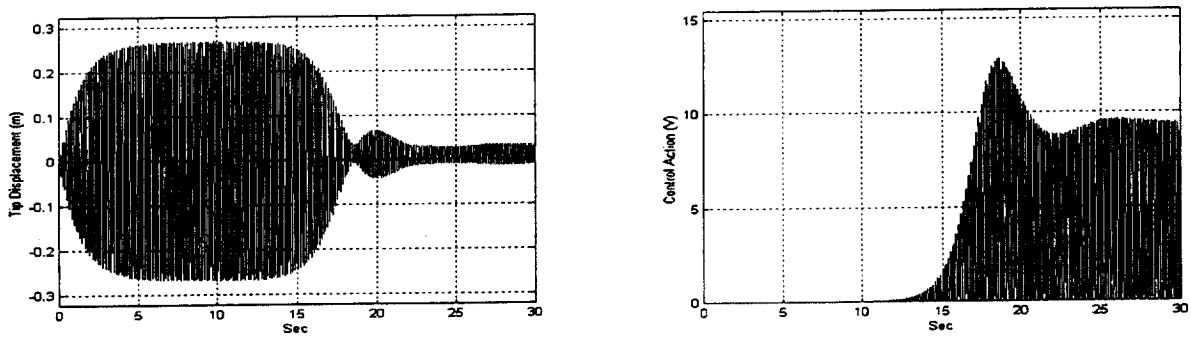

Figure 3. $\alpha = \bar{\alpha}/2$, $\gamma = \bar{\gamma}$, $u(0) = 1$, $f = \bar{f}$

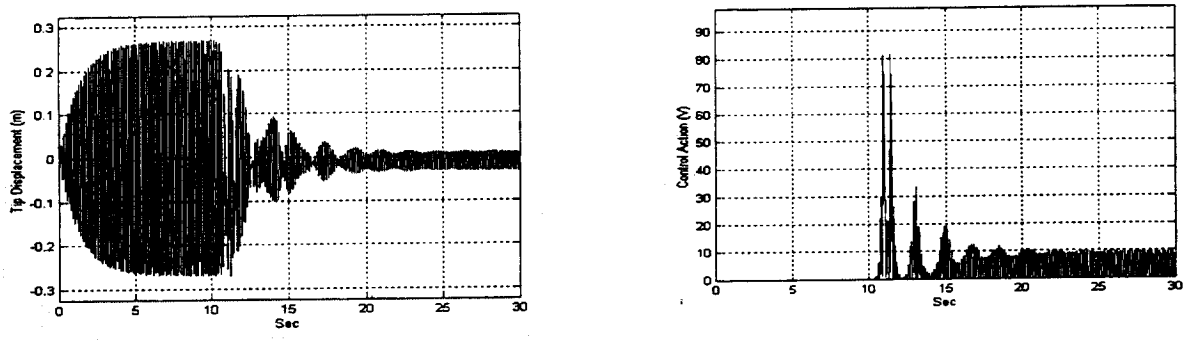

Figure 4. $\alpha = 5\bar{\alpha}$, $\gamma = \bar{\gamma}$, $u(0) = 1$, $f = \bar{f}$

Effect of changing γ

The effect of modifying γ is shown in Figs. 5-7. Changes in the value of γ has little effect on the magnitude and frequency of the beat-like responses. However, the lag between the absorber activation and its effect on the plant response is seen to decrease. In addition, the time required to reach a steady-state response decreases slightly, due to the decrease in the response lag. The γ

is too large, the initial response of the beam will increase slightly (Fig. 7). Again, the steady-state response of the beam is the same, as is the control action.

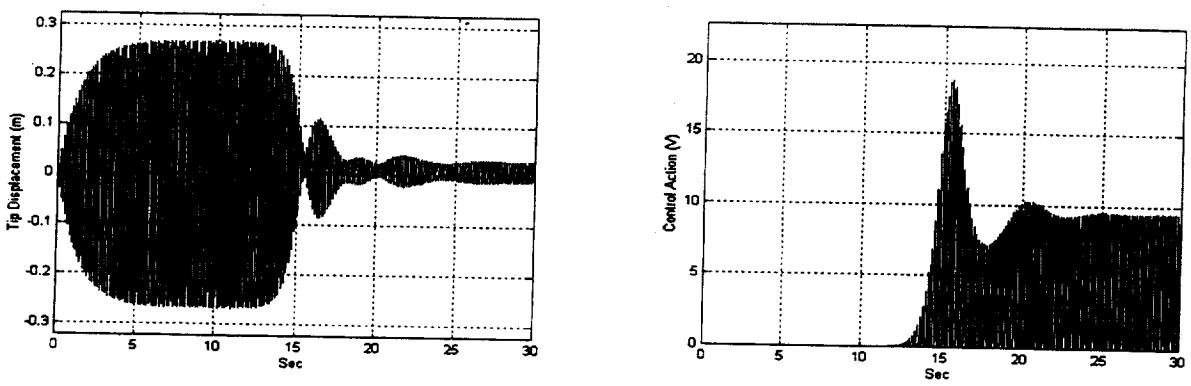

Figure 5. $\alpha = \bar{\alpha},\ \gamma = \bar{\gamma}/10,\ \ u(0) = 1,\ \ f = \bar{f}$

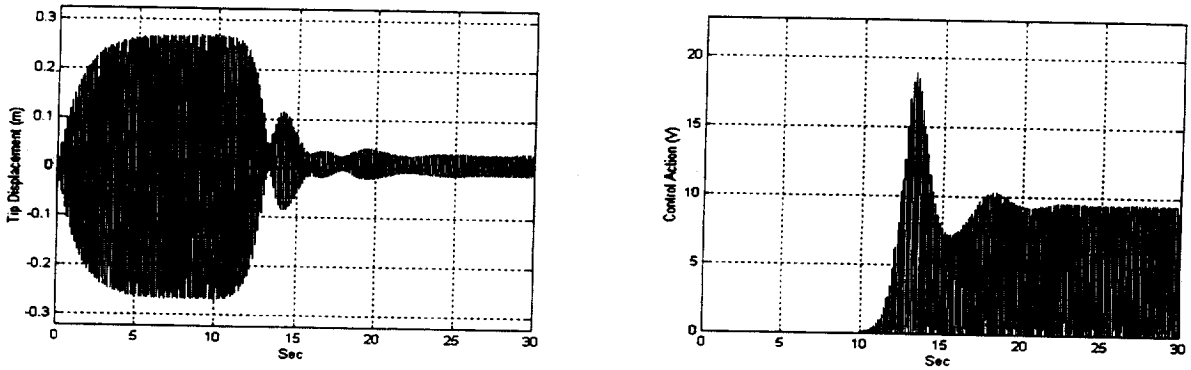

Figure 6. $\alpha = \bar{\alpha},\ \gamma = 10\bar{\gamma},\ \ u(0) = 1,\ \ f = \bar{f}$

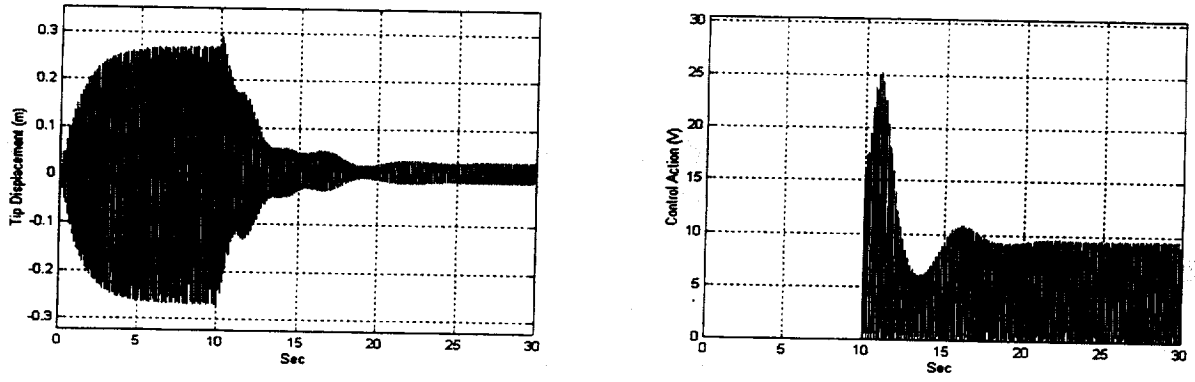

Figure 7. $\alpha = \bar{\alpha},\ \gamma = 10^3\bar{\gamma},\ \ u(0) = 1,\ \ f = \bar{f}$

Effect of changing the initial condition of the absorber.

Simulations showed that saturation control can work with any initial value greater than zero. As the initial value increases, the response to the absorber being turned on will be more rapid (Fig. 8). However, if the initial value is too large, the beam response will increase initially when the absorber is turned on.

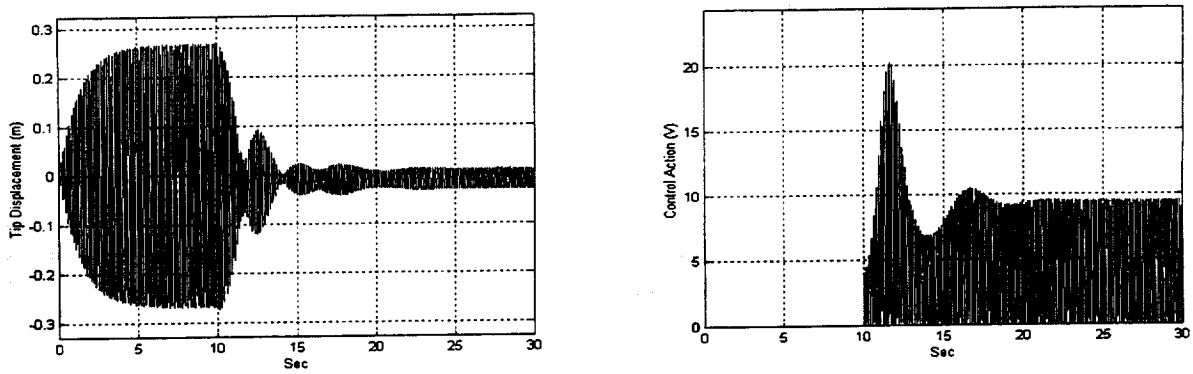

Figure 8. $\alpha = \bar{\alpha}$, $\gamma = 10\bar{\gamma}$, $u(0) = 5$, $f = \bar{f}$

Effect of changing the magnitude of the forcing function.

The simulations showed that as the forcing function increases, the system responds in a manner similar to the case of increasing α. If both f and α are very large, the system could become unstable. Therefore, to assure that the system is stable for large values of f, α should be decreased. Physically, the increase in α causes an increase in the magnitude of the absorber forcing function. When f is large, the response of the beam will be large, which also results in an increase in the magnitude of the absorber forcing function.

PD Controller

The PD controller is a member of the family of classical PID controllers, which are widely used in industrial control processes because of its simple structure and robust performance in a wide range of operating conditions. The PD and the optimal feedback controller are also used in active vibration control [13,14].

The classical PD controller used herein has the form

$$v = K_p W(x_s) + K_d \dot{W}(x_s) \tag{15}$$

If the system is represented as a single degree of freedom, the magnitude of the steady-state response of the system can be determined from

$$A_b(\Omega) = \frac{A f}{\sqrt{(\omega_c^{\,2} + K_p - \Omega^2) + (2\xi\omega_c + K_d)^2}} \tag{16}$$

where A is a constant. It is clear from Eq. (16) that increasing the PD gains (K_p, K_d) decreases the magnitude of the steady-state system response, which is independent from the forcing frequency. There are many methods that can be used to determine the optimal gains, but obtaining optimal gains is not the objective of this investigation. It is the effect of the gains on the beam response for this type of controller that is being determined.

The simulations using different values of the derivative and proportional gains are shown in Figs. 9-11. Note that as the proportional gain increases, the steady-state response as well as the initial control action increases. The same observation is valid for the derivative gain. Thus, the steady-state response cannot be decreased without increasing the initial control action. In a practical

application, a low-pass filter is needed which may distort the phase of the signal and lead to bad output from the controller (which depends on the phase). Using different gains in each stage of a multistage controller can solve this problem, but the controller will be nonlinear.

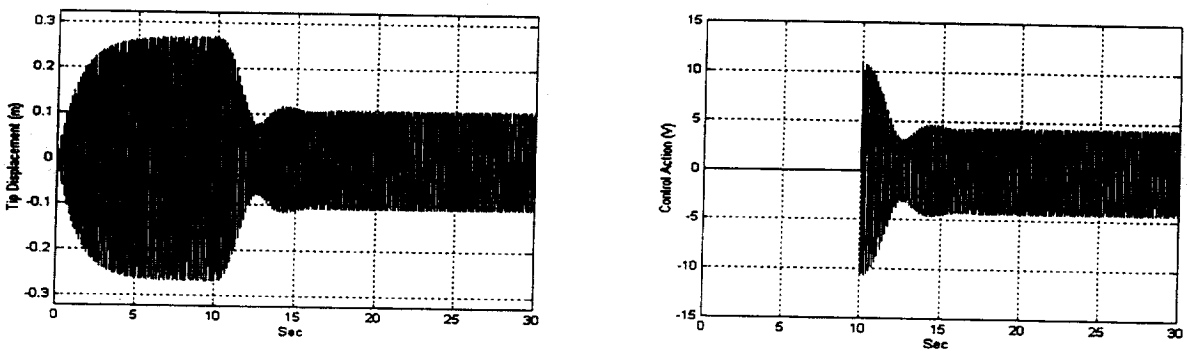

Figure 9. $K_p = 40$, $K_d = 0$

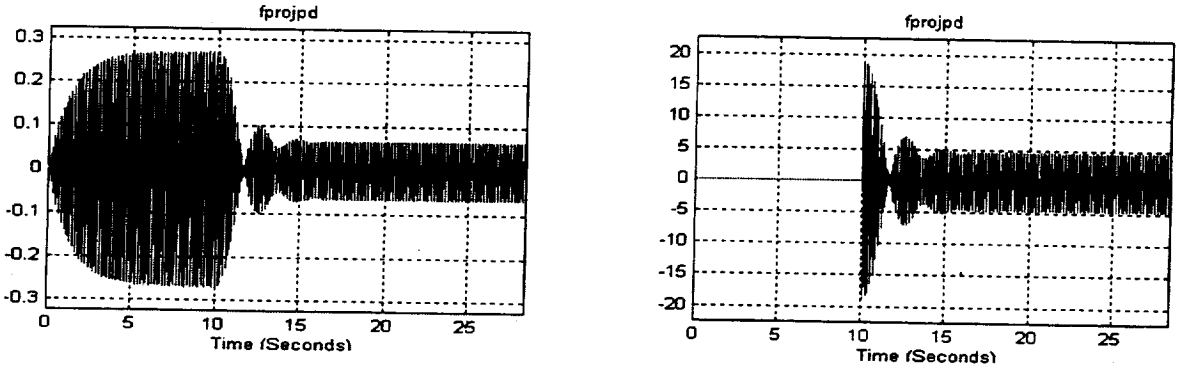

Figure 10. $K_p = 70$, $K_d = 0$

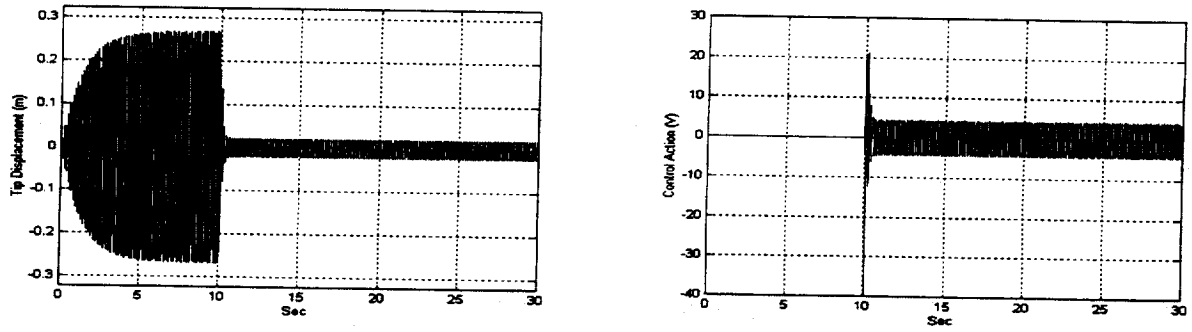

Figure 11. $K_p = 40$, $K_d = 5$

Fuzzy Logic Controller (FLC)

The FLC is based on the work of Zadah [15]. Fuzzy logic is a generalization of Boolean logic. The state of a variable is not one or zero but rather a degree of membership. This gives fuzzy logic the ability to deal with imprecise information, which is found in most processes. FLC is a set of linguistic rules which governs the relationship between the system response and the

controller output. Research in FLC by Mamdani [16] and his students started by applying FLC to a steam engine. Many research applications were tried on different processes. This research concluded that fuzzy control can work well for ill-defined systems in which a deterministic mathematical model can not be obtained. It also has good performance and is more robust if it is designed well [17].

The first application of FLC on structural vibrations was done by Tsouks and Vanladingham. They proposed a controller with 49 rules. These rules can be considered as a PD controller in a fuzzy shape. Kwak *et al.* [18] reduced these rules to only four. That research considered only free vibration. Forced vibration control using FLC is discussed in Ref. 19. The vibration was first suppressed using optimal control, by minimizing the displacement using a linear programming technique. The algorithm was then converted to fuzzy rules to form the FLC.

There is currently no theory for determining the stability of a FLC, and the rules are determined from the engineering judgment or the experience of the designer. The phase plane and the idea of the switching surface with a boundary layer [18] can be used to derive the fuzzy rules. The switching surface is defined as

$$s = \beta W(x_s) + \dot{W}(x_s) \tag{17}$$

Due to the switching delay and chattering problem along the switching surface, a boundary layer is added to smooth the control discontinuity. Those rules can be written as

If abs(d_i) is ZO then $\overline{u}_i$ is ZO

If abs(d_i) is PS then $\overline{u}_i$ is PS

If abs(d_i) is PM then $\overline{u}_i$ is PM

If abs(d_i) is PB then $\overline{u}_i$ is PB

where d is the normal distance from the nominal point to the switching surface

$$d = s_i / \sqrt{1 + \beta^2} \tag{18}$$

ZO = Zero, PS = Positive Small, PM = Positive Medium, PB = Positive Big. The membership function of these terms are shown in Fig. 12.

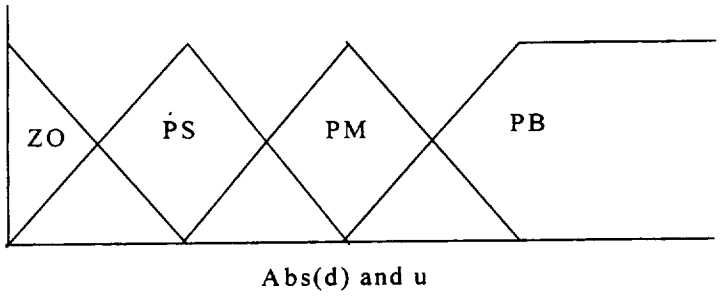

Figure 12. Fuzzy logic membership functions for d and u

The control action is given by

$$u_i = -\alpha \operatorname{sgn}(d_i)\, defuzz(\overline{u}_i) \tag{19}$$

Defuzz is known as the defuzzification process by which the fuzzy variable (control action) is converted to a crisp value suitable to be directed to the physical system.

The FLC can be considered to be a PD controller with variable gains, so it can overcome the disadvantage of the PD controller. The responses of the system with different parameters of the FLC are shown in Figs. 13-14. Note that the same steady-state response is obtained with smaller initial control action, as compared with the PD controller.

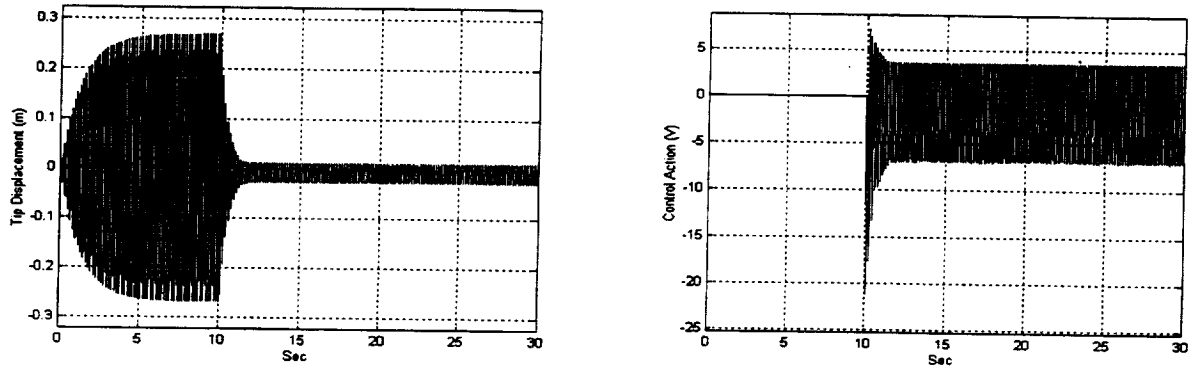

Figure 13. $G_s = 0.5,\ G_u = 30,\quad s = -0.2W + \dot{W}$

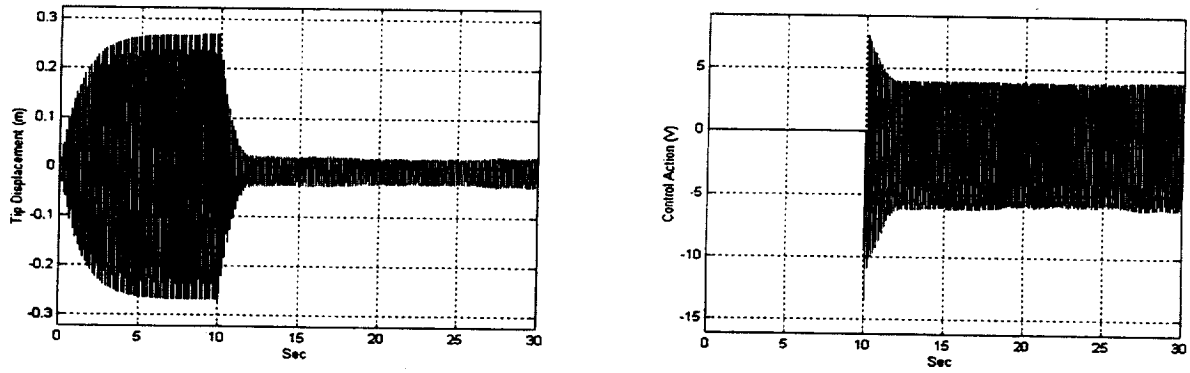

Figure 14. $G_s = 0.5,\ G_u = 30,\quad s = -0.1W + \dot{W}$

Conclusions and Recommendations

The saturation absorber possesses the characteristic that the controlled steady-state response is always small, whatever the values of its parameters. The parameters can, however, be used to shape the plant transition response between the time that the absorber is turned on and a steady-state response is reached. The following guidelines can be used:

- The smoothness of the transition response can be improved by decreasing α. However, decreasing α introduces a lag between the initiation of the absorber and the initial response of the plant.

- The lag between the initiation of the absorber and the initial response of the plant can be decreased by increasing γ. Within limits, the increase in γ has little effect on the smoothness of the transition response.
- Increases in the initial value of the absorber have a similar effect to increases in g. If either becomes too large, there will be an initial increase in the plant response before it starts to decrease.

A comparison of the three methods of control show the following:

- Saturation control achieves the smallest steady-state response with the least control output, but is limited by the frequency requirements placed on the plant, absorber, and forcing function. The PD and the fuzzy logic controllers have no such limitations.
- The large gains required by the PD controller in order to achieve a small steady-state response results in a requirement for large control outputs. In a design environment, this translates into the need for a larger power supply.
- Fuzzy logic controllers can overcome some of the problems of the PD controller, but selection of the gains and definition of rules are difficult.

It was observed that the PD controller with fixed gains requires large gains to get a small controlled steady-state response. Because of these gains, the initial control output is very large. The fuzzy logic controller avoids this problem by the proper choice of gains and rules. Applying this concept to saturation control, it might be possible to use fuzzy logic to control the saturation parameters and improve the transition response.

References

1. S.S. Oueini A.H. Nayfeh, and J.R. Pratt, "A Nonlinear Vibration Absorber for Flexible Structures", *Nonlinear Dynamics*, 1998, pp. 259-282.

2. S.S. Oueini and A.H. Nayfeh, "Multimode Control of Flexible Structures Using Saturation," AIAA Paper No. 97-1207, AIAA/ASME/ASC/AHS Structures, Structural Dynamics and Materials Conference, Kissimmee, Florida, 1997, pp. 597-602.

3. C.R. Fuller, S.J. Elliot and P.A. Nelson, Active Control of Vibration, Academic Press, 1997.

4. R.S. Haxton and A.D.S. Barr, "The Autoparametric Vibration Absorber," *Journal of Engineering for Industry*, 1997, pp. 119-125.

5. H. Hatwal, A.K. Mallik and A. Ghosh, "Non-Linear Vibrations of a Harmonically Excited Autoparametric System," *Journal of Sound and Vibration*, 1982, pp. 153-164.

6. M.F. Golnaraghi, "Regulation of a Flexible Structure Via Nonlinear Coupling", *Journal of Dynamics and Control*, 1991, pp. 405-428.

7. K.L. Tuer, M.F. Golnaraghi and D. Wang, "Development of a Generalized Active Vibration Supression Strategy for a Cantilever Beam Using Internal Resonance", *Nonlinear Dynamics*, 1994, pp. 131-151.

8. K.L. Tuer, A.P. Duquette and M.F. Golnaraghi, "Vibration Control of a Flexible Beam Using a Rotational Internal Resonance Controller, Part I: Theoretical Development and Analysis" *Journal of Sound and Vibration*, 1993, pp. 41-62.

9. S.S. Oueini, K.L. Tuer and M.F. Golnaraghi, "Design of Two Degrees of Freedom Using Internal Resonance," *ASME Journal of Dynamic Systems, Measurement and Control*, 1995, pp. 247-252.

10. S.S. Oueini and M.F. Golnaraghi, "Experimental Implementation of the Internal Resonance Control Strategy," *Journal of Sound and Vibration*, 1996, pp. 377-396.

11. S.S. Oueini and A.H. Nayfeh, "Saturation Control of a DC Motor," AIAA Paper No. 96-1642, AIAA/ASME/ASC/AHS Structures, Structural Dynamics and Materials Conference, Salt Lake City, Utah, 1996, pp. 1151-1157.

12. P.F. Pai, B. Wen, M.J. Schulz, "Structural Vibration Control Using PZT Patches and Non-Linear Phenomena," *Journal of Sound and Vibration*, 1996, pp. 377-396.

13. H. Oz and G. Yen, "Direct Optimal Vibration Control," Proceedings of the American Control Conference, Albuquerque, New Mexico, 1997, pp.1789-1793.

14. S. Hanagud, M.W. Obal and A.J Calise, "Optimal Vibration Control by Use of Piezoceramic Sensors and Actuators," *Journal of Guidance, Control and Dynamics*, 1992, pp.291-298.

15. L.A. Zadeh, "Fuzzy Sets", *Information and Control*, 1965, pp.28-44.

16 E.H. Mamdani, "Twenty Years of Fuzzy Control: Experiences Gained and Lessons Learned," IEEE Proceedings, 1993, pp. 339-344.

17. M. Jamshidi and T.J. Ross, Fuzzy Logic and Control, Software and Hardware Applications, Prentice-Hall, Inc., 1993.

18. M.K. Kwak and D. Sciulli, "Fuzzy-Logic Based Vibration Suppression Control Experiments on Active Experiments on Active Structures," *Journal of Sound and Vibration*, 1996, pp. 15-28.

19. M.G. Shalin and S.A. Timashev "Forced Beam Vibration Control," Proceedings of the European Conference on Structural Control, Barcelona, Spain, 1996, pp. 543-550.

Creation of a finite element model for F/A – 18 structural dynamic analyses based on ground vibration test data.

S.A. Dunn
Senior Research Scientist, Airframes & Engines Division
Aeronautical & Maritime Research Laboratory
Defence Science & Technology Organisation
PO Box 4331, Melbourne, Victoria, Australia
Shane.Dunn@dsto.defence.gov.au

Abstract

In this paper, a technique for creating structural dynamic models directly from experimental data is proposed. The method is based on having a finite element model with prescribed geometry for nodes and beams and using the artificial intelligence optimisation tool of genetic algorithms. The aim is then to create an optimal model by selecting mass and stiffness properties such that the resulting model gives the best approximation to the real data. Such a process has been the subject of a number of earlier papers by the author and in this paper, results are presented for the creation of a complete aircraft model with symmetric boundary conditions based on actual ground vibration test data.

Introduction

Mathematical modelling of complex systems inevitably requires assumptions and idealisations (eg. a representation of the structural dynamic model of an F/A-18 is shown in Figure 1.

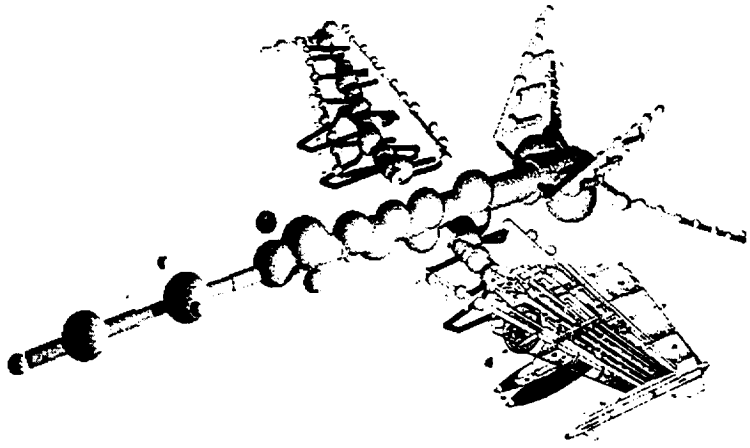

Figure 1. Finite element model for structural dynamic analysis of an F/A –18; such a model is a considerable idealisation of the actual structure that is shown on the port wing.

As the system becomes more complex, these assumptions typically lead to a model with poor predictive capabilities: this is the case with finite element modelling of

aircraft structures for dynamic analyses. Such a finite element model is developed when the aircraft is in the design stage; when built, the aircraft is then subjected to a ground vibration test (GVT) and the finite element model is typically a poor predictor of the true result.

The question that must then be addressed is: How should the model then be developed to better reflect the true behaviour of the structure? A process that has been proposed by this author in previous publications, and is further developed in this paper, involves throwing away the initial model and developing a new model based on the GVT data. The basis of this procedure involves using the artificial intelligence optimisation tool of genetic algorithms to create an optimal finite element model (FEM), where optimal is defined as the model that gives the best correlation with the experimentally determined transfer function. Previous work has demonstrated how such processes can be used on the relatively simple models representing an aircraft tailplane and a truss structure based on true experimental data (Dunn, 1996). These two models were similar in that they involved relatively few unknowns. The complexity of such optimisations, however, grows rapidly with the number of unknowns. For traditional optimisation techniques, this growth in complexity typically involves an exponential growth in processing time as the number of unknown parameters grows. Such a process has been demonstrated for a full aircraft structure using simulated experimental data for a General Dynamics F-111C (Dunn, 1998a).

In this paper, the technique of using genetic algorithms to create an optimal structural dynamic model for a CF – 18 will be demonstrated. The ground vibration test data used were collected by Bombardier inc. (Canadair) for the Canadian Forces and have been forwarded to the Australian Department of Defence for the purpose of creating an optimal finite element model. Details of how such a technique can lead to a unique, or minimum order, model will be discussed.

Genetic Algorithms

Some introductory reading focussing on the philosophy of genetic algorithms (GAs) can be found in Holland (1992) and Forrest (1993). A good introduction to the technical aspects of GAs can be found in Goldberg (1989).

The idea for genetic algorithms came about from a realisation that, according to the concepts of evolution by natural selection, nature finds relatively optimal solutions in a naive way to the problem of how to exist on earth. That is, natural evolution does not occur by looking ahead and attempting to determine which features will improve the fitness of a species, but rather tries out different features and those which prove beneficial are preferentially selected. This preferential selection, through an increased likelihood of mating, leads to a higher probability that a fit individual's genes will be spread throughout the species over subsequent generations. The observation that the forces of nature are really the impetus behind a massive highly non-linear optimisation routine led workers to consider whether mimicking natural evolution on computers could be used to solve the relatively much more simple problems which arise in human endeavours; this led to the creation of genetic algorithms.

Genetic algorithms are based on starting with a randomly generated population of individual possible solutions scattered over a pre-determined search space (the region in which the answer is thought to lie). Each population member will be composed of n parameters, each of which is to be optimised, forming an n-dimensional search space. The relative fitness of each population member is determined and a stochastic selection process biased towards the fitter individuals is used to select parents for mating. In mating, attributes of the parents are mixed to form offspring which may, or may not, be fitter than one or both of the parents. In forming offspring, occasional random mutations can occur which also have the possibility of leading to a fitter individual. The process of selection, mating and mutation is repeated over a number of generations to allow the solution to evolve towards the optimum.

Experimental Data

The gathering of the experimental data was described in a *pers.comm.* by M. Dickinson of Canadair Inc. A ground vibration test was performed on a CF-18 with wing tip stores and two different 2000lb class stores under each wing by Canadair Inc. for the Canadian Forces at the Aerospace Test Engineering Establishment (AETE), Cold Lake, Alberta. The aircraft was sitting on its undercarriage with reduced tyre pressures. For wing and store excitation, two shakers were used as symmetric or anti-symmetric pairs and for fuselage excitation, a single shaker was used; in all, 16 shaker configurations were used. The aircraft was instrumented with 85 accelerometers. For the analysis used here, three of the shaker configurations and data from 57 accelerometers were used. The shaker and accelerometer locations are shown in Fig. 2. All of the recorded data were not used in order to keep processing times tractable. Also, only the data from the shakers being used to excite symmetric modes have been analysed here, so the resulting model has symmetric boundary conditions.

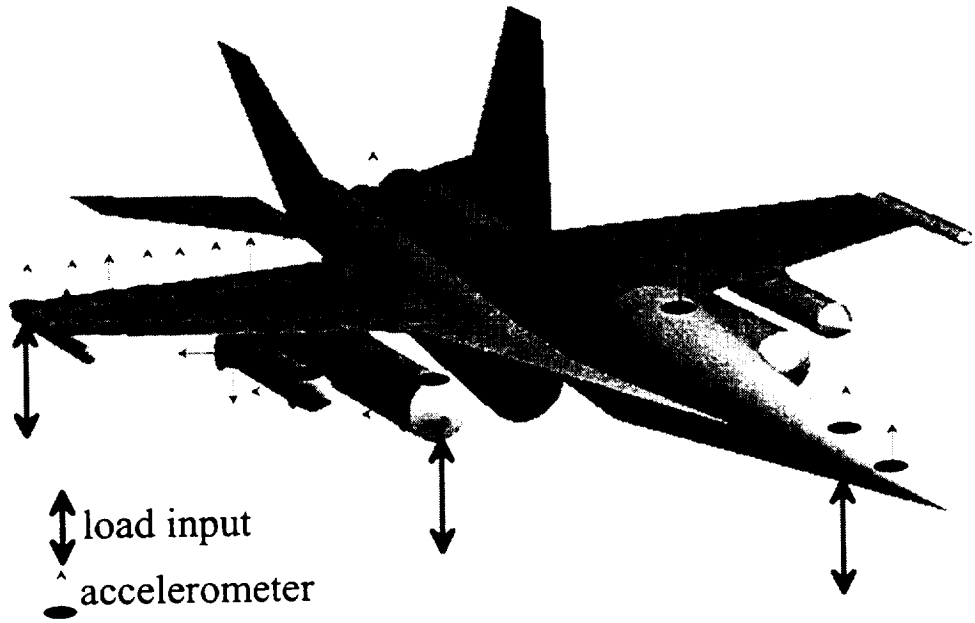

Fig. 2 showing load inputs and accelerometers for data used in analysis (note: loads and accelerometers were placed symmetrically, though only those on one side of the aircraft are shown).

For each of the three load inputs used, the transfer functions of the accelerometers shown were processed (eg. averaging port+starboard+fore+aft for wing heave and similarly for the wing pitch, but with differencing the fore and aft accelerations and allowing for the distance between the accelerometers). Examples of the resulting transfer functions are shown in Fig. 3.

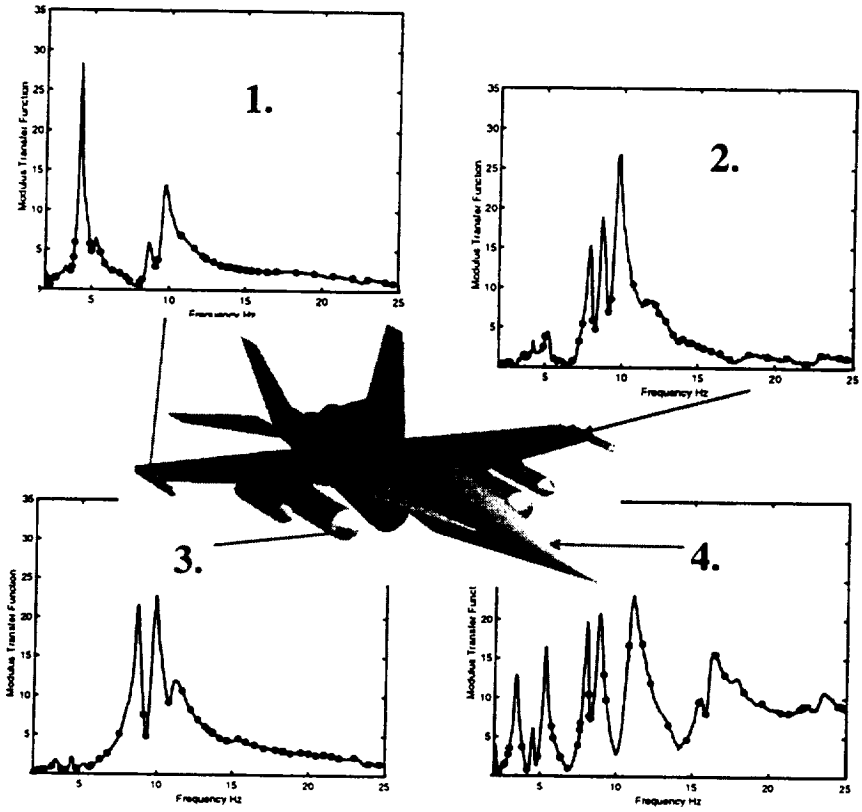

Fig. 3. Examples of transfer functions used. The circles indicate points to be used in determining the cost function in the model optimisation process.

The transfer functions shown in Fig. 3. are: 1. wing tip heave due to wing load; 2. wing tip torsion due to wing load; 3. inboard store pitch due to store load, and; 4. fuselage nose heave due to fuselage load. These are just a very few examples; results from all accelerometers were used in the optimisation process for each of the three load cases.

Model Optimisation Process

The fundamental approach used here to create optimised mathematical models for the structural dynamics of aircraft structures is to determine an optimal set of finite element properties which will give a minimum error between measured frequency response functions, and those predicted by the model as described in eqn. 1.

$$\min(\varepsilon(\mu,\kappa)) = \sum_{j=1}^{N}\sum_{i=1}^{n}\left\| y_{i,j}(\mu,\kappa)\right| - \left|y'_{i,j}\right\| \qquad (1)$$

where the cost function ε, the error between model prediction and measurement, is defined as a function of the mass and stiffness properties, μ and κ respectively. ε is determined for the model frequency response function, $y_{i,j}(\mu,\kappa)$, at the ith frequency and jth freedom, and the corresponding experimental measurements, $y'_{i,j}$. This concept is illustrated for a simulated jth freedom in Fig. 4.

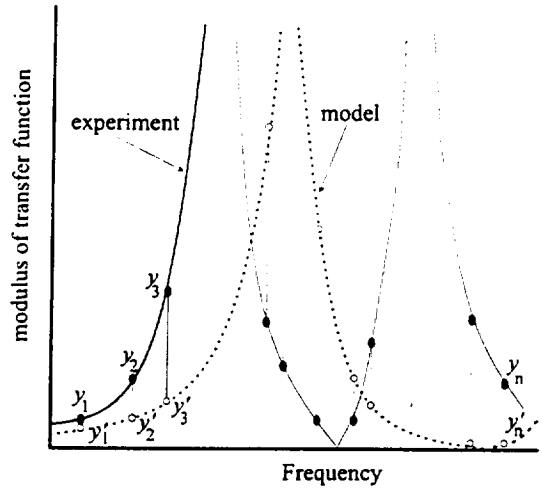

Fig. 4. Schematic depicting the use of a frequency response function in the evaluation of ε as used in Equation (1).

In carrying out this optimisation, all of the mass and stiffness properties required for the description of the model are considered to be unknown. The number of properties to be estimated is typically large and many will have a high degree of interaction; in other words, such a process is typically a high–order, highly non–linear optimisation problem. Genetic algorithms can be very useful in solving such problems, and for the specific case of structural dynamic model estimation, have been shown to be far more efficient than more traditional optimisation processes (Dunn, 1998b).

The FEM is prescribed in its geometry (ie. the nodes are fixed in space), but the physical properties required to describe the mass and stiffness properties are allowed to fall anywhere within a large search space. Stiffness properties may be allowed to range over a number of orders of magnitude, (eg. beam bending stiffnesses may vary from 10^6 to 10^{10}Nm^2). Masses can require up to seven properties to be fully defined: offset from the node in each of the axis directions, mass, rotational inertias about each of the thee axis directions.

Towards a Minimum Order Model.

In determining the nature of the FEM to be developed for aircraft structural dynamic analyses, it is typical that an overly complex model is developed (complexity here can be defined as the number of properties required to describe the model). In such cases, the following procedure can be carried out:

- Run the optimisation procedure – in this case a GA – a number of times such that there are a number of results where the better cost functions (eqn. 1) are very similar and the model predictions give a satisfactory representation of the experimental data;

- compare the properties found for these results;
- where this comparison shows little variation, assume the property is being determined uniquely;
- where the comparison shows a great deal of variation for a similar cost function, assume that either the property is not required, or that the property and one or more of its neighbours can be combined into one;
- repeat this process until all parameters appear to be defined uniquely and the model still gives a satisfactory representation of the data.

Described above is the process to be followed in the typical case where the original model is too complex, the opposite process where the model is insufficiently complex is discussed and demonstrated in Dunn (1998c).

Results

As discussed previously, the genetic algorithm is run a number of times and the results examined for uniqueness; this process is best illustrated by examining the results for the wing bending and torsion stiffness as the optimisation proceeds.

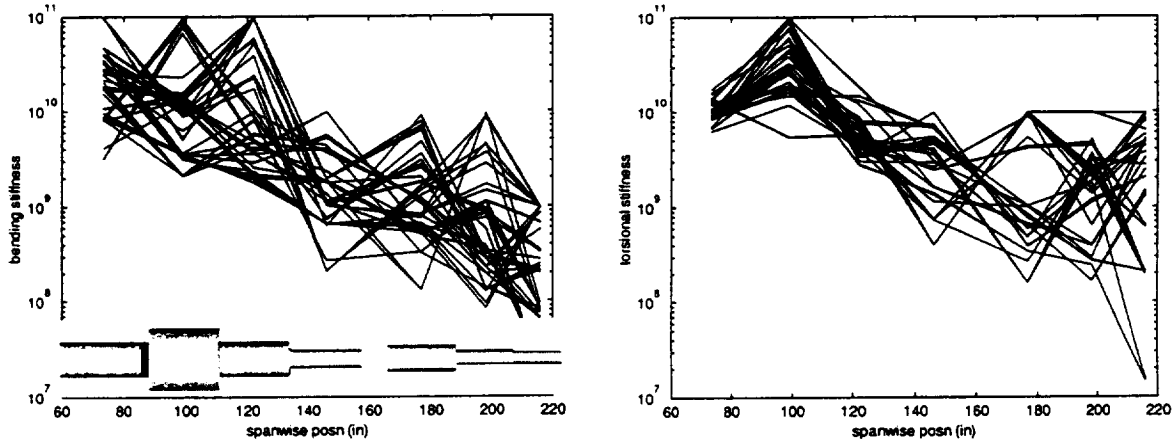

Fig. 5. Optimisation results for wing with 7 bending and 7 torsion stiffness elements – the gap at ~160in. represents the wingfold which is modelled with springs. (The shaded figure represents the vertical wing bending stiffness elements for the result with the best cost function).

In Fig. 5, each line represents the bending stiffness and torsional stiffness distribution found for a separate completed genetic algorithm run, each of which had very similar final cost functions (as defined in eqn. 1). The results are clearly non-unique in that they exhibit a large degree of scatter whilst having very similar correlation with the experimental data, as defined by the cost function in eqn(1) . The solution to this is to reduce the complexity of the model until a more unique solution is found. The next step in this process is demonstrated in Fig. 6 (it should be noted that only the results for the wing stiffness properties are shown, the actual reduction in model complexity also affects wing inertial properties and fuselage properties).

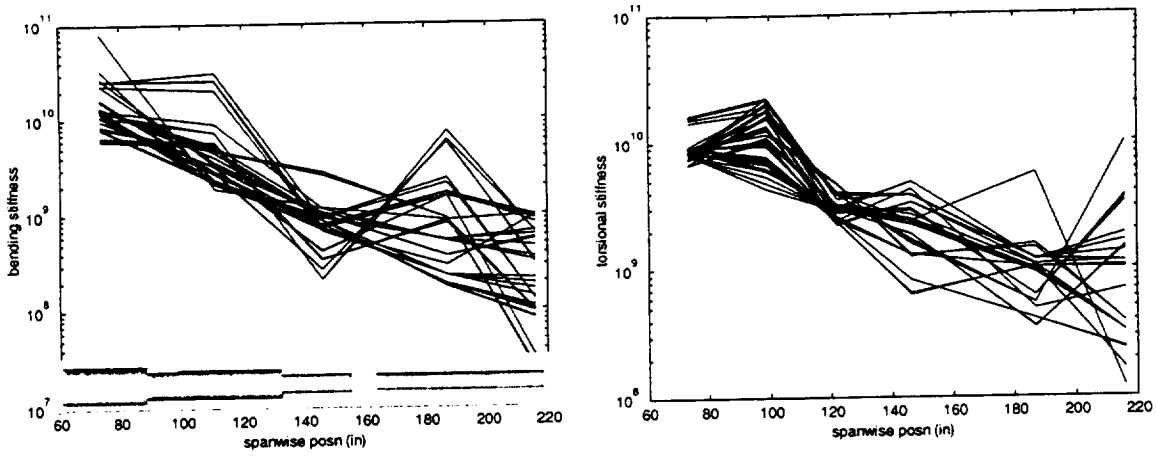

Fig. 6. Optimisation results for wing with 5 bending and 6 torsion stiffness elements.

The results in Fig. 6 still show a degree of non-uniqueness. Following the same procedures, the results shown in Fig. 7 were finally settled upon.

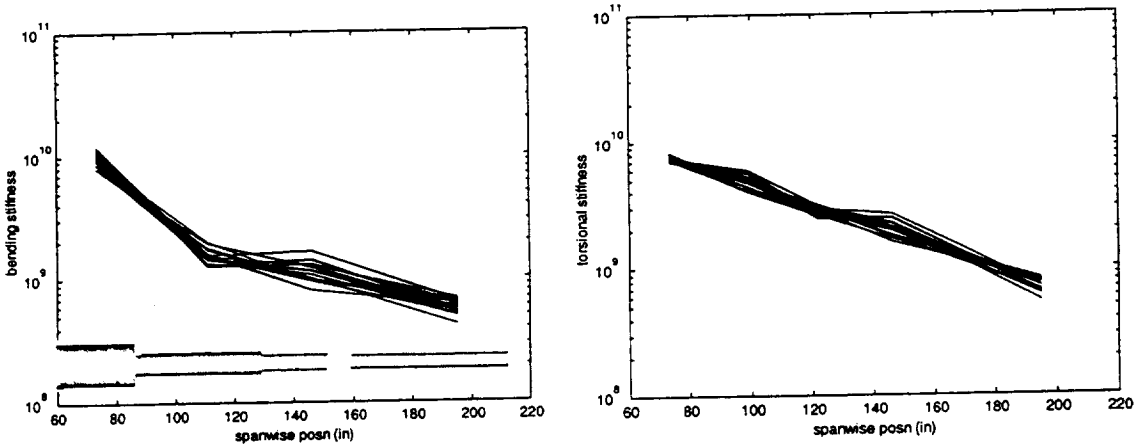

Fig. 7. Optimisation results for wing with 4 bending and 5 torsion stiffness elements.

The final form of the complete model is shown in Fig. 8.

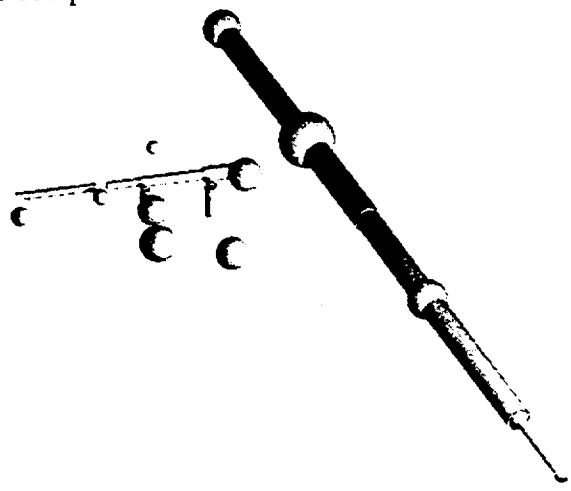

Fig. 8. Form of the final CF-18 symmetric finite element model.

Some examples of the correlation between the experimental and model results are presented in the forcing point transfer functions in Figs 9,10,11 & 12 (in all of theses figures, the dashed line represents the model results and the circles are the points used in the cost function evaluation).

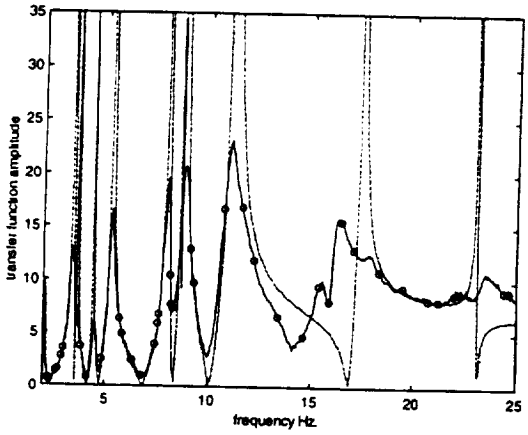

Fig. 9. Fuselage nose response due to fuselage load.

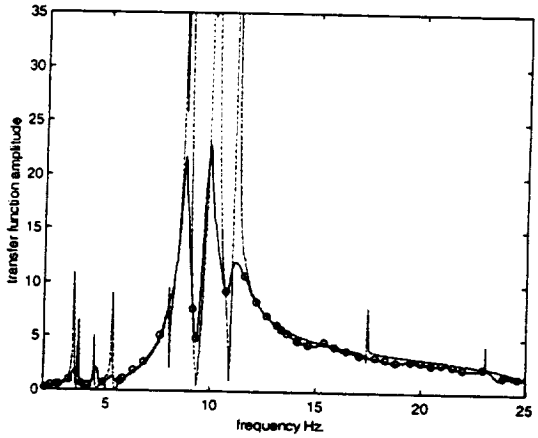

Fig. 10. Inboard store pitch response due to i/b store load

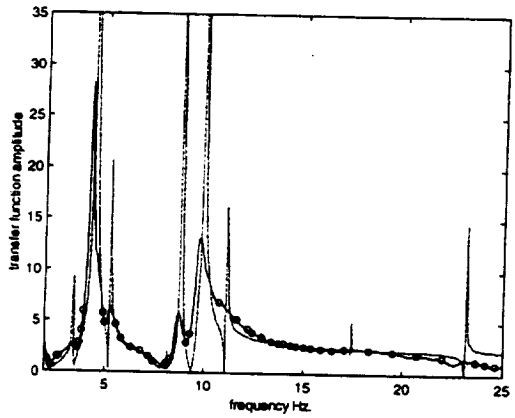

Fig. 11. Wing tip heave due to wing tip load.

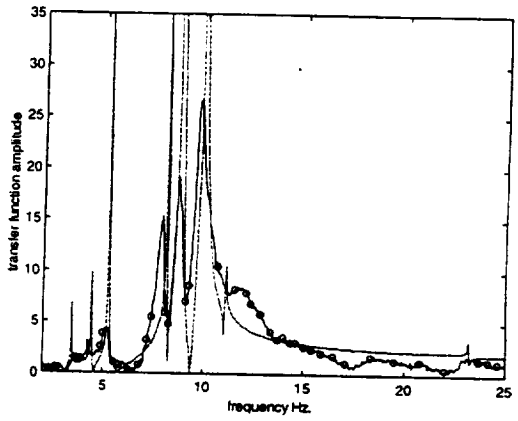

Fig. 12. Wing tip pitch due to wing tip load.

Discussion

The results shown in Figs. 9 – 12 for the model depicted in Fig. 8 show very good agreement between experimental and model responses. There are some features in the region >15Hz that are not very well represented, but it is hoped that further work of the type discussed below will help to address such issues. Irrespective of the region that is not modelled as well as the rest of the frequency range, the agreement is much better than would be expected from the more typical highly complex models.

A feature which is immediately evident in Figs. 9 – 12 is that the peak response in the model predictions is always much greater than that found for the actual structure. The reason for this is simply the existence of damping in the actual structure which is not

present at all in the mathematical model. The reason damping has not been included is because these sorts of finite element models typically do not include damping. The main reason for this is that quantifying the damping for the numerous damping elements that would be required would be a very difficult process. The methods outlined here, however, would allow such damping elements to be quantified and this will be the subject of further work.

Another area of further work involves increasing the generality of the model by moving away from the requirement that the geometry of the model be prescribed beforehand. For example, it would be desirable to allow the location of the wing torque-box elements to also be subject to the optimisation procedure. The modification to allow this is simply one of further increasing complexity in the optimisation procedure (though not the resulting model) and presents no conceptual difficulties.

Conclusion

In this paper, it has been demonstrated how the optimisation tool of genetic algorithms can be used to create an optimal structural dynamic finite element model for a complete aircraft structure. This has been demonstrated for a symmetric model of a CF-18 using actual ground vibration test data. A significant component of deriving such a model involves defining the model complexity such that the most simple, and unique, model is defined; the process behind this has been presented and an example of how this was done for wing stiffness properties has been shown. How this work can be further developed has also been briefly discussed.

Acknowledgments

The author would like to gratefully acknowledge the assistance of Canadair Inc. and the Head of Flight Services Branch, Canadian Forces for supplying the CF-18 ground vibration test data for the purposes of this research.

References

Dunn, S.A., 'The Use of Genetic Algorithms in Dynamic Finite Element Model Identification for Aerospace Structures', *20th Congress of the International Council of the Aeronautical Sciences,* Sorrento, Napoli, Italy, pp. 398-406, 8-13 September, 1996.

Dunn, S.A., 'Optimisation of the Structural Dynamic Finite Element Model of a Complete Aircraft', *21st Congress of the International Council of the Aeronautical Sciences,* Melbourne, Australia, 13-18 September, ICAS 98,9,4-3, 1998a.

Dunn, S.A. 'Optimal Genetic Algorithm properties for Dynamic Finite Element Model Optimisation', Submitted to *Computers & Structures,* 1998b.

Dunn, S.A. 'A Technique for Unique Optimisation of Dynamic Finite Element Models', Submitted to *Journal of Aircraft,* 1998c

Forrest, S. 'Genetic Algorithms: Principles of Natural Selection Applied to Computation', *Science*, pp. 872-878, **261**, 13th August, 1993.

Goldberg, D.E., 'Genetic Algorithms in Search Optimisation & Machine Learning', Addison Wesley Publishing Co. Inc. Reading, Massachusetts, USA, 1989.

Holland, J.H., 'Genetic Algorithms', *Scientific American*, pp. 44-50, July, 1992.

EFFECTS OF TRANSIENT HYPERSONIC FLOW CONDITIONS ON FAILURE PREDICTION OF PANELS

Radu UDRESCU*
COMOTI-National Institute
for R&D of Turbomachinery
Bd.Iuliu Maniu 220, P.O.Box 76/174,
76194 Bucharest, ROMANIA

Giuseppe SURACE**
POLITECNICO DI TORINO
Corso Duca degli Abruzzi 24,
10129 TORINO, Italy

A new approach of the transient flow conditions (simultaneous transitory behaviour of thermal load and fluid velocity) is proposed in the nonlinear panel flutter analysis. Applying proper aeroelastic theories (von Karman elasticity, piston aerodynamic theory) and fatigue life estimation (Heywood's approach) the results confirm differences in failure predictions, compared with the classical approach (case of constant flow and kinetic heating parameters). This study demonstrates the sensitivity of the aerothermoelastic system to the transitory hypersonic flow conditions: the pattern of the motion changes in amplitude even when modifying the increasing slope of the thermal and flow parameters that govern the motion, but maintaining the same steady state values. The panel behaves like a chaotic system and needs to be carefully investigated for a reliable design.

INTRODUCTION

The design of the re-entry space vehicles and high-speed aircraft structures requires special attention to the nonlinear thermoelastic and aerodynamic instabilities. The phenomenon depends on the structural configurations and flow conditions acting over this kind of mechanical systems. Thus, the dynamic aeroelastic instability of a wing structure (called *wing flutter*) involves a critical dynamic pressure (which corresponds to a limiting speed), growing an explosive failure due to an exponential increasing of the amplitudes. In this case, it is sufficiently to use a linear model by searching for the solution of the associated eigenvalue problem.

Panel flutter describes self-excited oscillations of an external panel of a flight vehicle when exposed to supersonic or hypersonic airflow (Fig.1). The phenomenon has received resurgent interest due to the development of aircraft and missiles at supersonic speed. The earliest reported structural failures that can be attributed to panel flutter were the failure of the 60-70 early German rockets during the World War II[1]. Also, most recently, after the flight tests of the F-117A stealth fighter, cracks were found in about half of the laminated composite skin panels (which had to be redesigned and stiffened)[2]. A linear analysis of the panel flutter could offer incomplete or erroneous information: critical dynamic pressure, frequency of vibration, and mode shape at the instability can be determined, but usually this yields no direct information about panel deflection and stresses.

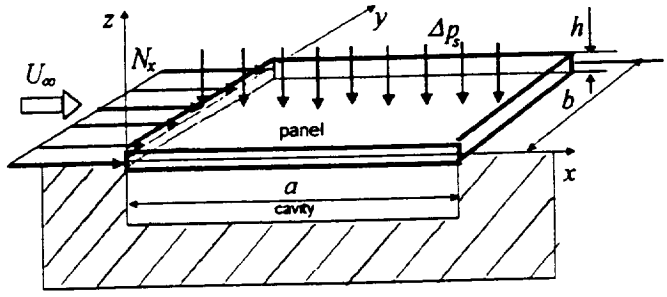

Fig.1 Skew of the panel configuration

Two successive stages can distinguish this problem: panel flutter analysis and failure prediction, respectively. Each of these problems has been gradually studied by previous authors.

---

* Research Scientist, member AIAA
** Professor, Department of Aeronautical & Space Engineering

The studies of panel flutter began during the Sixties. The Dowell's article[3] contains classical solutions of nonlinear isotropic panel flutter found through the use of Galerkin's method in the spatial domain and subsequent numerical integration. The first application of the finite element method (FEM) to study the linear panel flutter was due to Olson[4]. Then, extensions of the FEM were reported into nonlinear oscillations of 2D-isotropic panels (Mei[5]), and 3D-rectangular and triangular isotropic plates (Mei and Wang[6], and Han and Yang[7]). Analysis of composite plates, control and suppression of nonlinear panel flutter were given by Mei et all[8,9,10,11,12]. The high-order FE model presented in this paper has already been used in classical analysis[13] and in advanced studies of the transitory phenomena of hypersonic flow-field [14].

Though in flutter experiments it has been observed that many panels failed before the steady state flutter motion were reached, no significant studies have been directed towards failure mechanisms. However, at least two are readily identifiable and have occurred in practice:
-if the stress amplitude due to flutter exceeds the yield stress of the plate material over a substantial portion of the structure, then catastrophic or rapid failure occurs;
-on the other hand, if the stresses are relatively small, then fatigue or longue-time failure may occur.

From a knowledge of stress amplitude and frequency of the oscillation, an estimation of the fatigue life can be done, based on the maximum cycle stress together with the stress cycles to failure and material data. Recently, Xue & Mei[15] solved the influence of temperature and dynamic pressures on panel fatigue life for a two-dimensional nonlinear. The endurance and failure of a general nonlinear aerothermoelastic model were also reported[16] by using the presented model.

GOVERNING EQUATIONS

The stresses arisen in an isotropic Hookean plate subjected to uniform temperature difference ΔT can be written as the sum of the tension created by the stretching of the plate due to bending and the thermal applied in-plane load:

$$\begin{aligned}
\sigma_{xx} &= \frac{E}{(1-\nu^2)}\left[\varepsilon_{yy} + \nu\varepsilon_{xx}\right] - \frac{E}{(1-\nu)}\alpha\Delta T \\
\sigma_{yy} &= \frac{E}{(1-\nu^2)}\left[\varepsilon_{xx} + \nu\varepsilon_{yy}\right] - \frac{E}{(1-\nu)}\alpha\Delta T \\
\sigma_{xy} &= \frac{E}{2(1+\nu)}\varepsilon_{xy}
\end{aligned} \tag{1}$$

The von Karman nonlinear strain-displacement relations for a plate element undergoing both extension and bending at any point z is a sum of membrane and change of curvature strain components:

$$\begin{aligned}
\varepsilon_{xx} &= \frac{\partial u}{\partial x} + \frac{1}{2}\left(\frac{\partial w}{\partial x}\right)^2 - z\frac{\partial^2 w}{\partial x^2} = \varepsilon_{xx0} - z\frac{\partial^2 w}{\partial x^2} \\
\varepsilon_{yy} &= \frac{\partial v}{\partial y} + \frac{1}{2}\left(\frac{\partial w}{\partial y}\right)^2 - z\frac{\partial^2 w}{\partial y^2} = \varepsilon_{yy0} - z\frac{\partial^2 w}{\partial y^2} \\
\varepsilon_{xy} &= \frac{\partial v}{\partial x} + \frac{\partial u}{\partial y} + \frac{\partial w}{\partial x}\frac{\partial w}{\partial y} - 2z\frac{\partial^2 w}{\partial x \partial y} = \varepsilon_{xy0} - 2z\frac{\partial^2 w}{\partial x \partial y}
\end{aligned} \tag{2}$$

Combining the above two relations, the general normal stresses state can be represented by three significant components:

(i) nonlinear stretching stress:

$$\sigma_{1xx}=\frac{E}{(1-\nu^2)}\left[\frac{\partial u}{\partial x}+\frac{1}{2}\left(\frac{\partial w}{\partial x}\right)^2\right]$$
$$\sigma_{1yy}=\frac{E}{(1-\nu^2)}\left[\frac{\partial v}{\partial y}+\frac{1}{2}\left(\frac{\partial w}{\partial y}\right)^2\right] \tag{3}$$

(ii) pure bending stress:

$$\sigma_{2xx}=\frac{E}{(1-\nu^2)}\left[-z\frac{\partial^2 w}{\partial x^2}\right]$$
$$\sigma_{2yy}=\frac{E}{(1-\nu^2)}\left[-z\frac{\partial^2 w}{\partial y^2}\right] \tag{4}$$

(iii) thermal stress:

$$\sigma_{3xx}=\sigma_{3yy}=\frac{-\alpha E}{(1-\nu)}\Delta T \tag{5}$$

We note that a general formulation in terms of thermal effect should include the complete expression of the temperature change:

$$\Delta T=\Delta T(x,y,z,t) \tag{6}$$

meaning fully unsteady nonuniform temperature distribution. The classical approach in nonlinear panel flutter theory usually took into account a constant temperature distribution. Xue and Mei[17] extended the study to the case of nonuniform distribution over the panel surface and into the panel thickness, respectively. This paper will extend also the analysis to the case of a particular unsteady temperature distribution:

$$\Delta T=\Delta T(t) \tag{7}$$

having the pattern of a transitory behaviour until a stagnation temperature change between panel and its supports is reached.

The tensions:

$$N_x=\int_{-h/2}^{h/2}\sigma_{xx}dz;\ N_y=\int_{-h/2}^{h/2}\sigma_{yy}dz;\ N_{xy}=\int_{-h/2}^{h/2}\sigma_{xy}dz \tag{8}$$

are used to express the strain energy as a sum of pure bending and stretching components:

$$U_B=\frac{D}{2}\iint\left[\left(\frac{\partial^2 w}{\partial x^2}\right)^2+\left(\frac{\partial^2 w}{\partial y^2}\right)^2\right]dxdy+\frac{D}{2}\iint\left[2\nu\frac{\partial^2 w}{\partial x^2}\frac{\partial^2 w}{\partial y^2}+2(1-\nu)\left(\frac{\partial^2 w}{\partial x\partial y}\right)^2\right]dxdy \tag{9}$$

$$U_S = \frac{1}{2}\iint\left[N_x\varepsilon_{xx0} + N_y\varepsilon_{yy0} + N_{xy}\varepsilon_{xy0}\right]dxdy \tag{10}$$

The governing equation of the general model is obtained through the application of the Hamilton's principle:

$$\int(\delta T - \delta U + \delta W)dt = 0 \tag{11}$$

and becomes:

$$D\Delta^2 w - N_x\frac{\partial^2 w}{\partial x^2} - N_y\frac{\partial^2 w}{\partial y^2} + m\frac{\partial^2 w}{\partial t^2} + \Delta p_a = \Delta p_s \tag{12}$$

where Δp_S is the transversal static aerodynamic pressure. For the aerodynamic terms we will consider the simplest approximation of the aerodynamic forces valid for the domain of hypersonic velocities (first order piston theory):

$$\Delta p_a = \frac{2q_\infty}{M_\infty^2}\left(\frac{\partial w}{\partial x} + \frac{1}{v_\infty}\frac{\partial w}{\partial t}\right) \tag{13}$$

We chose this popular aerodynamic approximation because we are interested in an accurate prediction at high Mach numbers. Moreover, Bailie and McFeely[18] have shown that their results in panel flutter analysis obtained using a full unsteady hypersonic theory agree very closely with the results of this approximate theory.

FAILURE PREDICTION PROCEDURE

The fatigue life estimation can be obtained by using the Heywood's approach (as Xue and Mei[17] analysed for two-dimensional panels). The method is based on the expression of the alternating stress σ_a as:

$$\sigma_a = \pm\sigma_t\left(1 - \frac{\sigma_m}{\sigma_t}\right)[A_0 + \gamma(1 - A_0)] \tag{14}$$

where:

$$A_0 = \frac{\left(1 + \dfrac{0.0031n^4}{1 + 0.045\sigma_t}\right)}{1 + 0.0031n^4};\ n = \log(N);\ \gamma = \frac{\left(\dfrac{\sigma_m}{\sigma_t}\right)}{\left[1 + \left(\dfrac{\sigma_t n}{320}\right)^4\right]} \tag{15}$$

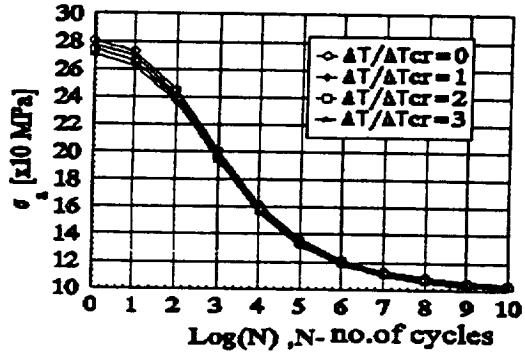

Fig.2 Heywoods's σ_x-N curve

We denote σ_t the ultimate tensile strength of the material, σ_m the mean stress and N is the number cycles to failure. The mean stresses correspond to various temperature changes related to the critical temperature change. Eq.(14) can be used to estimate the fatigue characteristic of panel knowing any three of the parameters σ_a, σ_m ,N or σ_a and solving for the fourth parameter. The fatigue life estimation (N-no. of cycles) is found from σ_x-N curves (as they are shown in Fig.2 -case of a simply

supported square panel having thickness/length ratio $h/a=0.005$, $\Delta T_{cr}=1.344^{o}C$), knowing the alternanting stress σ_a (max. values of σ_{xx}) and the mean stress σ_m equal to the thermal stress σ_{3xx}.

FINITE ELEMENT FORMULATION

The finite element idealisation is based on the Argyris' natural elastic theory[19] of the strains and stresses along the natural directions of a triangular finite element. The natural stresses state having the components $\sigma_\alpha,\sigma_\beta,\sigma_\gamma$ along the three sides of the triangle (see Fig.3a) is equivalent to the classical Cartesian stresses vector. This natural stress state can be considered as an effect of the equivalent system of natural nodal forces shown in Fig.3b. The modelling procedure consists of the Argyris' high-order triangular finite elements TUBA6 and TRIM6 (fully compatible elements for the out-of-plane and, respectively in-plane displacements, based on the natural geometry concept).

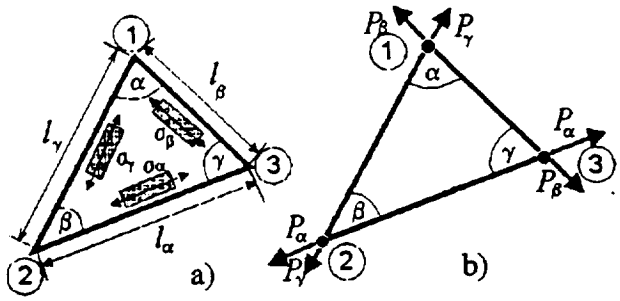

Fig.3 Natural stresses (a) and (b) equivalent nodal forces

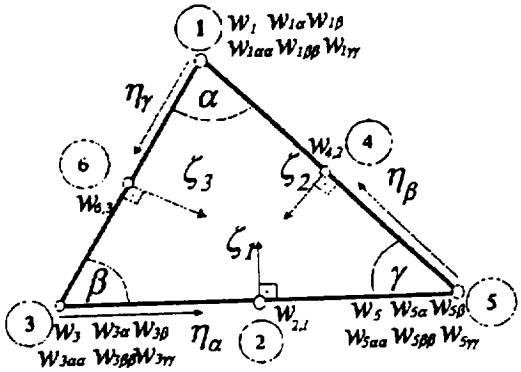

Fig.4 TUBA6 -natural directions and dofs

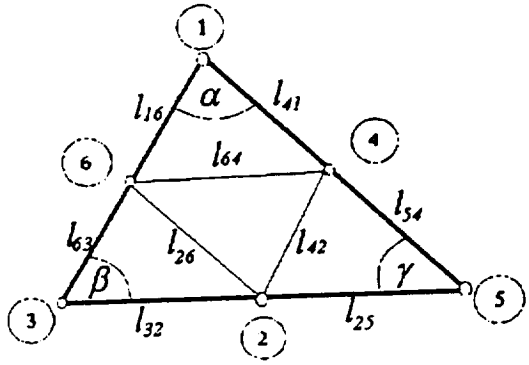

Fig.5 TRIM6 -natural dofs

Two nets of identical topology and material properties create the finite elements model: one composed of fifth order (six nodes) triangular plate TUBA 6 elements (Fig.4). The 21 degrees of freedom of this element consist of displacement, all first and second derivatives at the vertices -for satisfying the continuity condition in curvature- and the normal derivative in the middle-points of the edges; the other composed of a second order triangular membrane elements (Fig.5) with 12 degrees of freedom per element, having no flexural stiffness and carrying loads by axial and central shear forces. The FE formulation of the general equation (12) can be expressed in a non-dimensional form which includes separately the plate and membrane terms (denoted by the subscripts *"b"* and *"m"*):

$$\begin{bmatrix} \mathbf{M}^0_{bb} & \mathbf{0} \\ \mathbf{0}^t & \mathbf{M}^0_{mm} \end{bmatrix} \begin{bmatrix} \ddot{\mathbf{r}}^0_b \\ \ddot{\mathbf{r}}^0_m \end{bmatrix} + \sqrt{\frac{\lambda^r \delta}{M_\infty}} \begin{bmatrix} \mathbf{B}^0 & \mathbf{0} \\ \mathbf{0}^t & \mathbf{0} \end{bmatrix} \begin{bmatrix} \dot{\mathbf{r}}^0_b \\ \dot{\mathbf{r}}^0_m \end{bmatrix} + \left(\lambda^r \begin{bmatrix} \mathbf{A}^0 & \mathbf{0} \\ \mathbf{0}^t & \mathbf{0} \end{bmatrix} + \begin{bmatrix} \mathbf{K}^0_{bb} + \sigma_x \mathbf{K}^0_g & \mathbf{0} \\ \mathbf{0}^t & \mathbf{K}^0_{mm} \end{bmatrix} + \begin{bmatrix} \mathbf{K}^0_{1bb} & \mathbf{K}^0_{1bm} \\ \mathbf{K}^0_{1mb} & \mathbf{0} \end{bmatrix} + \begin{bmatrix} \mathbf{K}^0_{2bb} & \mathbf{0} \\ \mathbf{0}^t & \mathbf{0} \end{bmatrix} \right) \begin{bmatrix} \mathbf{r}^0_b \\ \mathbf{r}^0_m \end{bmatrix} = \begin{bmatrix} p\mathbf{P}^0_s \\ \mathbf{0} \end{bmatrix} \tag{16}$$

M,B,A and **K** are the global mass, aerodynamic damping, aerodynamic influence, and linear stiffness matrices, respectively; $\mathbf{K_g}$ is the geometric stiffness due to thermal forces; $\mathbf{K_1}$, $\mathbf{K_2}$ are the nonlinear stiffness matrices that depend linearly and quadratically on element plate "$\mathbf{r_b}$" and membrane "$\mathbf{r_m}$" displacements, respectively; $\mathbf{P_S}$ is the externally applied out-of-plane load (static pressure). The Dowell's non-dimensional parameters, obtained by using plate rigidity D, mass per square meter m, and geometrical characteristics (panel length a, and thickness h):

$$\tau = t\sqrt{\frac{D}{ma^4}}; W = \frac{w}{h}; \lambda^r = \frac{\rho_\infty U_\infty^2 a^3}{M_\infty D}; \delta = \frac{\rho_\infty a}{m}; \sigma_x = \frac{N_{x0}a^2}{D}; p_r = \frac{\Delta p_s a^4}{Dh} \qquad (17)$$

have the advantage of expressing the various results in a most compact form and establishing scaling laws to extrapolate results for other physical situations.

TRANSIENT HYPERSONIC FLOW EFFECTS

We consider that the transient hypersonic flow conditions consist of changes in dynamic pressures and kinetic heating. In Dowell's notation the dynamic pressure λ^r is related to Mach number M_∞ panel geometry and material properties (Young's modulus E, length/thickness ratio a/h), as well as to the characteristics of the altitude of flight (air density ρ_∞ and speed of sound). The typical trajectory of a hypersonic vehicle can be considered as in Fig.6. Also, the accelerations (as transient changes of velocities) have significant influence on dynamic pressure. This is exemplified in the Table 1 (from ref.[20]) showing the flight characteristics that correspond to a metallic panel substructure. Thus, it can be considered that the dynamic pressures evolves as a function with an increasing slope, until the steady level is reached.

Flight time (sec)	Altitude (Km)	Mach No.
1000	85.34	25
1500	73.15	22
2000	47.24	9

Table 1

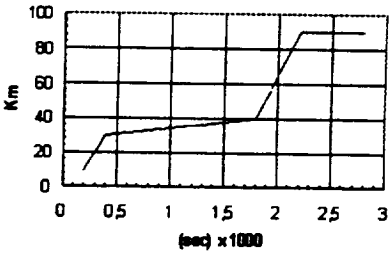

Fig.6 Typical trajectory of a hypersonic vehicle

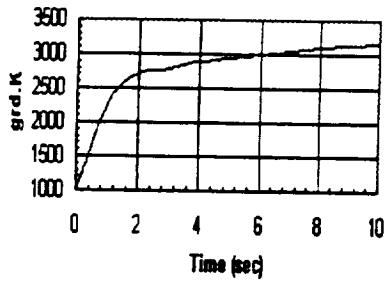

Fig.7 Transient kinetic heating of a wing leading edge

Thermal buckling load (arising when the kinetic heating of the panel surface yields a temperature difference between the panel and its fixed edges) is the second parameter that governs the aerothermoelastic behaviour. Under the conditions of the hypersonic flow, the kinetic heating is a complex phenomenon determined by using standard compressible flow and shock relations. We exemplify a transient simulation of a wing leading edge with Fig.6, presenting the kinetic heating of a wing leading edge[21], simulated from 1000 °K initial condition in the Mach 15 flowfield at H=30.54 Km (material: advanced diboride ceramic, ρ=5238.09 Kg/m^3). In the case of the square panel having completely restrained edges against in-plane motions, the in-plane stress resultants due to the temperature change between panel and its supports are equal:

$$N_x = N_y = -\frac{Eh\alpha\Delta T(t)}{1-\nu} \tag{18}$$

and could be related to the critical buckling conditions ΔT_{cr} by the relation:

$$-\frac{\sigma_x(t)}{2\pi^2} = \frac{\Delta T(t)}{\Delta T_{cr}} \tag{19}$$

Applying non-dimensional time parameter τ, the variation of the temperature change can be assumed as having the same pattern as the transient kinetic heating: increasing values (over a time span τ_1) until a stagnation temperature difference ΔT_1 is reached. The functions showed in Fig.8 are simple approximations for the real phenomena in hypersonic flow.

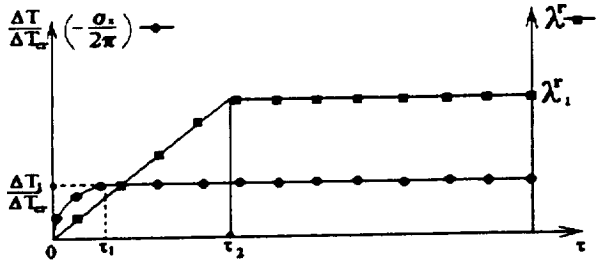

Fig.8 Pattern of transitory functions

RESULTS

A stress analysis of the fluttering panel is based on the identification of the dynamic response from which the characteristics of the oscillations (amplitude and frequency) are extracted to perform the fatigue life estimation. It is known that the non-linear structural effect consists in the in-plane stretching stresses induced by the large amplitudes of the out-of-plane motion. Since the tension increases at higher and higher deflections and remains positive for any sign of the amplitude, a limited aeroelastic response (limit cycle flutter -Fig.9, case of a simply supported square panel, *h/a=0.01*) arises at supercritical dynamic pressures. This means that the limit-cycle oscillations (LCO) of the flutter phenomenon are fatigue cycles, due to the total induced alternating stress σ_{txx} expressed as sum of the components: nonlinear stretching stress σ_{1xx}, pure-bending stress σ_{2xx}, and thermal stress σ_{3xx}. As the classical map of stability boundaries (Fig.10) shows, the dynamic behaviour becomes more complex under certain combinations of dynamic pressures and thermal buckling loads: the limit cycle motion domain is extended at large temperature change ΔT, as well as chaotic motions arise for moderate temperature and dynamic pressure conditions.

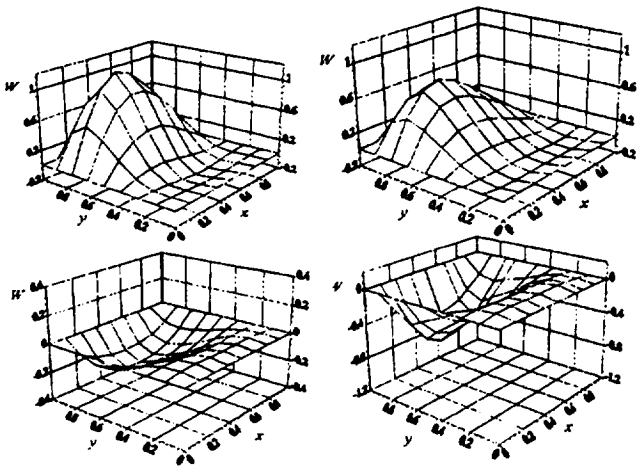

Fig.9 Limit-cycle oscillations of the panel (λ^r=800, $\sigma_x/2\pi$=0)

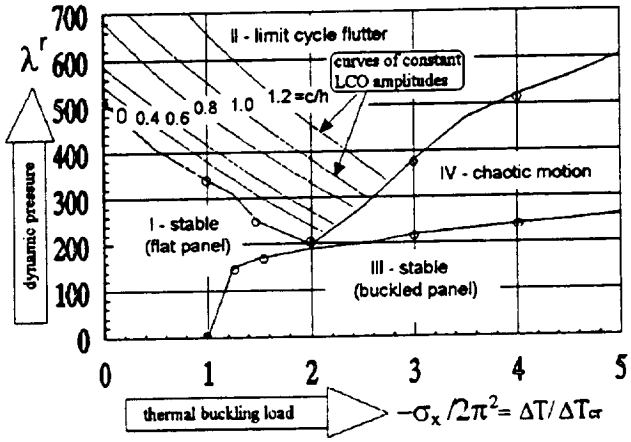

Fig.10 Map of the aero-thermoelsatic stability boundaries (simply supported panel)

The critical cases are related to the limit-cycle oscillations and chaotic behaviour. The classical dynamic stress analysis uses especially curves of the maximum amplitude plotted in the LCO domain of the map of aeroelastic stability boundaries. In other words, under the conditions of a certain pair of values of the dynamic pressure and thermal load (acting as constant parameters in the nonlinear aero-thermoelastic system), a unique pair of LCO amplitude and frequency of oscillation characterizes the limit-cycle motion. So, there are completely defined the parameters for the fatigue analysis within Heywood's theory: the maximum limit-cycle deformed shape determines the corresponding alternating stress distribution and the failure prediction can be estimated (in life hours) by extracting the number of cycles to failure from the Heywood's diagram.

More interesting results arise when taking into account the effects of transient hypersonic flow conditions. Thus, changing only the slope of the dynamic pressure function in transition to the same steady value (λ^r=500) and under the same thermal condition (transient heating at $\Delta T/\Delta T_{cr}$=2.5), the dynamic responses change their steady-state amplitudes and patterns (Fig.11: buckled → chaos → limit-cycle flutter, Fig.12: buckled → limit-cycle flutter). Other patterns (buckled → chaos → buckled) have also been found by varying the transient change of the same parameters.

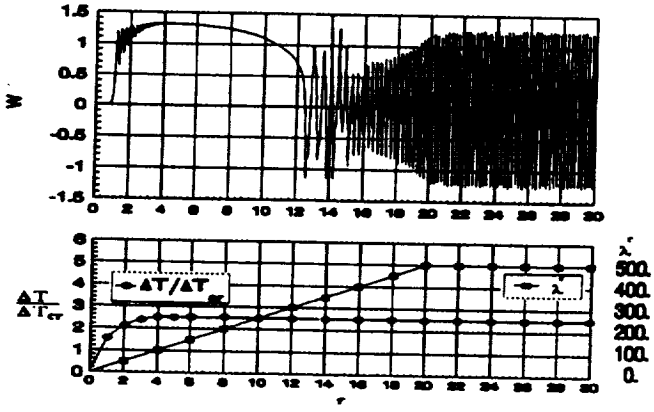

Fig.11 Transient behaviour ($\Delta T/\Delta T_{cr}$=2.5, λ^r=500) at moderate change in dynamic pressure

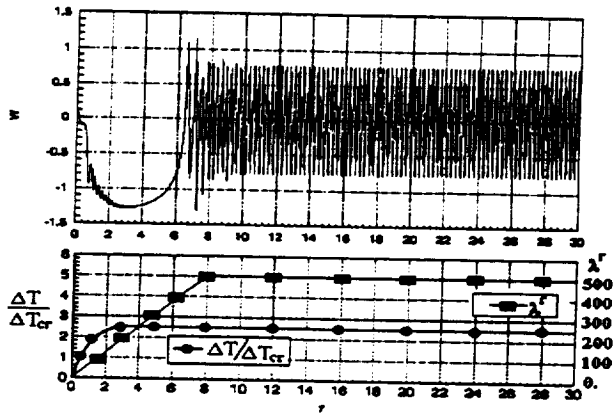

Fig.12 Transient behaviour ($\Delta T/\Delta T_{cr}$=2.5., λ^r=500) at rapid change in dynamic pressure

The dynamic stress analysis can be performed using directly the finite element dofs (all combinations of the first and second order derivatives of the displacements) in the relations of the von Karman nonlinear elastic theory (eqs 3, 4, 5). The σ_{xx} stresses distribution corresponding to the steady-state domain of Fig.11 is presented (Fig.13) in the section $x=a/2$ which is the most representative in a strength analysis. All components are alternating stresses (having the frequency of the limit cycle oscillation), except the thermal stress σ_3 that is constant. It can be seen that the nonlinear stretching stress σ_{1xx} plays a significant role in location of the maximum total stress σ_{txx}. By comparison to this case, a similar analysis (Fig.14) is performed by taking into account the case of a rapid transition in thermal and dynamic pressure conditions (shown in Fig.12). In this case the values of the stress components are smaller, corresponding to smaller limit cycle flutter amplitude, though the stationary conditions are the same as in the previous case ($\Delta T/\Delta T_{cr}$=2.5, λ^r=500). As a consequence, the corresponding fatigue analysis through Heywood's theory (Fig.2) gives different results: a limited life of about 10^4 cycles (in dimensionless time) in the first case and an unlimited life in the second case, though the classical analysis states that in the LCO domain the motion is uniquely determined in amplitude and frequency at certain parameters $\Delta T/\Delta T_{cr}$ and λ^r.

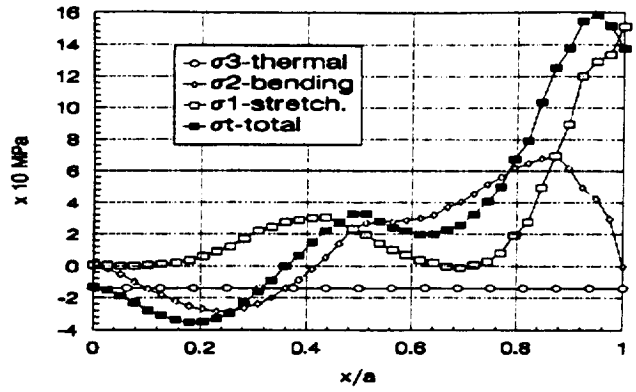

Fig.13 Stress distribution σ_{xx} (case 1)

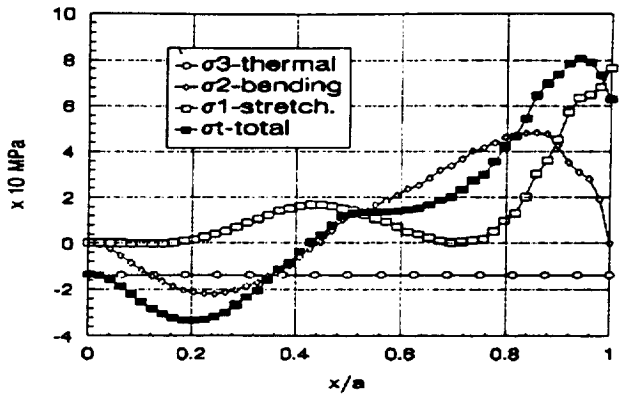

Fig.14 Stress distribution σ_{xx} (case 2)

The sensitivity of the nonlinear system exhibiting changeable patterns of the aerothermoelastic response when exposed to transient thermal and velocity effects could determine another interesting case. Thus, investigations into the flutter domain of the map of the aeroelastic boundaries showed also a local phenomenon of exponential increasing amplitudes at certain transitory conditions (Fig.16). In other circumstances, this behaviour does not arise (Fig.15).

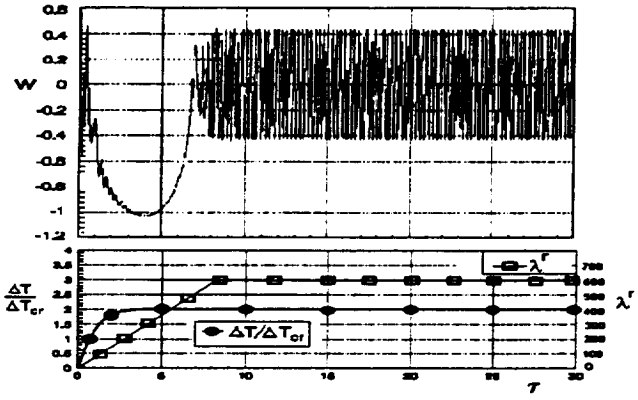

Fig.15 Transient behaviour ($\Delta T/\Delta T_{cr}$=2., λ^r=600) at rapid change in dynamic pressure

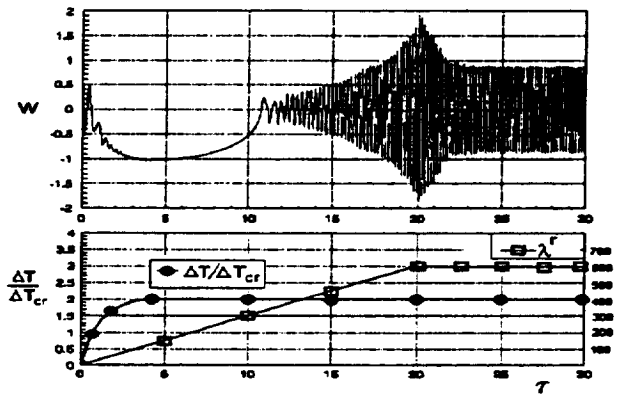

Fig.16 Transient behaviour ($\Delta T/\Delta T_{cr}$=2., λ^r=600) at moderate change in dynamic pressure

In this case, even if the limit-cycle amplitudes of the steady-state domain are smaller than the previous studied case (and consequently do not involve a failure by fatigue), conditions of a local damage during the explosive phenomenon could appear due to the larger displacements that could exceed the ultimate strain of material. Then the catastrophic failure can be accelerated by the periodic motion at smaller amplitudes of the flutter motion. Also, another phenomenon can not be neglected: the rapid buckling that precedes the limit-cycle behaviour in almost cases of the transitory conditions. Due to the large amplitudes which change very fast, the behaviour is like a shock and can cause damages.

CONCLUSIONS

This study demonstrate the sensitivity of the aerothermoelastic system to the transitory hypersonic flow conditions: the pattern of the motion changes in amplitude even when modifying the

increasing slope of the parameters that govern the motion (thermal forces and dynamic pressures), but maintaining the same steady state values. The panel behaves like chaotic system.

Applying proper theories for elastic (von Karman) and aerodynamic (piston theory) model, and the Heywood's approach for fatigue life estimation, the results confirm differences in stress predictions, compared with the classical approach (case of constant flow and kinetic heating parameters).

The engineers and designers of the high speed aircraft structures could find new information about the failure mechanism of panels, searching not only for the fatigue analysis of limit-cycle flutter solutions (involving certain frequencies and maximum cyclic stresses in LCO domain), but also taking into account the possibility of a fast failure during a rapid buckling phenomenon, or a long term failure due to the irregularly oscillations as an effect of the transient conditions.

REFERENCES

[1] Bisplinghoff,R.,L., Ashley,H., -"Principles of Aeroelasticity", Wiley, New York, 1962, pp.419,420.

[2] Backer,R., -"F-117A Structures and Dynamics Design Considerations", Plenary Session 8, AIAA Dynamics Specialists Conference, Dallas, TX April 1992.

[3] Dowell,E.,H., "Nonlinear Oscillations of a Fluttering Plate II", AIAA Journal, Vol.5, No.10, 1967, pp.1856-1862.

[4] Olson,M.,D., -"Some Flutter Solutions Using Finite Elements", AIAA Journal, Vol.8, No.4, 1970, pp.747-752.

[5] Mei,C., "A Finite Element Approach for Nonlinear Panel Flutter", AIAA Journal, Vol.15, No.8, 1977, pp.1107-1110.

[6] Mei,C., Wang,H.,C., -"Finite Element Analysis of Large Amplitude Supersonic of Panels", Proceeding of the International Conference on FEM, (Shanghai, China), Gordon & Breach, New York, Aug.1982, pp.944-951.

[7] Han,A.,D., Yang,T.,Y., -"Nonlinear Panel Flutter Using High-Order Triangular Finite Elements", AIAA Journal, Vol.21, No.10, 1983, pp.1453-1461.

[8] Dixon, R.,I., Mei,C., -"Finite Element Analysis of Large-Amplitude Panel Flutter of Thin Laminates, AIAA Journal, Vol.31, No.4, 1993, p.701-707.

[9] Zhou,R.,C., Xue,Y., Mei,C., -"Finite Element Time Domain -Modal Formulation for Nonlinear Flutter of Composite Panels", AIAA Journal, Vol.32, No.10, Oct.1994, pp.2044-2052.

[10] Lai,Z., Xue,D., Huang,J-K., Mei,C., -"Panel Flutter Limit-Cycle Suppression with Piezoelectric Actuation", Journal of Intelligent Material Systems and Structures, Vol.6 -March 1995, pp.274-282.

[11] Zhou,R.,C., Lai,Z., Xue,D., Huang,J-K., Mei,C., -"Suppression of Nonlinear Panel Flutter with Piezoelectric Acuators Using Finite Element Method", AIAA Journal, Vol.33, No.6, June 1995, pp.1098-1105.

[12] Zhou,R.,C., Mei,C., Huang,J-K., -"Suppression of Nonlinear Panel Flutter at Supersonic Speeds and Elevated Temperatures", AIAA Journal, Vol.34, No.2, Feb.1996, pp.347-354.

[13] Udrescu,R., "A Higher Finite Element Model in Nonlinear Panel Flutter Analysis", AIAA paper no. 98-1843, A collection of techical papers of the 39th AIAA/ASME/ASCE/AHS/ACS Structures, Structural Dynamics and Materials Conference, Part 2, pp.1252-1262.

[14] Udrescu,R., "Aero-Thermoelastic Behaviour of Panel Substructures Subjected to Rapid Accelerations in Supersonic Flow", AIAA paper #98-4838, the 7th AIAA/USAF/NASA/ISSMO Simposium on Multidisciplinary Analysis and Optimization, Sept.2-4, 1998, St.Louis, USA.

[15] Xue,D.,Y., Mei,C., -"Finite Element Nonlinear Panel Flutter with Arbitrary Temperatures in Supersonic Flow", AIAA Journal, Vol.31, No.1, 1993, pp.154-162.

[16] Udrescu,R., "Stress Analysis of the Panel Flutter and Divergence in Supersonic Flow", Buletinul Institutului Politehnic din Iasi, Tom XLIII, sectia V, Construcctii de masini (Proceedings of the 4th International Conference on Boundary and Finite Element", Iasi, ROMANIA, 4-6th of June, 1997), section 2.1, pp.172-177.

[17] Xue,D.,Y., Mei,C., "Finite Element Nonlinear Flutter and Fatigue Life of Two-Dimensional Panels with Temperature Effects", Journal of Aircraft, Vol.30, No.6, 1993, pp.993-1001.

[18] Bailie,J.,A., McFeely, "Panel Flutter in Hypersonic Flow", AIAA Journal, Vol.6, No.2, 1968, pp.332-337.

[19] Argyris,J., Mlejnek,H.,P., "Die Metoden der Finiten Elementen", Band I, Vieveg, Braunschweig/Wiesbaden, 1986.

[20] Kontinos,D., "Coupled Thermal Analysis Method with Application to Metallic Thermal Protection Panels", Journal of Thermophysics and Heat Transfer, Vol.11, No.2, April-June 1997, pp.173-181.

[21] Colwell, G.,T., Moldin,J.,M., "Heat Pipe and Surface Mass Transfer Cooling of Hypersonic Vehicle Structures", Journal of Thermophysics and Heat Transfer, Vol.6, No.3, July -Sept. 1992, pp.492-499.

Nonlinear Regular and Chaotic Flutter of an Airfoil with a Trailing Edge Flap in Supersonic Flow

Z. Dżygadło, I. Nowotarski and A. Olejnik
Military University of Technology
00-908 Warszawa, ul. Kaliskiego 2, Poland

An airfoil in supersonic flow, having deformable nonlinear supports, is an aeroelastic system for which various types of instability, bifurcations and regular or chaotic motions can appear (see [5 - 9]).

The airfoil has three degrees of freedom - that is, plunge displacement, angle of pitch and angle of flap deflection. The stiffness force and moments for all those motions are assumed to be nonlinear ones [2, 3]).

The airfoil is subjected to the pressure difference produced by its motion in supersonic flow. Stability and bifurcations occurring in the system, limit cycles of self-excited vibrations and regions of regular or chaotic motions have been investigated. The effect of some parameters of the system on the course of linear and nonlinear vibrations has been studied.

1. Introduction

Recently some investigations of nonlinear vibrations of aeroelastic systems have been made in which regular and chaotic motions were studied [6 - 9].

In the present paper nonlinear vibrations of an airfoil with a trailing edge flap in supersonic flow are considered (Fig.1). The airfoil has three degrees of freedom, where $z_c = z_c(t)$ is plunge displacement, $\alpha = \alpha(t)$ is angle of pitch and $\beta = \beta(t)$ is angle of flap deflection. The airfoil suspension is assumed to be nonlinear and the stiffness force and the moments for airfoil motions are nonlinear functions.

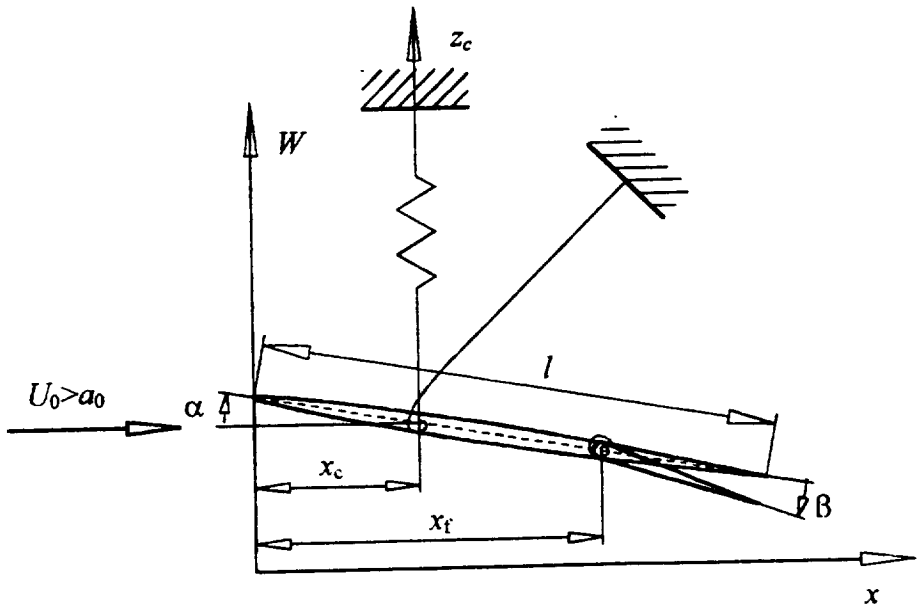

Fig.1. Sketch of the airfoil

The airfoil is subjected to the pressure difference caused by its motion in the gas stream having unperturbed velocity $U_0 > a_0$, where a_0 is sound velocity of the flowing gas.

The airfoil is assumed to be a thin and plane nondeformable structure (Fig.1). The pressure difference acting upon the airfoil can be determined by making use of the potential theory of unsteady supersonic flow [1 - 4].

Finally, we obtain a set of three nonlinear differential equations describing the motion of the system under consideration, which enables us to study linear and nonlinear flutter of the airfoil with the trailing edge flap in supersonic flow, where bifurcations and regular or chaotic vibrations can appear.

2. Equations of Motion

Equations of airfoil motion can be written in the form [2, 3]

$$\begin{aligned} m_a \frac{d^2 z_c}{dt^2} - S_a \frac{d^2\alpha}{dt^2} - S_f \frac{d^2\beta}{dt^2} &= Q_z + P_z \\ I_a \frac{d^2\alpha}{dt^2} - S_a \frac{d^2 z_c}{dt^2} + (I_f + (x_f - x_c)S_f)\frac{d^2\beta}{dt^2} &= Q_\alpha + M_\alpha \\ I_f \frac{d^2\beta}{dt^2} + (I_f + (x_f - x_c)S_f)\frac{d^2\alpha}{dt^2} - S_f \frac{d^2 z_c}{dt^2} &= Q_\beta + M_\beta \end{aligned} \tag{2.1}$$

where m_a, S_a, I_a are mass, static moment and moment of inertia, respectively, per unit span of the complete airfoil (moments S_a and I_a are taken in relation to the axis x_c of airfoil suspension Fig.1), S_f, I_f are static moment and moment of inertia of the flap (taken in relation to the axis x_f of flap rotation Fig.1).

$$\begin{aligned} P_z &= P_z(z_c) = -k_{z0}(z_c + k_{z1} z_c^3) \\ M_\alpha &= M_\alpha(\alpha) = -k_{\alpha 0}(\alpha + k_{a1}\alpha^3) \\ M_\beta &= M_\beta(\beta) = -k_{\beta 0}(\beta + k_{\beta 1}\beta^3) \end{aligned} \tag{2.2}$$

represent nonlinear stiffness force and moments for airfoil and flap motions, while Q_z, Q_α and Q_β are aerodynamic force and moments produced by the airfoil motion in supersonic flow

$$Q_z = \int_0^l \Delta p dx; \qquad Q_\alpha = \int_0^l \Delta p (x_c - x) dx; \qquad Q_\beta = \int_{x_f}^l \Delta p (x_f - x) dx \tag{2.3}$$

The pressure difference Δp can be determined making use of the potential theory of unsteady supersonic flow [1, 3, 4]

$$\Delta p = p_l - p_u = \Delta p_1 + \Delta p_2 \tag{2.4}$$

where

$$\Delta p_1 = -\frac{2\rho_0 U_0}{\mu}\left[U_0 \frac{\partial W}{\partial x} + \left(1 - \frac{1}{\mu^2}\right)\frac{\partial W}{\partial t}\right] \tag{2.5}$$

is the linear part of the pressure difference [9] and

$$\mu^2 = M^2 - 1; \qquad M = \frac{U_0}{a_0} > 1 \tag{2.6}$$

ρ_0, M are density and Mach number of unperturbed flow, while

$$W = W(x,t) = z_c + \alpha(x_c - x) + \beta(x_f - x)H(x - x_f) \tag{2.7}$$

is displacement of the airfoil surface (Fig.1) and $H(x)$ is Heaviside's function.

Nonlinear, the second order part of the pressure difference can be obtained in the form [4]

$$\Delta p_2 = -\frac{\rho_0}{2}(\kappa+1)\left(U_0\frac{\partial W}{\partial x}+\frac{\partial W}{\partial t}\right)^2 - \frac{\rho_0}{\mu^2}\left[(\kappa-1)U_0\frac{\partial W}{\partial x}\left(U_0\frac{\partial W}{\partial x}+\frac{\partial W}{\partial x}\right)-\left(\frac{\partial W}{\partial t}\right)^2\right] \tag{2.8}$$

where κ is the ratio of specific heats.

Aerodynamic force and moments (2.3) acting upon the airfoil can be determined for linear approximation making use of (2.5) and (2.7)

$$Q_z = \int_0^l \Delta p_1 dx = \frac{2\rho_0 U_0^2 l}{\mu}(\alpha+\lambda_f\beta) - \frac{2\rho_0 U_0 l}{\mu}\left(1-\frac{1}{\mu^2}\right)\left[\dot z_c + \dot\alpha\left(x_c-\frac{l}{2}\right)-\dot\beta\frac{l}{2}\lambda_f^2\right] \tag{2.9}$$

$$\begin{aligned} Q_\alpha = \int_0^l \Delta p_1 (x_c - x)dx = {} & \frac{2\rho_0 U_0^2 l}{\mu}\left\{\alpha\left(x_c-\frac{l}{2}\right)+\beta\lambda_f\left[x_c-\frac{1}{2}\left(l+x_f\right)\right]\right\}+ \\ & -\frac{2\rho_0 U_0 l}{\mu}\left(1-\frac{1}{\mu^2}\right)\left\{\dot z_c\left(x_c-\frac{l}{2}\right)+\dot\alpha\left(x_c^2-x_c l+\frac{l^2}{3}\right)+\right. \\ & \left.+\dot\beta\left[\lambda_f x_c x_f-\frac{1}{2}\lambda_f\left(x_c+x_f\right)\left(l+x_f\right)+\frac{l^3-x_f^3}{3l}\right]\right\} \end{aligned} \tag{2.10}$$

$$\begin{aligned} Q_\beta = \int_{x_f}^l \Delta p_1 (x_f - x)dx = {} & -\frac{\rho_0 U_0^2 l^2 \lambda_f^2}{\mu}(\alpha+\beta)+\frac{2\rho_0 U_0 l}{\mu}\left(1-\frac{1}{\mu^2}\right)\left\{\frac{1}{2}\lambda_f^2 l\dot z_c+\right. \\ & -\dot\alpha\left[\lambda_f x_c x_f-\frac{1}{2}\lambda_f\left(x_c+x_f\right)\left(l+x_f\right)+\frac{l^3-x_f^3}{3l}\right]+ \\ & \left.-\dot\beta\left[\lambda_f x_f^2-\lambda_f x_f\left(l+x_f\right)+\frac{l^3-x_f^3}{3l}\right]\right\} \end{aligned} \tag{2.11}$$

where $\lambda_f = \dfrac{l_f}{l}$ (2.12)

and l_f is flap chord.

The problem of airfoil vibrations will be considered in a dimensionless form assuming that the displacement z_c is referred to the chord l of airfoil and time t to $1/\omega_\alpha$, where

$$\omega_\alpha = \sqrt{\frac{k_{\alpha 0}}{I_a}}\ ; \qquad \omega_z = \sqrt{\frac{k_{z0}}{m_a}}\ ; \qquad \omega_\beta = \sqrt{\frac{k_{\beta 0}}{I_f}} \tag{2.13}$$

are natural frequencies of linearized uncoupled vibrations of the airfoil and its flap under study. Equations of motion (2.1) will be transformed making use of Eqs. (2.2), (2.9) - (2.11) and we can obtain

$$\begin{aligned} \frac{d^2 z}{d\tau^2} - e_a\frac{d^2\alpha}{d\tau^2} - e_f\overline{m}_f\frac{d^2\beta}{d\tau^2} + \chi_z(z+\bar k_{z1}z^3) = {} & \gamma_1 r_a^2(\alpha+\lambda_f\beta)+ \\ & -\gamma_1\delta r_a^2\left(\frac{dz}{d\tau}+\xi_0\frac{d\alpha}{d\tau}-\frac{\lambda_f^2}{2}\frac{d\beta}{d\tau}\right) \end{aligned} \tag{2.14}$$

$$\frac{d^2\alpha}{d\tau^2}-\frac{e_a}{r_a^2}\frac{d^2z}{d\tau^2}+\bar{I}_{fc}\frac{d^2\beta}{d\tau^2}+\alpha+k_{\alpha 1}\alpha^3=\gamma_1\left[\alpha\xi_0+\beta\lambda_f\left(\xi_0-\frac{1}{2}\xi_f\right)\right]+$$
$$-\gamma_1\delta\left[\xi_0\frac{dz}{d\tau}+\frac{d\alpha}{d\tau}\left(\xi_0^2+\frac{1}{12}\right)\right]-\gamma_1\delta\frac{d\beta}{d\tau}\lambda_f\left[\frac{1}{3}-\frac{1}{2}\lambda_f\xi_c-\frac{1}{6}\xi_f\left(1+\xi_f\right)\right] \quad (2.15)$$

$$\frac{d^2\beta}{d\tau^2}+e_{fc}\frac{d^2\alpha}{d\tau^2}-\frac{e_f}{r_f^2}\frac{d^2z}{d\tau^2}+\chi_\beta(\beta+k_{\beta 1}\beta^3)=-\gamma_1\frac{\lambda_f^2}{2\bar{I}_f}(\alpha+\beta)+$$
$$+\gamma_1\delta\frac{\lambda_f}{\bar{I}_f}\left\{\frac{dz}{d\tau}\frac{\lambda_f}{2}-\frac{d\alpha}{d\tau}\left[\frac{1}{3}-\frac{1}{2}\lambda_f\xi_c-\frac{1}{6}\xi_f(1+\xi_f)\right]-\frac{1}{3}\lambda_f^2\frac{d\beta}{d\tau}\right\} \quad (2.16)$$

where

$$\tau=\omega_\alpha t;\qquad z=\frac{z_c}{l};\qquad e_a=\frac{S_a}{m_a l}$$

$$r_a^2=\frac{I_a}{m_a l^2};\quad \xi_0=\frac{x_c}{l}-\frac{1}{2};\quad e_f=\frac{S_f}{m_f l};\quad r_f^2=\frac{I_f}{m_f l^2};\quad \xi_c=\frac{x_c}{l}$$

$$\bar{m}_f=\frac{m_f}{m_a};\quad \bar{I}_{fc}=\left[I_f+(x_f-x_c)S_f\right]/I_a;\quad e_{fc}=1+(x_f-x_c)\frac{S_f}{I_f};\quad \xi_f=x_f/l \quad (2.17)$$

$$\lambda_f=\frac{l_f}{l};\quad \gamma_1=\frac{2\rho_0U_0^2l^2}{\mu k_{\alpha 0}};\quad \delta=\frac{l\omega_\alpha}{a_0M}\left(1-\frac{1}{\mu^2}\right);\quad \chi_z=\frac{\omega_z^2}{\omega_\alpha^2};\quad \chi_\beta=\frac{\omega_\beta^2}{\omega_\alpha^2};\quad \bar{k}_{z1}=l^2k_{z1}$$

Equations (2.14) - (2.16) together with relations (2.17) will be applied to the analysis of airfoil vibrations. In those equations, the coefficient γ_1 defines the reduced dynamic pressure of supersonic flow, which is the decisive factor for self-excitation of the system, $\gamma_1\delta$ is the coefficient of aerodynamic damping, ξ_0 is the dimensionless distance of the airfoil suspension axis (elastic axis) from the mid-chord point and χ_β determines the ratio of natural frequencies for angles of pitch and flap deflection, which has also the essential effect on the course of vibrations.

3. Analysis of Stability

At the beginning Eqs.(2.14)-(2.16) will be linearized assuming that

$$k_{z1}=k_{\alpha 1}=k_{\beta 1}=0 \quad (3.1)$$

and the solution of Eqs. (2.14)-(2.16), (3.1) can be found in the form

$$z(\tau)=z_0e^{ip\tau};\qquad \alpha(\tau)=\alpha_0e^{ip\tau};\qquad \beta(\tau)=\beta_0e^{ip\tau} \quad (3.2)$$

On substituting (3.2) into Eqs. (2.14)-(2.16), (3.1), a set of algebraic equations is obtained from which the equation of frequencies can be found

$$\Delta=a_{11}(a_{22}a_{33}-a_{23}a_{32})-a_{21}(a_{12}a_{33}-a_{13}a_{32})+a_{31}(a_{12}a_{23}-a_{13}a_{22})=0 \quad (3.3)$$

where

$$a_{11}=\chi_z-p^2+ip\gamma_1\delta r_a^2;\qquad a_{12}=p^2e_a-\gamma_1r_a^2+ip\gamma_1\delta r_a^2\xi_0;$$

$$a_{13}=p^2e_f\bar{m}_f-\gamma_1r_a^2\lambda_f-ip\gamma_1\delta r_a^2\tfrac{1}{2}\lambda_f^2;\quad a_{21}=p^2\frac{e_a}{r_a^2}+ip\gamma_1\delta\xi_0;$$

$$a_{22}=1-p^2-\gamma_1\xi_0+ip\gamma_1\delta(\xi_0^2+\tfrac{1}{12});\qquad a_{23}=\gamma_1\lambda_f(\tfrac{1}{2}\xi_f-\xi_0)-p^2\bar{I}_{fc}+ip\gamma_1\delta w_{23};$$

$$a_{31}=p^2\frac{e_f}{r_f^2}-ip\gamma_1\frac{\delta}{\bar{I}_f}\tfrac{1}{2}\lambda_f^2;\qquad a_{32}=\gamma_1\frac{\lambda_f^2}{2\bar{I}_f}-p^2e_{fc}+ip\gamma_1\frac{\delta}{\bar{I}_f}w_{23}$$

$$a_{33} = \chi_\beta - p^2 + \gamma_1 \frac{\lambda_f^2}{2\bar{I}_f} + ip\gamma_1 \frac{\delta}{\bar{I}_f} \frac{1}{3}\lambda_f^3; \qquad w_{23} = \lambda_f[\tfrac{1}{3} - \tfrac{1}{2}\lambda_f \xi_c - \tfrac{1}{6}\xi_f(1+\xi_f)] \tag{3.4}$$

Equation (3.3) enables us to investigate stability of the system under study. In a general case, we can obtain from Eq. (3.3) complex eigenvalues of Eqs. (2.14)-(2.16), (3.1)

$$p = q - i\varepsilon \tag{3.5}$$

for stable ($\varepsilon < 0$) or unstable ($\varepsilon > 0$) vibrations, depending on γ_1, δ, ξ_0, χ_β and other parameters of the system. From Eq. (3.3) we can also find critical parameters of self-excited (flutter) vibrations

$$\gamma_1 = \gamma_{1cr}; \qquad p = q = \omega_{cr}; \qquad \varepsilon = 0 \tag{3.6}$$

or divergence of the system

$$\gamma_1 = \gamma_{1\,div}; \qquad p = 0 \tag{3.7}$$

Equations (3.6) define the Hopf bifurcation limit and Eqs. (3.7) - the divergence bifurcation limit for the system under study [5].

4. Numerical Analysis of Stability and Nonlinear Vibrations of the Airfoil

Numerical calculations of stability parameters (3.6) and (3.7) have been carried out for the following data

$$\chi_z = 0.2,\ e_a = 0.125;\ r_a^2 = 0.12;\ \bar{m}_f = 0.1;\ \lambda_f = 0.2;\ r_f^2 = 0.01;\ \xi_f = 0.8;$$
$$\bar{I}_f = 0.1;\ e_f = 0; 0.1;\ \delta = 0{,}001; 0.1;\ \xi_c = 0.4 \div 0.8;\ \chi_\beta = 0 \div 10 \tag{4.1}$$

Nonlinear airfoil vibrations have been investigated for (4.1) and

$$k_{z1} = 0; \quad k_{\alpha 1} = k_{\beta 1} = 20 \tag{4.2}$$

For nonlinear vibrations, we have also included torsional free-play in the deflection of flap, which is acting together with nonlinear stiffness moment $M_\beta = M_\beta(\beta)$ of (2.2), (4.2). The amplitude of free-play is taken

$$\beta = 0.05 \tag{4.3}$$

The range of parameters applied in this investigation enabled us to study regular and chaotic limit cycle vibrations. In Fig.2 diagrams of critical parameters γ_{1cr}, ω_{cr} versus χ_β are presented for $\xi_c = 0.4 \div 0.8$, $\delta = 0.001$ and balanced flap, $e_f = 0$. In Fig.3 similar diagrams and γ_{1div} are shown for unbalanced flap, $e_f = 0.1$.

It can be seen that the sensitivity of the system to flutter vibrations increases for $\xi \to 0.8$ - that is, for back position of elastic axis, and critical frequency decreases in this case.

For balanced flap (Fig.2) we can see interesting irregularities for $\chi_\beta \approx 1$ and $\chi_\beta < 0.2$ (Fig.2c).

In the next figures results of numerical analysis of nonlinear airfoil vibrations are shown, where phase plane plots, time histories and power spectrum density plots P are presented for $z(\tau)$, $\alpha(\tau)$ and $\beta(\tau)$.

In Fig.4, we have asymptotically stable vibrations for $\xi_c = 0.4$; $\chi_\beta = 0.9$; $\gamma_1 = 1.7$ and in Fig.5 we see quasi-periodic limit cycle vibrations for $\xi_c = 0.4$; $\chi_\beta = 0.9$; $\gamma_1 = 2{,}0$.

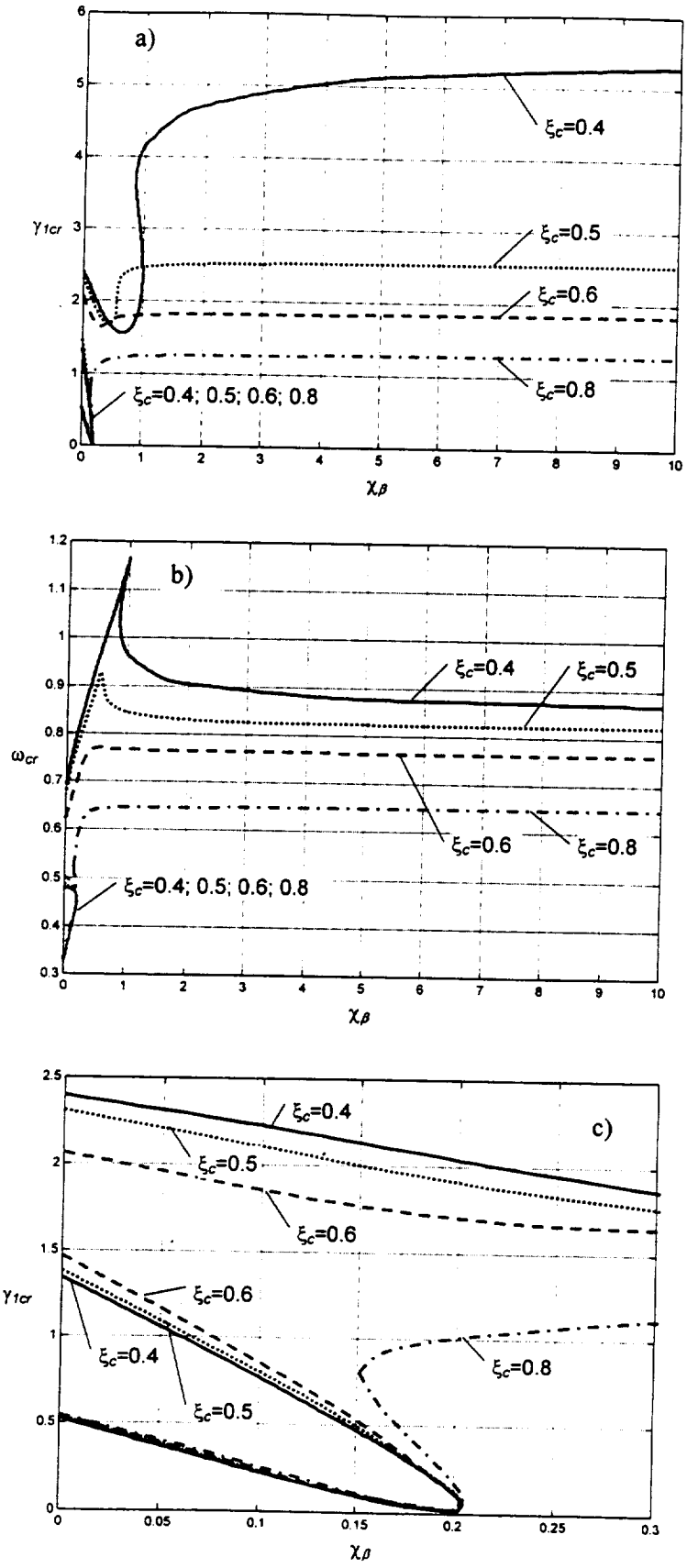

Fig. 2. Stability boundaries for $e_f = 0$

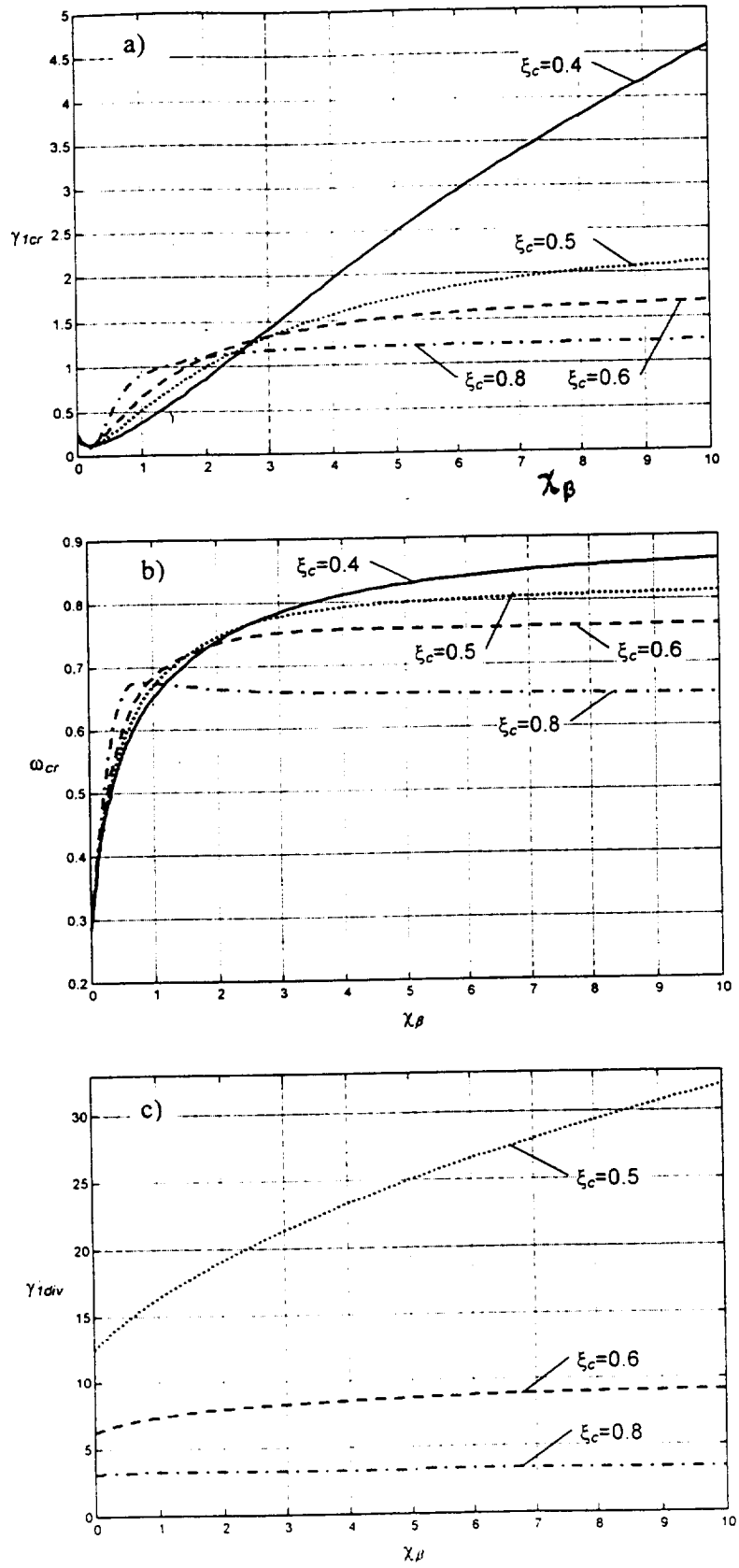

Fig. 3. Stability boundaries for $e_f = 0.1$

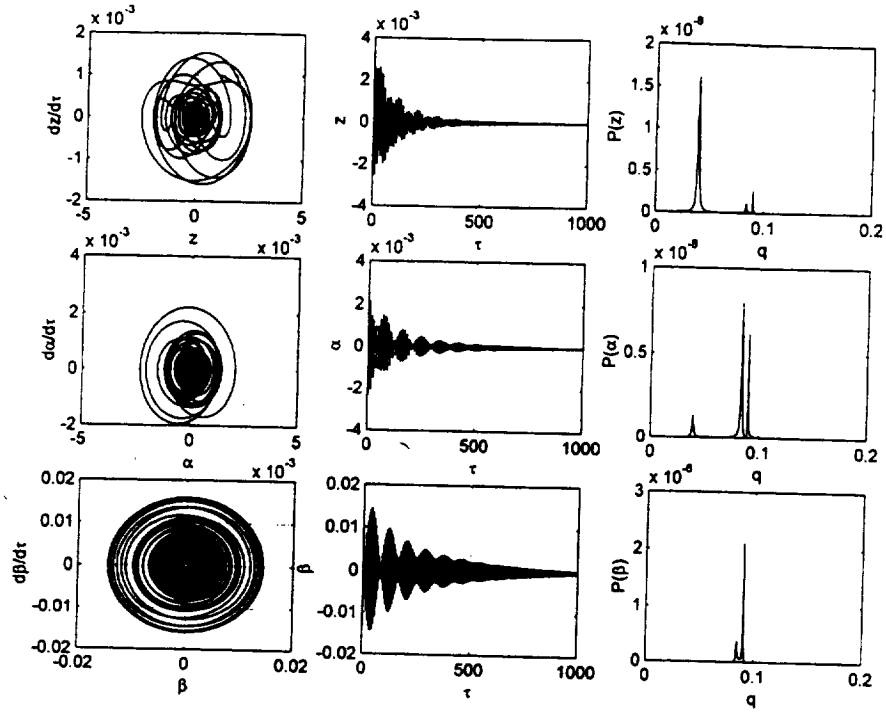

Fig. 4. Airfoil vibrations for ξ_c=0.4
(χ_β=0.9; γ_1=1.7; δ=0.1; e_f=0; k_{z1}=0; $k_{\alpha 1}$=$k_{\beta 1}$=20)

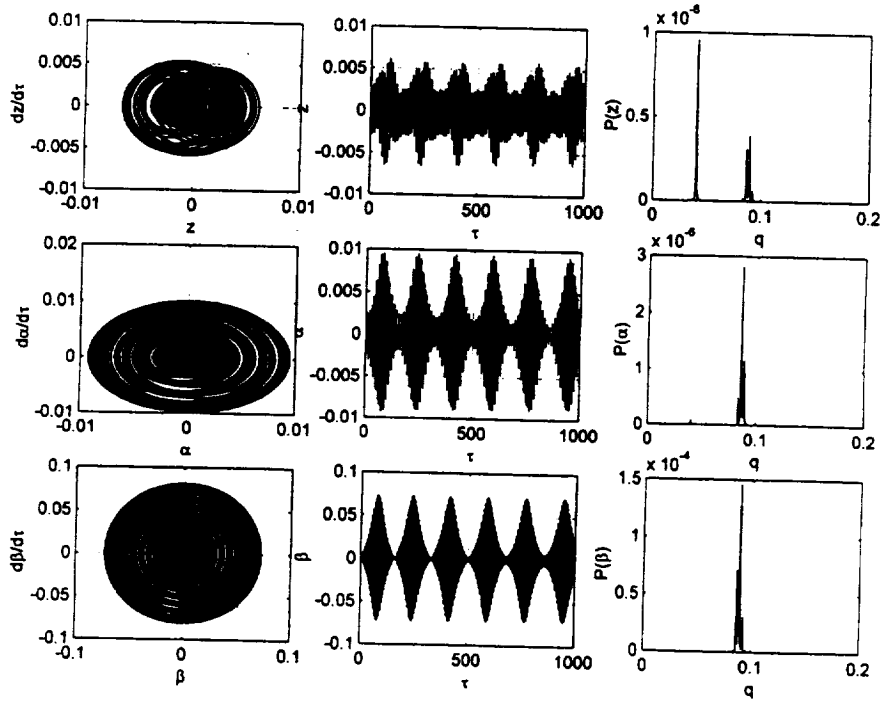

Fig. 5. Airfoil vibrations for ξ_c=0.4
(χ_β=0.9; γ_1=2.0; δ=0.001; e_f=0; k_{z1}=0; $k_{\alpha 1}$=$k_{\beta 1}$=20)

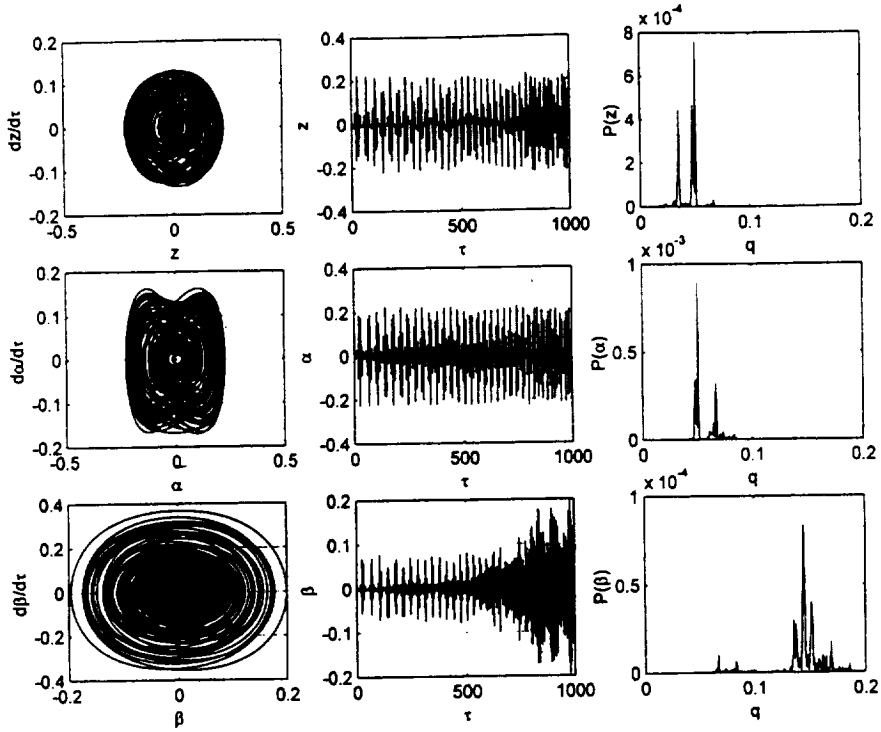

Fig. 6. Airfoil vibrations without free-play for ξ_c=0.8
(χ_β=2.0; γ_1=2.0; δ=0.001; e_f=0; k_{z1}=0; $k_{\alpha 1}$=$k_{\beta 1}$=20)

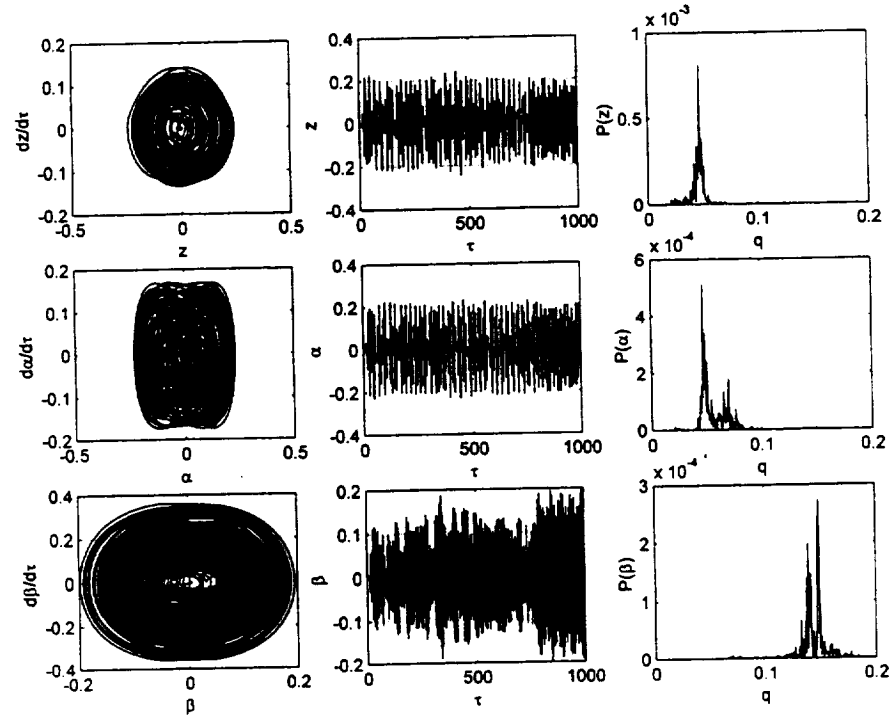

Fig. 7. Airfoil vibrations with free-play for ξ_c=0.8
(χ_β=2.0; γ_1=2.0; δ=0.001; e_f=0; k_{z1}=0; $k_{\alpha 1}$=$k_{\beta 1}$=20)

In Figs.6 and 7 chaotic limit cycle vibrations are shown for $\xi_\alpha = 0{,}8$; $\chi_\beta = \gamma_1 = 2{,}0$, without free-play (Fig.6) and with free-play (Fig.7).

It can be seen that near flutter limit γ_{1cr} regular quasi-periodic motions occur (Fig.5) and for greater values of γ_1 chaotic motions are developing. The most developed chaotic motion can be seen for back position of the elastic axis and free-play flap deflection (Fig.7).

References

1. J. W. Miles, The Potential Theory of Unsteady Supersonic Flow, Cambridge, University Press, 1959.

2. Y. C. Fung, An Introduction to the Theory of Aeroelasticity, John Wiley and Sons, New York 1955.

3. R. L. Bisplinghoff and H. Ashley, Principles of Aeroelasticity, Ed. John Wiley and Sons, New York London, 1962.

4. B. Gajl, Pressure acting on the oscillating surface of an airfoil in nonlinear supersonic potential flow, Proc. of Vibr. Probl., v.9, No.1, 1968.

5. J. Guckenheimer and P. Holmes, Nonlinear Oscillations, Dynamical Systems, and Bifurcations of Vector Fields, Ed. Springer-Verlag, New York Berlin, 1983.

6. L. C. Zhao and Z. C. Yang, Chaotic motions of an airfoil with non-linear stiffness in incompressible flow, Journal of Sound and Vibration, v.138, No 2, 1990.

7. S. J. Price, B. H. K. Lee and H. Alighanbari, Post - instability behavior of a two-dimensional airfoil with a structural nonlinearity, Journal of Aircraft, v.31, No 6, 1994.

8. K. Y. Fung and T. H. Shieh, Modeling, analysis and prediction of flutter at transonic speeds, AIAA Journal, v.31, No.1, 1993.

9. Z. Dżygadło, I. Nowotarski and A. Olejnik, Nonlinear regular and chaotic flutter of an airfoil in supersonic flow, International Forum on Aeroelasticity and Structural Dynamics, 17-20 June, 1997, vol.III, Rome, Italy.

CORRELATION OF FIN BUFFET PRESSURES ON AN F/A-18 WITH SCALED WIND-TUNNEL MEASUREMENTS

Robert W. Moses
Aeroelasticity Branch
NASA Langley Research Center
Hampton, VA

Gautam H. Shah
Vehicle Dynamics Branch
NASA Langley Research Center
Hampton, VA

Abstract

Buffeting is an aeroelastic phenomenon occurring at high angles of attack that plagues high performance aircraft, especially those with twin vertical tails. Previous wind-tunnel and flight tests were conducted to characterize the buffet loads on the vertical tails by measuring surface pressures, bending moments, and accelerations. Following these tests, buffeting responses were computed using the measured buffet pressures and compared to the measured buffeting responses. The calculated results did not match the measured data because the assumed spatial correlation of the buffet pressures was not correct. A better understanding of the partial (spatial) correlation of the differential buffet pressures on the tail was necessary to improve the buffeting predictions. Several wind-tunnel investigations were conducted for this purpose. When compared, the results of these tests show that the partial correlation scales with flight conditions. One of the remaining questions is whether the wind-tunnel data is consistent with flight data. Presented herein, cross-spectra and coherence functions calculated from pressures that were measured on the High Alpha Research Vehicle (HARV) indicate that the partial correlation of the buffet pressures in flight agrees with the partial correlation observed in the wind tunnel.

Background

For high performance aircraft at high angles of attack, vortices emanating from wing/fuselage leading edge extensions (LEX) burst at some flight conditions, immersing the vertical tails in their wake, as shown in Figure 1 for the F/A-18. The resulting buffeting of the vertical tails are a concern from airframe fatigue and maintenance points of view. A summary of previous wind-tunnel[1-8] and flight tests [2, 5, 13] conducted to quantify fin buffet on the F/A-18 follows.

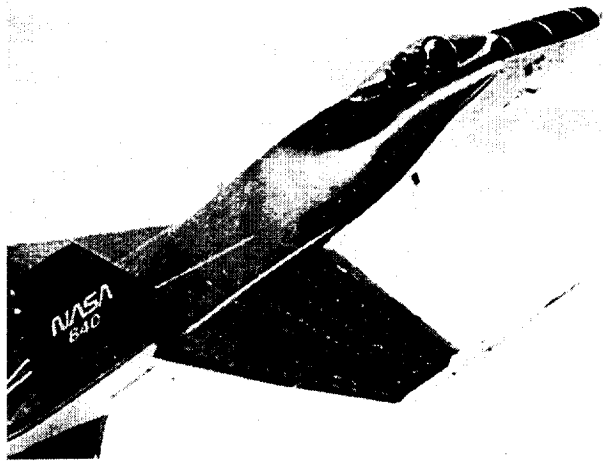

Figure 1. Flow Visualization of Leading Edge Extension (LEX) Vortex Burst, 30 Degrees Angle of Attack

Industry Test

The spectral nature of the unsteady differential (inboard surface minus outboard surface) pressures on the F/A-18 vertical tail caused by a burst LEX vortex are well documented[1]. As illustrated in Reference 1, the power spectral densities and root mean square (rms) values of the differential pressures vary with flight speed, angle of attack (AOA), dynamic pressure, and tail position. The worst case buffet condition, defined by the highest rms values of differential pressure at design limit load, occurs on the F/A-18 aircraft at a dynamic pressure of 340 pounds per square foot (psf) and 32 degrees angle of attack. Other findings of Reference 1 were that the rms value of the differential pressure varies linearly with dynamic pressure, and that Strouhal (proportional

to reduced frequency) scaling provides a means for comparing model and flight spectral data. Also, the highest rms values of differential pressure occur at stations closest to the leading edge while the lowest rms values occur near the trailing edge with a gradual change in rms values between these two regions of the tail. Another conclusion from this investigation was that the unsteady differential pressures were considered fully correlated (spatially in phase) since the pressures measured at five stations did not indicate a significant phase shift.

Canadian Measurements

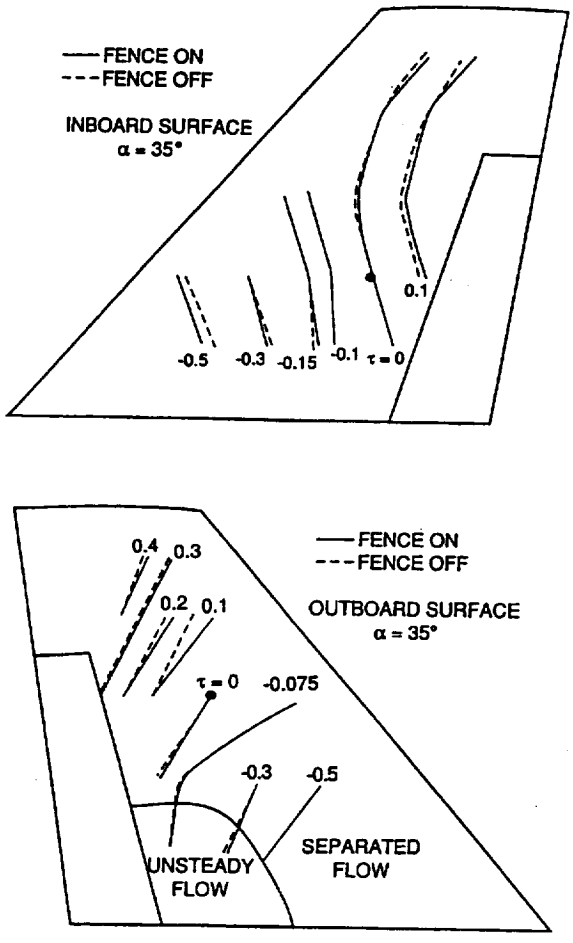

Figure 2. Peak Correlation Contours (msec) of the Fin Unsteady Pressure Signals, Starboard-Side Rigid Tail, 6% F/A-18 Model, M=0.6, 35 Degrees AOA (From Reference 2)

After the research of Reference 1, wind-tunnel tests of a 6% rigid F/A-18 model were conducted to investigate the spatial characteristics of the unsteady surface pressures on the tail[2]. Contour plots of the time delays of the unsteady pressures on each surface at Mach 0.6 were constructed using cross-correlation analyses of the measured unsteady pressures. As shown in Figure 2 for the two surfaces of the starboard-side fin, the contours above mid-span for inboard and outboard surfaces are quite different. It is in this region that the differential pressures contribute most to buffeting due to their distance from the root attachment at the fuselage. Therefore, the spatial characteristics of the unsteady differential pressures that contribute most to buffeting are unclear.

Prior Buffeting Predictions

Because of the perceived complexity in transcribing partially-correlated unsteady pressures into the analyses of buffet and buffeting, the differential pressures on the tail have been assumed to be in phase (fully correlated) at any given time[3-5]. These analyses do not estimate the buffet loads accurately, and it was concluded that an understanding of the spatial correlation of the pressures is a key to successful buffet load prediction and should be the subject of more research.

Full-Scale Wind-Tunnel Test

To learn more about the spatial correlation, a full-scale F/A-18 was tested in a wind tunnel [6-9] at high angles of attack at a maximum speed of M=0.15. Plots of the magnitudes and phase delays of the unsteady differential pressures at two stream-wise stations were constructed using cross-spectral analyses of the unsteady pressures measured on each tail surface at two different angles of attack (20 degrees and 32 degrees). The results shown in Figure 3a and 3b represent, respectively, harmless and worst case buffet conditions for the F/A-18. As shown in the Figures, the phase steadily decreases with increasing frequency. This trend is consistent for both angles of attack and indicates that the differential pressures acting on the tail are not in phase and therefore are not fully correlated.

However, the relationship of flight conditions on pressure correlation was not clearly understood from these results. Therefore, scaled model tests [8, 10-12] were conducted in the Transonic Dynamics Tunnel (TDT) where this relationship was determined, as summarized below.

The purpose of this paper is to evaluate whether the spatial correlation of the buffet pressures on an F/A-18 fin in flight agrees with the spatial correlation observed on a 1/6-scale F/A-18 fin in the TDT.

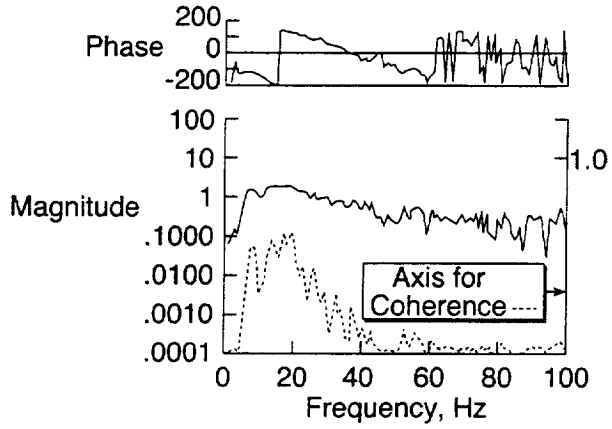

a) 20 Degrees AOA

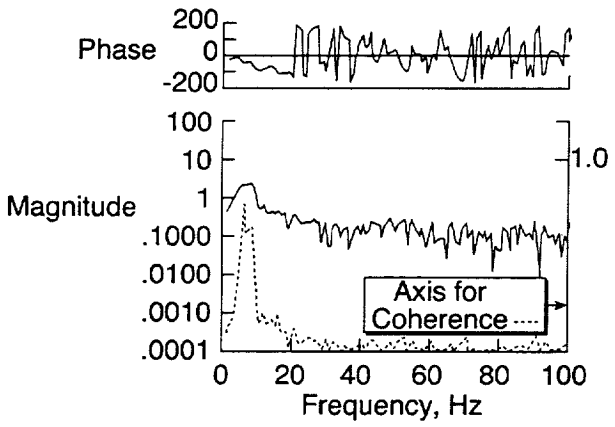

b) 32 Degrees AOA

Figure 3. Cross-Spectral Density and Coherence Functions Between the Differential Pressures Near the Leading-Edge Tip and the Trailing-Edge Tip, Full-Scale Tail, M=0.15, (From Reference 6)

Scaled Wind-Tunnel Measurements

Figure 4. 1/6-Scale F/A-18 Model Mounted in the Transonic Dynamics Tunnel

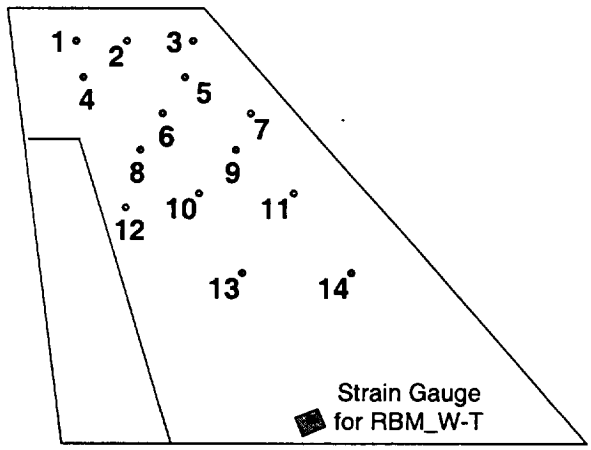

Figure 5. Pressure Transducer Stations, 1/6-Scale Flexible Tail

To better understand the pressure correlation during buffet, an available 1/6-scale, sting-mounted, F-18 wind-tunnel model, shown in Figure 4, was modified and tested in the Transonic Dynamics Tunnel (TDT) at the NASA Langley Research Center as part of the ACROBAT (Actively Controlled Response Of Buffet-Affected Tails) program[8]. Surface pressures were measured for scaled flight conditions at high angles of attack on rigid and flexible tails. Using the transducer spread shown in Figure 5, cross-correlation and cross-spectral analyses[9] were

performed for identifying any consistent spatial characteristics of the unsteady differential pressures.

Cross-correlation and cross-spectral density (CSD) functions of the unsteady differential pressures on the flexible tail are shown in Figures 6 and 7, respectively, and compared to results of References 2 and 6, shown in Figures 2 and 3, respectively [10-12]. These comparisons show that the time and phase delays of the unsteady differential pressures scale with wind-tunnel speed. In fact, the unsteady differential pressures were found to resemble waves that move along the tail, as indicated by the non-zero time delays. So, one remaining question was the correlation of the wind-tunnel data with flight measurements.

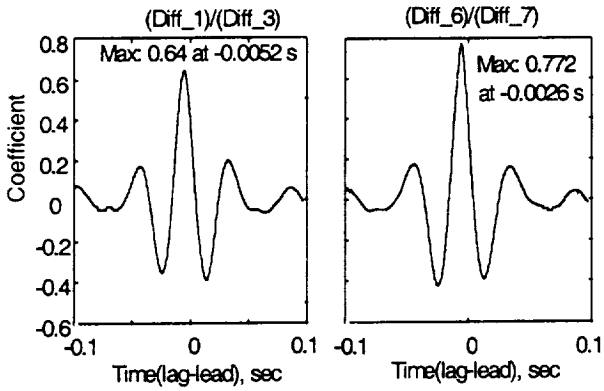

a) Near Tip and 75% Span

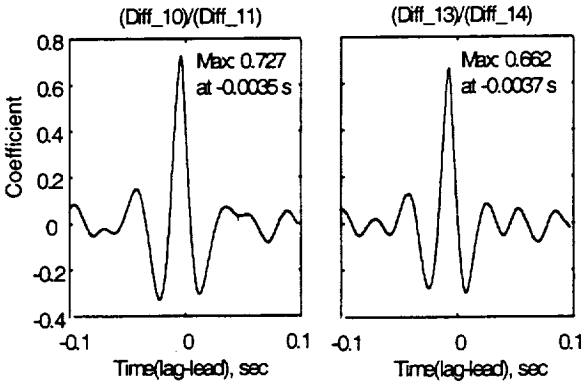

b) Near 60% and 40% Span

Figure 6. Cross-Correlation Functions Between Differential Pressures at Stations on Flexible Tail, 1/6-Scale F/A-18 Model, 34 Degrees AOA

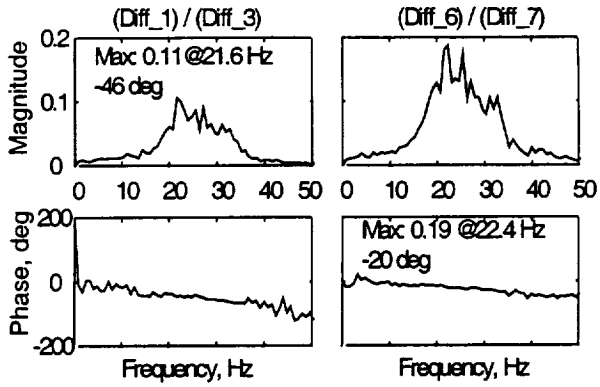

a) Near Tip and 75% Span

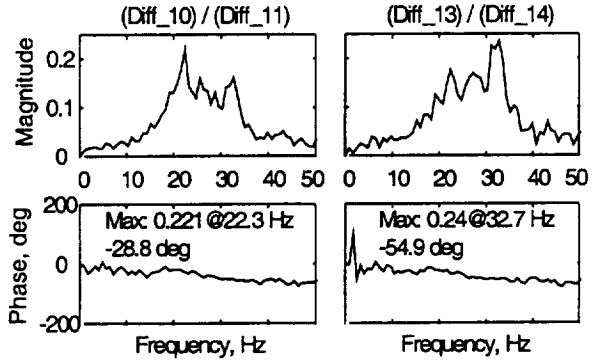

b) Near 60% and 40% Span

Figure 7. CSD Functions Between Differential Pressures at Stations on Flexible Tail, 1/6-Scale F/A-18 Model, 34 Degrees AOA

Flight Test Results

Pressures on the surfaces of the starboard vertical tail of the HARV, shown in Figure 1, were measured at various flight conditions using a sampling rate of 320 Hz. Referring to the HARV fin shown in Figure 8, the even numbers represent pressure transducers on the shown surface (notation KS) while the odd numbers represent transducers on the hidden surface (notation KP). Therefore, the differential pressure computed for the station located at 85% span and 90% chord would be designated "KP31-KS32". This notation is used consistently herein for reporting the differential pressures on the HARV fin.

CSD functions of the unsteady differential pressures at Mach 0.3 and 30 degrees angle of attack were computed from the digitized time histories of 43 seconds in length using a block size of 2048 with 75% overlapping and a rectangular window.

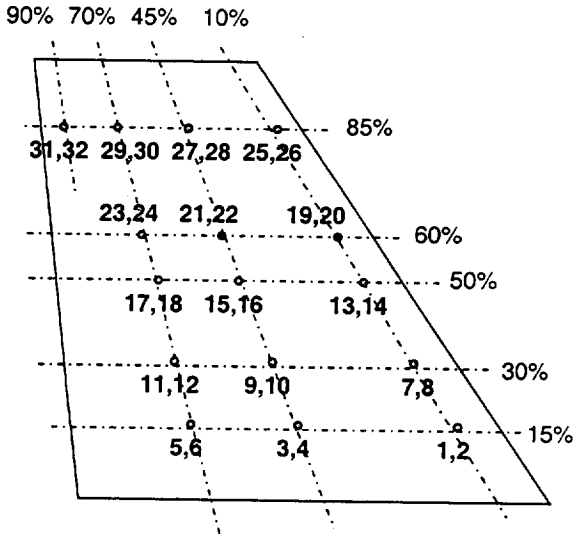

Figure 8. Location of Pressure Transducer on Starboard Vertical Tail, HARV

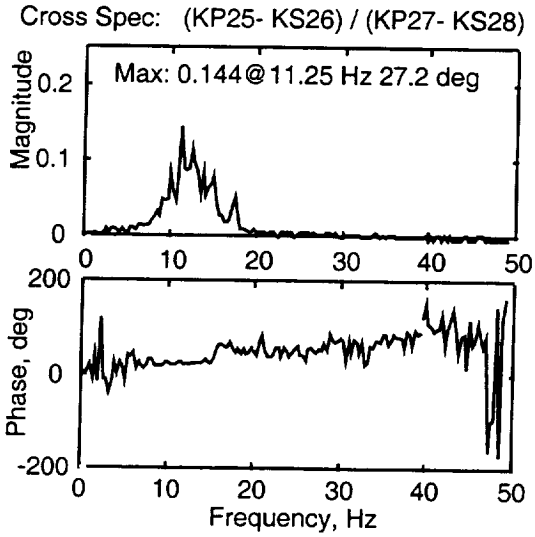

Figure 9a. CSD Function Between Differential Pressures, Station KP25-KS26 with Respect to KP27-KS28, on HARV, Mach 0.3, 30 Degrees AOA, LEX Fence Off

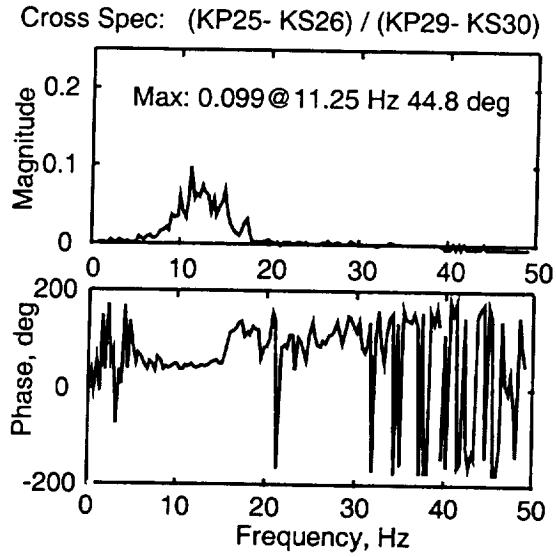

Figure 9b. CSD Function Between Differential Pressures, Station KP25-KS26 with Respect to KP29-KS30, on HARV, Mach 0.3, 30 Degrees AOA, LEX Fence Off

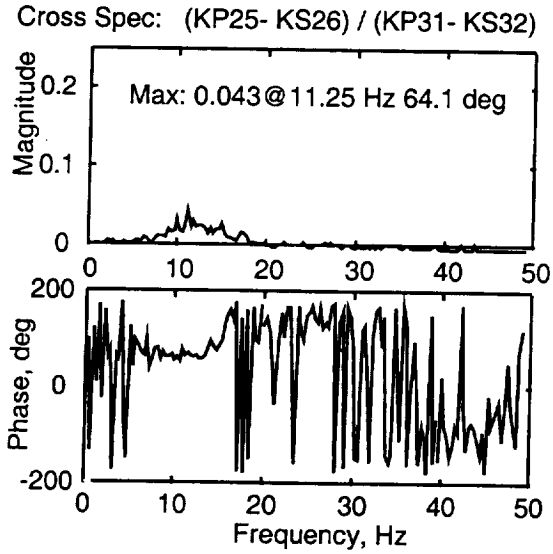

Figure 9c. CSD Function Between Differential Pressures, Station KP25-KS26 with Respect to KP31-KS32, on HARV, Mach 0.3, 30 Degrees AOA, LEX Fence Off

The magnitude and phase of the CSD functions, plotted in Figure 9, illustrate the spatial features of the differential pressures along the 85% span line. Based on the location of the peak magnitude in the upper plots in Figures 9a, 9b and 9c, the dominant

frequency component of the buffet pressures at these locations is approximately 11.25 Hz. In fact, the overall shape of the curve shown in all three magnitude plots are quite similar except for the relative scale in the vertical direction. The magnitudes of the CSD functions decrease with increase in distance between stations moving aft. This effect is expected since the rms of the differential pressures is generally highest at the stations near the leading edge and generally lowest near the stations near the trailing edge.

The value of phase between stations is conversely affected by distance. As shown in Figure 9, the value of the phase at the dominant frequency of 11.25 Hz is different in each of the lower plots. For instance, in Figure 9a, the phase at 11.25 Hz is approximately 27 degrees while, in Figure 9b, the phase is approximately 45 degrees, and while in Figure 9c, the phase is approximately 64 degrees. With reference to the 85% span-line in Figure 8, the pressure wave, represented by the CSD in Figure 9a, traveled 35% of the chord while the pressure wave, represented by the CSD in Figure 9b, traveled 60% of the chord length. Therefore, the phase increases with increases in distance between stations. Furthermore, this relationship appears to be linear.

As a check of linearity, the phase, shown in Figure 9a, is computed for the pair of differential pressure transducers KP25-KS26 and KP27-KS28 which are 1.54 feet apart. At 30 degrees AOA, the velocity of the streamlines in the vicinity of the tail will be less than the flight speed of Mach 0.3 (330 feet per second). In Reference 12, the velocity near the tail is shown to be approximately 70% of the free stream value. Therefore, using Equation 1, where "f" is the frequency of interest (11.25 Hz in this case), "d" is the distance between stations, and "U" is the velocity of the streamline near the 85% span line, the phase at 11.25 Hz is computed as 27 degrees, which agrees well with the value shown in Figure 9a. Similarly, the phase may be computed for other pressure transducer pairs. Equation 1 may be simplified further by introducing the Strouhal number, defined by Equation 2, and canceling like terms, to yield Equation 3.

$$\phi(\text{rad}) = \omega \cdot t = 2\pi f \cdot \frac{d}{U} \qquad (1)$$

$$n = \frac{f\,d}{U} \qquad (2)$$

$$\phi\,(\text{deg}) = \phi\,(\text{rad}) \cdot \frac{180}{\pi} = 360\,n \qquad (3)$$

Since dispersion (break down of eddies into higher harmonics) and dissipation (energy loss) are expected in this highly turbulent flow near the tail, the pressure wave is expected to deform as it travels along the tail[12]. Therefore, the magnitude of the partial correlation of the differential pressures at two stations is expected to drop as the distance between these two pressure stations increases. The coherence function provides a tool for assessing this drop in correlation. In Figure 10, coherence functions are computed, with respect to KP25-KS26, for the differential pressures at selected stations along the 85% span line for Mach 0.3, 30 degrees AOA.

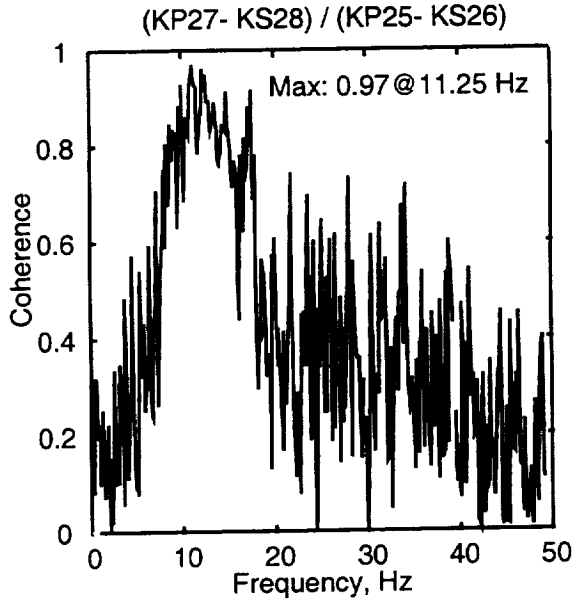

Figure 10a. Coherence Function Between Differential Pressures on HARV, Along 85% Span Line, Station KP27-KS28 with Respect to KP25-KS26, Mach 0.3, 30 Degrees AOA, LEX Fence Off

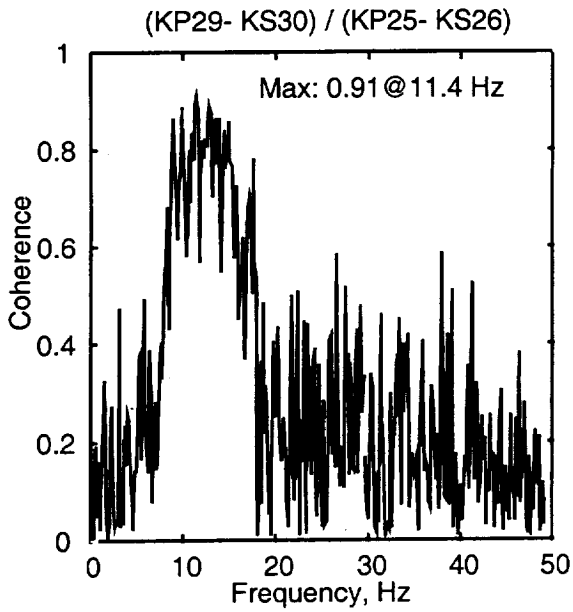

Figure 10b. Coherence Function Between Differential Pressures on HARV, Along 85% Span Line, Station KP29-KS30 with Respect to KP25-KS26, Mach 0.3, 30 Degrees AOA, LEX Fence Off

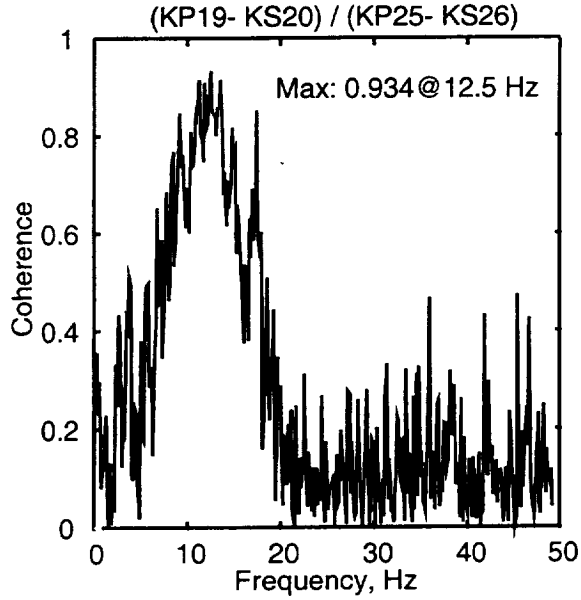

Figure 11a. Coherence Function Between Differential Pressures on HARV, Along 10% Chord Line, Station KP19-KS20 with Respect to KP25-KS26, Mach 0.3, 30 Degrees AOA, LEX Fence Off

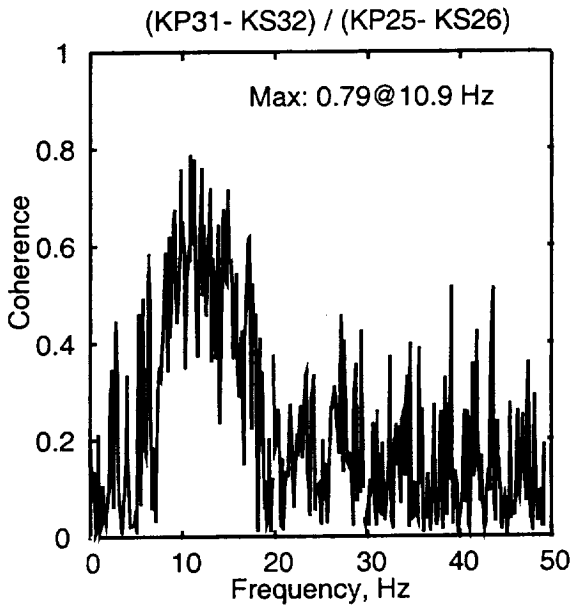

Figure 10c. Coherence Function Between Differential Pressures on HARV, Along 85% Span Line, Station KP31-KS32 with Respect to KP25-KS26, Mach 0.3, 30 Degrees AOA, LEX Fence Off

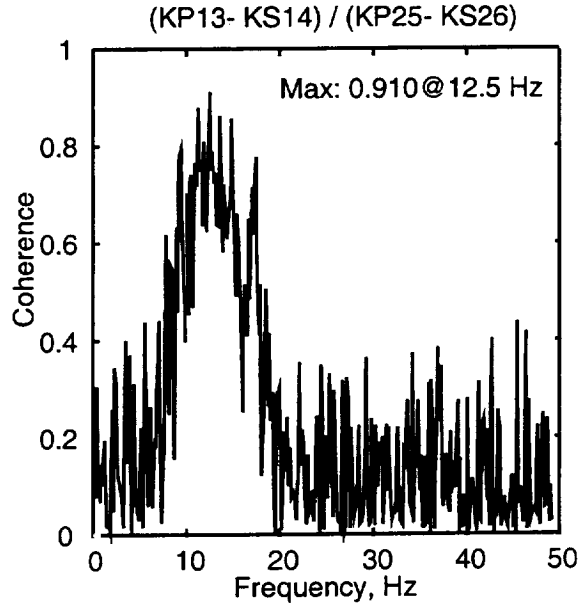

Figure 11b. Coherence Function Between Differential Pressures on HARV, Along 10% Chord Line, Station KP13-KS14 with Respect to KP25-KS26, Mach 0.3, 30 Degrees AOA, LEX Fence Off

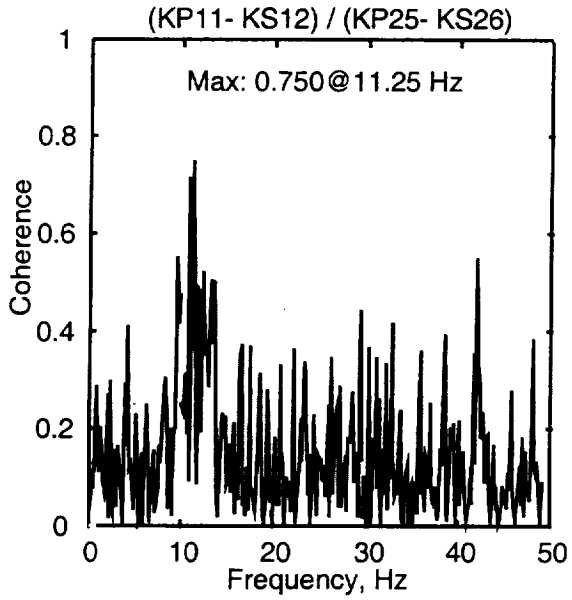

Figure 12. Coherence Function Between Differential Pressures on HARV, Well Separated Stations, Station KP11-KS12 with Respect to KP25-KS26, Mach 0.3, 30 Degrees AOA, LEX Fence Off

In Figure 10a, the maximum value of the coherence is 0.97 (out of a possible 1.0) at 11.25 Hz, the dominant frequency in the pressure wave form. The values of the coherence for other frequency components in the pressure wave are less than 0.97. This feature indicates that some dispersion of the frequency components is occurring as the wave moves along the tail. For instance, if the values of the coherence for all frequency components are unity, then no dispersion occurs in the wave as it moves along the tail. Conversely, if the values of the coherence for all frequency components get smaller as the distance between stations increases, then all frequency components in the wave are dispersing as a function of distance. The latter case is the nature of the unsteady differential pressures that occur on the vertical tails during buffet caused by LEX vortex burst.

As the pressure wave moves aft along the 85% span line, the maximum value in the coherence function falls from 0.97, shown in Figure 10a, to 0.91, shown in Figure 10b, to 0.79, shown in Figure 10c. Therefore, some dispersion and possibly some dissipation are occurring along a chord line. For the 10% chord line, the maximum value in the coherence functions are 0.934, shown in Figure 11a, and 0.91, shown in Figure 11b. Therefore, more dispersion occurs along a constant span line than along a constant chord line. The smallest maximum values of the coherence functions occur for stations that are farthest apart, as seen in Figure 12, where the maximum value is 0.75. Therefore, the worst coherence occurs between the most separated stations.

Comparison of Flight Results With Scaled Wind-Tunnel Results

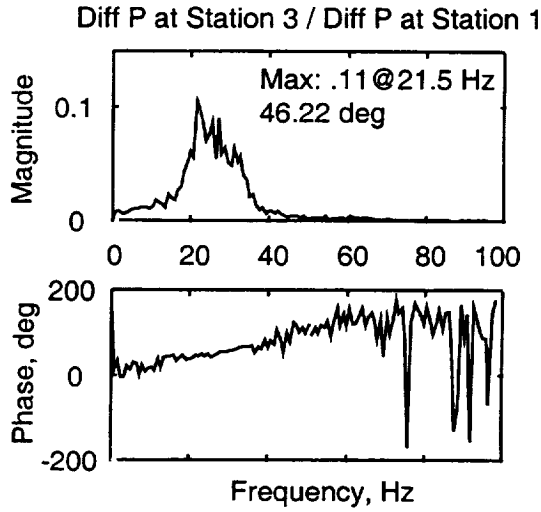

Figure 13. Cross-Spectral Density Function Between Differential Pressures, 1/6-Scale F/A-18 Model, Along Constant Span Line, Station 3 with Respect to Station 1, Mach 0.6 (Simulated), 34 Degrees AOA

Based on Strouhal scaling, the CSD functions, shown in Figure 7, that were computed for pressures measured in the TDT on a 1/6-scale F/A-18 vertical tail at Mach 0.1 (110 feet per second) at 34 degrees AOA, are representative of an F/A-18 at Mach 0.6 (660 feet per second) at 34 degrees AOA. Shown in Equation 1, a doubling of flight speed will reduce the phase shift by 50%, and from Reference 1, a doubling of the flight

speed will also double the frequency value at which the peak magnitude of the CSD occurs. This latter effect can be seen also in Equation 2 when maintaining a constant value of n. Therefore, since the two effects cancel each other in this case, a direct comparison of the phase value at the peak magnitude of the CSD function is possible between wind-tunnel results for the 1/6-scale F/A-18 model and the results of the HARV at Mach 0.3.

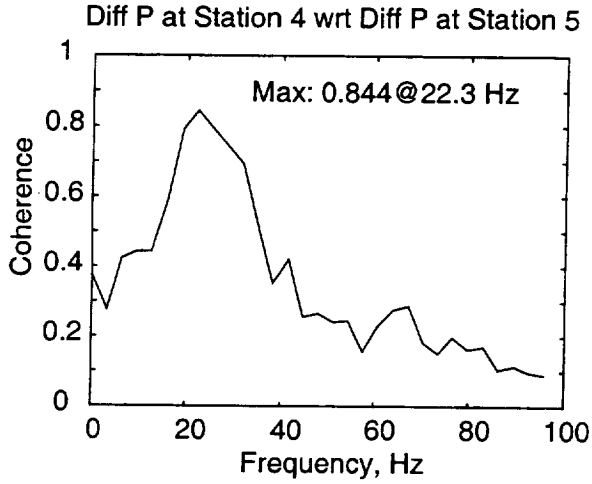

Figure 14. Coherence Function Between Differential Pressures, 1/6-Scale F/A-18 Model, Station 4 with Respect to Station 5, Mach 0.6 (Simulated), 34 Degrees AOA

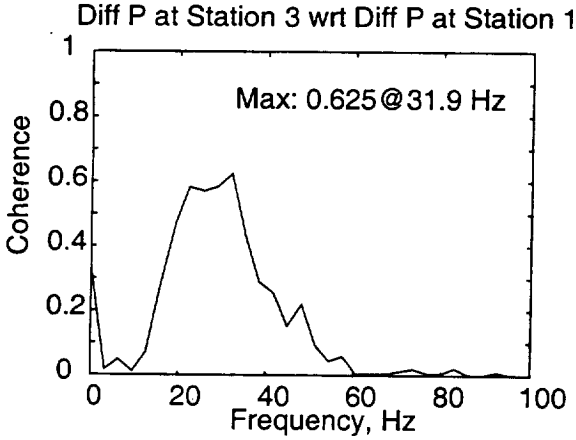

Figure 15. Coherence Function Between Differential Pressures, 1/6-Scale F/A-18 Model, Station 3 with Respect to Station 13, Mach 0.6 (Simulated), 34 Degrees AOA

In Figure 13, the CSD plot shows that the phase between the differential pressure at Station 3 with respect to Station 1 on the 1/6-scale F/A-18 vertical tail at 34 degrees AOA is approximately 46 degrees. For similar conditions and stations on the HARV, the phase is approximately 45 degrees, as shown in Figure 9b.

Coherence functions were computed for selected stations on the 1/6-scale F/A-18 flexible vertical tail for comparing coherence functions computed for the HARV. Shown in Figure 14, the maximum value of the coherence function between stations 4 and 5 on the 1/6-scale F/A-18 vertical tail (see Figure 5) is 0.844. This value of 0.844 agrees well with the values of the coherence functions, shown in Figures 10b (0.91) and 10c (0.79), for similar stations on the HARV vertical tail (see Figure 8). For an additional comparison, the coherence function between two of the most separated stations on the 1/6-scale F/A-18 flexible vertical tail was computed, as shown in Figure 15. The maximum value of the coherence between stations 3 and 13 on the 1/6-scale F/A-18 vertical tail (see Figure 5) is 0.625. This value is less than but not too different from the maximum value of 0.75 for the coherence function, shown in Figure 12, between stations that are similarly separated in terms of percent chord and percent span. Therefore, the level of dispersion occurring on the fins of the 1/6-scale model and the HARV agree well.

Conclusions

CSD and coherence functions were presented for indicating the partial (spatial) correlation that occurs on the vertical tail of the F/A-18 configuration during LEX vortex burst. The unsteady buffet pressures that are caused by LEX vortex burst during high angle of attack maneuvers on the F/A-18 (HARV) are not fully correlated as previously assumed. In fact, the local Strouhal number may be used to relate the phase shift of the unsteady buffet pressures among stations on the vertical tail.

The magnitude of the CSD functions presented herein indicates that the vortex disturbance

reduces as it travels along the tail. In agreement with this finding, the magnitudes of the coherence functions illustrate that the correlation of the unsteady pressures is affected by the distance between the stations. One issue that surfaces from this finding is the role, if any, that the vertical tail plays in affecting the spatial correlation and dispersion of the unsteady buffet pressures.

As shown herein, the results presented for the HARV agree well with the partial correlation of the buffet differential pressures measured on a 1/6-scale F/A-18 model tested in the TDT. Comparisons between the 1/6-scale F/A-18 data and the F/A-18 (HARV) data consistently illustrate the partial correlation of the differential pressures that occur on the vertical tail during LEX vortex burst at high angles of attack.

Acknowledgments

Gratitude is extended to the test crews that conducted the investigations and reduced the pressure data to useable format: NASA Dryden Flight Center, NASA Langley Research Center, and the Air Force Research Laboratory; and to Ms. Sherwood Hoadley and Ms. Carol Wieseman for the computational and plotting software.

References

1 Zimmerman, N. H., and Ferman, M. A., "Prediction of Tail Buffet Loads for Design Application," Vols. I and II, Rept. No. NADC-88043-60, July 1987.

2 Lee, B., Brown, D., Zgela, M., and Poirel, D., "Wind Tunnel Investigation and Flight Tests of Tail Buffet on the CF-18 Aircraft", in Aircraft Dynamic Loads Due to Flow Separation, AGARD-CP-483, NATO Advisory Group for Aerospace Research and Development, Sorrento, Italy, April 1990.

3 Lee, B. and Tang, F. C., "Unsteady Pressure and Load Measurements on an F/A-18 Vertical Fin at High-Angles-of-Attack," AIAA-92-2675-CP, 10th Applied Aerodynamics Conference, Palo Alto, CA, June 22-24, 1992.

4 James, K. D. and Meyn, L. A., "Dependence on Integrated Vertical-Tail Buffet Loads for F/A-18 on Sensor Density," SAE Technical Paper 94110, Aerospace Atlantic Conference and Exposition, Dayton, Ohio, April 18-22, 1994.

5 Bean, D. E. and Lee, B., "Correlation of Wind Tunnel and Flight Test Data for F/A-18 Vertical Tail Buffet," AIAA-94-1800-CP, 12th AIAA Applied Aerodynamics Conference, Colorado Springs, CO, June 20-22, 1994.

6 Pettit, C. L., Banford, M., Brown, D., and Pendleton, E., "Pressure Measurements on an F/A-18 Twin Vertical Tail in Buffeting Flow," Vols 1-4, United States Air Force Wright Laboratory, TM-94-3039, August 1994.

7 Meyn, L. A. and James, K. D., "Full-Scale Wind-Tunnel Studies of F/A-18 Tail Buffet," Journal of Aircraft, Vol. 33, No. 3, May-June 1996.

8 Moses, R. W., "Active Vertical Tail Buffeting Alleviation on a Twin-Tail Fighter Configuration in a Wind Tunnel," presented at the CEAS International Forum on Aeroelasticity and Structural Dynamics 1997, 17-20 June 1997, Rome, Italy.

9 Bendat, J. S. and Piersol, A. G., Engineering Applications of Correlation and Spectral Analysis, Second Edition, John Wiley & Sons, Inc., 1993.

10 Moses, R. W. and Pendleton, E., "A Comparison of Pressure Measurements Between a Full-Scale and a 1/6-Scale F/A-18 Twin Tail During Buffet," AGARD Report 815, p. 6-1 to p. 6-12, Florence, Italy, September 4-5, 1996.

11 Moses, R. W. and Ashley, H., "Spatial Characteristics of the Unsteady Differential Pressures on 16% F/A-18 Vertical Tails," AIAA 98-0519, 36th AIAA Aerospace Sciences Meeting and Exhibit, Reno, Nevada, January 12-15, 1998.

12 Moses, Robert W., "Spatial Characteristics of the Unsteady Differential Pressures on Vertical Tails of a Twin-Tailed Aircraft at High Angles of Attack with an Emphasis on

Buffeting Alleviation," Ph.D. Dissertation, Stanford University, August 1997.

13 Moses, R. and Shah, G., "Spatial Characteristics of F/A-18 Vertical Tail Buffet Pressures Measured in Flight," AIAA-98-1956, 39th AIAA/ASME/ASCE/AHS/ASC Structures, Structural Dynamics, and Materials Conference and Exhibit, Long Beach, CA, 20-23 April 1998.

TWIN-TAIL BUFFET SIMULATION USING A MULTI-DISCIPLINARY COMPUTING ENVIRONMENT (MDICE)

Essam F. Sheta, John M. Siegel, Jr., Freddy N. Golos and Vincent J. Harrand
CFD Research Corporation, Huntsville, AL 35805

ABSTRACT

The current paper presents a state-of-the-art approach for performing efficient multi-disciplinary simulations. A Multi-Disciplinary Computing Environment (MDICE) is presented and validated with a twin-tail buffet simulation of a generic fighter aircraft. MDICE is an object-oriented computing environment which allows several analysis modules to run and communicate with each other over a distributed network of computers. In a buffet condition, the leading-edge vortices of a delta wing break down producing an unsteady turbulent flow which empennages on the surfaces of the tails, causing severe premature structural fatigue. The application of MDICE to the twin-tail buffet problem involves four types of modular functionality: a fluid-dynamics module, a fluid-structure interfacing technique, a structural dynamics module, and grid motion technique. The configuration model is pitched at a wide range of angles of attack at Mach and Reynolds numbers of 0.4 and 1.25 million, respectively. The computational results are in very good agreement with the experimental data.

INTRODUCTION

The Multi-Disciplinary Computing Environment (MDICE) has been developed by CFD Research Corporation in collaboration with AFRL and NASA Glenn Research Center. MDICE provides an environment in which several engineering analysis programs run concurrently and cooperatively to perform a multi-disciplinary design, analysis, or optimization problem. Using MDICE, engineers are able to couple inherently dissimilar disciplines and programs from a variety of sources, performing distinct tasks such as geometry modeling, grid generation, CFD-structural analysis, controls, and post processing into a single software system. Besides CFDRC's own engineering analysis codes, a large number of commercial, US Government and public domain codes have already been integrated into the MDICE environment. Examples of the third party codes are Pro-Engineer, Unigraphics, CATIA, MSC-NASTRAN, Cobalt (AFRL), NPARC (NASA LeRC), ADPAC (NASA LeRC), Splitflow (Lockheed Martin), GCNS (Northrop Grumman), etc. An MDICE developers toolkit is available so that the end user can easily include his own application modules with this environment. For more information, see http://www.cfdrc.com, select 'Products', then select 'MDICE'.

The current paper presents a state-of-the-art multi-disciplinary application of MDICE to the twin-tail buffet problem of fighter aircraft. These fighter aircraft maneuver at high angle of attack causing the flow to separate from the sharp leading edges of the wing or leading-edge extension (LEX), as the case of F/A-18 fighter. At some flight conditions, the leading-edge vortices break down before reaching the vertical twin tail which get bathed in a wake of highly turbulent, swirling flow. The vortex-breakdown flow produces unsteady, unbalanced loads on the vertical tails. This, in turn, produces severe buffet on the tails and has led to their premature fatigue failure.

Several experimental investigations have been conducted to examine various aspects of this phenomenon [1-4]. These experiments showed

that the vortical flow breaks down ahead of the vertical tails at angles of attack of 25° and higher. The buffet responses occur in the first bending mode, increases with increasing dynamic pressure and is larger at M=0.3 than at higher Mach numbers. Washburn et al [5] conducted an extensive experimental investigation of the problem. They showed that the aerodynamic loads were more sensitive to the chordwise tail location than its spanwise location. As the tails were moved laterally toward the vortex core, the buffeting response and excitation were reduced. Recently, Moses and Ashley [6] conducted an extensive wind tunnel tests on a refurbished 16%, rigid, full-span model of the F/A-18 A/B aircraft with three flexible and two rigid vertical tails. These tests have shown that the time and phase lags of the unsteady pressure differentials are functions of the distance between the measuring stations and the transport velocity, and tail flexibility does not appear to affect the time or phase delays of the unsteady differential pressures.

Kandil, Sheta and Massey [7] studied the buffet response of twin-tail model in turbulent flow over wide range of angles of attack. The computational results were in good quantitative agreement with the experimental data of Washburn et al. [5]. Recently, Sheta, Kandil and Yang [8] studied the effect of tangential leading-edge blowing (TLEB) and flow suction from the vortex cores along the vortex path (FSVC) on twin-tail buffet alleviation. The investigation concluded that FSVC in position with large volumetric flow rate provided the best buffet control. In a very recent paper by Sheta and Kandil [9], the effects of dynamic rolling maneuvers of the configuration model on twin tail buffet response were investigated. The model was forced to roll dynamically around the symmetry axis by a constant amplitude of 4° and reduced frequency of π and 2π. The unsteady aerodynamic loads have never reached to a complete periodicity due to the irregular deflection motion of the left and right tails. Increasing the reduced frequency has led to higher buffet loads, higher frequencies of loads, and higher excitation peaks in the loads spectra. However, it also has led to lower bending and torsion deflections and accelerations than those at lower reduced frequency.

MDICE ARCHITECTURE

MDICE is a distributed object oriented environment which is made up of several major components. The first component in MDICE is a central controlling process that provides network and application control, serves as an object repository, carries out remote procedure calls, and coordinates the execution of the several application programs via MDICE specific script language. The second component is a collection of libraries, each containing a set of functions callable by the application programs. These libraries provide low level communication and control functions that are hidden from the application programs, as well as more visible functionality such as object creation and manipulation, interpolation of flow data along interfaces, and safe dynamic memory allocation services. Finally, the environment also encompasses a comprehensive set of MDICE compliant application programs. MDICE provides capabilities for parallel execution of participating application programs and has a full Fortran interface for those codes written in Fortran 77 or 90, C, in addition to C++.

The MDICE Graphical User Interface includes facilities for control the application. Figure 1 shows the control panel used to set up and control a simulation with some of MDICE compliant modules. The application modules are selected; for each module, the computer on which the program is to be run is chosen. Other information is provided, such as specifying a directory to run each module and any command line arguments the module might require. Once the simulation has been set up, it is run and controlled by MDICE using a simple script. The

MDICE script contains all the conveniences found in most common script languages. In addition, MDICE script supports remote procedure calls and parallel execution of the application modules. These remote procedure calls are the mechanism by which MDICE controls the execution and synchronization of the participating applications. Each application posts a set of available functions and subroutines. These function are invoked from MDICE script, but are executed by the application program who posted the function.

There are many advantages to the MDICE approach. Using this environment one can avoid giant monolithic codes that attempt to provide all needed services in a single large computer program. Such large programs are difficult to develop and maintain and by their nature cannot contain up-to-date technology. The MDICE allows the reuse of existing, state-of-the-art codes that have been validated. The flexibility of exchanging one application program for another enables each engineer to select and apply the technology best suited to the task at hand. Efficiency is achieved by utilizing a parallel distributed network of computers. Extensibility is provided by allowing additional engineering programs and disciplines to be added without modifying or breaking the modules or disciplines already in the environment. For more details of MDICE architecture, see Kingsley et al [10].

MULTI-DISCIPLINARY AEROELASTIC APPLICATION OF TWIN-TAIL BUFFET VIA MDICE

The application of MDICE computing environment to the aeroelastic twin-tail buffet problem involves four types of modular functionality: a fluid-dynamics module, a fluid-structure and fluid-fluid interfacing technique, a structural dynamics module, and grid motion technique. Next, the particular set of analysis modules used for twin-tail buffet simulation is presented.

Fluid-Dynamics Modules

The fluid-dynamics analysis module used for the current study is CFD-FASTRAN (CFD Research Corporation). CFD-FASTRAN is a state-of-the-art full Navier-Stokes flow solver for modeling compressible, turbulent flow problems using structured and/or unstructured grids. The solution of full Navier-Stokes equations is crucial for this problem to account accurately for the massive three-dimensional separations, vortex breakdown and vorticity evolution, convection and shedding, and strong fluid-structure interaction. CFD-FASTRAN employs an upwind scheme with Roe's flux-difference splitting or Van-Leer's flux-vector splitting for spatial differencing. Temporal differencing is done using Runge-Kutta scheme, point-implicit scheme or a fully-implicit scheme. Turbulent models in CFD-FASTRAN include Baldwin-Lomax, k-ε, and k-ω models. CFD-FASTRAN also provides the state-of-the-art for modeling flow problems with multiple moving bodies using Chimera overset gridding methodology coupled with a 6DOF model. The current simulation used fully-implicit scheme with Roe's flux-difference splitting.

Other fluid-dynamics analysis modules currently integrated into the MDICE environment include CFD-ACE (CFD Research Corporation), ADPAC (NASA), SPLITFLOW (Lockheed Martin), NPARC (NPARC Alliance), COBALT (AFRL), GCNS (Northrop Grumman), WIND (Boeing), NISTAR, NASTAR, and CORSAIR (Pratt&Whitney).

Structural-Dynamics Module

The current structural-dynamics modules, which are MDICE compliant, include the nonlinear FEM code MSC/NASTRAN, and the CFDRC's FEM code FEMSTRESS with capabilities for various linear structural simulation (LSS) models, such as influence coefficient, modal

analysis, and beam models. In the current analysis, the linear beam model of FEMSTRESS is used. The vertical tails are modeled as cantilevered beams fixed at the root. The tail bending and torsional deflections occur about an elastic axis that is displaced from the inertial axis. The equations for the bending deflection, w, and the torsion deflection, θ, are given by

$$\frac{\partial^2}{\partial z^2}\left[EI(z)\frac{\partial^2}{\partial z^2}w(z,t)\right] + m(z)\frac{\partial^2}{\partial t^2}w(z,t) + m(z)x_\theta(z)\frac{\partial^2}{\partial t^2}\theta(z,t) = N(z,t) \quad (1)$$

$$\frac{\partial}{\partial z}\left[GJ(z)\frac{\partial}{\partial z}\theta(z,t)\right] - m(z)x_\theta(z)\frac{\partial^2}{\partial t^2}w(z,t) - I_\theta(z)\frac{\partial^2}{\partial t^2}\theta(z,t) = -M(z,t) \quad (2)$$

where z is the vertical distance from the tail-root fixed support, EI(z) and GJ(z) are the bending and torsional stiffness of the tail section. m(z) is the mass per unit length, I_θ is the mass moment of inertia per unit length about the elastic axis, x_θ is the distance between the elastic axis and the inertia axis, N and M are the normal force and twisting moment per unit length. The geometric and natural boundary conditions on w and θ are given by

$$w(0,t) = \frac{\partial}{\partial z}w(0,t) = 0 \quad (3)$$

$$\frac{\partial^2}{\partial z^2}w(h,t) = \frac{\partial}{\partial z}\left[EI(h)\frac{\partial^2}{\partial z^2}w(h,t)\right] = 0 \quad (4)$$

$$\theta(0,t) = \frac{\partial}{\partial z}\theta(h,t) = 0 \quad (5)$$

The equations are transformed into a set of coupled second-order ODE using Galerkin method and modal analysis. The resulting aeroelastic equations are solved using fifth-order accurate Runge-Kutta scheme. Details of the aeroelastic equations and their solution procedure are presented by Sheta [11].

Fluid-Structure Interaction Technology

The Fluid-Structure interface algorithm is used to project the forces and moments from the fluid flow to the flexible-body structure and to feedback the aeroelastic deflections of the structure to the flow field. The interfacing is formulated in the most general sense for maximum flexibility. There are no inherent assumptions that the fluids grid is matched with the structure grid, either through different mesh densities, mesh architecture, or through physical separation between the interfaces as seen with thick shell finite-element models. The current simulation uses a conservative and consistent interface, adapted from Brown [12]. Conservative interfaces aim to conserve the forces and moments in the interpolation process between the two grids. In this case, the sum of all forces and moments on the fluid interface is equivalent to the sum of all forces and moments on the structure interface.

$$\sum_{fluid\ faces} \vec{F}_{fluid} = \sum_{solid\ nodes} \vec{F}_{solid} \quad (6)$$

$$\sum_{fluid\ faces} \vec{M}_{fluid} = \sum_{solid\ nodes} \vec{M}_{solid} \quad (7)$$

Consistency or virtual work conservation is also provided by requiring that the virtual work performed by the solid interface is equivalent to the virtual work performed by the fluid interface.

$$\sum_{fluid\ faces} W_{fluid} = \sum_{solid\ nodes} W_{solid} \quad (8)$$

$$W_{fluid} = \vec{F}_{fluid} \bullet \Delta\vec{r}_{center} \quad (9)$$

$$W_{solid} = \vec{F}_{solid} \bullet \Delta\vec{x} + \vec{M}_{solid} \bullet \vec{\omega}_{solid} \quad (10)$$

The above equations apply only to the degrees of freedom of the structure-dynamics equations. MDICE environment contains many types of function-matching interfaces and conservative interfaces techniques. For more details, see Siegel et al [13].

Communication Between Modules

Communication between the modules is controlled by the user from within the MDICE graphical user interface. The user specifies the modules that will be used for a particular simulation, the necessary input files for each module, the platforms upon which each module will run (each module can be run on a different computer) and other input parameters. The user then executes a short script in the graphical user interface which explicitly specifies the synchronization between the modules. For example, the user could specify that the flow solver should iterate 10 times, then interpolate fluid pressures to solid forces, then solve 1 iteration on the structural analysis, then loop. Interpolation is invoked automatically, using transfinite interpolation functions, when a fluid-structure interface is exchanged between application programs.

Generic Fighter Aircraft

In the current study, a generic model of fighter aircraft is chosen to study the twin-tail buffet. The configuration model consists of a 76°-swept back, sharp-edged delta wing of aspect ratio of one and dynamically scaled, flexible, swept-back twin tail of aspect ratio of 1.4, shaped after Washburn et al [5]. The vertical tails are oriented normal to the upper surface of the delta wing and have a leading-edge sweep of 62.5°. The separation distance between the twin-tail is 78% of the wing span, see Figure 2. Each tail is modeled as a single aluminum spar and balsa wood covering, as shown in Figure 3. The aluminum spar has a taper ratio of 0.3 and is constructed from 6061-T6 alloy. The balsa-wood covering has a taper ratio of 0.23 and aspect ratio of 1.4. The details of the configuration model and material properties are discussed in details in Sheta [11]. The computational grid used in this study is a multi-block H-H grid structure consisting of 10 blocks, C^0-continuous, with a total size of 450,000 grid points. The delta-wing/twin-tail configuration is statically pitched at wide range of angles of attack at Mach number of 0.4 and Reynolds number of 1.25×10^6.

RESULTS AND DISCUSSION

Figure 4 shows side-view and front-view snapshots of the total pressure iso-surfaces over the configuration model at different angles of attack. The figure shows that at AOA=26° the leading-edge vortices break down aft the twin tail. However, as the angle of attack increases, the vortex-breakdown flow moves upstream ahead of the twin tail. This is the reason behind the increase of the buffet responses at angles of attack higher than 25, as observed in many experimental work. The figure also shows increase in the size of the breakdown bubbles with the increase of the angle of attack. Figure 5 shows MDICE aeroelastic twin-tail buffet simulation of generic fighter aircraft. The MDICE script is shown in the background of the figure. A snapshot of the total pressure iso-surfaces over the configuration model at 34° angle of attack is shown in the figure. Also shown are the histories of the bending and torsional displacements of the right-tail tip and right-tail root bending moment. These images are graphically displayed in conjunction with MDICE GUI and can be invoked from MDICE as s separate display modules.

Aeroelastic Results

Figure 6 shows the history of the root bending moment of the right tail at different angles of attack. Positive moments correspond to an outward force on the tail. At AOA=26 deg., there is

no apparent variation in the root bending moment. This is because of the absence of vortex breakdown flow in front of the twin tail, as shown in Figure 4. As the angle of attack increases, the root bending moment increases due to the upstream motion of the vortex breakdown flow which causes the unsteady dynamic loads on the tails.

Figure 7 shows the histories of the bending and torsion deflections of the left and right tail tips at different angles of attack. The figure shows that increase the angle of attack has led to an increase in both the bending and torsion deflections. The frequency of the torsion deflections is more than twice the frequency of the bending deflections, in agreement with the experimental observations. The figure also shows a slight phase lag in the bending deflections with the increase of the angle of attack. The right and left tails have the same level of deflection. However, they are moving to the outboard direction in asymmetric manner due to the irregular vibrations of the left and right tails. Figure 8 shows the histories of the right-tail-tip bending and torsion accelerations at different angles of attack. The frequency of the bending accelerations is almost the same as that of the torsion accelerations. The bending and torsion accelerations are also increasing with the increase of the angle of attack. However, the bending acceleration is maximum at AOA=34°.

Figure 9 shows the RMS buffet pressure and RMS surface pressures at the five transducers (shown in Figure 3) of the inner and outer surfaces of the right tail. The buffet pressure is defined as the instantaneous differential pressure across the tail surface, and it is normalized by the free-stream dynamic pressure. The buffet pressures show sharp increase after 26° angle of attack. The sharp increase in the buffet pressures corresponded with the vortex breakdown position crossing the trailing edge. The RMS buffet pressures were a strong function of transducer location and locations 4 and 5 yielded the greatest levels. In the experimental data of Washburn, location 4 yielded the greatest level. The surface pressure fluctuations were sensitive to the tail side and transducer location. Generally, the inner surface RMS pressure levels were larger than those of the outer surface, in agreement with the experimental observations of Washburn et al [5]. The lowest RMS pressure levels were observed at transducer location 2. This location corresponds to the transducer furthest from the tail leading edge. In the experimental data of Washburn, locations 2 and 5 show the lowest levels.

Validation

Figure 10 shows the mean and RMS values of the right-tail root bending moment coefficients as a function of the angle of attack. The experimental data of Washburn et al [5] are also shown in the figure. The computed results agree well with the experimental data. At an angle of attack higher than 25, the RMS of the root bending moment increases with the increase of the angle of attack due to the upstream motion of the vortex breakdown flow in front of the twin tails, as shown in Figure 4.

Figure 11 shows the variation of the first two dominant non-dimensional frequencies (nfreq_d = f_d * b / U) of the tip transducer versus the angle of attack. The experimental data of Washburn et al [5] is also shown in the figure. The results are in very good agreement with the experimental data. The frequency peaks shift to a lower frequency as the angle of attack increases. The first two frequency peaks are moderately close to each other, which indicate that the pressure field contains energy over a narrow frequency band. This is in agreement with the observations of Washburn [5] and Martin and Thompson [14].

CONCLUSION

The MDICE Multi-Disciplinary Computing Environment was successfully used and vali-

dated for the fluid-structure interaction problem of twin-tail buffet. A good comparison with experimental data was achieved. A sharp increase in the buffet pressures was observed as the vortex breakdown crossed the wing trailing edge. The frequency of the torsion deflections was almost twice that of the bending deflections. Future applications will involve using the nonlinear FE code (MSC/NASTRAN) to model different nonlinear transient aeroelastic phenomena. The integration of MSC/NASTRAN with high-end full Navier-Stokes flow solvers by means of a conservative/consistent fluid-structure interfacing mechanism is imperative to model the nonlinear behavior of such nonlinear phenomena.

ACKNOWLEDGMENTS

The authors wish to acknowledge Joel Luker, Don Kinsey and Larry Huttsell of Wright-Patterson Air Force base for their support of the MDICE-aerostructures environment. The authors also wish to thank Steve Brown, Ed Blosch, Charlie Peavy and John Volk of Northrop-Grumman for technical guidance and collaboration on the development of the fluid-structure interfacing algorithms. Viji Parthasarathy of CFDRC also provided invaluable support with the integration of MDICE modules.

References

1. Sellers, W. L. III, Meyers, J. F. and Hepner, T. E., "LDV Survey Over a Fighter Model at Moderate to High Angle of Attack," SAE Paper 88-1448, 1988.
2. Erickson, G. E., Hall, R. M., Banks, D. W., Del Frate, J. H., Shreiner, J. A., Hanley, R. J. and Pulley, C. T., "Experimental Investigation of the F/A-18 Vortex Flows at Subsonic Through Transonic Speeds," AIAA 89-2222, 1989.
3. Wentz, W. H., "Vortex-Fin Interaction on a Fighter Aircraft," AIAA 87-2474, 1987.
4. Cole, S. R., Moss, S. W. and Dogget, R. V., Jr., "Some Buffet Response Characteristics of a Twin-Vertical-Tail Configuration," NASA TM-102749, October 1990.
5. Washburn, A. E., Jenkins, L. N. and Ferman, M. A., "Experimental Investigation of Vortex-Fin Interaction," AIAA 93-0050, AIAA 31st ASM, Reno, NV, January 1993.
6. Moses, R. W. and Ashley, H., "Spatial Characteristics of the Unsteady Differential Pressures on 16\% F/A-18 Vertical Tails," AIAA-98-0519, AIAA 36th ASM, Reno, NV, January 1998.
7. Kandil, O. A., Sheta, E. F. and Massey, S. J., "Fluid/Structure Twin Tail Buffet Response Over A Wide Range of Angles of Attack," AIAA 97-2261-CP, 15th AIAA Applied Aerodynamics Conference, Atlanta, GA, June 23-25, 1997.
8. Sheta, E. F., Kandil, O. A. and Yang, Z., "Effectiveness of Flow Control for Alleviation of Twin-Tail Buffet," WAC Paper No. 985501, SAE-AIAA World Aviation Cogress and Exposition, Anaheim, CA, September 28-30, 1998.
9. Sheta, E. F. and Kandil, O. A., "Effect of Dynamic Rolling Oscillations on Twin-Tail Buffet Response," AIAA 99-0792, AIAA 37th ASM, Reno, NV, January 1999.
10. Kingsley, G. M., Siegel, J. M., Harrand, V. J., Lawrence, C., and Luker, J., "Development of the Multi-Disciplinary Computing Environment (MDICE)," AIAA-98-3857, 7th AIAA/USAF/NASA/ISSMO Symposium of MDO, September 1998.
11. Sheta, E. F., "Computational Investigation and Validation of Twin-Tail Buffet Response Including Dynamics and Control," Ph.D. Dissertation, Old Dominion University, Norfolk, VA, May 1998.
12. Brown, S. A., "Displacement Extrapolation for CFD and CSM Analysis," AIAA-97-1090, 1997.
13. Siegel, J. M., Jr., Parthasarathy, V., Kingsley, G. M., Dionne, P. J., Harrand, V. J. and Luker, J. J., "Application of A Multi-Disciplinary Computing Environment (MDICE) for Loosely Coupled Fluid-Structural Analysis," AIAA-98-4866, 7th AIAA/USAF/NASA/ISSMO Symposium of MDO, September 1998.
14. Martin, C. A. and Thompson, D. H., "Scale Model Measurements of Fin Buffet due to Vortex Bursting on F/A-18," AGARD-CP-497, 1991.

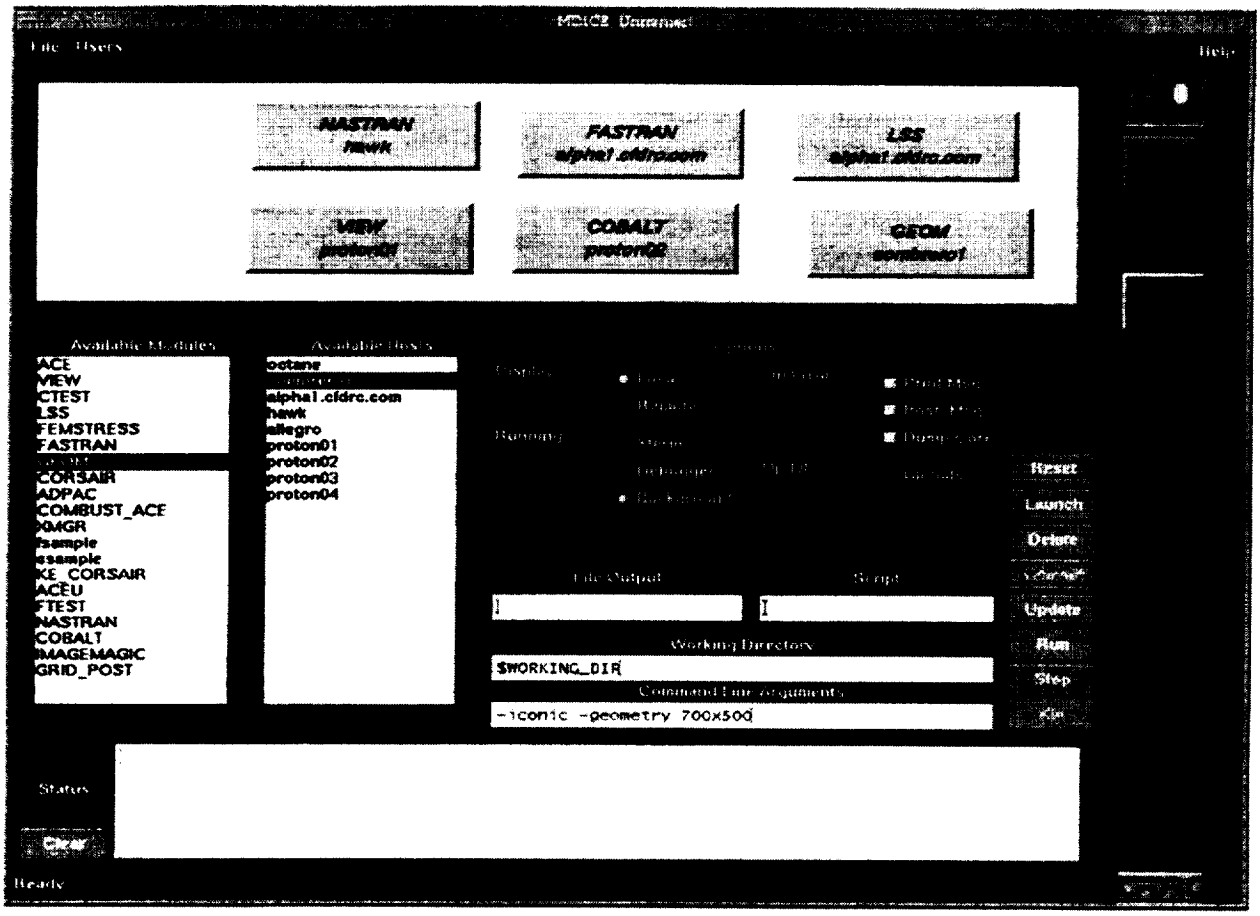

Figure 1: Application control panel of MDICE showing some of the compliant computer analysis modules

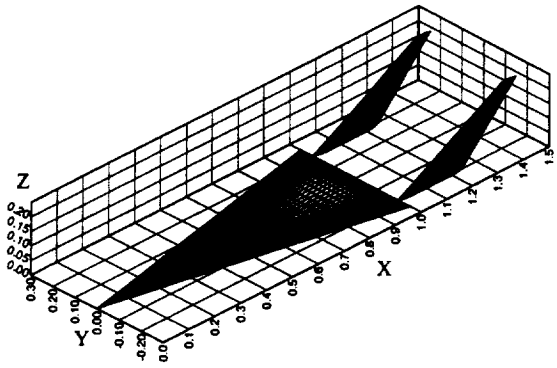

Figure 2: Surface grid of the delta-wing/twin-tail configuration model.

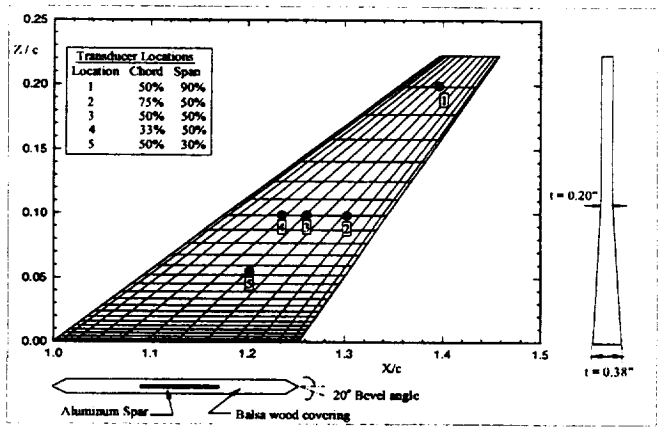

Figure 3: A schematic view of the tail construction and dimensions showing the pressure transducers locations.

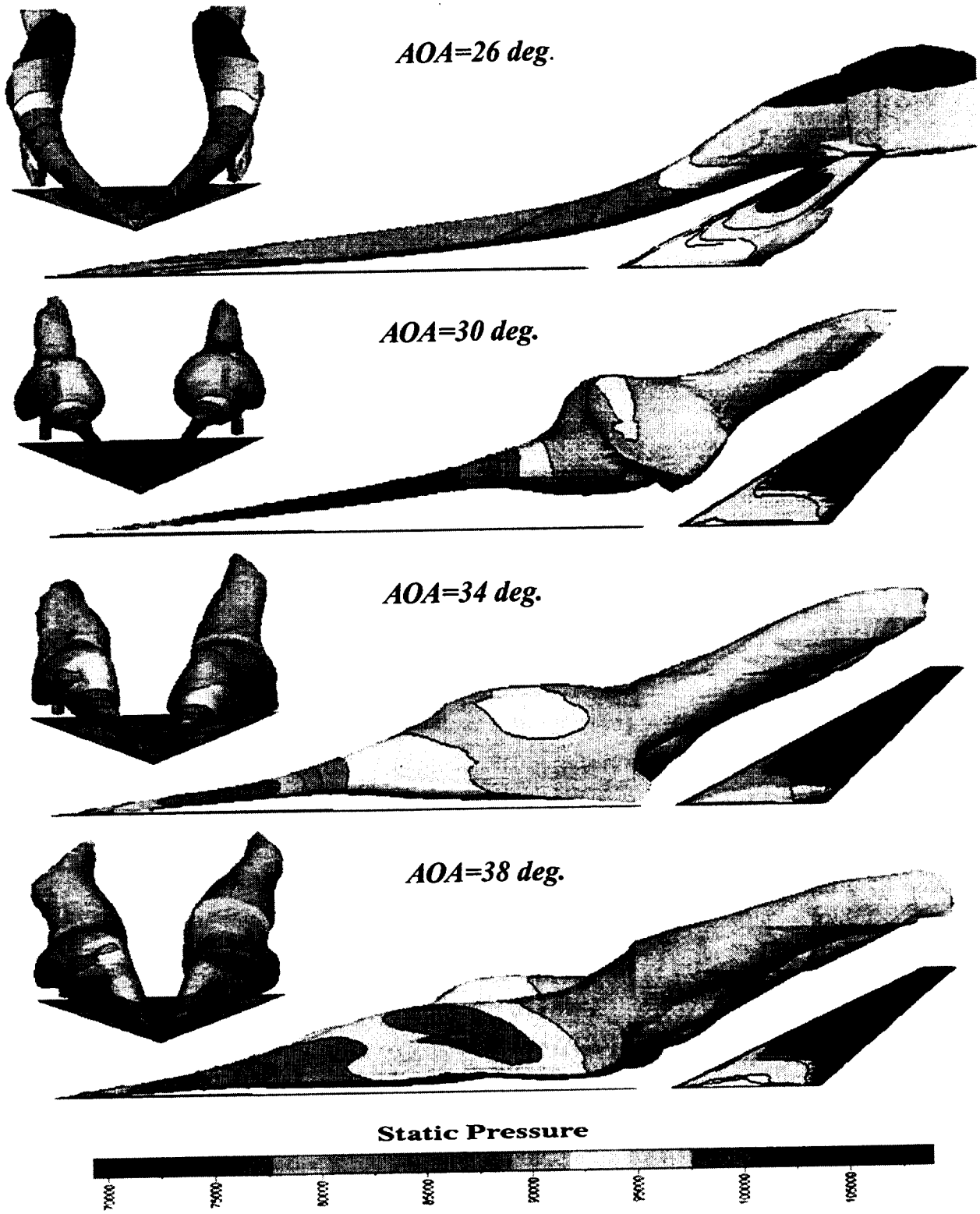

Figure 4: Side-view and front-view snapshots of the total pressure iso-surfaces and the break-down of the leading-edge vortex cores at different angles of attack. Delta-wing/Flexible twin tail model.

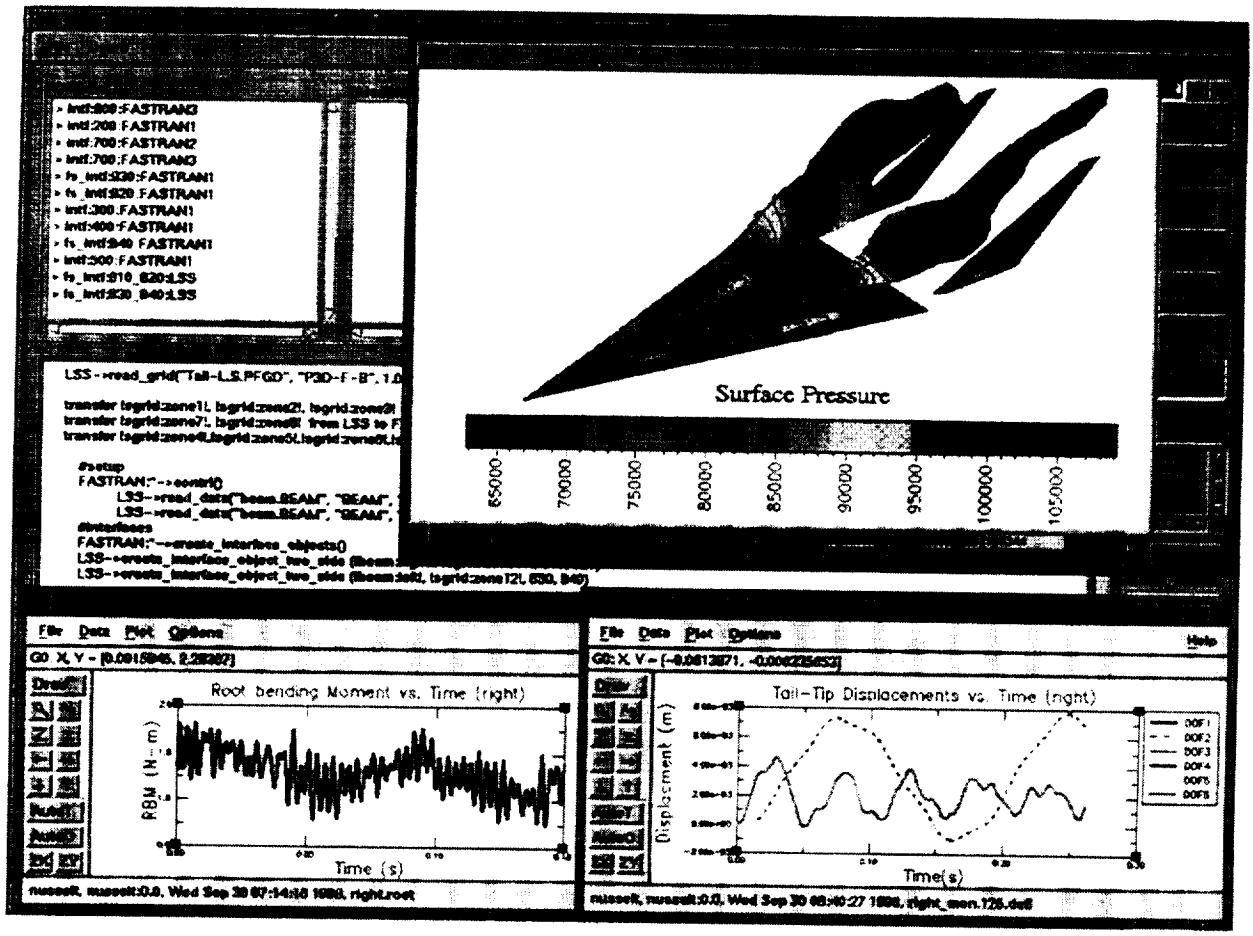

Figure 5: Multi-Disciplinary Computing Environment (MDICE) aeroelastic twin-tail buffet simulation of generic fighter aircraft. α=34°, M = 0.4, Re = 1.25×10^6.

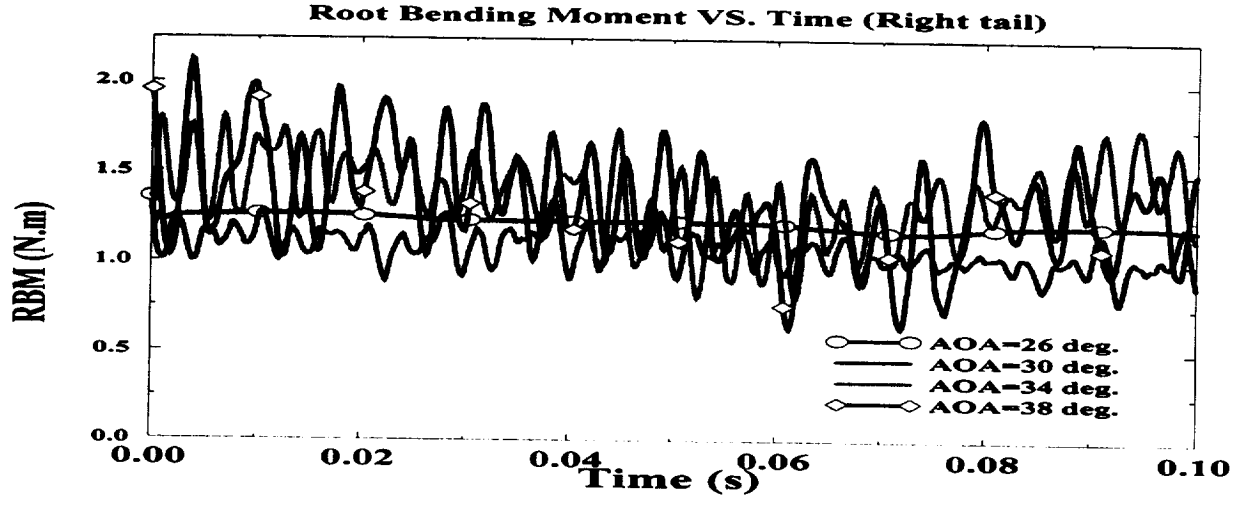

Figure 6: Effect of angle of attack on the history of the right-tail root bending moment. M = 0.4, Re = 1.25×10^6.

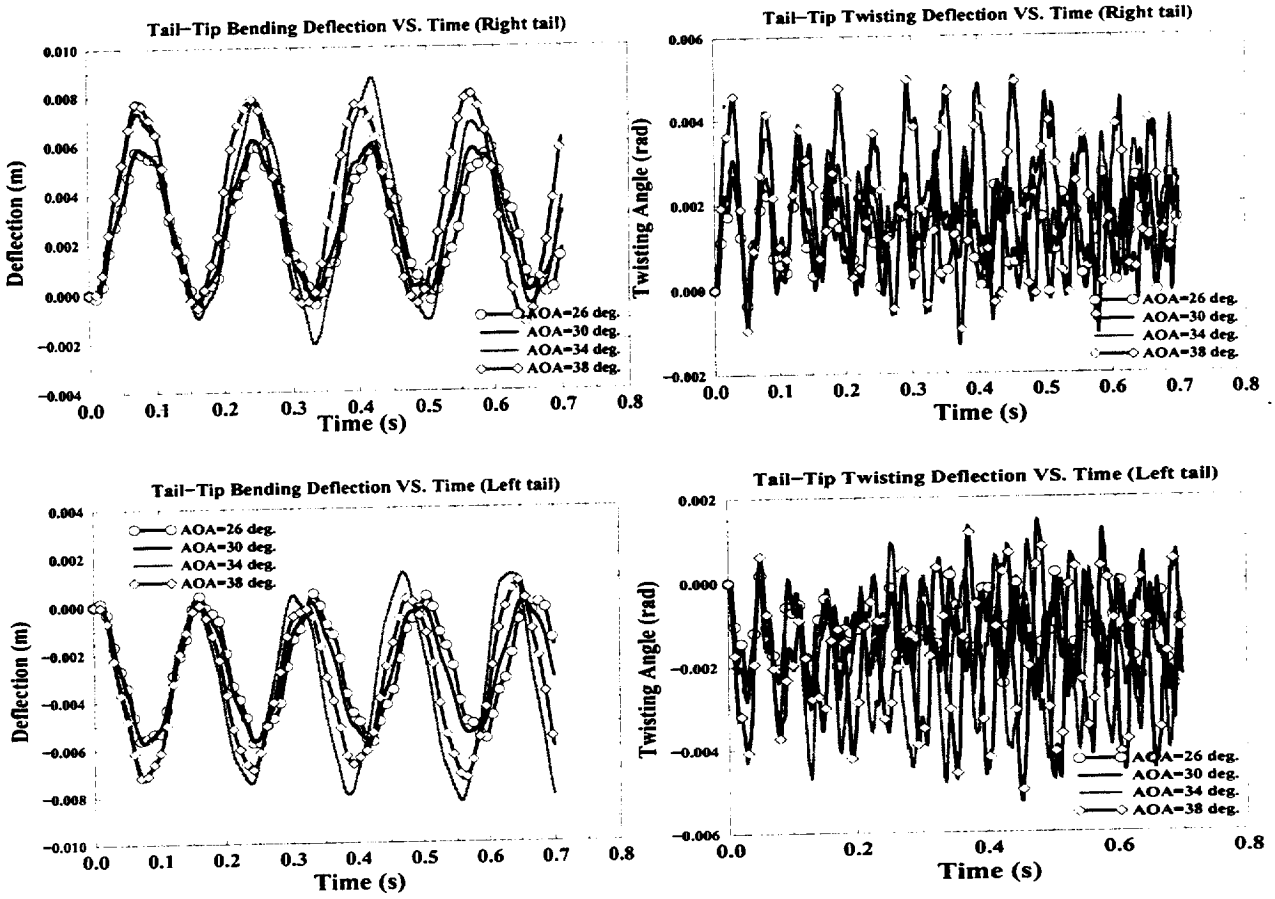

Figure 7: Effect of angle of attack on the history of tail-tip bending and torsion deflections of the right and left tails. M = 0.4, Re = 1.25×10^6.

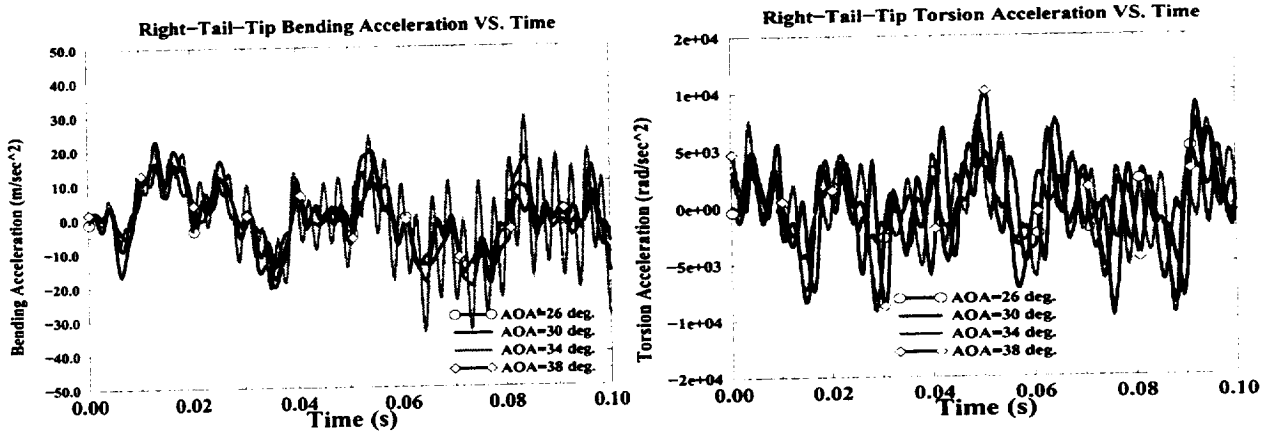

Figure 8: Effect of angle of attack on the history of right-tail-tip bending and torsion accelerations. M = 0.4, Re = 1.25×10^6.

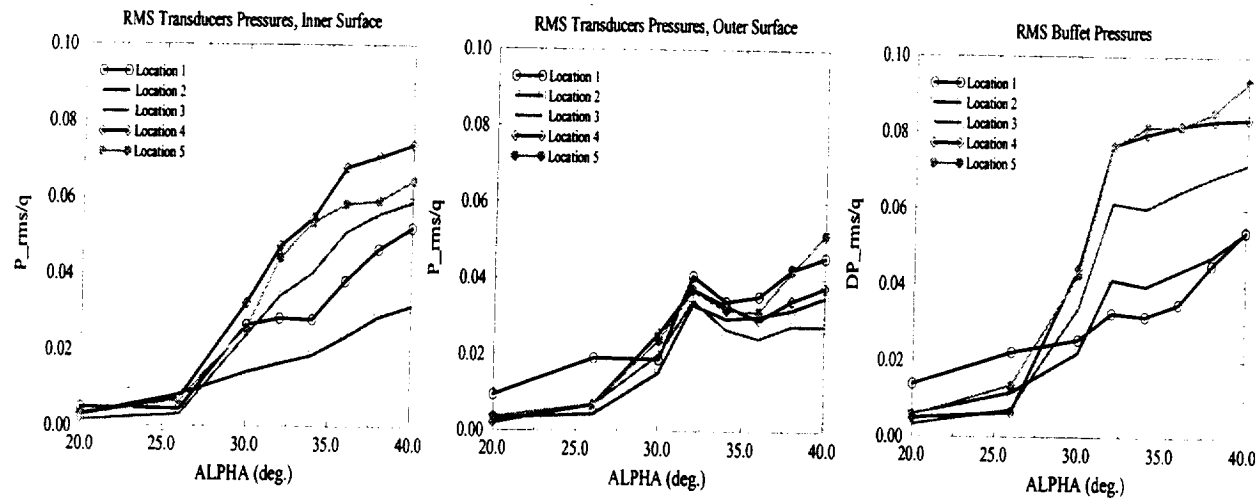

Figure 9: RMS buffet pressures and RMS surface pressures at the five transducers locations of the inner and outer surfaces of the right tail.

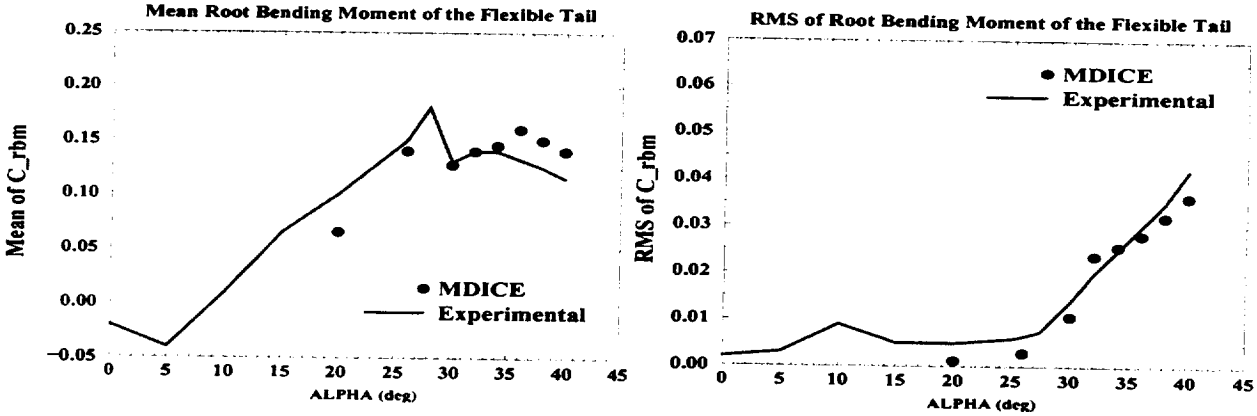

Figure 10: RMS and mean values of the right-tail root bending moment coefficients, compared with the experimental data of Washburn et al [5].

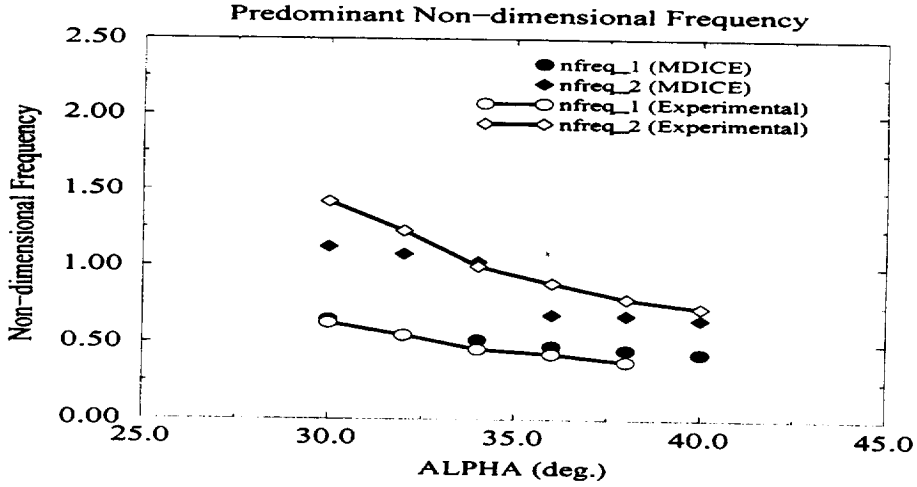

Figure 11: Non-dimensional predominant frequencies of the tail-tip transducer, compared with the experimental data of Washburn et al [5].

ADAPTIVE SUCTION AND BLOWING FOR TWIN-TAIL BUFFET CONTROL

Osama A.Kandil[1] and Zhi Yang[2]
Aerospace Engineering Department
Old Dominion University, Norfolk, VA 23529

ABSTRACT

Adaptive active flow control for twin-tail buffet alleviation is investigated. The concept behind this technique is to place control ports on the tail outer and inner surfaces with flow suction or blowing applied through these ports in order to minimize the pressure difference across the tail. The suction or blowing volume flow rate from each port is proportional to the pressure difference across the tail at this location. A parametric study of the effects of the number and location of these ports on the buffet response is carried out. The computational model consists of a sharp-edged delta wing of aspect ratio one and swept-back flexible twin tail with taper ratio of 0.23. This complex multidisciplinary problem is solved sequentially using three sets of equations for the fluid flow, aeroelastic response and grid deformation, using a dynamic multi-block grid structure. The computational model is pitched at 30° angle of attack. The freestream Mach number and Reynolds number are 0.3 and 1.25 million, respectively. The model is investigated for the inboard position of the twin tails, which corresponds to a separation distance between the twin tails of 33% of the wing span. Comparison of the time history and power spectral density responses of the tails for various distributions of the control ports are presented and discussed.

INTRODUCTION

The maneuver capabilities of the F/A-18 fighter aircraft are achieved through the combination of a leading-edge extension (LEX) with a delta wing and the use of twin vertical tails. The LEX maintains lift at high angles of attack by generating a pair of vortices that trail aft over the top of the aircraft. The vortex entrains air over the vertical tails to maintain stability of the aircraft. At some flight conditions, the vortices emanating from the highly swept LEX of the delta wing breakdown before reaching the vertical tails, which get bathed in a wake of unsteady highly-turbulent, swirling flow. This flow produces severe buffet of the tails and has led to their premature fatigue failure. Applying active flow control and/or active structural control could alleviate this problem. In this paper we address active flow control methods.

The twin-tail buffet response was predicted and analyzed recently by the senior author and his co-workers. Kandil, Sheta and Massey[1] studied the buffet response of twin-tail model in turbulent flow over wide range of angles of attack. The computational results were in good quantitative agreement with the experimental data of Washburn et al[2]. In a recent paper by Kandil and Sheta[3], the effects of

[1] Professor, Eminent Scholar and Department Chair, Associate Fellow AIAA
2 Ph.D. Graduate Research Assistant, Member AIAA

using coupled and uncoupled bending-torsion aeroelastic equations on the twin-tail buffet response were also investigated.

The main objective of active flow control methods is to modify the flow field in the region of the twin tail. Unsteady vortex breakdown of the leading-edge vortex cores develops upstream of the twin tail and moves downstream in close proximity to the twin tail. This highly unsteady vortex-breakdown flow produces unsteady differential pressure on each tail forcing it to oscillate through wide ranges of amplitudes and frequencies, which eventually result into a tail fatigue failure. Hence, flow control methods should be designed in such a way as to move the vortex breakdown location downstream behind the twin tail and displace the vortex core path away from the twin tail. These flow control methods are expected to produce these objectives over the whole ranges of angle of attack and Mach number during the configuration maneuverability. Moreover, these control methods should not produce adverse effects on the aerodynamic performance of the configuration. Obviously, this is a challenging multidisciplinary, time-dependent, control problem.

The approach that we had adopted to deal with this complex problem was to break it up into a step-by-step investigation of simple and combined flow control methods[4]. The first method, which we investigated, was the tangential leading edge blowing (TLEB)[5]. The second method was the flow suction along the vortex cores (FSVC). In the TLEB method, an air jet was blown tangential to the delta wing surface along its whole leading edge. The volume flow rate of this jet was varied linearly along the wing leading edge. The control effect of this method was modifying the path of the leading-edge vortex core, moving it closer to the tail and intersecting it. This vortex path modification increased the aerodynamic damping of the tail, and hence it damped its forced oscillation. An additional effect of this method was the increase of the vortex core axial momentum, which in turn moved the vortex breakdown location further downstream. In the FSVC method, flow suction was applied along the leading-edge vortex core in order to remove the low-level axial momentum flow from the vortex-breakdown region. This flow control method increased the axial momentum of the vortex flow and moved the vortex breakdown further downstream.

It has been shown that the TLEB method moved the vortex breakdown location downstream and the leading-edge vortices laterally toward the twin tail. The TLEB control produced lower tail root bending and twisting moments as well as lower torsion deflection and acceleration than those of the no-control case. However, the bending deflection and acceleration were higher than those of the no-control case. In the FSVC method (out position location), it has been shown that the vortex-breakdown size has been reduced and was moved in the downstream direction. It also reduced the tail bending deflection and has also shown some initial reduction of the tail root twisting moment. However, the root bending moment, bending and torsion accelerations and torsion deflection of the tail were higher than those of the no-control case. Next, the TLEB and FSVC (out position) methods were combined and applied simultaneously to the same configuration. The results of this case have shown that no improvement was achieved in comparison with those results that were obtained with each method being applied separately.

Further investigation of the FSVC method has shown that moving the suction tubes in the spanwise direction toward the tail location produced favorable aeroelastic control. This control is called The FSVC (in position) method. The results of this case have shown additional reduction in the tail root bending and twisting moments, its tip bending and torsion accelerations and its tip torsion deflection than those of the no-control case. Increasing the suction volumetric flow rate produced further

reduction in the tail aeroelastic responses. Next, the axial orientation of the FSVC method was investigated [6]. The direction of suction tubes was tilted to the right at an angle of + 10 deg. or to the left at an angle of – 10 deg. with respect to an observer looking in the upstream direction . The best control results were obtained with the suction tubes tilted at –10 deg.

In this paper adaptive suction and blowing flow control is applied through ports which are located on the tail outer and inner surfaces. The suction or blowing volume flow rate is proportional to the pressure difference across the tail at the corresponding port location. A parametric study of the effects of the number and location of these control ports is presented.

HIGHLIGHTS OF THE FORMULATION AND COMPUTATIONAL SCHEMES

The formulation of the problem consists of three sets of governing equations along with certain initial and boundary conditions. The first set is the unsteady, compressible, full Navier-Stokes (NS) equations. The second set consists of the aeroelastic equations for bending and torsion modes. The tail bending and torsion deflections occur about an elastic axis that is displaced from the inertial axis. The third set consists of equations for moving the grid according to the tail deflections. In these equations, the tail bending displacement, $w_{i,j,k}$, and the tail twist angle, $\theta_{i,j,k}$, are interpolated through cosine functions. Details of these sets of equations are given in Ref. 3.

The first step in this multidisciplinary problem is to solve for the fluid flow problem keeping the twin tail rigid. The NS equations are solved using the implicit, flux-difference-splitting finite-volume scheme. The grid speed is set equal to zero in this step. This step provides the initial flow field conditions along with the pressure difference across the tails. The pressure difference is used to generate the normal force and twisting moment per unit length of each tail. Next, the aeroelastic equations are solved sequentially along with the other two sets of equations, to obtain the bending and torsion deflections of each tail, $w_{i,j,k}$ and $\theta_{i,j,k}$. The grid displacement equations are then used to compute the new grid coordinates. In the NS equations, the metric coefficients of the coordinate Jacobian matrix are updated as well as the grid speed. At each time step, the computational cycle consisting of the NS solver, the aeroelastic equation solver, and the grid displacement solver is repeated. This solution is called the "No Control" solution. Next, the adaptive flow control is applied starting with the initial flow field conditions, which are obtained with the twin tail kept rigid. The suction or blowing volume flow rate is proportional to the instantaneous pressure difference across the tail at the location of the port. If the pressure on the outer tail surface is greater than the pressure on the inner tail surface, suction volume flow rate is applied at the outer port and an equal volume of blowing flow rate is applied at the corresponding inner port. Figure 1 shows different arrangements for active flow control ports on the tail. They are referred to as ¼ cells, 1/3 cells and ¾ cells.

COMPUTATIONAL APPLICATIONS

Twin Tail-Delta Wing Configuration:

The twin tail-delta wing configuration consists of a 76° swept back, sharp-edged delta wing (aspect ratio of one) and dynamically scaled flexible twin tail similar to those used by Washburn et. Al[2]. The vertical tails are oriented normal to the upper surface of the delta wing and have a centerline

sweep of $53.5°$. Each tail is made of a single Aluminum spar and Balsa wood covering. The Aluminum spar has a taper ratio of 0.3 and a constant thickness of 0.001736. The Aluminum spar is constructed from 6061-T6 alloy with density, ρ, modulii of elasticity and rigidity, E and G of 2693 kg/m^3, 6.896×10^{10} N/m^2 and 2.5925×10^{10} N/m^2, respectively. The Balsa wood covering has a taper ratio of 0.23 and aspect ratio of 1.4. The Balsa thickness decreases gradually from 0.0211 at the tail root to 0.0111 at the tail midspan and then constant thickness of 0.0111 is maintained to up the tail tip. The tail cross section is a semi-diamond shape with bevel angle of $20°$. The Balsa density, modulii of elasticity and rigidity, E and G, are 179.7 kg/m^3, 6.896×10^8 N/m^2 and 2.5925×10^8 N/m^2, respectively. The tails are thought of to be magnetically suspended, and the tail apex is positioned at $x/c=1.0$, as measured from the wing apex. The configuration is statically pitched at $30°$ angle of attack. The freestream Mach number and Reynolds number are 0.3 and 1.25×10^6, respectively. A multi-block grid consisting of 4 blocks is used for the solution of the problem. The first block is O-H grid for the wing and upstream region, with $101\times50\times54$ grid points in the wrap around, normal and axial directions, respectively. The second block is H-H grid for the inboard region of the twin tail, with $15\times50\times13$ grid points in the wrap around, normal and axial directions, respectively. The third block is H-H grid for the outboard region of the twin tail, with $87\times50\times13$ grid points in the wrap around, normal and axial directions, respectively. The fourth block is O-H grid for the downstream region of the twin tail, with $101\times50\times25$ grid points in the wrap around, normal and axial directions, respectively. The grid topology of the twin tail-delta wing configuration is shown in Ref. 6.

Flow Field Results of Adaptive Flow Control:

Figure 2 shows a snap shot of the flow field results with no control at $\tau=19$ after allowing the tails to move and interact with the flow. The figure shows a top view of the vortex cores total pressure isosurfaces. Breakdown of the vortex cores is observed to occur at 64% chord station.

Figures 3-5 show the flow field results for the adaptive flow control when all the cells have control ports .The top view figure of vortex cores, Fig. 3, shows that the vortex breakdown location has moved downstream to the 70% chord station and the bubble size decreased substantially, Fig.4. Figure 5 shows that the vortex cores are smaller than those of the no-control case . Figures 6-8 show the flow field results for the adaptive flow control when ¾ of the cells have control ports. The results show a small increase in the size of the vortex breakdown bubble.

Load and Aeroelastic Results of Adaptive Flow Control:

Figure 9 shows the distribution histories of bending deflection, w, rotation angle deflection, θ, normal force, N, and twisting moment, M, versus the tail height, z for the ¾ cells adaptive control. Each figure shows the distribution every dimensionless time unit after the adaptive flow control is applied. These curves are labeled as A, B, ...etc. It is observed that the bending deflections are in the first mode shape only, and the rotation angle deflections are also in the first mode shape only. For the no-control case, three mode shapes were observed for the bending and rotation angle deflections. These values are substantially lower than those of the no-control case, particularly for the rotation angle deflections. On the other hand, the maximum normal forces and twisting moments have been decreased by 80% in comparison with those of the no-control case.

Figures 10-13 show comparisons of the time history of the root bending moment, the root twisting moment, their power spectral densities and the time history of the tip bending and rotation angle accelerations and their power spectral densities for different adaptive flow control and the no-control case. It is observed that the best adaptive flow control is achieved with the all cells and ¾ cells cases. The power spectral curves show that good to excellent control results are also obtained using the 1/3 and ¼ cells cases.

CONCLUDING REMARKS

The fundamental issue of twin-tail buffet alleviation was addressed using adaptive flow control. The concept behind this technique is to place control ports on the tail outer and inner surfaces and apply flow suction or blowing through these ports. The suction or blowing volume flow rate from each port is proportional to the pressure difference across the tail at the location of the port. It has been shown that the all cells and ¾ cells adaptive control are very effective in moving the vortex breakdown downstream and substantially reducing the root bending and twisting moments and the tip bending and rotation accelerations as well.

ACKNOWLEDGMENT

This research work is supported under Grant No. NAG-1-648 by the Aeroelasticity Branch of NASA Langley Research Center.

REFERENCES

1. Kandil, O. A., Sheta, E. F. and Massey, S. J., "Fluid/Structure Twin Tail Buffet Response Over A Wide Range of Angles of Attack," AIAA 97-2261-CP, 15th AIAA Applied Aerodynamics Conference, Atlanta, GA, June 23-25, 1997, pp. 221-232.

2. Washburn, A. E., Jenkins, L. N. and Ferman, M. A., "Experimental Investigation of Vortex-Fin Interaction," AIAA 93-0050, AIAA 31st ASM, Reno, NV, January 1993.

3. Kandil, O. A. and Sheta, E. F., " Coupled and Uncoupled Bending-Torsion Responses of Twin-Tail Buffet," Journal of Fluids and Structures, Academic Press, 12, 1998, pp. 677-701.

4. Sheta, E. F., Kandil, O. A. and Zhi Y., "Effectiveness of Flow Control for Alleviation of Twin-Tail Buffet," SAE Paper No. 985501, 1998 World Aviation Conference, Anaheim, CA, September 28-30, 1998.

5. Wong, G. S., Rock, S. M., Wood, N. J. and Roberts, L., ``Active Control of Wing Rock Using Tangential Leading-Edge Blowing," Journal of Aircraft, Vol. 31, No. 3, May-June 1994.

6. Kandil, O. A., Yang, Z. and Sheta, E. F., " Flow Control and Modification for Alleviating Twin-Tail Buffet," AIAA 99-0138, AIAA 37th ASM, Reno, NV, January 1999.

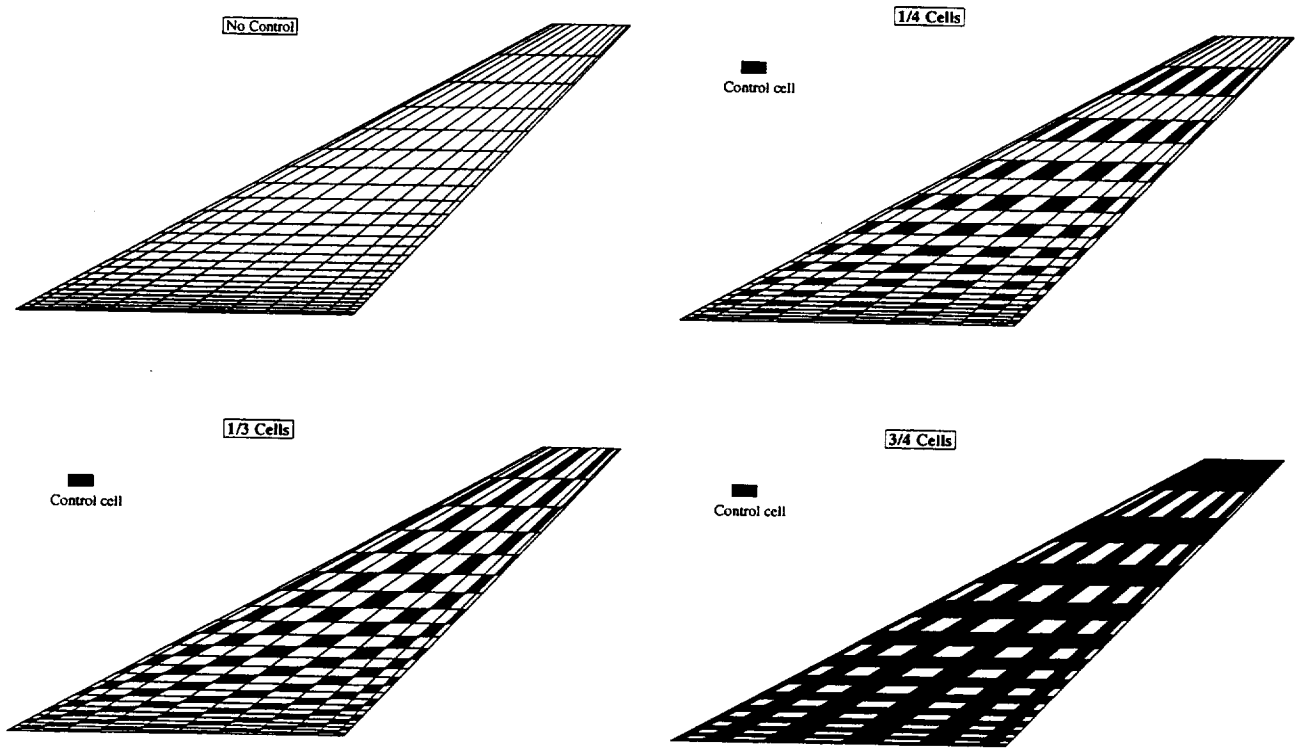

Figure 1: Schematic view showing the arrangement for Active Control cells.

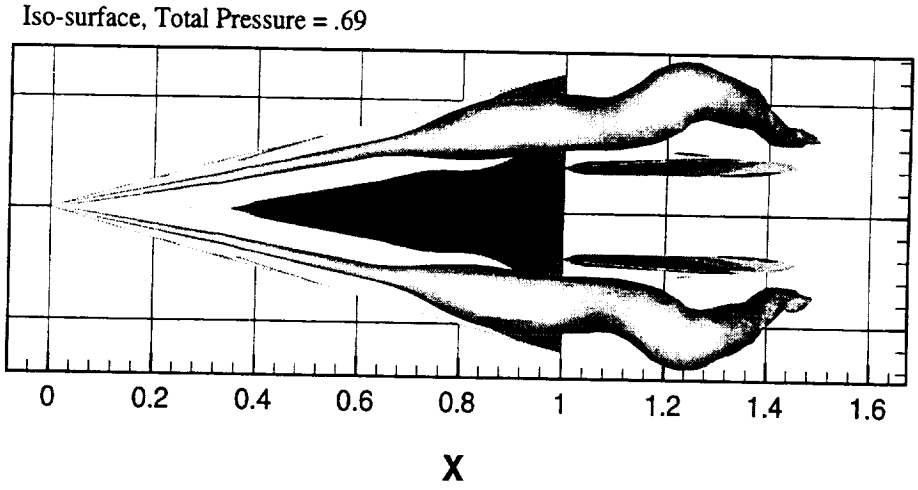

Figure 2: Top view showing the vortex core total pressure iso-surface. No-control case at $\tau = 19$, $M_\infty = 0.3$, $\alpha = 30°$, $R_c = 1.25\times10^6$. (Inboard twin-tail position).

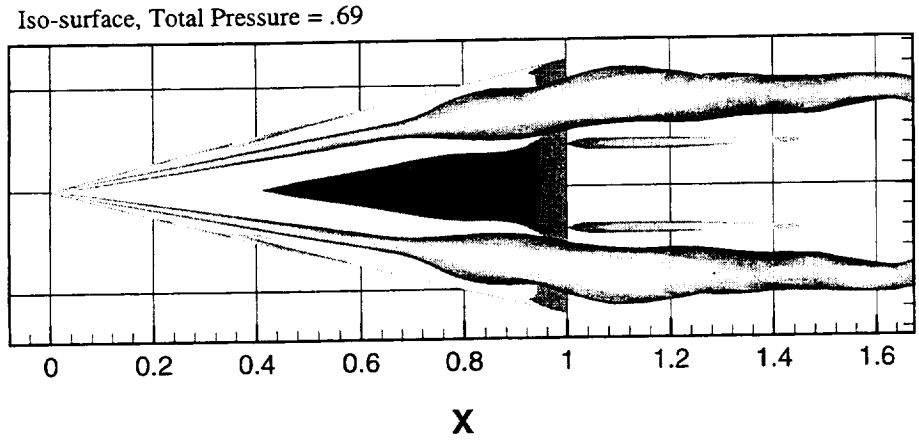

Figure 3: Top view showing the vortex core total pressure iso-surface. Active Control (all cells) case at $\tau = 11$, $M_\infty = 0.3$, $\alpha = 30°$, $R_e = 1.25\times10^6$. (Inboard twin-tail position).

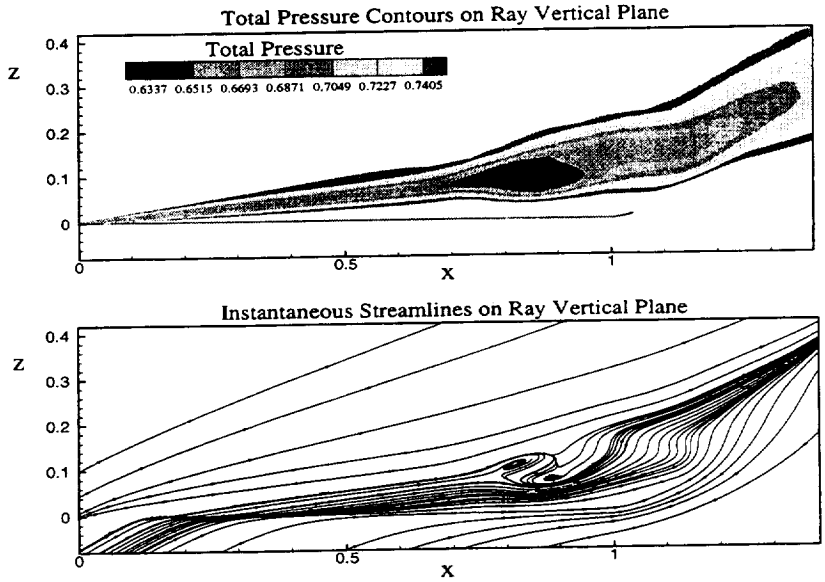

Figure 4: Total pressure contours on a ray vertical plane passing through the wing leading-edge vortex. Active Control (all cells) case at $\tau = 11$, $M_\infty = 0.3$, $\alpha = 30°$, $R_e = 1.25\times10^6$. (Inboard twin-tail position).

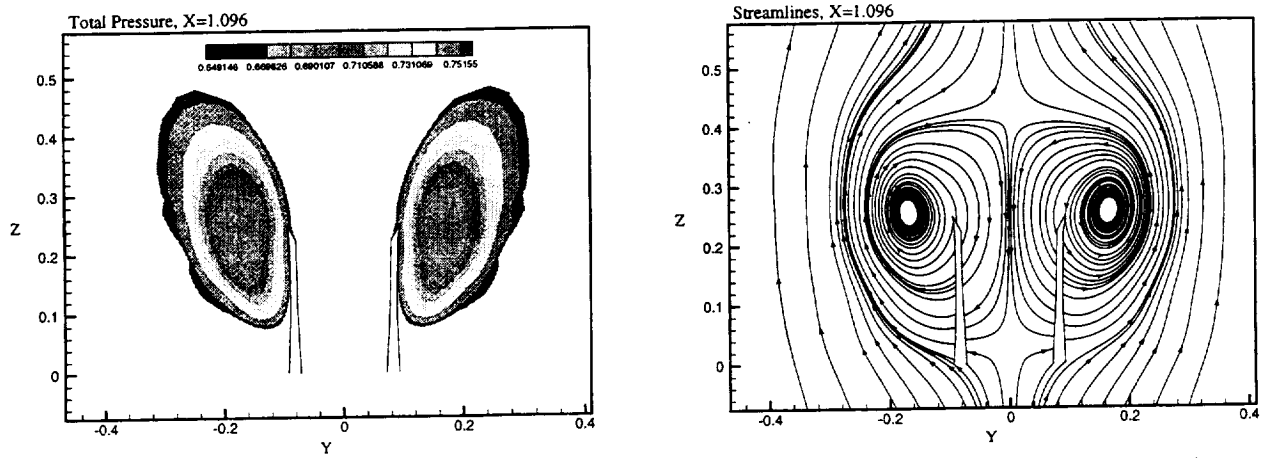

Figure 5: Snap shots of total pressure contours and instantaneous streamlines on cross plane, $x = 1.096$. Active Control (all cells) case at $\tau = 19$, $M_\infty = 0.3$, $\alpha = 30°$, $R_e = 1.25\times10^6$. (Inboard twin-tail position).

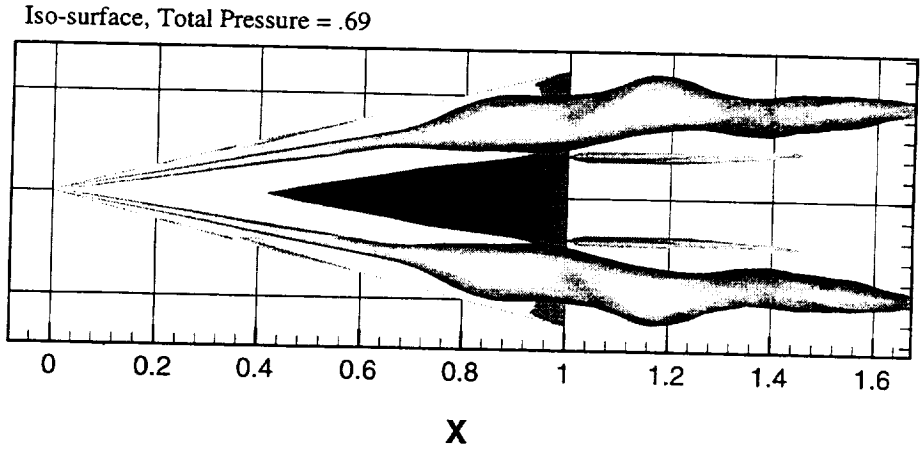

Figure 6: Top view showing the vortex core total pressure iso-surface. Active Control (3/4 cells) case at $\tau = 11$, $M_\infty = 0.3$, $\alpha = 30°$, $R_e = 1.25\times10^6$. (Inboard twin-tail position).

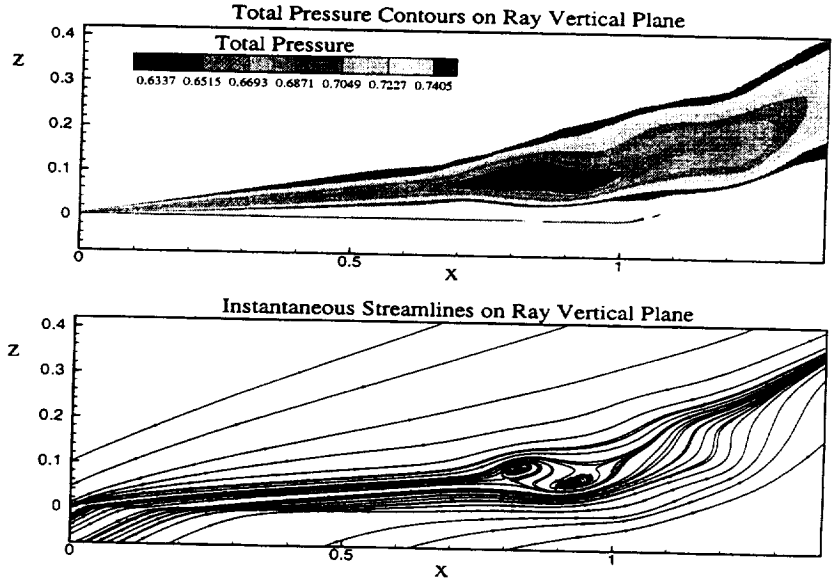

Figure 7: Total pressure contours on a ray vertical plane passing through the wing leading-edge vortex. Active Control (3/4 cells) case at $\tau = 11$, $M_\infty = 0.3$, $\alpha = 30°$, $R_e = 1.25\times10^6$. (Inboard twin-tail position).

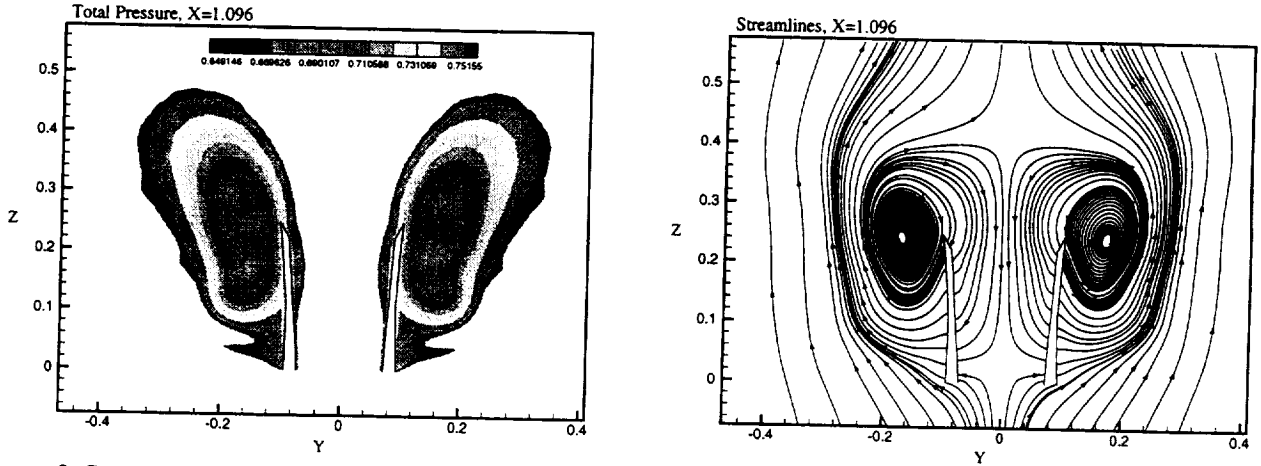

Figure 8: Snap shots of total pressure contours and instantaneous streamlines on cross plane, $x = 1.096$. Active Control (3/4 cells) case at $\tau = 11$, $M_\infty = 0.3$, $\alpha = 30°$, $R_e = 1.25\times10^6$. (Inboard twin-tail position).

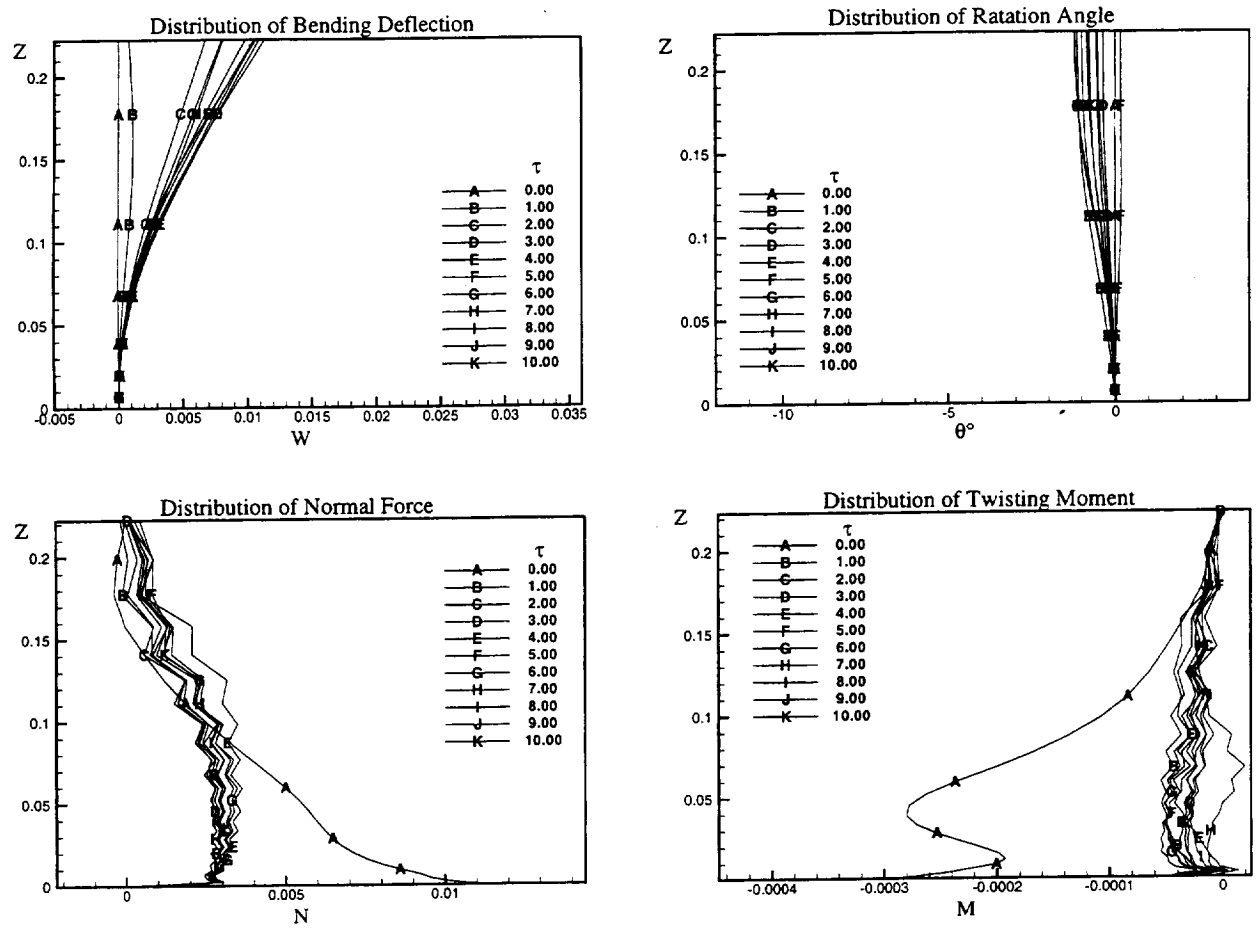

Figure 9: Distribution of bending deflection, rotation angle, normal force and twisting moment along the tail span. Active Control (3/4 cells) case at $\tau = 11$, $M_\infty = 0.3$, $\alpha = 30°$, $R_e = 1.25\times10^6$. (Inboard twin-tail position).

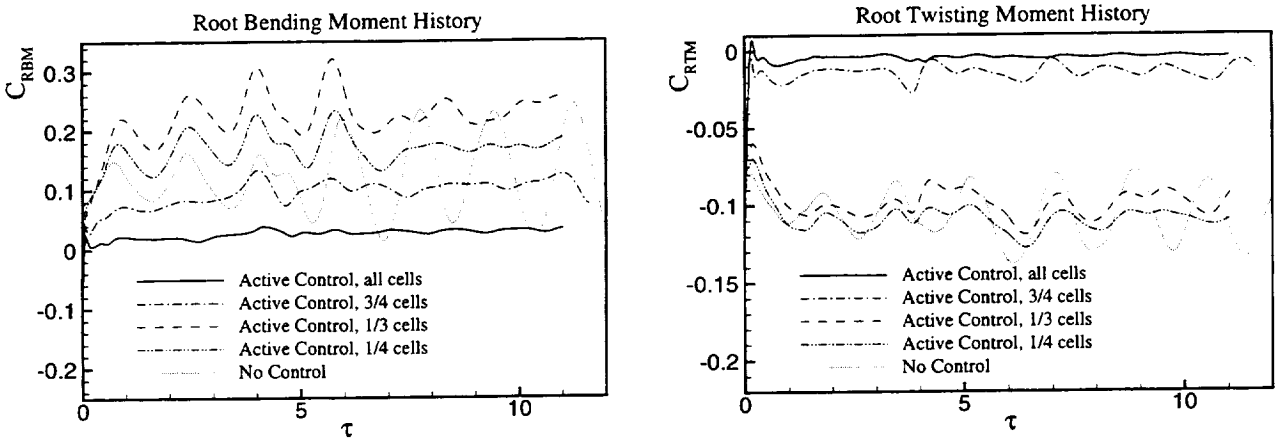

Figure 10: Effect of Active Control on the history of right tail root bending moment and twisting moment coefficients for uncoupled bending-torsion modes. $M_\infty = 0.3$, $\alpha = 30°$, $R_e = 1.25\times10^6$.(Inboard twin-tail position).

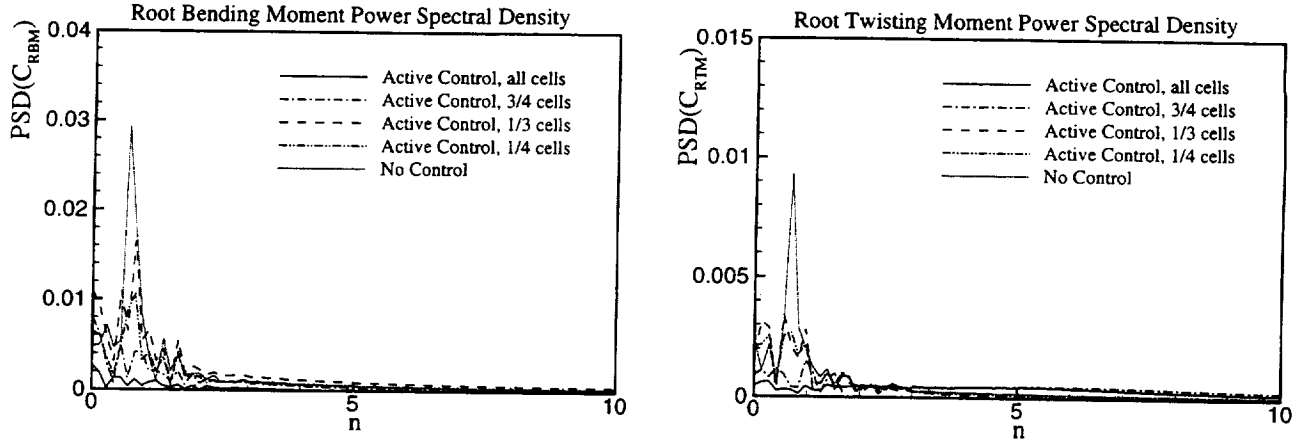

Figure 11: Effect of Active Control on power spectral density of right tail root bending moment and twisting moment coefficients for uncoupled bending and torsion modes. $M_\infty = 0.3$, $\alpha = 30°$, $R_e = 1.25\times10^6$.(Inboard twin-tail position).

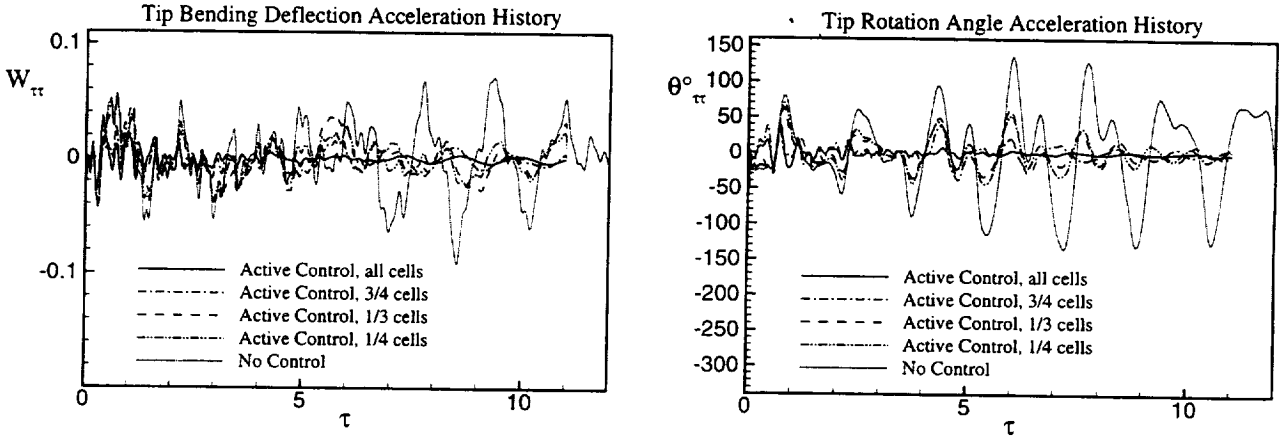

Figure 12: Effect of Active Control on the history of right tail tip bending and torsion accelerations for uncoupled bending and torsion modes. $M_\infty = 0.3$, $\alpha = 30°$, $R_e = 1.25\times10^6$.(Inboard twin-tail position).

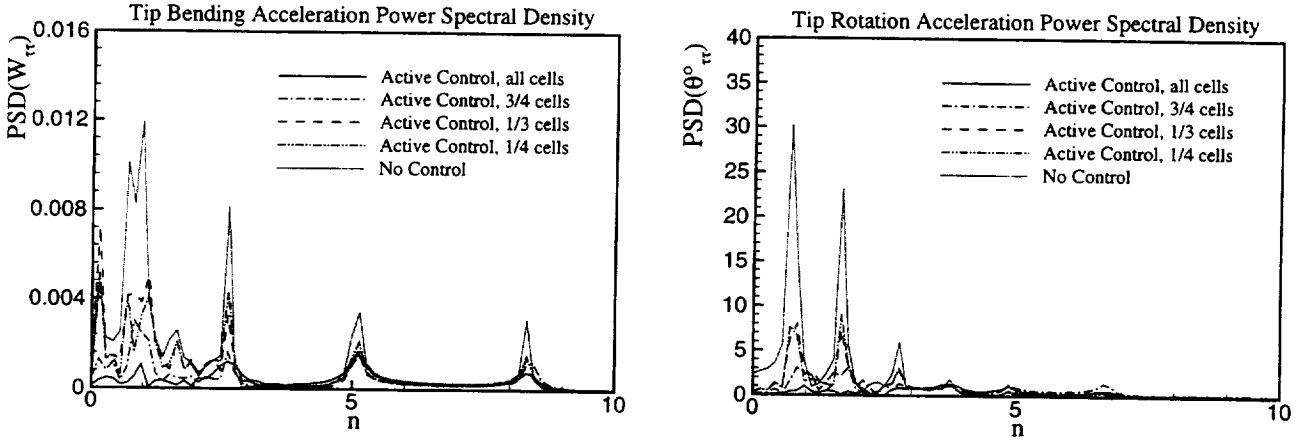

Figure 13: Effect of Active Control on power spectral density of right tail tip bending and torsion accelerations for uncoupled bending and torsion modes. $M_\infty = 0.3$, $\alpha = 30°$, $R_e = 1.25\times10^6$.(Inboard twin-tail position).

An Overview Of Landing Gear Dynamics

by

Jocelyn Pritchard

Abstract

One of the problems facing the aircraft community is landing gear dynamics, especially shimmy and brake-induced vibration. Although neither shimmy nor brake-induced vibrations are usually catastrophic, they can lead to accidents due to excessive wear and shortened life of gear parts and contribute to pilot and passenger discomfort. Recently, NASA has initiated an effort to increase the safety of air travel by reducing the number of accidents by a factor of five in ten years. This safety initiative has spurred an increased interest in improving landing gear design to minimize shimmy and brake-induced vibration that are still largely misunderstood phenomena. In order to increase the understanding of these problems, a literature survey was performed. The major focus of the paper is to summarize work documented from the last ten years to highlight the latest efforts in solving these vibration problems. Older publications are included to understand the longevity of the problem and the findings from earlier researchers. The literature survey revealed a variety of analyses, testing, modeling, and simulation of aircraft landing gear. Experimental validation and characterization of shimmy and brake-induced vibration of aircraft landing gear are also reported. This paper presents an overview of the problem documented in the references together with a history of landing gear dynamic problems and solutions. Based on the assessment of this survey, recommendations of the most critically needed enhancements to the state of the art are given.

Problem Definition

Landing gear vibration includes self-induced oscillations referred to as shimmy and brake-induced vibration. Shimmy may be caused by a number of conditions such as low torsional stiffness, excessive freeplay in the gear, wheel imbalance, or worn parts. Brake-induced vibration includes conditions known as gear walk, squeal and chatter which are caused by the characteristics of friction between the brake rotating and nonrotating parts. Squeal refers to the high frequency rotational oscillation of the brake stator assembly whereas chatter and gear walk refer to the low frequency fore and aft motion of the gear.

Shimmy

History and Background

It is generally acknowledged that the fundamental contributions to understanding shimmy were made by the French whereas the Germans were responsible for much of the subsequent systematic development. In France and Germany shimmy was regarded as a problem that should be dealt with early in the design stages. In the United States, the general tendency was to fix a problem after it had occurred. The U.S. literature is quite extensive but was not considered to be representative of a systematic development. There were also significant contributions from other countries, including Russia whose papers did not begin to appear in the literature until the 1930's. (Ref.1)

The first fundamental contributions toward understanding the shimmy phenomenon emerged from the automobile industry in France around 1920. Of particular significance was that given by Broulhiet

published in 1925. (Ref. 2) His observations on the role of tire mechanics on shimmy behavior are still followed today. While Broulhiet concentrated his attention on the tire, Sensaud de Lavaud (Ref.3) formulated the first fundamental shimmy theory. His theory incorporated a rigid tire that disregarded any effect of ground forces on the tire. Fromm (Ref. 4) also studied wheel shimmy in automobiles and recognized the similarities between the wheel vibration problems in automobiles and aircraft. He was one of the first to identify the vertical elasticity of the tire as the main contribution to the vertical displacement of the vehicle. His earlier investigations on rolling slip of deformable wheels led him to study the effect of sideslip or yaw of the rolling wheel due to lateral forces. Fromm's studies of lateral forces acting on the wheels led to the realization that these forces were coupled with the shimmy oscillation through the moment of the forces about the longitudinal axis. Either damping or build-up of the initial disturbance would occur depending upon the phase shift between the coupled motions. Von Schlippe and Dietrich (Ref. 5) made significant progress in defining the yaw angle and the swivel angle as arbitrary functions of time. Their tire concept was simplified as a thin band with lateral elasticity leading to simple expressions for the forces and moments. This eventually became known as the String Theory.

Some of the earliest investigations of shimmy problems in aircraft took place at Wright Field in Dayton, Ohio. In 1944 (Ref. 6) initial taxi testing of a fighter aircraft (Me 309) exhibited severe shimmy of the nose gear. Design of new piston shimmy dampers in coordination with landing gear manufacturers eliminated shimmy entirely for this aircraft. Other efforts at Wright Field (Ref. 7) included analysis development and validation by test. One such effort utilized a steel drum to perform studies on various airplane tires to correlate lateral deformation and lateral tractive force to banking angle and lateral-load force. In 1950, even though the shimmy problem had been studied for many years it was still a very common occurrence in automobiles, trailers, and aircraft. Physical control of shimmy was available in hardware such as shimmy dampers, but little was known about the cause of shimmy. Wright Air Development Center (WADC) started a program in 1951 to study the problem of shimmy and to learn the deficiencies of earlier efforts to combat the problem. The program included the development of a theory of shimmy, computer studies, experimental research on a laboratory model, and full scale testing. Even though earlier efforts traced the shimmy problem to the mechanical properties of the pneumatic tire, it was during this study that Moreland (Ref. 8) theorized that the tire support flexibility was a more important consideration than the tire mechanics. He contended that a shimmy theory based on the elastic properties of the tire alone was insufficient and that torsional and lateral rigidities, the wheel moment of inertia, and the weight of the strut were also critical in defining system stability. (Ref. 9) Only a fairly complete model of the structure including the tire properties could properly evaluate the stability of the system.

During the 1970's many investigators attributed landing gear vibration to wheel and tire imperfections and road surface roughness. References 10 and 11 found that when the frequency of the normal load oscillation was approximately twice the shimmy frequency, a decrease in the shimmy stability would occur. This loss of stability was primarily due to the variations of tire parameters with normal load. Other investigations found that shimmy motion was large when the frequency of wheel shimmy was close to the frequency of the wheel rotation. This resonance occurred at a particular forward velocity that was a function of the trail of the system. Studies concluded that braking forces tended to increase stability and that traction forces decreased stability even though these effects are small. By 1980 gear designs were having to adapt to increasing gross weight of the aircraft, increasing aircraft flexibility, higher ground roll speeds, and substandard landing fields. By now it was apparent that in order to fully understand the shimmy problem it was necessary to account for airframe flexibility and the coupling between the gear and airframe, and to weigh the effects of free play in gear components and damping devices on the system. There were many new areas of landing gear design that had emerged and needed attention. For example, ground simulators were being developed for pilot evaluation of steering capabilities that created a need for

accurate mathematical models and flight testing for simulator verification. Structural and system testing were performed both during and after the design stage to substantiate the strength and performance of the gear. Tire braking and cornering data were practically non-existent during this time and oversimplification of many system parameters made for inaccurate models. Shimmy damping requirements often conflicted with good high-speed directional control. Composite carbon brakes were introduced and anti-skid systems were being used to optimize the braking performance and prevent skids and tire blowouts. Air-over-oil shock struts typically provided shock absorption where the damping was a function of the shock strut stroke. (Ref. 12)

Airframe Flexibility Effects

In references 8 and 9 Moreland characterizes shimmy by defining the relationship between a single non-dimensional quantity called the inertia ratio and the dynamics of the airframe. In most cases he studied, when the simplest systems were stable, the higher order systems were not less stable. To precisely describe the system and the shimmy phenomena, the mathematical model required 5 degrees of freedom: tire deflection, swivel angle, strut deflection, damper-linkage strain, and airframe motion. Comparisons of various systems were made with and without tire elasticity. The stability of the gear was influenced by 15 system parameters that were brought together in the shimmy analysis by a seventh order characteristic equation of the model. Routh's stability criterion was applied to the equation to study the effects of changing gear parameters on the stability of the gear. Plots of dimensionless quantities such as velocity ratio, damping ratio, mass ratio, trail ratio, and inertia ratio defined the stability boundaries.

In 1960 at NASA Langley Research Center a simple experimental model of an aircraft was used to study the effects of gear and airframe variables on nose landing gear shimmy behavior. (Ref. 13) A dynamically scaled skeleton model of an aircraft with a single main skid and castering wheel was towed on a moving belt runway at constant speed. The simplicity and size of the model made it relatively easy to vary model parameters for different configurations. This enabled evaluation of the gear through repeated observations of the model's response to varying conditions. Nose wheel steering and forms of shimmy damping were shown to have a stabilizing effect when the wheel was at an angle to the direction of motion. Another study of the role of airframe dynamics in shimmy analysis is described in reference 14. This report describes the theoretical and experimental study of the F-101 and F-104 nose landing gear shimmy. The dynamic response characteristics of the airplane fuselage were simulated during these tests with a mechanical fixture attached to an overhead platform that served as a mounting structure for landing gear. Frequency response characteristics were obtained experimentally by applying a periodic input to the fuselage at the nose gear station and recording the resultant bending and torsional motions. A graphical technique was used to fit the theoretical frequency response data to the experimental data to determine the parameters of the simulator from the transfer functions. Fuselage simulators were then designed and used to test the F-101 and F-104 aircraft systems.

Reference 15 presents an analytical method to determine the random vibration response of a flexible aircraft caused by runway irregularities transmitted through the main gear struts. The runway profile is represented as a stationary Gaussian random process. The statistical or power spectral approach yields only an average or root mean square value of the response. This method is useful for estimating fatigue effects in airframes and landing gear and has value for investigating the effect of parameter variations in the average sense. The major drawback of this approach is that in order for the probability distribution to be independent of the position along the length of the runway, the profile has to have the same degree of roughness at all points which is usually not the case. In 1976 a simplified model of the longitudinal vibration of a landing gear strut during landing and spin-up of the wheel was developed. The influence of

the lateral forces on the rotating wheels during landing was studied while accounting for the interface between the strut and airframe. (Ref. 16) The elastic forces produced in the strut were calculated from landing gear and aircraft fuselage modes.

There have been recent efforts to approach the landing gear shimmy problem as a "flexible landing gear interaction with flexible aircraft" problem as in reference 17. This paper presents their approach to integrating the flexible properties of the aircraft into the shimmy investigation of nose landing gear during the development phase of a fighter aircraft. Taxi tests of the prototype indicated a severe shimmy oscillation at a frequency of 25.7 Hz. After considering several potential fixes, it was found that increasing the pressure level in the nose gear tire removed the oscillation. Higher order models of landing gear legs were used to include all the features that are needed to represent the interactions with other subsystems during ground roll and landing simulations. The most important parameters in this shimmy investigation were the relaxation length or length of the ground contact area of the tire and the damping (friction) of the piston against the cylinder. The elastic fuselage modes were not considered to be important if the leg mode frequencies were well separated from the aircraft mode frequencies.

Role of Tire Theories

As previously mentioned, tire mechanics are intimately related to the shimmy problem. Tire models were very difficult to define due to the influence of the ground forces on tire behavior. Since the problem of shimmy and self-excited vibration of landing gear has existed for such a long time, many theories on the elastic deformation of tires had been proposed. There was much controversy over the advantages and disadvantages of these theories due to erroneous conclusions presented in previous papers on tire mechanics and shimmy. (Ref. 18) The tire theories were categorized into two basic groups. (Ref. 19) The major difference between the two groups is the number of coordinates used to describe the tire deformation. The first group yielded the simplest theory because there was no tangible model. The tire was taken into account by considering its kinematical behavior in the overall system. This group includes Moreland's point contact theory that assumed the interaction between the ground and the tire could be treated as a single point. (Ref. 8) This theory accounts for the effect of side force on the yaw angle of the tire and a time delay between the application of the side force and the steady state yaw. (Ref. 18) The second group utilizes a physical model of the tire. The most renowned example of this group is the string model. (Ref. 5) In this theory, the tire is approximated by an elastic string stretched around the outer edge of the wheel and attached by elastic springs. The elastic restoring effect of the tire is based on a linear principle that the deviation from the original swivel angle is proportional to the lateral deflection of the tire. The tire force and moment are found by integrating the infinitesimal effects of the deformations. (Ref. 18) This theory assumes pure rolling of the tire. Pacejka (Ref. 20) improved this approximation by using multiple stretched strings to simulate the width of the tire and nonstationary properties of the rolling tire are included. Most theories are linear which meant only small perturbations and no sliding in the contact area of the tire are addressed. These methods are considered to be effective for low frequency applications. Pacejka's method is particularly applicable to vibration problems of steering and suspension systems of vehicles at high speed and frequency. Simple equations are derived that relate inertial forces to dynamic displacements and external ground forces to static displacements of the tire center plane. His analytical results compared well with experimental data.

In 1957 Smiley (Ref. 21) developed a summary theory that combined many features of the existing theories and included comparisons with experimental data. The summary theory is a minor modification of the basic theory of Von Schlippe and Dietrich (Ref. 5) that includes tilting of the tire in more detail while omitting Pacejka's refinements necessary for wide tires. The kinematic relations of the lateral deflection of

the tire ground-contact center point with the corresponding wheel coordinates of lateral deflection, swivel angle, and tilt angle are given for a rolling tire. Information about tire distortion is utilized in the derivation of these kinematic relations. Equations for the forces and moments on the wheel together with the kinematic relations establish the equations of motion for a rolling wheel. The theory was not validated for full-scale conditions and there was no reliable method at that time to predict the elastic characteristics of tires that were needed for shimmy analysis. Discrepancies were contributed to tire hysteresis effects and other nonlinear influences however, there were no strong indicators that nonlinear theory was necessary to predict stability boundaries. References 18 and 19 provide comparisons of the two basic theories from a validation standpoint as well as from computational and clarity aspects. It was found that both of these fundamental linear theories predicted shimmy characteristics of landing gear systems if the input parameters were properly chosen.

Brake-induced Vibration

Technological advances in aircraft led to smaller brakes with more energy to dissipate, lighter shock struts with higher strength materials, and increased flexibility all of which increased the likelihood of vibrations of landing gear due to braking action. Brake-induced vibrations in landing gear may be induced for several reasons. The self-excitation of modes due to negative damping arises from variations in the coefficient of friction with instantaneous slip velocity. Forced oscillations are due to irregularities in the friction surfaces. Self-excited whirl vibration is caused by eccentricity of rotating and non-rotating brake parts. The Information Report on brake dynamics of the SAE Committee A5 in 1997 (Ref. 22) categorized these landing gear dynamic vibration problems. A uniform method of classifying brake characteristics was given in terms of coefficient of friction, dynamic variation of friction coefficient, wear variation, and torque versus pressure characteristics. Self-excitation may be induced by large variations in the stiffness of brake components, poorly phased feedback in the anti-skid system, and tire lock-up corresponding to maximum drag. Solutions to these vibration problems included provision of basic aircraft parametric data from airframe manufacturers for analysis and testing. Data collection from flight testing is needed for skid control on wet and dry surfaces at shimmy speeds. Brake history and frequency and amplitude of vibration are desirable in order to characterize a pattern.

One of the early investigations on brake vibration was reported in reference 23 where a study of landing gear vibration due to brake chatter and squeal during taxi and landing was performed. The report contains both experimental (static, dynamic, and taxi tests) and theoretical studies explaining the basic phenomena and pointing out the important design considerations. Static tests were conducted to determine parameters such as weight and mass moments of inertia, damping ratios, and spring rates that were needed for analytical studies. Dynamic tests included brake and strut dynamometer testing that measured drag loads, brake pressure, wheel speed, side force, fore and aft motion of the axle, and angular acceleration of the axle. Taxi tests involved a number of relatively uncontrollable variables which is why it is difficult to achieve the same results with the dynamometer tests. Systems of individual masses, springs, and dampers were used to represent the landing gear to aid in studying the effects of friction characteristics of the brake on the dynamic stability of the gear. Only linear solutions were considered in this report, however, it was recommended that non-linear friction characteristics be included in future theoretical studies. The dynamometer tests revealed a connection between the chatter frequencies and the wheel rotation. Theoretically, decreases in chatter amplitudes were noticed for increases in strut damping, rolling radius, and total mass. Another effort to study landing gear chatter and brake squeal vibrations was at the Naval Research Laboratory during the development of a digital program to simulate the DC-9 aircraft main gear slowing to a stop. (Ref. 24) The analytical model represented the fore and aft motion of the gear with

accompanying rotational motion at the gear axle. Comparison of computed responses and measured data indicated reasonable simulation accuracy. The analysis showed that brake torque was the primary contributor to chatter and squeal vibration. Increasing the brake torque in combination with diminishing brake rotor to stator angular velocity instigated the vibration. This function effectively produced a negative damping that sustained or increased the vibration amplitudes. Attenuation methods included using a mix in the brake lining that ensured a flat brake torque function. Vibration absorbers were also suggested even though an excessive weight penalty existed for chatter vibration absorbers.

At Wright Patterson AFB dynamometer tests were performed to simulate normal service conditions experienced by the brake on the T-38A aircraft for the purpose of investigating the brake characteristics (Ref. 25). Brake torque, hydraulic pressure, dynamometer flywheel speed, and test wheel speed were measured during dynamometer tests performed on a B. F. Goodrich 2-727 brake assembly at three different deceleration and brake initiation speeds to determine the kinetic friction and relative rubbing velocities. The experimental data and the analysis both indicated that the system was stable. Dynamometer test temperatures were used to investigate the temperature response of the brake rotor and stator during braking. A comparison to the analytical model showed good reliability for predicting rubbing surface temperatures. Predicting these temperatures accurately is advantageous to designers due to the potential for strut chatter and metallurgical design criteria. All tests were conducted on new brakes, however, it was suggested that these tests and analyses should also be performed on worn brakes to observe any differences in the results. More recent investigations emphasized the effect of the variation of friction coefficient with slip velocity between rotors and stators as in reference 26. This report also gives an overview of the stability and modal interactions caused by nonlinear negative damping at the brake friction interface. It was emphasized in reference 27 that the braking system should be analyzed as a global system rather than as separate components due to the coupling between the parts. Nonlinear modeling of aircraft landing gear brake whirl and squeal was discussed in references 28-30. These studies found that system stability could be altered by changes in the brake friction coefficient, pressure, stiffness, geometry, and various brake design parameters.

Modeling and Simulation

Traditionally the emphasis in analytical prediction capability was on landing impact loads since these were considered to be the largest that the aircraft would experience. The oscillatory loads from taxiing were deemed as secondary. The emphasis eventually included the requirement to more accurately model the gear to improve the dynamic response predictions. The state-of-the-art in modeling techniques for landing gear prior to 1980 was summarized in reference 31. There was a need for experimental verification of the details of the gas compression process and determination of the parameters that affect this process such as hydraulic fluid compressibility, fluid-gas mixing, and deformation of the gear chamber. The orifice coefficients were considered extremely important for calculating the response of the gear and very accurate procedures were needed to determine these values for hydraulic damping. Since the orifice flow is highly unsteady, problems arose when steady flow hydraulic force models were used in taxi simulations. Most models included friction as dry or Coulomb friction but frictional forces were sometimes left out of the analysis because a good method for measuring these forces was not known. Normal forces on the bearings that create friction forces were dependent on the gear geometry and the wheel loading. For flexible models where the deformation of the gear was included in the analysis, determination of the normal forces became very complex. The tire was modeled as a simple spring (linear and nonlinear) with point contact with the ground and linear viscous damping. Tire stiffness was represented by static load deflection curves either provided from experiment or manufacturer. The tire interface with the ground and the geometry of the tire footprint was an area that needed more attention. Numerical simulations could be used

with some confidence to predict fatigue and peak loads if the analysis had been evaluated with taxi or drop test data. Modeling and simulation efforts over the past ten years have become fairly sophisticated as input data has been carefully scrutinized and experiments are conducted to validate models. Efforts to model nonlinearities such as damping and friction characteristics were becoming more prevalent. Several examples of modeling gear systems are given below.

In reference 32 an analysis of fatigue of light aircraft landing gear using random properties and surface profiles was developed. The system was modeled as a linear, 1 DOF nonstationary vibrating system referred to as a random parametric vibration problem that uses a recently developed random matrix method. Reference 33 is a follow up to the work described in reference 3 with nonstationary damping and random nonstationary loads included. The random matrix method was shown to be better suited for this type of problem than a hybrid Monte Carlo technique. In reference 34 modeling and parameter identification of single degree of freedom structural systems are investigated. Experiments were conducted to measure the free response of these structural systems and the measurements were used to formulate system models and parameters. Models include a linear, damped oscillator and a nonlinear shock strut with and without friction forces. Results showed that it is possible to model and identify a physical structure such as a damped oscillator with damping effects. Comparisons between the response predicted by the model and the response measured experimentally agreed for the first few seconds of motion but then deteriorated in later stages. This was due in part to ill-conditioning of the equations even though experimental measurements were used to identify the model parameters of the system. Models developed in references 35-39 include the effects of linkage dynamics, damper mounting characteristics, Coulomb friction, nonlinear tire, air spring, oleo damping forces, torsional freeplay, and spring hardening effects of bending and torsional stiffness.

An example of non-linear modeling involved an A-6 Intruder nose gear. The model included nonlinear effects in the pneumatic air spring, stick-slip friction, velocity squared damping, geometry governed discharge coefficients, and tire model. Analytical results were in excellent agreement with test data that was acquired at NASA Langley Research Center. (Ref. 40) Reference 41 describes linear and nonlinear analysis methods applied to investigate the shimmy of a simple nose gear model. The nonlinear shimmy model consisted of torsional dynamics of the gear, the forces, moments, and lateral elasticity of the tire using elastic string theory. Results showed that the occurrence of shimmy increases with increasing velocity, lower torsional damping, and increasing vertical force. The numerical simulation results confirm the stability of the linear system and provided additional information concerning the nonlinear regions. Reference 42 is an example of a model that includes an error feedback control law for anti-skid braking simulation used in determining the effects of structural parameters on gear walk instability. The effect of longitudinal stiffness of the tire, the vertical damping of the tire, and the inclination angle of the strut on gear walk stability were investigated.

There were also efforts to study and compare modeling techniques. Reference 43 developed simulations and analyses of conventional oleo-pneumatic landing gear during taxi and landing impact. Simplification of the model and the effect of certain element omissions on the model fidelity were pointed out. For example, constant spring and damping coefficients will not provide a realistic simulation effect. The hydraulic force is a function of metering pin and strut closure and therefore cannot be represented by a single force closure rate. This curve is different for acceleration and deceleration phases. Reference 44 gives a review of two landing gear shimmy models demonstrating the use of the Moreland tire model and the Von Schlippe-Dietrich tire model. The models were used to perform a parametric study of the effect of numerical variation of several input parameters on the stability of the gear. A comparison is made of the analytical results to experimental data showing good agreement of the limit cycle oscillation frequency. Both analyses were considered to be successful in determining the stability characteristics of landing gear.

The results suggested that dynamic modeling of the gear would significantly improve the accuracy of the analytical predictions. It was discovered that the spring stiffness values were stability critical parameters and if the fuselage flexibility effects are not taken into account, the measured values of the stiffness parameters may be in error by as much as 3 times the actual values.

General-purpose computer programs were also being developed to model complete landing gear systems. An example of this type of modeling is described in reference 45 where the Dynamic Analysis and Design System (DADS) program is used to model the response of two types of landing gear on damaged and repaired runways during landing, taxiing, and take off. Both the cantilevered and the articulated models included nonlinear effects such as the hydraulic orifice damping, pneumatic air spring, bearing friction forces in the strut, and a tire-load deflection curve. These models could be used as stand alone gear on a runway surface or combined together to simulate an entire aircraft. The dynamic analysis and simulation show results such as strut loads and stroke for different runway profiles. The plots indicate stick motion of the strut and the animation capability in DADS gives an advantageous view of the response of the gear rolling over a runway.

Finite Element Modeling

Finite element modeling has become a useful tool for studying dynamic stability issues of landing gear. Reference 27 describes finite element modeling of the whirl and squeal modes of landing gear and braking systems. Correlation between the analysis and various system component tests as well as the performance of the complete model and actual system during operation are performed. Models include landing gear, wheels, brakes, and tires. Design sensitivity studies are also used to evaluate component changes during the design process. A feasibility study of computing nonlinear finite element simulations of whirl and squeal dynamics is discussed in reference 28. DYNA3D is an explicit finite element code that uses the central difference method to integrate the equations of motion in time. The model includes the aircraft inertia and tire flexibility effects without adding extensive computational expense. Advantages of using this method over more commonly used linear complex finite element analysis are evident in the nonlinear transient analysis capability, the ability to model nonlinear stiffness and damping effects of hydraulic fluid, modeling whirl and squeal instabilities with negative damping, and provision for modeling a sliding interface.

Software Development

Reference 46 uses a library of components based on finite element methods which range from beams and springs to very specific landing gear elements such as shock absorbers, actuators, flexible sliders, and flexible wheel elements. Customization of elements is also available through user defined elements. Results presented include simulation of a drop test, taxiing on repaired runway, tire burst during rollout, and shimmy of a two-wheeled cantilever gear. Reference 47 developed a very comprehensive landing gear model and simulation software capability that integrates landing gear and braking systems with an aircraft for the purpose of parametric design. The software can be used during the conceptual design stage or to evaluate proposed modifications for an existing configuration. All phases of aircraft landing gear dynamics have been included to a fairly high level of detail including take-off, landing, steering, and taxiing. Also flexibility of the strut and bogie were modeled. The software is composed of modules that correspond to different subsystems or components such that a wide range of configurations can be modeled from a single landing gear strut to a whole aircraft with multiple gear. The software has the capability of modeling the aircraft as a flexible body that may be important in configurations that have more than two

main gear across the fuselage. A finite element model is used for the strut component of the gear. Since the frequencies and mode shapes change as the gear is extended or compressed the model is evaluated at several different positions and interpolated in between. A modal reduction routine is used for removing unwanted modes in order to preserve the efficiency of the software. The oleo, bogie, brakes and wheels, braking servo, steering actuation, control systems, tires, and runway profile are also included in the model. The software has been validated with test data and an example of a drop test is given in the paper.

Sensitivity Analysis and System Studies

With the development of more accurate models for analyzing gear vibration problems, system sensitivity studies became feasible and valuable in the design and evaluation of landing gear dynamics. Ref 14 describes a sensitivity study of several service variables on the dynamic stability of the F-101 and F-104 landing gear systems. Among the studies are the effects of wear, manufacturing tolerances, and normal maintenance procedures on the nominal gear. These studies were helpful in determining if optimum performance of the gear could be achieved by changing the values of the nominal service variables. Also, it was important to establish guidelines that stated if any deviations in these service variables from their nominal values would be detrimental to the performance of the aircraft. Torsional free play of the F-104 gear was found to have the most profound effect on the stability of the gear, particularly for fully extended operation. Tire unbalance reduced the dynamic stability of the gear when adverse values of other service variables were present such as air in the steer-damp unit or excessive torsional free play. For the F-101 gear, tire unbalance was shown to have a severe effect on the stability. Reference 48 describes an analytical method of determining the sensitivity of various parameters of the landing gear and the braking system on the landing gear dynamics during landing. The differential equations of motion of an 11 degree of freedom system in generalized coordinates are written using Lagrange equations which are solved with variations of the parameters. During the design modifications of the F-15 reported in reference 49, landing gear shimmy tests were performed using a dynamometer facility and prototype landing gear. Several instances of shimmy were encountered during testing and the results indicated that shimmy speed was a function of strut torsional free play. Nonlinear analyses showed the sensitivity of shimmy speed to changes in tire parameter values and frictional coefficients. The sensitivity analysis reported in reference 50 showed that forward speed, vertical velocity, pitch attitude, and damping coefficients of the landing gear have the largest effect on the g loads at touchdown. The nonlinear model described in reference 37 varied system parameters to study the dynamic behavior of a dual wheel nose-gear system. The study included parameters such as wheel span and cant angle, mass of the torque arms and its relative position to the shock strut, torque arm stiffness, damper stiffness, wheel size and mass, and tire vertical and lateral stiffness.

Messier-Dowty has studied shimmy phenomena in order to improve the prediction of the dynamic behavior of landing gear systems. In reference 51 they have developed several models with many input parameters, particularly non-linear parameters and made comparisons to test data. Simulations show sensitivities of shimmy stability to variations in these parameters and reinforce the need for taking nonlinearities into account. The effects of longitudinal tire stiffness, vertical damping, and inclination angle of the strut on gear walk stability are investigated in reference 42. The analytical model was developed to study the behavior of main landing gear during taxi and braking. The model includes an error feedback control law for anti-skid braking simulation. In Reference 52 system studies were performed for landing impact and taxi for three types of dual-chamber shock struts to aid in the selection process when designing landing gear for different applications. The strut behavior was calculated for the design energy conditions of a transport aircraft. No validation of the equations and results was performed. Reference 53 gives an example of a shock strut model for an articulated landing gear that was used for the purpose of

comparing different linkage system configurations. Linkage mechanisms are important for achieving mechanical advantages and other improvements in weight, reduced friction, and steering. The strut model included hydraulic damping and pneumatic spring forces, but seal and bearing friction were neglected during landing conditions. The tire model was relatively simple having empirical coefficients obtained from static testing. The simulation also included aerodynamics, engine model, and ground effects. Reference 54 developed a numerical to study the advantages and disadvantages of decreasing the initial charge pressure of the air-oil chamber in the strut. The analysis was performed with and without the effects of the relaxation properties of the tire which influences the maximum load point in the lower part of the strut but does not affect the upper part of strut or fuselage. The advantage of shortening the strut did not outweigh the disadvantage of increasing the stiffness of the strut both caused by "soft-filling".

Testing and Validation

The literature was reviewed for examples of testing for verification of analytical models, accurate parameter identification for input into analytical models, and determining the stability of gear designs. Reference 55 describes analytical and experimental studies of shimmy for the DASH 7 and DASH 8 aircraft to understand nose gear shimmy and to aid in the development of analysis methods for predicting shimmy. Shimmy occurred during service of the DASH 7 nose gear and was predicted during the design of the DASH 8 main gear. Aircraft ground testing of a DASH 7 nose gear investigated variables such as free-play in the scissors, effects of spin-up transient oscillations, and time-delay steering mechanism. The analysis model used represents backlash, bearing friction, scissors stiffness and free play, and fuselage torsional stiffness and free play. The frequencies predicted were 20% higher than the values measured and was attributed to mass and stiffness modeling inaccuracies. Effects of free play and mass balance on stability were investigated. The main landing gear of the DASH 8 was prone to shimmy due to its long flexible design. Analytical results showed that increasing torsional stiffness and side bending stiffness of the gear would increase stability. Mechanical trail was increased to the maximum to improve stability also. The DASH 7 nose landing gear shimmy problem was contained at the expense of increased maintenance cost, pilot workload, and in some cases airplane weight. In the case of the DASH 8, all 400 airplanes in service are shimmy free but at the expense of increased time and effort to establish the final design with a weight penalty.

There are different approaches to testing landing gear. Test results may therefore differ as discussed in reference 56. Large differences still exist between dynamometer and airplane test results. Although it is possible to predict the dynamometer results with an analytical model of the dynamometer test setup if the dynamics of the overhead rig are included, the dynamometer predicts much more stable behavior than the actual landing gear on the aircraft. The lack of complete simulation of the torsional squeal modes interaction with the rest of the landing gear structure, and the lack of simulation of low frequency modes can result in significant differences between the stability of important modes in the lab as compared to the actual aircraft. Another large difference between the dynamometer and the aircraft landing gear is the modal density in the low frequency range between 0 and 50 Hz. For the example discussed in the reference the main landing gear had fifteen modes in this range where the simulator of the gear had only two. The lack of simulation of the low frequency modes of the landing gear system can result in significant differences between the stability of important modes in the laboratory as compared to the aircraft. The author states that a simulator of this type can be used to predict airplane performance only if it is used in conjunction with a detailed analytical model of the complete landing gear system. Reference 57 gives a brief overview of a 1993 NASA test program to study aircraft nose gear shimmy. The parameters were torsional stiffness, torsional freeplay, wheel balancing, and worn parts. Steerable nose wheels were

particularly susceptible to shimmy problems. Test results of the Shuttle nose landing gear compared with that of a steel dynamometer showed little difference except in the case of a simulated flat tire test. This test was shown to be significant only in the dynamometer data. Basically vertical load had little effect on maximum steering collar rotation, maximum axle acceleration and maximum wheel swivel acceleration for the shuttle nose gear tests which also confirmed earlier dynamometer data that shimmy did not appear to be a problem. Reference 58 describes methodology to measure nose landing gear shimmy parameters using T-46 static test article and static force-deflection measurements. The shimmy stiffness and torsional freeplay parameters were then input into a shimmy analysis that incorporated the Moreland tire model. Stability was predicted over a speed range of 20 to 140 knots. The prediction was validated through taxi tests of the T-46. In reference 59 a mathematical model was developed to analyze the stability of the F-28 and other similar gear and then validated through ground vibration tests and aircraft taxi tests. It was found that this gear was basically unstable. An examination of the modes of the gear model found that the torsional-yaw mode had negative damping for velocities above 70 m/s at a .25 m vertical deflection of the shock absorber. A shimmy damper was included at the apex of the torque links that proved to be stabilizing in the analysis as well as subsequent flight tests. Eventually experimental testing in landing gear systems and components was performed to determine critical input parameters for improving analytical methods. Taxi tests of the airplane were not conducive to developmental work on the gear or for broad investigations of the effects of system parameters, therefore laboratory tests were the most cost-effective way to investigate the stability of the gear.

Stability characteristics have been examined in the laboratory over the complete range of speed, vertical load, and service parameter changes. Reference 60 examines several major differences between laboratory tests and airplane tests. The mounting structure to which the landing gear is attached affects the frequency and damping. The curvature of the flywheel surface affects the rolling dynamics of the tire such as cornering power, relaxation length, and tire lateral spring rate. The melted rubber on the flywheel surface will change the friction between the tire and the flywheel surface causing the gear to be more stable than the actual. Landing gear exhibit non-linear characteristics such as friction and damping that are dependent on the level of excitation. Lab testing usually involves gear in new condition that is non-typical of actual landing gear systems. Because of these differences, the predictions are carried out by an experimentally verified analysis rather than directly from lab test results. Reference 60 describes one such effort to examine shimmy instability analytically during the design stages and by experimental testing. The critical input parameters for the analytical study were flexibility coefficients, damping and steering characteristics, fuselage frequency response, frictional torques, deadband values, and tire parameters which were determined in lab tests. Correlation between the lab tests and the analysis was very good. The complete landing gear was then tested either in laboratory simulation or taxi tests on the actual airplane.

Assessment and Recommendations for Future Work

Significant improvements in analytical predictions can be made if gear and tire parameters such as stiffness, damping, and friction are known as functions of load on the gear or aircraft ground speed. (Ref. 61) Obtaining these parameters can be very labor intensive. Some landing gear dynamicists are of the opinion that there is a need for standardized analytical modeling capabilities that are comprehensive and accurate but not cumbersome or computer intensive. These tools should be versatile enough to handle different types of gear as well as wheel/tire configurations and should be well maintained and documented. A database of predictions of aircraft contributions to the gear parameters would eliminate the need for labor intensive measurements on the aircraft. The need for a better understanding of damping and friction in the gear still exists today. Reference 62 gives an overview of the needs for improvements in analytical

modeling and testing. They contend that simulation models can be used in parametric studies to improve shimmy stability of gear designs, however, a total assessment of the system stability requires analyzing the entire operating range of the aircraft and can be difficult to obtain in this manner. In the open literature they found few publications that dealt with model simulations having significant impact on landing gear design. Still simulation can provide a less expensive alternative to full scale testing. Test findings indicate that torsional freeplay tends to destabilize the system whereas friction forces have a stabilizing effect. Separation of lateral and torsional frequencies through lateral and torsional stiffness modifications, adding negative or large positive mechanical trail, mass balance applied to the wheel axle, steering systems, and shimmy dampers are all methods for improving shimmy stability according to the references cited. Worn parts, tire wear, and tire inflation also adversely affect shimmy stability.

Landing dynamics issues have been the focus of the Aircraft Landing Dynamics Facility (ALDF) at NASA Langley Research Center since its inception in 1956. Landing gear vibration could be studied further in this facility. In January 1998 a workshop was held at NASA Langley where the aircraft landing gear community was invited to discuss vibration problems. Landing gear and tire manufacturers, commercial airline and general aviation personnel, FAA, and WPAFB were in attendance. The overall consensus was that analytical tools were available to predict shimmy and brake-induced vibration, but there was a need for accurate tire characterization to provide input for the models. They requested an update to the NASA Technical Report R-64 cataloging mechanical properties of aircraft tires including dynamic properties of radial and advanced bias-ply tires. Since the data for the original R-64 document were acquired at the ALDF it seemed appropriate to perform the update activity there as well. The test plan and schedule has been initiated and testing is projected to start in the summer of 1999.

Concluding Remarks

In order to increase understanding of landing gear shimmy and brake-induced vibration problems, a literature survey on landing gear dynamics was performed. The major focus of the paper was to summarize work documented from the last ten years to highlight the latest efforts in solving these vibration problems. Older publications are included to understand the longevity of the problem and the findings from earlier researchers. The literature survey revealed a variety of analyses, testing, modeling, and simulation of aircraft landing gear. Experimental validation and characterization of shimmy and brake-induced vibration of aircraft landing gear were also reported. This paper presented an overview of the problem documented in the references together with a history of landing gear dynamic problems and solutions. Based on the assessment of this survey, recommendations of the most critically needed enhancements to the state of the art were given.

References

1. Dengler, M; Goland, M.; Herrman, G., "A Bibliographic Survey of Automobile Aircraft Wheel Shimmy", WADC-TR-52-141, December 1951.
2. Broulhiet, G., "The Suspension of the Automobile Steering Mechanism: Shimmy and Tramp", Bull Soc. Ing. Civ. Fr. 78, pp. 540-554, July 1925.
3. Sensaud de Lavaud, D. "Shimmy, Pseudo-Shimmy and Tramp of an Automobile", C.R. Acad. Sci., Paris, Fr. 185, pp. 254-257, July 1927.
4. Fromm, H., "Brief Report on the History of the Theory of Shimmy", NACA TM 1365, pp.181, 1954.
5. Schlippe, V.B. and Dietrich, R. "Shimmying of a Pneumatic Wheel", NACA TM 1365, 1954.

6. Maier, E. and Renz, M., "Tests On Shimmy with the Nose Landing Gear of the Me 309 and the FKFS Trailer", N-579 AAF, Air Material Command, Wright Field Technical Intelligence, Dayton, Ohio, 1947.
7. Dietz and Harling, "Examination of Lateral Stress and Shimmy Phenomena on Airplane Wheel Tires", 1156.2 48, Headquarters Air Material Command, Wright Field, Dayton, Ohio, Aug. 1950.
8. Moreland, W.J., "Landing Gear Vibration", AF Technical Report No. 6590, October 1951.
9. Moreland, W.J., "The Story of Shimmy", Journal of the Aeronautical Sciences, Vol. 21, No. 12, December 1954.
10. Ho, F.H. and Lai, J.L., "Parametric Shimmy of a Nosegear", Journal of Aircraft, Vol.7, pp. 373-375, 1970.
11. Podgorski, W.A.; Krauter, A.I.; and Rand, R.H., "The Wheel Shimmy Problem: Its Relationship to Wheel and Road Irregularities", Vehicle System Dynamics, Netherlands, pp. 9-41, March 1975.
12. Attri, N.S. and Amberg, R.L., "Advances in Landing Gear Systems", AGARD CP-299, pp. 13/1-20, 1981.
13. Faber, S. "Dynamic Model Investigation of a Landing-Gear Configuration Consisting of a Single Main Skid and a Nose Wheel", NASA TN D-213, February 1960.
14. Black, R.J., "An Experimental and Theoretical Study of the Effects of Service Variables on the Dynamic Stability of Airplane Nose Landing Gear Shimmy", Bendix Report No. SV-62-4 (870), Bendix Products Aerospace Division, The Bendix Corporation, November 1962.
15. Kirk, C.L., "Analysis of Taxiing Induced Vibrations in Aircraft by the Power Spectral Density Method", Technical Report AFFDL-TR-72-74, January 1973.
16. Maksimova, T.I., "Vibrations of the Principal Struts of a Landing Gear During Landing", Theory and Practice of Designing Passenger Aircraft, (A77-27126 11-01), pp.345-350, 1976.
17. Luber, W.; Kempf, G.; and Krauss, A., "Self-Induced Oscillations of Landing Gear as an Integral Landing Gear Aircraft System Problem", AGARD-R-800, March, 1996.
18. Collins, R. L., Theories on the Mechanics of Tires and Their Applications to Shimmy Analysis", Journal of Aircraft, Vol.8, No.4, April 1971.
19. Sperling, E., "Shimmy Problems of Landing Gears Caused By Elastic Deformation of Tires", Proceedings of The 15th Congress of the International Council of the Aeronautical Sciences, London, U.K., September 7-12, 1986.
20. Pacejka, H.B., "Approximate Dynamic Shimmy Response of Pneumatic Tires", Vehicle System Dynamics 2, pp.49-60, 1973.
21. Smiley, R.F., "Correlation, Evaluation, and Extension of Lineraized Theories For Tire Motion and Wheel Shimmy", NACA Report 1299, 1957.
22. Society of Automotive Engineers Subcommittee A-5A, Wheel, Brakes, and Skid Controls, of SAE Committee A5, Aerospace Landing Gear Systems, "Brake Dynamics Information Report", SAE AIR 1064C, January 1997.
23. Edman, J.L., "Aircraft Vibrations Due To Brake Chatter and Squeal", WADC Technical Report 55-326, Wright Air Development Center, Air Research and Development Command, USAF, Wright Patterson Air Force Base, OH, October 1955.
24. Biehl, F.A., "Aircraft Landing Gear Brake Squeal and Strut Chatter Investigation", The Shock and Vibration Bulletin, Naval Research Laboratory, Washington, D.C., January 1969.
25. Brewer, J.D., "Experimental Investigation of Brake Characteristics Conductive to Strut Chatter", Report #: AD-780505 GAW/MC/74-2, Thesis for Master's Degree, Air Force Institute of Technology, Wright Patterson AFB, OH, March 1974.

26. Black, R.J., "Self Excited Multi-Mode Vibrations of Aircraft Brakes With Nonlinear Negative Damping", Proceedings of The 15th Biennial Conference on Mechanical Vibration and Noise, Boston, MA, September 17-20, 1995.
27. Chang, C.F., "Dynamic Finite Element Modeling of Aircraft Landing System", Proceedings of the ASME Design Engineering Technical Conference, Boston, MA, 1995.
28. Travis, M.H., "Nonlinear Transient Analysis of Aircraft Landing Gear Brake Whirl and Squeal", Proceedings of The 15th Biennial Conference on Mechanical Vibration and Noise, Boston, MA, September 17-20, 1995.
29. Liu, S.Y.; Gordon, J.T.; and Ozbek, M.A., "A Nonlinear Model For Brake Squeal Analysis I – Model Description and Solution Methodology", AIAA Dynamics Specialists Conference, Salt Lake City, UT, April 18, 1996.
30. Liu, S.Y.; Gordon, J.T.; and Ozbek, M.A., "A Nonlinear Model For Brake Squeal Analysis II – Stability Analysis and Parametric Studies", AIAA Dynamics Specialists Conference, Salt Lake City, UT, April 18, 1996.
31. Batill, Stephen M., "A Study of Analytic Modeling Techniques For Landing Gear Dynamics", AFWAL-TR-82-3027, May 1982
32. Huntington, D.E., and Lyrintzis, C.S., "Random Parametric Vibration in Aircraft Landing Gear", Proceedings of the 37th AIAA/ASME/ASCE/AHS/ASC Structures, Structural Dynamics, and Materials Conference, Salt Lake City, UT, April 1996.
33. Huntington, D.E. and Lyrintzis, C.S., "Nonstationary Random Vibration in Light Aircraft Landing Gear", Journal of Aircraft, Vol. 35, No. 1, pp.145-151, February 1998.
34. Batill, S.M. and Bacarro, J.M., "Modeling and Identification of Nonlinear Dynamic Systems With Application to Aircraft Landing Gear", Proceedings of the 29th AIAA/ASME/ASCE/AHS Structures, Structural Dynamics, and Materials Conference-Part 2, Williamsburg, VA, April 18-20, 1988.
35. Yadov, D. and Ramamoorthy, R. P., "Nonlinear Landing Gear Behavior at Touchdown", Journal of Dynamic Systems, Measurement, and Control, Vol. 113, pp. 677-683, December 1991.
36. Baumann, J.: Barker, C.R.: and Koval, L.R., "A Nonlinear Model For Landing Gear Shimmy", Proceedings of the ASME Winter Annual Meeting, Atlanta, GA, December 1-6, 1991.
37. Li, G.X., "Modeling and Analysis of a Dual-Wheel Nose Gear: Shimmy Instability and Impact Motions", Proceedings of the SAE Aerospace Atlantic Conference and Exposition, Dayton, Ohio, April 20-23, 1993.
38. Bespalov, V.A.; Metrikin, V.S.; and Peisel, M.A., "On the Dynamic Stiffness of a Landing Gear Nose Strut Hydraulic Damper System", Izvestiya VUZ. Aviatsionnaya Tekhnika, Vol. 32, No. 3, pp. 3-6, 1989.
39. Feld, Dennis J., "Analytical Investigation of Damping of Landing Gear Shimmy", Proceedings of the Aerospace Technology Conference and Exposition, Long Beach, CA, Oct. 1-4, 1990.
40. Daniels, J.N., "A Method for Landing Gear Modeling and Simulation With Experimental Validation", NASA CR 201601, June 1996.
41. Somieski, G., "Shimmy Analysis of a Simple Aircraft Nose Landing Gear Model Using Different Mathematical Models", Aerospace Science and Technology, Vol.1, No. 8, pp.545-555, 1997.
42. Zhagn, L. "Numerical Analysis of the Stabilities on Main Landing Gear Walking", Proceedings of the Third Asian-Pacific Conference on Computational Mechanics, Seoul, Korea, September 16-18, 1996.
43. Kapadoukas, G. and Self, A., "The Simulation of Aircraft Landing Gear", Systems Analysis Modeling Simulation, Vol. 21, No. 4, pp. 237-245, 1995.
44. Krabacher, W.E., "A Review of Aircraft Landing Gear Dynamics", AGARD-R-800, March, 1996.

45. Lee, T.W., "Dynamic Response of Landing Gears on Rough Repaired Runway", Proceedings of The Aerospace Technology Conference and Exposition, Long Beach, CA, September 23-26, 1991.
46. Thomas, P.; Geradin, M.; and Guyot, B., "Dynamic Simulation of Landing Gears", International Forum on Aeroelasticity and Structural Dynamics, Strasbourg, France, pp.1077-1096, May 1993.
47. Cowling, D. and Shepherd, A., "The Prediction of Landing Gear Behavior Using Dynamic Simulation", Proceedings of the International Forum on Aeroelasticity and Structural Dynamics, Manchester Business School, U.K.,June 26-28, 1995.
48. Maksimova, T.I.; Priven, V.D.; and Tomin, B.P., Vibrations of Landing Struts During Braking", Theory and Practice of Designing Passenger Aircraft, (A77-27126 11-01), pp. 337-345, 1976.
49. Grossman, D.T., "F-15 Nose Landing Gear Shimmy, Taxi Test and Correlative Analyses", Proceedings of The Aerospace Congress and Exposition, Los Angeles Convention Center, CA, October 3-16, 1980.
50. Kothari, S.S.; Ananthasayanam, M.R.; and Rajaiah, K., "Analysis of Dynamical Behaviour of an Aircraft at Touchdown", Proceedings of the 31st Aircraft Symposium, Hikoki Shinpojiumu Koenshu, Japan, Vol. 31, pp. 82-85, 1993.
51. Woerner, P. and Noel, O., "Influence of Nonlinearity on the Shimmy Behaviour of Landing Gear", AGARD-R-800, March, 1996.
52. Nie, H. and Qiao, X., "Dynamic Bahavior Analysis For Landing Gear With Different Types of Dual-Chamber Shock Struts", Chinese Journal of Aeronautics, Vol. 4, May 1991.
53. Cameron, A.M.; Hogg, C.R.; and Harris, C.J., "Flight Simulation: Comparison of Articulated Gear Leg Models", Proceedings of The 27th Summer Computer Simulation Conference, Ottowa, ON, Canada, July 24-26, 1995.
54. Zhu, D., "Some Dynamic Problems in Design of Aircraft Landing Gear", Proceedings of the 18th Congress of the International Council of the Aeronautical Sciences, Beijing, China, September 20-25, 1992.
55. Glaser, J. and Hrycko, G., "Landing Gear Shimmy – De Havilland's Experience", AGARD-R-800, March, 1996.
56. Black, R.J., "Realistic Evaluation of Airplane Brake Vibration By Laboratory Test and Analysis", Proceedings of The 15th Biennial Conference on Mechanical Vibration and Noise, Boston, MA, September 17-20, 1995.
57. Yager, T.J., "Aircraft Nose Gear Shimmy Studies", Proceedings of the SAE Aerospace Atlantic Conference and Exposition, Dayton, Ohio, April 20-23, 1993.
58. Krabacher, William E., "The Experimental Measurement of the T-46 Nose Landing Gear Shimmy Parameters", Proceedings of the Aerospace Atlantic Conference, Dayton, OH, May 1996.
59. Van Der Valk, R. and Pacejka, H.B., "An Analysis of a Civil Aircraft Main Gear Shimmy Failure", Vehicle System Dynamics, Vol. 22, No. 2, pp. 97-121, 1993.
60. Black, R. J., "Realistic Evaluation of Landing Gear Shimmy Stabilization by Test and Analysis", SAE Paper No. 760496, Business Aircraft Meeting, Wichita, Kansas, April 6-9, 1976.
61. Krabacher, W.E., "Aircraft Landing Gear Dynamics Present and Future", Proceedings of The SAE Aerospace Atlantic Conference and Exposition, Dayton, OH, April 20-23, 1993.
62. Kruger, W.; Besselink, I.; Cowling, D.; Doan, D.B.; Kortum, W.; and Krabacher, W., "Aircraft Landing Gear Dynamics: Simulation and Control", Vehicle System Dynamics, Vol. 28, No.2-3, pp.119-158, 1997.

Actively Controlled Landing Gear For Aircraft Vibration Reduction

Lucas G. Horta, Robert H. Daugherty, and Veloria J. Martinson

Abstract

Concepts for long-range air travel are characterized by airframe designs with long, slender, relatively flexible fuselages. One aspect often overlooked is ground induced vibration of these aircraft. This paper presents an analytical and experimental study of reducing ground-induced aircraft vibration loads using actively controlled landing gears. A facility has been developed to test various active landing gear control concepts and their performance. The facility uses a NAVY A6-intruder landing gear fitted with an auxiliary hydraulic supply electronically controlled by servo valves. An analytical model of the gear is presented including modifications to actuate the gear externally and test data is used to validate the model. The control design is described and closed-loop test and analysis comparisons are presented.

1. Introduction

Long, slender, flexible fuselage configurations, especially those with a long overhang from the nose gear to the cockpit, are susceptible to ground-induced vibration problems, particularly those produced by operating over long-period, low-amplitude elevation disturbances on runways. Although in-flight vibrations are also a concern, the work discussed herein will address the mitigation of vibrations transmitted from the ground to the aircraft fuselage. The mitigation is accomplished by embedding a control system directly into the landing gear.

This paper presents results from an activity at NASA investigating three aspects of actively controlled landing gear; analytical modeling, control system design, and experimental validation. This work is aimed at improving the fidelity of analytical models to the point where they can be used for control design; experimental demonstration of various control philosophies, and to develop an experimental facility that permits development of realistic concepts that can be transitioned to commercial applications.

Development of landing gear analysis dates back to the late fifties[1,2]. Work has included numerical simulation techniques and experimental measurements to validate the various computer programs. A significant volume of the work available in the literature deals with military aircraft requiring accurate prediction of taxi loads over repaired, bomb-damaged runways [3-6]. A computer simulation program named HAVE BOUNCE[6] was developed to simulate the dynamic response of military aircraft over bomb damaged runways. To validate the computer code, model validation was performed at the Aircraft Ground Induced Loads Excitation (AGILE)[7] test facility at Wright-Patterson Air Force Base. Recently, attention has focused on ride quality during taxi, takeoff and landing[8,9]. A simulation program, developed by Stirling Dynamics[8,9], is a good example of new simulation capabilities.

Since the primary design driver in landing gear design is impact loading, landing gear are typically tuned passively for impact loading upon landing. Ross and Edson[10,11] are among the first to consider an actively controlled landing gear to reduce landing loads. Their work led to the actively control landing gear concept described in this paper. Ross and Edson demonstrated the benefits of using an actively controlled landing gear system to reduce impact loads upon landing and while traversing bombed damage runways. Work by Freymann[12] demonstrated analytically and experimentally the benefits of actively controlled landing gears in reducing landing loads and vibrations under various runway profiles. Daniels[13] presented analysis and test results for an A6 intruder landing gear system. This paper discusses an extension of the work in reference 13 to incorporate active controls. An A6-Intruder landing gear was used in the laboratory because it was readily available. Necessary modifications to the gear are described along with the facility used in the experimental validation phase.

2. Analytical Model

To extend the work by Ross and Edson[10], this research discusses an independent development of a mathematical model of a main landing gear. The nonlinear equations of motion were developed for a telescoping main gear modified with an external hydraulic system for actuation and control of the gear. Specific details of the landing gear were taken from technical drawings supplied by the Grumman Company.

Figure 1 shows a schematic of a landing gear used in the development of the equations of motion. This schematic is representative of a general telescoping-type main landing gear. The model includes the aerodynamic lift on the airplane L, the mass of the airplane's fuselage lumped with the mass of the main cylinder as M_u, and the mass of the piston lumped with the mass of the tire as M_L. The inertial position of the upper mass is X_{wg} with zero value when the gear is fully extended and the tire just touching the ground. From this same configuration X_a is the position of the lower mass taken as zero at the axle of the tire. When the gear is compressed, X_a measures the deflection of the tire to an inertial reference ground input $U(t)$. Part of the upper cylinder chamber is filled with compressed nitrogen to provide the system with a spring. The cross sectional area of the upper chamber is denoted by A_u and the corresponding pressure is P_u. Likewise, the lower chamber has cross sectional area denoted A_L and a corresponding pressure P_L. Hydraulic fluid moves between the upper and lower chamber through an orifice plate with a hole of diameter D_{op}. A tapered pin attached to the piston, known as a metering pin, is used to obstruct the flow and effectively vary the orifice diameter as the pin moves through the orifice. The pin diameter is a function of X_s and is denoted as $D_{pin}(X_s)$. Hydraulic fluid reaches the snubber chamber through several orifices of diameter D_s. In the snubber chamber, the annulus area is denoted by A_R and the pressure is P_S. The diameter of the piston is D_p. The figure denotes entry/exit ports in the upper and lower chambers for the exchange of hydraulic fluid used by the active control system. Tire spring and damping coefficients are denoted by K_t and C_t.

Figure 2 shows the forces acting on the upper mass. Balancing the forces acting on the upper mass yields the following equation:

$$\begin{aligned} M_u\ddot{X}_{wg} &= M_u g - L - P_u A_o - P_L(A_L - A_o) + P_s A_R - f \\ &= F_1 - f \end{aligned} \tag{1}$$

where F_1 is a newly defined term in Eq. (1), g is the gravitational acceleration, f is friction force between the piston and the cylinder wall, and all other terms were described previously. This equation assumes that the hydraulic fluid pressure in the upper cylinder is identical to the nitrogen pressure. Also, in this development, the variable A_o, the main orifice area, reflects the fact that the metering pin is included, i.e. it is a variable cross-sectional area depending on stroke of the piston.

Figure 3 shows the forces acting on the piston. Summing the forces on the lower mass (piston) the force balance equation is:

$$\begin{aligned} M_L\ddot{X}_a &= M_L g + P_L(A_L - A_S) - P_s(A_R - A_S) - F_t + f \\ &= F_2 + f \end{aligned} \tag{2}$$

where F_2 is a newly defined in Eq. (2). F_t is the force that is transmitted through the tire from the ground and has the form:

$$F_t = K_t(X_a + U) + C_t(\dot{X}_a + \dot{U})$$

where the tire force is defined as a linear function of tire stiffness and damping. The tire stiffness and damping coefficients are obtained by linearizing the behavior of the tire about its nominal operating point. Since all the pressures are functions of stroke, a more convenient coordinate to use is stroke. Defining the stroke coordinate as $X_s = X_{wg} - X_a$, Eqs. (1) and (2) can be written as

$$\begin{aligned} M_u \ddot{X}_{wg} &= F_1 - f \\ M_L \ddot{X}_s &= {}^{M_L}\!/_{M_u} F_1 - F_2 - (1 + {}^{M_L}\!/_{M_u}) f \end{aligned} \tag{3}$$

The discussion so far relates forces F_1 and F_2 to corresponding pressures. The pressures are functions of the displacements and velocities of the landing gear components. Details of derivations relating chamber pressures, forces, and actuation commands to landing gear motion are discussed in reference 14, but a few key expressions are included here for completeness. The expression governing hydraulic fluid flow into the landing gear system is

$$Q_c' = -C_c x_c \sqrt{P_{High} - P_L} \qquad x_c < 0 \tag{4}$$

where Q_c' is flow into the landing gear system, C_c is an experimentally determined orifice discharge coefficient, x_c is the control command, P_{High} is the high pressure value, and P_L is the lower chamber internal pressure. A typical expression relating pressures to stroke is

$$E_1 \sqrt{P_u - P_L} + C_c x_c \sqrt{P_{High} - P_L} = (A_L - A_R)\dot{X}_s, \quad x_c < 0 \tag{5}$$

where E_1 includes all the main orifice parameters. Equation (5) is an algebraic equation for P_L that needs to be solved for each value of $\dot{X}_s$ during the numerical simulation. In the following, a description of a general approach for control design is presented.

3. Control System Design

To control the motion of the landing gear, hydraulic fluid from auxiliary tanks is used in conjunction with electronically controlled valves to actuate the gear. The goal for control design is to minimize disturbance propagation from the ground into the fuselage. To aid the discussion on control design methodology, consider a linearized representation of the landing gear and servo valves transformed using Laplace's transform into *G(s)*. Using feedback control, as indicated in figure 4, one can design a controller *k(s)* to command the servo valves.

Define *r(s)* as an arbitrary input reference signal, *d(s)* as an unknown external disturbance, *y(s)* as the controlled response, and *m(s)* as sensor noise. After some block diagram manipulation, the controlled response is given by:

$$y(s) = (I + G(s)k(s))^{-1}\left[d(s) + G(s)k(s)r(s) - G(s)k(s)m(s)\right] \tag{4}$$

The factor $I + G(s)k(s)$ is the output return difference and multiplies every term in the right hand side of the equation. To minimize the effects of the disturbance *d(s)* on the response, the factor multiplying the disturbance term *d(s)* must be made small, i.e. the return difference must be large (i.e. $G(s)k(s) >> 1$) in the frequency range of interest. Since *G(s)* is fixed, the control designer's task is to maximize the return difference value by adjusting $k(s)$ while maintaining the stability of the system. To ensure a stable design, Nyquist criterion is used for this single-input single-output problem. Since the landing gear behavior is highly non-linear one must examine bounds of variations in the system dynamics to ensure a stable design. Nyquist criterion was computed experimentally to assess stability and gain margins of the design. Although

application of these techniques to nonlinear systems is limited, they provide tremendous insight into design philosophy and stability analysis.

4. Experimental Facility

Figure 5 shows an A6 Intruder main landing gear installed underneath a drop carriage in the standard vertical position. A connecting plate was fabricated to allow for normal mounting of the gear to the plate, and the plate was then rigidly connected to the drop carriage. The drop carriage is a truss-structure that weighs about 4.5 tons and allows unrestrained vertical motion. The drop carriage rests on the landing gear. This mass simulates the rigid portion of the aircraft mass carried by the gear. Once the gear is loaded, a shaker table is used to input forces into the gear. Hydraulic lift cylinders, powered by a hydraulic pump, are used to lift the drop carriage and unload the landing gear. Once the landing gear has been lifted, the ability exists to lock the landing gear in that position with hydraulic valves.

The hydraulic shaker table was built specifically for the task of testing landing gears. The specifications included the capability to perform a one-inch step bump in 2 milliseconds while bearing 12,000 lbm. Input waveforms such as 1-cos(x), sin(x), trapezoidal with user-selected rise time, and a saw-tooth wave-form are all accurately reproduced by the shaker table . General profiles using runway elevation versus time data are also reproduced well for low frequencies. The shaker table is capable of applying dynamic forces of up to 12,000 lbf. on the test mass and allows actuator movement of 6 inches.

The landing gear was modified in a number of ways. Two electro-hydraulic servo valves were attached to the outside of the landing gear on flat areas that had been machined on the outer cylinder of the landing gear. One valve was located above the orifice plate of the landing gear (in the upper chamber), and the other valve was located below the orifice plate (in the lower chamber). Holes were machined into the landing gear so that the valves could transfer pressurized hydraulic fluid either into or out of the desired chamber. Both valves were designed to have flow rates of at least 26 gallons per minute (gpm) at 600 PSI with a response approaching 100 Hz. A high-pressure accumulator was mounted on the upper mass (drop carriage) and kept charged to a pressure approximately twice that of the static, loaded charge pressure in the landing gear. A low-pressure accumulator was also installed so that when desired, pressurized hydraulic fluid in the landing gear could be directed there, reducing the transient back-pressure that would tend to restrict the outward flow of hydraulic fluid. The low-pressure accumulator was maintained at essentially atmospheric pressure. Ultimately, the low-pressure accumulator was attached to an atmospheric pressure reservoir where the pump used to supply the high-pressure accumulator was located. The system was thus pressure-balanced evenly around the nominal static, loaded charge pressure of the landing gear, permitting roughly equal flow rates into or out of the landing gear at similar servo command levels.

The piston head of the landing gear was also modified. Normally, a landing gear such as this has a snubber chamber that is designed to limit the speed of piston extension to prevent a significant "bottoming out" shock on the landing gear components such as might occur after a catapult during an aircraft carrier launch. Thus, normally the hydraulic damping characteristics of the landing gear vary depending on the direction of piston travel. In this experiment, it was desirable to remove the "snubber" effect so that the damping behavior was more even in both directions. To that end, a ring mounted directly under the piston head, which normally acts as a directional valve and restricts hydraulic fluid motion in one direction, was modified by drilling additional holes in it so that it provided equal flow past it regardless of the direction of hydraulic fluid motion. These changes were accurately reflected in the modeling of the landing gear for analytical purposes.

The top of the landing gear was modified slightly to accept a high-strength site glass. This site glass allowed a visual indication of the proper servicing level of hydraulic fluid prior to being pressurized with nitrogen, and saved a significant amount of time in pre-test operations.

The landing gear was instrumented to provide the necessary information for model validation. There were two accelerometers, one placed at the upper mass and the second one at the lower mass. Two relative displacement transducers were also used, one to locate the upper mass with respect to a fixed position on the carriage and one to measure the relative position between the upper and lower masses of the landing gear. Two pressure transducers were used to verify some basic model assumptions, mainly that the hydraulic fluid and the gas do not mix to any significant degree after initial shaking. One pressure transducer was located just outside the charge port of the upper cylinder, and the other was embedded in the piston head. Vertical load was inferred by measuring bending moments induced by the tire using a strain gage on the wheel axle.

5. Test Results and Model Validation

The following section discusses experimental results from tests conducted on the landing gear system. First, the servo loop dynamics and electronics were characterized and are compared with the analytical model. Second, the simulation model which was constructed using a commercially available software is described. Finally, test results for various open-loop and closed-loop cases are presented.

5.1 Numerical Solution of Equations of Motion

The fundamental equations presented in Section 2 along with key expressions discussed in Ref. 14 were programmed and numerically integrated using Simulink/Matlab[15] computer simulation program. Two types of tests were conducted as part of the analytical model validation; parameter estimation tests for characterization of the servo loop dynamics and system tests to compare overall behavior of the landing gear when operating. In the following sections test and analysis results are discussed.

5.2 Servo Loop Dynamic Characterization

Figure 6 presents a plot of hydraulic fluid flow rate as a function of servo command. These data were measured by removing nitrogen from the unrestrained landing gear and computing flow rates by measuring piston stroke rates as a result of discrete servo commands. Tests were then conducted with the piston restrained from moving to characterize the servo loop dynamics with minimum interference from piston motion. The slope of the measured flow rate versus command gives the product $C_c\sqrt{\Delta P}$, where ΔP is the pressure difference between the supply or return and the strut internal pressure. Using these results, the servo effective discharge coefficient was calculated to be $C_c = 1.0765 \times 10^{-6}$. To compare simulated chamber pressures to test, a test was conducted using a sinusoidal sweep from 0.5 Hz to 10 Hz. Input voltages from test were input into the simulation and the computed frequency response for upper chamber pressure to servo command is shown in figure 7. Test results are depicted using a solid line and simulation with a dashed line. Lower chamber tests results (not shown) are similar but with slightly more phase delay between commands and internal pressure variations. The initial pressure in the chamber was recorded as 350 PSI, the initial stroke was 10.3 inches, and the high pressure accumulator pressure was 750 PSI. The nitrogen level was estimated to be 4.78 inches. The upper curve in figure 7 shows the magnitude ratio of upper pressure to input voltage as a function of frequency, whereas the lower curve shows a phase comparison. This transfer function represents the servo valve hydraulic system response at the conditions mentioned previously.

5.3 Landing Gear Dynamic Characterization and Model Validation

Runway elevations and servo command voltages were the two inputs used to characterize the landing gear. Since the system is highly nonlinear, sine sweeps were the main form of excitation. Time simulations were performed using Simulink.

Since the simulation is nonlinear, initial conditions for the different parameters have to be set properly or time integration will fail. Conditions such as upper mass position and velocity, piston stroke, stroke rate, upper chamber pressure, and nitrogen level must all be specified. In the initial design, two sensors were used to control the motion of the landing gear; piston stroke and upper mass acceleration. Since the axle load signal from the strain gage is proportional to the upper mass acceleration, the strain gage output was used for later tests. The axle-mounted strain gages had the additional benefit of being relatively "quiet" and avoided the more dynamic nature of acceleration measurements on stiff structures such as those observed using the upper mass accelerometer.

The controller used for all the closed-loop tests was synthesized with the aid of an experimentally determined Nyquist diagram. To compensate for phase lag of the servo valves and hydraulic system, a lead-lag compensator was used to add about 10 degrees of lead at 1.5 Hz. Direct axle load feedback with a loop gain of 1 volt/6731 lbf. was used for all the closed-loop test results shown.

Shaker head position, servo-input command, piston position, upper mass position, internal pressures, and acceleration responses are compared to simulation results in figure 8. Solid lines correspond to test and dashed lines are simulation results. The input runway elevation is a sinusoid with amplitude of 0.75 inches at a frequency of 1.5 Hz. Piston position feedback is always used to maintain inter-chamber leakage through the servo valve from depleting the hydraulic fluid in the strut. This control loop is toggled on and off during an experiment. Data shown in figure 8 had the acceleration feedback loop turned on after 14 seconds. The upper mass position is reduced to 25 % of the uncontrolled position after the axle load feedback loop is turned on. Drift after the initiation of control in the stroke and upper mass position histories in figure 8 could be attributed, in part, to a continuous decrease in the control system hydraulic supply pressure. All simulation results assume a constant control system hydraulic supply pressure. To experimentally minimize the effect of reduced control system hydraulic supply pressure, long duration tests were interrupted periodically to allow for the recovery of system hydraulic pressure. Discrepancies in stroke levels between test and simulation are not well understood.

Friction played a key role in unrestrained tests performed with this testbed. To illustrate the problem, figure 9 shows a frequency response function of the upper accelerometer to servo command. Note that the landing gear locks-up above 0.7 Hz due to friction. Control authority is lost beyond 0.7 Hz due to high friction levels, about 2000 lbf. statically and 400 lbf. dynamically. This static friction level causes a condition in which pressure versus stroke equilibrium can be in error by as much as plus or minus 45 psi. Also important is the use of nitrogen in the upper chamber. Nitrogen serves as a soft cushion for load transfer through the landing gear. In the absence of nitrogen the strut is full of hydraulic fluid, which is incompressible, and therefore small amounts of hydraulic fluid into or out of the strut causes large changes in the internal pressures. Since the servo hydraulic has a limited supply of external hydraulic fluid, the absence of nitrogen allows for longer test time and higher forces in the system but requires higher pressures for the external supply.

Controlled tests like the one shown in figure 8 can only be performed at discrete frequencies with the capabilities of the existing hydraulic system. To test the frequency range between 0.1 Hz to 4 Hz, a spectrum analyzer was set for a sine-sweep and the test was conducted over a long period of time, stopping periodically to allow for the hydraulic system to be re-supplied. Open and closed-loop results from this test

are shown in figure 10. Note that in this test the shaker table was used as the input disturbance and provided enough energy to prevent the system from locking up below 1.2 Hz. Feedback from position and axle load signals were used in the control system to attenuate responses between 1.5 and 3.5 Hz. The maximum amplitude reduction is a factor of 4.4 at 1.4 Hz with reductions beyond 3.5 Hz of about 20%. Using the strain gage sensor to measure axle load provides a cleaner signal for feedback and reduces the risk of high frequency instabilities in the feedback loop. Note that in the ideal case with the control system fully charged, a gain optimized for a single frequency, and controlling the system at its natural frequency, amplitude reductions of a factor of 10 have been observed.

6. Summary

Equations of motion for a telescoping landing gear system have been developed incorporating an external servo-hydraulic system which allows for landing gear actuation. The electronic servo hydraulic system model combined the electronic and hydraulic dynamics in one relatively simple formulation. A number of aspects of actively controlled landing gear design have been demonstrated in this study. Fuselage vibration reduction levels by a factor of 4 have been demonstrated along with some of the fundamental limitations of implementing such systems in landing gear design. High friction levels hindered the ability to achieve higher performance without a major re-design of the landing gear. However, even modest vibration reductions may translate into reductions in landing gear loads and therefore aircraft structural weight.

References

1. Currey N.S.: *Aircraft Landing Gear Design: Principles and Practices*. AIAA Education Series, 1988.
2. Milwitzky, B.; and Cook F.E.: Analysis of Landing-Gear Behavior. NACA Report No. 1154, 1953.
3. Ottens, H.H.: Predicted and Measured Landing Gear Loads for the NF-5 Aircraft Taxiing over a Bumpy Runway. AGARD-CP 326, 1982.
4. Payne, B.W.; Dudman A.E.; Morris, B.R.; and Hockenhull, M.: Development of a Cost Effective Approach to Modeling Aircraft Response to Repaired Runways. *Proceedings of the 52nd meeting of the AGARD Structures and Materials Panel*, Cesne, Turkey, April 1981.
5. Freymann R.: An Experimental-Analytical Routine for the Dynamic Qualification of Aircraft Operating on Rough Runway Surfaces. AGARD R-731, March 1987.
6. Gerardi T.G.; and Ninnetyan L.: Status of Computer Simulations of USAF Aircraft and an Alternative Simulation Technique. AGARD CP-326, April 1982.
7. Freymann R.; and Johnson W.: Simulation of Aircraft Taxi Testing on the AGILE Shaker Test Facility. *Second International Symposium on Aeroelasticity and Structural Dynamics*, sponsored by Deutsche Gesellschaft fur Luft- und Raumfahrt e.V. in Aachen, W. Germany, April 1985.
8. Sheperd A.; Catt T.; and Cowling D.: The Simulation of Aircraft Landing Gear Dynamics. *18th Congress of the International Council of the Aeronautical Sciences*, Beijing, People's Republic of China, Sept. 1992.
9. Catt T.; Cowling D.; and Sheperd A.: Active Landing Gear Control for Improved Ride Quality During Ground Roll. AGARD Smart Structures for Aircraft and Spacecraft, Oct. 1992.
10. Ross I.; and Edson R.: An Electronic Control for an Electro-hydraulic Active Control Aircraft Landing Gear. NASA CR 3113, April 1979.
11. Ross I.; and Edson R.: An Electronic Control for an Electro-hydraulic Active Control Landing Gear for the F-4 Aircraft. NASA CR 3552, April 1982.

12. Freymann R.: Actively Damped Landing Gear System. AGARD CP-484, 1990.
13. Daniels, J.N.: A Method for Landing Gear Modeling and Simulation with Experimental Validation. NASA Contractor Report 201601, June 1996.
14. Horta, L.G.: Daugherty, R.H.: and Martinson, V.J: " Modeling and Validation of an A6-Intruder Actively Controlled Landing Gear System," NASA TP-1999-209124
15. Matlab/simulink User's manual, *Using Simulink, Version 2.0,* The Mathworks, Inc, Natick, MA, 1997

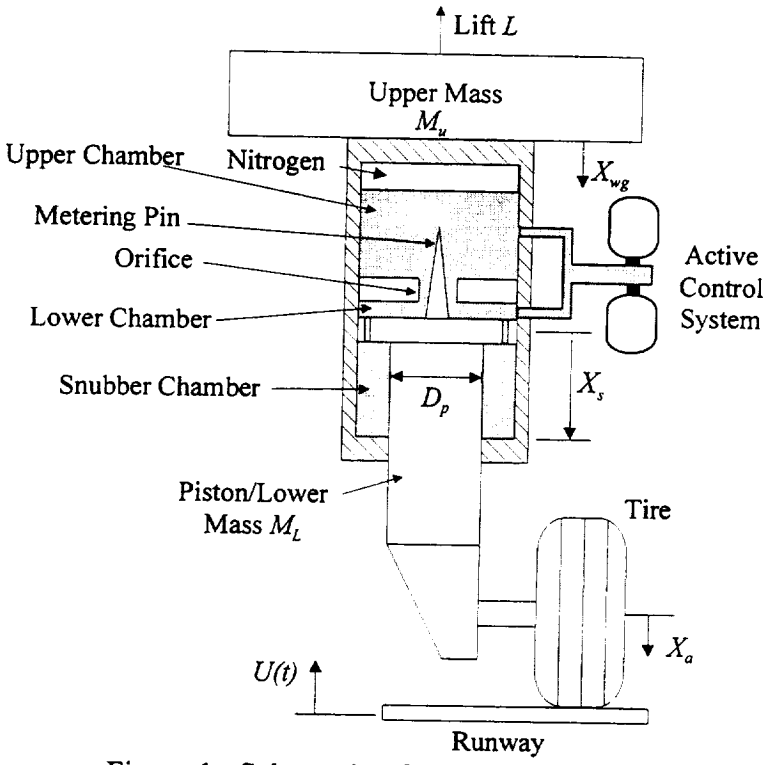

Figure 1. Schematic of a telescoping landing gear

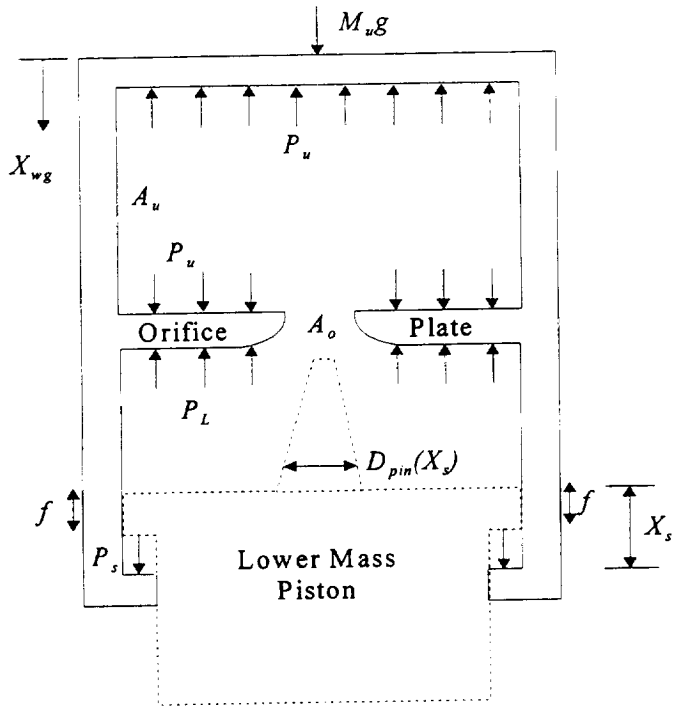

Figure 2. Schematic of upper mass and main cylinder.

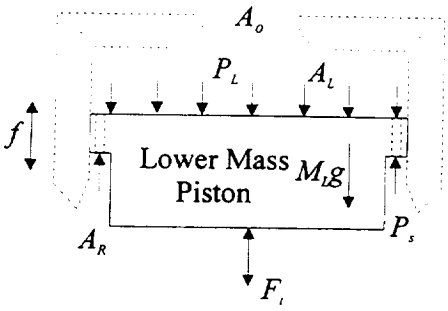

Figure 3. Schematic of lower mass.

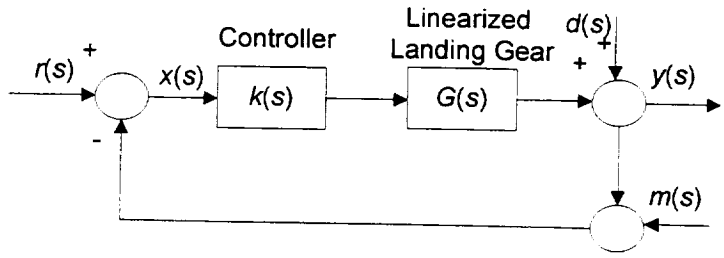

Figure 4. Block diagram of control system.

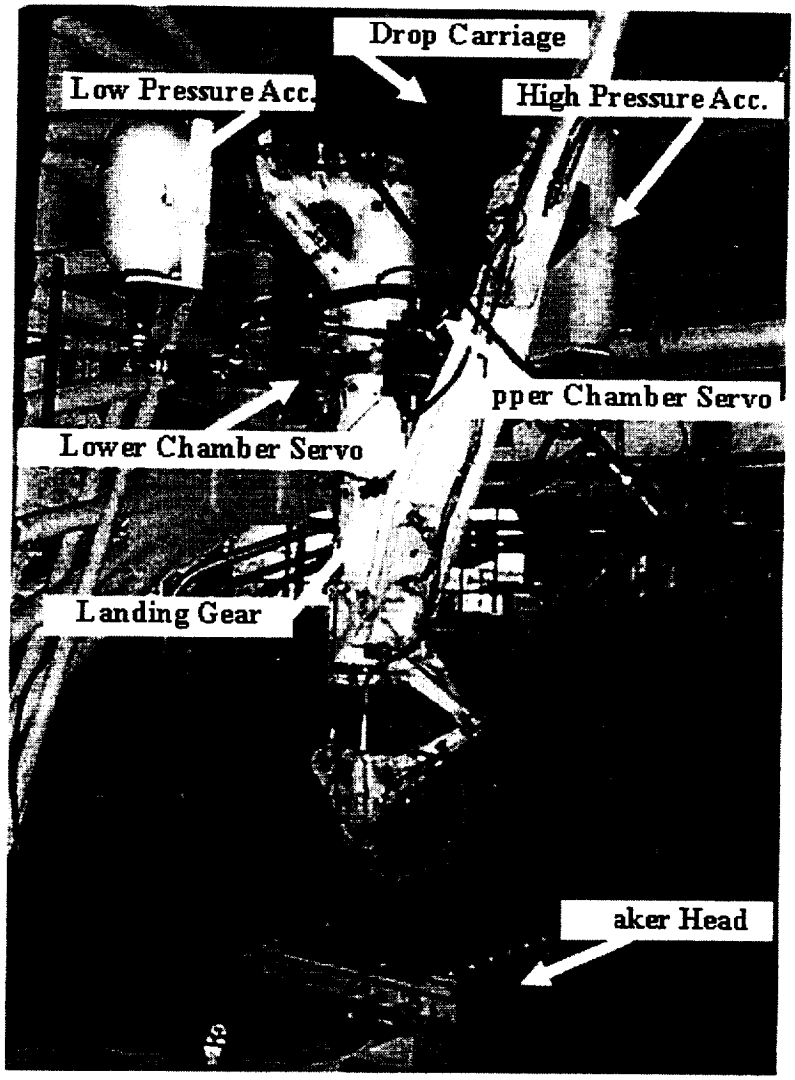

Figure 5. Test set-up for validation of analysis model and control system.

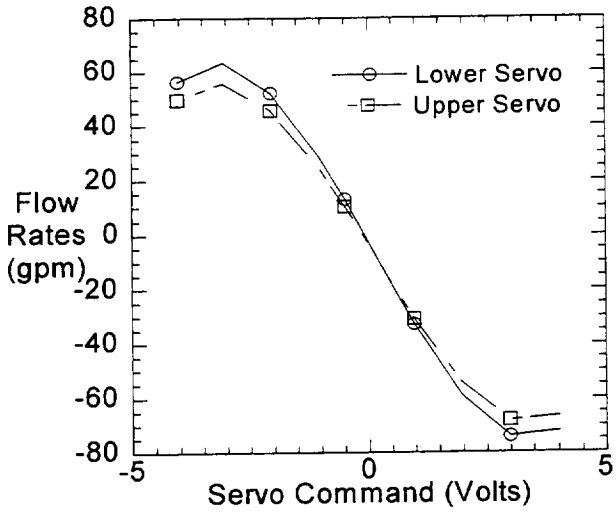

Figure 6. Flow rate as a function of servo commands with unrestrained landing gear and no nitrogen.

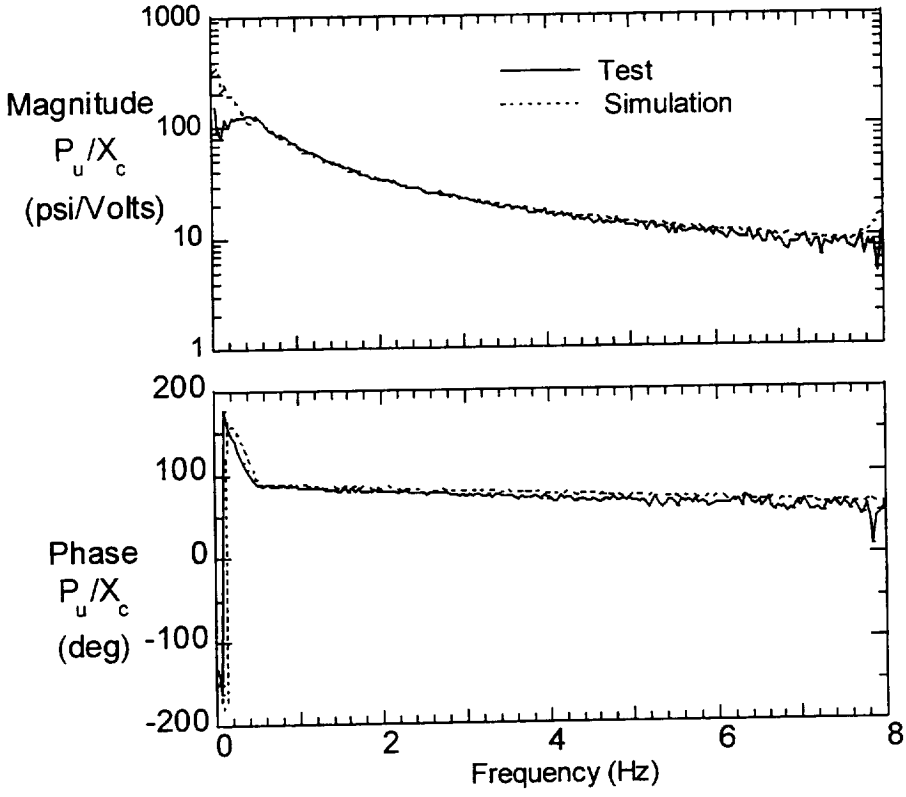

Figure 7. Upper chamber pressure to servo command transfer function.

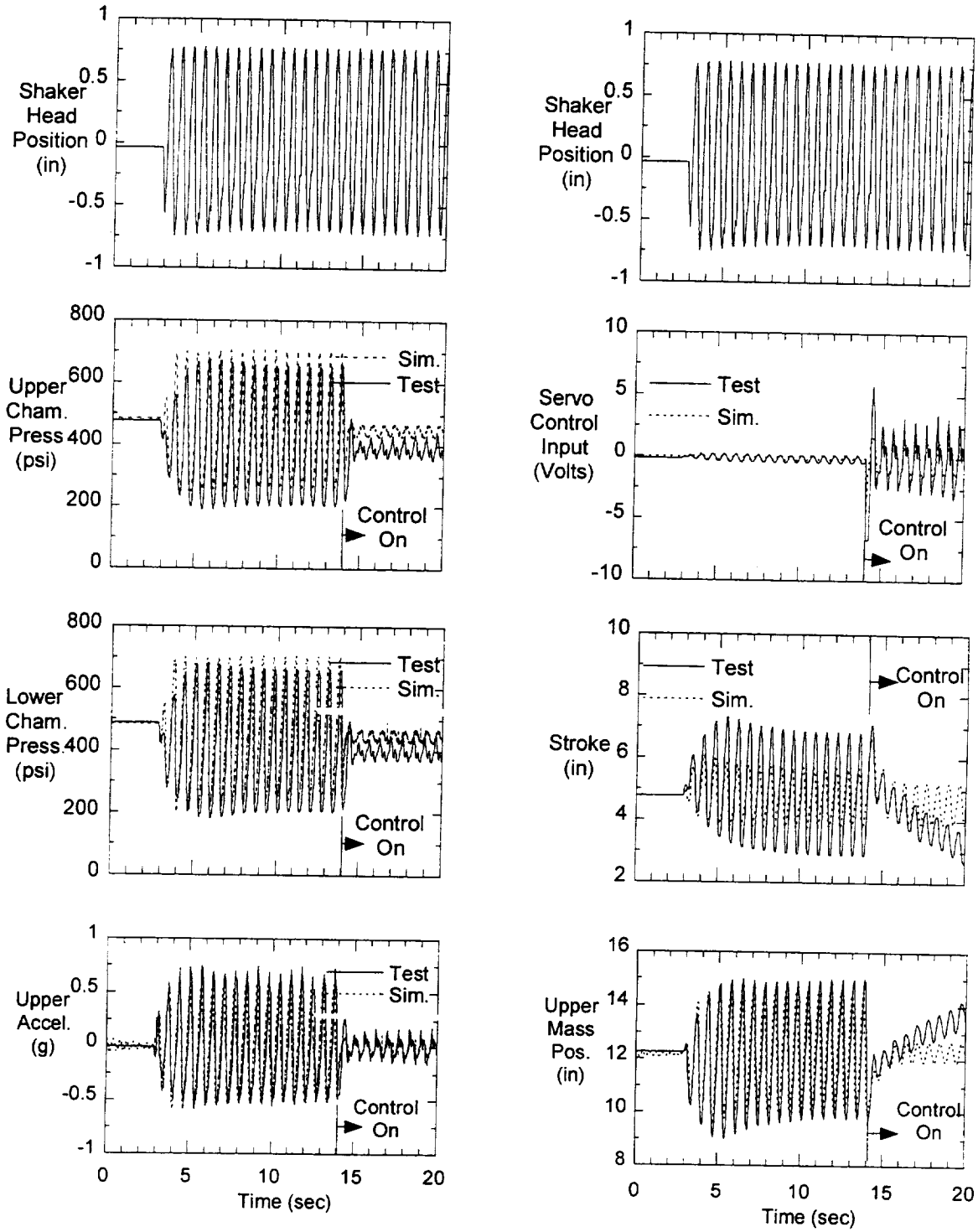

Figure 8. Controlled test and analysis results due to a periodic disturbance at 1.5 Hz.

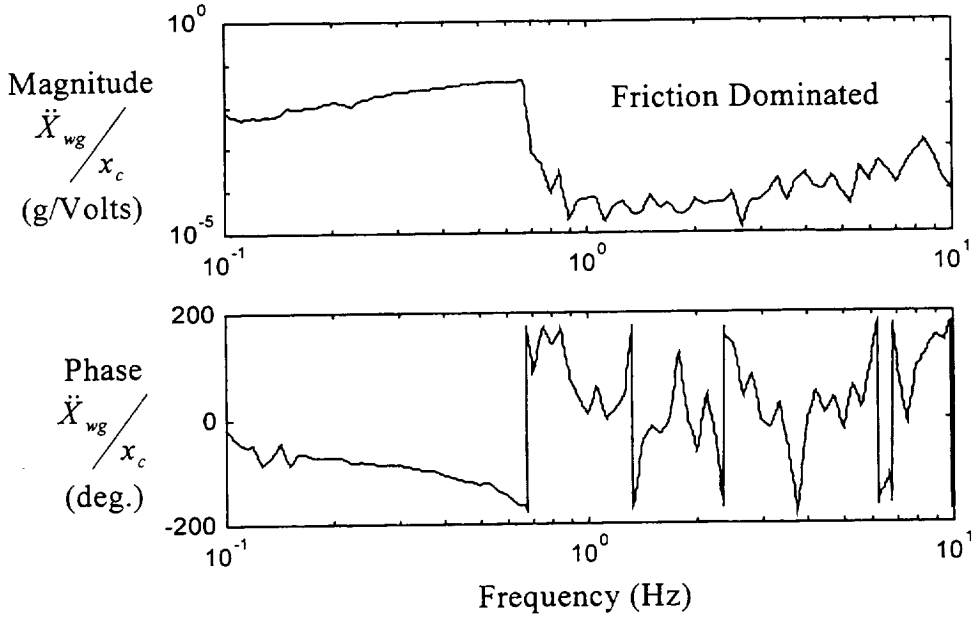

Figure 9. Frequency response from upper servo command to upper accelerometer.

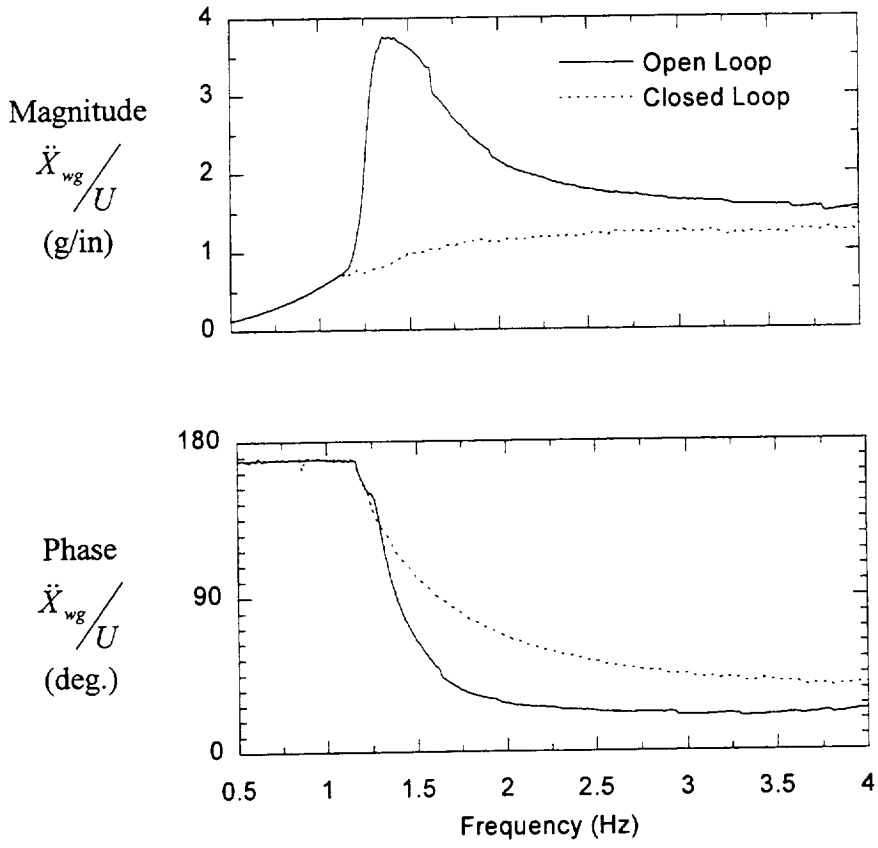

Figure 10. Upper acceleration to shaker position transfer function.

Aircraft and Ground Vehicle Winter Runway Friction Assessment

by

Thomas J. Yager
Senior Research Engineer
NASA Langley Research Center

Presented at
The International Forum on Aeroelasticity
and Structural Dynamics
June 22-25, 1999
Williamsburg, VA

ABSTRACT

Some background information is given together with the scope and objectives of a 5-year, Joint Winter Runway Friction Measurement Program between the National Aeronautics & Space Administration (NASA), Transport Canada (TC), and the Federal Aviation Administration (FAA). Participants recently completed the fourth winter season of testing. The primary objective of this effort is to perform instrumented aircraft and ground vehicle tests aimed at identifying a common number that all the different ground vehicle devices would report. This number, denoted the International Runway Friction Index (IRFI) will be related to all types of aircraft stopping performance. The range of test equipment, the test sites, test results and accomplishments, the extent of the substantial friction database compiled, and future test plans will be described.

Several related studies have also been implemented including the effects of contaminant type on aircraft impingement drag and the effectiveness of various runway and aircraft de-icing chemical types and application rates. New equipment and techniques to measure surface frictional properties are also described. The status of an international friction index calibration device for use in ensuring accuracy of ground vehicle friction measurements will also be discussed. NASA considers the success of this joint program critical in terms of ensuring adequate ground handling capability in adverse weather conditions for future aircraft being designed and developed as well as improving the safety of current aircraft ground operations.

INTRODUCTION

Improving aviation safety has long been one of the principal goals of NASA, Transport Canada and the Federal Aviation Administration. With global aviation safety as one of NASA's three pillars or thrusts for research activities, the announced metrics of "five fold reduction in commercial transport fatal accident rates within 10 years and a ten fold reduction within 20 years" were deemed achievable. In today's economic climate, aviation industries are committed to affordable, cost-effective technology for improved safety and profitability. Hand in hand with

this outlook, government agencies such as the FAA, NASA and Transport Canada, are partnering to share cost, expertise and facilities to achieve program objectives in a timely and acceptable manner with industry's guidance. The Joint Winter Runway Friction Measurement Program will contribute significantly towards meeting these one and two decade metrics by providing better tools for airport operators to use and more accurate and reliable runway friction data for pilots in making their "go/no go" decisions during operations in adverse weather conditions.

Inconsistent, inaccurate reporting of winter runway conditions to pilots has contributed to a disproportionate number of ground handling accidents as shown in **Figure 1**. This recent Boeing survey of commercial jet transport landing/taxi accidents indicates that over a 35 year period (1958-93), many accident events occurred on wet/icy runways with aircraft going off the end or side of the runway. An obvious step in the solution of these ground handling accidents is to standardize and harmonize ground friction measuring vehicle values to provide the pilot with uniform and reliable runway condition information that is independent of the type of measuring device.

One objective of this program includes harmonizing friction measurements obtained with a variety of ground test vehicles (13 thus far) on a wide range of winter runway conditions. Accurately relating these harmonized vehicle friction measurements to aircraft braking performance is also a goal of this program. To ensure the accuracy of these different devices including a new RUNAR trailer and an Airfield Surface Friction Tester (ASFT), the American Society for Testing and Materials E17 Committee has formed a task group to design an international friction index calibration tester with completion of prototype next year. A variety of instrumented test aircraft have been involved since testing in this 5-year program started in January 1996. During the course of conducting the aircraft test runs, a determination has been made on the magnitude of runway contaminant-produced drag on aircraft takeoff performance. The general test schedule for the joint program is given in **Figure 2** and it is hoped that a sixth instrumented aircraft, preferably a wide-body type, will participate in the fifth winter season of testing. The United States Air Force as well as two civil transport aircraft manufacturers have been approached to provide or support such wide-body aircraft testing.

BACKGROUND AND SCOPE

This study is being led by NASA and Transport Canada with support from the Canadian National Research Council (NRC) and the FAA. Also participating are organizations and equipment manufacturers, both aircraft and ground vehicle, from North America, Europe and several Scandinavian countries. A variety of instrumented test aircraft and ground friction measuring vehicles have been used at different test sites in the U.S., Canada and elsewhere. The NASA Langley B-737 transport and an NRC Dassault Falcon-20 aircraft were used during January and March 1996 at the Jack Garland Airport in North Bay, Ontario. Seven ground friction measuring devices from six different countries collected comparable friction data for several winter runway conditions including solid ice, dry loose snow and compacted snow. In the January-March 1997 winter season, similar tests were performed at North Bay with an FAA B-727 transport, the NRC Falcon-20 and a De Havilland Dash-8 aircraft together with 13 ground friction measuring devices. Data obtained during these investigations helped define the methodology for an International Runway Friction Index (IRFI) to harmonize the friction

measurements obtained with the different ground test vehicles. In the January-February 1998 winter season, additional data were collected at North Bay, ON with the Falcon-20 and Dash-8 aircraft, together with 11 different ground test vehicles, to further refine the IRFI methodology and to establish a Canadian Runway Friction Index (CRFI) to be used by pilots to determine their aircraft stopping distance under compacted snow and ice conditions from Electronic Recording Deceleration (ERD) readings. In March 1998, several different ground friction measuring devices participated in conducting nearly 800 test runs under compacted snow- and ice-covered surface conditions at a new test track facility located at Gardermoen Airport near Oslo, Norway. During the January-March 1999 winter season, Falcon-20 aircraft and ground vehicle data was collected at North Bay, NASA B-757 aircraft and ground vehicle data was collected at a new test site, Sawyer Airbase, Gwinn, MI and additional ground vehicle (9 different devices) obtained friction data at the Gardermoen test track site in Oslo, Norway. Data from these tests were used to further refine and improve the IRFI methodology. It is interesting to note that under similar runway conditions at these three different test sites, friction data from ground vehicles tested at all three sites were in close agreement and IRFI methodology was further substantiated. The joint program friction database collected during testing in 1996-99 includes nearly 400 instrumented aircraft test runs and more than 8000 ground vehicle runs under bare and dry, rain and artificially wet, artificially flooded, loose and compacted snow, smooth and rough ice, sanded and chemically-treated ice, and slush. Five weeks of NASA Aircraft Tire/Runway Friction Workshop data (1994-98) have been combined with data from thirteen weeks of winter testing at North Bay, ON (1996-99), one week at Sawyer Airbase, Gwinn, MI (1999) and two weeks at Oslo, Norway (1998-99). References 1 to 11 provide documentation of the 1996-98 test results obtained with instrumented aircraft and ground friction measuring vehicles.

Future testing with other aircraft types such as the B-777 or A320 aircraft and with new or improved ground test vehicles will further validate the IRFI methodology and help identify an Aircraft Friction Index (AFI) to harmonize different aircraft braking friction performance to the IRFI. Dissemination, acceptance and implementation of these test results by the aviation community is expected through the guidance and assistance of several organizations including the FAA, the International Civil Aviation Authority (ICAO), the American Society for Testing and Materials (ASTM), the Joint Aviation Authority (JAA), the International Federation of Air Line Pilots (IFALPA), the U.S. and Canadian Air Line Pilots Association (ALPA and CALPA) and the Air Transport Association (ATA). The overall results from this program are expected to increase aircraft ground operational safety as well as the capacity of airports and may also be applicable to vehicular safety where winter conditions are severe.

PRELIMINARY TEST RESULTS

Figure 3 shows four friction data comparisons between ground vehicles on six different runway conditions which varied from bare and dry (high values) to ice-covered (low values). The devices each operatedwith a fixed-slip value which varied from 12 to 100 percent with zero percent equal to a free rolling and 100 percent equal to a locked-wheel skid. The NASA Instrumented Tire Test Vehicle (ITTV) is used in comparisons with the ERD, the Surface Friction Tester (SFT), the IMAG trailer and the GripTester trailer. These comparisons of actual measured friction values obtained with different test vehicle and tire combinations are considered

quite good. The relative agreement, expressed by the "r squared" values with 1 being perfect agreement, in each of the four comparisons is nearly 0.92 on an average.

Figure 4 shows range of friction values obtained with a Norwegian variable slip trailer device (RUNAR) on several similar runway surface conditions. It should be noted that not only do the overall values of friction change with the different surface conditions, but the percent slip at the peak friction and the slope after the peak are also functions of the surface conditions. One can also conclude from this data that as the peak friction magnitude decreases, the difference between individual ground test vehicle measurements would also decrease. This has been observed in comparing data under different runway conditions obtained at all three test sites.

Figure 5 shows a comparison between the friction values measured in 1996 by the instrumented Falcon-20 aircraft and the ERD ground vehicle during testing on several different snow- and ice-covered runway conditions. The comparison in actual aircraft and ERD measurements is not as close as between the ERD and ITTV (r squared of 0.841 vs. 0.924) but that is to be expected because of differences in test tire slip ranges (100 percent for ERD, 15 to 20 percent for aircraft) and tire contact areas.

Figure 6 shows the effect of speed on the instrumented B-737 aircraft braking friction data. For the variety of runway conditions listed, the friction range varies from 0.5 under dry conditions down to 0.07 for patchy thin ice. A decrease in friction with speed is noted for the wet conditions whereas an increase is shown for dry loose snow (2 – 3 in. in depth), which may be attributed to a change in temperature during the test run series. The lower depth loose snow conditions and the patchy thin ice showed little effect of speed on the measured friction values. This trend was still evident after removing the contaminant drag values from the snow covered runway data. As expected, the patchy thin ice produced the lowest aircraft braking friction measurements which were obtained at a constant below-freezing temperature. Along with tire temperature, tire load or contact area has been found to be a significant factor in the level of friction developed by a given vehicle and/or aircraft on snow- and ice-covered runway conditions. Ground speed, on the other hand, does not have the influence on friction values developed on these winter runway conditions that it has under wet pavement conditions.

Figure 7 shows the effect of contaminant drag on the B-737 aircraft deceleration values with speed for three different snow-covered runway conditions. The contaminant drag values were a combination of the displaced contaminant drag by the aircraft tires together with that developed from impingement onto the aircraft. For these nonbraking tests, the aircraft was operated in the takeoff configuration. In general, the deceleration values increase with increased speed and contaminant depth as expected. The specific gravity of the base snow contaminant varied between 0.5 and 0.6. Similar data trends were found during nonbraking test run series with the Falcon-20, the Dash-8 and the B-727 aircraft.

FUTURE PLANS

More testing with the Falcon-20 and Dash-8 aircraft are planned for the 1999-00 winter seasons in North Bay, ON and additional testing with NASA Langley's instrumented B-757 aircraft will be conducted at Sawyer Airbase, Gwinn, Michigan. At least six of the ground friction measuring devices will participate in these tests at North Bay and Gwinn, MI and also in tests planned for the Gardermoen Airport test track facility near Oslo, Norway. Further participation of the FAA's

B-727 aircraft is expected. Efforts are also ongoing to get a wide-body aircraft, i.e. B-777 or Airbus 320 to participate in the 2000 winter season at Sawyer Airbase, MI. The United States Air Force has also been approached relative to use of an instrumented C-17 or C-130J transport aircraft in the testing. More ground vehicle tests evaluating friction, texture and pavement roughness are planned during the Sixth Annual NASA Tire/Runway Friction Workshop at Wallops Flight Facility, VA, May 10-14, 1999. In the fall, a 2-3 day international conference is planned with site and dates yet to be determined, to review all the joint program data and findings with the aviation community and get their guidance and recommendations for next year's program activities. The year 2000 marks the fifth and final year of the program.

CONCLUDING REMARKS

In the four years of testing aircraft and ground vehicles in the joint program, a substantial friction database has been established. Both an International Runway Friction Index (IRFI) and a Canadian Runway Friction Index (CRFI) have been identified from ground vehicle and aircraft friction data measurements. Data analysis is underway to improve the harmonization of ground vehicle friction measurements and determine a suitable Aircraft Friction Index (AFI), based on calculated aircraft stopping distances using IRFI, that pilots could use in making their "go/no go" decisions. Although next year marks the end of this ambitious 5-year program, discussions have taken place between the various participating government organizations and the International Civil Aviation Organization (ICAO) on extending this 5-year period to include different aircraft types and conditions. More aircraft and ground vehicle data are needed for the slush covered runway conditions and manufacturers and airlines are interested in reverse thrust performance data. Aircraft braking performance and contaminant drag measurements at speeds from 120 to 170 knots have also been identified as part of future aircraft test run matrices together with monitoring aircraft wheel brake torque variations during braking efforts.

REFERENCES

1. Yager, Thomas J.; Vogler, William A.; and Baldasare, Paul: *Evaluation of Two Transport Aircraft and Several Ground Test Vehicle Measurements Obtained for Various Runway Surface Types and Conditions.* NASA TP 2917, 1990.

2. Yager, Thomas J.: *Factors Influencing Aircraft Ground Handling Performance.* NASA TM-85652, 1983.

3. Barnes, Arthur G.; and Yager, Thomas J.: *Enhancement of Aircraft Ground Handling Simulation Capability.* AGARDograph 333, 1998.

4. Anon: *Proceedings of the International Meeting on Aircraft Performance on Contaminated Runways (IMAPCR'96).* TP 12943, 1996.

5. Anon: *Proceedings of the Technical Advisory Group Steering Committee Meeting on Aircraft Performance on Contaminated Runways.* TP 13257, 1997.

6. Comfort, George; and Gong, Shawn Y.: *Preliminary Analysis of the Friction Measured by the Ground Vehicles at the 1998 North Bay Trials.* TP XXXXXE, 1998.

7. Green, Carl: *Correlation Testing of Decelerometers.* TES Limited Doc. No. C2254-002-rev., 1998.

8. Doogan, Mark; Herrmann, Eric; and Lamont, Phillip J.: *Dash 8 Aircraft Performance Testing on Contaminated Runway Surfaces (Winter 1997/1998).* Doc. DHC-D4547-98-06, 1998.

9. Croll, John B.; Martin, Jim C.T.; and Bastian, Matthew: *Determination of Falcon 20 Landing Distances on Winter Contaminated Runways as a Function of the James Brake Index.* Canadian National Research Council No. 32173, 1996.

10. Croll, John B.; Martin, Jim C.T.; and Bastian, Matthew: *Falcon 20 Aircraft Performance Testing on Contaminated Runway Surfaces During the Winter of 1996/1997.* Canadian National Research Council No. LTR-FR-137, 1997.

11. Bastian, Matthew; and Lamont, Phillip J.: *Braking Friction Coefficient and Contaminated Drag of a B727 on Contaminated Runways.* Canadian Research Council No. LTR-FR-147, 1998.

[redacted]

Problem: Inconsistent, inaccurate reporting of winter/wet runway conditions to pilots...results in disproportionate number of accidents

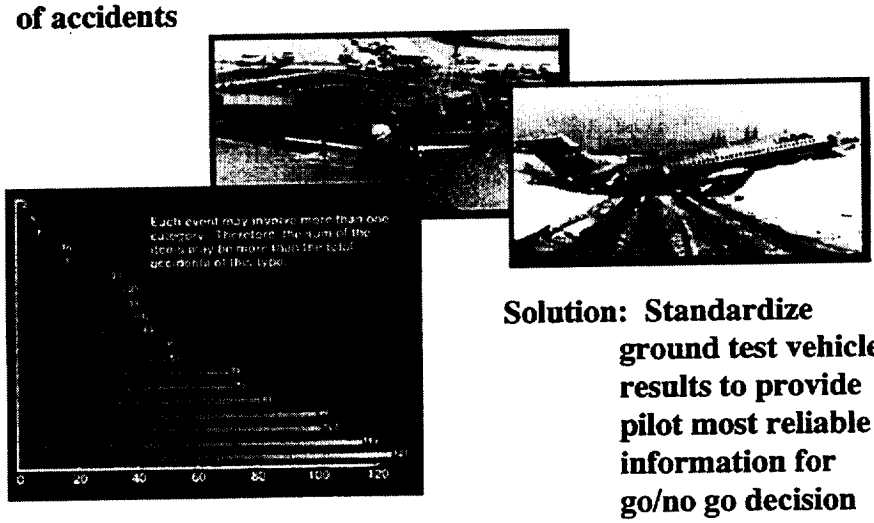

Solution: Standardize ground test vehicles results to provide pilot most reliable information for go/no go decision

1958-1993 Commercial Jet Transport Landing / Taxi Accidents

Figure 1

OVERALL JOINT NASA/TC/FAA WINTER RUNWAY FRICTION PROGRAM SCHEDULE

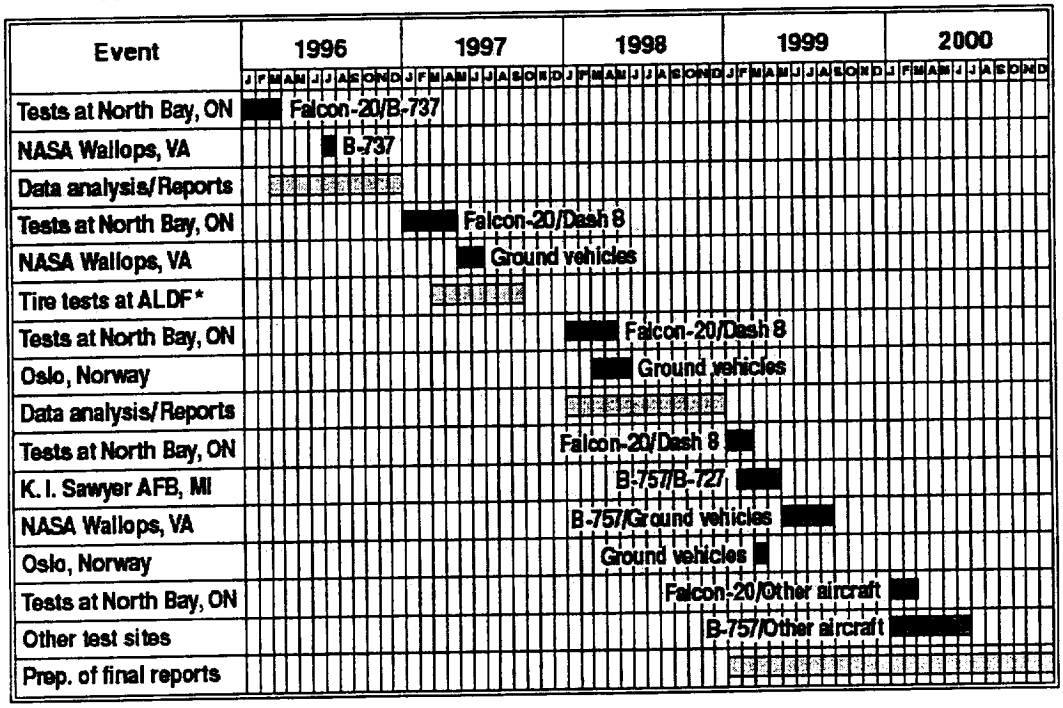

*ALDF – Aircraft Landing Dynamics Facility

Figure 2

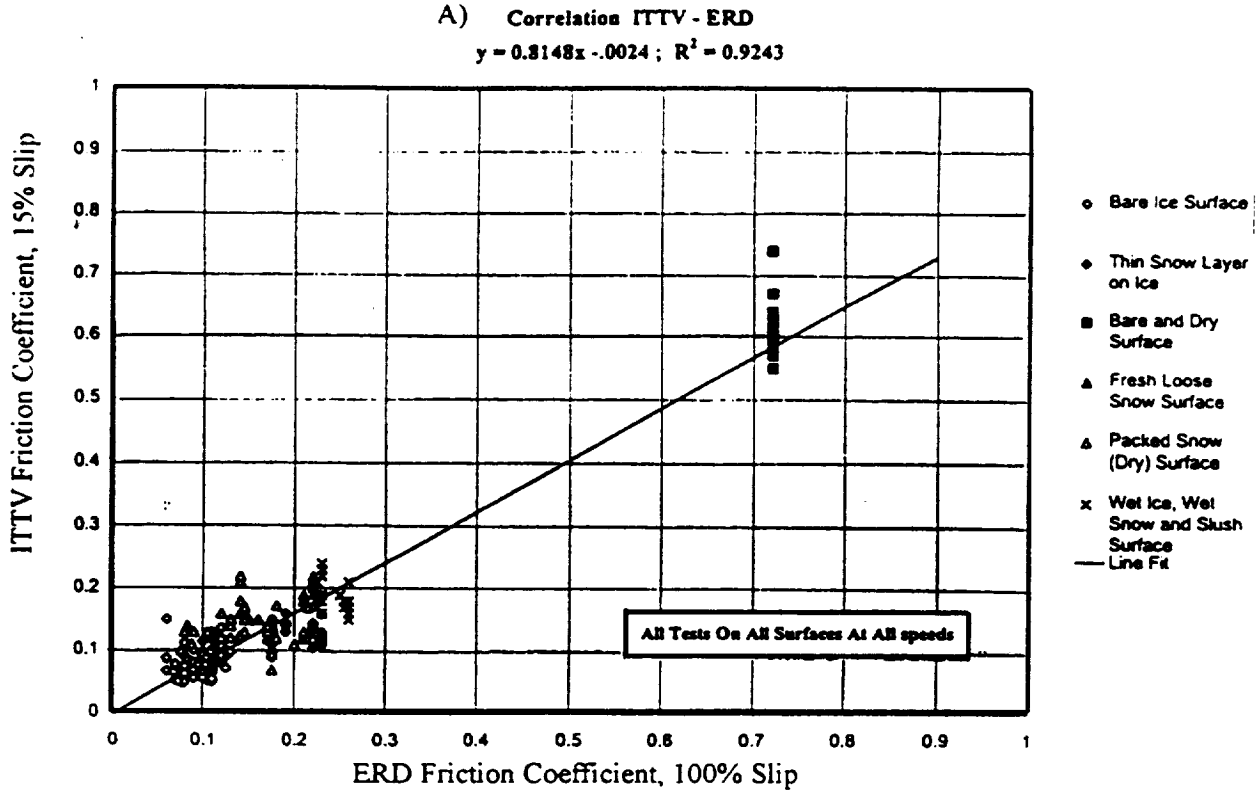
A) Correlation ITTV - ERD
y = 0.8148x -.0024 ; R² = 0.9243
ITTV Friction Coefficient, 15% Slip
ERD Friction Coefficient, 100% Slip
All Tests On All Surfaces At All speeds
Bare Ice Surface
Thin Snow Layer on Ice
Bare and Dry Surface
Fresh Loose Snow Surface
Packed Snow (Dry) Surface
Wet Ice, Wet Snow and Slush Surface
Line Fit

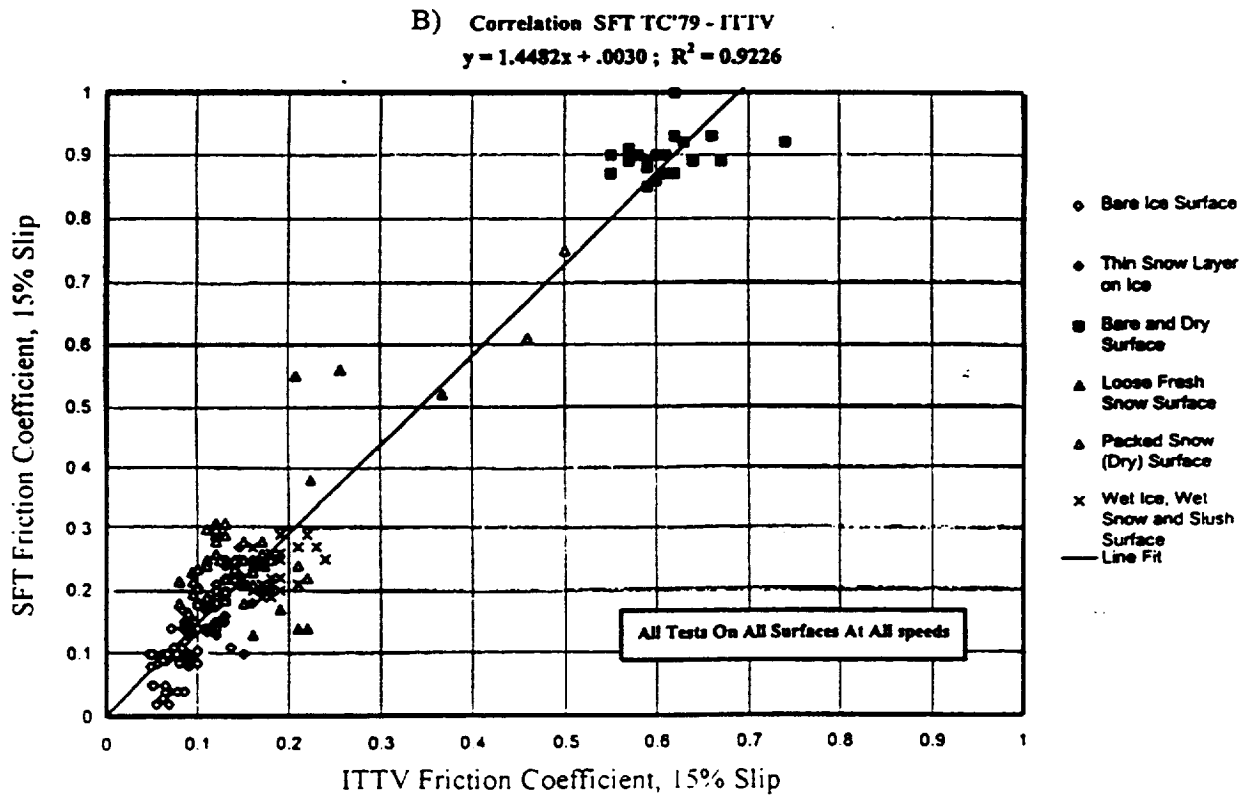
B) Correlation SFT TC'79 - ITTV
y = 1.4482x + .0030 ; R² = 0.9226
SFT Friction Coefficient, 15% Slip
ITTV Friction Coefficient, 15% Slip
All Tests On All Surfaces At All speeds
Bare Ice Surface
Thin Snow Layer on Ice
Bare and Dry Surface
Loose Fresh Snow Surface
Packed Snow (Dry) Surface
Wet Ice, Wet Snow and Slush Surface
Line Fit

Figure 3

C) CORRELATION OF IMAG AND ITTV

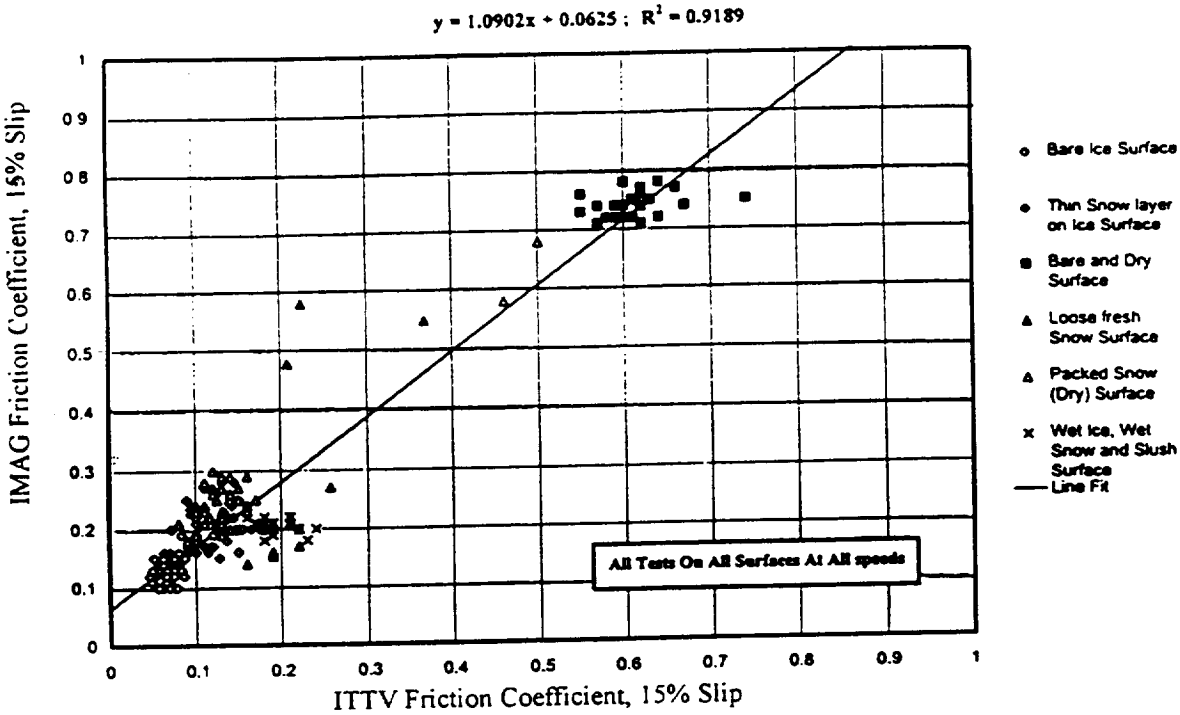

D) CORRELATION OF GRIPTESTER AND ITTV

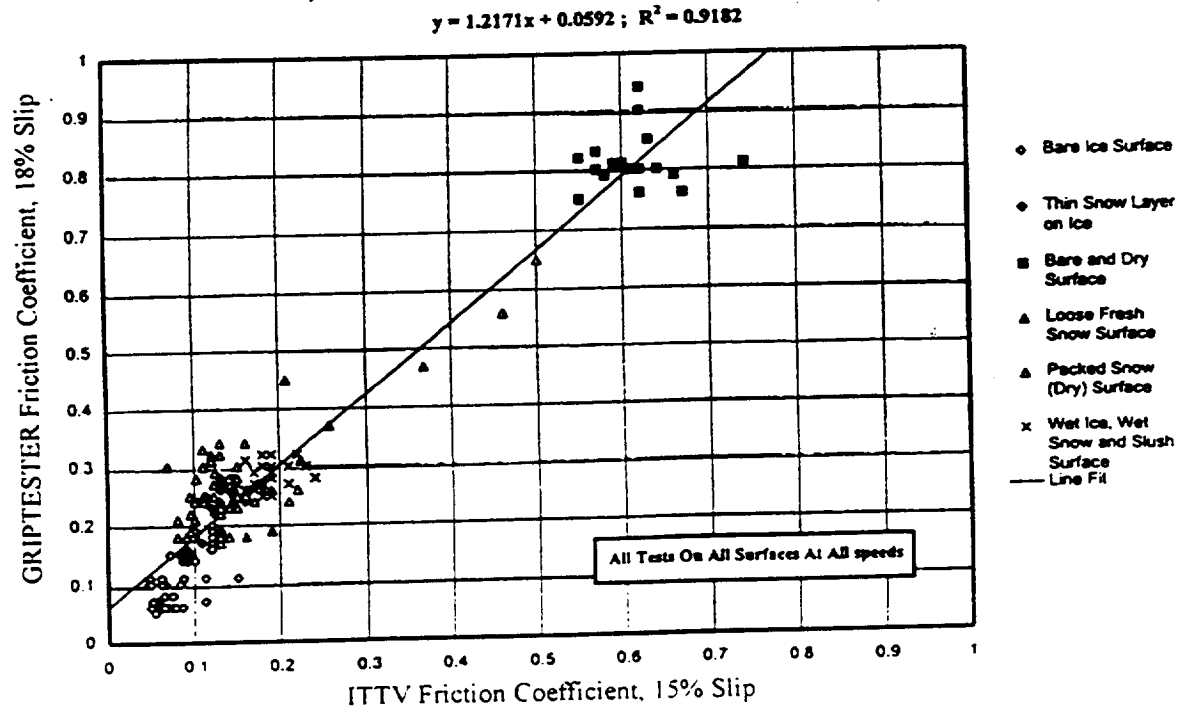

Figure 3 - Concluded

RUNAR TRAILER FRICTION VARIATION WITH PERCENT SLIP FOR DIFFERENT RUNWAY CONDITIONS
North Bay, ON and NASA Wallops; 65 km/hr (40 mph)

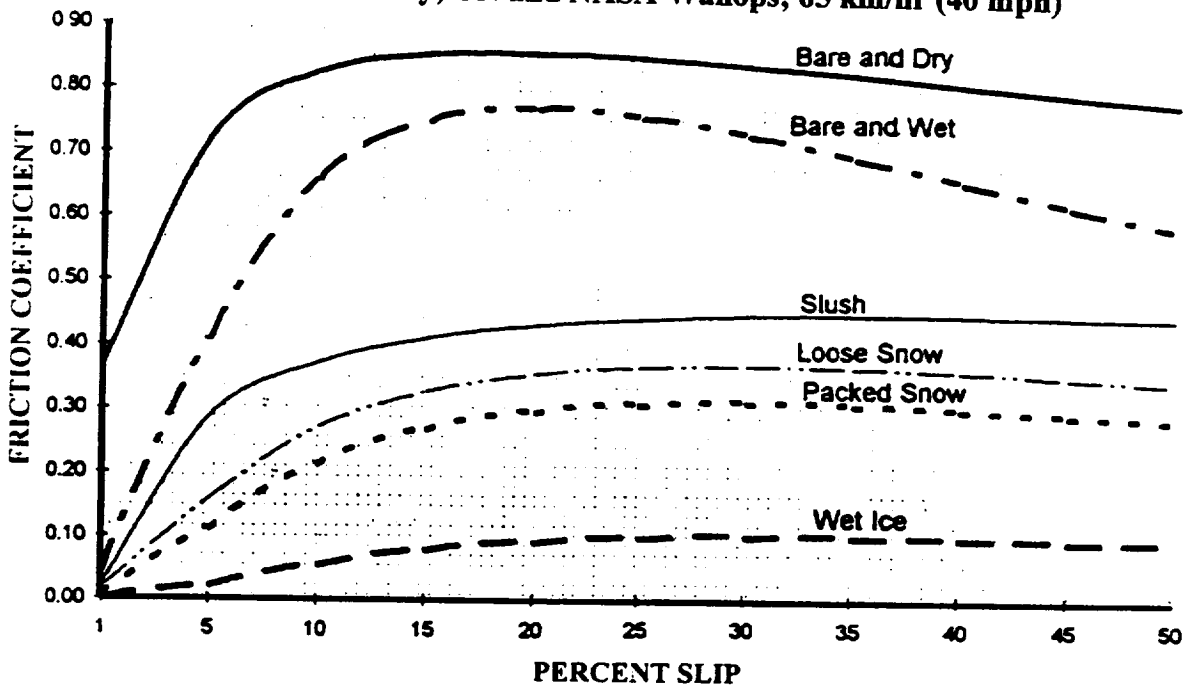

Figure 4

COMPARISON OF FALCON-20 AIRCRAFT AND ERD BRAKING FRICTION
North Bay, ON; Compacted snow conditions

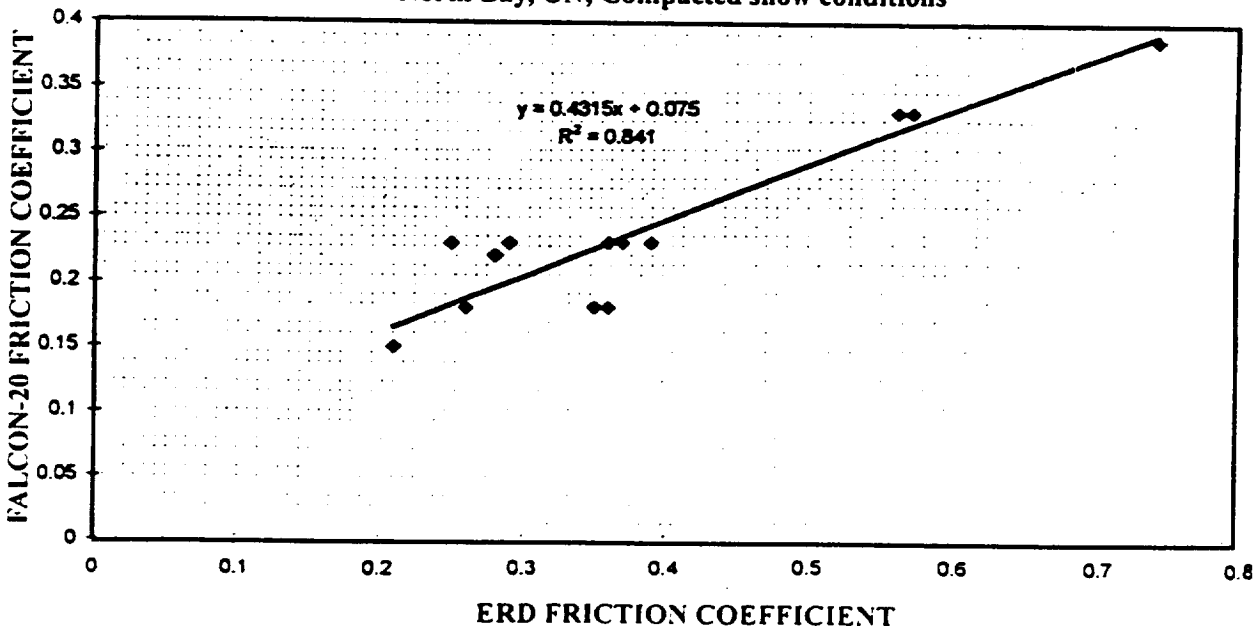

Figure 5

NASA B-737 AIRCRAFT BRAKING PERFORMANCE

Landing Configuration; North Bay, Ontario; R/W 8/26; March 1996
NASA Wallops Flight Facility; R/W 4/22; August 1996

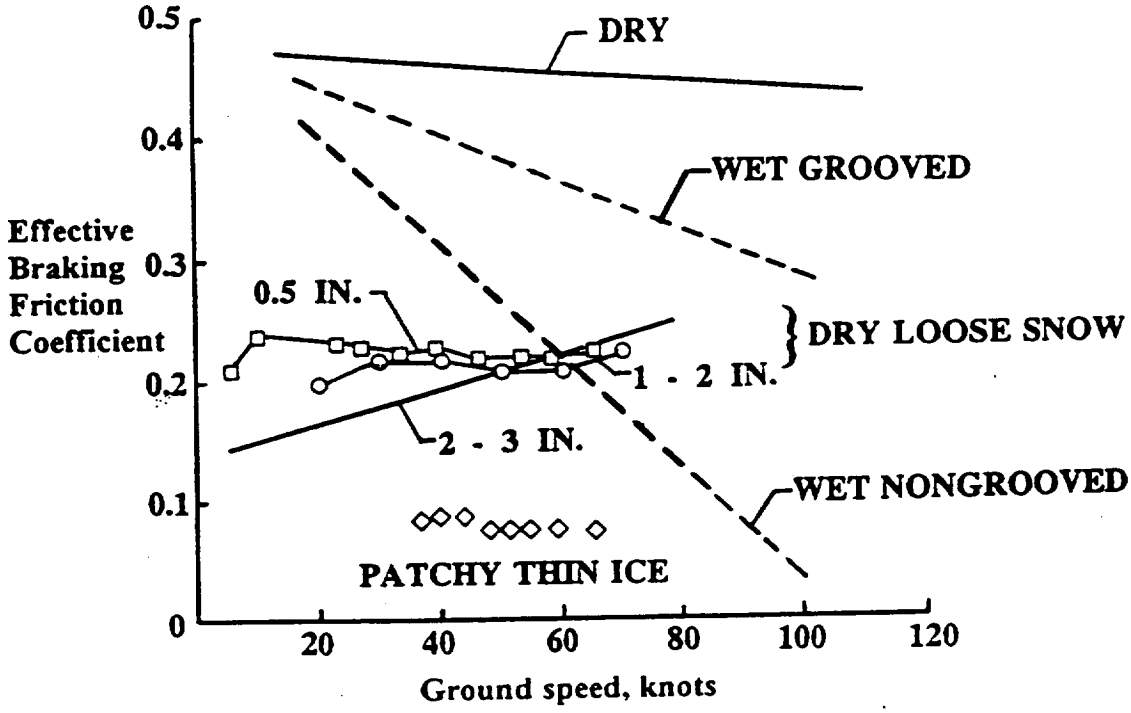

Figure 6

NASA B-737 Contaminant Drag Measurements
North Bay, ON; March 1996; takeoff configuration; loose dry snow

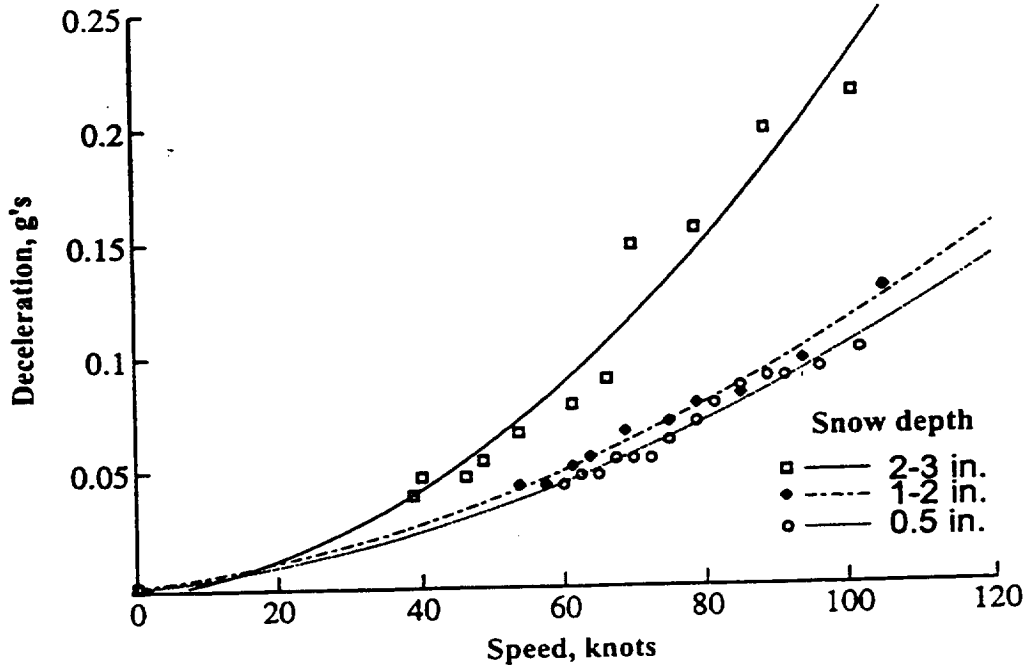

Figure 7

APPLICATION OF DIRECT SEARCH METHOD TO AEROELASTIC TAILORING OF AN ARROW WING CONFIGURATION

Koji Isogai
Department of Aeronautics and Astronautics
Kyushu University
6-10-1 Hakozaki Higasiku Fukuoka 812-8581, Japan
E-mail: isogai@aero.kyushu-u.ac.jp

Abstract. A computer code for areoelastic tailoring of an arrow wing supersonic cruise configuration is developed. A direct search method is employed to find the optimum fiber orientation angles and thickness distributions of the upper and lower skin panels of the wing box for the minimum weight design under the multiple constraints. The static strength, symmetric and antisymmetric flutter velocities are taken into account at the same time as the constraints. The code is applied to a typical arrow wing configuration to demonstrate its capabilities.

Key words: Aeroelasticity, SST, Arrow wing, Aeroelastic tailoring, Composite, Optimization

1. Introduction

The flutter characteristics, especially in the transonic regime, play the critical role in structural design of an arrow wing supersonic cruise configuration[1]. For example, the design studies performed by Turner and Grande[2] of the early Boeing Supersonic Transport (SST) Model 969-512B disclosed that the strength designed configuration does not meet the flutter requirement and an unrealistically high mass penalty was expected to achieve the flutter clearance ($1.2V_D$=259 m/s EAS at M=0.90 which was initially set. In order to improve the flutter characteristics of an arrow wing configuration without mass penalty, the application of the aeroelastic tailoring technology might be one of the most promising approaches. However, its effectiveness for the arrow wing configuration has not yet been well examined, though it has been shown that it is highly effective for the high aspect-ratio transport type wings[3)~5)].

In order to perform the trend study on the effectiveness of the aeroelastic tailoring for the structural design of an arrow wing supersonic cruise configuration, a preliminary design code is developed. In the present code, a direct search method (the Complex Method [5), 6)]), which does not depend on the derivatives of the objective and constraint functions, is employed to find the optimum fiber orientation angles and the thickness distributions of the upper and lower skin panels and the thickness of the spar and rib materials of the wing box for the minimum weight design under the multiple constraints. One of the characteristics of the code is that it can treat the static strength, the symmetric/antisymmetric flutter velocities and the minimum gauges at the same time as the constraints. In the next sections, the outline of the code and the results obtained by applying the present code to a typical arrow wing configuration will be presented.

2. The Outline of the Optimum Design Code

In order to perform the aeroelastic tailoring, we need several analysis codes as the elements of the optimization code. For the strength and vibration analyses, the in-house Finite Element Method (FEM) code is developed since we should know the fine-details of the FEM code to develop the aeroelastic optimization code by combining it with the aeroelastic analysis code. The in-house FEM code, in which the membrane elements are employed, is specialized to an arbitrary arrow wing configuration. That is, only a few parameters can generate, automatically, the FEM grids for the wing box of an arbitrary double delta type wing planform. For aeroelastic analyses, the modal approach is taken by using the symmetric/antisymmetric natural vibration

modes (16 mode shapes including rigid body modes are employed) obtained by the FEM code. The unsteady aerodynamic forces are calculated by Doublet Lattice Method (DLM)[7] code in which the 100 panels (10 chordwise by 10 spanwise) are employed. In order that the aeroelastic analysis code is integrated effectively in the optimization code, the symmetric/antisymmetric flutter velocities should be calculated automatically.

As to the optimization algorithm, the Complex Method which is originally proposed by Box[6] is employed. Applicability of the complex method to the aeroelastic tailoring of the high aspect-ratio transport type wings are extensively examined in Ref. 5. The complex method can handle multiple (inequality type) constraints without recourse to gradients. According to our experiences[5] in the aeroelastic tailoring study of the high aspect-ratio transport type wings, the complex method is very effective and robust in finding the optimum fiber orientation angles and the thickness distributions of the upper/lower skin panels of the wing box, while the deficiency of the method is that the rate of convergence of the objective function degrades rapidly with increasing number of design variables. Therefore, it is indispensable to reduce the number of design variables as small as possible when we apply the complex method to the aeroelastic tailoring. (See Refs. (5), (6), (8) for the detailed procedure of the complex method.)

In Fig. 1, the planform of the arrow wing model, for which the present design study is performed, is shown. (The further details of the model specification will be given in the next section.) The hatched part of the planform shown in Fig. 1 indicates the wing box location. Fig. 2 shows the arrangement of ribs and spars, and it also shows the FEM grids on the upper and lower skin panels. The total 670 triangular elements are used for the present FEM analyses. In order to reduce the number of the design variables in the optimization process, the upper/lower skin panels are divided into 7 blocks for each panels, respectively, as shown in Fig. 3, and the thickness of the skin within each block is assumed to be the same. It is also assumed that the laminate construction of the upper/lower skin panels is symmetric and the thickness of each layer having different fiber orientation angle is the

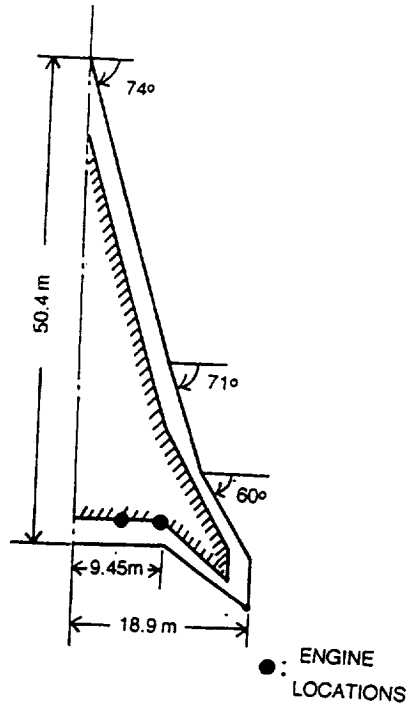

Fig. 1 Planform of Arrow Wing Model

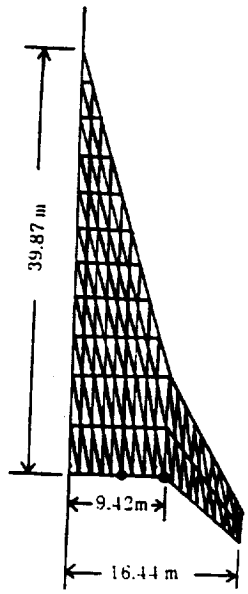

Fig. 2 Finite Element Grid

same for each other. As to the spars and ribs, the several elements which seems to be sensitive to the static strength and stiffness are selected as the design variables as shown later. In addition to this, the laminate constructions of the spars and ribs are assumed to be quasi-isotropic.

Thus, the following 25 design variables are selected:

(a) The thickness of each block of the upper/lower skin panels (the number of design variable: 7x2=14)

(b) The fiber orientation angles of the upper/lower skin panels (2)

(c) The thickness of the fore- and hind-spars of the inroad wing (2)

(d) The thickness of the fore- and hind-spars of the outboad wing (2)

(e) The thickness of the spars other than (c) and (d) (1)

(f) The thickness of the rib at the span station where the inboad engine is located (1)

(g) The thickness of the rib at the span station where the outboard engine is located (1)

(h) The thickness of the rib at the tip station of the wing box (1)

(i) The thickness of the rib other than (f), (g) and (h) (1)

Although the total 25 design variables mentioned above is employed for the present study, the design variables up to 34 (the maximum number of blocks up to 10 for each upper/lower skin panels and the maximum number of fiber orientation angle up to 5) can be taken in the present optimization code.

The objective function is the structural weight of the wing box, namely, the total sum of the weights of the upper/lower skin panels, spar materials and ribs.

The constraints are the static strength, the symmetric/antisymmetric flutter velocities and the minimum gauges for the upper/lower skin panels,

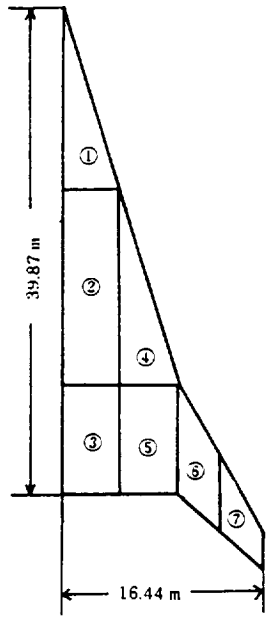

Fig. 3 Zoning of Upper/Lower Skin Panels

the spars and ribs. Tasi-Wu failure criterion[9] is employed to identify the structural failure.

3. Results and Discussions

As an example of the application of the present optimization code, the design study has been performed of an arrow wing configuration shown in Fig. 1. The length of the root chord is 50.4 m and the semispan length is 18.9 m. The leading edge sweep angles of the inner and outer wings are 74° and 60°, respectively. The full-span wing area is about 830 m^2 and the aspect ratio is 1.61. The airfoil section is 3 percent thick circular-arc. The engine mass is assumed to be 6,500 Kg for each of the four engines. The engines are expressed by the concentrated masses at the locations indicated in Fig. 1. For the full fuel condition, which is the most critical for flutter, 200,000 Kg of the fuel mass is assumed. The maximum gross take-off mass is assumed to be 374,500 Kg. Therefore the zero fuel mass becomes 174,500 Kg. The structural materials used in the present study is Graphite/PEEK (APC2), whose material properties are E_L=134 GPa, E_T=8.90 GPa, ν_{LT}=0.28, and G_{LT}=5.10 GPa.

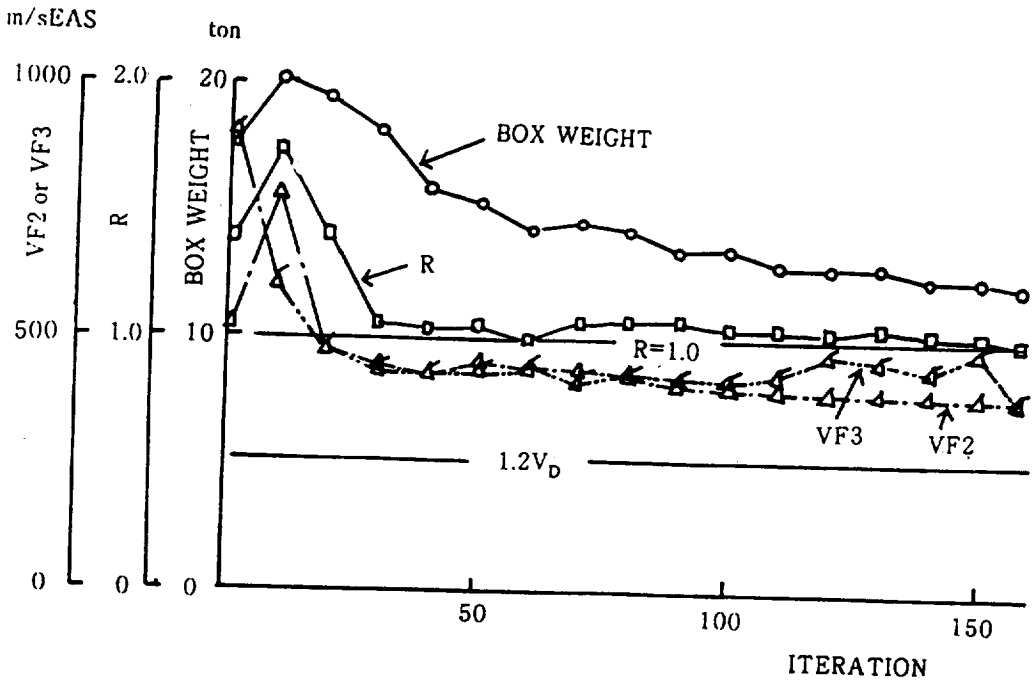

Fig. 4 Convergence Histories of the Box Weight, Strength Ratio and Symmetric/Antisymmetric Flutter Velocities during Optimization Process

The minimum weight design is performed under the following design conditions (inequality constraints):

a) Static Strength

The strength requirement is to sustain 2.5g load of the maximum take off gross weight which corresponds with 9.175×10^6 N. This static load can be realized at M=0.90 and $\alpha=5.1^{\circ}$. The load distributions calculated by using DLM is applied at each node point of the FEM grid.

b) Flutter Velocity Requirement

The symmetric/antisymmetric flutter velocities should clear 1.2 V_D=259 m/s EAS at M=0.90.

c) Minimum Gauges

Since the laminate construction of the upper/lower skin panels of the present model is assumed to be $(\beta_1:50\%; \beta_2:50\%)_s$ where β_1 and β_2 are the fiber orientation angles (design variables), the minimum gauge for the upper/lower skin panels is taken to be 0.52 mm. As to the minimum guage for the spars and ribs, 1.04 mm is assumed since the laminate constructions of them are quasi-isotropic.

In Fig. 4, the convergence histories of the wing box structural weight (the objective function), the strength ratio R, the symmetric (VF2) and antisymmetric (VF3) flutter velocities during optimization process are plotted. The value of the wing box weight has converged to 12.148 ton after 158 iterations. As seen from the figure, the strength ratio R has reached to 1.0 at the optimum point, while the flutter velocities at the optimum point are VF2=387 m/s EAS and VF3=388 m/s EAS, that are considerably higher than 1.2 V_D=259 m/s EAS. This fact suggests that the structure obtained by the present optimum design is strength critical rather than flutter critical.

The total wing box structural weight of 12.148 ton is composed from 3.656 ton of the upper/lower skin panels, 6.604 ton of the spar materials and 1.888 ton of the ribs. The optimum fiber orientation angles and the thickness distributions of the upper/lower skin panels are shown in Fig. 5. The 12.148 ton of the wing box

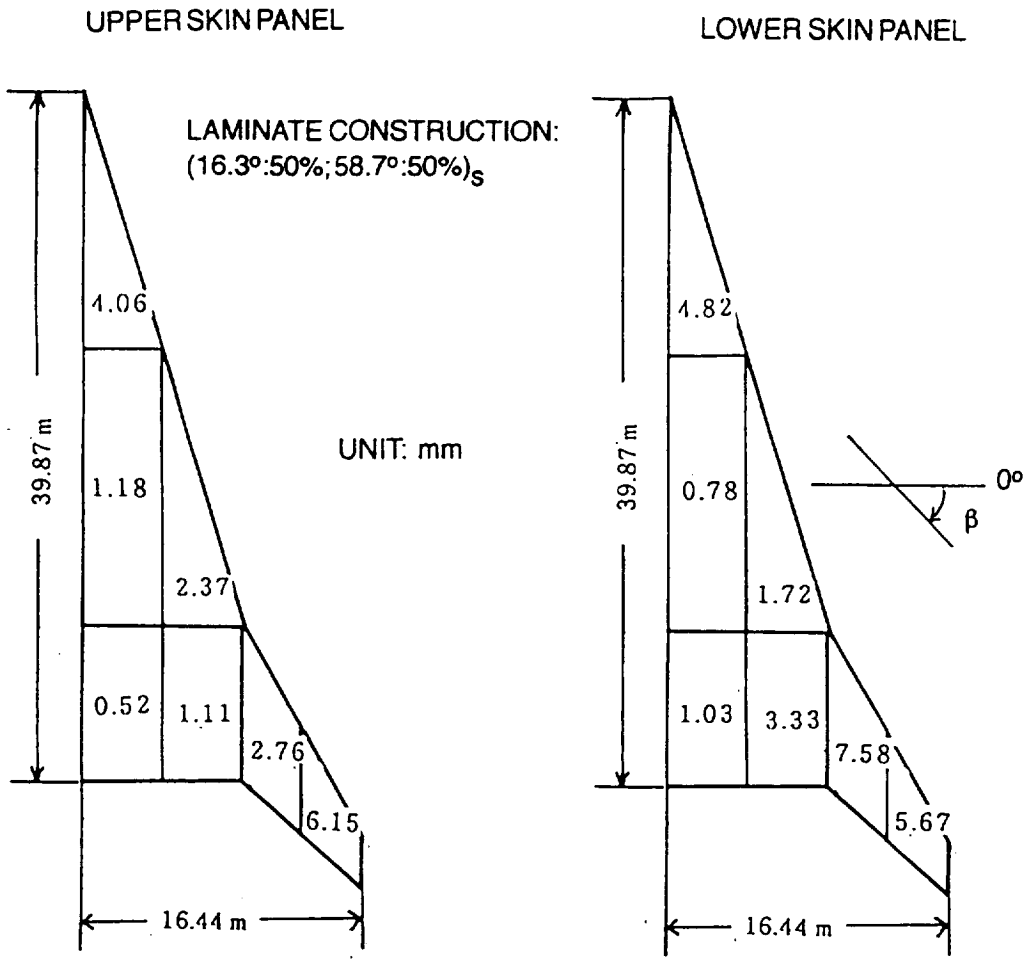

Fig. 5 Fiber Orientation Angles and Thickness Distributions of Upper/Lower Skin Panels

structural weight obtained by the present optimum design is about 19% reduction of the corresponding wing box structural weight of our previous design[10], which was obtained by the trial and error design under the same design conditions.

In Figs. 6a and 6b, the symmetric and antisymmetric natural vibration mode shapes and frequencies of the present optimized structure are shown, respectively. It should be noted that the first three modes are the rigid body modes, namely, $f_1=f_2=f_3=0$ and that only the elastic modes are shown in the figures.

As already mentioned, the structural weight reduction attained by the present optimization is about 19 % compared with our previous trial and error design. When we notice that the present optimized model is strength critical rather than flutter critical, it could be said that the aeroelastic tailoring might be more effective than the present example if we apply the present code to the arrow wing model which is flutter critical rather than strength critical.

4. Concluding Remarks

A preliminary design code for aeroelastic tailoring of an arrow wing supersonic cruise configuration has been developed. A direct search method, which does not depend on the derivatives of the objective and constraint functions, is employed to find the optimum fiber orientation angles and thickness distributions of the upper and lower skin panels, and to find the optimum thickness of the spar and rib materials of the wing box structure for the minimum weight design under the multiple constraints. The static

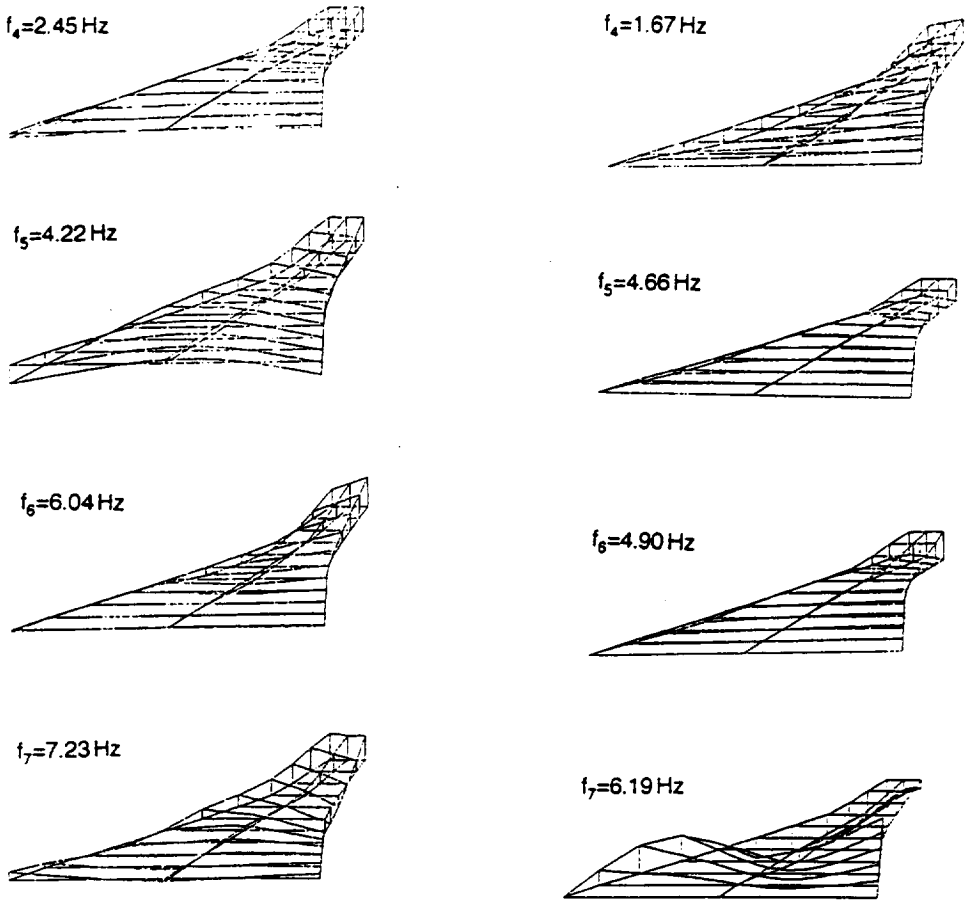

Fig. 6 Natural Vibration Mode Shapes and Frequencies of Optimum Designed Structure

strength, symmetric and antisymmetric flutter velocities are taken into account at the same time as the constraints. The code is applied to a typical arrow wing configuration to demonstrate its capabilities. It has been shown that the 19% reduction of the structural weight can be attained by the optimization compared with our previous trial and error design obtained under the same design conditions.

References

1. Bhatia, K. G. and Wertheimer, J.,"Aeroelastic Challenges for a High Speed Civil Transport," AIAA-93-1478-CP, 1993.

2. Turner, M. J. and Grande, D. L.,"Study of Metallic Structural Design Concepts for an Arrow Wing Supersonic Cruise Configuration," NASA Contractor Report 2743, Dec. 1977.

3. Isogai, K., Ejiri, H., Kukuchi, T., Yamane, K., Kumakura, I., Sotozaki, T., Minegishi, M., and Noguchi, Y.,"Effects of an Optimized Fiber Orientation on Transonic Flutter Characteristics of a High-Aspect-Ratio Composite Wing," TR-930, National Aerospace Laboratory, Japan, May 1987.

4. Isogai, K.,"Transonic Flutter/Divergence Characteristics of Aeroelastically Tailored and Non-Tailored High Aspect-Ratio Forward Swept Wings," Journal of Fluids and Structures, 6, 1992, pp. 525-537.

5. Isogai, K.,"Direct Search Method to Aeroelastic Tailoring of a Composite Wing under Multiple Constraints," Journal of Aircraft, Vol.26, No. 12, Dec. 1989. pp. 1076-1080.

6. Box, M.J.,"A New Method of Constrained Optimization and a Comparison with Other Methods," Computer Journal, Vol. 8, 1965, pp. 42-52.

7. Albano, E. and Rodden, W. P.,"A Doublet-Lattice Method for Calculating Lift Distributions on Oscillating Surfaces in Subsonic Flows," AIAA Journal Vol. 7, Feb. 1969, pp.279 ~285.

8. Beveridge, G.S.G. and Schechter, R.S. Optimization, Theory, and Practice, Chemical Engineering Series, McGraw-Hill, New York, 1970, pp. 453-456.

9. Tasi, S. W. and Wu, E. M.,"A General Theory of Strength for Anisotropic Materials," Journal of Composite Materials, Vol. 5, Jan. 1971, pp. 58-80.

10. Isogai, K.,"Study on Transonic Flutter Characteristics of an Arrow Wing Configuration," Proceedings of CEAS International Forum on Aeroelasticity and Structural Dynamics, June 1997, pp. 87-95.

Ply Angle Optimization of Non-Uniform Composite Beams Subject to Aeroelastic Constraints

T. Evrard*, R. Butler, S. W. Hughes
Department of Mechanical Engineering, University of Bath, Bath BA2 7AY, UK

J. R. Banerjee
Department of Mechanical Engineering and Aeronautics, City University, London EC1V OHB, UK

ABSTRACT

This paper investigates the effect that varying the orientation α of a $[90+\alpha/0+\alpha/+45+\alpha/-45+\alpha]_S$ lay-up has on the flutter and divergence behaviour of a uniform flat composite beam, in both swept and unswept configurations. Minimum-mass optimization of non-uniform flat composite beams, with varying orientation of the same lay-up, is also presented. Results show a reduction in mass of 23% for optimum α compared to the baseline $\alpha = 0$ case. It is also found that the lay-up orientation giving maximum permissible airspeed for a uniform beam corresponds to the optimum orientation for a non-uniform beam. Hence, the wing designer may quickly and accurately determine the optimal lay-up orientation by performing flutter and divergence analyses at a range of values of α between +90° and -90°. The current limitations of the technique, concerning strength requirements and manufacturing considerations, are recognized. Furthermore, some of the designs are shown to be highly imperfection-sensitive.

1. INTRODUCTION

Several studies on the optimization of aeroelastically constrained, composite wings with cantilever end conditions have been conducted. For example, recent optimizations[1,2] have examined the design of non-uniform, flat composite beams for frequency, flutter and divergence constraints. During these studies, variation of the thickness of a generic lay-up with fixed values of ply angles was considered, and an experimental validation was carried out. Other related work[3-6] has investigated the influence that ply orientation, sweep angle, wash-in and wash-out, as well as various other parameters, has on flutter speed. This work showed that modal interchange can significantly alter the flutter speed of a composite wing[4], and that for flutter of an unswept composite wing, torsional rigidity and coupled bending-torsional rigidity[5] are the most influential parameters. It was also found that, contrary to traditional thinking, wash-out can be beneficial from a flutter point of view[6]. A recent independent study[7] has examined the effect of both ply angle variation and the position of lumped masses on flutter speed for uniform thickness wind tunnel

**Placement student at the University of Bath. Now at French Institute for Advanced Mechanical Engineering, Campus des Cezeaux, B.P. 265, 63175 Aubiere Cedex, France.*

models. Here, the principal findings were that small variations in thickness can have a significant effect on flutter speed, and that practical application of optimization should allow for uncertainties in the aerodynamic and structural models.

For all of the above studies in which ply angle has been varied, the lay-up has been constructed from either unidirectional material [0°] or woven $[0/90]_S$ material. Also, the wing structure has previously consisted of a flat composite beam of uniform thickness. The current paper describes the effect that varying the orientation α of a $[90+\alpha/0+\alpha/+45+\alpha/-45+\alpha]_S$ lay-up has on the flutter and divergence speeds of such uniform beams which are both unswept and swept back, where the effect of such variation is to alter the influence of each layer on the beam rigidities. Following this, the design optimization of non-uniform beams with varying orientation of the same lay-up, is considered. These studies have led to the development of a strategy, the aim of which is to guide the designer using a quick and accurate conceptual model to determine the best lay-up orientation, i.e. the orientation that will give the minimum mass whilst satisfying flutter and divergence speed constraints. Such a strategy is very efficient compared to a complete optimization study for each possible lay-up orientation. The work also provides information on the effect of imperfections in lay-up orientation, which may be of interest to composite manufacturers.

2. Analysis and optimization

2.1 *Wing model*

The wing model used in this study has previously been presented[1,2]. It consists of 10 uniform beam elements, where each element has a lay-up of $[90+\alpha/0+\alpha/+45+\alpha/-45+\alpha]_S$, a length of 0.04 m and a width of 0.08 m, see Fig.1. The lay-up orientation α is defined as the angle that the 0° fibres are inclined to the y-axis of the beam. (Note that for a swept wing the y-axis is the centroidal axis of the beam.) The composite material properties are given in Table 1 and the structural beam is enclosed in a NACA 0015 aerofoil of (unswept) chord 0.195 m. The mid-chord position of this aerofoil is positioned 0.04 m in front of the beam centre.

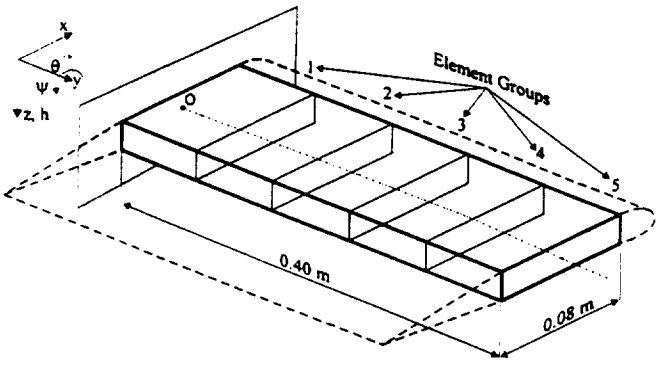

Fig. 1: Unswept wing model with coordinate system. θ shows the direction of both positive lay-up orientation and positive ply angle.

Parameter	Value
E_1	165.0 GPa
E_2	8.8 GPa
G_{12}	5.0 GPa
υ_{12}	0.30
ρ	1550 kg/m^3

***Table 1:** Material properties of carbon fibre/epoxy composite.*

It is assumed that each element obeys the following differential equations:

$$M = -EI\frac{\partial^2 h}{\partial y^2} + K\frac{\partial \psi}{\partial y} \qquad ...(1)$$

$$T = GJ\frac{\partial \psi}{\partial y} - K\frac{\partial^2 h}{\partial y^2} \qquad ...(2)$$

where M is the bending moment, T is torque, h is vertical displacement and ψ is torsional displacement. Hence $\frac{\partial \psi}{\partial y}$ is the rate of change of twist along the beam and $\frac{\partial^2 h}{\partial y^2}$ is the curvature of the beam. The bending, torsional and coupled bending-torsional rigidities, EI, GJ and K respectively, are constant for each element and have been derived[8] from the [D] matrix produced by classical laminate analysis, i.e.

$$EI = b\left[D_{22} - \frac{D_{12}^2}{D_{11}}\right]; \quad GJ = 4b\left[D_{66} - \frac{D_{16}^2}{D_{11}}\right]; \quad K = 2b\left[D_{26} - \frac{D_{12}D_{16}}{D_{11}}\right] \qquad ...(3)$$

where b is the width of the element. The coupled bending-torsional rigidity K may be either positive or negative. For positive K the wing will twist leading edge down when it is bent upwards, i.e. the wing will wash-out, whereas negative K will cause the wing to twist leading edge up (wash-in) when it is bent upwards, see Fig. 1.

2.2 *Free vibration and aeroelastic analysis*

The Dynamic Stiffness Method (DSM) is used to carry out free vibration analysis for the non-uniform composite beam[9] by idealizing it as a series of uniform beam elements. The dynamic stiffness matrix represents an exact continuous model of the element and so the major difference between this method and the Finite Element Methods (FEM), is that FEM approximates displacements with shape functions to obtain separate mass and stiffness matrices. To improve the accuracy, FE methods often require more elements, whereas the DSM is independent of the number of elements used.

Aeroelastic analysis is carried out using the program CALFUN[10]. Here, the dynamic stiffness matrix and aerodynamic matrix are expressed in terms of generalised co-ordinates; the generalised dynamic stiffness matrix being obtained by diagonalising the dynamic stiffness matrix using normal modes. The generalised aerodynamic matrix is obtained by applying the principle of virtual work, using strip theory based on Theodorsen expressions[11] and the normal modes obtained from the dynamic stiffness matrix. (In the results that follow the first six normal modes of the wing are used.) An accurate value of the flutter speed V_f and flutter frequency can be found using the V-g method and the divergence speed V_d is obtained by considering it as a static (zero frequency) instability problem.

2.3 Optimization

During optimization, the beam is divided into 5 element groups of length and width 0.08 m, see Fig. 1. The thickness of each of the (90° + α), (0° + α), (45° + α), and (–45° + α) layers within each group is allowed to vary within the limits of 0.125 mm and 2.0 mm. To find a minimum-mass wing design that satisfies aeroelastic constraints, a sequential quadratic programming strategy (SQP) combined with the modified methods of feasible directions (MMFD) optimizer contained in the optimization package DOT[12] is used. The minimum acceptable flutter and divergence speeds for this beam are set to 36.91 and 37.91 m/s, respectively, these being the values used in the previous study[2] in which lay-up orientation was not varied.

3. Results

3.1 Parametric study for uniform thickness beam

The analysis of a uniform thickness beam model for varying lay-up orientation α, where each of the 8 layers within the $[90+\alpha/0+\alpha/+45+\alpha/-45+\alpha]_S$ lay-up has the same thickness, is firstly considered. Figure 2 shows the variation of the rigidities EI, GJ and K against α where the values of rigidity have been normalized against the EI value for α = 0°. It can be seen that when α = 0° the beam has a small amount of positive K, since of the two layers of diagonal plies, the +45° layer is positioned outermost. As expected, maximum values of GJ occur at around α values of +49° and -50° whereas α = ± 90° gives maximum EI. It can also be seen that maximum value of positive (negative) K occurs at around α = -64° (α = +66°) and that K is zero when α is around +42° and –43°.

3.1.1 Unswept wing

Figure 3 shows the variation of flutter and divergence speed with varying α for an unswept wing. Here, as in Figs. 4 and 5, airspeed has been normalized against the flutter speed found when α = 0°. In Fig. 3, maximum flutter speed occurs at around α = 52°, which from Fig. 2, corresponds to a large value of GJ, low EI and a small amount of negative K. It is also evident that divergence speed approaches infinity for maximum values of positive K. Peak values on the flutter and divergence envelope shown in the figure occur at α values of around +41° and –45°.

All the calculations described above did not account for any offset x_α between the mass axis and the elastic axis of the beam, which in this case is taken as the beam centroidal axis. Thus a further study to evaluate the influence of the offset on the flutter speed was carried out. Figure 4 shows the variation of flutter speeds against α for different values of x_α, where positive x_α means that the mass axis is in front of the elastic axis. The figure shows that, as expected, flutter speed is reduced when the mass axis is positioned behind the elastic axis, which is usually the case for most practical wings. This can be explained by considering the lift of a wing due to local changes in angle of attack. A mass axis in front of the elastic axis tends to lower this angle and hence attenuates the flutter phenomenon, although a mass axis behind the elastic axis tends to increase the angle and hence amplify flutter. It is interesting to see that the offset has little influence on the shape of the curves. Minimum and maximum values are obtained for similar values of α to the zero offset case. Hence, the offset would not significantly change the optimum α, and only the $x_\alpha = 0$ case is considered henceforth.

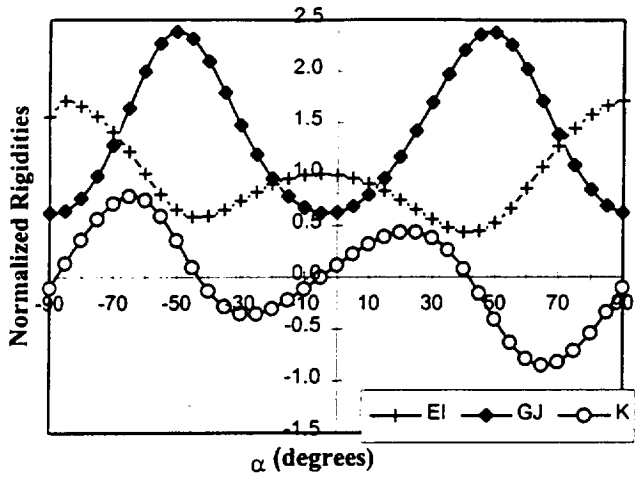

Fig. 2: Rigidities EI, GJ and K against lay-up orientation α for uniform beam.

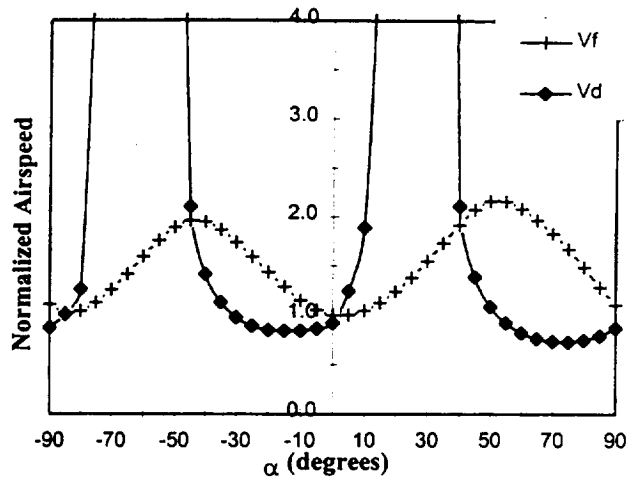

Fig. 3: Flutter and divergence speed against lay-up orientation α for unswept wing.

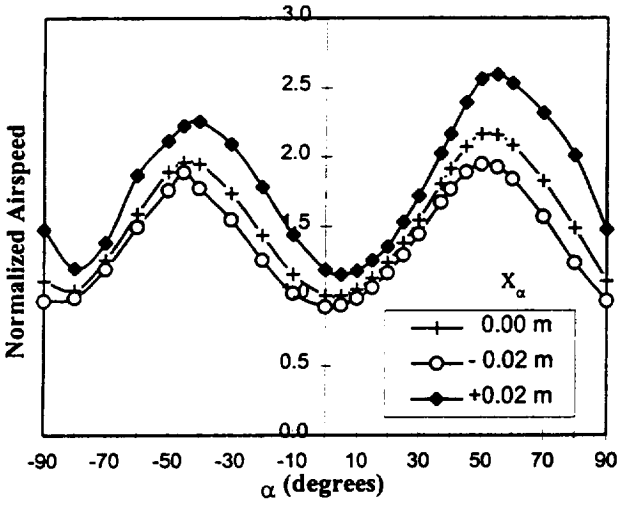

Fig. 4: Flutter speeds against α for different values of offset x_α.

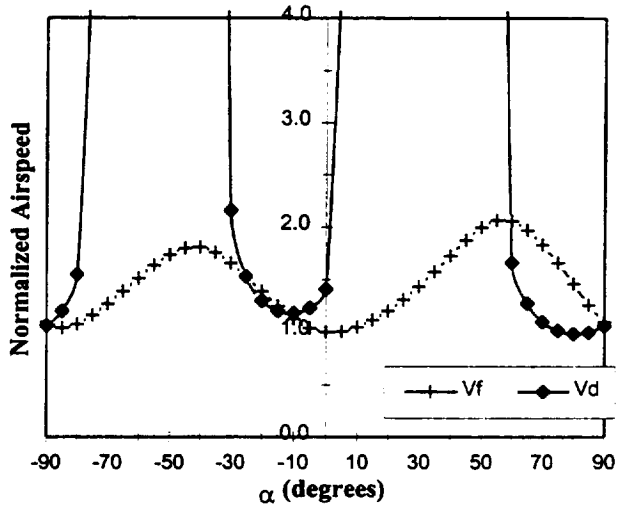

Fig. 5: Flutter and divergence speed against lay-up orientation α for wing with 20° sweep.

3.1.2 Swept wing

When the wing model is swept back 20°, the flutter and divergence results of Fig. 5 are obtained. As expected, the regions in which divergence is critical are reduced compared with the unswept case. These regions are confined to the range α = 60 to 90°, and around α = -20°. From Fig. 2, these regions have low values of GJ and negative K. The flutter/divergence boundary maximum now occurs when flutter speed reaches a maximum, i.e. at around α = 60°. This corresponds to relatively high values of both GJ and negative K.

3.2 *Optimization of non-uniform thickness beam*

3.2.1 Unswept wing

Initially, the unswept beam was optimized for a range of α values, see Fig. 6. Each point in the figure gives the optimum mass produced by a single optimization run for a single α value, taking on average 4 CPU hours on an Silicon Graphics O_2 (175 MHz/R10,000) workstation. The relationship between this figure and the flutter/divergence boundary of Fig. 3 is clearly apparent. For instance, the optimum (minimum-mass) values of α in Fig. 6, occurring at around +42° and –45° correspond to maximum points in Fig. 3. These optimum designs show a 23% reduction in mass compared to the $\alpha = 0$ case. Furthermore, values of α which produce high minimum-mass designs (α values of around –20° and 75°) correspond to minimum points on the flutter and divergence boundary of Fig. 3.

The $\alpha = 0°$ optimum design for zero sweep ($\Omega = 0°$), which was obtained previously[2], and the $\alpha = 45°$ optimum design are compared in Table 2. It can be seen that the (-45°+ α) layer is thickest for the $\alpha = 0°$ optimum whilst for the $\alpha = 45°$ optimum the (0° + α) layer is thickest. In the latter case, the (0° + α) layer is torsionally more efficient than the $\alpha = 0°$, (-45° + α) layer, as a result of being located further from the centre of the beam. Hence, although the torsional rigidity of both designs is similar, see Fig. 7(b), the α = 45° mass is considerably lower. Figure 7(a) shows that, as a result of the position of 0° fibres in the $\alpha = 0°$ design, its bending rigidity is high when compared with the $\alpha = 45°$ design. This will result in reduced separation between first bending and first torsional natural frequencies giving reduced flutter speed. Hence the required minimum flutter speed is achieved for the $\alpha = 0°$ case by a comparatively large value of positive coupled bending-torsional rigidity, see Fig. 7(c), causing the wing to wash-out. This effect reduces the coupling between aerodynamic forces (acting at quarter chord) and the torsional centre of the wing.

Table 2 shows that for the $\alpha = 0°$ optimum both the (90° + α) and (0° + α) layers are at their lower bound. Although this bound may be thought of as representing the practical constraints of strength and lay-up stability which are not considered here, an additional optimization with a lower bound of 0.001 mm was performed to investigate the effect of allowing the optimizer to remove this material altogether. This gave an optimum mass of 81.39 g, which is still around 10% heavier than the $\alpha = 45°$ optimum. Hence the advantage associated with the inclusion of α as a design variable would appear to be confirmed.

3.2.2 Swept wing

A similar study, performed for the wing with 20° sweep, also confirmed that the optimum value of α corresponds to the α producing maximum airspeed values on the flutter/divergence boundaries of Fig. 5. Hence, optimization results for the optimum orientation, $\alpha = 60°$, are given in Table 2 and the associated rigidities are plotted in Fig. 7. It can be seen that the optimum design in this case has negative coupled bending-torsional rigidity, see Fig. 7(c), causing the wing to wash-in.

In order to check the sensitivity of the above $\Omega = 20°$, $\alpha = 60°$ optimum design to small changes in α which may arise from manufacturing imperfections, the optimum design was re-analyzed with α values of 55° and 65°. This analysis gave, respectively, flutter speeds of 36.76 and 35.39 m/s and divergence speeds of

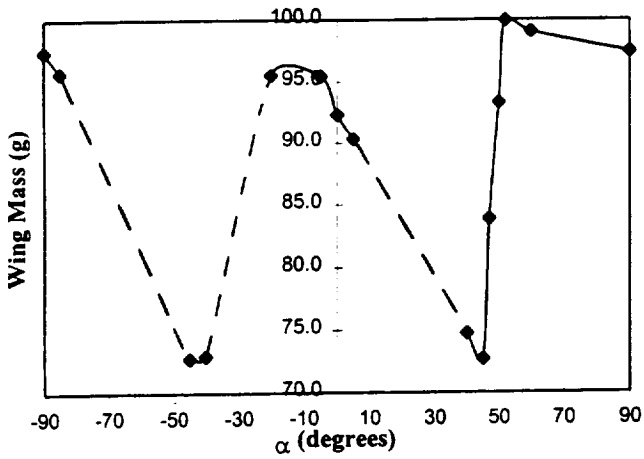

Fig. 6: Optimum mass against lay-up orientation α.

Ω (degrees) :	0.0	0.0	20.0
α (degrees) :	0.0	45.0	60.0
V_f (m/s) :	36.91	37.10	36.91
V_d (m/s) :	37.94	37.89	37.89
Thicknesses (mm) :			
(90° + α) Layer :			
1	0.125	0.125	0.125
Element 2	0.125	0.125	0.134
Group: 3	0.125	0.125	0.204
4	0.125	0.125	0.198
5	0.125	0.125	0.125
(0° + α) Layer :			
1	0.125	0.432	0.230
Element 2	0.125	0.411	0.263
Group: 3	0.125	0.374	0.262
4	0.125	0.309	0.203
5	0.125	0.132	0.125
(45° + α) Layer :			
1	0.271	0.183	0.285
Element 2	0.292	0.173	0.244
Group: 3	0.287	0.144	0.183
4	0.248	0.126	0.137
5	0.160	0.125	0.125
(−45° + α) Layer :			
1	0.548	0.126	0.237
Element 2	0.507	0.126	0.210
Group: 3	0.452	0.126	0.171
4	0.383	0.126	0.137
5	0.254	0.125	0.125
Total Mass (g) :	92.3	72.7	73.8

***Table 2:** Optimum thicknesses for unswept (Ω = 0°) and swept (Ω = 20°) wings with different values of lay-up orientation α.*

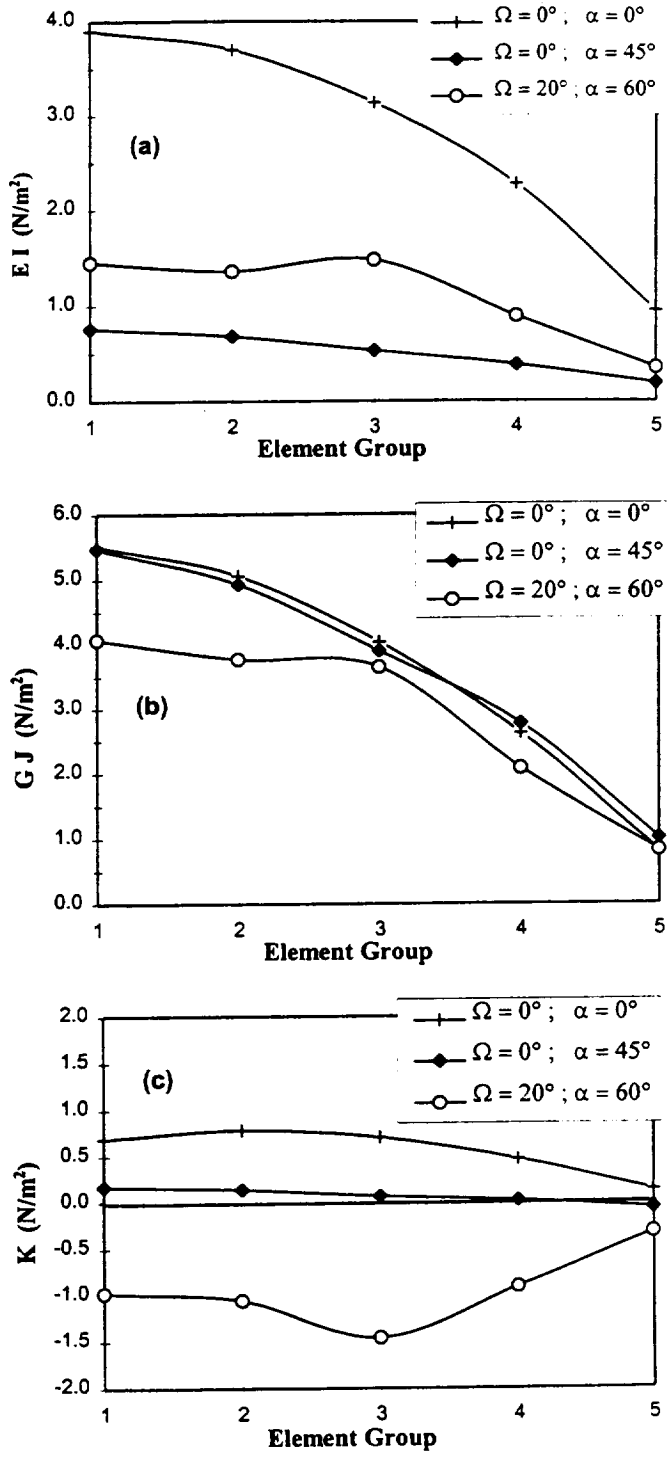

***Fig. 7:** Spanwise variation in (a) bending rigidity EI; (b) torsional rigidity GJ, and (c) coupled bending-torsional rigidity K for optimum designs of Table 2.*

114.88 and 25.35 m/s. Hence the divergence speed of the optimum is very sensitive to imperfection, which can be explained by the very steep variation in divergence speed at α values of around 60° in Fig. 5.

4. Conclusions and future work

The results described above show the variation of flutter and divergence speeds of a uniform composite wing with lay-up $[90+\alpha/0+\alpha/+45+\alpha/-45+\alpha]_S$ when subject to variations in lay-up orientation α. Following this, optimum non-uniform beam designs have been obtained for both swept and unswept wings for varying values of α. At the conceptual structural design stage a wing designer cannot afford to run a series of optimization runs to cover the full range of α between +90° and -90° in order to find the optimum α. Hence it is anticipated that the proposed strategy, in which the lay-up orientation giving maximum airspeed on the flutter/divergence boundary for a uniform wing is found to correspond to the optimum α for non-uniform wings, would be very advantageous. Furthermore, this method of finding the optimum α typically takes only 5% of the CPU time required for a single optimization run.

It is obviously important to consider the practicality of the above optimization results, particularly from a manufacturing point of view. It has been shown that the optimum designs may be sensitive to small changes (imperfections) in α. Furthermore, any continuous optima would need to be converted to a discrete number of layers as has been done previously[2]. This may be difficult, if not impossible, considering the small range of thicknesses in some cases. However, the aim of the paper is to show the potential benefit associated with design involving variable lay-up orientation.

For practical application of the proposed strategy there would be a need to adapt it to be able to deal with the design of a wing box structure and to handle strength constraints. This could be achieved via the extension of an existing wing box optimization program[13].

Acknowledgement

The authors are grateful for the helpful comments received from Dr M. Lillico (University of Bath).

References:

1. Taylor J.M. and Butler R., "Optimum Design and Validation of Flat Composite Beams Subject to Frequency Constraints", *AIAA J.*, 1997, Vol. 35, No. 4, pp. 540-545.

2. Taylor J.M., Butler R. and Harrison C., "Optimisation of Composite Wind-Tunnel Wing Models for Frequency, Flutter and Divergence", *Aeronautical Journal*, 103, No. 1020, 1999, pp. 105-111.

3. Georghiades, G.A., Guo, S. J., and Banerjee, J. R., "Flutter Characteristics of Laminated Composite Wings", *AIAA J.*, Vol. 33, No. 6, 1996, pp.1204-1206.

4. Georghiades, G.A., and Banerjee, J. R., "Role of Modal Interchange on the Flutter of Laminated Composite Wings", *J Aircraft*, Vol. 35, No. 1, 1997, pp.157-161.

5. Georghiades, G.A., and Banerjee, J. R., "Flutter Prediction for Composite Wings Using Parametric Studies", *AIAA J.*, Vol. 35, No. 4, 1997, pp.746-748.

6. Georghiades, G.A., and Banerjee, J. R., "Significance of Wash-Out on the Flutter Characteristics of Composite Wings", *J Aircraft*, Vol. 35, No. 5, 1998, pp. 823-825.

7. Kuttenkeuler, J. and Ringertz, U., "Aeroelastic Design Optimization and Experimental Verification", *J Aircraft*, Vol. 35 No. 3, 1997, pp. 505-507.

8. Weishaar, T.A., and Foist, B.L., "Vibration Tailoring of Advanced Composite Lifting Surfaces", *J Aircraft*, Vol. 22, 1985, pp. 254-269.

9. Banerjee, J.R. and Williams, F.W., "Free Vibration of Composite Beams - an Exact Method Using Symbolic Computation", *AIAA J*, Vol.32, No. 3, 1995, pp. 636-642.

10. Banerjee, J.R., "Use and Capability of CALFUN - A Program for Calculation of Flutter Speed Using Normal Modes", *ASME International Conference on Modelling and Simulation*, Athens, Greece, 1984, Vol. 27-29, pp.121-131.

11. Theodorsen, T., "General Theory of Instability and Mechanisms of Flutter", *NACA Tech Report*, No. 496, 1934.

12. Vanderplaats Research & Development, *Dot User Manual Version 4.20*, 1995.

13. Lillico, M., Butler, R., Guo, S. and Banerjee, J.R., "Aeroelastic Optimisation of Composite Wings Using the Dynamic Stiffness Method", *Aeronautical Journal*, 101, No. 1002, 1997, pp. 77-86.

INFLUENCE OF AEROELASTIC TAILORING IN THE MULTIDISCIPLINARY DESIGN OF A NEW AIRCRAFT

Dr.-Ing. Roland Kelm
DaimlerChrysler Aerospace Airbus GmbH, Hamburg, Germany
email address: roland.kelm@airbus.dasa.de

Dipl.-Ing. Michael Dugas and Prof. Dipl.-Ing. Rudolf Voit-Nitschmann
BFE Universität Stuttgart, Stuttgart, Germany
email address: dugas@ifb-uni.stuttgart.de
email address: rvn@ifb-uni.stuttgart.de

Dipl.-Ing. Michael Grabietz
Ingenieurbüro Michael Grabietz, Schmallenberg, Germany
email address: michael.grabietz@img-online.de

Abstract. This paper discusses ways of determining the effects of aeroelastic tailoring in the predevelopment phase of wings. At DaimlerChrysler Aerospace Airbus, the program system FAME (Fast and Advanced Multidisciplinary Engineering) has been developed. The part FAME-W deals with the mass prognosis of wings. In order to achieve reliable data within a short period of time, it is imperative to take into account the elastic properties of the structure for the determination of the aerodynamic loads and for the preliminary dimensioning. Only by regarding these effects, the FAME-W program has been successful in providing reliable prognoses of wing mass and, of course, of the occurring loads and deformation. This report describes the extensions carried out so far which make it possible to investigate the effects and possibilities of composite wings, as well, using FAME-W.

1. Introduction

Large primary structural parts made from composite materials were first used in civil aircraft engineering in 1982 for the A300 of Airbus Industries. On this aircraft, the complete vertical tail box which had been manufactured from aluminium before was replaced by a corresponding component made from CFRP. Thereby, a saving of 20% in structural weight has been possible.

The main reason for the increasing use of composite materials during the subsequent years was the necessity of continuous performance improvement caused by the tough competitive situation. In 1987, the horizontal stabilizer box of the A320, and in 1994 the complete empennage of the B777 were next to be designed using CFRP.

As a consequence of the expanding use of modern composite materials, however, the development of metallic materials was consistently continued, as well. For example, the aluminium alloys 7055 and 2525 were first used on the B777. Due to the improved strength and damage tolerance properties, the weight could be reduced by comparison with the aluminium alloys used before, too.

Apart from the weight aspect, costs and certification issues play a decisive role in the selection of materials. The use of CFRP for other primary structural parts such as the wing box has not been implemented yet. Preparations for this, however, have been going on for years at Airbus and Boeing, for example. Figure 1 shows structural testing of a CFRP test wing carried out at DaimlerChrysler Aerospace Airbus in Hamburg.

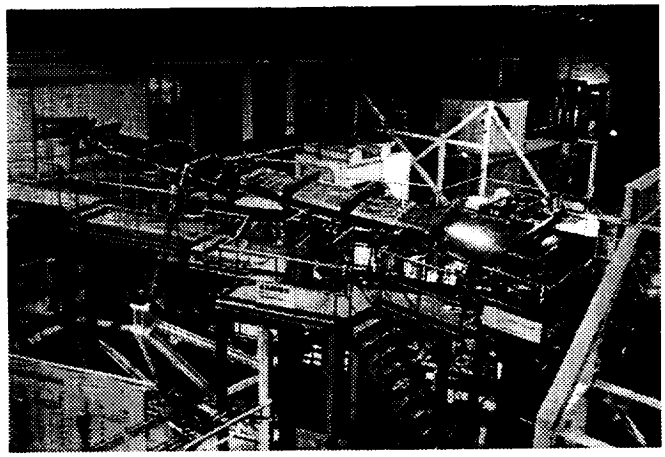

Figure 1. Testing of CFRP wing box

Besides good specific strength and low density CFRP offers the possibility to build up anisotropic laminates having properties which cannot be realized by the use of metallic materials. Thereby the aeroelastic

behaviour of wings can be altered deliberately, especially through the development of wing structures using composites.
The idea of using composite materials to influence the deformation behaviour of wings dates back to the year 1980. In those days the divergence problem of the forward-swept wing was discussed in papers written by e.g. Weishaar [12, 13], Piening [10] and Librescu [8]. It is considered to be one possibility to avoid divergence by varying the fiber orientations in the laminate in order to shift the elastic axis. By doing so, Weishaar and Librescu designed the wing structure in such a way as if the stiffnesses appear to be solely determined by the upper and lower shell of the wing, whereas Piening takes into account the webs, as well, in his box model.
Eastep et al. [2] shows the effects of damaged composite structures on the divergence speed. For this purpose, he employs a FE model to describe the structure. The examinations were expanded, e.g. by Lottati, to determine the influences of anisotropic laminates on flutter behaviour [9]. Shirk's publication [11] gives a comprehensive survey of the possibilities of aeroelastic tailoring.
The practical implementation of these results has been carried out mostly on military experimental aircraft (e.g. the X29 [7]). However, the aspect ratio of such wings is relatively small (approx. 2-4) compared with that of large commercial aircraft (7-10). Along with a growing aspect ratio, the aeroelastic deformation increases, and thus new possibilities are opening up for aeroelastic tailoring. The quantitative identification of this potential requires a complex multidisciplinary approach.

2. Task definition - Goals

With the coupling of bending and torsional deformation achieved by aeroelastic tailoring, two different directions are possible. Bending deformation that points upward (e.g. due to an increase of the load factor) can cause both a torsion deformation that is nose-up and one that is nose-down.
The advantage of a nose-down deformation lies in the reduction of the aerodynamic angle of attack, which in turn will cause a reduction of the bending moment and, thus, a reduction of the weight. With a nose-up deformation, on the other hand, it is possible to reduce changes of the wing lift distribution at a backswept wing which are occurring during cruise flight due to the continuously changing aircraft weight. This results in a reduction of fuel consumption due to an improved average lift to drag ratio. But, since the weight reduction achieved with the nose-down deformation, can also lead to less fuel consumption, a specific analysis is inevitable.
In order to make optimum use of the possibilities of aeroelastic tailoring, these aspects have to be assessed as early as in the predevelopment phase of a new aircraft. This is the only way of taking into account the resulting repercussions for defining the optimum aircraft configuration (aspect ratio, sweep, etc.).
At DaimlerChrysler Aerospace Airbus, the development of a new aircraft is subdivided into 14 milestones (figure 2). It begins with milestone M0 with a first three sided view and ends with M14, i.e. the entry into service. The earlier exact data for the new configuration can be determined in this chain of process, the more effectively the goal of an optimum development is achieved.

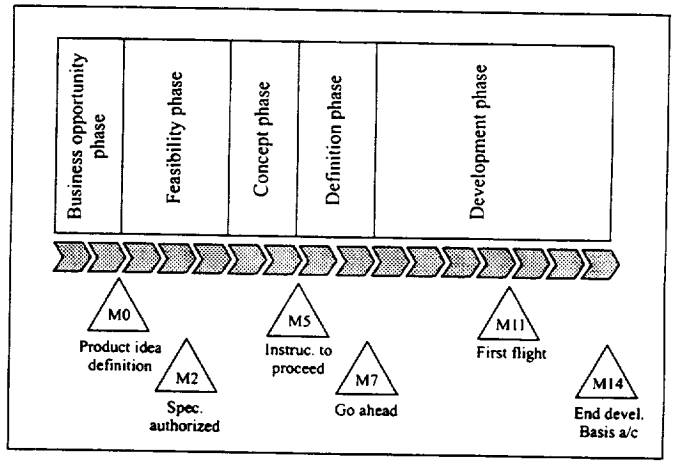

Figure 2. A/C development Phase (milestones)

In the predevelopment phase of a new aircraft, however, knowledge of numerous influences (dimensioning load cases, stiffness distribution, etc.) is still rather limited. Making it even more difficult, the number of free geometric parameters (wing area, thickness distribution, etc.) is very large. By coupling bending and torsional deformation, the dimensioning loads are effected. These, in turn, require an adaptation of the required cross sections from which, in turn, new stiffnesses and deformation will result.
The solution to this design problem can only be achieved iteratively and requires the integration of a multidisciplinary context within a suitable software

environment. The software has to meet the following requirements:

- full applicability in the predevelopment phase
- short computing time
- free modeling of the wing using parametric geometry
- consideration of any desired laminate structure
- automatic generation of a structural model
- integrated load and deformation calculation
- dimensioning of the primary wing structure
- determination of the stiffness and mass distributions
- calculation of aerodynamic coefficients of the elastic wing

At DaimlerChrysler Aerospace Airbus, the software system FAME (Fast and Advanced Multidisciplinary Engineering) [1, 3, 4, 5] was expanded by a calculation module to determine the possibilities offered by aeroelastic tailoring. In this paper, the theoretical context as well as the practical results will be introduced.

3. Theory

3.1. FAME-W FAST AND ADVANCED MULTIDISCIPLINARY ENGINEERING - WING

The program FAME-W used by DASA is a fast-working tool for the predevelopment of wings. The work presented here focuses on the extensions for the design of wings made of composite material. The deformation couplings can be achieved by symmetrically rotating the laminates in the upper and lower shell of the wing.

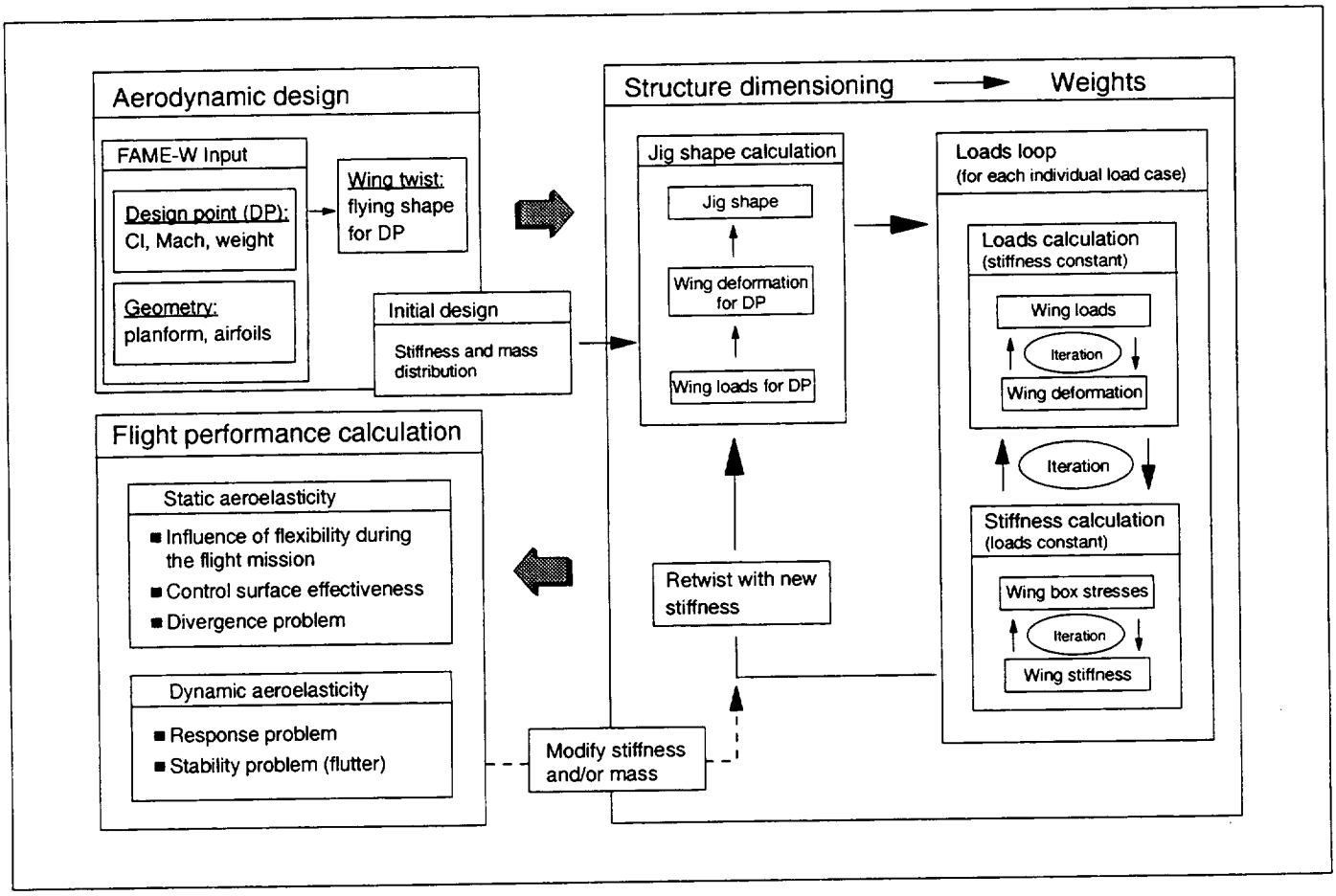

Figure 3. FAME-W Wing design process

FAME-W offers the possibility of being able to evaluate very different wing variations very fast and as early as in the predevelopment phase. By doing so, the program takes the elastic lift distribution into account for the determination of the loads. Wing deformations for different load cases and different types of deformation occurring during cruise flight can be determined.

The predesign process within the FAME-W program can be subdivided into three iteration loops. After determining a starting solution for the stiffness and mass distributions, the wing loads are calculated at constant stiffnesses on the basis of the lift distribution of the elastic wing. In the next loop, the loads remain constant, and the stiffnesses are newly calculated. In order to fulfill the aerodynamic design point, the jig shape must also be iterated (figure 3). For further information on the dimensioning process and the calculation procedure in FAME-W, please refer to the bibliography given hereafter [1, 3, 4, 5].

3.2. STRUCTURAL CALCULATION

3.2.1. *Deformation calculation*

The determination of the beam stiffnesses of the wing box is based on the equations of stress and strain of a plane laminate (CLT). For this purpose, only the smeared stiffnesses are calculated (figure 4).

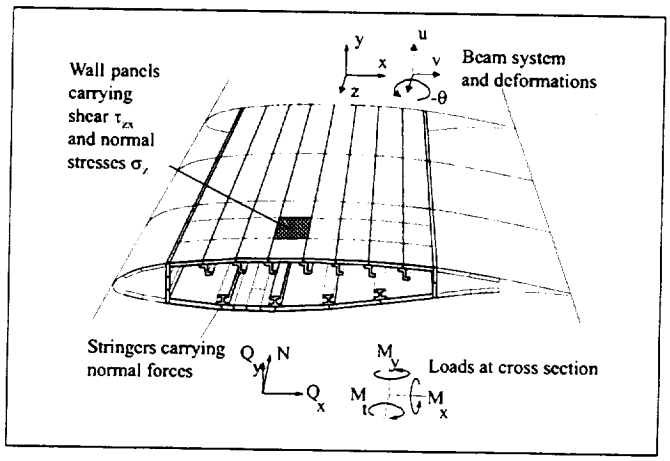

Figure 4. Wingbox model

The complete (plane) laminate matrices (A,B,D matrices) are not determined as information about the laminate stacking sequence is not available at the predevelopment stage. The general equation for the stress/strain ratio of the k^{th} individual layer of the general plane laminate is:

$$\begin{pmatrix} \sigma_{11} \\ \sigma_{22} \\ \tau_{12} \end{pmatrix}_k = \begin{pmatrix} Q_{11} & Q_{12} & Q_{16} \\ Q_{21} & Q_{22} & Q_{26} \\ Q_{61} & Q_{62} & Q_{66} \end{pmatrix}_k \begin{pmatrix} \epsilon_{11} \\ \epsilon_{22} \\ \gamma_{12} \end{pmatrix}_k \quad (1)$$

The smeared stiffness matrix $\bar{Q}$ of the laminate, together with the transformation matrix T, results from the following equation:

$$\bar{Q} = \sum_{k=1}^{N} T(\beta_k) \begin{pmatrix} Q_{11} & Q_{12} & Q_{16} \\ Q_{21} & Q_{22} & Q_{26} \\ Q_{61} & Q_{62} & Q_{66} \end{pmatrix}_k T(\beta_k)^T \frac{t_k}{t_{ges}} \quad (2)$$

If the transverse stress $\sigma_{xx} = 0$ (the stress perpendicular to the beam axis of the wing is small compared with the longitudinal stress) is neglected, the reduced stiffness matrix of the structure can be expressed as follows:

$$\bar{Q}_{red} = \begin{pmatrix} \bar{Q}_{11} - \frac{\bar{Q}_{16}^2}{\bar{Q}_{66}} & \bar{Q}_{16} - \frac{\bar{Q}_{16}\bar{Q}_{26}}{\bar{Q}_{22}} \\ \bar{Q}_{16} - \frac{\bar{Q}_{12}\bar{Q}_{26}}{\bar{Q}_{22}} & \bar{Q}_{66} - \frac{\bar{Q}_{26}^2}{\bar{Q}_{22}} \end{pmatrix} \quad (3)$$

After introducing the coupled stiffnesses EK_{xx} and EK_{yy} the deformation behaviour of a wing with deformation coupling can be described by the used beam modell as:

$$\begin{pmatrix} u'' \\ v'' \\ \theta' \end{pmatrix} = \begin{pmatrix} EI_{yy} & EI_{xy} & EK_{yy} \\ EI_{xy} & EI_{xx} & EK_{xx} \\ EK_{yy} & EK_{xx} & GJ_t \end{pmatrix}^{-1} \begin{pmatrix} M_x \\ -M_y \\ M_t \end{pmatrix} \quad (4)$$

3.2.2. *Effects of the different laminate variations*

In order to achieve the coupling of bending and torsion, the simplest possibility is to rotate the laminates in the upper and lower shell of the wing box symmetrically. By this, the couplings (coupling stiffnesses $\bar{Q}_{red16}$) can be achieved in different ways. So far, the following variations have been investigated (figure 5):

- rotation of the entire laminate
- rotation of the 0° layers
- rotation of the ±45° layers
- rotation of the stringers

Good results can be obtained here if the influence of the rotated stringers is taken into account by introducing the coupled stiffnesses. In contrast to the

rotated laminates, the transverse strain has to be assumed to be negligible ($\epsilon_{xx} = 0$) for the reduction of the stiffness matrix. The expression to calculate the reduced stiffness matrix of the stringers, according to Wiedemann [14] is as follows:

$$\bar{Q}_{red,Strg} = \begin{pmatrix} cos(\beta)^4 & cos(\beta)^3 sin(\beta) \\ cos(\beta)^3 sin(\beta) & cos(\beta)^2 sin(\beta)^2 \end{pmatrix} E_{Strg} \tag{5}$$

With β being the stringer rotation angle and E_{Strg} representing Young's modulus of the stringer laminate.

Of course, there are further possible ways of producing a coupling of bending and torsion (e.g. by unbalanced laminates). Here we will only discuss the variations named so far.

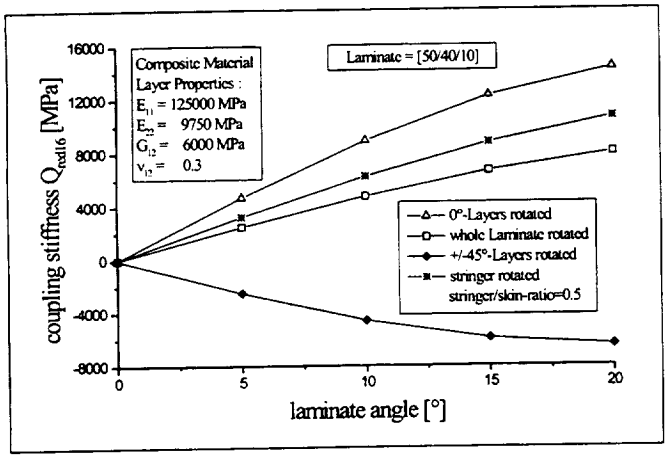

Figure 5. Comparison of the coupling stiffness

The effects of warping are neglected in the present FAME calculations. It is clear and well known through the work of Weisshaar [12, 13] and Librescu [8] that warping is influencing the wing deformations, espacially when working with coupled designs. And it is of course influencing the stress distribution in the wing box at the root of the wing (higher rear spar loading etc.). But the effect is reduced depending on the design of the wing fuselage joint. As usually done a design of the wing joint consists of a center wing box only carrying the wing bending moments. The wing root shear forces and torsion moments are transfered into the fuselage via a wing root rib. In this case the center wingbox provides additional elasticity to reduce warping effects.

To validate the FAME-W process the change of spanwise angle of attack of an Airbus A340-300 in cruise is calculated. The results of the FAME-W run show

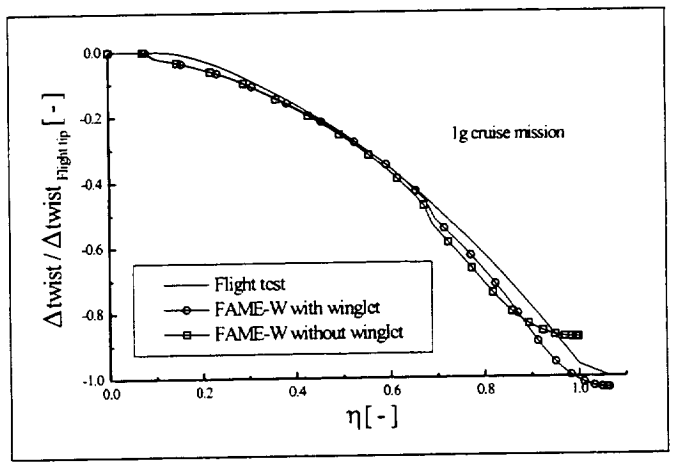

Figure 6. Comparison of flight test and calculation

good agreement in comparison with the flight test data (figure 6).

3.2.3. *Stress Calculation*

The analysis of the wing box stress distribution is based on the elemenary theory of bending, according to Navier and Bernoulli. The theory states that the cross sections have to stay plane after deformation. In the case of an uncoupled but orthotropic wingbox design the different moduli of elasticity have to be considered when calculating the wing box stiffnesses. The stresses in the wing box skin are found by

$$\sigma_z(x,y) = -\left[\frac{M_y[EI]_{xx} + M_x[EI]_{xy}}{[EI]_{xx}[EI]_{yy} - [EI]_{xy}^2}\right] E_z(x,y)\, x + \left[\frac{M_x[EI]_{yy} + M_y[EI]_{xy}}{[EI]_{xx}[EI]_{yy} - [EI]_{xy}^2}\right] E_z(x,y)\, y + N\frac{E_z(x,y)}{[EA]}$$

In case of a cross section with coupling stiffnesses the equation can be extended as follows:

$$\sigma_z(x,y) = -\left[A_x M_z + B_x M_x + C_x M_t\right] x\, \bar{Q}_{red11}\, F^{-1} + \left[A_y M_z + B_y M_x + C_y M_t\right] y\, \bar{Q}_{red11}\, F^{-1} + N\frac{\bar{Q}_{red11}}{EA} \tag{6}$$

with

$$A_x = EI_{xx}\, GJ_t - EK_{xx}{}^2$$
$$B_x = EI_{xy}\, GJ_t - EK_{xx}\, EK_{yy}$$
$$C_x = -EI_{xy}\, GJ_t + EK_{xx}\, EK_{yy}$$

$$A_y = -EI_{xy}\,GJ_t - EK_{xx}\,EK_{yy}$$
$$B_y = -EI_{yy}\,GJ_t - EK_{yy}{}^2 \qquad (7)$$
$$C_y = EI_{xx}\,GJ_t - EI_{xy}\,EK_{yy}$$

and

$$F = GJ_t(EI_{xx}\,EI_{yy} - EI_{xy}^2) - EK_{yy}^2\,EI_{xx}$$
$$+2\,EI_{xy}\,EK_{xx}\,EK_{yy} - EK_{xx}^2\,EI_{yy} \qquad (8)$$

The influence of the shear flow on the stress distribution (and vice versa) due to coupling stiffness is neglected in the current FAME version.

3.2.4. *Dimensioning of a CFRP-wing in the pre-design phase*

The dimensioning process for skins and stringers used by FAME-W to determine the thickness distribution of the wingbox consists of an equivalent stress criterion which takes into account the open hole residual stresses and the allowed maximum shear stresses. The maximum normal stress is taken from experimental investigations testing notched specimens [6]. The resulting allowable shear stress is found using the ZTL-criterion (σ_{xx} is assumed to be zero). This leads to:

$$\sigma_{e,skin} = \sqrt{\sigma^2 + \left[\frac{\sigma_{allow}}{\tau_{allow}}\right]^2 \tau^2} \qquad (9)$$

This represents a failure ellipse as shown in figure 7.

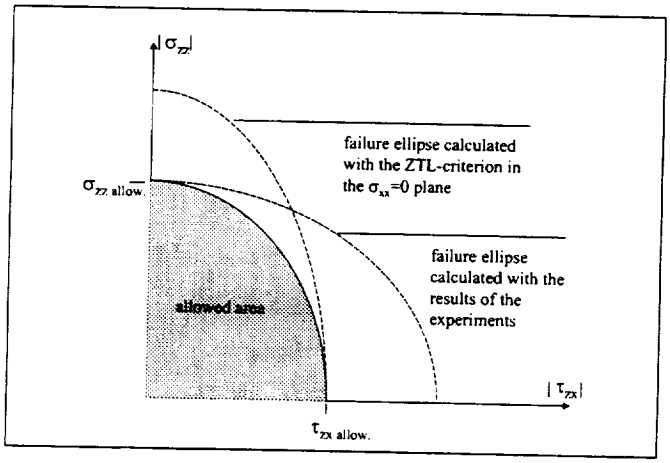

Figure 7. Failure criterion

The stringers of the wingbox are designed using a simple normal stress criterion.

4. Results

The substitution of a metallic structure by an orthotropic composite structure already offers a weight saving potential. The optimisation of a composite wing by consequent implementation of aeroelastic tailoring offers an additional improvement potential. Since the performance of an aircraft is influenced by weight and aerodynamic efficiency the results presented in this chapter include multidisciplinary interactions.

Two different solutions are possible by aeroelastic tailoring. The rotation of the laminate and/or stringers results in a nose up or a nose down twisting of the leading edge if the wing is bending. This can be used to create an 'aerodynamic rigid' wing with the shape of the lift distribution being nearly independent from the loads. Alternatively a design can be chosen with reduced loads. Since these are contrary effects which cannot be achieved simultaneously the best solution for a typical transport aircraft has to be found by consequent multidisciplinary analysis.

4.1. BASIC ASSUMPTIONS

The method described in the previous chapters was used for the assessment of the effects of aeroelastic tailoring for a typical midrange aircraft (figure 8). The goal of the performed calculations is the quantification of changes of the laminate orientation on the performance of the considered aircraft. The results cannot be transfered to each aircraft configuration since for example the influence of aerodynamic efficiency for a short range aircraft is reduced in relation

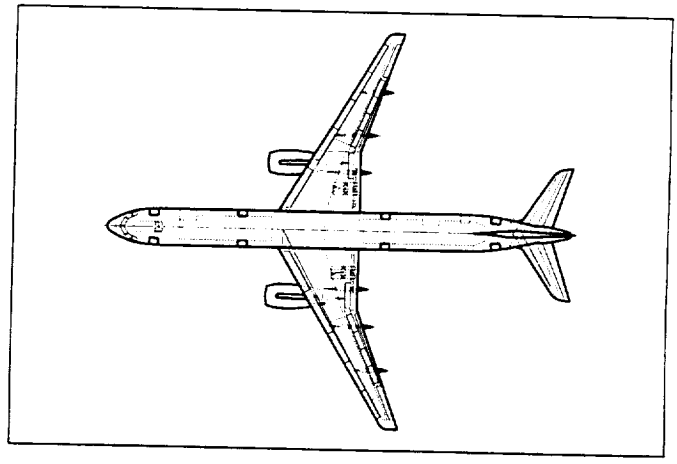

Figure 8. Midrange aircraft

to the influence of the weights. For the generic aircraft considered here the following design parameters were defined.

- MTOW 130 tons
- $\varphi_{c/4}$ sweep angle 26°
- wing area 200 m^2
- range 4400 NM
- wing aspect ratio 9
- Mach 0.80

Even small changes in aircraft weight or aerodynamics less than 1% accumulate to a large effect in fuel consumption since a typical transport aircraft remains in service for more than 25 years. For better identification of the potential of aeroelastic tailoring the results in the following chapters are presented with reference to a conventional aluminium wing.
A laminate lay-up typical for aircraft applications was used for the calculations. For the orthotropic case a laminate lay-up of [50/40/10] was selected which indicates that 50% of the fibres were oriented in beam axis direction, 40% in ±45° orientation and 10% perpendicular (90°) to the beam axis. For both, the wing box skins and the stringers the same laminate lay-up was chosen.
The rotation of the whole skin laminate showed a reduced effect on the coupling strength (section 3.2.2) compared with a rotation of the 0° fibres. Since it is the goal of this paper is to identify the principal potential of aeroelastic tailoring only the 0° skin fibres and for selected cases the stringer orientation were rotated.

4.2. Effects on deformations

Already the bending deformation of a swept wing results in a change of the local angle of attack. Changes in the stiffness distributions (e.g. caused by change of material or fibre orientation) therefore lead to an effect on the wing loads. For each change of the material composition in the following diagrams a complete dimensioning process for the wing primary structure was performed.
Figure 9 shows the bending deflection line if the orientation of the 0°-fibres is shifted to positive or negative angles. The increased deflections of the aluminium wing correspond to the smaller bending stiffness of the metallic structure. The nearly constant deflection lines for the composite designs indicate that the corresponding bending stiffnesses show only small sensitivity to the selected range of fibre orientations.

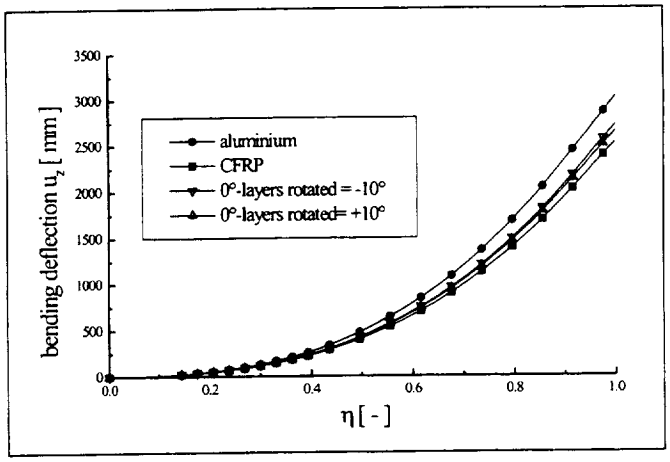

Figure 9. Bending deflection for 2.5g manoeuvre

The torsion deformation of the wing box (figure 10) shows a completely contrary behaviour. For the presented 2.5g manoeuvre load case increased torsion deformations in nose up or down direction depending on the fibre angle are calculated. This is a direct consequence of the bending/torsion coupling. Since the bending deformation of the wing is nearly unaffected by the fibre orientation the change of angle of attack in spanwise direction (figure 11) is dominated by the torsion effects. It can be seen that a rotation of the 0°-fibres to positive angles increases the change of angle of attack if the wing loading is increased. For a negative angle of −10° the change of angle of attack at the wing tip is nearly 0° compared to about −3° for the orthotropic composite wing or −5.3° for the metallic wing. These results demonstrate that with small angles already a significant influence on the elastic behaviour of a wing can be achieved.

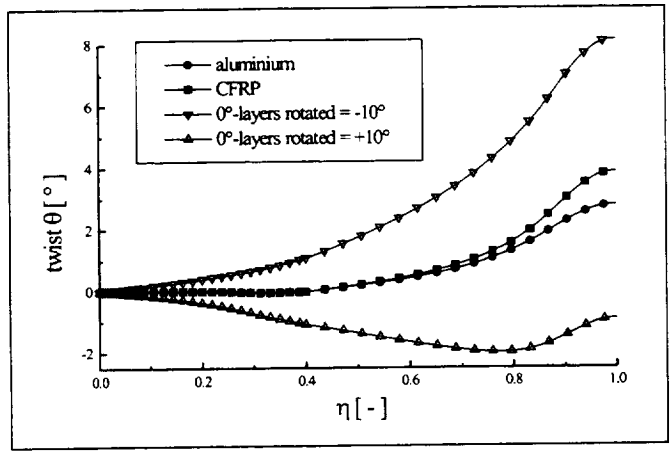

Figure 10. Torsion deflection for 2.5g manoeuvre

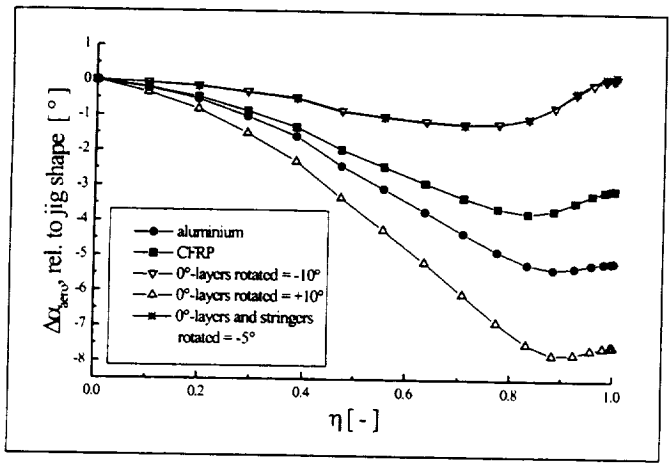

Figure 11. Change of angle of attack for 2.5g manoeuvre

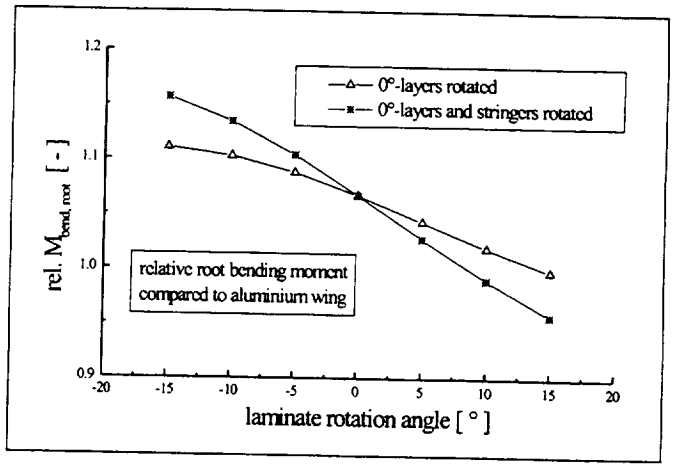

Figure 13. Change of bending moment due to laminate variation

4.3. Effects on weights

Based on the assumptions made here the substitution of the metallic wing primary structure by an orthotropic composite wing box results in a weight saving potential of about 20%. Figure 12 shows a

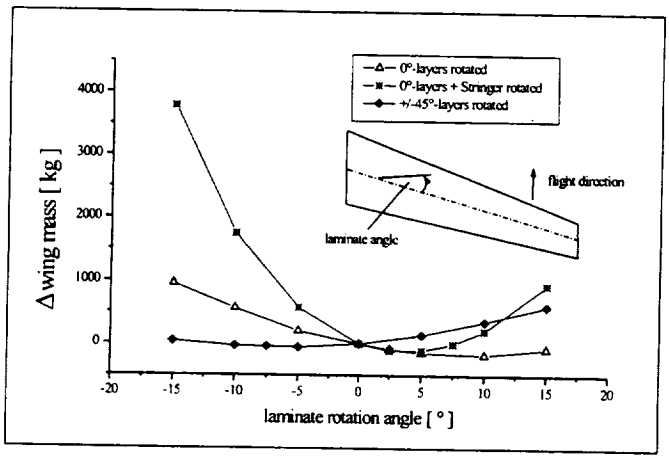

Figure 12. Change of weight due to laminate angle variation

strong effect of the fibre orientation (only 0° fibres were rotated) on the weight of the primary structure. A weight minimum can be identified for a fibre angle of 5°. The weight results show similar behaviour compared with calculations of Lerner [7].

A positive shift angle is corresponding with a nose down twist of the wing if it is bend upwards. A decrease of the aerodynamic load is the consequence. For higher angles the weight is increasing again although the bending moment distributions (figure 13) show the expected decrease. The clear relation between loads and weights for orthotropic wing structures failes for anisotropic designs. The dominating effect which leads to the weight increase for fibre angles higher respectively lower than 5° is the corresponding reduced bending stiffness of the wing box skins. Consequently the stresses in the stringers (which were not rotated for this calculation) are growing. This has to be compensated by an increase of the required skin thickness and stringer cross section.

Bending/torsion coupling can also be achieved by rotation of the ±45° layers. According to figure 5 a negative degree of coupling is following. Therefore the laminate angle for minimum weight is now shifted to a negative value of about −7°. Figure 12 additionally includes the result for a rotation of the stringers parallel to and simultaneously with the 0° fibre angle. The aeroelastic degree of coupling is inreased. Therefore the weight plot is compressed since now the same weight effect compared to the calculation with constant stringer orientation of 0° is shifted to smaller angles.

In the weight calculation the effect of a manoeuvre or gust load control system (e.g. by aileron deflections) was not included. If these systems should be included in the aircraft design additional investigations will have to be performed. It can be stated that an 'aerodynamic rigid' wing has an improved control surface effectiveness. This can now result in an advantageous combination of weight saving potential and aerodynamic drag reduction (see next section) by intelligent aeroelastic tailoring.

4.4. Effects on aerodynamics

For the assessment of the aerodynamics of the 1g cruise as well as the 2.5g manoeuvre load cases have

to be considered. The resulting 2.5g lift coefficient distributions for the investigated laminate angles show ΔC_l values of more than 10% at outer wing stations (figure 14). Consequently the stall behaviour

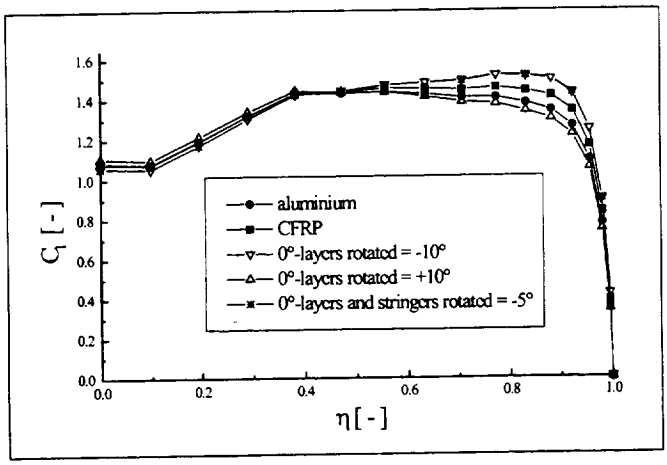

Figure 14. Lift coefficient distribution for 2.5g manoeuvre

of the wing is affected. The disadvantage of the increased outer wing stall probability is counteracted by the advantage of improved aileron efficiency and the improved flutter behaviour for the 'aerodynamic rigid' wing (negative laminate angles).
Results of the analysis of a 1g cruise mission are presented in figure 15. The ΔC_l distributions represent

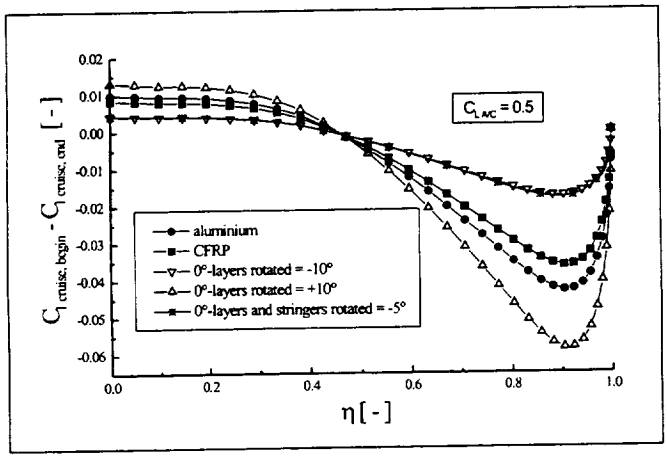

Figure 15. Lift coefficient variation during 1g cruise mission

the change of the local lift coefficient between the beginning and the end of the cruise mission. It is assumed that the C_l of the aircraft is constant during this mission. As already found for the 2.5g load case (figure 11) the nearly constant lift coefficient distribution for different wing loadings is a result of the corresponding stable angle of attack distribution.

If the shape of the lift distribution can be decoupled from the wing loading the airfoils can be optimised to a higher degree. Therefore aeroelastic tailoring offers clear advantages with respect to the aerodynamic drag. The induced drag of the aircraft which is a direct result of the shape of the lift distribution can be kept close to its minimum during a cruise mission. Changes of the lift distribution during a mission result in an effect on the pitching moment of the aircraft. This is presented in figure 16 where the pitching moment coefficient at zero lift C_{M0} is plotted. The

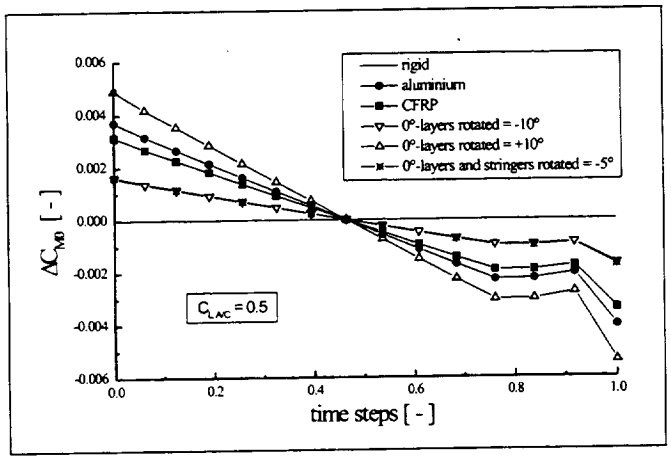

Figure 16. Zero moment coefficient during 1g cruise mission

disturbances of C_{M0} at the end of the mission are a result of the tank boundary definition, the defueling sequence and the following effect on deformations. The behaviour of C_{M0} has a strong effect on the trim forces and trim drag. Consequently from the aerodynamic point of view the 'aerodynamic rigid' wing offers significant advantages with respect to drag. Additionally the wave drag which for an aircraft in transonic flow regime strongly depends on the aerodynamic loading (local C_l) can remain constant at a low level.
Finally the buffet onset behaviour which is included in the certification requirements of transport aircraft is improved. The ΔC_l reserve of the 'aerodynamic rigid' wing for buffet onset is increased since it is not reduced by a local C_l increase during a cruise mission. Generally it can be concluded that aeroelastic tailoring can be equated with a 'passive system' which will have reduced certification problems compared with an 'active system' since system failure cases are minimized.

4.5. Effects on performance

For the assessment of the effects of aeroelastic tailoring on the performance of an aircraft a typical cruise mission has to be analysed. The effects of weight and drag e.g. on the fuel consumption have to be investigated. To quantify these effects a typical 4000 NM mission was chosen and the required sensitivities for the fuel consumption were evaluated. For the parameters chosen here a 1% total aircraft drag change can be set equal to a primary structure weight change of about 1000 kg at a constant fuel consumption rate. For the design point which is set to the middle of the mission minimum induced drag is achieved.

The drag changes during the mission strongly depend on the laminate lay-up. The average increase of drag relative to the design point is minimized for the 'aerodynamic rigid' wing ($-5°$ laminate angle, $0°$-layers and stringers rotated). The orthotropic wing ($0°$ laminate angle) has a 600 kg lower wing weight. If the drag increase for this wing is higher than 0.6% of the total aircraft drag a performance disadvantage is the consequence.

The airfoils of the orthotropic wing need more ΔC_l flexibility. Therefore geometric changes for a tailored wing (e.g. increased thickness) seem possible. It is recommended to include the effects of aeroelastic tailoring as soon as in the pre-design phase of a new aircraft when geometric changes of the wing design can be introduced easily.

5. Conclusions

A method was introduced to include the main effects of aeroelastic tailoring in the preliminary design phase of a new aircraft. The calculation procedure includes the repercussions on weight and aerodynamics. For a typical midrange transport aircraft it could be shown that by relative small changes of the laminate orientation an 'aerodynamic rigid' wing with a nearly constant lift distribution during a flight mission is achievable.

The most practical solution for a high degree of bending/twist coupling is the simultaneous rotation of $0°$-layers of the laminate and the stringers. The dimensioning process has to include the effects on loads as well as the impact on the stiffnesses if the laminate is rotated. A symmetrical bending stiffness reduction with a positive or negative laminate rotation is found.

Aeroelastic tailoring can be used either to minimise wing weight or to improve aerodynamics and control surface effectiveness. The effects on weights and aerodynamics have to be carefully evaluated to identify the best solution for optimum aircraft performance. The large impact of aeroelastic tailoring even for small laminate rotation angles shows the potential to influence specific properties of wings of transport aircraft.

References

1. Dugas M., Voit-Nitschmann R., Kelm R., Grabietz M.: Möglichkeiten zur Beeinflussung des Verformungsverhaltens von Tragflügeln am Beispiel einfacher Kastenträger, *Tagungsband, DGLR-Jahrestagung, Bremen, 5.-6.10.1998*
2. Eastep F. E., Venkayya V. B., Tishler V. A.: Divergence Speed Degradation of Forward-Swept Wings with Damaged Composite Skin, *J. Aircraft, Vol. 21, Nov. 1984*
3. Kelm R., Läpple M., Grabietz M. Wing primary structure weight estimation of transport aircrafts in the pre-development phase, SAWE paper No. 2283, *54th Annual Conference of Society of Allied Weight Engineers, Huntsville 1995*
4. Kelm R., Läpple M., Grabietz M.: Berechnungsverfahren zur Gewichtsprognose der Tragflügel-Primärstruktur von Transportflugzeugen im Vorprojekt, *Tagungsband, DGLR-Jahrestagung, Bonn, 26.-29.9.1995*
5. Kelm R., Grabietz M.: Multidisciplinary Aspects of Aeroelasticity in the Pre-design Phase for a new Aircraft, *CEAS International Forum on Aeroelasticity and Structural Dynamics, 17-20 June 1997, Rome, Italy*
6. Kröber I.: Zulässige Werte bei Druckbeanspruchung für verschiedene CFK-Laminate mit offener Bohrung und Impacts für Ciba 6376/HTA, *Technische Niederschrift TN-TK537-B/9504, DaimlerChrysler Aerospace Airbus*
7. Lerner E.: The Application of Practical Optimization Techniques in the Preliminary Structural Design of a Forward-Swept Wing, *Second International Symposium on Aerolelasticity and Structural Dynamics, Aachen, Germany, April 1-3 ,1985*
8. Librescu L., Thangjitham S.: Static Aeroelastic Behaviour of Swept Forward Composite Wing Structures Taking Into Account Their Warping Restraint Effect, *European Forum on Aeroelasticity and Structural Dynamics, 1989*
9. Lottati I.: Flutter and Divergence Aeroelastic Charakteristics for Composite Forward Swept Cantilevered Wing, *J. Aircraft, Vol. 22, Nov. 1985*
10. Piening M.: Die statische Aeroelastizität des anisotropen Tragflügels, *DGLR Bericht 84-02*
11. Shirk M. H., Hertz T. J., Weisshaar T. A.: Aeroelastic Tailoring -Theory, Practice, and Promise, *J. Aircraft, Vol. 23, Jan. 1986*
12. Weisshaar T. A.: Divergence of Forward Swept Composite Wings, J. Aircraft, *Vol. 17, June 1980*
13. Weisshaar T. A.: Aeroelastic Tailoring of Forward Swept Composite Wings, *J. Aircraft, Vol. 18, Aug. 1981*
14. Wiedemann J.: Leichtbau, Band I: Elemente, *Springer-Verlag, 1986*

SYNERGISTIC INTERACTION OF AEROELASTIC TAILORING AND BOUNDARY MOMENT CONTROL ON AIRCRAFT WING FLUTTER

Frank H. Gern+ and Liviu Librescu*
Virginia Polytechnic Institute and State University
Blacksburg, VA 24061-0203, USA

SUMMARY

The implications of active feedback control and aeroelastic tailoring on the flutter instability of straight/swept aircraft wings carrying external stores are discussed. The stabilizing feedback control is generated by a bending moment acting at the wing tip. Relating this bending moment with adequately selected kinematic response quantities, a complex eigenvalue problem is obtained. Its solution yields the closed-loop flutter speed and frequency of flutter.

The beneficial interaction of active feedback control in conjunction with aeroelastic tailoring upon the flutter boundary of aircraft wings made-up from advanced composite materials is emphasized. In addition, the prospects of an extension of the operational envelope of flight vehicles carrying external stores without weight penalties are revealed.

INTRODUCTION

In recent years, a great deal of work and important achievements in the design and analysis of feedback control stabilizers applied to mechanical systems prone to instability have been reached. The great progress in this field is due to the development of new methods and feedback control mechanisms. Among others, treatments of this problem based upon stabilizing feedback mechanisms consisting of forces and moments acting along a part of the boundary of the structure have been developed in a number of recent monographs (see e.g. Refs. 1 and 2). Such concepts can also be applied towards the structural control of new generations of aircraft/spacecraft vehicles. In spite of their increasing maneuvevability new generations of supermaneuverable airplanes have to be designed as to operate safely for all combinations of velocity and load factors compatible with their flight envelope. However, under special conditions, dramatic degradations of the flutter and dynamic response characteristics can occur with catastrophic repercussions upon flight safety.

This is specially the case for advanced aircraft carrying external stores. For such an aircraft, the classical means of flutter prevention, such as stiffness increase or mass balance are very expensive and penalize aircraft performance. The standard method of preventing the occurrence of flutter in the case of aircraft carrying external stores, namely that of limiting the flight speed, can be disastrous in special flight missions (i.e. during a ground

+ Research Associate, Department of Aerospace and Ocean Engineering
* Professor, Department of Engineering Science and Mechanics

attack), when the vulnerability of the aircraft dramatically increases.

As a result, an essential issue which must be addressed, even in the early design stages of advanced fighter-aircraft is the incorporation of appropriate techniques enabling one to control aeroelastic instabilities of such vehicles. The implementation of pertinent control techniques must result in the delay of the occurrence of aeroelastic instabilities and enhancement, without weight penalty, of their static and dynamic response behavior.

One of the possibilities consists of the further integration of advanced composite materials into the airframe. The directionality property featured by anisotropic composite materials provides, through the proper selection of the ply-angle scheme, the desired elastic couplings playing a positive role in this regard (see e.g. Ref. 3). At this point it should be noticed that the technique refered to as *aeroelastic tailoring* is passive in its nature in the sense that once implemented, the structure cannot respond to the variety of environmental factors, or to uncertainties in the structural parameters. As a result, the present authors fully agree with the opinion expressed in Ref. 4, according to which, "the increased use of composite materials will not solve all these wing store flutter problems."

A complementary option consists of the implementation of advanced feedback mechanisms. In a structure featuring such control capabilities, the deflection, bending moments at the wing root cross-section, natural frequencies, damping, mode shapes can be tuned as to enhance the vibrational behavior, avoid structural resonance and enhance aeroelastic response characteristics (see Refs. 5 through 11).

The basic goal of this paper is to implement a combined control methodology based on both, aeroelastic tailoring and feedback control, enabling one to enhance the flutter behavior of swept/straight aircraft wings carrying external stores. A solid plate-beam model incorporating a number of non-classical effects such as transverse shear, warping inhibition, anisotropy of the constituent materials and, arbitrarily located external stores along the wing span and chord is used to simulate the wing structure (see Refs. 12 and 13). The study is confined to the case of the flutter of straight/swept wings of high to moderate aspect ratios in an incompressible flow.

The active feedback control mechanism used in this paper is based on a bending moment applied at the wing tip which is coupled, via a prescribed functional relationship, with the mechanical quantities characterizing the response of the wing. The bending moment can be generated in various ways. One of the possibilities is based on the converse piezoelectric effect; consisting of the generation of localized strains (and implicitly of forces) in response to an applied voltage (see e.g. Refs. 5 through 11 and 14).

For such a case, considering the piezoactuators spread along the entire wing span and bonded to its top and bottom faces, bending control moments are induced at the wing tip via out-of-phase activation.

In the present paper, a comprehensive feedback control law is used, including as special cases acceleration, velocity and displacement feedback control.

As a by-product of this implementation, in the absence of unsteady aerodynamic loads, the closed-loop eigenfrequencies and induced damping for the considered wing structure, can be obtained.

In order to solve the complex closed-loop eigenvalue problem, a mathematical methodology based upon the Extended Galerkin Method was used.

It should be mentioned that earlier investigations on flutter feedback control based on piezoelectric strain actuation, have been carried out in Refs. 15 through 19, while in

Ref. 20, a survey-paper on the accomplishments in this area is provided. However, to the best of authors' knowledge, no analysis involving a comprehensive structural wing model incorporating anisotropy, transverse shear, warping inhibition and arbitrarily distributed external stores as well as such an encompassing feedback control methodology as the one considered in this paper, can be found in the specialized literature.

STRUCTURAL MODELING

The geometric details and notations related to wing and external store configuration considered in the present study are illustrated in Fig. 1. The case of straight/swept untapered wings is considered in this study.

The wing structure is idealized as a laminated composite plate beam whose constituent laminae are characterized by different orthotropicity angles and different material and thickness properties. Let N be the total number of constituent layers. The interface plane between the contiguous layers r and $r+1$ (where $1 \leq r < N$) is selected as the reference plane of the composite structure. The points of the reference plane (defined by $x_3 = 0$) are referred to a Cartesian system of in-plane coordinates (x_1, x_2), the upward x_3-coordinate being considered perpendicular to the (x_1, x_2) plane. The x_1 and x_2 coordinates are referred to as the chordwise and spanwise coordinates, respectively. Axis x_2 (referred here-after to as the reference axis) is selected to coincide with the midchord line.

The sweep angle (considered positive swept back and negative swept forward) is measured in the plane of the wing from the direction normal to the airstream to the reference axis. All geometrical and aerodynamical section parameters are based on sections normal to the reference axis.

The relevant equations of motion as well as the appropriate boundary conditions are obtained via Hamilton's Variational Principle and application of generalized function theory in order to exactly consider the spanwise location and properties of the attached stores. The energy functional of a composite wing carrying external stores, regarded as a 3-D elastic system, is expressed as

$$J = \int_{t_0}^{t_1} (\mathcal{U}_W - \mathcal{K}_W + \mathcal{A}_W - \mathcal{K}_S + \mathcal{A}_S) dt \tag{1}$$

In Eq. (1) $\mathcal{U}$ denotes the strain energy $\mathcal{K}$ represents the kinetic energy, and $\mathcal{A}$ the potential energy of body and surface forces, while t_0 and t_1 are two instants of time. The subscripts W and S affecting the various quantities appearing in Eq. (1) identify their affiliation to the wing and externally mounted stores, respectively.

From the stationary condition $\delta J = 0$, rendering explicitly $\mathcal{U}$, $\mathcal{K}$ and $\mathcal{A}$ and adopting the Einstein summation convention, one obtains

$$\delta J = 0 = \int_{t_0}^{t_1} dt \underbrace{\left\{ \left[- \int_{\tau} \sigma_{ij}\, \delta U_{i,j}\, d\tau + \int_{\tau} \rho(H_i - \ddot{U}_i) \delta U_i d\tau + \int_{\Omega_\sigma} \sigma_i\, \delta U_i d\Omega \right] \right.}_{\text{wing}}$$

$$\underbrace{+\sum_s \int_0^l \delta_D(x_2 - x_2^{(s)}) \Big[- \int_\tau \rho^{(s)} \ddot{U}_i^{(s)} \delta U_i^{(s)} d\tau + \mathcal{L}^{(s)} \delta h^{(s)} - \mathcal{M}^{(s)} \delta\theta^{(s)} + m^{(s)} \delta U_3^{(s)} \Big] dx_2 \Big\}}_{\text{external stores}} \quad (2)$$

In Eq. (2), δ denotes the variation operator; δ_D represents Dirac's distribution, the superposed dots denote time derivatives; the terms underscored by a tilde represent prescribed quantities; superscript (s) identifies the affiliation of the respective quantity to the s-th store; $\mathcal{L}$ and $\mathcal{M}$ denote the sectional lift (positive upward) and sectional aerodynamic torque, (positive nose up), respectively, about wing elastic axis; U_i denote the components of the 3-D displacement vector; h and θ are the plunging (positive upward), and elastic twist angle (positive nose up), respectively; σ_{ij} and σ are the stress tensor and stress vector, respectively; ρ is the mass density; τ and Ω denote the volume and external surface of the body, respectively, while H_i denote the components of the body force vector.

As shown in Ref. 21, the 3-D displacement components are represented as:

$$\begin{aligned} U_1 &= x_3\theta(x_2;t), \\ U_2 &= u_2(x_2;t) + x_3[f_2(x_2;t) + x_1 g_2(x_2;t)], \\ U_3 &= h(x_2;t) - (x_1 - x_0)\theta(x_2;t), \end{aligned} \quad (3a-c)$$

where $x_0 = x_0(x_2)$ defines the position of the elastic axis and $f_2(x_2;t), g_2(x_2;t)$ and $u_2(x_2;t)$ are generalized 1-D displacement components.

For $f_2 = -h_{,2} - (x_0\theta)_{,2}$ and $g_2 = \theta_{,2}$, it results that $\gamma_{13} = \gamma_{23} = 0$, which is consistent with the traditional assumption of the infinite stiffness of the wing structure in transverse shear (Kirchhoff's Theory).

In the case of a straight wing, the pitching angle $\theta^{(s)}$ of the stores coincides with that of the wing, angle θ. Having in view the case of wings featuring the sweep angle Λ, in order to express the stores' main inertia properties which are in chordwise direction, the 3-D displacement quantities of the stores have to be referred to the wing coordinate system. This transformation yields

$$\begin{aligned} U_1^{(s)} &= x_3\theta \cos\Lambda - u_2 \sin\Lambda - x_3(f_2 + x_1 g_2) \sin\Lambda \\ U_2^{(s)} &= x_3\theta \sin\Lambda + u_2 \cos\Lambda + x_3(f_2 + x_1 g_2) \cos\Lambda \\ U_3^{(s)} &= h(x_1 - x_0)[\theta \cos\Lambda - f_2 \sin\Lambda - x_1 g_2 \sin\Lambda] \end{aligned} \quad (4a-c)$$

Replacement of displacement components as given by Eqs. (3) and (4) in (2) and performing the indicated mathematical operations, results, in the case of a composite aircraft wing

carrying external stores, in the following expression (see Refs. 12 and 13):

$$\delta J=0=\int_{t_0}^{t_1} dt \Bigg\{ \underbrace{\int_0^l [A_1\delta u_2+A_2\delta f_2+A_3\delta g_2+(A_4-\mathcal{M})\delta\theta+(A_5+\mathcal{L})\delta h]dx_2+A_6}_{\text{energy functional of the clean composite wing}}$$

$$-\sum_s m^{(s)}\delta_D(x_2-x_2^{(s)})[\ddot{u}_2+x_3\ddot{f}_2+x_1x_3\ddot{g}_2)\delta u_2$$

$$+(x_3\ddot{u}_2+(x_3^2+K_p^{2(s)}\ sin^2\ \Lambda)\ddot{f}_2+(x_1x_3^2+x_1K_p^{2(s)}\ddot{\theta}\ sin\ \Lambda\ cos\ \Lambda-E_p^{(s)}\ddot{h}\ sin\ \Lambda)\delta f_2$$

$$+x_1(x_3\ddot{u}_2+(x_3^2+(K_p^{2(s)}\ sin\ \Lambda)\ddot{f}_2+x_1x_3^2+x_1K_p^{2(s)}\ sin\ \Lambda)\ddot{g}_2$$

$$-K_p^{2(s)}\ddot{\theta}\ sin\ \Lambda\ cos\ \Lambda-E_p^{(s)}\ddot{h}\ sin\ \Lambda)\delta g_2$$

$$+(-K_p^{2(s)}\ddot{f}_2\ sin\ \Lambda\ cos\ \Lambda-x_1K_p^{2(s)}\ddot{g}_2\ sin\ \Lambda\ cos\ \Lambda+(x_3^2+K_p^{2(s)}\cos^2\ \Lambda)\ddot{\theta}$$

$$\underbrace{+E_p^{(s)}\ddot{h}\ cos^2\ \Lambda)\delta\theta+(-E_p^{(s)}\ddot{f}_2\ sin\ \Lambda-x_1E_p^{(s)}\ddot{g}_2\ sin\ \Lambda+E_p^{(s)}\ddot{\theta}\ cos\ \Lambda+\ddot{h})\delta h]}_{\text{kinetic energy of external stores}}$$

$$\underbrace{+\sum_s \delta_D(x_2-x_2^{(s)})[\mathcal{M}^{(s)}\ sin\ \Lambda\delta f_2+x_1\mathcal{M}^{(s)}\ sin\ \Lambda\delta g_2-\mathcal{M}^{(s)}\ cos\ \Lambda\delta\theta+\mathcal{L}^{(s)}\delta h]}_{\text{aerodynamic forces acting on external stores}}$$

$$\underbrace{+\sum_s m^{(s)}g\delta_D(x_2-x_2^{(s)})[E_p^{(s)}\ sin\ \Lambda\delta f_2+x_1E_p^{(s)}\ sin\ \Lambda\delta g_2-E_p^{(s)}\ cos\ \Lambda\delta\theta+\delta h]\Bigg\}}_{\text{potential energy of external stores}} \tag{5}$$

Herein, $E_p^{(s)}$ denotes the offset between the center of gravity of the store and the wing elastic axis, $K_p^{(s)}$ denotes the pitching radius of gyration of the store about its center of gravity, while g denotes the gravitational acceleration.

Collecting the terms associated with the respective variations δu_2, δf_2, δg_2, $\delta\theta$, and δh, and having in view that these variations have to be arbitrary and independent, from the stationary condition $\delta J = 0$ which concerns each instant belonging to the interval $[t_0,\ t_1]$, the equations of motion and boundary conditions are obtained.

The equations of motion are:

$$\delta u_2 : A_1+\sum_s \delta_D(x_2-x_2^{(s)})[-m^{(s)})(\ddot{u}_2+x_3\ddot{f}_2+x_1x_3\ddot{g}_2)]=0$$

$$\delta f_2 : A_2+\sum_s \delta_D(x_2-x_2^{(s)})\Big[-m^{(s)}(x_3\ddot{u}_2+(x_3^2+K_p^{2(s)}\ sin^2\ \Lambda)\ddot{f}_2+(x_1x_3^2+x_1K_p^{2(s)}\ sin\ \Lambda)\ddot{g}_2$$

$$-K_p^{2(s)}\ddot{\theta}\ sin\ \Lambda\ cos\ \Lambda-E_p^{(s)}\ddot{h}\ sin\ \Lambda)\mathcal{M}^{(s)}\sin\Lambda+\underline{m^{(s)}gE_p^{(0)}\ sin\ \Lambda}\Big]=0$$

$$\delta g_2 : A_3+\sum_s \delta_D(x_2-x_2^{(s)})x_1[-m^{(s)}(x_3\ddot{u}_2+(x_3^2+K_p^{2(s)}\ sin^2\ \Lambda)\ddot{f}_2+(x_1x_3^2+x_1K_p^{2(s)}\ sin\ \Lambda)\ddot{g}_2$$

$$-K_p^{2(s)}\ddot{\theta}\ sin\ \Lambda\ cos\ \Lambda-E_p^{(s)}\ddot{h}\ sin\ \Lambda)+\mathcal{M}^{(s)}\ sin\ \Lambda+\underline{m^{(s)}gE_p^{(s)}\ sin\ \Lambda}\Big]=0$$

$$\delta\theta : A_4 + \sum_s \delta_D(x_2 - x_2^{(s)})\Big[- m^{(s)}(-K_p^{2(s)}\ddot{f}_2 \; sin\,\Lambda \; cos\,\Lambda - x_1 K_p^{2(s)}\ddot{g}_2 \; sin\,\Lambda \; cos\,\Lambda$$

$$+ (x_3^2 + K_p^{2(s)} \; cos^2\,\Lambda)\ddot{\theta} + E_p^{(s)}\ddot{h} \; cos^2\,\Lambda) - \mathcal{M}^{(s)} \; cos\,\Lambda - \underline{m^{(s)} g E_p^{(s)}} \; cos\,\Lambda\Big] = 0$$

$$\delta h : A_5 + \sum_s \delta_D(x_2 - x_2^{(s)})\Big[- m^{(s)}(-E_p^{(s)}\ddot{f}_2 \; sin\,\Lambda - x_1 E_p(s)\ddot{g}_2 \; sin\Lambda + E_p^{(s)}\ddot{\theta} \; cos\,\Lambda + \ddot{h})$$

$$+ \mathcal{L}^{(s)} + \underline{m^{(s)} g}\Big] = 0 \qquad (6a - e)$$

Herein the coefficients A_1 through A_5 are recorded in Ref. 21 and consequently, will not be displayed here. In their expressions the 1-D generalized stress couples and generalized body forces and mass terms measured per unit wing span appear explicitly and are given by:

$$T_{ij}^{(m,n)}(x_2) = \int_A \sigma_{ij} \; x_1^m \; x_3^n \; dA; \quad \left\{ \begin{matrix} F_i^{(m,n)}(x_2) \\ I^{(m,n)}(x_2) \end{matrix} \right\} = \int_A \gamma \left\{ \begin{matrix} \mathcal{H}_i \\ 1 \end{matrix} \right\} x_1^m \; x_3^n \; dA \qquad (7a - b)$$

where A denotes the wing cross-section area.

In addition to the equations of motion, the geometrical and statical boundary conditions at the wing root and tip are obtained. For a cantilevered wing, the boundary conditions at the root ($x_2 = 0$) are purely geometrical, expressed as:

$$u_2 = \underset{\sim}{u}_2, \; f_2 = \underset{\sim}{f}_2, \; g_2 = \underset{\sim}{g}_2, \; \theta = \underset{\sim}{\theta}, \; h = \underset{\sim}{h} \qquad (8a - e)$$

In the case of the wing without tip store, the boundary conditions at the wing tip ($x_2 = l$) are purely statical:

$$\begin{aligned} &\delta u_2 : T_{22}^{(0,0)} = \underset{\sim}{T}_{22}^{(0,0)} \\ &\delta f_2 : T_{22}^{(0,1)} = \underset{\sim}{T}_{22}^{(0,1)} \\ &\delta g_2 : T_{22}^{(1,1)} = \underset{\sim}{T}_{22}^{(1,1)} \\ &\delta\theta : T_{12}^{(0,1)} - T_{23}^{(1,0)} = \underset{\sim}{T}_{12}^{(0,1)} - \underset{\sim}{T}_{23}^{(1,0)} \\ &\delta h : T_{23}^{(0,0)} = \underset{\sim}{T}_{23}^{(0,0)} \end{aligned} \qquad (9a - e)$$

When considering a wing tip store, the boundary conditions at $x_2 = l$ change to kinetic ones, taking into account inertia properties and the aerodynamics of the tip store:

$$\delta u_2 : T_{22}^{(0,0)} = -m^{(T)}(\ddot{u}_2 + x_3\ddot{f}_2 + x_1 \; x_3 \; \ddot{g}_2)$$

$$\delta f_2 : T_{22}^{(0,1)} = -m^{(T)}\Big[x_3\ddot{u}_2 + \Big(x_3^2 + K_p^{2(T)} \; sin^2\Lambda\Big)\ddot{f}_2 + \Big(x_1 x_3^2 + x_1 K_p^{2(T)} \; sin\,\Lambda\Big)\ddot{g}_2$$

$$- K_p^{2(T)}\ddot{\theta} \; sin\,\Lambda \; cos\,\Lambda - E_p^{(T)}\ddot{h} \; sin\,\Lambda\Big] + \mathcal{M}^{(T)} \; sin\,\Lambda + \underline{m^{(T)} g E_p^{(T)}} \; sin\,\Lambda$$

$$\delta g_2 : T_{22}^{(1,1)} = x_1\Big[- m^{(T)}\Big(x_3\ddot{u}_2 + \Big(x_3^2 + K_p^{2(T)} \; sin^2\,\Lambda\Big)\ddot{f}_2 + (x_1 \; x_3^2 + x_1 K_p^{2(T)} \; sin\,\Lambda\Big)\ddot{g}_2$$

$$- K_p^{2(T)}\ddot{\theta} \; sin\,\Lambda \; cos\,\Lambda - E_p^{(T)}\ddot{h} \; sin\,\Lambda\Big) + \mathcal{M}^{(T)} \; sin\,\Lambda + \underline{m^{(T)} g E_p^{(T)}} \; sin\,\Lambda\Big]$$

$$\delta\theta : T_{12}^{(0,1)} - T_{23}^{(1,0)} + x_0 T_{23}^{(0,0)} = -m^{(T)}\Big[-K_p^{2(T)}\ddot{f}_2 \sin\Lambda\cos\Lambda - x_1 K_p^{2(T)}\ddot{g}_2 \sin\Lambda\cos\Lambda$$

$$+\Big(x_3^2 + K_p^{2(T)}\cos^2\Lambda\Big)\ddot{\theta} + E_p^{(T)}\ddot{h}\cos^2\Lambda\Big] - \mathcal{M}^{(T)}\cos\Lambda - \underline{m^{(T)} g E_p^{(T)}\cos\Lambda}$$

$$\delta h : T_{23}^{(0,0)} + \underline{m^{(T)} g} = -m^{(T)}\Big(-E_p^{(T)}\ddot{f}_2 \sin\Lambda - x_1 E_p^{(T)}\ddot{g}_2 \sin\Lambda$$

$$+E_p^{(T)}\ddot{\theta}\cos\Lambda + \ddot{h}\Big) + \mathcal{L}^{(T)} \qquad (10a-e)$$

In these equations the superscript (T) identifies the quantities associated with the tip store.

In Eqs. (6) and (10) the terms underscored by an interrupted line help to define the *static equilibrium position* of the mechanical system carrying external stores. Consequently, as it can readily be shown, when dealing with the motion about the equilibrium, position these terms become immaterial. In this connection see Refs. 8 and 9.

Equations (6) through (10) represent the equations governing the aeroelastic equilibrium of advanced composite aircraft wings laminated of anisotropic layers and incorporating transverse shear and warping inhibition. In addition, these include arbitrarily distributed external stores in the wing's spanwise and chordwise directions, as well as the aerodynamics of the stores. Expressed in terms of the unknown displacement quantities $u_2(x_2;t), f_2(x_2;t), g_2(x_2;t), \theta(x_2;t)$ and $h(x_2;t)$, a tenth order governing system of ordinary differential equations is obtained.

Upon discarding the influence of the in-plane components of body forces $F_2^{(0,0)}$, as well as in-plane rotatory inertia terms (i.e. terms $I^{(0,0)}\ddot{u}_2, I^{(0,1)}\ddot{f}_2$, and $I^{(1,1)}\ddot{g}_2$), the displacement quantity $u_2(x_2;t)$ can be expressed in terms of $f_2(x_2;t), g_2(x_2;t), \theta(x_2;t)$ and $h(x_2;t)$, and thus be eliminated from the system. As a result, the system can be equivalently reduced to an eighth order differential equation system in terms of the unknowns $f_2(x_2;t), g_2(x_2;t), \theta(x_2;t)$ and $h(x_2;t)$. This governing equation system is not recorded here.

CONSTITUTIVE EQUATIONS

The constitutive equations relating the generalized stress couples $T_{ij}^{(m,n)}$ with the 1-D strain measures have been obtained in Ref. 21. In order to study the effects of external stores in conjunction with aeroelastic tailoring, the composite wing is considered to be made-up from a finite number N of linearly elastic homogeneous layers, the axes of orthotropy of each constituent layer being rotated by an angle φ with respect to the geometrical axes. It is further postulated a perfect bonding between the contiguous layers. In this case, the three-dimensional constitutive equations are

$$\begin{bmatrix}\sigma_{11}\\ \sigma_{22}\\ \sigma_{33}\\ \sigma_{23}\\ \sigma_{13}\\ \sigma_{12}\end{bmatrix} = \begin{bmatrix}\overline{Q}_{11} & \overline{Q}_{12} & \overline{Q}_{13} & 0 & 0 & \overline{Q}_{16}\\ \overline{Q}_{12} & \overline{Q}_{22} & \overline{Q}_{23} & 0 & 0 & \overline{Q}_{26}\\ \overline{Q}_{13} & \overline{Q}_{23} & \overline{Q}_{33} & 0 & 0 & \overline{Q}_{36}\\ 0 & 0 & 0 & \overline{Q}_{44} & \overline{Q}_{45} & 0\\ 0 & 0 & 0 & \overline{Q}_{45} & \overline{Q}_{55} & 0\\ \overline{Q}_{16} & \overline{Q}_{26} & \overline{Q}_{36} & 0 & 0 & \overline{Q}_{66}\end{bmatrix}\begin{bmatrix}\varepsilon_{11}\\ \varepsilon_{22}\\ \varepsilon_{33}\\ \gamma_{23}\\ \gamma_{13}\\ \gamma_{12}\end{bmatrix} \qquad (11)$$

where $\overline{Q}_{ij}$ denote the transformed elastic coefficients associated with the k-th layer in the coordinate system of the wing structure; $\gamma_{ij} = 2\varepsilon_{ij}, i \neq j$, and ε_{ij} denote the components of the strain tensor.

CONTROL LAW AND GENERATION OF THE WING TIP BENDING MOMENTS.

As previously mentioned, piezoactuators are considered to be spread over the entire span of the wing and symmetrically bonded to the upper and bottom surfaces. In the case of external voltages of opposite signs applied in the piezoactuator thickness direction (out-of-phase activation), it can readily be shown that only the piezoelectrically induced stress couples $\hat{T}_{22}^{(0,1)}$ and $\hat{T}_{22}^{(1,1)}$ survive, being non-zero quantities. Being spatially constant valued quantities, their contributions to the governing equations is immaterial, while in the homogeneous variant of boundary conditions, (obtained by discarding the terms underscored by a tilde sign), these intervene as boundary moments applied at the wing tip. The boundary conditions at $x_2 = l$ expressed in terms of displacement quantities are not displayed here. Their expressions are displayed in Ref. 17. This is one of the possibilities enabling one to generate the required bending moments at the wing tip.

For feedback control, the bending tip moments $\hat{T}_{22}^{(0,1)}$ and $\hat{T}_{22}^{(1,1)}$ must be related to one of the mechanical quantities characterizing the wing response. Consequently, a number of control laws can be implemented. For the problem at hand, their effectiveness must be measured by the ability to increase the flutter speed and even to eliminate, without weight penalties, the possibility of its occurrence.

Herein a combined feedback control law is implemented which concerns each of the boundary moments $\hat{T}_{22}^{(0,1)}$ and $\hat{T}_{22}^{(1,1)}$.

For the boundary moment control, $\hat{T}_{22}^{(0,1)}$, the following control law is implemented

$$\hat{T}_{22}^{(0,1)} = \hat{K}_p \ddot{h}, \text{ for } (x_2 = l) \tag{12}$$

whereas the boundary moment $\hat{T}_{22}^{(1,1)}$, associated with the secondary warping effect is considered to be related to the wing response quantities as:

$$\hat{T}_{22}^{(1,1)} = \hat{K}_w \ddot{\theta}_{,2}, \text{ for } (x_2 = l) \tag{13}$$

Herein, $\hat{K}_p$ and $\hat{K}_w$are the feedback gains in plunging and warping, respectively.

For the kinematic response variables the following representation which fulfills identically the boundary conditions at the wing root, is used:

$$\left[f_2(\eta;t), g(\eta;t), \theta(\eta;t), h(\eta,t)\right]^T = \sum_{j=1}^{n} \left[F_j, G_j, T_j, H_j\right]^T \eta^j e^{i\omega t} \tag{14}$$

where $\eta(\equiv x_2/l)$ is the dimensionless spanwise coordinate and $i(\equiv \sqrt{-1})$ is the imaginary unit.

At the same time, in order to be able to implement different combinations of feedback, the representation of h and θ in Eqs. (12) and (13), includes a variable phase shift ϕ:

$$\left[\theta(\eta;t), h(\eta;t)\right]^T = \sum_{j=1}^{n} \left[T_j, H_j\right]^T \eta^j e^{i(\omega t+\Phi)} \tag{15}$$

It can readily be seen that the control laws, Eqs. (12) and (13), considered in conjunction with (15), include as special cases acceleration, ($\Phi = 0$) , velocity ($\Phi = -\pi/2$), and displacement ($\Phi = -\pi$) feedback control. Continuous variation of Φ between the extreme values, $\Phi = 0$ and $\Phi = -\pi$, yields combinations of these basic control laws. Representations (14) and (15) are replaced in the Hamilton's functional, Eq. (5), wherefrom a complex closed-loop eigenvalue problem is obtained whose solution enables one to determine the closed-loop flutter and frequency.

It should be underlined that within the Extended Galerkin Method (EGM), the non-fulfillment of static boundary conditions at the wing tip is compensated by the appearance of associated residual terms in the energy functional. This ensures a great accuracy of flutter instability predictions. Moreover, application of the EGM enables one to accommodate the spanwise variability of the geometrical and mechanical characteristics of the wing structure as well as those associated with the sectional left-curve slope, aerodynamic center location, etc.

NUMERICAL SIMULATIONS

The performance of aeroelastic tailoring and active feedback control upon the dynamic aeroelastic response of advanced aircraft wings with or without external stores is underlined by the following numerical simulations.

The ply-angle φ represents the counterclockwise angle of rotation of the principal axis of orthotropy x_1' of the material with respect to the x_1-axis of the structure. In this context, the wing is considered to be made-up from a graphite-epoxy composite material, whose elastic properties are:

$$E_1 = 30.10^6 \text{ psi};\ G_{12} = 0.45 \cdot 10^6 \text{ psi};\ E_2 = 0.75 \cdot 10^6 \text{ psi};\ G_{13} = 0.37 \cdot 10^6 \text{ psi};$$
$$\nu_{12} = 0.25; \rho = 14.3 \cdot 10^6 \text{ lb sec}^2/\text{in}^4$$

For this material, the transverse shear flexibility parameter is $R = E_1/G_{13} = 81.081$. The dynamic aeroelastic instability is analyzed assuming an incompressible airflow. In this context, a 3-D flutter analysis based on Theodorsen's expression of the unsteady aerodynamic loads is carried out. Throughout the considered numerical simulations, the wing aspect ratio is $\mathcal{AR} = 6.67$.

Figures (2a-c) and (3a-c) depict of the combined effects of feedback plunging gain, phase shift and ply-angle on the flutter speed parameter ($\lambda_F \equiv V_F/b\,\omega_h$) and of frequency flutter $\Omega_F(\equiv \omega_F/\omega_h)$ respectively, for a clean unswept wing. The results displayed in these plots reveal the beneficial influence played by combining the tailoring technique with an active feedback control.

It can be seen that the effectiveness of the control system highly depends on the ply-angle orientation of the composite wing, with the maximum increase of the flutter speed

and flutter frequency being at a ply-angle $\varphi \cong 45°$. It is important to note that the control effectiveness also depends on the phase shift of the feedback signal. The optimum phase shift also varies with the ply-angle.

Figures 4a and 4b display variations of the flutter speed parameter λ_F and of the flutter frequency Ω_F versus the ply-angle for the case of the uncontrolled ($\hat{K}_p = 0$) and controlled ($\hat{K}_p \neq 0$) straight clean wings. Herein, the displacement feedback control ($\Phi = -\pi$) was used.

The results reveal that the efficiency of the active control strongly depends on the ply-angle. In this sense, it is readily seen that over a certain range of ply-angles, the active feedback control is almost inefficent, whereas in the range ($25° < \varphi < 50°$), the active control shows to be most efficient. The results of the Fig. 4b also reveal that the range of φ over which the active control is more efficient on the flutter frequency is larger than for the associated flutter speed.

Figures 5a and 5b depict the combined effects of the implementation of plunging and warping feedback controls with fixed phase shift, on the flutter of a straight wing featuring a fixed ply-angle $\varphi = 45°$. The results reveal that implementation of both feedback control strategies results in a significant increase of flutter speed and frequency.

Figures 6a and 6b display the influence of plunging feedback control and aeroelatic tailoring on flutter speed and frequency, respectively. In this case, an unswept wing carrying an external store of relative mass $\mu_w (\equiv m_{\text{wing store}}/m_{\text{wing}}) = 0.5.$, located at $0.5l$ on the reference axis was examined. The results reveal the high efficiency of the implementation of both techniques towards the enhancement of the flutter response of wings carrying external stores.

In Fig. 7, the 3-D plot depicts the variation of λ_F for a wing of ply angle $\varphi = 45°$ vs. the sweep angle in the range ($-20° \leq \Lambda \leq 60°$). The external store parameters are $\eta_w = 0.5$ and $\mu_w = 0.5$. It is considered that displacement feedback control ($\Phi = -\pi$) was implemented and $\hat{K}_p$ is the feedback gain in plunging. In addition to the trend concerning the variaton of λ_F with Λ similar to that reported in Refs. 12 and 13, the results reveal that the increase of $\hat{K}_p$ yields a substantial increase of the flutter speed.

Finally, in Figs. 8a and 8b, the variations of the flutter speed and frequency parameters, λ_F and Ω_F, respectively, for a clean wing characterized by the ply-angle $\varphi = 45°$ vs. the sweep angle Λ and phase shift ϕ are displayed. The numerical simulation has been obtained for the case of a fixed value of the feedback gain $\hat{K}_p = 10$, when only the control in plunging is activated.

The results reveal again the strong influence of the phase shift on both the flutter speed and frequency. It should be noticed that variation of Φ influences differently λ_F and Ω_F, in the sense that for the flutter speed, the maximum beneficial influence is played when displacement feedback is implemented whereas the minimum one, for acceleration feedback control law. In the case of the flutter frequency, the least influence is excerted when velocity feedback control is implemented.

CONCLUSION

A comprehensive structural model of aircraft wings built-up from advanced composite

materials was developed. It incorporates the anisotropy of the materials of constituent layers, transverse shear flexibility, warping inhibition and a system of arbitrarily distributed external stores. In addition, an active feedback control capability was included. This model reveals its efficiency in approaching the flutter problem of complex wing/store configurations in conjunction with active feedback flutter control and aeroelastic tailoring.

The results supplied here demonstrate in full the synergistic interaction of the application of both techniques, towards the enhancement of the flutter response of advanced wing structures carrying external stores, as well as an expansion of the flight envelope without weight penalties.

REFERENCES

1. Lagnese, J. E. and Lions, J. L., "Boundary Stabilization of Thin Plates," Masson, Paris, 1988.
2. Lagnese, J. E. "Boundary Stabilization of Thin Plates," *SIAM Studies in Applied Mechanics*, SIAM, Philadelphia, PA, 1989.
3. Weisshaar, T.A., "Aeroelastic Tailoring, Creative Uses of Unusual Materials," AIAA Paper 87-0976-CP, *AIAA/ASME/ASCE/AHS 20th Structures, Structural Dynamics and Materials Conference*, April 1987.
4. Hönlinger, H. and Destuynder, R. "External Store Flutter Suppression with Active Controls" in *Active Control Technology*, von Kármán Institute for Fluid Dynamics, Lecture Series 1979.
5. Song, O., Librescu, L. and Rogers, C. A., "Application of Adaptive Technology to Static Aeroelastic Control of Wing Structures," *AIAA Journal*, Vol. 30, No. 12, pp. 2882-2889, December 1992.
6. Librescu, L., Song, O. and Rogers, C. A., "Adaptive Vibrational Behavior of Cantilevered Structures Modeled as Composite Thin-Walled Beams," *International J. of Engineering Science*, Vol. 31, No. 5, pp. 775-792, 1993.
7. Librescu, L., Meirovitch, L. and Song, O., "Integrated Structural Tailoring and Control Using Adaptive Materials for Advanced Aircraft Wings," *Journal of Aircraft*, Vol. 33, 1, Jan.-Feb., pp. 203-213, 1996.
8. Song, O. and Librescu, L., "Bending Vibrations of Cantilevers Carrying Externally Mounted Stores and Incorporating Adaptive Capabilities," *International J. of Mechan. Science*, Vol. 38, No. 5, pp. 483-498, 1996.
9. Librescu, L. and Song, O., "Static and Dynamic Behavior of Adaptive Aircraft Wings Carrying Externally Mounted Stores," *Structronic Systems, Smart Structures, Devices and Systems*, (Ed. H. Tzou), pp. 1-85, 1966.
10. Librescu, L., Meirovitch, L., and Na. S. S., "Control of Cantilever Vibration via Structural Tailoring and Adaptive Materials," *AIAA Journal* Vol. 35, No. 8, pp. 1309-1315, August, 1997.
11. Weisshaar, T. A. and Ehlers, S. M., "Adaptive Aeroelastic Composite Wings-Control and Optimization Issues," *Composites Engineering* , Special Issue: Use of Composites in Rotorcraft and Smart Structures, Vol. 2, Nos. 5-7, pp. 457-476, 1992.

12. Gern, F. H. and Librescu, L., "Static and Dynamic Aeroelasticity of Advanced Aircraft Wings Carrying External Stores," *AIAA Journal,* Vol. 36, No. 7, pp. 1121-1129, July, 1998.
13. Gern, F. H., and Librescu, L., "Effects of Externally Mounted Stores on Flutter Characteristics of Advanced Swept Cantilevered Aircraft Wings," *Aerospace Science and Technology,* Vol. 2, No. 5, pp. 321-333, July, 1998.
14. Tzou, H. S., "Piezoelectric Shells, Distributed Sensing and Control of Continua," Kluwer Academic Publication, Dordrecht/Boston/London, 1993.
15. Heeg, J., "Analytical and Experimental Investigation of Flutter Suppression via Piezoelectric Actuation," Proceedings of the AIAA Dynamics Specialists Conference, (Dallas, TX), AIAA, Washington, DC, 1992, 237-248 (AIAA Paper 92-2106).
16. McGowan, A. M. R., Heeg, J. and Lake, R. C., "Results of Wind-Tunnel Testing From the Piezoelectric Aeroelastic Response Tailoring Investigation," Paper AIAA-96-1511-CP, 37th AIAA/ASME/ASCE/AHS/ASC Structures, Structural Dynamics and Materials Conference and Exhibit, April 15-16, Salt Lake City, UT, 1996.
17. Nam, C, Kim, Y. and Layton, J. B., "Active Aeroelastic Wing Design for Gust Load Alleviation and Flutter Suppression," *AIAA Paper*, 97-1265.
18. Karpouzian, G. and Librescu, L., "Flutter Instability Control of Aircraft Wings via Incorporation of Adaptive Materials Technology," *AIAA Paper 96-1213, AIAA Dynamics Specialists Conference*, Salt Lake City, UT, April, 1996.
19. Bendikson, O. O. and Hwang, G-Y., "Transonic Flutter Suppression Using Dynamic Twist Control," Paper AIAA-96-1343-CP, 37th AIAA/ASME/ASCE/AHS/ASE Structures Structural Dynamics and Materials Conference and Exhibit, April 15-17, Salt Lake City, UT, 1996.
20. Crawley, E. F., "Intelligent Structures for Aerospace: A Technology Overview and Assessment," *AIAA Journal*, **32**, 8, 1994, 1689-1699.
21. Karpouzian, G. and Librescu, L., "Non-Classical Effects on Flutter and Divergence of Anisotropic Swept Aircraft Wings," *AIAA Journal*, Vol. 34, No. 4, 1996, pp. 786-794.

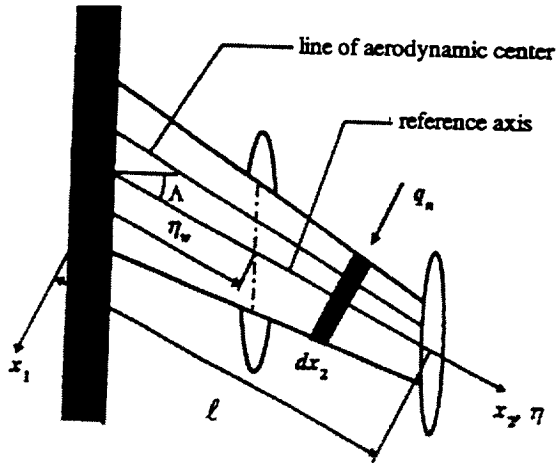

Fig. 1: Geometry of the composite wing carrying external stores.

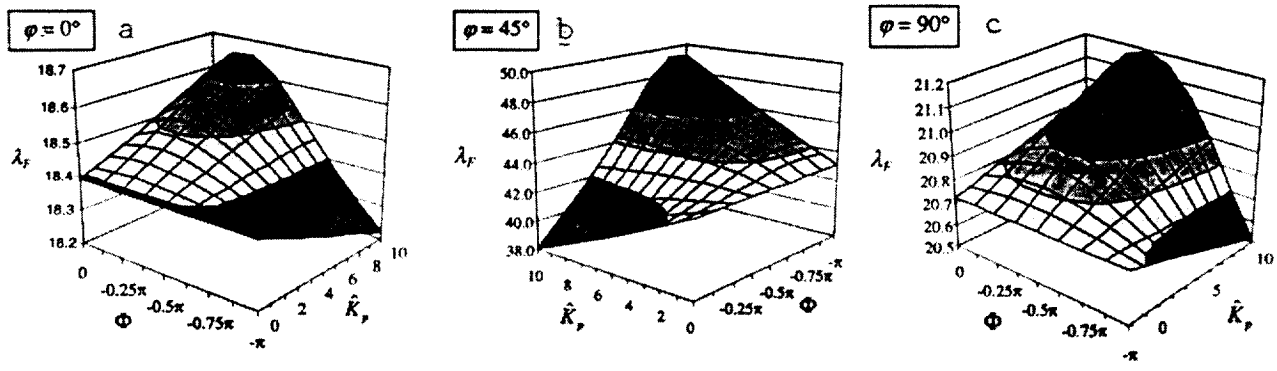

Figs. 2a-c: Flutter speed of the clean wing vs. phase shift Φ and feedback gain $\hat{K}_p$, for selected values of ply-angle φ.

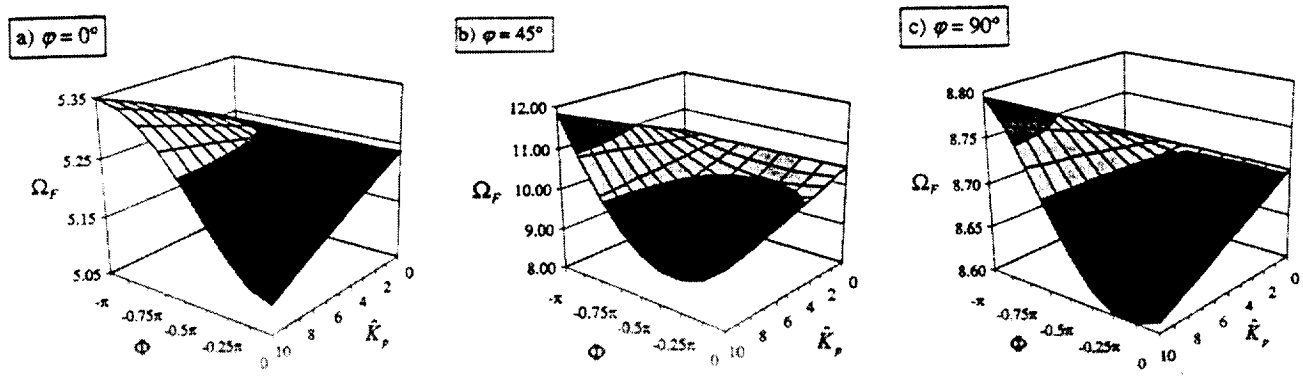

Figs. 3a-c: Flutter frequency of the clean wing vs. phase shift Φ and feedback gain $\hat{K}_p$, for selected values of ply-angle φ.

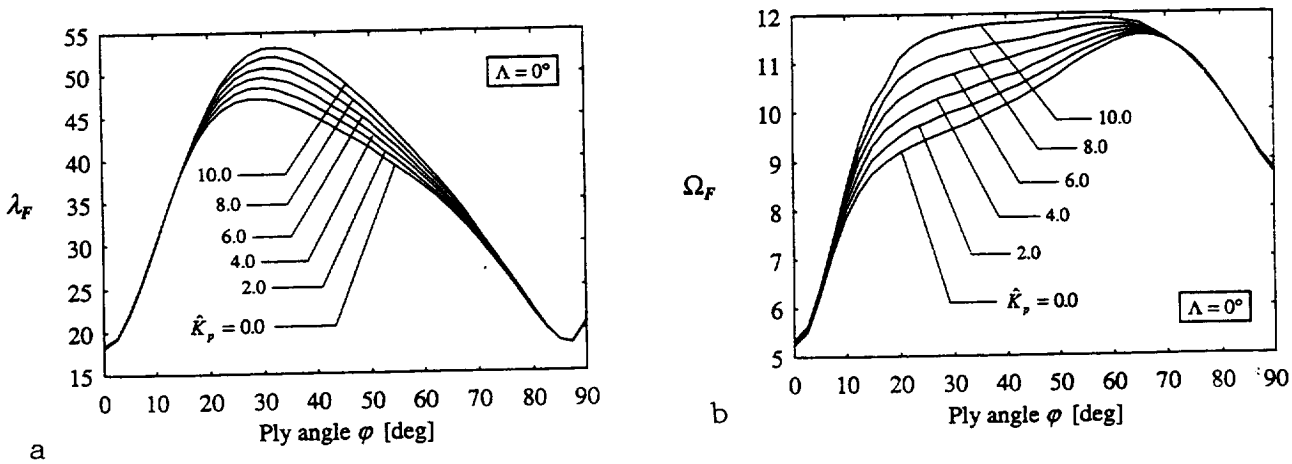

Figs. 4a,b: Effect of ply-angle φ and plunging feedback gain $\hat{K}_p$ on flutter speed (Fig. 4a) and frequency (Fig. 4b) of a straight wing including transverse shear flexibility, $\Phi = -\pi$

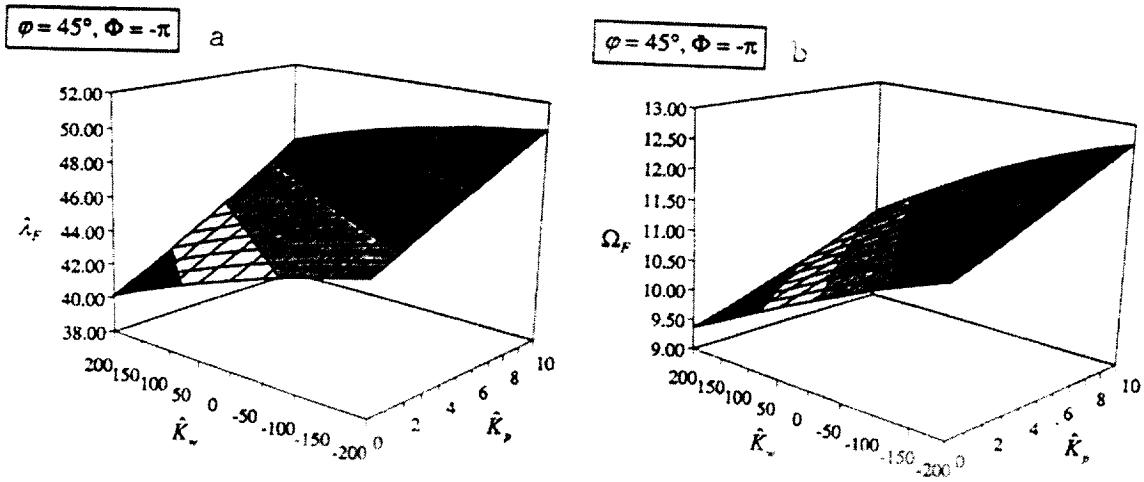

Figs. 5a,b: Flutter speed and flutter frequency of the composite wing vs. plunging and warping feedback gains $\hat{K}_p$ and $\hat{K}_w$, respectively. Displacement feedback control law.

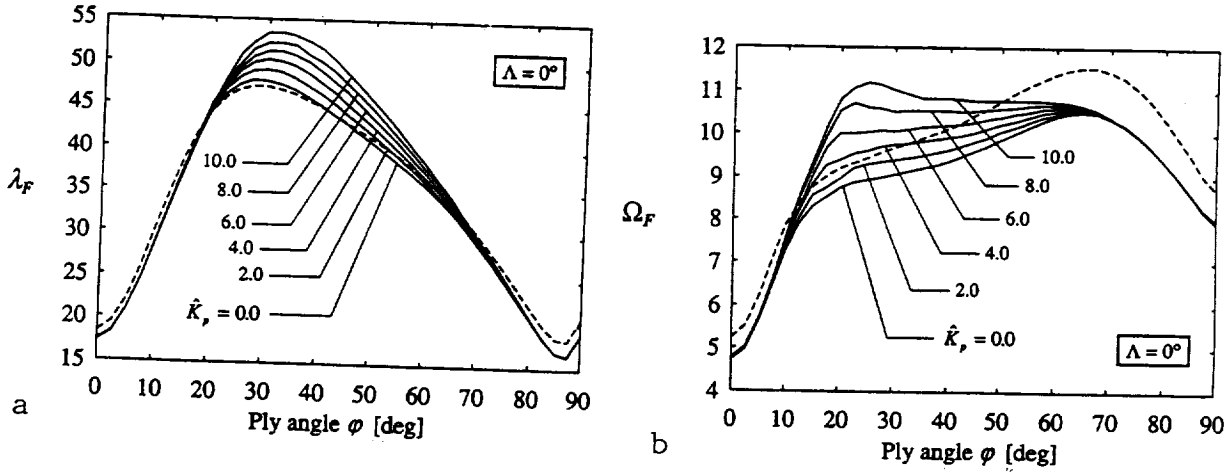

Figs. 6a,b: Effect of ply-angle φ and plunging feedback gain $\hat{K}_p$ on flutter speed (Fig. 6a) and frequency (Fig. 6b) for a straight wing carrying an external wing store ($\mu_w = 0.5$) and including transverse shear flexibility, $\Phi = -\pi$ (the dashed line indicates the uncontrolled clean wing)

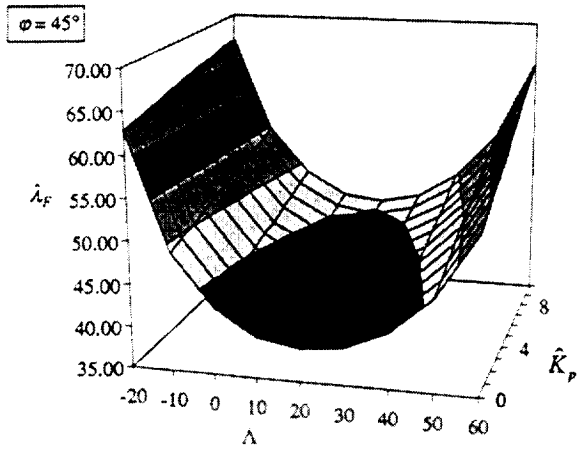

Fig. 7: Effect of sweep angle Λ and plunging feedback gain $\hat{K}_p$ on flutter speed parameter $\lambda_F = V_F/b\omega_h$ for a wing carrying an external wing store ($\mu_w = 0.5$) and including transverse shear flexibility, $\Phi = -\pi$

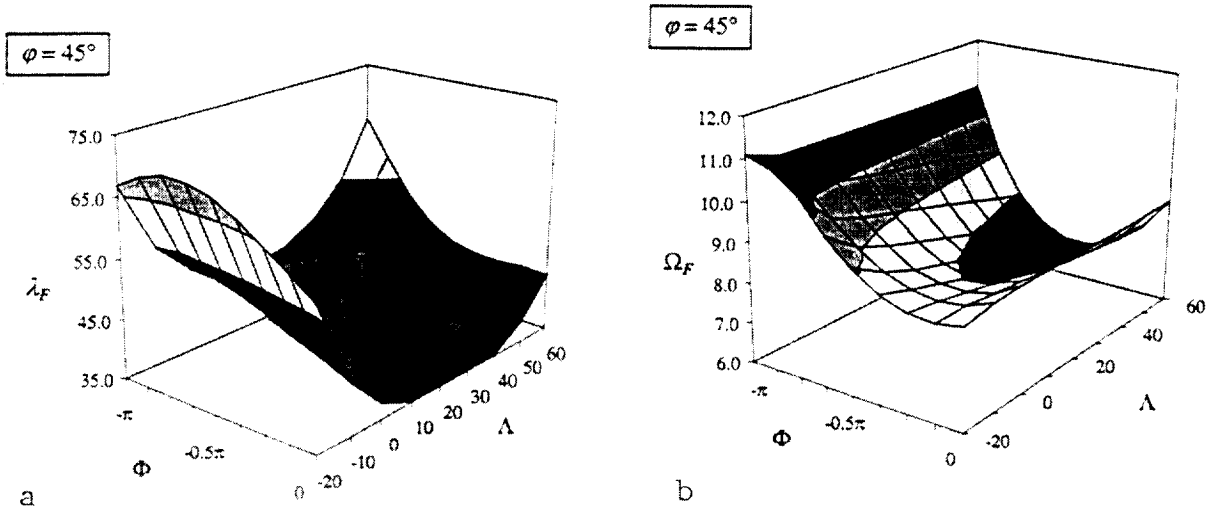

Figs. 8a,b: Flutter speed (Fig. 8a) and frequency (Fig. 8b) of the composite wing vs. plunging feedback gain phase shift Φ and wing sweep angle Λ (plunging gain $\hat{K}_p = 10.0$)

NON-LINEAR FLUID AND STRUCTURES INTERACTION SIMULATION

Reid B. Melville* and Raymond E. Gordnier†
Air Force Research Laboratory, Wright-Patterson Air Force Base, Ohio

Abstract

A dynamic aeroelastic solver is used to simulate several fluid-structure interactions with highly non-linear flow-fields. A Beam-Warming, approximate factored algorithm, coupled with a linear, second-order structural model via subiteration, becomes a fully implicit, second-order accurate aeroelastic solver. Key issues for accurate aeroelastic simulation are discussed and highlighted by examples. These include geometric conservation, temporal synchronization of the fluid and structural state, full coupling and feedback between the solvers, and non-linear flow features that drive aeroelastic stability and require high levels of spatial discretization.

Introduction

Flight vehicles performance and longevity are often limited because of adverse aeroelastic phenomena. Efforts to model and to account for these fluid-structure interactions have historically been done with simplified, linearized techniques. More recently, research has been directed at accounting for the inherent nonlinearities in flexible flight systems. For particular materials and under certain loading conditions, structural non-linearities become significant. In some flight regimes, namely transonic and separated, it is the fluid loading of the structure that becomes highly non-linear.

To capture the full range of fluid responses, advanced modeling techniques, like computational fluid dynamics (CFD), are required. CFD has matured as a field into a robust technological capability based on experience simulating rigid bodies surrounded by static volume grids. Extending these types of simulations to include elastic bodies and deforming grids, while not new, is a subject of ongoing research and development. The fidelity of the CFD simulation can be selected to capture sufficiently the non-linear fluid features that drive the elastic response. Further, the feedback of the structural dynamics to the fluid systems can also be correctly modeled. In this paper, an analysis methodology is outlined that includes high fidelity representation of non-linear fluids and their interactions with elastic surfaces. This method has been applied to several configurations that are representative of flight vehicles. The results of these dynamic, aeroelastic simulations yield considerable insight into the fluid mechanisms that drive the responses and the modeling requirements to represent them fully.

Aeroelastic simulation is most often performed by coupling separate fluid and structural solvers. Research has shown the importance of fully synchronizing the two solutions in time[1]. One method of achieving synchronization is to subiterate the solution, that is, to apply each solver successively until they converge on a single solution state at each time step. A subiterated strategy to coupling offers other well-known benefits[2]. Subiteration reduces linearization and factorization error, which for 3-D Beam-Warming solvers is a source of stability restriction. Lagged boundary conditions and turbulence models are also synchronized with subiteration. Finally, for parallel decomposed or overset configurations, subiterations provide a mechanism for communication between zones that are explicitly linked.

The base flow solver used in this work is a 3-D Beam-Warming algorithm with Newton-like subiteration. It has been used extensively to simulate a wide range of unsteady flow-fields[3] [4]. Previously[5], it has been extended to include second-order temporal accuracy, grid deformation capability, application of the Geometric Conservation Law[6], and a general, linear second-order structural solver. Much of the current work is performed using a parallel implementation on overset grids[7] via explicit message passing.

Methodology

In this section, the overall solution methodology is presented. Topics include the aerodynamic and structural governing equations and their boundary conditions. The time integration scheme is outlined along with the interface data exchange, parallel coupling of the solvers, and grid deformation.

---

*† Research Aerospace Engineer, Computational Sciences Branch, Aeronautical Sciences Division, *Member AIAA, †Associate Fellow AIAA.

Governing Equations

Aerodynamic Governing Equations

The aerodynamic governing equations are the unsteady compressible three-dimensional Navier-Stokes equations written in nondimensional strong-conservation law form employing a general time dependent transformation. The resulting system of governing equations is expressed as:

$$\frac{\partial}{\partial t}\widehat{U} + \frac{\partial}{\partial \xi}\left(\widehat{F} - \frac{1}{Re}\widehat{F}_v\right) + \frac{\partial}{\partial \eta}\left(\widehat{G} - \frac{1}{Re}\widehat{G}_v\right) + \frac{\partial}{\partial \zeta}\left(\widehat{H} - \frac{1}{Re}\widehat{H}_v\right) = S_{GCL} \quad (1)$$

With this formulation, the vector of dependent variables U is given as:

$$\widehat{U} = \frac{1}{J}U = \frac{1}{J}\left[\rho \;\; \rho u \;\; \rho v \;\; \rho w \;\; \rho E\right]^T \quad (2)$$

All variables have been normalized by freestream values of velocity and density and by a characteristic length scale, like wing root chord. For Euler simulations, the inviscid subset of Equation 1 was solved by neglecting the viscous fluxes.

The source vector term, S_{GCL}, is a term to enforce the geometric conservation law for moving meshes. This term is defined as[1]:

$$S_{GCL} = U\left[\frac{\partial J^{-1}}{\partial t} + \left(\frac{\xi_t}{J}\right)_\xi + \left(\frac{\eta_t}{J}\right)_\eta + \left(\frac{\zeta_t}{J}\right)_\zeta\right] \quad (3)$$

This term vanishes analytically, but not when discrete representations of the temporal and spatial derivatives are used. The most straightforward approach of accounting for this term is to simply include it in the discrete governing equations, completely representing the non-transformed governing equations.

Aerodynamic Boundary Conditions

For the solid surfaces, a dynamic flow tangency condition or a dynamic no-slip condition was enforced on the velocity, as appropriate. The remaining two conditions are the adiabatic wall condition and dynamic normal momentum equation, which accounts for the surface acceleration on the pressure gradient. Away from the wing, a quasi-1-D characteristic boundary condition was applied in the far-field except at the downstream plane where zeroth-order extrapolation was used. At planes of symmetry, zeroth-order extrapolation was also used to accommodate the oblique intersection of the spanwise gridlines. Where computational grids overlapped, boundary conditions were applied using data from neighboring grids via trilinear interpolation[8].

Structural Dynamic Governing Equations

In general a second-order, linear structural model coupled with a flow solver can be expressed:

$$M\ddot{q} + D\dot{q} + Kq = \Phi^T F_a \quad (4)$$

where q, M, D, and K are generalized displacement, mass, damping, and stiffness. F_a is the vector of forces on the aerodynamic grid and Φ^T is the transformation that maps F_a into generalized forces. The model can be made first order by defining $S = \left[q \;\; \dot{q}\right]^T$:

$$\begin{bmatrix} I & 0 \\ 0 & M \end{bmatrix}\dot{S} + \begin{bmatrix} 0 & -I \\ K & D \end{bmatrix}S = \begin{bmatrix} 0 \\ \Phi^T F_a \end{bmatrix} \quad (5)$$

For most cases, finite element structural analysis is used to simulate the elastic properties of the models and to generate modal representations of the structural response. Structural damping was assumed to be zero. The mode shapes (Φ^T) were matched to the aerodynamic grid using thin-plate splines from a specialized interpolation program (FASIT, ref. 9).

Fluid-Structure Interface

An important issue is the treatment of the boundaries between the two disciplines, fluids and structures[10]. The information exchange should be formulated so that the coupled system is energy conservative and consistent in the limit of refinement. As long as the mode shapes are sufficiently smooth, use of interpolated mode shapes on the aerodynamic grid maintains fidelity to the original mode shapes. The fidelity of the modal model to the original finite-element model is an important, but separate issue.

On the principle of reciprocity, the interchange of energy between the fluid and the structures can be conserved if the transformation operator (Φ^T, Equation 4) used to project the loads into generalized space is also used to map the generalized displacement state into physical space. For this simulation, the deflections are transferred in this conservative way. Also, the velocities are formed from the deflections with identical operators for the fluid and the structures, thus achieving conservative interchange to round-off precision. However, the acceleration term used in the surface pressure boundary condition is only approximately conservative.

Time-Integration Scheme

Solutions to equation Equation 1 are obtained numerically using the implicit approximately-factored finite-difference algorithm of Beam and Warming[11], employing a Newton-like subiteration procedure[2]. The numerical algorithm is obtained from Equation 1 by utilizing either a two- or three-point backward time differencing and linearizing about the solution at subiteration level p. The choice of first or second-order temporal accuracy is retained in the following iterative approach by specifying either $\phi = 0$ or $\phi = 1/2$, respectively. The numerical algorithm is written in approximately-factored, delta form as:

$$\left[J^{-1} + \phi^i \Delta t_s \delta_\xi \left(\frac{\partial F^p}{\partial U} - \frac{1}{Re}\frac{\partial F_v{}^p}{\partial U}\right)\right] x \tag{6}$$

$$\left[J^{-1} + \phi^i \Delta t_s \delta_\eta \left(\frac{\partial G^p}{\partial U} - \frac{1}{Re}\frac{\partial G_v{}^p}{\partial U}\right)\right] x$$

$$\left[J^{-1} + \phi^i \Delta t_s \delta_\zeta \left(\frac{\partial H^p}{\partial U} - \frac{1}{Re}\frac{\partial H_v{}^p}{\partial U}\right)\right] \Delta U$$

$$= -\phi^i \Delta t_s \left[J^{-1}\frac{(1+\phi)U^p - (1+2\phi)U^n + \phi U^{n-1}}{\Delta t}\right.$$

$$- U^p\left(\left(\frac{\xi_t}{J}\right)_\xi + \left(\frac{\eta_t}{J}\right)_\eta + \left(\frac{\zeta_t}{J}\right)_\zeta\right) + J^{-1}\delta_\xi\left(F^p - \frac{1}{Re}F_v{}^p\right)$$

$$\left. + J^{-1}\delta_\eta\left(G^p - \frac{1}{Re}G_v{}^p\right) + J^{-1}\delta_\zeta\left(H^p - \frac{1}{Re}H_v{}^p\right)\right]$$

where

$$\phi^i = \frac{1}{1+\phi}, \quad \Delta U = U^{p+1} - U^p \tag{7}$$

and for $p = 1$, $U^p = U^n$.

Here U^p is the subiteration approximation to U^{n+1} so that as $p \to \infty$, $U^p \to U^{n+1}$. It should be noted that with this subiteration approach the right-hand side of Equation 6 represents the numerical approximation to the governing equation, while the left-hand side vanishes as $p \to \infty$. The left-hand side then, may be modified for efficiency without loss of formal accuracy provided a sufficient number of subiterates is employed. The numerical procedure has been modified to include diagonalization, following the approach of reference 12. Although the diagonalized form of the ADI scheme is only first-order time-accurate, when coupled with subiterations, higher order time accuracy may be recovered. The numerical scheme reverts to the standard first-order Beam-Warming procedure for $\phi=0$, $\Delta t_s = \Delta t$, and $p=1$.

In Equation 6 all spatial derivatives are approximated by second-order accurate central differences, and common forms of both implicit and explicit nonlinear dissipation[13] are employed in order to preserve numerical stability. The temporal metric derivatives are discretized in a manner consistent with the temporal derivative of the conserved variables in Equation 6.

Structural Time Integration

The subiteration implicit formulation can also be applied to the structural equations (Equation 5). The resulting scheme is:

$$\begin{bmatrix} \gamma I & -I \\ K & \gamma M + D \end{bmatrix} \Delta S^p = \begin{bmatrix} 0 \\ \Phi^T F_a \end{bmatrix} - \begin{bmatrix} 0 & -I \\ K & D \end{bmatrix} S^p - \begin{bmatrix} I & 0 \\ 0 & M \end{bmatrix} \delta_t S^p \tag{8}$$

where $\gamma = \left(\frac{1+\phi}{\Delta t}\right)$.

Since the structural equations are cast in iterative form, successive applications of the solver yield a fully implicit coupling between the aerodynamic model and the structural model.

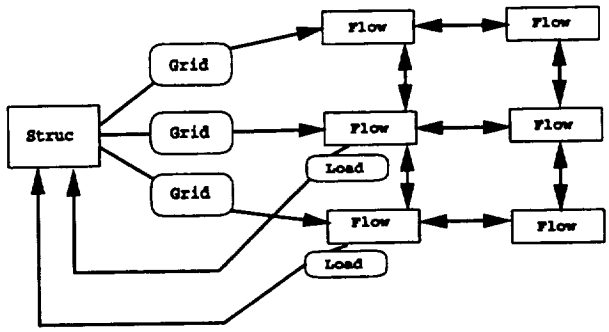

Figure 1 Fluid-Structure Coupling Message Passing Strategy

Temporal Coupling in Parallel

For parallel computing platforms, the fluid-structure coupling problem can include hardware issues. Although a number of configurations are possible, an intuitive method is to segregate the fluid and structures solvers into separate computational node pools[14]. This approach is employed here and specifically, a single compute node is dedicated to solving the structural equations and deforming the computational grids. The rest of the compute nodes are used to decompose the fluid solver (a representative configuration is illustrated in Figure 1). The nodes communicate via explicit message

passing (MPI), with flow nodes exchanging boundary condition information and flow and structures nodes exchanging surface loads and deformed grids, respectively. In general, only a subset of the flow nodes will require communication with the structural node, and the present algorithm allows for any combination of message dependency.

Once a hardware and software coupling between the solvers is established, the next issue is the temporal synchronization of the solutions. The simulations reported here utilized a serial coupling strategy where the flow nodes wait for an updated grid before advancing in time.

Grid Deformation

A grid deformation method which is suitable for aeroelastic simulations on overset grids was developed previously[5]. This new strategy is similar to TFI in that it is an algebraic approach based on redefining the normal grid lines. However, unlike TFI, this method maintains the grid quality of the initial mesh near deforming surfaces under arbitrary, moderate deflections and rotations. In addition, a specified region in the far-field may be held fixed so that the grid overlap regions, and their connectivities, remain unchanged.

Simulation Issues

Most engineering analysis pits competing requirements of accuracy and efficiency. Sometimes rapid turn around is paramount and only the most basic accuracy requirements need be met. Other times great expense is taken to assure the highest standards of accuracy. This paper focuses on the second scenario and specifically on high-fidelity, dynamic aeroelastic simulation. Several key issues that effect the accuracy of a fluid-structure interaction analysis will be presented and illuminated by example. This list is not exhaustive but serves to highlight critical issues of CFD-based aeroelastic simulation.

Geometric Conservation

The Geometric Conservation Law (GCL) describes the requirement to account for errors due to grid motion in dynamic simulations. There are a number of ways to satisfy a GCL constraint, either approximately or exactly. An effective method for finite-difference techniques was outlined in the previous section and used in the work presented here. The error caused by neglecting the GCL constraint is case dependent, and while it may be benign, it can, in the worst extreme, be catastrophic. One example that quantifies the effect of GCL is a 2-D panel flutter study[15], presented here.

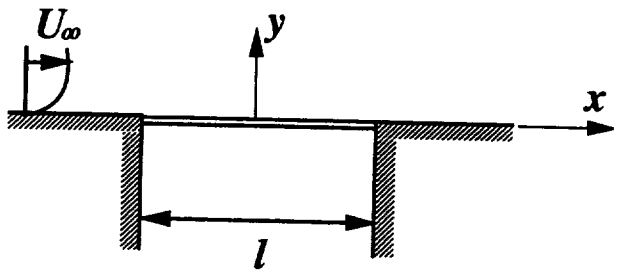

Figure 2 Panel Flutter Configuration

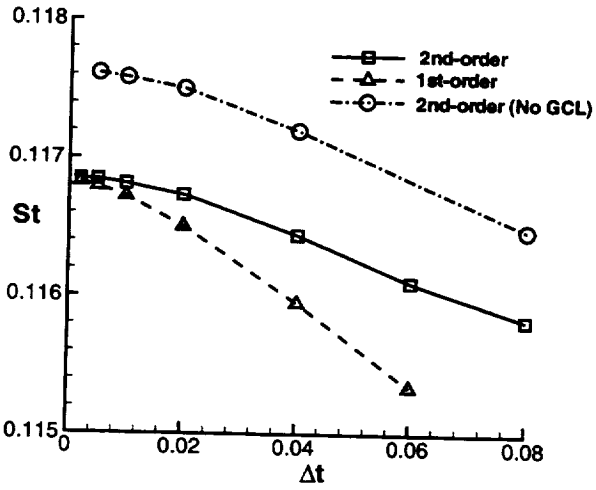

Figure 3 Impact of GCL under Temporal Refinement

For these computations, a simply-supported plate (see Figure 2) with thickness to width ratio of .00271 and typical aluminum material properties is modeled. Standard atmospheric properties at an altitude of 20,000 feet are assumed. The computational mesh has 50 equal streamwise intervals over the plate and a minimum vertical spacing next to the plate of 0.001. In this study, flutter calculations are initiated by first computing the steady flow over a rigid plate, and subsequently perturbing the panel by imposing a small vertical velocity. Results for an inviscid panel flutter case at Mach number 1.2 and a mass ratio of 0.1 are presented here.

Calculations were performed using either the first- or second-order accurate time-marching schemes combined with 3 sub-iterations. The effect of time step on the computed non-dimensional frequency is shown in Figure 3 for a wide range of timestep values (0.002 to

0.08). The first- and second-order time-integration methods asymptote to the same flutter frequency with temporal refinement, with the second-order scheme resulting in an improved convergence behavior.

The effect of the Geometric Conservation Law was also investigated. As shown in Figure 3, results obtained without the addition of the GCL correction term (Equation 3) asymptote to a different flutter frequency. In fact, the variation in frequency due to geometric conservation errors is found to be more significant than the changes associated with the order of accuracy of the time-integration algorithm.

Temporal Synchronization

It is common in aeroelastic analysis to solve the fluid equations and structural equations separately and sequentially. While this is the simplest of all approaches, it results in error due to the lag between the fluid and structural states. For accurate simulations, the lag error cannot be ignored, and for some cases refuses to be ignored. For example, in the panel flutter case mentioned previously, if lagging errors were allowed to persist, a long-time numerical instability would result[15].

Several techniques are available to eliminate the lag error, or more precisely to synchronize the fluid and structural states. The subiteration method used here is simple to implement in an existing solver. This method has a computational overhead, as the solvers are applied successively at each time step, but for many cases it allows larger time steps to be taken. The following example of an elastically mounted cylinder[1] demonstrates how subiteration can make a simulation more accurate and more efficient.

The structural model is depicted in Figure 4. The cylinder is assumed to be constrained to move by linear springs and dampers along the vertical and horizontal directions without rotation. The simulations were computed with freestream conditions of Reynolds number 500, Mach number 0.2, and a mass ratio of 5. The time-asymptotic solution is a periodic displacement driven by the alternating vortex shedding of the cylinder.

A temporal refinement study was accomplished comparing Strouhal frequency versus time step. Results for both first and second order time accurate methods are presented in Figure 5. The results for the second-order scheme asymptote quadraticly, implying that second-order accuracy was realized. The first order scheme produced a linear convergence rate with the same asymptotic Strouhal number of 0.2256. Higher-order temporal

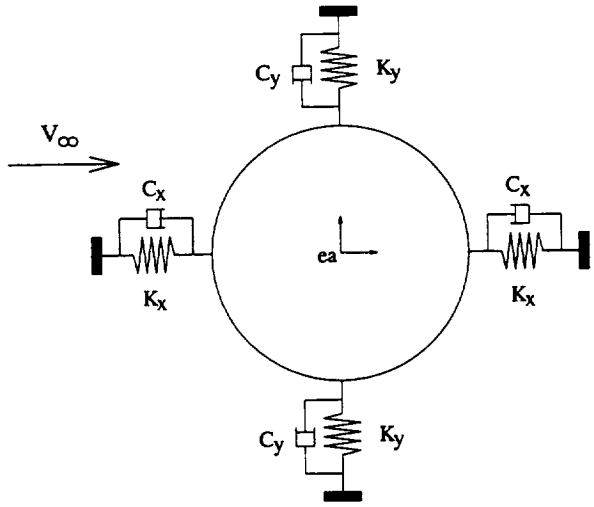

Figure 4 Elastically Mounted Cylinder Schematic

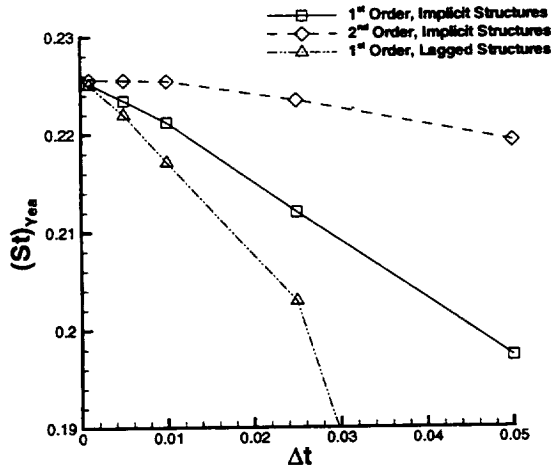

Figure 5 Temporal Accuracy of Synchronized and Lagged Coupling Methods

accuracy could not have been achieved with errors like lagging errors. The three subiterations employed effectively eliminated the lagging error as well as greatly reduced the factorization and linearization errors in the fluid solution, allowing the coupled system to approach second-order accuracy.

Comparison of the synchronized coupling method to a traditional lagged structures method was accomplished by removing the structural solver from the subiteration

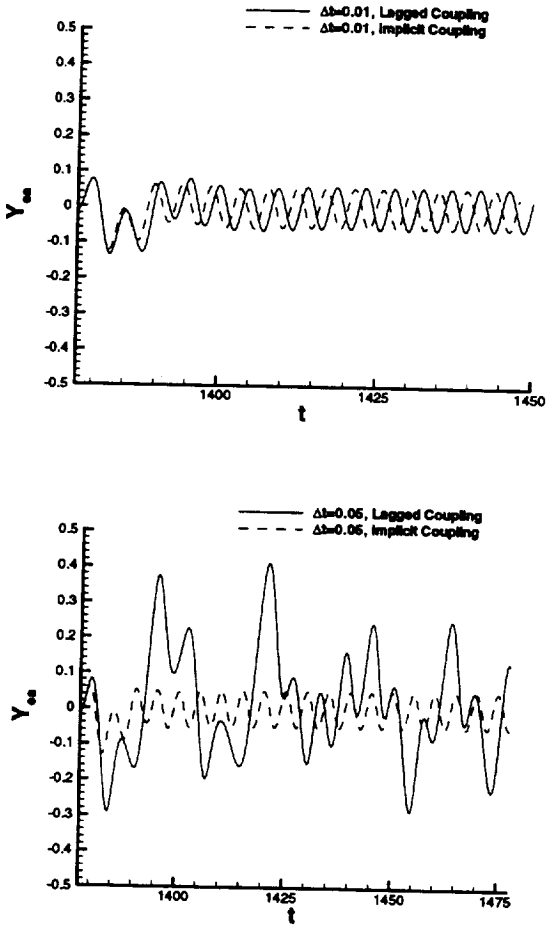

Figure 6 Coupled and Lagged Elastic Response

loop. The convergence curve is also depicted in Figure 5 and is clearly first-order in time. The increase in slope of the lagged structures convergence curve was attributed to the linearization, factorization, and lagging errors not eliminated through subiteration. A comparison between the second-order coupled scheme and the lagged structures scheme implies that higher levels of accuracy can be achieved for this case with less overall computational expense.

The impact of temporal synchronization is even more critical when larger time steps are investigated. Figure 6 shows the time history of the vertical displacement of the cylinder for two different time steps and two different coupling strategies. For the smaller time step, both responses are sinusoidal with constant amplitude. The lag effect in this case only causes a frequency that is higher. However for the larger time step the results are much different. The coupled response still accurately represents the solution behavior that is known to be correct, while the lagged response undergoes a dramatic change. The response is no longer sinusoidal and the amplitude changes over a considerable range. In this case, lag errors do not merely degrade accuracy but actually induce a spurious solution.

Spatial Resolution

The computational cost of analysis scales with spatial resolution, and this induces a natural frugality when it comes to spatial discretization. However, to achieve highly accurate simulations of non-linear flow conditions often requires considerable resources. The following example of a simple transonic wing flutter case[16] demonstrates the difficulty of achieving grid independent results.

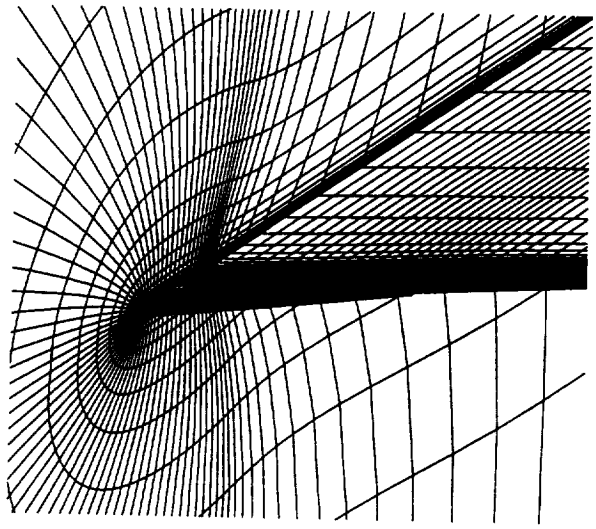

Figure 7 C-H Grid Topology for AGARD 445.6 Wing

The configuration to be computed is the AGARD 445.6 weakened wing model. The geometry consists of a wing with an aspect ratio, AR=1.6525, a taper ratio of 0.6576, a quarter-chord sweepback angle of 45 degrees and a NACA65A004 airfoil section in the streamwise direction. Experimental flutter results as well as a structural model for the wing using 4 mode shapes are presented in reference 16. A series of three C-H type grids (see Figure 7) have been developed for this geometry, with total number of points ranging from 300,000 to 2,000,000.

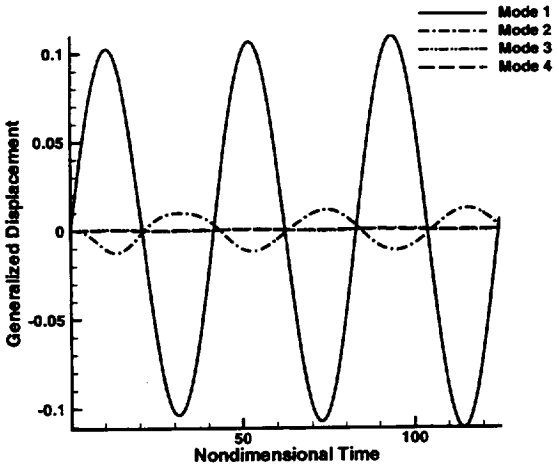

Figure 8 Dynamic Response of Structural Modes, Mach 0.96

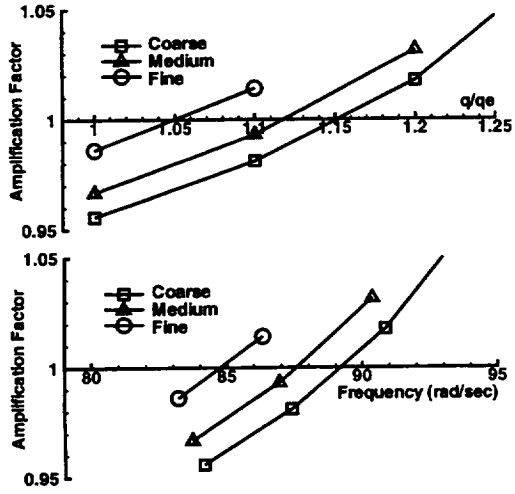

Figure 9 Dynamic Pressure and Frequency of Flutter, Mach 0.96

Dynamic computations of wing flutter are carried out for the AGARD wing for two Mach numbers, 0.96 and 1.141. Each Mach number case is run for a series of dynamic pressures to determine the flutter point. Reynolds numbers (based on the wing rootchord) for the two cases are in the range Re=614500 to 879000. In each case the flow is assumed turbulent and the Baldwin-Lomax turbulence model [CITE] is implemented to account for turbulence effects.

A nondimensional time step $\Delta t = 0.05$ is used for all the flutter computations, allowing for approximately 800 time steps per cycle of structural oscillation. All simulations are started from a steady-state, rigid, non-lifting condition, and then a small velocity perturbation is given to the first bending mode.

Figure 8 shows the response of the first four modes for the Mach 0.96 case on the medium mesh for a flutter condition $q/q_e=1.2$ (where $q_e=61.3$ lbf/ft^2 is the experimental dynamic pressure for flutter). The first bending mode appears to be the dominant mode with only the second mode showing any significant effect of the impulse applied to the first mode. The growth or decay of the first bending mode is analyzed, therefore, to determine the flutter location.

The results of all the computations performed for Mach 0.96 are summarized in Figure 9. In this figure the amplification factor is defined as the ratio of the magnitude of a peak with the magnitude of the previous peak of corresponding sign. The response frequency is determined from the period between two successive peaks of the same sign. A value of amplification factor greater than 1.0 implies flutter.

From this figure the effects of varying dynamic pressure, q, and mesh resolution can be clearly seen. As dynamic pressure is increased the amplification factor grows and eventually exceeds 1.0 and the wing begins to flutter. This figure indicates that the effect of improved mesh resolution is to reduce the computed flutter speed for the Mach 0.96 case, though grid independence has not yet been achieved. Inspection of the wing surface pressure reveals that a shock forms near the tip and is most clearly resolved only on the finest grid.

The next case computed, Mach 1.141, has proved much more challenging to reproduce the correct experimental flutter behavior. Unlike the Mach 0.96 case, this case has a strong shock that is located outboard, on the aft portion of the wing. The presence of the shock and the corresponding shock/boundary-layer interaction makes this a much more complicated flow condition. Figure 10 displays the time history of the first four modes for a dynamic pressure $q/q_e = 1.8$ (where $q_e = 105.3$ lbf/ft^2). As in the Mach 0.96 case, the first mode appears to be the dominant mode, though the higher modes appear to play more of a role for Mach 1.141. For this case it is also necessary to run significantly more cycles than for Mach 0.96 before a clear determination of the response is made.

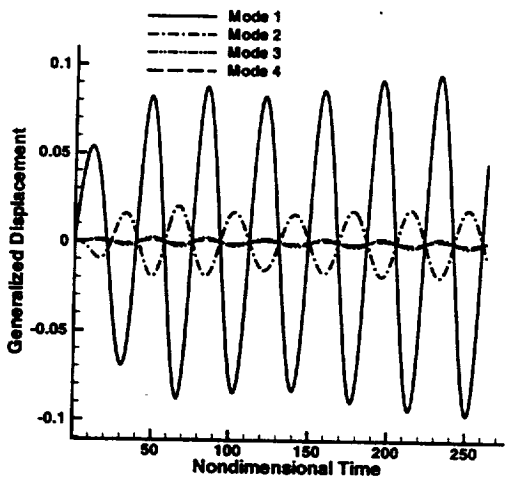

Figure 10 Dynamic Response of the Structural Modes, Mach 1.141

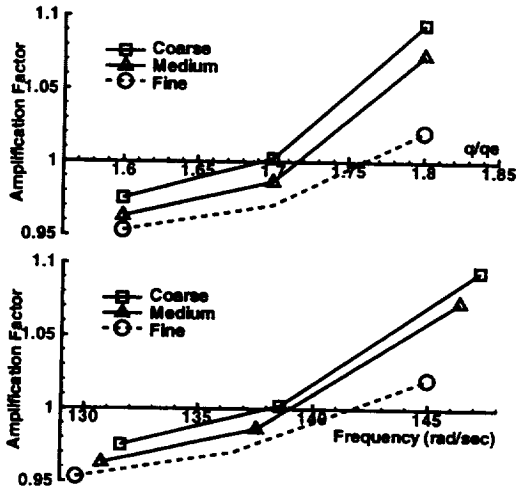

Figure 11 Dynamic Pressure and Frequency of Flutter, Mach 1.141

Figure 11 summarizes the results for the computations at increasing dynamic pressures on the three meshes. Since no computation was performed for q/qe = 1.7 on the fine mesh, the dashed line represents a best estimate of the shape of the curve for this grid. This figure demonstrates that the effect of grid resolution is to increase the flutter speed and frequency for this case. This trend is opposite from the situation for Mach 0.96. The most significant effect noted is a strengthening and sharpening of the shock wave on the wing.

Non-Linear Flow Features

The motivating reason for using CFD techniques for aeroelastic simulation is to capture non-linear flow features. The presence of shock systems and separated flow can effect the elastic stability of a structure in ways difficult to predict. An entire class of aeroelastic response, the limit-cycle oscillation (LCO), depends on some non-linear mechanism, usually from the fluid loads, to limit the growth of a classical flutter response[18], as seen in the following example.

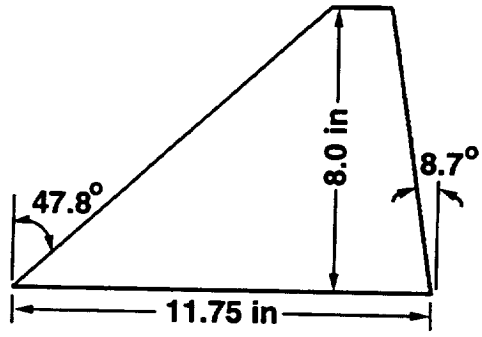

Figure 12 Thin Plate Wing Planform

For this LCO study, the simple, thin-plate wing model of reference 19 was chosen. This wing has a cropped delta planform cut from a 0.035 inch thick steel plate (see Figure 12). A computational grid system of eight grids totalling about 850,000 points was used to simulate the unsteady flow over the wing. The nature of the structural response is considered and details of the unsteady flowfield are indicated. The flow conditions chosen ranged from 0.869 to 0.879 Mach number. The wing is initially at rest with angle of attack of zero. The structural response was initiated by impulsively adding a discrete velocity to the first generalized displacement.

In order to understand the structural response of the wing, the time histories of the generalized displacements are plotted for four different values of dynamic pressure and shown in Figure 13. The first four modes are shown, although the fourth and higher modes (not shown) do not appear to participate significantly in the structural response.

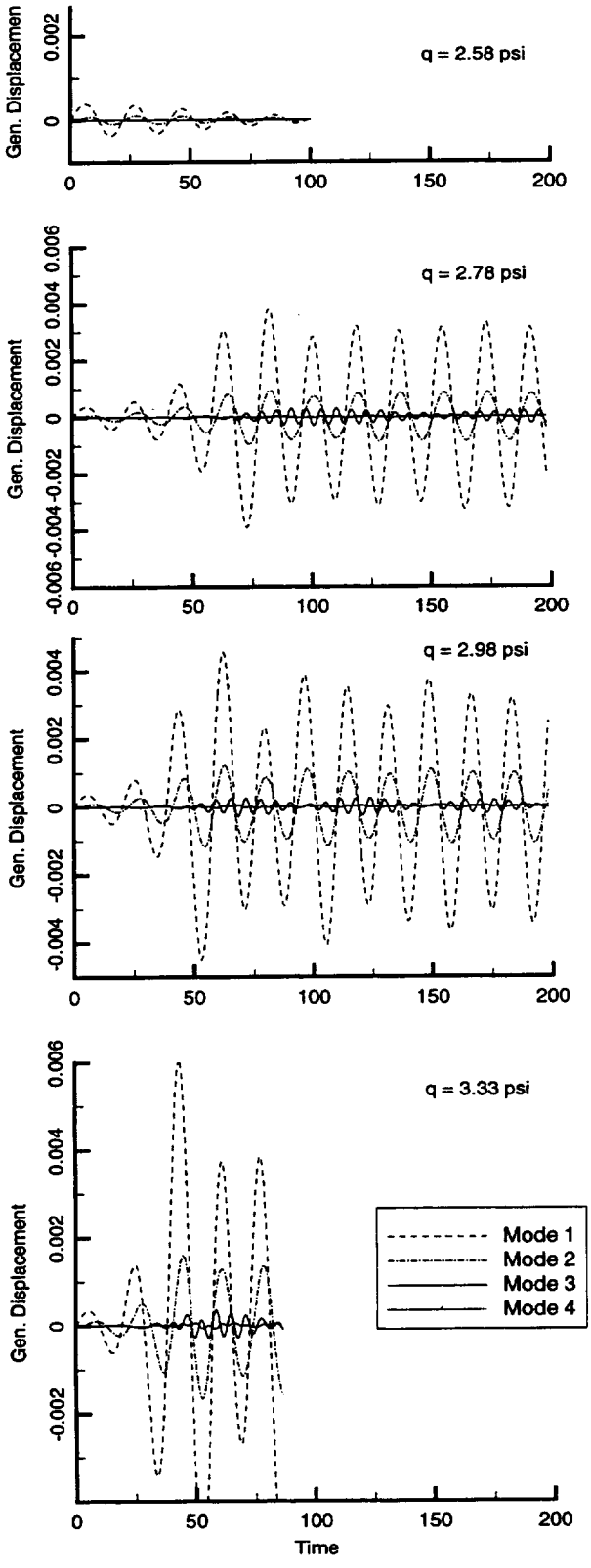

Figure 13 Gen. Displacement vs Dynamic Pressure

The dominate response is the first bending mode, a tail high bending, and it can be seen in all of the responses. For the lowest value of dynamic pressure (q=2.58 psi) the modal response does not grow from the initial input but damps out monotonically. This indicates that the flutter onset boundary lies at a larger value of dynamic pressure.

The next two values of dynamic pressure (q=2.78, 2.98 psi) are similar in their modal responses. Initially the amplitude grows in a manner consistent with classical, linear flutter. Afterward the amplitude rolls off and settles into a limit cycle oscillation with a single dominant frequency. The last value of dynamic pressure (q=3.33 psi) is similar, but the amplitude levels have increased to levels not observed experimentally.

In all the cases, the response initially consists of the first mode interacting with the second, primary torsion. Torsion lags bending such that it adds energy to the wing and increases the amplitude of the response, consistent with linear flutter theory. During this initial phase, the third mode, which is secondary bending, has a small amplitude and is in opposite phase with primary torsion.

After the amplitude of the response has grown, there is a change in the third mode. Where it responded at the fundamental frequency (~50 Hz) initially, it changes to the third harmonic of the fundamental frequency (~150 Hz, which is close to its natural frequency, ~130 Hz) and its amplitude increases rapidly. As the second bending response grows, the amplitude of first bending decreases. It can be seen that the interaction of second bending is stabilizing and balances the destabilizing interaction of the torsional mode.

Several contour plots have been included to highlight some of the highly non-linear flow features that are present during the sustained oscillation. Figure 14 shows the pressure contours on the upper surface of the wing and Figure 15 shows pressure contours in streamwise plane that cuts at 67% of span. In each figure there are plots from two sequential points in time that illustrate the flow structure during part of an oscillation.

In Figure 14, the surface shock structure can be seen strengthening initially and then weakening. From Figure 15 it can be seen that the shock strengthens and then lifts off of the surface of the wing as it weakens, indicating a stalled condition. The roll-up of the tip vortex can be seen at the top of Figure 14. It is initially small and coherent, then strengthens and grows, and

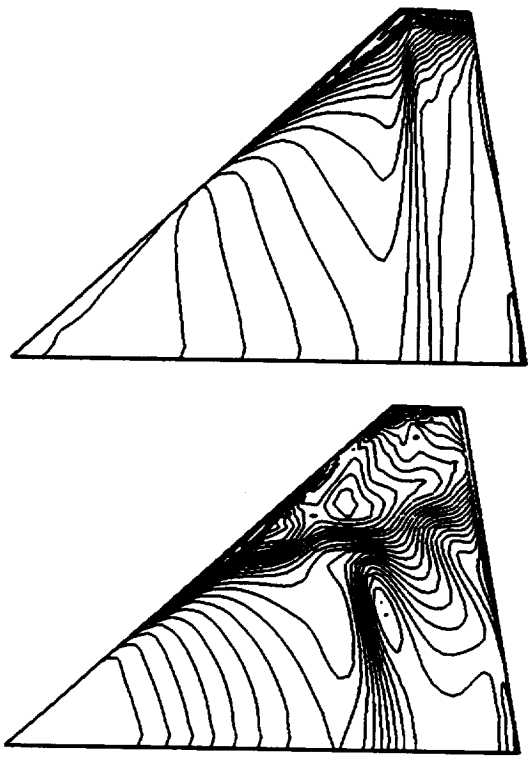

Figure 14 Pressure on the Upper Surface

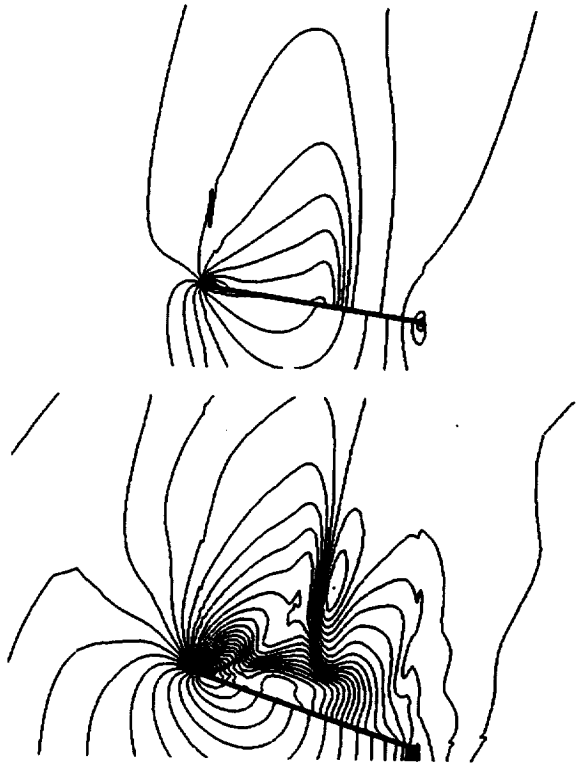

Figure 15 Pressure at 67% Span

finally interacts with the shock structure, becoming diffused.

This large amplitude limit cycle oscillation demonstrates several important nonlinear mechanisms that may effect dynamic aeroelastic stability. There is a complex shock pattern that moves across the wing, a stalled flow region, and a strong vortex roll-up over the wingtip. Exactly how these features may interact with each other and with the structural response of the wing is a research topic requiring experiment and simulation using the full capabilities of CFD.

Fluid-Structure Coupling

Sometimes to lessen the complexity of the fluid-structure interaction problem, a decoupling assumption is invoked. For an uncoupled analysis, the flow is calculated for a rigid configuration to provide representative loads to structural models that are solved separately. While this can be very expeditious, it may neglect critical feedback mechanisms between the two solutions. This potential is highlighted by the following study of a delta wing with flexible tails[20].

These solutions were obtained for a 70 degree sweep delta wing with twin tail configuration at an angle-of-attack of 23.2 deg and a freestream Mach number of 0.2 which duplicate the flow conditions of reference 21. The baseline solution consists of a time step of 0.0005, a dynamic pressure of 0.41144 lbs/in^2, a freestream density of 1.3757x10^{-6} slugs/in^3, vanishing structural damping, 10 structural modes describing the structural model and a baseline grid system of 17 grids and almost half a million points. The dynamic pressure was varied by holding velocity constant and increasing or decreasing the freestream density. The baseline conditions were chosen to simulate typical sea-level conditions.

For these conditions, a pair of leeside vortices roll-up from the edge of the delta wing, undergo a spiral-type vortex breakdown, and impinge on the tails downstream. A three-dimensional representation of the wing/tail flowfield is presented in Figure 16. Crossplane contours and an isosurface of total pressure are displayed. Following breakdown, the isosurface appears to 'wind' in a direction opposite to that of the rotational sense of the flow. The complete vortex structure rotates in the same sense as the flow causing the windings to impact the tail at different locations over time. Also, the vortex break-

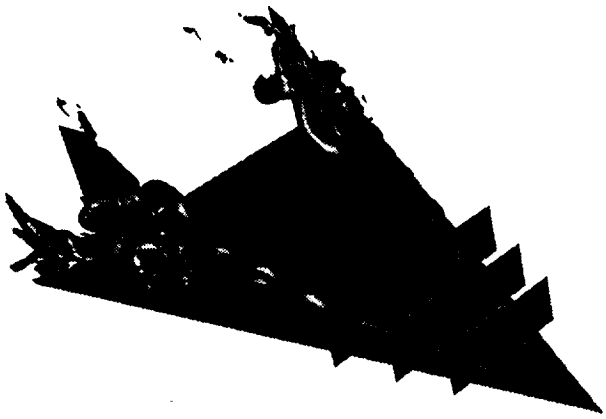

Figure 16 Crossplane Contours and Isosurface of Total Pressure over Delta Wing

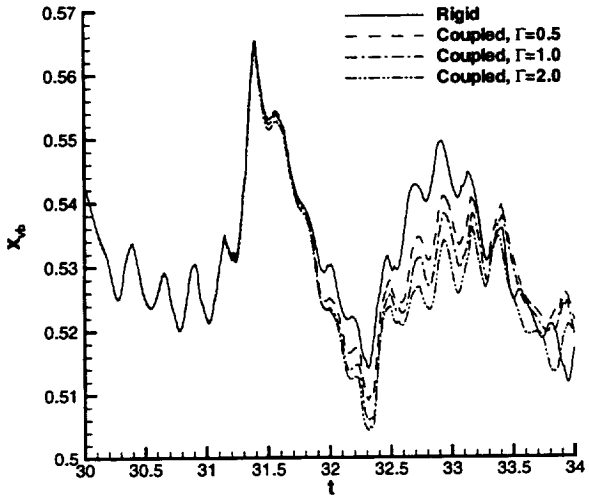

Figure 17 Time History of Vortex Position for Varying Dynamic Pressure

down position moves fore and aft over the delta wing as a function of time. The areas of reduced pressure produced by the windings impacting the tail in the lower outboard and mid inboard regions are apparent in the isosurface for this particular instant in time. Impact of the vortex with the tail precludes any further 'winding' of the isosurface downstream.

A study was done over a range of dynamic pressures. The amplitude of the tail response grows as a function of freestream dynamic pressure causing an increase in the disturbance propagating forward on the delta wing. The disturbances result in movement of the vortex breakdown position. Figure 17 shows the change in the vortex breakdown position time history as a function of dynamic pressure. The rigid tail vortex breakdown position is included as a reference. The qualitative behavior of the time history for each dynamic pressure considered is similar for the time period evaluated (four characteristic times), but the fluid-structure coupling is seen to be important. As the dynamic pressure is increased from the limiting case (rigid tail), the vortex breakdown position moves forward. It is interesting to note that it takes on the order of two characteristic times for the flexible tail disturbance to propagate forward and effect the breakdown position. This feedback between the fluid and structure would not take place in a load-linearized or uncoupled analysis.

Conclusions

This paper outlined a methodology for simulating non-linear fluid/structure interactions. A robust unsteady CFD capability was included that captures viscous effects, transonic conditions, and separated flow. The linear structural model, while not complex, was able to account for the basic structural dynamics of surfaces loaded in highly non-linear flow regimes. Several applications of this aeroelastic analysis technique yielded considerable insight into the critical issues of highly accurate simulation.

The importance of satisfying the GCL constraint was noted with an example of the effect of moving mesh error. Synchronizing the fluid and structural states was shown to be critical for high accuracy. The subiterating technique used here allowed for high orders of temporal accuracy and safeguarded against spurious solutions due to lagging error. Many non-linear flow features require high levels of spatial resolution. An example for a wing flutter case showed that even relatively fine grids may not achieve grid independent results.

CFD-class aerodynamic modeling is required for many types of aeroelastic interactions. A study of limit cycle oscillation indicated that complex shock systems, coherent vortex formations, and massive leading-edge separation were all present and contributing to a highly non-linear flow environment. Aeroelastic analysis is best done with full interaction between the fluid and structures solvers. For a case of vortical buffeting of a tail, the structural response had a directed impact on the aerodynamic flow field that was driving the buffet.

Acknowledgments

This work was sponsored by the Air Force Office of Scientific Research under Task 2307 AW, monitored by Dr. L. Sakell. This work was supported in part by a grant of HPC time from the DoD HPC Shared Resource Centers at ASC, CEWES, and NAVO.

References

[1] Morton, S. A., Melville, R. B., Visbal, M. R., "Accuracy and Coupling Issues of Aeroelastic navier-Stokes Solutions on Deforming Meshes," AIAA Paper 97-1085, April 1997.

[2] Rizzetta, D.P. and Visbal, M. R., "Comparative Numerical Study of Two Turbulence Models for Airfoil Static and Dynamic Stall," AIAA Paper 92-4649, June 1992.

[3] Visbal, M. R., "Structure of Vortex Breakdown on a Pitching Delta Wing," AIAA Paper 93-0434, January 1993.

[4] Gordnier, R. E. and Visbal, M. R., "Numerical simulation of Delta-Wing Roll," AIAA-93-0554, January, 1993.

[5] Melville, R.B., Morton, S. A., Rizzetta, D.P., "Implementation of a Fully-Implicit, Aeroelastic Navier-Stokes Solver," AIAA Paper 97-2039, July 1997.

[6] Thomas, P.D. and Lombard, C.K., "Geometric Conservation Law and Its Application to Flow Computations on Moving Grids," *AIAA Journal*, Vol. 17, No. 10, pp. 1030-1037.

[7] Melville, R., Morton, S., "Fully Implicit Aeroelasticity on Overset Grid Systems," AIAA Paper 98-0521, Reno, NV, 1998.

[8] Benek, J. A., Dougherty, F. C., Steger, J. L., Buning, P. G., "Chimera: A Grid-Embedding Technique," AEDC-TR-85-64, Dec. 1985.

[9] Smith, M. J., Hodges, D. H., Cesnik, C. E. S., *An Evaluation of Computational Algorithms to Interface Between CFD and CSD Methodologies*, WL-TR-96-3055, Nov. 1995

[10] Bendiksen, O. O., "Nonunique Solutions in Transonic Aeroelasticity," CEAS International Forum on Aeroelasticity and Structural Dynamics 1997, Rome, Italy, June 1997.

[11] Beam, R. and Warming, R., "An Implicit Factored Scheme for the Compressible Navier-Stokes Equations," *AIAA Journal*, Vol.16, April 1978, pp. 393-402.

[12] Pulliam, T.H. and Chaussee, D.S., "A Diagonal Form of an Implicit Approximate-Factorization Algorithm," Journal of Computational Physics, Vol 39, No 2, pp. 347-363.

[13] Jameson, A., Schmidt, W., and Turkel, E., "Numerical Solutions of the Euler Equations by Finite Volume Methods Using Runge-Kutta Time Stepping Schemes," AIAA Paper 81-1259, June 1981.

[14] Byun, C., Guruswamy, G. P., "Static Aeroelasticity Computations for Flexible Wing-Body-Control Configurations," AIAA Paper 96-4059, April 1996.

[15] Selvam, R. P., Visbal, M. R., Morton, S. A., "Computation of Nonlinear Viscous Panel Flutter Using a Fully-Implicit Aeroelastic Solver," AIAA Paper 98-1844, Long Beach, CA, 1998.

[16] Gordnier, R., Melville, R., "Accuracy Issues for Transonic FlutterUsing 3-D Navier-Stokes," AIAA Paper 98-1729, Long beach, CA, 1998.

[17] Yates, E. C. Jr., *AGARD Standard Aeroelastic Configurations for Dynamic Response I.-Wing 445.6*, AGARD-R-765, July 1988.

[18] Melville, R., Gordnier, R., "Numerical Simulation of Large Amplitude Aeroelastic Wing Response," AIAA Paper 98-2657, Albuquerque, NM, 1998.

[19] Schairer, E.T., Hand, L.A., "Measurements of Unsteady Aeroelastic Model Deformation by Stereo Photogrammetry," AIAA Paper 97-2217, Atlanta, GA, 1997.

[20] Morton, S., Rizzetta, D., Melville, R., "Numerical Simulation of the Interaction Between a Leading-edge Vortex and a Flexible Vertical Tail," AIAA Paper 98-1957, Long Beach, CA, 1998.

[21] Rizzetta, P., "Numerical Simulation of the Interaction Between a Leading-Edge Vortex and a Vertical Tail," AIAA Paper 96-2012, New Orleans, LA, 1996.

DIVERGENCE AND FLUTTER OF ADAPTIVE LAMINATED COMPOSITE AIRCRAFT WINGS FEATURING DAMAGED BONDING INTERFACES

L. Librescu* - U. Icardi+ and M. Di Sciuva+

* Virginia Polytechnic Institute and State University, Blacksburg, VA 24061-0219, USA
+ Politecnico di Torino, Corso Duca degli Abruzzi 24-10129 Torino, ITALY

SUMMARY

A study of the aeroelastic divergence and flutter of swept-aircraft wings made-up from laminated composite materials featuring nonrigidly bonded interfaces is presented.

Among the goals to be reached, those of capturing and revealing the effects played by interlaminae bonding imperfections on static and dynamic aeroelastic instabilities, and that of the incorporation of a feedback control methodology are investigated. Implementation of a feedback control methodology enabling one: a) to counteract the detrimental effects of bonding imperfections, and b) to enhance the overall aeroelastic response behavior, is also considered.

In order to obtain results emphasizing the implications of bonding imperfections, the aeroelastic problem will be considered in a restricted sense, i.e. for the case when only the bending degree of freedom is involved. In this context, results addressing the problem of the influence of interfacial bonding imperfection, and feedback control on static and dynamic aeroelastic instabilities of swept-aircraft wings are presented, and pertinent conclusions are outlined.

INTRODUCTION

Over the past two decades advanced composite material systems have been increasingly used in the design of structural elements of flight vehicles, and is more than sure that this trend will continue and even intensify in the years ahead. In addition to the well-known superior features over monolithic materials, the anisotropy and heterogeneous character of composites provide new degrees of freedom for an optimum design of advanced flight vehicle structures. In this context, it should be noticed that aeroelastic tailoring of wing structures composed of advanced composite materials can play a tremendous role in the design of next generation of space vehicles. The successful design of the experimental sweptforward wing aircraft X-29, in which the aeroelastic tailoring was used to eliminate the detrimental wash-in effect, jeopardizing its free flight, demonstrates in full the power of this technology towards the enhancement and optimization of the aeroelastic behavior of advanced flight vehicles.

Within the entire body of literature devoted to the *aeroelasticity of laminated composite aircraft wings,* a perfect bonding between the adjacent constituent laminae, implying continuous displacement and tractions across these interfaces was postulated. However, in many cases, this assumption does not always correspond to reality. Indeed, as a result of environmental and/or fatigue effects, interface bond deteriorations can appear in the

structure. Needless to say, the interlayer bond damages can have detrimental implications upon the overall behavior of the structure, involving its static, dynamic and stability response. The aim of this study is just to investigate the effects of these imperfections upon the divergence and flutter of laminated composite wing structures.

To this end, a newly developed theory of laminated structures featuring nonrigidly bonding interfaces will be used (Refs. 1-3). Such a theory can accommodate all the intermediate cases between the ones of the perfectly bonded and completely debonded interfaces. Due to the complexity of the associated aeroelastic governing equations resulting in the case of the inclusion of damaged bonding interfaces, in order to get a measure of their implications, two special cases will be investigated: a) the divergence in pure bending of sweptforward wings (see Ref. 4), and b) the pure-bending flutter of sweptback wings (see Ref. 5). In addition to the possibility of capturing in an easier way the effects of bonding imperfections, the approach of the bending flutter can provide the most critical instability conditions which can occur at large wing sweep angles.

As a result, after summarizing the aeroelastic governing system corresponding to the bending of wing structures composed of laminated composite structures featuring damaged bonding interfaces, the associated aeroelastic instability problems of swept wings will be investigated. As a preparatory step, and in order to be reasonably self-contained, the basic kinematic equations of laminated solid beams featuring damaged interfaces will be displayed. Moreover, based upon the converse piezoelectric effects, a feedback control capability will be incorporated, and results concerning the closed-loop divergence and flutter instabilities experienced by the composite wings featuring interlaminae imperfections will be supplied.

BASIC EQUATIONS FOR BENDING OF LAMINATED COMPOSITE AIRCRAFT WINGS FEATURING INTERLAMINAE DAMAGES

The case of symmetrically laminated composite cross-ply beams of solid rectangular cross-section $(b \times h)$, consisting of a finite number $\mathcal{N}$ of linearly elastic layers of uniform thickness $h^{(k)}$ is considered. One assumes that piezoactuator layers are bonded on the top and bottom faces of the beam, and that are spread over its entire span. In the forthcoming developments the affiliation of any quantity to the kth layer $(k = \overline{1,\mathcal{N}})$, is identified by the superscript (k) in brackets placed on the left of the respective quantity.

The points of the beam are referred to an orthogonal Cartesian coordinate system (x, y, z), where y, z are the cross-section coordinates and x is the spanwise coordinate. (see Fig. 1) For the sake of convenience, the undeformed bottom plane of the laminate is selected as the reference plane. The distances along z between the reference plane and the undeformed upper and bottom faces of the kth layer are denoted by ${}^{(k)}Z^{+}$ and ${}^{(k)}Z^{-}$, respectively.

It is assumed that the material of each layer of the host structure features orthotropic properties, the principal axes of orthotropy being parallel at each point to the in-plane geometrical axes, and that the piezoactuators exhibit transversal-isotropic properties, the surface of isotropy being parallel to the (x, y) plane. It is also assumed that the direction of polarization coincides with the z-axis, this implying that $\mathcal{E}_z$ is the only component of the electric field considered in the analysis. Under these assumptions, the following stress-strain

relations hold valid for each constituent layer:

$$\sigma_{xx} = \tilde{\sigma}_{xx} + \delta_p \hat{\sigma}_{xx} = \overline{Q}_{11}\epsilon_{xx} - \delta_p \overline{e}_{zx}\mathcal{E}_z; \quad \sigma_{xz} = \tilde{\sigma}_{xz} = 2\overline{Q}_{44}\epsilon_{xz}, \tag{1}$$

$\tilde{\sigma}_{xx}$ and $\hat{\sigma}_{xx}$ being the mechanical and piezoelectric contributions to the total stress, respectively. Herein δ_p is a tracer taking the value 0 or 1, depending on whether the layer belongs to the host structure or to the piezoactuator layer, respectively.

$\overline{Q}_{11}$ and $\overline{Q}_{44}(\equiv Q_{44})$ appearing in previous stress-strain relations are the reduced components of the stiffness tensor, whereas $\overline{e}_{zx}$ is the reduced piezoelectric constant.

In the light of Eq. (1), $\hat{\sigma}_{xx}$ is the only piezoelectrically induced stress and is proportional to the applied electric field $\mathcal{E}_z$, assumed constant through the thickness of piezoactuators.

In order to substantiate the theory of laminated composite plates featuring interlaminar slips, the following requirements at the interface between two consecutive kth and $(k+1)$th layers have to be fulfilled:

- the condition expressing the *continuity of transverse shear stresses*

$$S_{xz}|_{z=(k)Z^+} = S_{xz}|_{z=(k+1)Z^-} \tag{2}$$

and

- the condition expressing the *interlaminar jump of spanwise displacement* at the interface between two contiguous layers l and $l+1$

$$^{(l)}\hat{U} = {}^{(l+1)}U|_{z=(l+1)Z^-} - {}^{(l)}U|_{z=(l)Z^+} \tag{3}$$

In addition, the free shear traction condition at the top (i.e. $z = h$) and bottom (i.e. $z = 0$) planes of the beam, expressed as

$$\sigma_{xz}|_0^h = 0. \tag{4}$$

should be fulfilled, where h denotes the laminate thickness.

In developing a displacement field associated with the bending of plate-beam structures that fulfills the interfacial shear traction continuity requirement and exhibit the interfacial displacement jump the following representations for the spanwise U and transverse W displacement components are postulated (see Refs. 1 and 2)

$$U(x,z,t) = u(x,z,t) + \tilde{U}(x,z,t) + \hat{U}(x,z,t), \tag{5a}$$

$$W(x,z,t) = w(x,t). \tag{5b}$$

Equation (5b) states that the transverse deflection is uniform throughout the entire laminate thickness. The three terms intervening in Eq. (5a) are detailed as follows:

The first term

$$u(x,z,t) = \sum_{r=0}^{3} z^r u^{(r)}(x,t) \tag{6}$$

represents the contribution to the in-plane displacement which is a continuous function of the beam thickness coordinate z, and with the continuous first derivative across the laminate thickness. Herein, and in the following developments, index (r) in brackets placed on the right of a quantity represents its contribution to the development in power series across the thickness of the respective quantity. This presentation is consistent with the standard expansion used in the third-order single-layer or smeared laminate plate models.

The second term

$$\tilde{U}(x,z,t) = \sum_{k=1}^{\mathcal{N}-1} {}^{(k)}\phi(x,t)(z - {}^{(k)}Z^{+})\mathcal{H}_k \tag{7}$$

gives a contribution to the spanwise displacement which is continuous with respect to the z coordinate, but with discontinuous first derivative at the interfaces between the adjacent layers. This is the expansion used in the *zig-zag* multilayered plates models enabling one to fulfill the continuity of the transverse shear stresses at each layer interface (see, Refs. 6 and 7). Herein $\mathcal{H}_k(\equiv \mathcal{H}(z - {}^{(k)}Z^{+}))$ is the Heaviside step function and ${}^{(k)}\phi(x,t)$ are yet unknown functions to be determined by satisfying the continuity conditions, Eq. (2).

Enforcing the continuity of transverse shear stresses at the layer interface, Eq. (2), the functions ${}^{(k)}\phi(x,t)$ are determined as:

$${}^{(k)}\phi(x,t) = {}^{(k)}a w_{,x} + \sum_{r=0}^{3} {}^{(k)}a^{(r)} u^{(r)} \tag{8}$$

Herein ${}^{(k)}a$, ${}^{(k)}a^{(r)}$ are referred to as the, *continuity constants* that depend only on the transverse shear mechanical properties of constituent laminae.

These are defined as:

$${}^{(k)}a = {}^{(k)}A + {}^{(k)}A \sum_{q=1}^{k-1} {}^{(q)}a \tag{9}$$

and

$${}^{(k)}a^{(r)} = {}^{(k)}A r({}^{(k)}Z^{+})^{r-1} + {}^{(k)}A \sum_{q=1}^{k-1} {}^{(q)}a^{(r)} \tag{10}$$

with

$${}^{(k)}A = {}^{(k+1)}S_{44}({}^{(k+1)}Q_{44} - {}^{(k)}Q_{44}) \tag{11}$$

S_{44} being the transverse shear compliance.

Finally, the *third term* in Eq. (5a) represented as

$$\hat{U}(x,z,t) = \sum_{k-1}^{\mathcal{N}-1} {}^{(k)}\hat{U}(x,t)\mathcal{H}_k, \tag{12}$$

represents the jump of the spanwise displacement component across the interfaces featuring bonding imperfections of the slip type (see, Ref. 8).

For the interlaminar displacement jump ${}^{(k)}\hat{U}$ across the interface $z = {}^{(k)}Z^{+}$, we postulate a linear shear slip law

$${}^{(k)}\hat{U}(x,z) = {}^{(k)}\mathcal{R}(x,z)\ {}^{(k)}S_{xz}(x,z) \tag{13}$$

where $z = {}^{(k)}Z^{+}$

Herein ${}^{(k)}\mathcal{R} \geq 0$, denotes the imperfect bonding constant between the kth and $(k+1)$th layers.

In addition to the two extreme situations corresponding to: (i) perfect bonding assumption implying ${}^{(k)}\mathcal{R} = 0$ this, yielding ${}^{(k)}\hat{U} = 0$, and (ii) completely debonding

interfaces, implying ${}^{(k)}\mathcal{R} = \infty$ this yielding ${}^{(k)}S_{xz} = 0$, Eq. (13), covers also, for any finite postive value of $({}^{(k)}\mathcal{R} \neq 0, \infty)$ all the intermediate cases of imperfectly bonded interfaces.

This is the approach followed also in the earlier works dealing with bonding imperfections (see, Refs. 3, 9, and 10). It should be mentioned that using ultrasonic signature, a great deal of theoretical and experimental work directed toward characterization of interface imperfections and, implicitly, toward determination of sliding constant ${}^{(k)}\mathcal{R}$ was accomplished so far. The reader is referred to Ref. 11 where, in addition to a presentation of the state-of-the-art on this matter, rich references to the pertinent literature are supplied.

From the studies accomplished so far in this area, it becomes apparent that corresponding to small values of ${}^{(k)}\mathcal{R}$, strong variations in the local and global structural responses can emerge.

Upon enforcing the absence of shear traction at the top and bottom faces of the beam, Eq. (4), the following final form of the spanwise displacement compo nent across the thickness is obtained:

$$U(x, z, t) = -zw_{,x} + \mathcal{L}u^{(3)} \tag{14}$$

Equations (5b) and (14) supply the final form of the displacement field as used in this analysis. The expression of $\mathcal{L}$ appearing in Eq. (14) is as follows:

$$\mathcal{L} = \mathcal{P} + \sum_{k=1}^{\mathcal{N}-1} {}^{(k)}\mathcal{R}\ {}^{(k)}Q_{44}\mathcal{P}_{,z} \tag{15}$$

where

$$\mathcal{P} = z^2\left(z - \frac{A^{(3)}}{A^{(2)}}\right) + \sum_{k=1}^{\mathcal{N}-1} {}^{(k)}b^{(3)}(z - {}^{(k)}Z^{+})\mathcal{H}_k \tag{16}$$

and

$${}^{(k)}b^{(3)} = {}^{(k)}a^{(3)} - \frac{A^{(3)}}{A^{(2)}}{}^{(k)}a^{(2)} \tag{17}$$

whereas $A^{(2)}$ and $A^{(3)}$ are obtainable from $A^{(r)} = rh^{(r-1)} + \sum_{k=1}^{\mathcal{N}-1} {}^{(k)}a^{(r)}$ for r= 2 and r = 3, respectively. As a result, the non-zero axial and transverse shear strain components can be expressed in condensed form as:

$$2\varepsilon_{xx} = -2zw_{,xx} + 2\mathcal{L}u^{(3)}_{,x} \tag{18}$$

$$2\varepsilon_{xz} = \mathcal{L}_{,z}u^{(3)} \tag{19}$$

With the use of the constitutive equations (1) and of the expression for the transverse shear strain component Eq.(19), one obtains the following expression for the displacement jump at the kth upper interface (i.e. at $z = {}^{(k)}Z^{+}$,

$${}^{(k)}\hat{U} = {}^{(k)}R\ {}^{(k)}Q_{44}\ \mathcal{L}_{,z}u^{(3)} \tag{20}$$

It is worthwhile to note that the only component of the generalized displacement appearing in ${}^{(k)}\hat{U}$ is the transverse shear rotation $u^{(3)}$.

Consistent with the previously displayed displacement field, the equations of motion of symmetrically laminated beam featuring interfacial imperfections of the slip type, and

exposed to transversely distributed load P_z, as derived via the application of Hamilton's variational principle are:

$$\tilde{M}_{,xx} = -P_z + \mu_1 \ddot{u}^{(3)}_{,x} - m_2 \ddot{w}_{,xx} + m_0 \ddot{w} + \hat{M}_{,xx} \tag{21a}$$

$$\tilde{S}_{,x} - \tilde{T} = \pi_0 \ddot{u}^{(3)} - \mu_1 \ddot{w}_{,x} \tag{21b}$$

At the same time, the variationally consistent boundary conditions are:

$$\begin{array}{lll} w = \overline{w} & \text{or} & \tilde{M}_{,x} + \mu_1 \ddot{u}^{(3)} - m_2 \ddot{w}_{,x} = \hat{M}_{,x} \\ w_{,x} = \overline{w}_{,x} & \text{or} & M(\equiv (\tilde{M} - \hat{M})) = \overline{M} \\ u^{(3)} = \overline{u}^{(3)} & \text{or} & \tilde{S} = \overline{S} \end{array} \tag{22}$$

where the overbars denote prescribed quantities.

In the previously displayed equations the mechanical and piezoelectrically induced stress-resultants and stress couples are defined as:

$$(\tilde{M}; \tilde{S}); \tilde{T} = \langle \tilde{\sigma}_{xx}(z; \mathcal{L}); \tilde{\sigma}_{xz} \rangle, \tag{23a}$$

and

$$\hat{M} = \langle \overline{e}_{xz} \mathcal{E}_z z \rangle, \tag{23b}$$

respectively, while the mass quantities per unit wing span are:

$$(m_i,\ \mu_i,\ \pi_i) = \langle \rho_{(k)} z^i (1; \mathcal{L}; \mathcal{L}^2) \rangle, \tag{24}$$

$\rho_{(k)}$ being the mass density of the kth layer. Herein the operator $\langle \cdots \rangle$ identifies the stepwise integration through the laminate thickness as defined by

$$\langle \cdots \rangle = \sum_{k=1}^{\mathcal{N}} \int_{(k)_{Z^-}}^{(k)_{Z^+}} (\cdots)\, dz \tag{25}$$

In order to express the governing equations in terms of displacement quantities, the previously displayed equations of motion and the boundary conditions have to be supplemented by the constitutive equations. Expressed in terms of displacement quantities these are:

$$M = \tilde{M} - \hat{M} \tag{26}$$

$$\tilde{S} = F u^{(3)}_{,x} - E w_{,xx} \tag{27}$$

$$\tilde{T} = H u^{(3)} \tag{28}$$

where

$$\tilde{M} = E u^{(3)}_{,x} - D w_{,xx}$$

In these equations, the stiffness quantities are defined as follows:

$$(D;\ E;\ F) = \langle \overline{Q}_{11}(z^2; z\mathcal{L}; \mathcal{L}^2) \rangle;\ H = \langle Q_{44}\ \mathcal{L}^2_{,z} \rangle \tag{29}$$

It should be remarked that the effects of sliding imperfections are included in the last three stiffness quantities as defined in Eqs. (29) and in the last two mass terms appearing in Eq. (25).

The governing equations in terms of displacement quantities are obtained in a customary way and are given by:

$$Eu^{(3)}_{,xxx} - Dw_{,xxxx} = -P_z + \mu_1 \ddot{u}^{(3)}_{,x} - m_2 \ddot{w}_{,xx} + m_0 \ddot{w} + \hat{M}_{,xx} \tag{30}$$

$$Fu^{(3)}_{,xx} - Ew_{,xxx} - Hu^{(3)} = \pi_0 \ddot{u}^{(3)} - \mu_1 \ddot{w}_{,x} \tag{31}$$

Assuming that $\mathcal{E}_z(x,z,t) \equiv \mathcal{E}_z(t)$, i.e. that the applied electrical current is spatially uniform, under out-of-phase activation, the piezoelectrically induced couple $\hat{M}$ appearing only as a boundary moment control at the wing tip, becomes immaterial in the equations of motion. Assuming the wing clamped at its root ($x = 0$) and free at its tip, ($x = L$), the pertinent boundary conditions read:

At $x = 0$:

$$u^{(3)} = w = w_{,x} = 0 \tag{32a-c}$$

and at $x = \mathrm{L}$

$$\tilde{S} = \tilde{T} = 0; \ \tilde{M} = \hat{M} \tag{32e-f}$$

It should be remarked that the number of boundary conditions prescribed at each edge is consistent with the sixth order degree of the governing system, Eqs. (30) and (31).

UNSTEADY AERODYNAMICS FOR DIVERGENCE AND FLUTTER IN BENDING OF SWEPT AIRCRAFT WINGS

In order to put into evidence the implications of interlaminar bonding imperfections on static and dynamic aeroelastic instability boundaries , and to reduce the problem to a tractable one, the divergence and flutter in pure bending will be approached.

The instabilities in pure bending can be conceived to occur when the wing torsional stiffness is very large. In this case, as is well known, the sweptforward wing can experience divergence instability, while the sweptback wing can experience a rather low flutter speed (see Ref. 5). These cases will be considered in this analysis.

The angle of sweep, considered positive when the wing is sweptback and negative when it is sweptforward, is measured in the plane of the wing from the direction normal to the airstream to the middle axis of the wing.

The solution methodology based on Extended Galerkin Method, enables one to accommodate any variation of geometrical, mechanical and aerodynamic parameters along the wing span.

For the approach of the divergence problem, the local lift force is expressed as:

$$P_z(x) = q_n c(x) \frac{\partial C_L}{\partial \alpha} \frac{dw}{dx} \tan \Lambda \tag{33a}$$

where

$$q_n = q \cos^2 \Lambda \tag{33b}$$

$q(\equiv \rho_\infty U^2/2)$ denoting the dynamic pressure.

For the approach of the flutter in bending, assuming simple harmonic motion, the unsteady lift force is expressed as:

$$P_z(x,t) = -\pi\rho_\infty\omega^2 b^3\left\{\frac{\overline{w}}{b}L_{ww} + \frac{d\overline{w}}{dx}L_{ww'}\right\} \tag{34}$$

where $\overline{w}(\equiv \overline{w}(x))$ has to be considered in the sense of that displayed in Eq. (38a)

Herein L_{ww} and $L_{ww'}$ denote the dimensionless aerodynamic coefficients expressed as:

$$L_{ww} = 1 + \frac{b_r}{b(x)}\left[1 - 2i\left(\frac{U_n}{b_r\omega}\right)[F(k_n) + iG(k_n)]\right] \tag{35a}$$

$$L_{ww'} = \left[-i\frac{b_r}{b(x)}\left(\frac{U_n}{b_r\omega}\right)\tan\Lambda\right]L_{ww} \tag{35b}$$

where

$$k_n \equiv \omega b/U_n \tag{36}$$

and i $(\equiv \sqrt{-1})$ denotes the imaginary unit.

In addition, $b(x)$ $(\equiv c(x)/2)$ and $b_r(\equiv c_r/2)$ is the local semi-chord and that of the typical section located at 0.75 L from the wing root cross-section, respectively; $C(k_n)(\equiv F(k_n) + iG(k_n)$ is the Theordorsen's function, assumed not to vary along the wing span. Notice that all the geometrical and aerodynamical quantities are measured in the cross-sections normal to the spanwise coordinate of the actual sweptwing.

Since the Theodorsen's function is an intricate transcendental function, a highly accurate approximation of it has been used. Its expression can be found in Ref 12.

THE CONTROL LAW

In order to counteract the damaging effects of interfacial bonding imperfections and enhance the divergence and flutter instabilities, a feedback control law relating the applied electric field $\mathcal{E}_z$ to the mechanical quantities characterizing the beam's response, has to be implemented.

The control via a boundary moment acting at the beam tip is a methodology mathematically substantiated (see Ref 13), and proved to be efficient, among others towards the control of the dynamic response of cantilevered beams to transient loads (see Ref. 14) Herein, the feedback moment control law is adopted, this implying the following relationship between the piezoelectrically induced bending moment at the beam tip and the elastic restoring bending moment at the wing root

$$\hat{M}(L,t) = K_m\tilde{M}(0,t) \tag{37}$$

where K_m stands for the corresponding feedback gain. Use of Eq. (37) in the boundary condition, at the beam tip, and solution of the eigenvalue problems resulting from consideration of Eqs. (30) and (31) specialized for the static case) in conjunction with Eq. (33), for the divergence problem, and with Eqs. (34) and (35), for the flutter problem, yield the closed-loop divergence speed and the closed-loop frequency and flutter speed.

It should be mentioned, that in addition to this control law, other ones, as the velocity and acceleration feedback control laws, or combinations of these can be implemented. In various contexts, such control methodologies have been considered in Refs. (15 through 17).

SOLUTION METHODOLOGY

In order to discretize the problem and obtain the corresponding eigenvalue problems, the generalized displacement $u^{(3)}(x,t)$ and $w(x,t)$ are expressed in terms of combinations of trial functions selected as to fulfill identically all the kinematic boundary conditions.

As a result, for the flutter problem these representations are:

$$[u^{(3)}(x,t); w(x,t)] = \sum_{j=1}^{J} [G_j(x); \mathcal{W}_j(x)] e^{i\omega t}, \tag{38a}$$

whereas for the divergence problem are

$$[u^{(3)}(x); w(x)] = \sum_{j=1}^{J} [G_j(x); \mathcal{W}_j(x)]. \tag{38b}$$

In order to satisfy exactly the kinematic boundary conditions at the beam root $x = 0$, $\mathcal{W}_j$ are selected as the Williams' polynomials

$$\mathcal{W}_j(x) = 1 - \frac{(j+3)x}{L} - \left(1 - \frac{x}{L}\right)^{j+3}, \tag{39}$$

whereas G_j are selected as $G_j = \mathcal{W}_{j,x}$.

In addition, for the flutter problem, the time dependence of all field variables, i.e. of the unsteady lift, electric current, etc. is considered to be harmonic one, i.e. for any generic time dependent quantity $F(x,t)$ one assumes the following time dependence

$$F(x,t) = \overline{F}(x) e^{i\omega t}. \tag{40}$$

Replacing the representations given by Eq. (38), together with that resulting for the boudary moment $\hat{M}$, Eq. (37), and the specific expressions of lift loads directly in Hamilton's functional, a closed-loop complex eigenvalue for the flutter problem, and a real one, for the divergence problem are obtained.

In order to determine the flutter conditions, the eigenfrequency ω should be a real-valued quantity, whereas for the divergence instability, the eigenvalue λ defined in terms of the reduced speed as

$$\lambda = q_n \, \partial C_L / \partial \alpha \tan \Lambda \tag{41}$$

should be a postive real quantity. For the case of the divergence in bending this condition can be fulfilled only for sweptforward wings implying $\Lambda \to -\Lambda$.

It should be emphasized that the Extended Galerkin Method used here to obtain the eigenvalue problems compensates the non-fulfilment of the boundary conditions at the wing tip, by incorporation of residual terms obtained from the non-fulfilment of these boundary conditions.

The open (i.e. the non-activated) and closed-loop (i.e. the activated) flutter and divergence response characteristics of a composite laminated wing, as influenced by the bonding imperfections are investigated.

The host structure is a three-layered (0°/90°/0°) symmetric cross-ply beam. At the top and bottom of the beam, there are mounted thin piezoactuator layers, uniformly spread over its span and subjected to an out-of-phase activation, this resulting in a bending moment control $\hat{M}(L,t)$ applied at the beam tip. The material properties of the host structure are:

$$E_L/E_T = 25, \quad G_{LT}/E_T = 0.5, \quad G_{TT}/E_T = 0.2, \quad \nu_{LT} = 0.25,$$

E being the Young's modulus, G the shear modulus, and ν Poisson's ratio, where subscripts L and T denote the directions parallel and normal to the fibers, respectively.

As is evident, the main interest here is to emphasize the implications of the interlaminar bonding imperfections on the instability response behavior and on the way enabling one to enhance the response by using the feedback control methodology. Herein the characteristics of the top and bottom piezoactuator layers used in the numerical analysis are those used in Ref. (18) and correspond to the PVF-2 with a thickness of $40\mu m$.

Throughout the numerical illustrations, the sliding constants representing the degree of bonding imperfectons at the kth interface, are used in dimensionless form as

$$^{(k)}R = \frac{^{(k)}\mathcal{R}h}{E_T} \tag{42}$$

Unless otherwise stated, $^{(k)}R$ is assumed to be the same at all interfaces and indicated as R. Also notice that the feedback gain is used in normalized form as

$$\mathcal{K}_m = K_m \frac{1}{E_T h^2 L} \tag{43}$$

In Figs. 2 and 3, there are displayed plots of the variation of the divergence speed parameter λ_{Div} vs. chord ratio $\mathcal{C}(\equiv c_T/c_R)$, for the activated and unactivated wing, and for selected values of the damage parameter R, including the undamaged case as well. The results reveal: a) the deleterious effect of bonding imperfections, b) the fact that divergence speed diminishes with the increase of the chord parameter $\mathcal{C}$, c) that the incorporation of the feedback control yields an increase of the divergence speed, and d) that the sensitivity of the divergence instability to bonding imperfection is larger for the activated wing than for its unactivated counterpart.

In Figs. 4 and 5, the effect of the relative thickness of the wing L/h, coupled with that of bonding imperfections upon the divergence instability for the activated and unactivated wing, respectively, are displayed.

The results reveal that the increase of L/h coupled with that of R yields a decrease of λ_{Div}. In addition, the conclusions c) and d) related with the effect of the piezoelectric actuation previously presented, remain valid in this case, as well.

As revealed in Figs. 6 and 7, the increase of the ratio E_L/E_T of in-plane Young's moduli, where E_T is held fixed, results also in an increase of the divergence speed. Moreover, Fig. 7 reveals that the piezoelectric activation coupled with the increase of E_L/E_T results in a significant increase of λ_{Div}, which counteracts the detrimental effect of bonding imperfections.

Finally, in Figs. 8 and 9, the nomalized flutter speed of laminated damaged wing, for the unactivated and activated wing scenarios, respectively, versus the sweep angle, is displayed. The results reveal the power of the feedback control technology to increase the flutter speed, specially at high sweep angles, where the minimum flutter speed occurs. On the other hand, the results reveal that the wing is more sensitive to the interlaminar damages in the region of sweep angles where the flutter is very high, and less sensitive in that region of sweep angles where the flutter speed is low. In spite of this, even in that region, the effect of the feedback control does not appear to be negligeable, and so, it can play an significant role towards counteracting the effect of interfacial imperfections.

Herein the impact of incorporation of a *dynamic* feedback control methodology upon the enhancement of flutter instability of aircraft wings was not investigated. Adoption of such a control strategy is likely to play a more powerful role in this context.

Conclusion

In this paper several issues related with the implications of interfacial damages upon the divergence and flutter instabilities in pure-bending of swept aircraft wings, and with those involving the incorporation of a feedback control methodology have been addressed. Although the results concern only a specialized case of aeroelastic instability, a number of trends, which can play a postive role towards the reliable aeroelastic design of advanced aircraft wings composed of laminated composite materials, have been emphasized. Although obtained in a specialized context, it is believed that the results of this work will be extended as to investiage this problem in a context which would include the bending-twist degrees of freedom for both wing divergence and flutter instabilities.

ACKNOWLEDGMENTS

The financial support of this work by the Consiglio Nazionale delle Ricerche through Grants CTB97.00589.CT11 and CTB97.00459.CT11 is gratefully acknowledged by M. Di Sciuva, U. Icardi, while L. Librescu acknowledges with gratitude partial support of this research by NATO Grant, CRG960118.

REFERENCES

1. Di Sciuva, M. Icardi, U. and Librescu, L., "On Modeling of Laminated Composite Structures Featuring Interlaminar Bonding Imperfections," Advanced Methods in Materials Processing Defects, M. Predeleanu and P. Gilormini (Editors), *Studies in Applied Mechanics* **45**, Elsevier, Amsterdam, pp. 393-403, 1997.

2. Di Sciuva, M. "Geometrically Nonlinear Theory of Multilayered Plates with Interlayer Slips," *AIAA Journal*, **35**, 11, 1753-1759, 1997.

3. Schmidt, R. and Librescu, L., "Geometrically Nonlinear Theory of Laminated Anisotropic Composite Plates Featuring Interlayer Slips", *Nova Journal of Mathematics, Game Theory and Algebra*, Nova Sci. Publi., **5**, 2, pp. 131-148, 1996.

4. Flax, H. H., "Aeroelasticity and Flutter"in *High Speed Problems of Aircraft and Experimental Methods*, Vol. VIII High Speed Aerodynamics and Jet Propulsion, Eds. Donavan, H. F. and Lawrence, H. R., Princeton University Press, 1961, pp. 161-417.

5. Cunningham, H. J., "Analysis of Pure-Bending Flutter of a Cantilever Swept Wing and its Relation to Bending- Torsion Flutter," NACA TN 2461, 1951.

6. Di Sciuva, M. "An Improved Shear-Deformation Theory for Moderately Thick Multilayered Anisotropic Sheels and Plates," *Journal of Applied Mechanics*, **54**, pp. 589-596, 1987.

7. Di Sciuva, M. "A Generalization of the Zig-Zag Plate Models to Account for General Lamination Configurations," *Atti Accademia delle Scienze di Torino-Classe di Scienze Fisiche, Matematiche e Naturali*, **128**, 3, 4, pp. 81-103, 1994.

8. Icardi, U., Di Sciuva, M. and Librescu, L., "Smart Structures Featuring Imperfect Bonding Interfaces: Modeling and Implications," in *Smart Structures and Materials 1998: Mathematics and Control in Smart Structures,* V. V. Varadan, Editor, *Proceedings of SPIE*, Vol. 3323, pp. 202-213, 1998.

9. Cheng, Z. -Q, Jemah, A. K., Williams, F. W., "Theory for Multilayered Anisotropic Plates with Weakened Interfaces," *Journal of Aplied Mechanics*, bf 63, pp. 1019-1026, 1996.

10. Cheng, Z. -Q, Kennedy, D. and Williams, F. W., "Effect of Interfacial Imperfection on Buckling and Bending Behavior of Composite Laminates," *AIAA Journal*, **34**, 12, pp. 2590-2595, 1996.

11. Lavrentyev, A. I. and Rokhlin, S. I., "Ultrasonic Spectroscopy of Imperfect Contact Interfaces Between a Layer and Two Solids," *Journal of Acoustical Society of America* **103,** 2, pp. 657-664, 1998.

12. Gern, F. H., and Librescu, L., "Static and Dynamic Aeroelaticity of Advanced Aircraft Wings Carrying External Stores," *AIAA Journal* **36**, 7, pp. 1121-1129, 1998.

13. Lagnese, J. E. and Lions, J. L. "Boundary Stabilization of Thin Plates," Collection RMA, Masson, Paris, 1988.

14. Librescu, L., and Na, S. S., "Boundary Control of Free and Forced Oscillation of Shearable Thin-Walled Beam Cantilevers," *European Journal of Mechanics A/Solids*, **17** (4) pp. 687-700, 1998.

15. Song, O. and Librescu, L. "Bending Vibrations of Adaptive Cantilevers with External Stores," *International Journal of Mechanical Sciences*, **38**, 5, pp. 483-498, 1996.

16. Librescu, L., Meirovitch, L. and Song, O., "Integrated Structural Tailoring and Adaptive Materials Control for Advanced Aircraft Wings," *Journal of Aircraft*, **33**, 1, pp. 203-213, 1996.

17. Librescu, L. and Na, S. S., "Bending Vibration Control of Cantilevers Via Boundary Moment and Combined Feedback Control Law," *Journal of Vibration and Control*, 4, 6, pp. 733-746, 1998.

18. Icardi, U. and Di Sciuva, M. "Large-deflection and Stress Analysis of Multilayered Plates with Induced-Strain Actuators," *Smart Material and Structures*, 5, pp. 140-164, 1996.

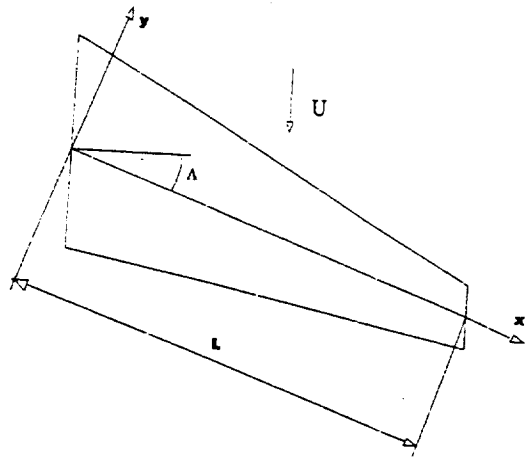

a In-plane geometry.

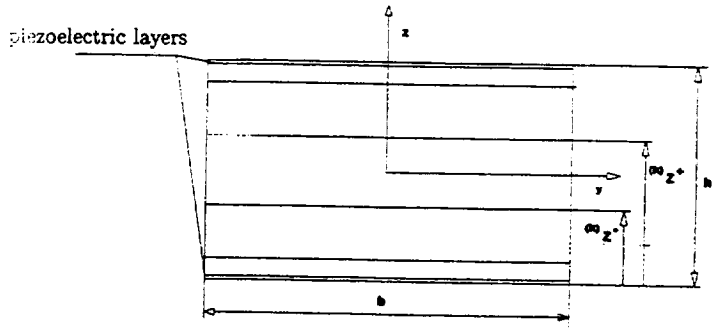

b Geometry of the cross section.

Figure 1 Geometry of the wing.

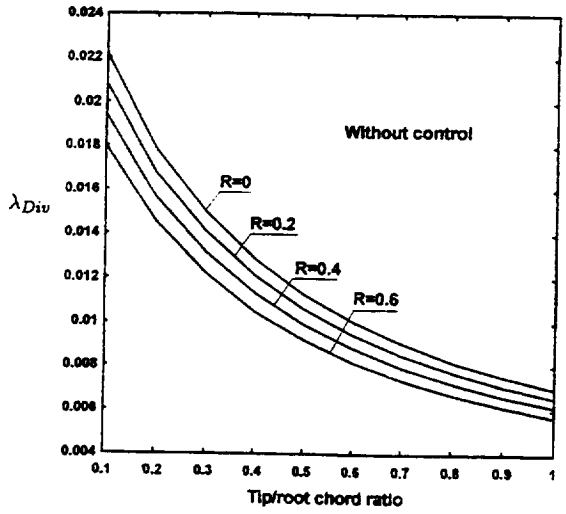

Figure 2 Divergence speed parameter λ_{Div} vs.c_T/c_R, for selected values of the damage parameter R. Unactivated wing.

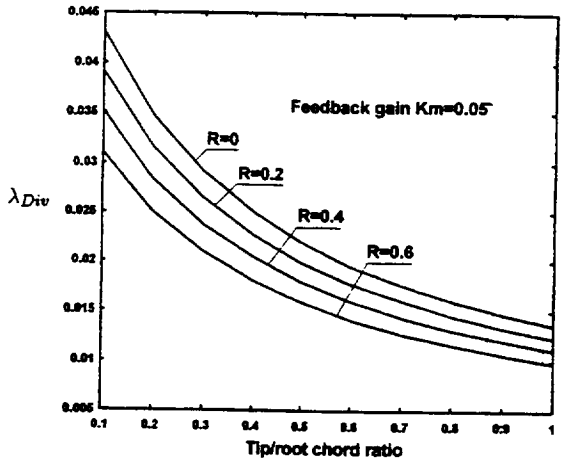

Figure 3 The counterpart of the case depicted in Fig. 2, for the case of the activated wing.

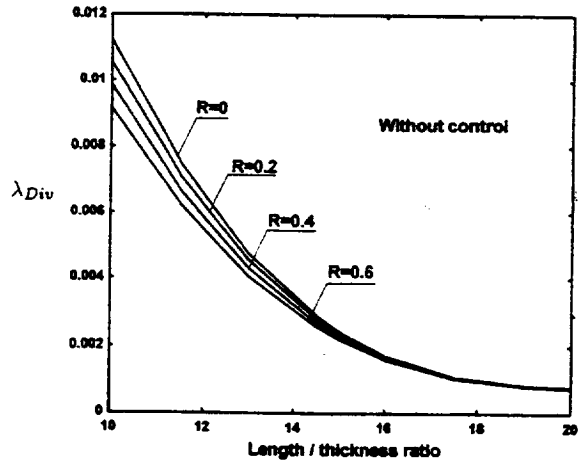

Figure 4 The effect of L/h on the divergence speed parameter λ_{Div}, for selected values of the damage parameter. Unactivated wing.

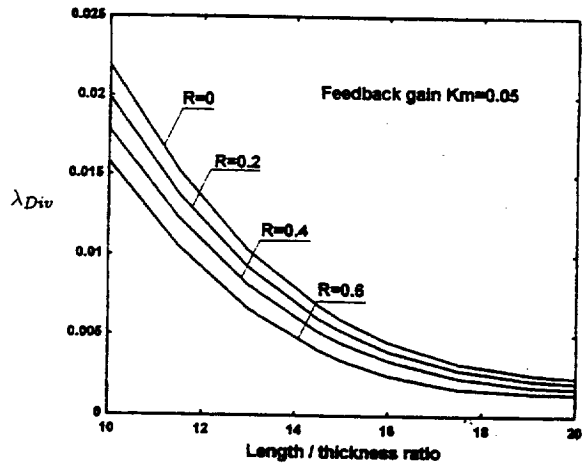

Figure 5 The counterpart of the case depicted in Fig. 4 for the case of the activated wing.

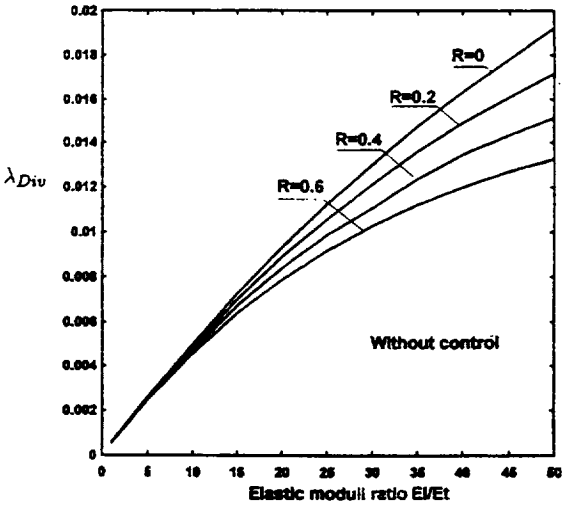

Figure 6 Effect of the ratio E_L/E_T on the divergence speed parameter λ_{Div}, for selected values of the damages parameter. Unactivated wing.

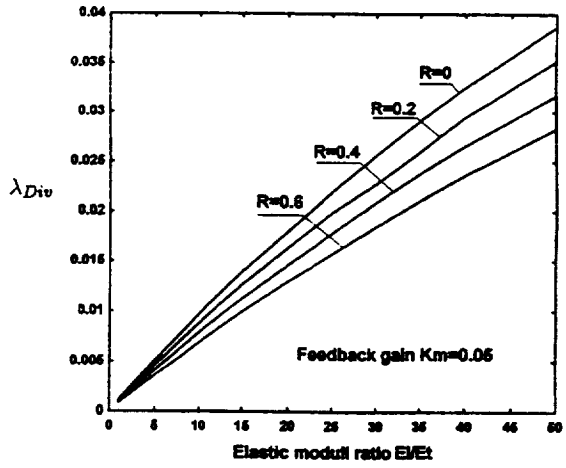

Figure 7 Counterpart of the case considered in Fig. 6 for the case of the activated wing.

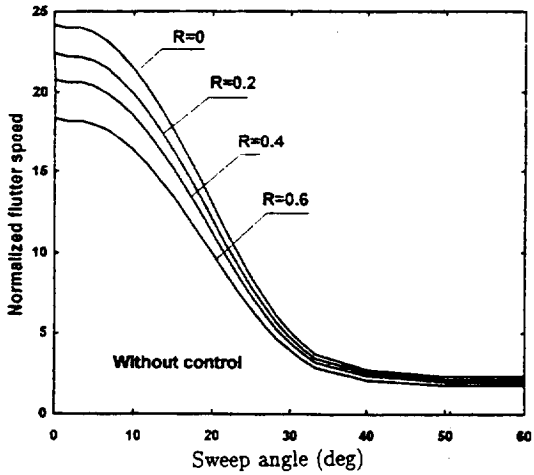

Figure 8 Normalized flutter speed as a function of the sweep angle for selected values of the damage parameter. Unactivated wing.

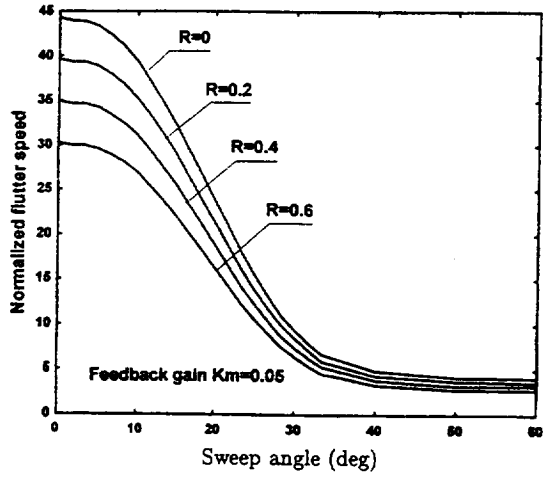

Figure 9 The counterpart of Fig. 8 for the case of the activated wing.

Improving the Convergence of the Doublet-Lattice Method Through Tip Corrections

Myles L. Baker
Senior Engineer, Loads and Dynamics
The Boeing Company
Long Beach, California 90807-5608, USA
myles.l.baker@boeing.com

William P. Rodden
Consulting Engineer
William P. Rodden, Ph.D., Inc.
La Canada Flintridge, California 92011-2831, USA
billrodden@aol.com

In 1973 Hough studied the slow convergence of the Vortex-Lattice Method (VLM) as the number of spanwise divisions (strips) is increased. Specifically, the lift curve slope of a lifting surface was shown to decrease significantly as the resolution of the lattice was increased, converging to the "true" value only with relatively fine spanwise divisions. Impressive improvements in the converged results were achieved when equally spaced divisions of the lifting surface were inset from the tip by a fraction of the strip width. Hough demonstrated the improvement via the tip inset on a number of wing planforms at a constant angle of attack.

Hough's argument was based on an elliptical lift distribution which is a reasonable assumption in the steady, symmetric case. The present paper investigates also cases where elliptical lift distributions are not expected, specifically, the antisymmetric motion of rolling, elastic motions, and oscillatory motions with high reduced frequencies. The beneficial effect of the tip inset is observed in all cases investigated

Keywords: Doublet, Lattice, Unsteady Aerodynamics, Convergence

1. Introduction

Following a suggestion of Rubbert[1] that equally spaced divisions on a lifting surface should be inset from the tip by a fraction d ($0<d<1$) of the strip width, Hough [2,3] has demonstrated impressive improvement in the estimation of lift curve slope ($C_{L\alpha}$) of a wing without using an inordinate number of spanwise strips, specifically for d = ¼. The tip inset concept is illustrated in Figure 1, and some of Hough's convergence results for $C_{L\alpha}$ are shown in Figure 2.

Hough's recommendation of d = ¼ was based on an analysis of an elliptical lift distribution which is typical of a steady symmetrical aerodynamic loading. It is the purpose of this paper to investigate

the convergence improvement that can be obtained by applying the tip inset correction to the oscillatory Doublet-Lattice Method (DLM, which reduces to the VLM in the steady case) for conditions in which elliptical lift distributions are not expected.

The tip correction is implemented by reducing the effective span of the wing (the span that is actually paneled with Doublet-Lattice boxes) by the factor NS/(NS+d), where NS is the number of spanwise strips, and d is the tip inset factor (typically ¼). The lack of an aerodynamic panel on the most outboard tip of the wing has the effect of driving the tip loading toward the correct value of zero. Since the DLM assumes constant loading (spanwise) within a box, it requires a very high resolution to capture the correct wingtip load distribution, and the DLM will typically over-predict the tip loading, and in the steady, symmetric case, the DLM results approach the correct results from above as the resolution is refined.

2. Results

Rectangular Wings: Two wings pitching about their midchords at a Mach number of M=0.80 are studied. The first wing has aspect ratio of AR=2. It is divided into various numbers of spanwise strips (NS), and various numbers of chordwise boxes (NC) such that the maximum box aspect ratio is less than 8.0. The value of NC necessary for convergence depends on the reduced frequency $k_r=\omega c/2V$, where ω is the angular frequency (rad/sec), c is the reference chord (c = 1.0 for the rectangular wings), and V is the freestream velocity. The guideline of Ref. 5 recommends 50 boxes per wavelength λ, where $\lambda = \pi c/k_r$.

The steady lift curve slope $C_{L\alpha}$ and the roll damping coefficient C_{lp} are obtained from the DLM at $k_r=0.001$. Oscillatory results are obtained for $k_r=0.1$, 0.5, 1.0, and 2.0. The results for the aspect ratio 2 wing are presented in Figures 3 and 4. Figure 3 shows the results for the symmetric case (lift curve slope), and Figure 4 shows the antisymmetric (roll damping coefficient) results. Figures 3 and 4 present the real parts on the left and the imaginary parts on the right. The solid lines are the results with the tip correction applied, and the dashed lines are the results without the tip correction. The data are plotted as functions of the reciprocal of the number of spanwise strips, so that extrapolation of 1/NS to zero should provide converged results. The steady case (based on $k_r=0.001$) is shown at the tops of the figures, with results for increasing reduced frequencies shown below. As the reduced frequency is increased, more chordwise boxes are required to satisfy the requirement of 50 boxes per wavelength. The figures only present data that satisfy the requirement.

Perusing Figure 3 from top to bottom, we make the following observations in the symmetric case. The top graph is the steady case and the convergence with the tip correction behaves as Hough has shown[2,3]. The next two graphs below are for $k_r=0.1$ and good convergence with the tip correction is found for the real part and significant improvement is seen in the imaginary part. The next two graphs are for $k_r=0.5$ and some dependence on the number of chordwise boxes appears, but both real and imaginary parts are improved with the tip correction over the results without it. Similar behavior is seen in the remaining graphs for $k_r=1.0$ and 2.0: There is some dependence on the number of chordwise boxes, and the tip correction improves the results but moreso in the real part than the imaginary part.

Figure 4 is similar to Figure 3 but for the antisymmetric case. The top graph is the steady damping-in-roll coefficient. Again, as in the symmetric case, the tip correction leads to converged results almost independent of the number of spanwise strips. Below the steady case is the damping-in-roll

coefficient at k_r=0.1. Both real and imaginary parts are improved with the tip correction. Both real and imaginary parts are improved with the tip correction also at k_r=0.5. At the higher reduced frequencies of k_r=1.0 and 2.0, the damping-in-roll coefficient exhibits some dependence on the number of chordwise boxes, but this dependence is less than that seen above in the symmetric case and the tip correction leads to better results.

The second wing has an aspect ratio of 7.0. As in the AR=2.0 case, the wing was analyzed in both symmetric and antisymmetric oscillatory rigid body motion. The results are presented in Tables 1 and 2. Table 1 contains the symmetric results, and Table 2 presents the results of the antisymmetric analysis. A tabular presentation of these results is made to give the reader a different perspective on the data from the graphical format (Note that tabulated results of the data for the figures in this paper are available from the authors). Blank entries in the tables indicate that the combination of NC and k_r do not satisfy the wavelength requirement.

The results in Tables 1 and 2 for the aspect ratio 7.0 rectangular wing are similar to the results plotted in Figures 3 and 4 for the aspect ratio 2.0 rectangular wing. The steady lift curve slope in Table 1 (found at k_r=0.001) is again found to be reasonably constant with the number of spanwise strips when the tip correction is made. At k_r=0.1, the oscillatory lift curve slope computed with the tip correction is also fairly constant with the number of strips. At k_r=0.5, the real parts with the tip correction are again insensitive to the number of spanwise strips, but there is some dependence of the imaginary parts on the number of chordwise boxes. Also, the variation in the imaginary parts is about the same whether or not the tip correction is made. At k_r=1.0 and 2.0, the real parts are again improved with the tip correction, but the imaginary parts are not significantly affected by it. As in the aspect ratio 2.0 results, a dependence on the number of chordwise boxes is observed.

In Table 2, the antisymmetric results follow the pattern of the symmetric case. The steady damping-in-roll coefficient is much improved by the tip correction. At all of the higher reduced frequencies, it is the real parts that are improved by the tip correction. At the low reduced frequency k_r=0.1, the tip correction improved the imaginary parts, especially for a small number of chordwise boxes (NC=10 and 20), but at the high frequencies, the tip correction does not have much effect on the imaginary parts.

LANN Wing: In order to investigate the convergence behavior of aeroelastic generalized forces as the box resolution is refined, a model with realistic elastic vibration modes is required. These generalized forces are extremely important in flutter and aeroservoelastic analysis. The LANN wing[6], which was chosen for this study, is a well-published sample case representative of a high aspect ratio transport wing, and is complete with elastic modal data. The wing has an aspect ratio of 7.9, a taper ratio of 0.40, and a leading edge sweep of 27.5 degrees. The first bending and first torsion mode shapes of the LANN wing are shown in Figure 5.

The unsteady generalized aerodynamic forces for the two mode shapes shown in Figure 5 were computed at reduced frequencies of k_r=0.01, 0.5,.1.0, and 2.0 for varying numbers of spanwise strips and chordwise boxes. The number of spanwise strips varied from 5 to 20, and the number of chordwise boxes varied from 5 to 25. Figure 6 shows the Generalized Aerodynamic Force coefficient (GAF) in first wing bending in a similar format to that used for the rectangular wing results discussed above. The top pair of graphs in Figure 6 show the real and imaginary parts of the GAF in first wing bending at a reduced frequency of k_r=0.01. As seen in the rigid symmetric and antisymmetric results for the rectangular wings, the generalized aerodynamic forces at this low

reduced frequency are rendered almost independent of the number of spanwise strips through the use of the tip correction. This observation applies to both the real and imaginary parts. The next set of graphs in Figure 6 show the results for a reduced frequency of k_r=0.5. Again, the convergence of the results is improved dramatically through the use of the tip correction. Note that there is some dependence of the real part of the GAF on the number of chordwise boxes. The next two pairs of graphs show the results for reduced frequencies of k_r=1.0 and 2.0. In each case, the real part of the GAF is either slightly improved or unaffected by the application of the tip correction, while the imaginary part is not significantly improved. In fact, at k_r=2.0, it appears that the tip correction offers a slight reduction in convergence properties. However, this is more than offset by the dramatic improvements seen in the other conditions.

Figure 7 shows the results for the first torsion mode of the LANN wing. In this case, the effect of the tip inset correction is much smaller. The real parts of the GAF's at all reduced frequencies are slightly improved, while the convergence of the imaginary parts is slightly reduced. The overall result is that the tip correction is not an obvious improvement in this case, but it is clearly not detrimental to convergence.

3. Concluding Remarks

The foregoing discussions of the results for the three configurations may be summarized as follows. In general, the tip inset correction improves the convergence by decreasing the sensitivity of the results to the number of spanwise strips. This is observed for both symmetric and antisymmetric rigid body motions of rectangular wings in both the steady and oscillatory cases up to a reduced frequency of 2.0. It is also observed in the case of oscillatory symmetric elastic modes of a swept, tapered wing representative of a subsonic transport.

The observations above are general, but some specific features may be pointed out. The improvement in the steady lift curve slope is observed again as Hough has shown before [2,3]. A comparable improvement in the steady roll damping coefficient is found here. However, as the frequency increases, the effectiveness of the correction is somewhat reduced. The tip inset correction also appears to be more effective in improving the real part of the unsteady aerodynamic forces than the imaginary part (although the benefits to the imaginary part are substantial in most cases).

There is sufficient benefit to the tip inset correction in all cases studied to make the recommendation that it be used routinely, particularly since the correction is so easily made. Only the case of equal width spanwise strips has been considered. Other spanwise distributions of strip width require further investigation.

4. References

1. P. E. Rubbert, "Theoretical Characteristics of Arbitrary Wings by a Non-Planar Vortex Lattice Method," D6-9244, 1964, The Boeing Co., Renton, WA.

2. G. R. Hough, "Remarks on Vortex-Lattice Methods," J. Aircraft, Vol. 10, No. 5, 1973, pp. 314-317.

3. G. R. Hough, "Lattice Arrangement for Rapid Convergence," Vortex-Lattice Utilization, NASA SP-405, Mat 17-18, 1976, pp. 325-342.

4. W. P. Rodden, P. F. Taylor, S. C. McIntosh, Jr., "Further Refinement of the Nonplanar Aspects of the Subsonic Doublet-Lattice Lifting Surface Method," 20th Congress of the International Council of the Aeronautical Sciences, Paper ICAS 96-2.8.2, September 1996, also *J. Aircraft*, Vol. 35, No. 5, 1998, pp. 720-727.

5. W. P. Rodden, P. F. Taylor, S. C. McIntosh, and M. L. Baker, "Further Convergence Studies of the Enhanced Subsonic Doublet-Lattice Oscillatory Lifting Surface Method," International Forum of Aeroelasticity and Structural Dynamics, 17-20 June 1997, Rome, Italy, pp. 401-408, to be published in *J. Aircraft*.

6. Horsten, J.J., den Boer, R. G., and Zwaan, R. J., "Unsteady Transonic Pressure Measurements on a Semispan Wind Tunnel Model of a Transport-Type Supercritical Wing (LANN Model), Part I," Air Force Wright Aeronautical Laboratory, Report AFWAL-TR-83-3039, March 1983.

No Tip Correction					
NS	**k_r=0.001**	**k_r=0.1**	**k_r=0.5**	**k_r=1.0**	**k_r=2.0**
5	**6.553**	**5.892-0.769i**	**4.882+0.325i**		
10	**6.358**	**5.735-0.733i**	**4.814+0.268i**		
20	**6.255**	**5.651-0.711i**	**4.753+0.270i**		
Tip Correction					
NS	**k_r=0.001**	**k_r=0.1**	**k_r=0.5**	**k_r=1.0**	**k_r=2.0**
5	**6.117**	**5.545-0.670i**	**4.637+0.322i**		
10	**6.139**	**5.561-0.683i**	**4.688+0.271i**		
20	**6.145**	**5.564-0.686i**	**4.689+0.272i**		

Table 1(a): Symmetric (lift curve slope) convergence behavior for aspect ratio 7.0 rectangular wing with 10 Chordwise Boxes

No Tip Correction					
NS	**k_r=0.001**	**k_r=0.1**	**k_r=0.5**	**k_r=1.0**	**k_r=2.0**
9	**6.381**	**5.755-0.741i**	**4.845+0.240i**	**5.021+0.814i**	
15	**6.290**	**5.681-0.727i**	**4.815+0.205i**	**4.979+0.725i**	
20	**6.255**	**5.653-0.720i**	**4.800+0.196i**	**4.958+0.702i**	
Tip Correction					
NS	**k_r=0.001**	**k_r=0.1**	**k_r=0.5**	**k_r=1.0**	**k_r=2.0**
9	**6.138**	**5.561-0.686i**	**4.706+0.243i**	**4.885+0.795i**	
15	**6.144**	**5.565-0.693i**	**4.730+0.208i**	**4.897+0.718i**	
20	**6.145**	**5.566-0.695i**	**4.736+0.198i**	**4.896+0.698i**	

Table 1(b): Symmetric (lift curve slope) convergence behavior for aspect ratio 7.0 rectangular wing with 20 Chordwise Boxes

No Tip Correction					
NS	k_r=0.001	k_r=0.1	k_r=0.5	k_r=1.0	k_r=2.0
14	6.300	5.690-0.729i	4.824+0.199i	4.991+0.714i	
20	6.255	5.654-0.722i	4.809+0.181i	4.968+0.669i	
25	6.234	5.637-0.719i	4.801+0.174i	4.956+0.652i	
Tip Correction					
NS	k_r=0.001	k_r=0.1	k_r=0.5	k_r=1.0	k_r=2.0
14	6.143	5.565-0.693i	4.733+0.202i	4.903+0.705i	
20	6.145	5.567-0.697i	4.745+0.183i	4.906+0.665i	
25	6.146	5.567-0.699i	4.750+0.176i	4.907+0.649i	

Table 1(c): Symmetric (lift curve slope) convergence behavior for aspect ratio 7.0 rectangular wing with 30 Chordwise Boxes

No Tip Correction					
NS	k_r=0.001	k_r=0.1	k_r=0.5	k_r=1.0	k_r=2.0
18	6.267	5.663-0.725i	4.815+0.181i	4.977+0.672i	5.913+0.728i
25	6.234	5.637-0.720i	4.805+0.167i	4.960+0.638i	5.907+0.660i
30	6.220	5.626-0.717i	4.799+0.162i	4.952+0.626i	5.902+0.636i
Tip Correction					
NS	k_r=0.001	k_r=0.1	k_r=0.5	k_r=1.0	k_r=2.0
18	6.145	5.566-0.697i	4.745+0.184i	4.909+0.666i	5.831+0.717i
25	6.146	5.567-0.699i	4.753+0.170i	4.910+0.635i	5.848+0.654i
30	6.147	5.568-0.701i	4.756+0.164i	4.911+0.624i	5.853+0.632i

Table 1(d): Symmetric (lift curve slope) convergence behavior for aspect ratio 7.0 rectangular wing with 40 Chordwise Boxes

No Tip Correction					
NS	k_r=0.001	k_r=0.1	k_r=0.5	k_r=1.0	k_r=2.0
22	6.245	5.646-0.722i	4.810+0.170i	4.967+0.645i	5.914+0.671i
30	6.220	5.626-0.718i	4.801+0.159i	4.954+0.619i	5.908+0.617i
35	6.209	5.618-0.716i	4.797+0.155i	4.948+0.610i	5.905+0.599i
Tip Correction					
NS	k_r=0.001	k_r=0.1	k_r=0.5	k_r=1.0	k_r=2.0
22	6.146	5.567-0.699i	4.752+0.173i	4.911+0.641i	5.847+0.663i
30	6.147	5.568-0.701i	4.758+0.161i	4.913+0.616i	5.859+0.613i
35	6.147	5.568-0.702i	4.760+0.157i	4.913+0.608i	5.863+0.595i

Table 1(e): Symmetric (lift curve slope) convergence behavior for aspect ratio 7.0 rectangular wing with 50 Chordwise Boxes

No Tip Correction					
NS	k_r=0.001	k_r=0.1	k_r=0.5	k_r=1.0	k_r=2.0
5	-0.6763	-0.6753-0.0112i	-0.6639-0.0549i		
10	-0.6312	-0.6308-0.0135i	-0.6314-0.0555i		
20	-0.6062	-0.6061-0.0143i	-0.6097-0.0573i		
Tip Correction					
NS	kr=0.001	kr=0.1	kr=0.5	kr=1.0	kr=2.0
5	-0.5646	-0.5753-0.0146i	-0.5703-0.0549i		
10	-0.5760	-0.5760-0.0148i	-0.5845-0.0557i		
20	-0.5789	-0.5789-0.0150i	-0.5864-0.0573i		

Table 2(a): Antisymmetric (roll damping) convergence behavior for aspect ratio 7.0 rectangular wing with 10 Chordwise Boxes

No Tip Correction					
NS	k_r=0.001	k_r=0.1	k_r=0.5	k_r=1.0	k_r=2.0
9	-0.6366	-0.6363-0.0131i	-0.6385-0.0525i		
15	-0.6148	-0.6148-0.0138i	-0.6226-0.0510i		
20	-0.6064	-0.6064-0.0140i	-0.6160-0.0507i		
Tip Correction					
NS	k_r=0.001	k_r=0.1	k_r=0.5	k_r=1.0	k_r=2.0
5	-0.5751	-0.5753-0.0146i	-0.5862-0.0528i		
10	-0.5782	-0.5785-0.0146i	-0.5913-0.0513i		
20	-0.5790	-0.5793-0.0146i	-0.5925-0.0510i		

Table 2(b): Antisymmetric (roll damping) convergence behavior for aspect ratio 7.0 rectangular wing with 20 Chordwise Boxes

No Tip Correction					
NS	k_r=0.001	k_r=0.1	k_r=0.5	k_r=1.0	k_r=2.0
14	-0.6172	-0.6172-0.0137i	-0.6251-0.0504i	-0.6243-0.1265i	
20	-0.6064	-0.6065-0.0139i	-0.6172-0.0493i	-0.6153-0.1223i	
25	-0.6012	-0.6015-0.0140i	-0.6132-0.0489i	-0.6109-0.1206i	
Tip Correction					
NS	k_r=0.001	k_r=0.1	k_r=0.5	k_r=1.0	k_r=2.0
14	-0.5780	-0.5783-0.0146i	-0.5916-0.0507i	-0.5906-0.1208i	
20	-0.5790	-0.5794-0.0145i	-0.5937-0.0496i	-0.5918-0.1185i	
25	-0.5794	-0.5798-0.0145i	-0.5945-0.0492i	-0.5921-0.1176i	

Table 2(c): Antisymmetric (roll damping) convergence behavior for aspect ratio 7.0 rectangular wing with 30 Chordwise Boxes

No Tip Correction					
NS	k_r=0.001	k_r=0.1	k_r=0.5	k_r=1.0	k_r=2.0
18	-0.6092	-0.6093-0.0138i	-0.6196-0.0492i	-0.6181-0.1227i	-0.7314-0.2080i
25	-0.6012	-0.6015-0.0140i	-0.6137-0.0484i	-0.6115-0.1194i	-0.7250-0.2011i
30	-0.5977	-0.5980-0.0140i	-0.6110-0.0481i	-0.6086-0.1181i	-0.7219-0.1986i
Tip Correction					
NS	k_r=0.001	k_r=0.1	k_r=0.5	k_r=1.0	k_r=2.0
18	-0.5788	-0.5791-0.0145i	-0.5935-0.0496i	-0.5920-0.1184i	-0.7011-0.2002i
25	-0.5794	-0.5798-0.0145i	-0.5950-0.0487i	-0.5927-0.1164i	-0.7032-0.1958i
30	-0.5796	-0.5800-0.0145i	-0.5954-0.0483i	-0.5929-0.1156i	-0.7037-0.1942i

Table 2(d): Antisymmetric (roll damping) convergence behavior for aspect ratio 7.0 rectangular wing with 40 Chordwise Boxes

No Tip Correction					
NS	k_r=0.001	k_r=0.1	k_r=0.5	k_r=1.0	k_r=2.0
22	-0.6040	-0.6043-0.0139i	-0.6160-0.0484i	-0.6141-0.1201i	-0.7281-0.2024i
30	-0.5977	-0.5981-0.0140i	-0.6113-0.0478i	-0.6089-0.1174i	-0.7231-0.1968i
35	-0.5952	-0.5956-0.0141i	-0.6094-0.0475i	-0.6068-0.1165i	-0.7209-0.1948i
Tip Correction					
NS	k_r=0.001	k_r=0.1	k_r=0.5	k_r=1.0	k_r=2.0
22	-0.5792	-0.5796-0.0145i	-0.5947-0.0488i	-0.5927-0.1166i	-0.7033-0.1962i
30	-0.5796	-0.5800-0.0144i	-0.5957-0.0480i	-0.5932-0.1150i	-0.7049-0.1924i
35	-0.5797	-0.5802-0.0144i	-0.5960-0.0477i	-0.5934-0.1144i	-0.7053-0.1911i

Table 2(e): Antisymmetric (roll damping) convergence behavior for aspect ratio 7.0 rectangular wing with 50 Chordwise Boxes

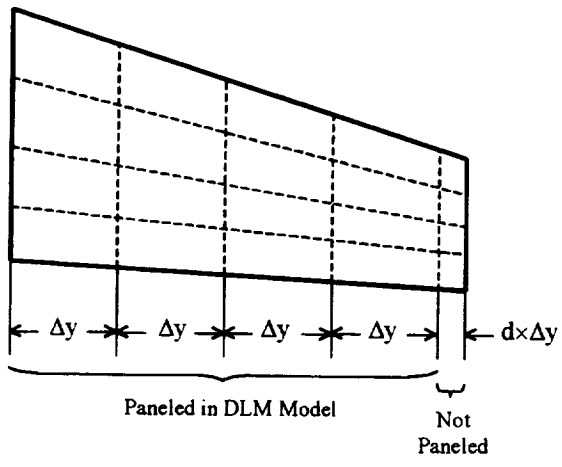

Figure 1: Tip Inset Illustration.

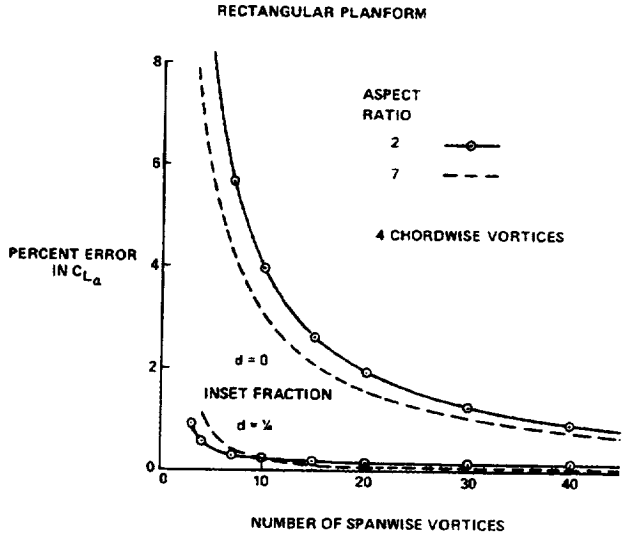

Figure 2: Effect of Tip Inset on Steady $C_{L\alpha}$ (Hough[2]).

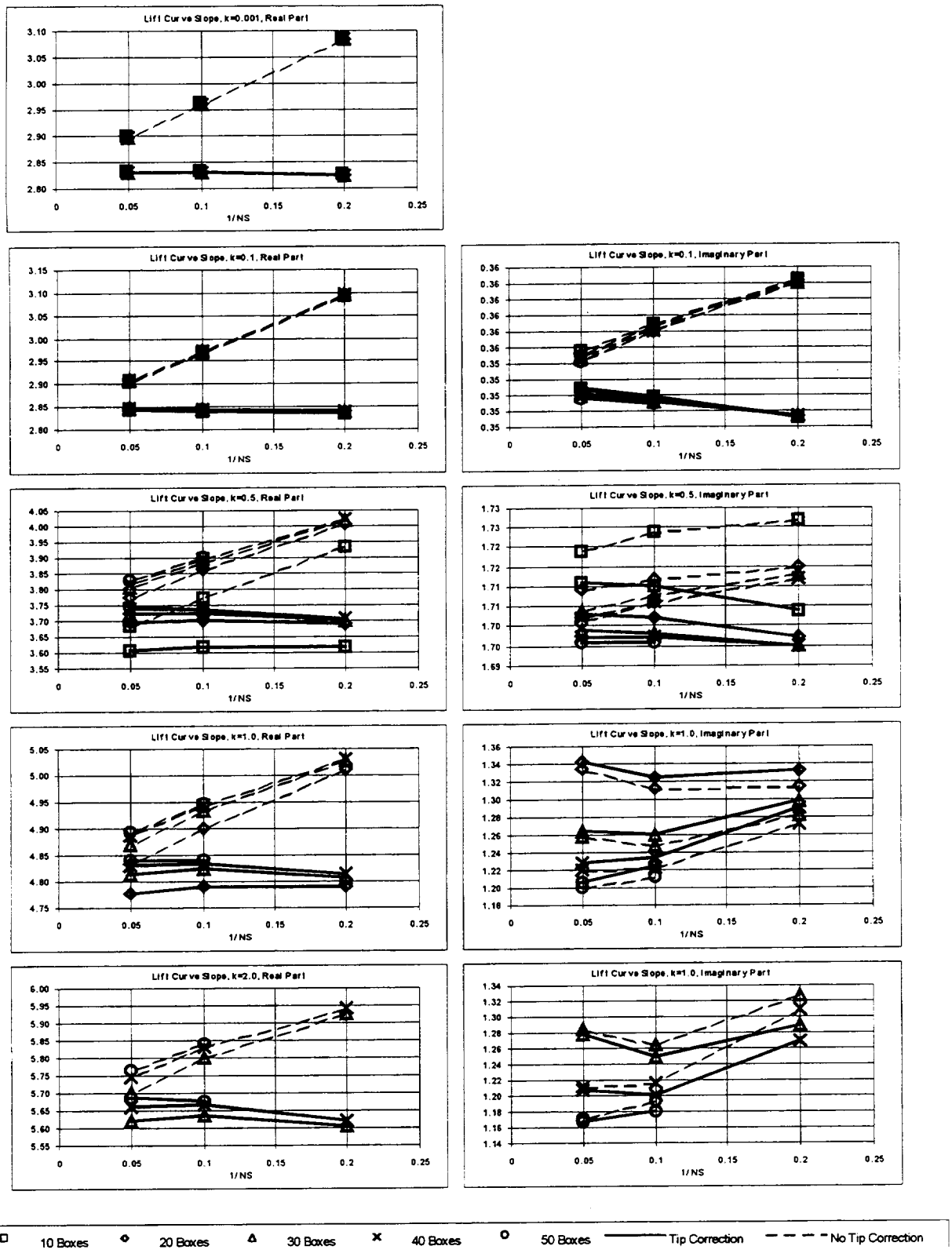

Figure 3: Convergence behavior of Lift due to pitching oscillations for the AR 2 rectangular wing. Real part on left, Imaginary part on Right.

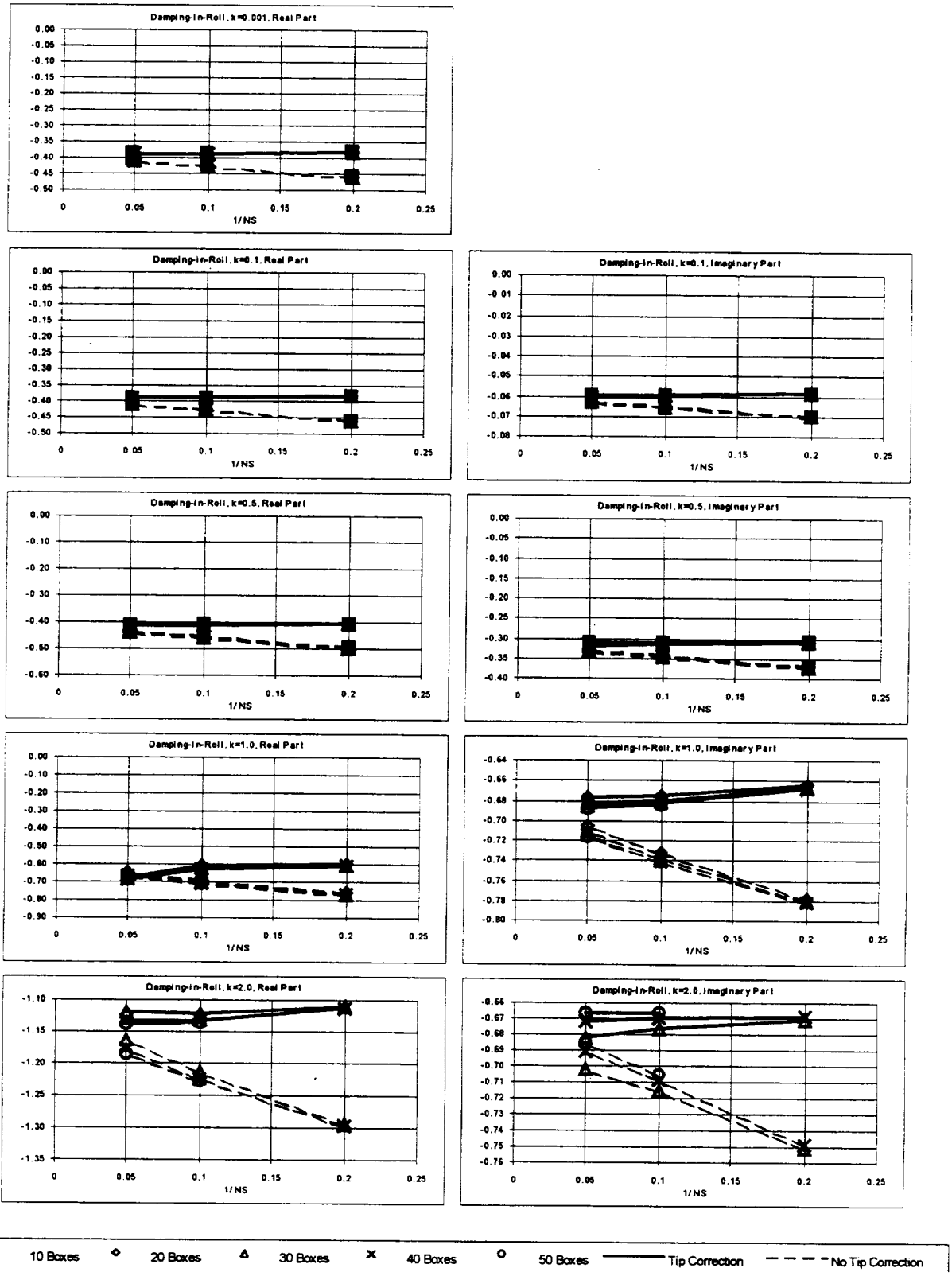

Figure 4: Convergence behavior of Rolling moment due to roll oscillations for the AR 2 rectangular wing. Real part on left, Imaginary part on Right.

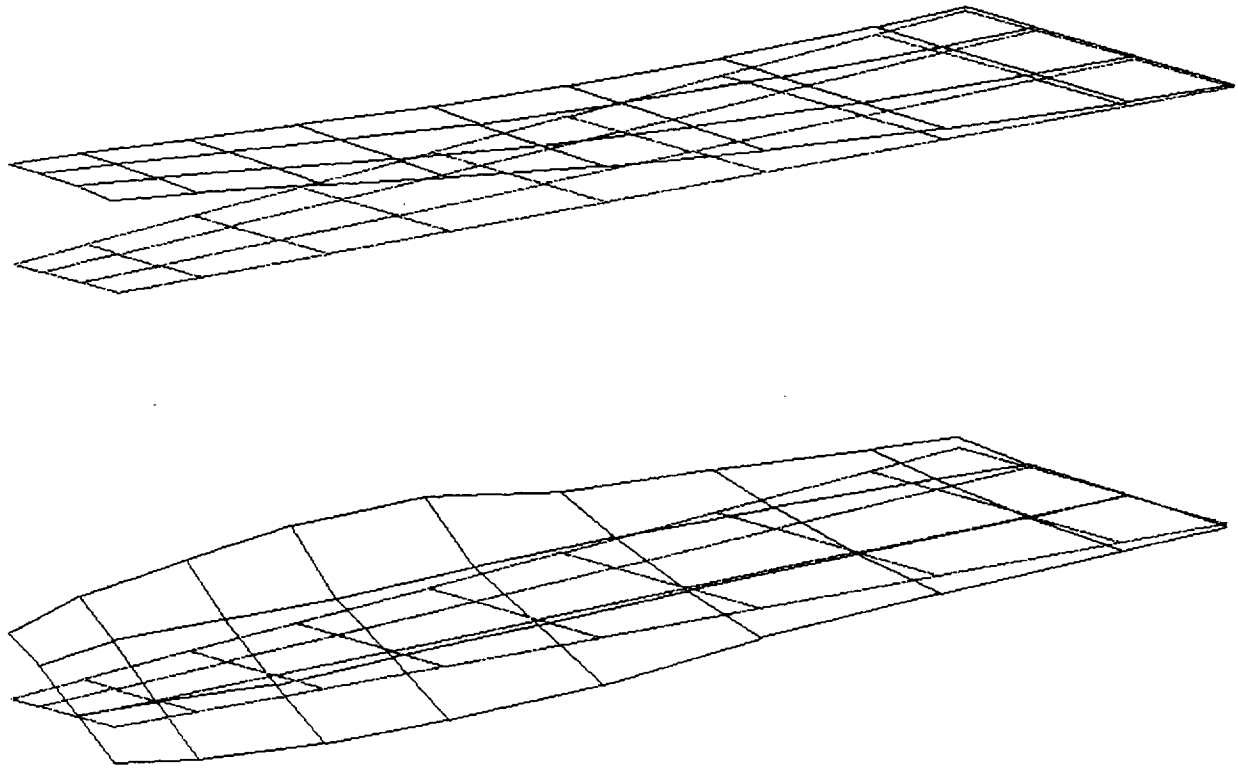

Figure 5: LANN Wing: First Bending and Torsion Mode Shapes.

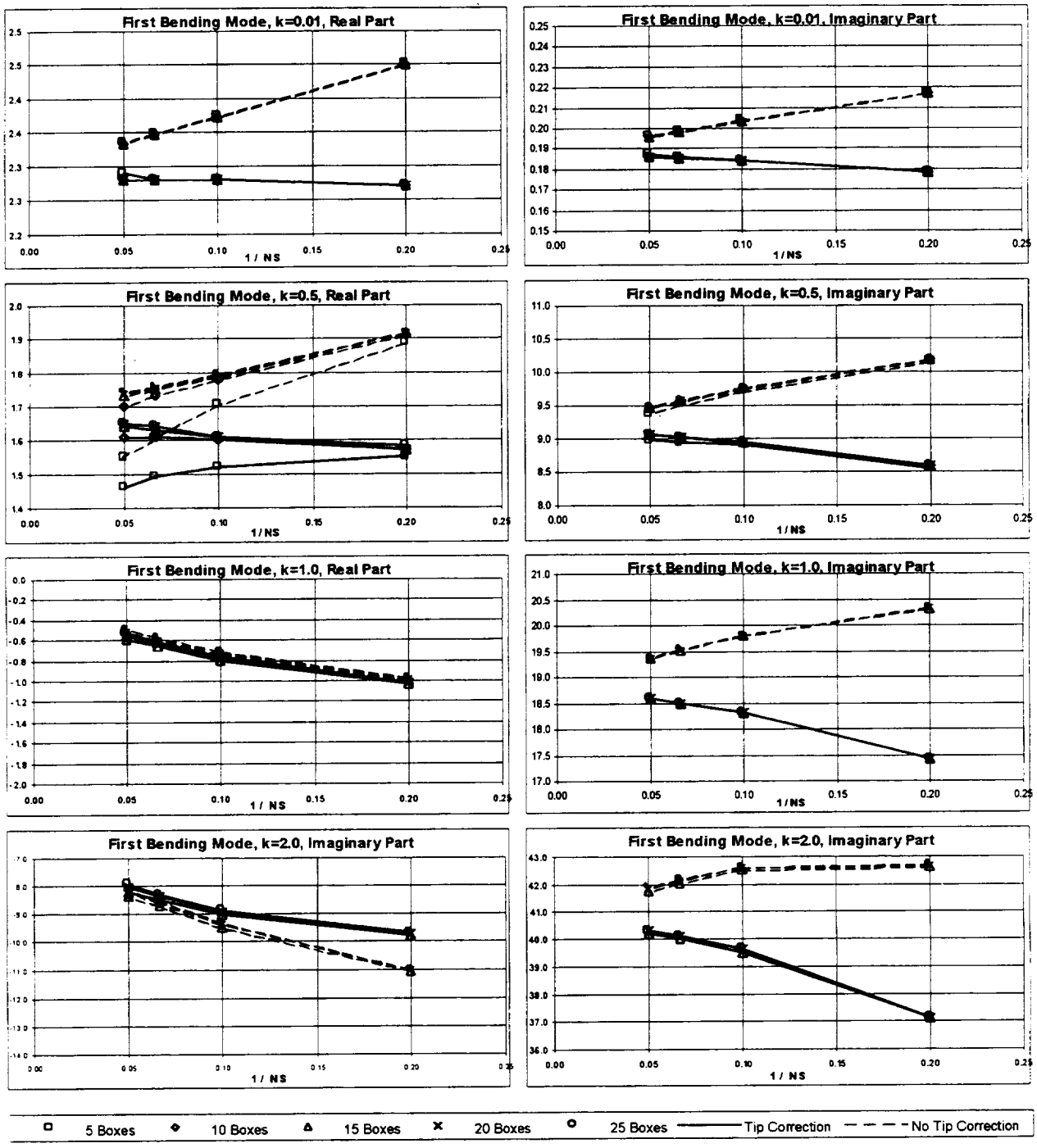

Figure 6: Convergence behavior of generalized aerodynamic force in first bending mode due to first bending mode excitation. Variation in chordwise boxes, spanwise strips, and tip configuration is shown vs. reduced frequency.

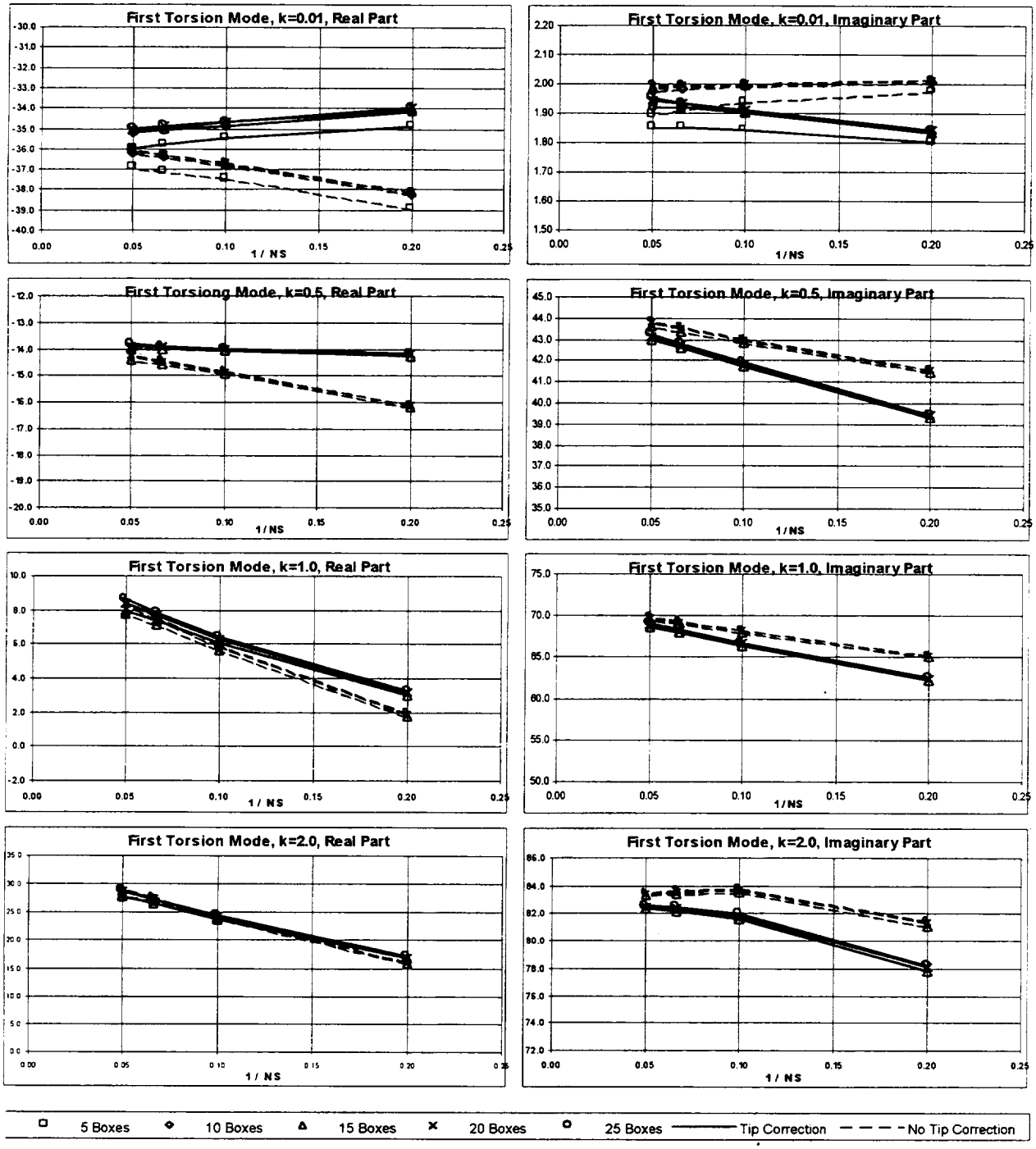

Figure 7: Convergence behavior of generalized aerodynamic force in first torsion mode due to first torsion mode excitation. Variation in chordwise boxes, spanwise strips, and tip configuration is shown vs. reduced frequency.

Aeroelastic Analysis of a Trimmed Generic Hypersonic Vehicle

I. Nydick* and P. P. Friedmann†
Mechanical and Aerospace Engineering Dept.
University of California
Los Angeles, California 90095 – 1597

ABSTRACT

The aeroelastic equations of motion governing a hypersonic vehicle in free flight are derived. The equations of motion for a translating and rotating flexible body using Lagrange's equations in terms of quasi-coordinates are presented. These equations are simplified for the case of a vehicle with pitch and plunge rigid body degrees of freedom and small elastic displacements. The displacements are approximated by a truncated series of the unrestrained mode shapes, which are obtained using equivalent plate theory. Subsequently, the nonlinear equations of motion are linearized about the trim state, which is obtained using a rigid body trim model and steady hypersonic aerodynamics. The appropriate flutter derivatives are calculated from piston theory. Results describing mode shapes, trim behavior, and aeroelastic stability of a generic hypersonic vehicle are presented.

NOMENCLATURE

A	Area
$\mathbf{A}$	Flutter boundary eigenproblem matrix
a_∞	Free stream sound velocity
$\mathbf{C}(\Theta)$	Orthogonal rotation matrix from the inertial axes to the body axes
C_p	Pressure coefficient
c_{ft}, c_{fr}	Chord length of fin tip and root, respectively
D	Domain of integration of the flexible body
$\mathbf{D}(\Theta)$	Transformation matrix relating the time derivatives of the Euler angles to the angular velocity vector

*Research Assistant
†Currently François-Xavier Bagnoud Professor, Dept. of Aerospace Engineering, University of Michigan, AnnArbor, MI 48109-2140

d_f	Distance from vehicle c.g. to leading edge of canted fin root chord
d_e	Distance from vehicle c.g. to aerodynamic center of elevon
e_T	Thrust eccentricity
$\mathbf{F}$	Nonconservative force vector, expressed in body axes
$\hat{\mathbf{F}}$	Vector of distributed generalized forces
g	Acceleration of gravity
h^b	Depth distribution of equivalent plate trapezoidal segment
$\mathbf{I}$	Identity matrix
$\mathbf{J}$	Matrix of mass moments of inertia of the deformed body
$\mathbf{J^o}$	Matrix of mass moments of inertia of the undeformed body
$J^o_{xx}, J^o_{yy}, J^o_{zz}, J^o_{xy}$	Mass moments of intertia of the undeformed body
$\hat{J}^o_{yy}$	Nondimensionalized mass moment of inertia for the undeformed hypersonic vehicle, $\frac{2J^o_{yy}}{\rho_\infty A_t l^3_{lb}}$
$\mathbf{K}$	Stiffness matrix
$\boldsymbol{\mathcal{L}}$	Matrix of structural operators on $\mathbf{u}$
L	Lagrangian of the hybrid system, written as a function of generalized coordinates
$\bar{L}$	Lagrangian of the hybrid system, written as a function of quasi-coordinates
$\bar{\mathrm{L}}$	Trim lift
l	length
M	Moment component in the y direction of the body axes
M_c	Mach number at which flutter occurs
$\mathbf{M}$	Moment vector written in terms of components along the body axes
$\mathbf{M^g}$	Generalized mass matrix
M_∞	Free-stream mach number
m	Mass of the flexible body
$\hat{m}$	nondimensionalized mass of the hypersonic vehicle, $\frac{2m}{\rho_\infty A_t l_{lb}}$
$\bar{m}$	Mass per unit area
N_m	Number of normal modes in truncated series
$\hat{\mathbf{n}}$	Unit normal
O	Origin of the body axes
P	Arbitrary point on flexible body
p, q, r	Angular velocity components referred to body axes, in x,y, and z directions respectively
p_l	Pressure on lower surface
p_u	Pressure on upper surface
p_∞	Free-stream pressure
$\mathbf{Q}$	Vector of discrete generalized forces
$\hat{\mathbf{Q}}$	Vector of generalized forces used in modal expansion method
$\mathbf{q}$	Vector of generalized coordinates
q_∞	Free-stream dynamic pressure
$\hat{q}$	Nondimensionalized pitch rate, $\frac{l_{lb}q}{V_{oz}}$
$\mathbf{q_x}, \mathbf{q_y}, \mathbf{q_z}, \mathbf{q_{\Phi_x}}, \mathbf{q_{\Phi_y}}$	Vectors of the unknown power series coefficients for $u_{xo}, u_{yo}, u_{zo}, \Phi_x, \Phi_y$,

	respectively
$\mathbf{R_o}$	Position vector of origin of body axes with respect to the inertial axes
$\mathbf{R_o^I}$	$\mathbf{R_o}$, but with components given with respect to unit vectors of the inertial axes
$\mathbf{r}$	Position vector of typical point P in the undeformed configuration with respect to the body axes
$\mathbf{r_p}$	Position vector of typical point P in the deformed body with respect to the inertial axes
s_f	Span of canted fin
T	Kinetic energy
t	Time
t_k	Thickness distribution of kth layer of equivalent plate trapezoidal segment cover skin
$\hat{t}$	Nondimensional time, $\frac{\bar{V}_{oz}t}{l_{lb}}$
U	Strain energy
U_o	Strain energy density
U_∞	Free-stream velocity
$\mathbf{u}$	Vector of elastic displacements
$\mathbf{u}_o$	Vector of elastic displacements of the reference surface
V	Potential energy
V_g	Potential energy due to gravity
$\mathbf{V_o}$	Velocity of origin of body axes, in body axis components
$\mathbf{v}$	Time derivative of $\mathbf{u}$ with respect to a reference frame attached to the body axes
v_p	effective piston velocity
$\mathbf{v_p}$	Velocity vector of typical point P in the deformed body with respect to the inertial axes
X, Z	Components of $\mathbf{F}$ in the x and z directions of the body axes, respectively
X_I, Y_I, Z_I	Inertial axes
x, y, z	Body axes
$\mathbf{\Delta x}$	vector of degrees of freedom for linearized model of the generic hypersonic vehicle
$\bar{Z}^{u,l}(x, y)$	initial curvature of vehicle upper(u) or lower(l) surface
Z_c	Camber distribution of equivalent plate trapezoidal segment

Greek Symbols

α	Angle of attack
γ	Specific heat
γ_c	Climb angle
$\delta()$	Variational symbol
δ_{ij}	Kronecker delta function
δ_e	Elevon deflection
$\Delta()$	Perturbed quantity
ϵ_T	Inclination of the thrust vector
ζ_k	Modal damping of the k'th mode

η	Spanwise local coordinate of equivalent plate trapezoidal segment
$\hat{\eta}_i$	Nondimensionalized modal coordinate, $\eta_i (i = 1, \ldots, N_m)$, $\frac{\eta_i}{l_{lb}}$
$\hat{\eta}_{N_m+i}$	Nondimensionalized modal coordinate, $\eta_{N_m+i} (i = 1, \ldots, N_m)$, $\frac{\eta_i}{V_{ox}}$
$\boldsymbol{\eta}$	Vector of generalized coordinates used in modal expansion
ξ	Streamwise local coordinate of equivalent plate trapezoidal segment
$\boldsymbol{\Theta}$	3×1 Matrix of Euler angles
θ_f	Angle of the X33 fins, measured from horizontal
ϕ, θ, ψ	Euler angles, elements of $\boldsymbol{\Theta}$
$\boldsymbol{\phi_x}, \boldsymbol{\phi_y}, \boldsymbol{\phi_z}$, $\boldsymbol{\phi_{\Phi_x}}, \boldsymbol{\phi_{\Phi_y}}$	Vectors of power series terms for the approximating polynomials of $u_{xo}, u_{yo}, u_{zo}, \Phi_x, \Phi_y$, respectively
$\boldsymbol{\Phi}_k$	k'th normal mode
$\boldsymbol{\Phi}$	Modal matrix
Φ_x, Φ_y	Rotations due to transverse shear in the xz and yz planes respectively
ρ	Vehicle density
$\boldsymbol{\omega}$	Angular velocity
ω_k	Natural frequency of k'th normal mode
$\hat{\omega}_k$	Nondimensionalized natural frequency, $\frac{\omega_k l_{lb}}{V_{ox}}$

Special Symbols

$\dot{()}$	Derivative with respect to time
$()'$	Derivative with respect to spatial coordinate
$\hat{()}$	Indicates energy density of variable or nondimensionalized quantity, depending on context.
$\tilde{()}$	Skew symmetric matrix
$\bar{()}$	Trimmed value
$()_{lb}$	Quantity with respect to the lifting body only
$()_f$	Quantity with respect to the canted fins only
$()_e$	Quantity with respect to the elevon only
$()_t$	Quantity with respect to the total vehicle

INTRODUCTION

Recent efforts aimed at designing prototype hypersonic vehicles, such as the NASA/Lockheed X33 reusable launch vehicle (RLV) and the NASA Hyper-X program, reflect the need for reliable, low cost flight vehicles capable of sustained hypersonic flight. However, the aeroelastic characteristics and the fundemental aeroelastic behavior of this class of vehicles is not well understood, and experimental verification of such behavior using dynamically scaled aeroelastic models in the hypersonic speed regime is not feasible. Due to the stringent minimum weight requirements of such a design, the vehicle structure will be quite flexible. Furthermore, the requirements of the flight profile, which specifies a large Mach number variation in the range of $0 < M_\infty < 12$, also introduces severe aerodynamic heating, which couples the

thermal and aeroelastic problem into an aerothermoelastic problem, which is quite difficult to handle.

Previous studies in this area have focused primarily on two classes of problems: the localized phenomenon of panel flutter and the aeroelastic behavior of the vehicle in the transonic regime, where experimental wind tunnel studies indicated potential aeroelastic problems [1–4]. Hypersonic panel flutter has been studied by a number of researchers, focusing on important effects such as aerodynamic heating [5], composite structure [6,7], nonlinear structural model [8], and initial panel curvature [9]. Approaches to the solution of the governing equations include the global Galerkin method [10] and the finite element method [11].

An aeroelastic analysis of the entire vehicle in free flight in the hypersonic regime requires the formulation of the governing equations of motion for an unrestrained flexible vehicle. A general discussion of the governing equations of motion for unrestrained flight vehicles can be found in the text by Bisplinghoff, Ashley, and Halfmann [12] and the series of papers by Milne [13,14]. Application to hypersonic vehicles has been studied by Schmidt, et. al. [15,16], where the primary emphasis has been on stability and control. A novel approach to the determination of the governing equations of motion of a flexible body using quasi-coordinates has been presented by Meirovitch [17]. The method of quasi-coordinates, which is discussed later in this paper, is an effective and labor-saving procedure for obtaining the governing equations for flexible structures involving rigid body and flexible degrees of freedom.

When representing the dynamics of a flexible aerospace vehicle, several alternatives exist. One can develop a finite element model for a vehicle, which usually involves a large number of degrees of freedom. The finite element degrees of freedom can be reduced by calculating a limited number of free vibration modes and using a normal mode transformation. An alternative to the finite element method is the equivalent plate theory, which produces significant savings in both computational time and model set-up effort while retaining acceptable modeling accuracy [18]. Recently, equivalent plate theory has received renewed attention and its modeling capabilities have been expanded so that it is now capable of representing complex aerospace vehicle structural configurations [19–21]. Such enhancements include the ability to model asymmetric fin cross-sections, out-of-plane fin segments, internal web and spar structures including transverse shear effects, thermal stresses, and general boundary conditions, as well as the ability to specify multiple trapezoidal segments and multiple sets of assumed displacement functions. In this study, equivalent plate theory is employed to calculate the free vibration modes of the unrestrained vehicle using the ELAPS code.

While the studies mentioned in this section have contributed to the understanding of hypersonic vehicle aeroelastic behavior, the fundamental question of coupling between rigid body dynamics and aeroelastic behavior has not been explored in detail, and the effect of the trim state on aeroelastic behavior is also not well understood. This paper has several objectives: (1) Present a derivation of the unrestrained aeroelastic equations of motion for a generic hypersonic vehicle resembling the X-33 configuration, (2) Use the formulation to determine the trim state of the flexible vehicle, (3) Develop a methodology for calculating the aeroelastic stability boundaries for this class of vehicles, including the effect of trim state and rigid body dynamics, (4) Calculate the mode shapes for a typical generic unrestrained vehicle and use them in aeroelastic stability calculations.

EQUATIONS OF MOTION OF UNRESTRAINED VEHICLE

The derivation of the equations of motion for the unrestrained generic hypersonic vehicle is based upon Lagrange's equations of motion in terms of quasi-coordinates following the approach described in [17].

Lagrange's Equations for Quasi-Coordinates

The motivation for using quasi-coordinates arises from the fact that Lagrange's equations in terms of generalized coordinates are difficult to apply because a transformation from body axes to inertial axes must be performed, producing complicated expressions for the kinetic energy. The rotational kinetic energy is most compactly written down in terms of the components of angular velocity of the body which are time derivatives of quasi-coordinates. Quasi-coordinates are defined in terms of their time derivatives. Specifically, these time derivatives are defined as *nonintegrable* linear combinations of the generalized velocities. Because the time derivatives are nonintegrable, the quasi-coordinate itself is undefined.

The Lagrangian for an unrestrained flexible body, often called a hybrid system, may be written in the functional form [17]

$$L = L(q_i, \dot{q}_i, u_j, \dot{u}_j, u'_j, u''_j, \cdots, u_j^{(p)}, t) \tag{1}$$

where $q_i(t)(i = 1, 2, \ldots, m)$ are the generalized coordinates governing rigid body motion and $u_j(P,t)(j = 1, 2, \ldots, n)$ are the distributed coordinates of elastic deflections at point P on the body. Lagrange's equations may then be written in symbolic vector form as

$$\frac{\mathrm{d}}{\mathrm{d}t}\left(\frac{\partial L}{\partial \dot{\mathbf{q}}}\right) - \frac{\partial L}{\partial \mathbf{q}} = \mathbf{Q} \tag{2a}$$

$$\frac{\partial}{\partial t}\left(\frac{\partial \hat{T}}{\partial \dot{\mathbf{u}}}\right) - \frac{\partial \hat{T}}{\partial \mathbf{u}} + \frac{\partial \hat{V}^*}{\partial \mathbf{u}} + \boldsymbol{\mathcal{L}}\mathbf{u} = \hat{\mathbf{F}} \tag{2b}$$

where $\boldsymbol{\mathcal{L}}$ is an $n \times n$ matrix of structural operators and the following notation has been used:

$$\frac{\partial L}{\partial \dot{\mathbf{q}}} = \left[\frac{\partial L}{\partial \dot{q}_1}, \frac{\partial L}{\partial \dot{q}_2}, \cdots, \frac{\partial L}{\partial \dot{q}_m}\right]^T \tag{3}$$

The other derivatives of scalars with respect to vectors that appear in Eqs.(2) are to be interpreted similarly. Appropriate boundary conditions for the elastic deflections must be appended to Eqs.2 for a properly posed initial-boundary value problem.

The coordinate systems needed to describe the translating and rotating elastic body are shown in Fig. 1. The body axes translate and rotate with the body, though they are not necessarily attached to a specific material point in the body. Possible choices for the body axes include attached axes, mean axes, and principal axes [13]. Attached axes are attached to

a specific material point in the body, mean axes are oriented such that no linear or angular momentum is generated by the flexible motion, and principal axes are oriented such that they are the principal axes of the deforming body at all times. Mean axes are used in this study, as described later in the paper.

Natural choices for the generalized coordinates of the translating and rotating elastic body are the components of the position vector of the body axes origin referred to inertial axes, and the Euler angles, $\Theta = [\phi, \theta, \psi]^T$, shown in Fig. 2. Time derivatives of these generalized coordinates are denoted by the symbols, $\dot{\mathbf{R}}_{\mathbf{o}}^{\mathbf{I}}$ and $\dot{\Theta}$, respectively. The Lagrangian has a simpler form when written in terms of time derivatives of the position vector referred to body axes and the angular velocity vector of the body axes, when compared to its form in terms of the time derivatives of these generalized coordinates. The transformations required to write Lagrange's equations in terms of the former set of coordinates are given by [17]

$$\mathbf{V_o} = \mathbf{C}(\Theta)\dot{\mathbf{R}}_{\mathbf{o}}^{\mathbf{I}} \tag{4a}$$

$$\omega = D(\Theta)\dot{\Theta} \tag{4b}$$

where $\mathbf{C}(\Theta)$ is

$$\mathbf{C} = \begin{bmatrix} c\theta c\psi & c\theta s\psi & -s\theta \\ s\phi s\theta c\psi - c\phi s\psi & s\phi s\theta s\psi + c\theta c\psi & s\phi c\theta \\ c\phi s\theta c\psi + s\phi s\psi & c\phi s\theta s\psi - s\phi c\psi & c\phi c\theta \end{bmatrix} \tag{5}$$

and $D(\Theta)$ is

$$D(\Theta) = \begin{bmatrix} 1 & 0 & -s\theta \\ 0 & c\phi & s\phi c\theta \\ 0 & -s\phi & c\phi c\theta \end{bmatrix} \tag{6}$$

and 's' and 'c' are abbreviations for 'sin' and 'cos', respectively. Examination of Eqs.(4) shows that the components of both $\mathbf{V_o}$ and ω meet the definition of time derivatives of quasi-coordinates stated earlier, that is, both are given as nonintegrable linear combinations of the generalized velocities.

After considerable algebraic manipulation, it can be shown that when using Eqs.(4), Lagrange's equations (Eqs.(2)) may be rewritten in terms of time derivatives of the quasi-coordinates as

$$\frac{\mathrm{d}}{\mathrm{dt}}\left(\frac{\partial \bar{L}}{\partial \mathbf{V_o}}\right) + \tilde{\omega}\frac{\partial \bar{L}}{\partial \mathbf{V_o}} - \mathbf{C}\frac{\partial \bar{L}}{\partial \mathbf{R}_{\mathbf{o}}^{\mathbf{I}}} = \mathbf{F} \tag{7a}$$

$$\frac{\mathrm{d}}{\mathrm{dt}}\left(\frac{\partial \bar{L}}{\partial \omega}\right) + \tilde{\mathbf{V}}_{\mathbf{o}}\frac{\partial \bar{L}}{\partial \mathbf{V_o}} + \tilde{\omega}\frac{\partial \bar{L}}{\partial \omega} - (\mathbf{D}^T)^{-1}\frac{\partial \bar{L}}{\partial \Theta} = \mathbf{M} \tag{7b}$$

$$\frac{\mathrm{d}}{\mathrm{dt}}\left(\frac{\partial \hat{T}}{\partial \mathbf{v}}\right) - \frac{\partial \hat{T}}{\partial \mathbf{u}} + \frac{\partial \hat{V}^*}{\partial \mathbf{u}} + \mathcal{L}\mathbf{u} = \hat{\mathbf{F}} \tag{7c}$$

where $\mathbf{F}$ and $\mathbf{M}$ are nonconservative force and torque vectors, respectively, written in terms of components along the body axes and the displacements $\mathbf{u}$ are subject to appropriate

boundary conditions. Note the notation

$$\tilde{\mathbf{a}} = \begin{bmatrix} 0 & -a_z & a_y \\ a_z & 0 & -a_x \\ -a_y & a_x & 0 \end{bmatrix} \tag{8}$$

where $\mathbf{a} = [a_x, a_y, a_z]^T$ is a 3×1 vector and $\tilde{\mathbf{a}}$ is used to denote the 3×3 skew-symmetric matrix formed from $\mathbf{a}$. Also the bar above the Lagrangian indicates that it is to be expressed in terms of time derivatives of quasi-coordinates.

The equations for a translating and rotating flexible body may be completed by substituting appropriate expressions for the Lagrangian into Eqs.(4). Using the geometry given in Fig. 1, the position and velocity of material point P can be written as

$$\mathbf{r_p} = \mathbf{R_o} + \mathbf{r} + \mathbf{u} \tag{9a}$$

$$\mathbf{v_p} = \dot{\mathbf{R}}_\mathbf{o} + \boldsymbol{\omega} \times (\mathbf{r} + \mathbf{u}) + \mathbf{v} \tag{9b}$$

and expressions for the kinetic and potential energy may be obtained. When small elastic deformations are assumed, the displacements are expressed as a sum of unrestrained normal modes

$$\mathbf{u}(\mathbf{r}, t) = \sum_{k=1}^{N_m} \boldsymbol{\Phi}_k(\mathbf{r}) \eta_k(t) = \boldsymbol{\Phi}\boldsymbol{\eta} \tag{10}$$

where the modes satisfy the orthogonality relations given by

$$\int_V \boldsymbol{\Phi}_i \cdot \boldsymbol{\Phi}_j \rho \, dV = M_i^g \delta_{ij} \tag{11}$$

where M_i^g is the i'th generalized mass. This orthogonality property holds for both the rigid body and flexible modes.

Simplification of the kinetic energy expression can be obtained by employing mean axes with the origin at the center of gravity of the deformed vehicle as the body axes. Mean axes reduce the inertial coupling between the rigid and flexible equations of motion. Mean axes are chosen such that, at every instant, the linear and angular momenta of the relative motion with respect to the body axes are identically zero, which leads to the relations [13]

$$\int_V \rho \mathbf{u} \, dV = 0 \tag{12}$$

$$\int_V \rho \mathbf{r} \times \mathbf{u} \, dV = 0 \tag{13}$$

Using Eqs.(9)-(11) and employing mean axes, the kinetic energy expression becomes

$$T = \frac{1}{2} m \mathbf{V}_\mathbf{o}^T \mathbf{V}_\mathbf{o} + \frac{1}{2} \boldsymbol{\omega}^T \mathbf{J}^\circ \boldsymbol{\omega} + \frac{1}{2} \int_D \rho \left[2\mathbf{r}^T \tilde{\boldsymbol{\omega}}^T \tilde{\boldsymbol{\omega}} \boldsymbol{\Phi} \boldsymbol{\eta} + \boldsymbol{\eta}^T \boldsymbol{\Phi}^T \tilde{\boldsymbol{\omega}}^T \tilde{\boldsymbol{\omega}} \boldsymbol{\Phi} \boldsymbol{\eta} \right] dD + \frac{1}{2} \dot{\boldsymbol{\eta}}^T \mathbf{M}^\mathbf{g} \dot{\boldsymbol{\eta}} \tag{14}$$

where $\mathbf{M^g}$ is a $N_m \times N_m$ diagonal matrix with the k'th diagonal element equal to the generalized mass

$$M_k^g = \int_D \rho \Phi_k^T \Phi_k \, dD \tag{15}$$

The potential energy is written

$$U = \frac{1}{2} \boldsymbol{\eta}^T \mathbf{K^g} \boldsymbol{\eta} \tag{16}$$

where $\mathbf{K^g}$ is a $N_m \times N_m$ diagonal matrix with the k'th diagonal element equal to

$$K_k^g = \omega_k^2 M_k^g \tag{17}$$

where ω_k is the natural frequency corresponding to the k'th normal mode. Finally, the potential energy due to gravity is written as

$$V_g = -mgR_{oZ}^I \tag{18}$$

Substituting Eqs.(14),(16),and (18) into Eqs.(7) yields the following nonlinear equations of motion

$$m\dot{\mathbf{V}}_\mathbf{o} = m\tilde{\mathbf{V}}_\mathbf{o}\boldsymbol{\omega} - \mathbf{C}\frac{\partial V_g}{\partial \mathbf{R_o^I}} + \mathbf{F} \tag{19a}$$

$$\mathbf{J^o}\dot{\boldsymbol{\omega}} = -\tilde{\boldsymbol{\omega}}\mathbf{J^o}\boldsymbol{\omega} + \mathbf{M} \tag{19b}$$

$$\mathbf{M^g}\ddot{\boldsymbol{\eta}} + \mathbf{C^g}\dot{\boldsymbol{\eta}} + (\mathbf{K^g} - \int_D \rho \Phi^T \tilde{\boldsymbol{\omega}}^T \tilde{\boldsymbol{\omega}} \Phi \, dD)\boldsymbol{\eta} = \int_D \rho \mathbf{r}^T \tilde{\boldsymbol{\omega}}^T \tilde{\boldsymbol{\omega}} \Phi \, dD + \hat{\mathbf{Q}} \tag{19c}$$

This study focuses on the longitudinal dynamics of a symmetric vehicle in horizontal flight. The fact that pure longitudinal motion cannot give rise to any lateral motion for such a configuration, even for large values of the motion variables, permits the lateral motion variables to be eliminated from Eqs.(19a) and (19b), resulting in the following rigid body equations of motion

$$m(\dot{V}_{ox} + qV_{oz}) = X - mg\sin\theta \tag{20a}$$

$$m(\dot{V}_{oz} - qV_{ox}) = Z + mg\cos\theta \tag{20b}$$

$$J_{yy}^o \dot{q} = M \tag{20c}$$

The equation governing the elastic motion remains unchanged.

Trim State of the Vehicle

Aeroelastic stability boundaries are obtained from dynamic equations linearized about a static trim state. Lateral trim is assumed to be satisfied and decoupled from the longitudinal trim state. Longitudinal trim is obtained for level, ascending or descending flight by using elevons located at the trailing edge of the lifting body, as shown in Fig 3(a). The trim state

of the vehicle involves three primary quantities: $\bar{\alpha}$, $\bar{\delta}_e$, and $\bar{T}$. These quantities are depicted in Fig. 3(a), which shows the hypersonic vehicle in climb at an angle, $\bar{\gamma}_c$, which is equal to the Euler angle, $\bar{\theta}$.

Four sets of axes are used to describe the vehicle. The first set is an inertial axis system, X_I, Y_I, Z_I, attached to a flat earth. The second set is a stability axis system, x_s, y_s, z_s, located at the vehicle CG and initially aligned with the equilibrium flight velocity, $\bar{\mathbf{V}}_\mathbf{o}$. It is obtained from the inertial axes by locating them at the vehicle center of mass and rotating about Y_I by the angle, $\bar{\gamma}_c + \Delta\theta$, where $\Delta\theta = 0$ in the trim state. The third is a body axis system, x_b, y_b, z_b, obtained by rotating the stability axes about y_s by the trim angle of attack, $\bar{\alpha}$, which aligns the x_b axis with the zero lift line (Z.L.L.). The fourth system is the x_{bi}, y_{bi}, z_{bi} body axis (shown in Fig. 4), obtained from the x_b, y_b, z_b system by shifting the axes origin to the junction of the right fin trailing edge and the main lifting body and rotating about x_b by the fin inclination angle, θ_f, which directs the y_{bi} axis outward along the right fin. This additional system is needed to represent the aerodynamic loads on the canted fin surfaces.

The net aerodynamic force acting on the vehicle is given by the lift, $\bar{\mathrm{L}}$, and the drag, $\bar{\mathrm{D}}$, also shown in Fig. 3(a). Alternatively, the net aerodynamic force may be resolved into components, $\bar{\mathrm{N}}$, normal to the zero lift line, and $\bar{\mathrm{A}}$, parallel to the zero lift line; or components, $\bar{Z}^a$ and $\bar{X}^a$, directed along the stability axes, z_s and x_s, respectively. Because the x_s-axis is initially oriented in the direction of $\bar{V}_o$, $\bar{Z}^a_s$ equals the trim lift, $\bar{\mathrm{L}}$, and $\bar{X}^a_s$ equals the trim drag, $\bar{\mathrm{D}}$. However, if the vehicle is perturbed from the trim state the forces $\bar{Z}^a_s$ and $\bar{X}^a_s$ will differ from L and D, respectively.

In order to account for the effect of thrust on the trim state, a general case is considered where the thrust has an eccentricity, e_T, and can be inclined by an angle, ϵ_T, relative to the vehicle zero lift line, as shown in Fig. 5.

Force and moment equilibrium conditions in the vertical plane, with respect to the stability axes, are:

$$\sum \mathcal{F}_{x_s} = 0 \tag{21a}$$

$$\sum \mathcal{F}_{z_s} = 0 \tag{21b}$$

$$\sum \mathcal{M}_{y_s} = 0 \tag{21c}$$

Using Figs. 3(a) and 5 and dividing the forces by $\frac{1}{2}\rho_\infty \bar{V}^2_{ox} A_t$ and the moments by $\frac{1}{2}\rho_\infty \bar{V}^2_{ox} A_t l_{lb}$, the nondimensional trim equations for the rigid vehicle are obtained:

$$C_{\bar{T}_R}\cos(\epsilon_T + \bar{\alpha}) - C_{\bar{\mathrm{D}}_R} = C_W \sin\bar{\gamma}_c \tag{22a}$$

$$C_{\bar{T}_R}\sin(\epsilon_T + \bar{\alpha}) + C_{\bar{\mathrm{L}}_R} = C_W \cos\bar{\gamma}_c \tag{22b}$$

$$C_{\bar{M}_R} + C_{\bar{T}_R} e_T = 0 \tag{22c}$$

where

$$C_{\bar{\mathrm{L}}_R} = \frac{\bar{\mathrm{L}}_R}{\frac{1}{2}\rho_\infty \bar{V}^2_{ox} A_t}, \quad C_{\bar{\mathrm{D}}_R} = \frac{\bar{\mathrm{D}}_R}{\frac{1}{2}\rho_\infty \bar{V}^2_{ox} A_t}, \quad C_{\bar{M}_R} = \frac{\bar{M}^a_R}{\frac{1}{2}\rho_\infty \bar{V}^2_{ox} A_t l_{lb}}$$

$$C_{\bar{T}_R} = \frac{\bar{T}_R}{\frac{1}{2}\rho_\infty \bar{V}^2_{ox} A_t}, \quad C_W = \frac{mg}{\frac{1}{2}\rho_\infty \bar{V}^2_{ox} A_t}$$

The steady aerodynamic loads are obtained by treating the vehicle as a rigid flat plate. For flow in the hypersonic regime, which is highly nonlinear, the aerodynamic loads may be approximated using modified newtonian theory[22], which states that the pressure coefficient is given by: [23]

$$C_p = \begin{cases} C_{p_{\max}} \left(\frac{\bar{\mathbf{V}}_o \cdot \hat{\mathbf{n}}}{\bar{V}_\infty}\right)^2 & \bar{\mathbf{V}}_o \cdot \hat{\mathbf{n}} < 0 \\ 0 & \bar{\mathbf{V}}_o \cdot \hat{\mathbf{n}} \geq 0 \end{cases} \tag{23}$$

where $C_{p_{\max}}$ is the maximum value of the pressure coefficient, evaluated at a stagnation point behind a normal shock wave, i.e.,

$$C_{p_{\max}} = \frac{2}{\gamma M_\infty^2}\left[\left(\frac{\gamma+1}{2}M_\infty^2\right)^{\frac{\gamma}{\gamma-1}}\left(\frac{\gamma+1}{2\gamma M_\infty^2-\gamma+1}\right)^{\frac{1}{\gamma-1}}-1\right] \tag{24}$$

Note from Eq.(23) that the pressure is assumed to be equal to the free stream pressure on those parts of the body for which $\bar{\mathbf{V}}_o \cdot \hat{\mathbf{n}} \geq 0$. These parts of the body are said to lie in the *aerodynamic shadow.*

The lift, drag, and moment are obtained by integrating the pressure over the fuselage, canted fins, and elevon separately , and summing each contribution:

$$\begin{aligned} \bar{\mathrm{L}} &= \cos\bar{\alpha}\int\int_{A_{lb}} \Delta\bar{p}_{lb}(x_s,y_s)\,dx_s dy_s + 2\cos\theta_f\cos\bar{\alpha}\int\int_{A_f}\Delta\bar{p}_f(x_{bi},y_{bi})\,dx_{bi}dy_{bi} \\ &\quad + \cos(\bar{\alpha}+\bar{\delta}_e)\int\int_{A_e}\Delta\bar{p}_e(x_e,y_e)\,dx_e dy_e \end{aligned} \tag{25a}$$

$$\begin{aligned} \bar{\mathrm{D}} &= \sin\bar{\alpha}\int\int_{A_{lb}} \Delta\bar{p}_{lb}(y_s,z_s)\,dy_s dz_s + 2\cos\theta_f\sin\bar{\alpha}\int\int_{A_f}\Delta\bar{p}_f(y_{bi},z_{bi})\,dy_{bi}dz_{bi} \\ &\quad + \sin(\bar{\alpha}+\bar{\delta}_e)\int\int_{A_e}\Delta\bar{p}_e(y_e,z_e)\,dy_e dz_e \end{aligned} \tag{25b}$$

$$\begin{aligned} \bar{M} &= \int\int_{A_{lb}} \Delta\bar{p}_{lb}(x_s,y_s)\,dx_s dy_s + 2\cos\theta_f\int\int_{A_f}\Delta\bar{p}_f(y_{bi},z_{bi})x_s\,dy_{bi}dz_{bi} \\ &\quad + \bar{\mathrm{L}}_e d_e \end{aligned} \tag{25c}$$

Nondimensionalizing Eqs.(25) by dividing the lift and drag by $\frac{1}{2}\rho_\infty \bar{V}_o^2 A_t$ and the moment by $\frac{1}{2}\rho_\infty \bar{V}_o^2 A_t l_{lb}$, then using Eqs.(23) results in

$$\begin{aligned} C_{\bar{\mathrm{L}}} &= C_{p_{\max}}\left[\sin^2\bar{\alpha}\cos\bar{\alpha}\frac{A_{lb}}{A_t} + 2\sin^2\bar{\alpha}\cos\bar{\alpha}\cos^3\theta_f\frac{A_f}{A_t} + \right. \\ &\quad \left. \sin^2(\bar{\alpha}+\bar{\delta}_e)\cos(\bar{\alpha}+\bar{\delta}_e)\frac{A_e}{A_t}\right] \end{aligned} \tag{26a}$$

$$C_{\bar{\mathrm{D}}} = C_{p_{\max}}\left[\sin^3\bar{\alpha}\frac{A_{lb}}{A_t} + 2\sin^3\bar{\alpha}\cos^3\theta_f\frac{A_f}{A_t} + \sin^3(\bar{\alpha}+\bar{\delta}_e)\frac{A_e}{A_t}\right] \tag{26b}$$

$$C_{\bar{M}} = C_{p_{\max}}\left\{\frac{\sin^2\bar{\alpha}}{A_t l_{lb}}\left[\frac{s_1 w_{lb}^3}{24} - \frac{1}{4}s_1 s_2 w_{lb}^2 + \frac{1}{2}(s_2^2 - d_f^2 - c_{fr}^2 - 2d_f c_{fr})w_{lb}\right] - \right.$$

$$\sin^2\bar{\alpha}\cos^3\theta_f\left[\frac{2(d_f+c_{fr}+c_{ft})}{l_{lb}}\frac{A_f}{A_t}-\frac{1}{A_t l_{lb}}\left(\frac{1}{3}(s_4^2-s_3^2)s_f^3+s_4 m_2 s_f^2+m_2^2 s_f\right)\right]$$
$$-\sin^2(\bar{\alpha}+\bar{\delta}_e)\cos(\bar{\alpha}+\bar{\delta}_e)\frac{d_e}{l_{lb}}\frac{A_e}{A_t}\Bigg\} \tag{26c}$$

where

$$s_1 = \frac{2(l_{lb}-c_{fr})}{w_{lb}}, \quad s_2 = l_{lb}-c_{fr}-d_f$$
$$s_3 = \frac{c_{ft}}{s_f}, \quad s_4 = \frac{c_{fr}}{s_f}$$

The trim state is calculated by solving Eqs.(22) with the aerodynamic loads given by Eqs.(26) using a nonlinear rootfinding routine.

Linearization of Equations of Motion

The quantities in Eqs.(20) can be expressed as the sum of a steady state trim value and a time dependent small perturbation, indicated by the symbol Δ preceeding the quantity, thus

$$X_s(t)=\bar{X}_s+\Delta X_s(t), \quad Z_s(t)=\bar{Z}_s+\Delta Z_s(t), \quad M_s(t)=\bar{M}_s+\Delta M_s(t),$$
$$\hat{Q}_k(t)=\hat{\bar{Q}}_k+\Delta\hat{Q}_k(t) \tag{27a}$$
$$V_{ox}(t)=\bar{V}_{ox}+\Delta v_{ox}(t), \quad V_{oz}(t)=\Delta v_{oz}(t) \tag{27b}$$
$$q=\Delta q, \quad \theta(t)=\bar{\theta}+\Delta\theta(t), \quad \phi(t)=0 \tag{27c}$$
$$\eta_k(t)=\bar{\eta}_k+\Delta\eta_k \tag{27d}$$

Note that since the vehicle was trimmed by referencing forces and moments to the stability axes, the subscript 's' has been added to these terms to indicate that they are to be interpreted as components taken along the stability axes. The various vehicle axes which were previously discussed are shown for the vehicle in perturbed flight in Fig. 3b. Also, because a linear structural model is used for the vehicle, coupling between the steady state deflections due to the trim forces, $\bar{\eta}_k$, and the perturbed motion variables is neglected. The linear structural model is justified because generic hypersonic vehicles can be asssumed to be relatively stiff.

Substitution of the expressions for the perturbed motion variables into the nonlinear longitudinal equations of motion, and subsequent elimination of all higher order terms, results in the linearized equations

$$m\Delta\dot{v}_{ox} = -mg\cos\bar{\theta}\Delta\theta+\Delta X_s \tag{28a}$$
$$m\Delta\dot{v}_{oz} = m\bar{V}_{ox}\Delta q-mg\sin\bar{\theta}\Delta\theta+\Delta Z_s \tag{28b}$$
$$J^o_{yy}\Delta\dot{q} = \Delta M_s \tag{28c}$$
$$\Delta\dot{\theta} = \Delta q \tag{28d}$$
$$\Delta\ddot{\eta}_k+2\xi_k\omega_k\Delta\dot{\eta}_k+\omega_k^2\Delta\eta_k = \frac{\Delta\hat{Q}_k}{M^g_k} \quad k=1,\ldots,N_m \tag{28e}$$

Further simplification of the linearized equations is obtained by recognizing that coupling between the rigid body and elastic degrees of freedom will only involve the short period mode. Coupling is assumed to be negligible between the long period (phugoid) mode and the elastic degrees of freedom due to the large separation in the natural frequencies. Furthermore, the perturbation in forward speed, Δv_{ox}, has a negligible effect on the short period mode, for typical flight vehicles (ref.22,p.231). Thus, $\Delta v_{ox} = 0$ and the equation governing Δv_{ox} is discarded. The rigid body equations of motion after this simplification are:

$$m\Delta\dot{v}_{oz} = m\bar{V}_{ox}\Delta q + \Delta Z_s \tag{29a}$$

$$J^o_{yy}\Delta\dot{q} = \Delta M_s \tag{29b}$$

The force and moment perturbations, ΔZ_s and ΔM_s, are expressed in terms of partial derivatives with respect to the degrees of freedom. Equations (28e), (29a), and (29b) are rewritten below in terms of these dimensional flutter derivatives:

$$\begin{aligned} m\Delta\dot{v}_{oz} &= Z_{v_{oz}}\Delta v_{oz} + (m\bar{V}_{ox} + Z_q)\Delta q + Z_{\eta_1}\Delta\eta_1 + \cdots + Z_{\eta_{N_m}}\Delta\eta_{N_m} + \\ &\quad Z_{\dot{\eta}_1}\Delta\eta_{N_m+1} + \cdots + Z_{\dot{\eta}_{N_m}}\Delta\eta_{2N_m} + Z_{\delta_e}\Delta\delta_e \end{aligned} \tag{30}$$

$$\begin{aligned} J^o_{yy}\Delta\dot{q} &= M_{v_{oz}}\Delta v_{oz} + M_q\Delta q + M_{\eta_1}\Delta\eta_1 + \cdots + M_{\eta_{N_m}}\Delta\eta_{N_m} + \\ &\quad M_{\dot{\eta}_1}\Delta\eta_{N_m+1} + \cdots + M_{\dot{\eta}_{N_m}}\Delta\eta_{2N_m} + M_{\delta_e}\Delta\delta_e \end{aligned} \tag{31}$$

$$\left.\begin{aligned} M^g_k\Delta\dot{\eta}_{N_m+k} &= \hat{Q}_{k_{v_{oz}}}\Delta v_{oz} + \hat{Q}_{k_q}\Delta q + \textstyle\sum_{l=1}^{N_m}(\hat{Q}_{k_{\eta_l}} - \hat{\omega}^2_k M^g_k\delta_{kl})\Delta\eta_l \\ &\quad + \textstyle\sum_{l=1}^{N_m}(\hat{Q}_{k_{\dot{\eta}_l}} - 2\xi_k\hat{\omega}_k M^g_k\delta_{kl})\Delta\eta_{N_m+l} \\ \Delta\dot{\eta}_k &= \Delta\eta_{N_m+k} \end{aligned}\right\} \quad k = 1,\ldots,N_m \tag{32}$$

where the equation governing the elastic deflections is written in first order form.

It is convenient to work with the linearized equations of motion in nondimensional form. Equations (30-32) may be rendered nondimensional by dividing by the quantities $\frac{1}{2}\rho_\infty\bar{V}^2_{ox}A_t$, $\frac{1}{2}\rho_\infty\bar{V}^2_{ox}A_t l_{lb}$, and $\frac{1}{2}\rho_\infty\bar{V}^2_{ox}A_t$, respectively. The resulting nondimensional equations are

$$\begin{aligned} \hat{m}D_{\hat{t}}\Delta\alpha &= C_{z\alpha}\Delta\alpha + (\hat{m} + C_{zq})\Delta\hat{q} + \sum_{i=1}^{N_m}\{C_{z\eta_i}\Delta\hat{\eta}_i + C_{z\dot{\eta}_i}\Delta\hat{\eta}_{N_m+i}\} \\ &\quad + C_{z\delta_e}\Delta\delta_e \end{aligned} \tag{33a}$$

$$\begin{aligned} \hat{J}^o_{yy}D_{\hat{t}}\hat{q} &= C_{m\alpha}\Delta\alpha + C_{mq}\Delta\hat{q} + \sum_{i=1}^{N_m}\{C_{m\eta_i}\Delta\hat{\eta}_i + C_{m\dot{\eta}_i}\Delta\hat{\eta}_{N_m+i}\} \\ &\quad + C_{m\delta_e}\delta_e \end{aligned} \tag{33b}$$

$$\begin{aligned} \hat{M}^g_k D_{\hat{t}}\hat{\eta}_{N_m+k} &= C_{Q_k\alpha}\Delta\alpha + C_{Q_kq}\Delta\hat{q} + \sum_{l=1}^{N_m}\left\{\left(C_{Q_k\eta_l} - \hat{\omega}^2_k\hat{M}^g_k\delta_{kl}\right)\Delta\hat{\eta}_l + \right. \\ &\quad \left.\left(C_{Q_k\dot{\eta}_l} - 2\xi_k\hat{\omega}_k\hat{M}^g_k\delta_{kl}\right)\Delta\hat{\eta}_{N_m+l}\right\} + C_{Q_k\delta_e}\Delta\delta_e \end{aligned} \tag{33c}$$

$$D_{\hat{t}}\Delta\hat{\eta}_k = \Delta\hat{\eta}_{N_m+k}, \quad k = 1,\ldots,N_m \tag{33d}$$

where the various nondimensional quantities are given by

$$\hat{m} = \frac{2m}{\rho_\infty A_t l_{lb}}, \quad \hat{J}^o_{yy} = \frac{2J^o_{yy}}{\rho_\infty A_t l^3_{lb}}, \quad \hat{t} = \frac{\bar{V}_{ox} t}{l_{lb}}, D_{\hat{t}}(\ ) = \frac{d}{d\hat{t}}(\ ), \quad \hat{M}^g_k = \frac{2M^g_k}{\rho_\infty A_t l_{lb}}, \quad \hat{\omega}_k = \frac{\omega_k l_{lb}}{\bar{V}_{ox}}$$
$$\Delta\alpha = \frac{\Delta v_{oz}}{\bar{V}_{ox}}, \quad \Delta\hat{q} = \frac{l_{lb}\Delta q}{\bar{V}_{ox}}, \quad \Delta\hat{\eta}_i = \frac{\Delta\eta_i}{l_{lb}}, \Delta\hat{\eta}_{N_m+i} = \frac{\Delta\eta_{N_m+i}}{\bar{V}_{ox}} \tag{34}$$

and the flutter derivatives are related to their dimensional counterparts as

$$Z_{v_{oz}} = \frac{1}{2}\rho_\infty \bar{V}_{ox} A_t C_{z\alpha} \tag{35a}$$
$$Z_q = \frac{1}{2}\rho_\infty \bar{V}_{ox} A_t l_{lb} C_{zq} \tag{35b}$$
$$Z_{\eta_i} = \frac{1}{2l_{lb}}\rho_\infty \bar{V}^2_{ox} A_t C_{z\eta_i} \tag{35c}$$
$$Z_{\dot{\eta}_i} = \frac{1}{2}\rho_\infty \bar{V}_{ox} A_t C_{z\dot{\eta}_i} \tag{35d}$$
$$Z_{\delta_e} = \frac{1}{2}\rho_\infty \bar{V}^2_{ox} A_t C_{z\delta_e} \tag{35e}$$

$$M_{v_{oz}} = \frac{1}{2}\rho_\infty \bar{V}_{ox} A_t l_{lb} C_{m\alpha} \tag{35f}$$
$$M_q = \frac{1}{2}\rho_\infty \bar{V}_{ox} A_t l^2_{lb} C_{mq} \tag{35g}$$
$$M_{\eta_i} = \frac{1}{2}\rho_\infty \bar{V}^2_{ox} A_t C_{m\eta_i} \tag{35h}$$
$$M_{\dot{\eta}_i} = \frac{1}{2}\rho_\infty \bar{V}_{ox} A_t l_{lb} C_{m\dot{\eta}_i} \tag{35i}$$
$$M_{\delta_e} = \frac{1}{2}\rho_\infty \bar{V}^2_{ox} A_t l_{lb} C_{m\delta_e} \tag{35j}$$

$$\hat{Q}_{k_{v_{oz}}} = \frac{1}{2}\rho_\infty \bar{V}_{ox} A_t C_{Q_k\alpha} \tag{35k}$$
$$\hat{Q}_{k_q} = \frac{1}{2}\rho_\infty \bar{V}_{ox} A_t l_{lb} C_{Q_k q} \tag{35l}$$
$$\hat{Q}_{k_{\eta_l}} = \frac{1}{2l_{lb}}\rho_\infty \bar{V}^2_{ox} A_t C_{Q_k\eta_l} \tag{35m}$$
$$\hat{Q}_{k_{\dot{\eta}_l}} = \frac{1}{2}\rho_\infty \bar{V}_{ox} A_t C_{Q_k\dot{\eta}_i} \tag{35n}$$

Stability Derivatives of the Vehicle

Previous studies [9] have indicated that piston theory is a suitable tool for generating unsteady aerodynamic loads for exploratory studies at high Mach numbers, and therefore it is used as the basis for deriving the aerodynamic loads. The local pressure on the vehicle surface due to combined rigid body motion and structural deformation is

$$p_s = \rho_\infty a_\infty v_p + p_\infty \tag{36}$$

where v_p is the velocity of a fluid particle on the surface of the vehicle in the direction normal to the surface.

The hypersonic vehicle considered here has three principal types of lifting surfaces: a clipped delta-shaped lifting body, two canted fins, and an elevon. The flutter derivatives of the entire vehicle are obtained by combining the individual contributions. From Fig. 6, the velocities of fluid particles on the upper and lower surfaces of the clipped delta-shaped lifting body are given by (assuming $V_{ox} >> V_{oz}$):

$$v_p^u(x_b) = V_{ox}\cos\bar{\alpha}\left(\frac{\partial u_z}{\partial x_b}+\frac{\partial \bar{Z}^u}{\partial x_b}\right) - \dot{u}_z + x_b q - V_{oz}\cos\bar{\alpha} \tag{37a}$$

$$v_p^l(x_b) = -V_{ox}\cos\bar{\alpha}\left(\frac{\partial u_z}{\partial x_b}+\frac{\partial \bar{Z}^l}{\partial x_b}\right) + \dot{u}_z - x_b q + V_{oz}\cos\bar{\alpha} \tag{37b}$$

The net pressure is the sum of the trimmed pressure and the change in pressure due to the small perturbations in the rigid body and flexible degrees of freedom. This change in pressure is given by

$$\Delta p_s = \rho_\infty a_\infty \Delta v_p \tag{38}$$

where Δv_p is the portion of v_p due to the perturbed motion.

$$\Delta v_p^u(x) = \bar{V}_{ox}\cos\bar{\alpha}\frac{\partial \Delta u_z}{\partial x} - \Delta\dot{u}_z + x\Delta q - \cos\bar{\alpha}\Delta v_{oz} \tag{39a}$$

$$\Delta v_p^l(x) = -\bar{V}_{ox}\cos\bar{\alpha}\frac{\partial \Delta u_z}{\partial x} + \Delta\dot{u}_z - x\Delta q + \cos\bar{\alpha}\Delta v_{oz} \tag{39b}$$

Substitution of Eqs.(39) into Eq.(38) gives the net pressure difference between the upper and lower surfaces due to the perturbed motion:

$$\Delta p_s^u - \Delta p_s^l = 2\rho_\infty a_\infty\left(\bar{V}_{ox}\cos\bar{\alpha}\frac{\partial \Delta u_z}{\partial x} - \Delta\dot{u}_z + x\Delta q - \cos\bar{\alpha}\Delta v_{oz}\right) \tag{40}$$

Using Eq.(10) for the elastic displacement and Eq.(40) for the net pressure, the aerodynamic force in the z_b-direction on the main lifting body may be written as:

$$\begin{aligned}\Delta Z_{lb,b} &= \int_{A_{lb}} (\Delta p_s^u - \Delta p_s^l)\, dA_{lb} \\ &= 2\rho_\infty a_\infty \bar{V}_{ox}\cos\bar{\alpha}\sum_{i=1}^{N_m}\left(\int_{A_{lb}}\frac{\partial \Phi_i^z}{\partial x_b}\, dA_{lb}\ \Delta\eta_i\right) - 2\rho_\infty a_\infty \sum_{i=1}^{N_m}\left(\int_{A_{lb}}\Phi_i^z\, dA_{lb}\ \Delta\dot{\eta}_i\right) \\ &\quad + 2\rho_\infty a_\infty \int_{A_{lb}} x_b\, dA_{lb}\ \Delta q - 2\rho_\infty a_\infty A_{lb}\cos\bar{\alpha}\Delta v_{oz}\end{aligned} \tag{41}$$

We require the force component along the z_s-axis, which is given by

$$\Delta Z_{lb} = \Delta Z_{lb,b}\cos\bar{\alpha}$$

$$= \sum_{i=1}^{N_m} Z_{lb_{\eta_i}} \Delta\eta_i + \sum_{i=1}^{N_m} Z_{lb_{\dot{\eta}_i}} \Delta\dot{\eta}_i + Z_{lb_q} \Delta q + Z_{lb_{v_{oz}}} \Delta v_{oz} \tag{42}$$

The contributions of the lifting body to the Z flutter derivatives are

$$Z_{lb_{\eta_i}} = 2\rho_\infty a_\infty \bar{V}_{ox} \cos^2\bar{\alpha} \int_{A_{lb}} \frac{\partial \Phi_i^z}{\partial x}\, dA_{lb} \tag{43a}$$

$$Z_{lb_{\dot{\eta}_i}} = -2\rho_\infty a_\infty \cos\bar{\alpha} \int_{A_{lb}} \Phi_i^z\, dA_{lb} \tag{43b}$$

$$Z_{lb_q} = 2\rho_\infty a_\infty \cos\bar{\alpha} \int_{A_{lb}} x\, dA_{lb} \tag{43c}$$

$$Z_{lb_{v_{oz}}} = -2\rho_\infty a_\infty A_{lb} \cos^2\bar{\alpha} \tag{43d}$$

The contribution of the main lifting body to the pitching moment flutter derivatives may be evaluated in a similar manner. Using Eqs.(10) and (40), the pitching moment contributed by the clipped delta-shaped lifting body may be expressed as

$$\Delta M_{lb} = -\int_{A_{lb}} (\Delta p_s^u - \Delta p_s^l) x_b\, dA_{lb} \tag{44}$$

Substitution of Eqs.(10) and (40) into Eq.(44) yields the contributions of the lifting body to the pitching moment flutter derivatives

$$M_{lb_{\eta_i}} = -2\rho_\infty a_\infty \bar{V}_{ox} \cos\bar{\alpha} \int_{A_{lb}} \frac{\partial \Phi_i^z}{\partial x_b} x_b\, dA_{lb} \tag{45a}$$

$$M_{lb_{\dot{\eta}_i}} = 2\rho_\infty a_\infty \int_{A_{lb}} \Phi_i^z x_b\, dA_{lb} \tag{45b}$$

$$M_{lb_q} = -2\rho_\infty a_\infty \int_{A_{lb}} x_b^2\, dA_{lb} \tag{45c}$$

$$M_{lb_{v_{oz}}} = 2\rho_\infty a_\infty \cos\bar{\alpha} \int_{A_{lb}} x_b\, dA_{lb} \tag{45d}$$

The final set of flutter derivatives to be calculated are those associated with the generalized forces, $\hat{Q}_i$. These forces are determined by examining the expression for the virtual work done by a virtual elastic displacement over an arbitrary surface area, A.

$$\begin{aligned} \delta W &= \int_A (\Delta p_s^u - \Delta p_s^l) \delta u_z\, dA \\ &= \int_A (\Delta p_s^u - \Delta p_s^l) \left(\sum_{i=1}^{N_m} \Phi_i^z \delta\eta_i \right) dA \\ &= \sum_{i=1}^{N_m} \hat{Q}_i \delta\eta_i \end{aligned} \tag{46}$$

From Eq.(46), with $A = A_{lb}$, the contribution of the main lifting body to $\hat{Q}_i$ is

$$\hat{Q}_i^{lb} = \int_{A_{lb}} \left(\Delta p_s^u - \Delta p_s^l\right) \Phi_i^z \, dA_{lb} \tag{47}$$

Substituting Eq.(40) into Eq.(47) and expanding yields the contributions of the lifting body to the elastic generalized force derivatives:

$$\hat{Q}_{i_{\eta_j}}^{lb} = 2\rho_\infty a_\infty \bar{V}_{ox} \cos\bar{\alpha} \int_{A_{lb}} \Phi_i^z \frac{\partial \Phi_j^z}{\partial x_b} \, dA_{lb} \tag{48a}$$

$$\hat{Q}_{i_{\dot{\eta}_j}}^{lb} = -2\rho_\infty a_\infty \int_{A_{lb}} \Phi_i^z \Phi_j^z \, dA_{lb} \tag{48b}$$

$$\hat{Q}_{i_q}^{lb} = 2\rho_\infty a_\infty \int_{A_{lb}} \Phi_i^z x_b \, dA_{lb} \tag{48c}$$

$$\hat{Q}_{i_{v_{oz}}}^{lb} = -2\rho_\infty a_\infty \cos\bar{\alpha} \int_{A_{lb}} \Phi_i^z \, dA_{lb} \tag{48d}$$

The contribution of the canted fins to the flutter derivatives is obtained in a similar manner. The velocities of fluid particles on the upper and lower surfaces of the fin due to the perturbed motion are given by

$$\Delta v_p^u(x) = \bar{V}_{ox} \cos\bar{\alpha} \frac{\partial u_{z'}}{\partial x'} - \dot{u}_{z'} + x\Delta q \cos\theta_f - \Delta v_{oz} \cos\bar{\alpha} \cos\theta_f \tag{49a}$$

$$\Delta v_p^l(x) = -\bar{V}_{ox} \cos\bar{\alpha} \frac{\partial u_{z'}}{\partial x'} + \dot{u}_{z'} - x\Delta q \cos\theta_f + \Delta v_{oz} \cos\bar{\alpha} \cos\theta_f \tag{49b}$$

where an additional primed coordinate system for the fin has been introduced, as shown in Fig 4. Substitution of Eqs.(49) into Eq.(38) gives the net pressure difference between the upper and lower surfaces of the fin due to the perturbed motion:

$$\Delta p_s^u - \Delta p_s^l = 2\rho_\infty a_\infty \left(\bar{V}_{ox} \cos\bar{\alpha} \frac{\partial u_{z'}}{\partial x'} - \dot{u}_{z'} + x\Delta q \cos\theta_f - \Delta v_{oz} \cos\bar{\alpha} \cos\theta_f \right) \tag{50}$$

The net aerodynamic force in the z_s-direction on the two fins is given by

$$\Delta Z_f = 2 \cos\bar{\alpha} \cos\theta_f \int_{A_f} \left(\Delta p_s^u - \Delta p_s^l\right) dA_f \tag{51}$$

where the contributions from each fin can be summed because both the vehicle and the motion are symmetric. Substituting Eq.(50) into Eq.(51) yields the following contribution of the two canted fins to the Z flutter derivatives:

$$\begin{aligned} \Delta Z_w = {} & 4\cos\theta_f \rho_\infty a_\infty \bar{V}_{ox} \int_{A_w} \sum_{i=1}^{N_m} \frac{\partial \phi_i^{z'}}{\partial x'} \, dA_w \eta_i - 4\cos\theta_f \rho_\infty a_\infty \int_{A_w} \sum_{i=1}^{N_m} \phi_i \, dA_w \dot{\eta}_i \\ & + 4\cos^2\theta_f \rho_\infty a_\infty \int_{A_w} x \, dA_w \delta q - 4\cos^2\theta_f \rho_\infty a_\infty A_w \delta v_{oz} \end{aligned} \tag{52}$$

Examining Eq.(52), the contribution of the fins to the Z flutter derivatives are found to be

$$z_{f_{\eta_i}} = 4\cos\theta_f \cos^2\bar{\alpha}\rho_\infty a_\infty \bar{V}_{ox} \int_{A_f} \frac{\partial \phi_i^{z'}}{\partial x'}\, dA_f \tag{53a}$$

$$z_{f_{\dot{\eta}_i}} = -4\cos\theta_f \cos\bar{\alpha}\rho_\infty a_\infty \int_{A_f} \phi_i^{z'}\, dA_f \tag{53b}$$

$$z_{f_q} = 4\cos^2\theta_f \cos\bar{\alpha}\rho_\infty a_\infty \int_{A_f} x\, dA_f \tag{53c}$$

$$z_{f_{v_{oz}}} = -4\cos^2\theta_f \cos^2\bar{\alpha}\rho_\infty a_\infty A_f \tag{53d}$$

The contribution of the canted fins to the pitching moment is given by

$$\Delta M_f = -2\cos\theta_f \int_{A_f} x(\Delta p_s^u - \Delta p_s^l)\, dA_f \tag{54}$$

Since Eq.(54) differs from Eq.(51) only by the factor $\cos\bar{\alpha}$ outside the integral and the factor $-x$ inside the integral, the M_f flutter derivatives may be obtained from the Z_f flutter derivatives by dividing by $\cos\bar{\alpha}$, multiplying the integrands by the factor $-x$, and carrying out the required integrations.

$$M_{f_{\eta_i}} = -4\cos\theta_f \cos\bar{\alpha}\rho_\infty a_\infty \bar{V}_{ox} \int_{A_f} x\frac{\partial \phi_i^{z'}}{\partial x'}\, dA_f \tag{55a}$$

$$M_{f_{\dot{\eta}_i}} = 4\cos\theta_f \rho_\infty a_\infty \int_{A_f} x\phi_i^{z'}\, dA_f \tag{55b}$$

$$M_{f_q} = -4\cos^2\theta_f \rho_\infty a_\infty \int_{A_f} x^2\, dA_f \tag{55c}$$

$$M_{f_{v_{oz}}} = 4\cos^2\theta_f \cos\bar{\alpha}\rho_\infty a_\infty \int_{A_f} x\, dA_f \tag{55d}$$

Using the principle of virtual work in a manner similar to Eq.(46), the contribution of the canted fins to $\hat{Q}_i$ is given by

$$\hat{Q}_i^f = 2\int_{A_f} (\Delta p_s^u - \Delta p_s^l)\, \Phi_i^{z'}\, dA_f \tag{56}$$

Comparison of Eq.(56) to Eq.(47) and Eq.(50) to Eq.(40) indicates that the $\hat{Q}_i^f$ flutter derivatives may be obtained from the $\hat{Q}_i^{lb}$ flutter derivatives by referring the mode shapes to the primed (fin) coordinate system and multiplying the derivatives with respect to q and v_{oz} by $\cos\theta_f$.

$$\hat{Q}_{i_{\eta_j}}^f = 4\rho_\infty a_\infty \bar{V}_{ox} \cos\bar{\alpha} \int_{A_f} \Phi_i^{z'} \frac{\partial \Phi_j^{z'}}{\partial x'}\, dA_f \tag{57a}$$

$$\hat{Q}_{i_{\dot{\eta}_j}}^f = -4\rho_\infty a_\infty \int_{A_f} \Phi_i^{z'} \Phi_j^{z'}\, dA_f \tag{57b}$$

$$\hat{Q}^f_{i_q} = 4\cos\theta_f \rho_\infty a_\infty \int_{A_f} \Phi_i^{z'} x \, dA_f \tag{57c}$$

$$\hat{Q}^f_{i_{voz}} = -4\cos\theta_f \rho_\infty a_\infty \cos\bar{\alpha} \int_{A_f} \Phi_i^{z'} \, dA_f \tag{57d}$$

Using the same procedure with which the flutter derivatives of the lifting body and canted fins were calculated, the contribution of the rigid elevon to the flutter derivatives is found to be:

$$\Delta Z_{e_{voz}} = -2\rho_\infty a_\infty \cos^2(\bar{\alpha}+\bar{\delta}_e) A_e \tag{58a}$$

$$\Delta Z_{e_{\Delta q}} = -2\rho_\infty a_\infty \cos(\bar{\alpha}+\bar{\delta}_e)\cos\bar{\delta}_e d_e A_e \tag{58b}$$

$$\Delta M_{e_{voz}} = -2\rho_\infty a_\infty \cos(\bar{\alpha}+\bar{\delta}_e)\cos\bar{\delta}_e d_e A_e \tag{58c}$$

$$\Delta M_{e_{\Delta q}} = -2\rho_\infty a_\infty \cos^2\bar{\delta}_e d_e^2 A_e \tag{58d}$$

Note that since the elevon is assumed to be rigid, all of the flutter derivatives involving elastic deflection are zero. In particular, the effect of the deformation of the main lifting body on the perturbation aerodynamic forces experienced by the elevon is assumed to be negligible.

The overall flutter derivatives of the entire vehicle can be written as a combination of the individual components for which the flutter derivatives have been evaluated in the preceeding parts of this section. Using Eqs.(43,45,48,53,55,57,58) and nondimensionalizing the derivatives using Eqs.(35), the flutter derivatives for the entire vehicle are given by

$$C_{z\alpha} = -\frac{4\cos^2\bar{\alpha}}{M_\infty}\left\{\left(\frac{A_{lb}}{A_t}\right) + 2\left(\frac{A_f}{A_t}\right)\cos^2\theta_f + \left(\frac{A_e}{A_t}\right)\frac{\cos^2(\bar{\alpha}+\bar{\delta}_e)}{\cos\bar{\alpha}}\right\} \tag{59a}$$

$$C_{zq} = \frac{4\cos\bar{\alpha}}{M_\infty A_t l_{lb}}\left(\int_{A_{lb}} x\, dA_{lb} + 2\cos^2\theta_f \int_{A_f} x\, dA_f - A_e d_e \cos\delta_e \frac{\cos(\bar{\alpha}+\bar{\delta}_e)}{\cos\bar{\alpha}}\right) \tag{59b}$$

$$C_{z\eta_i} = \frac{4 l_{lb}\cos^2\bar{\alpha}}{M_\infty A_t}\left(\int_{A_{lb}} \frac{\partial\phi_i^z}{\partial x}\, dA_{lb} + 2\cos\theta_f \int_{A_f} \frac{\partial\phi_i^{z'}}{\partial x'}\, dA_f\right) \tag{59c}$$

$$C_{z\dot{\eta}_i} = -\frac{4\cos\bar{\alpha}}{M_\infty A_t}\left(\int_{A_{lb}} \phi_i^z\, dA_{lb} + 2\cos\theta_f \int_{A_f} \phi_i^{z'}\, dA_f\right) \tag{59d}$$

$$C_{m\alpha} = \frac{4\cos\bar{\alpha}}{M_\infty A_t l_{lb}}\left(\int_{A_{lb}} x\, dA_{lb} + 2\cos^2\theta_f \int_{A_f} x\, dA_f - A_e d_e \cos\delta_e \frac{\cos(\bar{\alpha}+\bar{\delta}_e)}{\cos\bar{\alpha}}\right) \tag{60a}$$

$$C_{mq} = -\frac{4}{M_\infty A_t l_{lb}^2}\left(\int_{A_{lb}} x^2\, dA_{lb} + 2\cos^2\theta_f \int_{A_f} x^2\, dA_f + A_e d_e^2 \cos^2\bar{\delta}_e\right) \tag{60b}$$

$$C_{m\eta_i} = -\frac{4\cos\bar{\alpha}}{M_\infty A_t}\left(\int_{A_{lb}} \frac{\partial\phi_i^z}{\partial x} x\, dA_{lb} + 2\cos\theta_f \int_{A_f} \frac{\partial\phi_i^{z'}}{\partial x'} x\, dA_f\right) \tag{60c}$$

$$C_{m\dot{\eta}_i} = \frac{4}{M_\infty A_t l_{lb}}\left(\int_{A_{lb}} \phi_i^z x\, dA_{lb} + 2\cos\theta_f \int_{A_f} \phi_i^{z'} x\, dA_f\right) \tag{60d}$$

$$C_{Q_k\alpha} = -\frac{4\cos\bar{\alpha}}{M_\infty A_t}\left(\int_{A_{lb}} \phi_k^z\, dA_{lb} + 2\cos\theta_f \int_{A_f} \phi_k^{z'}\, dA_f\right) \tag{61a}$$

$$C_{Q_k q} = \frac{4}{M_\infty A_t l_{lb}}\left(\int_{A_{lb}} \phi_k^z x\, dA_{lb} + 2\cos\theta_f \int_{A_f} \phi_k^{z'} x\, dA_f\right) \tag{61b}$$

$$C_{Q_k \eta_l \cos\bar{\alpha}} = \frac{4l_{lb}}{M_\infty A_t}\left(\int_{A_{lb}} \phi_k^z \frac{\partial \phi_l^z}{\partial x}\, dA_{lb} + 2\int_{A_f} \phi_k^{z'} \frac{\partial \phi_l^{z'}}{\partial x'}\, dA_f\right) \tag{61c}$$

$$C_{Q_k \dot{\eta}_l} = -\frac{4}{M_\infty A_t}\left(\int_{A_{lb}} \phi_k^z \phi_l^z\, dA_{lb} + 2\int_{A_f} \phi_k^{z'} \phi_l^{z'}\, dA_f\right) \tag{61d}$$

Structural Dynamic Model Based on Equivalent Plate Approach

The configuration selected for the generic hypersonic vehicle resembles the X33 RLV, as shown in Fig. 7. The initial structural model consists of isotropic equivalent plate segments and nonstructural masses for the canted fins, clipped delta-shaped main lifting body, fuel, and payload. The mass and stiffness properties of the equivalent plate model are determined by matching the calculated mode shapes and frequencies to those obtained from a detailed NASTRAN model of the empty vehicle[24]. This simple configuration was chosen to facilitate methodology developement. However a more complex model, which includes curved, laminated composite cover skins and complex internal structure, is also under development.

The solution of the governing equations of motion for the unrestrained vehicle requires the determination of the normal modes and frequencies of the unrestrained (or free-free) vehicle. The equivalent plate code, ELAPS, is used to model the vehicle and compute the unrestrained mode shapes. A concise description of the equivalent plate model is provided for completeness.

In equivalent plate theory, the vehicle planform geometry is divided into multiple trapezoidal segments with cross-sectional geometry specified by the analyst in the form of polynomial series in the global coordinates, x and y:

$$\begin{aligned} Z_c(x,y) &= \sum_{i=0}^{m}\sum_{j=0}^{n} z_{ij} x^i y^j \\ h^b(x,y) &= \sum_{i=0}^{m}\sum_{j=0}^{n} h^b_{ij} x^i y^j \\ t_k(x,y) &= \sum_{i=0}^{m}\sum_{j=0}^{n} t_{ij} x^i y^j \end{aligned} \tag{62}$$

where the physical description of the quantities used in Eq.(62) is shown in Fig. 8. The displacement field for the equivalent plate is assumed to be of the form

$$u_x = u_{xo} - z\frac{\partial u_{zo}}{\partial x} + z\Phi_x \tag{63a}$$

$$u_y = u_{yo} - z\frac{\partial u_{zo}}{\partial y} + z\Phi_y \tag{63b}$$

$$u_z = u_{zo} \tag{63c}$$

where u_{xo}, u_{yo}, and u_{zo} are the middle surface displacements in the x, y, and z directions, respectively, and Φ_x, Φ_y are additional degrees of freedom that are necessary for transverse shear deformation modeling. The reference surface displacements and transverse shear rotations are approximated by polynomial displacement functions as

$$u_{xo} = \boldsymbol{\phi}_{\mathbf{x}}^T \mathbf{q}_{\mathbf{x}}, \quad u_{yo} = \boldsymbol{\phi}_{\mathbf{y}}^T \mathbf{q}_{\mathbf{y}}, \quad u_{zo} = \boldsymbol{\phi}_{\mathbf{z}}^T \mathbf{q}_{\mathbf{z}} \tag{64a}$$

$$\Phi_x = \boldsymbol{\phi}_{\boldsymbol{\Phi}_{\mathbf{x}}}^T \mathbf{q}_{\boldsymbol{\Phi}_{\mathbf{x}}}, \quad \Phi_y = \boldsymbol{\phi}_{\boldsymbol{\Phi}_{\mathbf{y}}}^T \mathbf{q}_{\boldsymbol{\Phi}_{\mathbf{y}}} \tag{64b}$$

where $\boldsymbol{\phi}_{\mathbf{x}}, \mathbf{q}_{\mathbf{x}}$ are (expressions for $\boldsymbol{\phi}_{\mathbf{y}} - \mathbf{q}_{\boldsymbol{\Phi}_{\mathbf{y}}}$ are similar)

$$\boldsymbol{\phi}_{\mathbf{x}}^T = [1, x, x^2, \ldots, y, xy, x^2y, \ldots, x^I y^J] \tag{65a}$$

$$\mathbf{q}_{\mathbf{x}}^T = [q_{x_{00}}, q_{x_{10}}, q_{x_{20}}, \ldots, q_{x_{01}}, q_{x_{11}}, q_{x_{21}}, \ldots, q_{x_{IJ}}] \tag{65b}$$

In Eq. (65b), $\mathbf{q}_{\mathbf{x}} - \mathbf{q}_{\boldsymbol{\Phi}_{\mathbf{y}}}$ are the unknown generalized coordinates, obtained from the solution of the global system of equations.

Equations (63) with Eqs.(64-65) comprise a displacement system. Out-of-plane sections, such as the canted fins on the X33, are accomodated by defining an additional displacement system for the section and connecting the displacement systems with stiff springs to ensure displacement compatibility. Boundary conditions may be enforced either by using springs or by setting the appropriate coefficients in the assumed displacement function to zero. For example, zero transverse slope in the y-direction at $y = 0$ may be enforced by setting $q_{z_{01}} - q_{z_{I1}}$ to zero. Taking advantage of symmetry, the vehicle shown in Fig. 7 is modeled in ELAPS by defining only the right half plane, with boundary conditions enforced at the vehicle centerline as follows. To calculate the symmetric modes, the following quantities are set equal to zero: $\frac{\partial u_{x0}}{\partial y}(x,0), u_{yo}(x,0), \frac{\partial u_{z0}}{\partial y}(x,0), \frac{\partial \phi_x}{\partial y}(x,0), \phi_y(x,0)$.

Contribution of each structural component (cover skins, ribs, spars, etc...) to the global stiffness and mass matrices is obtained from the strain and kinetic energy expressions for the component, expressed in terms of the assumed displacement functions, Eqs (63). The global mass and stiffness matrices are assembled from the contributions of each structural component, and the natural modes and frequencies of the unrestrained vehicle are then obtained by solving the linear eigenvalue problem. For a comprehensive discussion of equivalent plate theory and recent enhancements, see references [19,20]. Mode shapes and frequencies based on this approach are presented in the results section.

STABILITY BOUNDARY COMPUTATION

The stability boundaries for the generic hypersonic vehicle are determined from the eigenproblem generated from the governing equations of motion. Therefore, the equations of motion, Eqs.(33) are rewritten in matrix form:

$$D_{\hat{t}}\Delta\mathbf{x} = \left[\begin{array}{c|c|c} \mathbf{A_r} & \mathbf{A_{rf}} & \mathbf{A_{r\dot{f}}} \\ \hline \mathbf{0} & \mathbf{0} & \mathbf{I} \\ \hline \mathbf{A_{\dot{f}r}} & \mathbf{A_{\dot{f}f}} & \mathbf{A_{\dot{f}\dot{f}}} \end{array}\right] \Delta\mathbf{x} = \mathbf{A}\,\Delta\mathbf{x} \tag{66}$$

where

$$\Delta\mathbf{x} = \left\{\begin{array}{c} \Delta\alpha \\ \Delta\hat{q} \\ \Delta\hat{\eta}_1 \\ \vdots \\ \Delta\hat{\eta}_{2N_m} \end{array}\right\} \tag{67}$$

and the sub-matrices of the partitioned matrix, $\mathbf{A}$, are given in Appendix I. Solutions to Eqs.(66) can be written as

$$\Delta\mathbf{x} = \boldsymbol{\xi} e^{\lambda\hat{t}} \tag{68}$$

which produce the eigenvalue problem from which the aeroelastic stability boundaries are obtained

$$(\mathbf{A} - \lambda\mathbf{I})\,\boldsymbol{\xi} = \mathbf{0} \tag{69}$$

The eigenvalues, $\lambda_n = \zeta_n + i\omega_n$, must be calculated in an iterative manner. Starting at low values of the flight speed, V_{ox}, the eigenvalues are computed, and the process is repeated until the real part of any particular eigenvalue becomes zero. At each iteration, the trim state is calculated using the current value of V_{ox}. This process is repeated at a number of altitudes representing the operational envelope of the vehicle.

RESULTS

Baseline Configuration and Mode Shapes

The baseline hypersonic vehicle configuration chosen for this study has the following properties. The vehicle has a length of 65 ft. and a width of 65 ft. (l_{lb} and w in Fig. 7, respectively). The vehicle is made of aluminum and has a structural weight of 73,000 lbs. Fuel weight at takeoff is 210,000 lbs. Four fuel configurations were studied: the empty vehicle, 10% fuel, 50% fuel, and 100% fuel. Natural frequencies for each configuration were computed using ELAPS and are shown in Table 1. As mentioned, the model was tuned to approximately match the frequencies with those from a detailed NASTRAN model.

The first four unrestrained flexible mode shapes for the empty vehicle are shown in Fig. 10. A perspective view of the undeformed configuration is shown in Fig. 9 to aid in visualization of the mode shapes. The mode shapes in Fig. 10 were calculated for a vehicle configuration which differs slightly from the one used to calculate the results in this study,

but the mode shapes of both vehicles are qualitatively similar. The first flexible mode shape, labeled 'mode 7' in Fig. 10 due to the six rigid body modes, is a symmetric mode composed of bending and twisting of the rear fins with no appreciable deformation of the fuselage. The second flexible mode is an antisymmetric mode affecting similar areas of the vehicle. The third flexible mode is a symmetric full vehicle mode composed of longitudinal fuselage bending as well as fin bending and twisting. The fourth flexible mode is an antisymmetric full vehicle mode composed of fuselage and fin twisting. Higher modes are also composed of both fin modes and full vehicle modes, but involve increasingly complex deformations.

Trim Results and Flutter Boundaries

Typical trim curves for the generic hypersonic vehicle are given in Fig. 11 for the four different fuel configurations. The trim angles are quite small at large Mach. numbers; this is due to the large aerodynamic forces at these flight conditions. Effect of the c.g. location on the trim state is shown for the 100% fuel case in Figs.12 and 13. In these figures, x is the c.g. location measured from the vehicle nose and is given as a fraction of total vehicle length. The angle of attack decreases as the c.g. moves rearward but the elevon angle increases to large values due to the need to balance the increasing contribution to the moment from the main lifting body.

The flutter boundaries for the baseline vehicle configuration with four fuel conditions as well as a half-stiffness model with two fuel conditions are shown in Fig. 14. The flutter Mach number is very high for the altitudes at which the vehicle will fly in the hypersonic regime. For example, at 100,000 ft., $M_c = 160$ for the empty vehicle. The fully fueled vehicle is less stable, and flutter begins at around $M_c = 140$. If the stiffness is reduced by a factor of two, M_c decreases significantly. For the empty and fully fueled vehicles, it decreases to 86 and 68 respectively. The reduced stiffness model has practical importance due to the fact that the X33, which the generic hypersonic vehicle is modeled after, is a half-scale prototype of the Venture Star vehicle. Since the X33 is geometrically scaled, the Venture Star may be significantly more flexible than the X33 and the effect of reduced stiffness on the stability boundaries of such a vehicle can be pronounced. The effect of c.g. location on the flutter boundaries is shown in Fig. 15 for the half stiffness/100% fuel configuration. Moving the c.g. rearward initially reduces the stability but between $x_{cg} = .65$ and $x_{cg} = .7$ the stability begins to increase. Interestingly, the curves for these two values of x_{cg} cross at an altitude of about 35,000 ft. More research will be performed to determine the reason for this behavior.

Figure 16 contains typical frequency and damping curves. It can be seen that the flutter is due to strong coupling between modes 1 and 3. Mode 1 is primarily a wing-bending mode and mode 3 is a more complex mode that involves deformation of the complete vehicle, including significant wing twist. The behavior closely resembles the classic bending-torsion flutter. The frequencies of the two modes begin to coalesce and the damping of Mode 3 increases to zero at the critical Mach number while the damping of mode 1 continues to decrease. Note that this calculation was carried out under contrived conditions, since the altitude was assumed to be at sea level.

CONCLUDING REMARKS

A procedure for calculating the aeroelastic stability boundaries of an unrestrained generic hypersonic vehicle is presented in the paper. The formulation and solution procedure are general, and the most limiting assumption is the decoupling between the longitudinal and lateral dynamics of the vehicle. Thus, it is applicable to any generic hypersonic vehicle. The second limitation in the paper is associated with the aerodynamic theory used, namely piston theory. Preliminary results [9] have indicated that, for generic hypersonic vehicles, the unsteady aerodynamic loads may require the solution of the Navier Stokes equations, possibly with some simplifying assumptions, and the coupling of the aeroelastic problem with the heat transfer problem, thereby leading to a complete aerothermoelastic problem. Obviously, this approach was deemed to be too complicated for the trend type study conducted here.

The results presented in this paper lead to a number of useful conclusions. The X-33 type vehicle appears to have wide aeroelastic stability margins at hypersonic speeds, since flutter at the high altitudes occurs at very high Mach numbers. However, the flutter boundaries are quite sensitive to the trim state and the C.G. locations.

Reduced stiffness configurations, having half the stiffness of the baseline configuration have significantly lower stability margins. Since the X-33 is a geometrically scaled version of the Venture Star, it is conceivable that the full-scale vehicle would be much more flexible, and therefore it would be subject to considerable aeroelastic constraints. Thus aeroelastic effects will have to be carefully addressed in the design of the full-scale vehicle.

APPENDIX I

The components of the sub-matrices of matrix A in Eq.(66) are given below:

$$\mathbf{A_r} = \begin{bmatrix} \frac{C_{z\alpha}}{\hat{m}} & 1+\frac{C_{zq}}{\hat{m}} \\ \frac{C_{m\alpha}}{\hat{J}^o_{yy}} & \frac{C_{mq}}{\hat{J}^o_{yy}} \end{bmatrix}_{(2\times 2)} \tag{70}$$

$$\mathbf{A_{rf}} = \begin{bmatrix} \frac{C_{z\eta_1}}{\hat{m}} & \cdots & \frac{C_{z\eta_{N_m}}}{\hat{m}} \\ \frac{C_{m\eta_1}}{\hat{J}^o_{yy}} & \cdots & \frac{C_{m\eta_{N_m}}}{\hat{J}^o_{yy}} \end{bmatrix}_{(2\times N_m)} \tag{71}$$

$$\mathbf{A_{r\dot{f}}} = \begin{bmatrix} \frac{C_{z\dot{\eta}_1}}{\hat{m}} & \cdots & \frac{C_{z\dot{\eta}_{N_m}}}{\hat{m}} \\ \frac{C_{m\dot{\eta}_1}}{\hat{J}^o_{yy}} & \cdots & \frac{C_{m\dot{\eta}_{N_m}}}{\hat{J}^o_{yy}} \end{bmatrix}_{(2\times N_m)} \tag{72}$$

$$\mathbf{A_{\dot{f}r}} = \begin{bmatrix} \frac{C_{Q_1\alpha}}{\hat{M}^g_1} & \frac{C_{Q_1 q}}{\hat{M}^g_1} \\ \vdots & \vdots \\ \frac{C_{Q_{N_m}\alpha}}{\hat{M}^g_{N_m}} & \frac{C_{Q_{N_m} q}}{\hat{M}^g_{N_m}} \end{bmatrix}_{(N_m\times 2)} \tag{73}$$

$$\mathbf{A}_{\dot{\mathbf{f}}\mathbf{f}} = \begin{bmatrix} \frac{C_{Q_1\eta_1}}{\hat{M}_1^g} - \hat{\omega}_1^2 & \frac{C_{Q_1\eta_2}}{\hat{M}_1^g} & \cdots & \frac{C_{Q_1\eta_{N_m}}}{\hat{M}_1^g} \\ \frac{C_{Q_2\eta_1}}{\hat{M}_2^g} & \frac{C_{Q_2\eta_2}}{\hat{M}_2^g} - \hat{\omega}_2^2 & \cdots & \frac{C_{Q_2\eta_{N_m}}}{\hat{M}_2^g} \\ \vdots & \vdots & \ddots & \vdots \\ \frac{C_{Q_{N_m}\eta_1}}{\hat{M}_{N_m}^g} & \frac{C_{Q_{N_m}\eta_2}}{\hat{M}_{N_m}^g} & \cdots & \frac{C_{Q_{N_m}\eta_{N_m}}}{\hat{M}_{N_m}^g} - \hat{\omega}_{N_m}^2 \end{bmatrix} \quad (N_m \times N_m) \qquad (74)$$

$$\mathbf{A}_{\dot{\mathbf{f}}\dot{\mathbf{f}}} = \begin{bmatrix} \frac{C_{Q_1\dot{\eta}_1}}{\hat{M}_1^g} - 2\xi_1\hat{\omega}_1 & \frac{C_{Q_1\dot{\eta}_2}}{\hat{M}_1^g} & \cdots & \frac{C_{Q_1\dot{\eta}_{N_m}}}{\hat{M}_1^g} \\ \frac{C_{Q_2\dot{\eta}_1}}{\hat{M}_2^g} & \frac{C_{Q_2\dot{\eta}_2}}{\hat{M}_2^g} - 2\xi_2\hat{\omega}_2 & \cdots & \frac{C_{Q_2\dot{\eta}_{N_m}}}{\hat{M}_2^g} \\ \vdots & \vdots & \ddots & \vdots \\ \frac{C_{Q_{N_m}\dot{\eta}_1}}{\hat{M}_{N_m}^g} & \frac{C_{Q_{N_m}\dot{\eta}_2}}{\hat{M}_{N_m}^g} & \cdots & \frac{C_{Q_{N_m}\dot{\eta}_{N_m}}}{\hat{M}_{N_m}^g} - 2\xi_{N_m}\hat{\omega}_{N_m} \end{bmatrix} \qquad (75)$$

$(N_m \times N_m)$

ACKNOWLEDGEMENT

This research was supported by NASA grant NCC-2-374 provided under the auspices of the UCLA/NASA Dryden Flight Systems Research Center. The useful comments of the grant monitor, Dr. K. Gupta, from Dryden are gratefully acknowledged. The authors are very grateful to Dr. Gary Giles from NASA/Langley for providing the ELAPS code and his help on questions regarding the code. We also thank Dr. David McGhee from NASA Marshall Flight Center for providing modal information from an X33 NASTRAN model.

References

[1] Ricketts, R., Noll, T., Whitlow, W., and Huttsell,L., "An Overview of Aeroelasticiey Studies for the National Aerospace Plane," AIAA Paper No. 93-1313, *Proc. 34st AIAA/ASME/ASCE/AHS/ASC Structures, Structural Dynamics and Materials Conference*, La Jolla, CA, April 19-22 1993, pp. 152 - 162.

[2] Spain, C., Zeiler, T.A., Gibbons, M.D., Soistmann, D.L., Pozefsky, P., DeJesus, R.O., and Brannon,C.P., "Aeroelastic Character of a National Aerospace Plane Demonstrator Concept," *Proc. 34st AIAA/ASME/ASCE/AHS/ ASC Structures, Structural Dynamics and Materials Conference*, La Jolla, CA, April 19-22 1993, pp. 163–170.

[3] Heeg, J., Zeiler, T., Pototzky, A., Spain, C., and Engelund, W., "Aerothermoelastic Analysis of a NASP Demonstrator Model," AIAA Paper No. 93-1366, *Proc. 34st AIAA/ASME/ASCE/AHS/ ASC Structures, Structural Dynamics and Materials Conference*, La Jolla, CA, April 19-22 1993, pp. 617–627.

[4] Soistmann, D. and Spain, C., "An Experimental and Analytical Study of a Lifting Body Wind Tunnel Model Exhibiting Body-Freedom Flutter," AIAA Paper No. 93-1316, *Proc.*

34st AIAA/ASME/ASCE/AHS/ ASC Structures, Structural Dynamics and Materials Conference, La Jolla, CA, April 19-22 1993, pp. 171–181.

[5] Xue, D.Y. and Mei, C., "Finite Element Two-Dimensional Panel Flutter at High Supersonic Speeds and Elevated Temperature," AIAA Paper No. 90-0982, *Proc. 31st AIAA/ASME/ASCE/AHS/ASC Structures, Structural Dynamics and Materials Conference*, 1990, pp. 1464–1475.

[6] Gray, E.G. and Mei, C., "Large-Amplitude Finite Element Flutter Analysis of Composite Panels in Hypersonic Flow," AIAA Paper No. 92-2130, *Proc. 33rd AIAA/ASME/ASCE/AHS/ASC Structures, Structural Dynamics and Materials Conference*, Dallas, TX, April 16-17 1992, pp. 492–512.

[7] Abbas, J.F. and Ibrahim,R.A., "Nonlinear Flutter of Orthotropic Composite Panel Under Aerodynamic Heating," *AIAA J.*, Vol. 31, No. 8, No. 8, 1993, pp. 1478–1488.

[8] Bein, T., Friedmann, P., Zhong, X., and Nydick, I., "Hypersonic Flutter of a Curved Shallow Panel with Aerodynamic Heating," AIAA Paper No. 93-1318, *Proc. 34st AIAA/ASME/ASCE/AHS/ASC Structures, Structural Dynamics and Materials Conference*, La Jolla, CA, April 19-22 1993.

[9] Nydick, I., Friedmann, P.P., and Zhong, X., "Hypersonic Panel Flutter Studies on Curved Panels," AIAA Paper no. 95-1485, *Proc. 36th AIAA/ASME/ASCE/AHS/ASC Structures, Structural Dynamics and Materials Conference*, New Orleans, LA, April 1995, pp. 2995–3011.

[10] Friedmann, P. and Hanin, M., "Supersonic Nonlinear Flutter of Orthotropic or Isotropic Panels with Aribitrary Flow Direction," *Israel Journal of Technology*, Vol. 6, No. 1-2, No. 1-2, 1968, pp. 46–57.

[11] Olson, M.D., "Some Flutter Solutions Using Finite Elements," *AIAA Journal*, Vol. 8, April 1970, pp. 747–752.

[12] Bisplinghoff, R.L., Ashley, H., and Halfman, R.L., *Aeroelasticity*, Addison-Wesley, 1955.

[13] Milne, R.D., "Dynamics of the deformable aeroplane, parts i and ii." Great Britian Aeronautical Research Council, R.& M. No. 3345, 1964.

[14] Milne, R.D., "Some Remarks on the Dynamics of Deformable Bodies," *AIAA Journal*, Vol. 6, March 1968, p. 556.

[15] Waszak, M.R. and Schmidt, D.K., "Flight Dynamics of Aeroelastic Vehicles," *Journal of Aricraft*, Vol. 23, No. 6, June 1988, pp. 562–571.

[16] Bilimoria, K.D. and Schmidt, D.K., "Integrated Development of the Equations of Motion for Elastic Hypersonic Flight Vehicles," *Journal of Guidance, Control, and Dynamics*, Vol. 18, No. 1, No. 1, 1995, pp. 73–81.

[17] Meirovitch, L., "Hybrid State Equations of Motion for Flexible Bodies in Terms of Quasi-Coordinates," *Journal of Guidance, Control, and Dynamics*, Vol. 14, No. 5, No. 5, 1991, pp. 1008–1013.

[18] Giles, G.L., "Equivalent Plate Analysis of Aircraft Wing-Box Structures with General Planform Geometry," *J. of Aircraft*, Vol. 23, No. 11, November 1986, pp. 859–864.

[19] Giles, G.L., "Further Generalization of an Equivalent Plate Representation for Aircraft Structural Analysis," *Journal of Aircraft*, Vol. 26, No. 1, January 1989, pp. 67–74.

[20] Giles, G.L., "Equivalent Plate Modeling for Conceptual Design of Aircraft Wing Structures," AIAA Paper No. 95-3945, *Proc. 1st AIAA Aircraft Engineering, Technology and Operations Congress*, Los Angeles, CA, September 19-21 1995.

[21] Livne, E., "Recent Developments in Equivalent Plate Modeling for Wing Shape Optimization," AIAA Paper No. 93-1647, *Proc. 34th AIAA/ASME/ASCE/AHS/ASC Structures, Structural Dynamics, and Materials Conference*, La Jolla, CA, April 19-22 1993, pp. 2998–3011.

[22] Lees, L., "Hypersonic Flow," *Fifth International Aeronautical Conference*, Los Angeles, CA, 1955, pp. 241–276.

[23] Rasmussen, M., *Hypersonic Flow* New York, John Wiley & Sons, 1994.

[24] McGhee, D. private communication.

mode no.	empty	10% fuel	50% fuel	100% fuel
1	5.21	5.17	5.1	5.01
2	5.53	5.43	5.23	5.12
3	11.1	9.8	7.05	5.61
4	12.46	11.34	8.48	6.78
5	13.48	12.93	10.1	8.07
6	13.91	13.51	10.71	8.67

Table 1: Natural frequencies (Hz) calculated from ELAPS

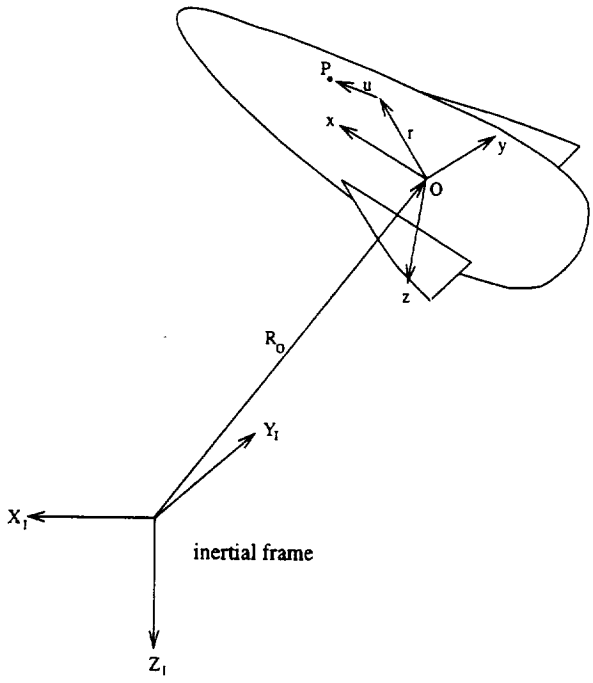

Figure 1: Flexible body

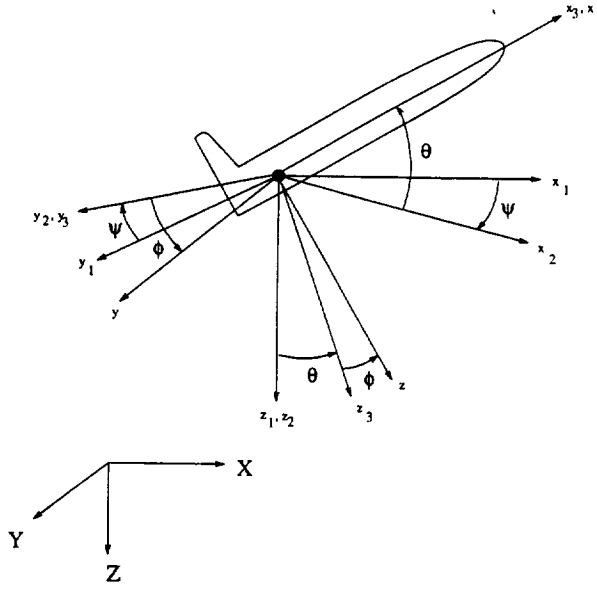

Figure 2: Definition of Euler angles

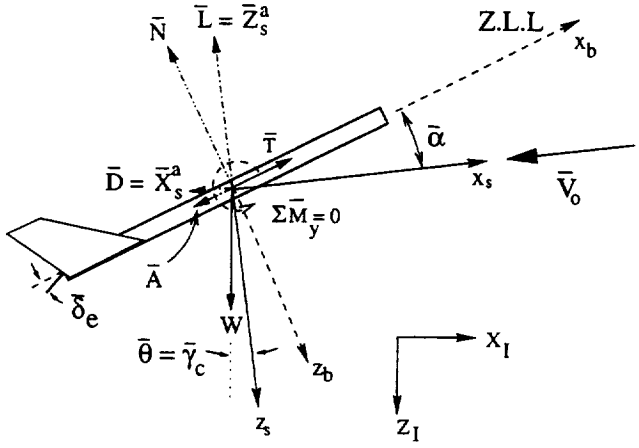

(a) Trim Flight Condition

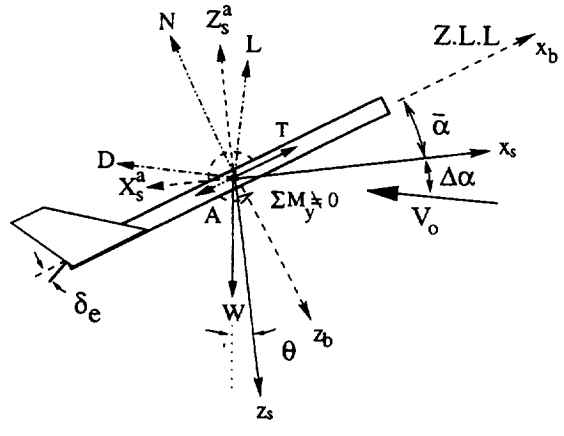

(b) Perturbed Flight Condition

Figure 3: Forces and moments on vehicle

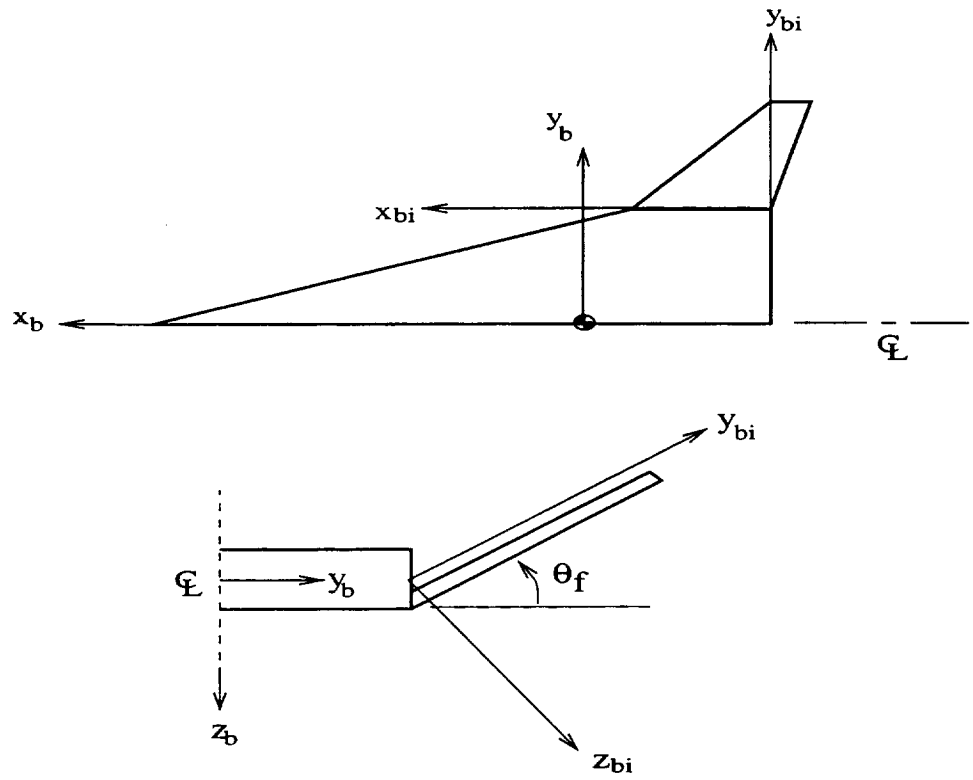

Figure 4: Coordinate Systems for X33 Main Lifting Body and Wing

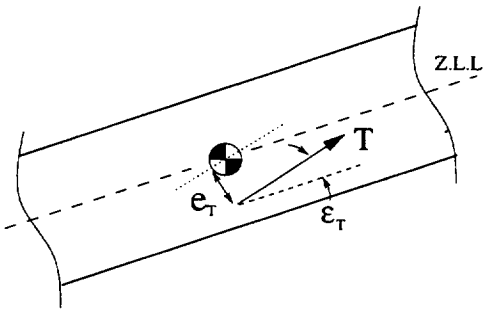

Figure 5: Orientation of the thrust vector

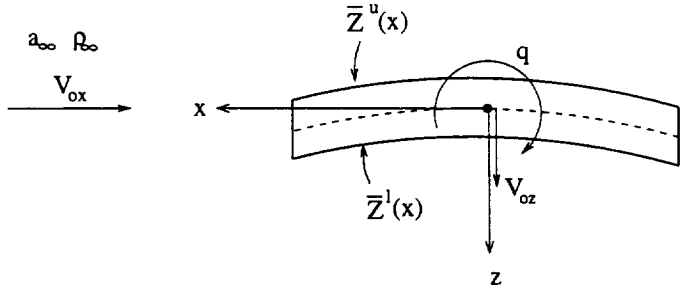

Figure 6: Airflow on Main Lifting Body

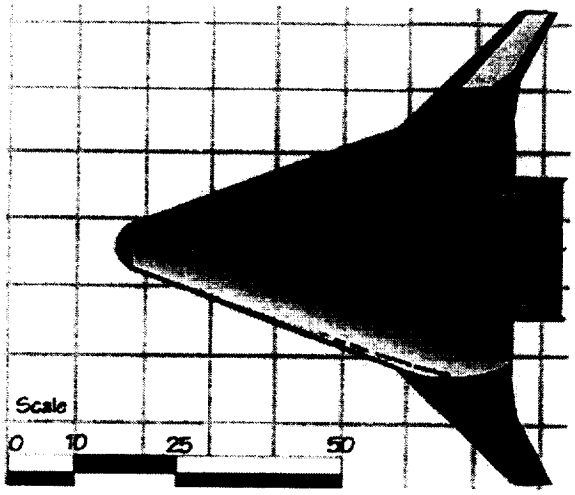

TOP VIEW

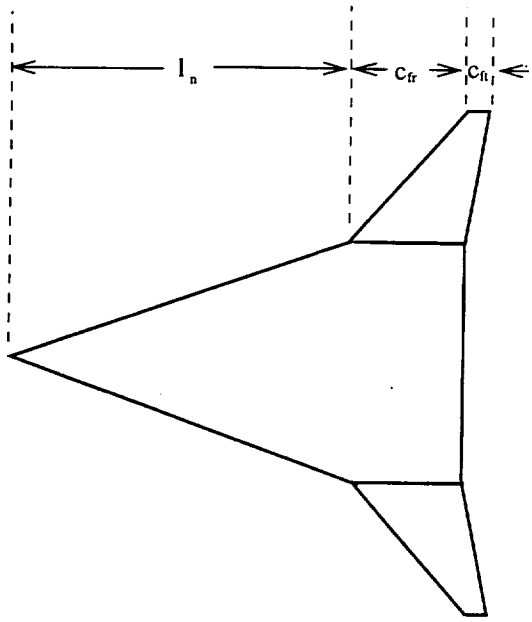

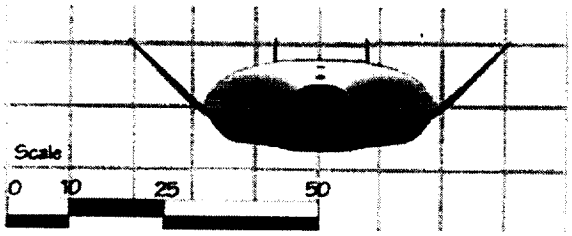

FRONT VIEW

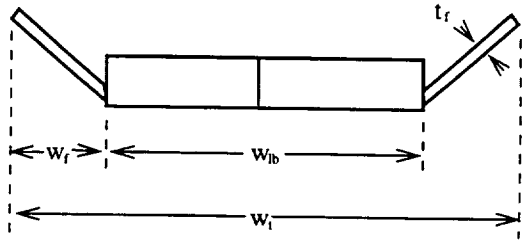

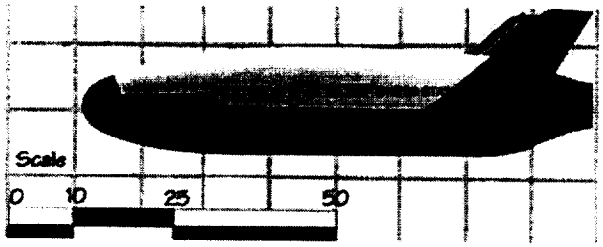

SIDE VIEW

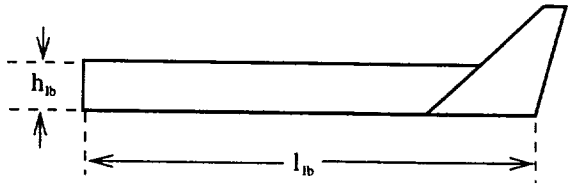

Figure 7: Actual and Idealized X33 Configurations

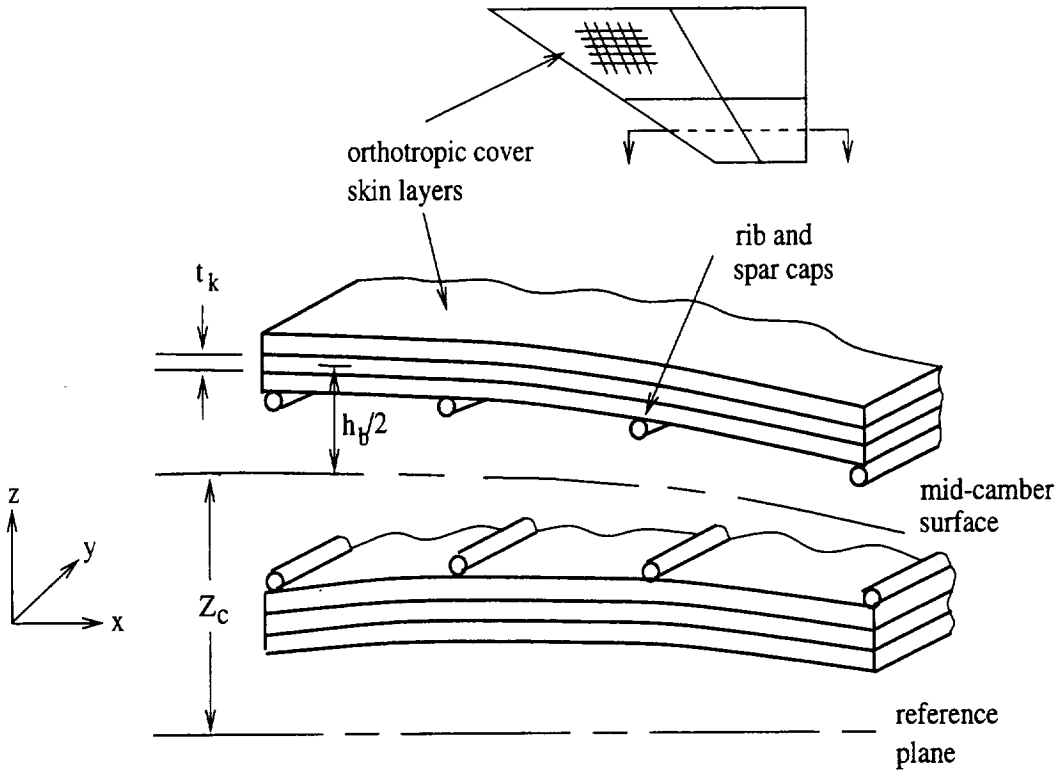

Figure 8: Vehicle structural box

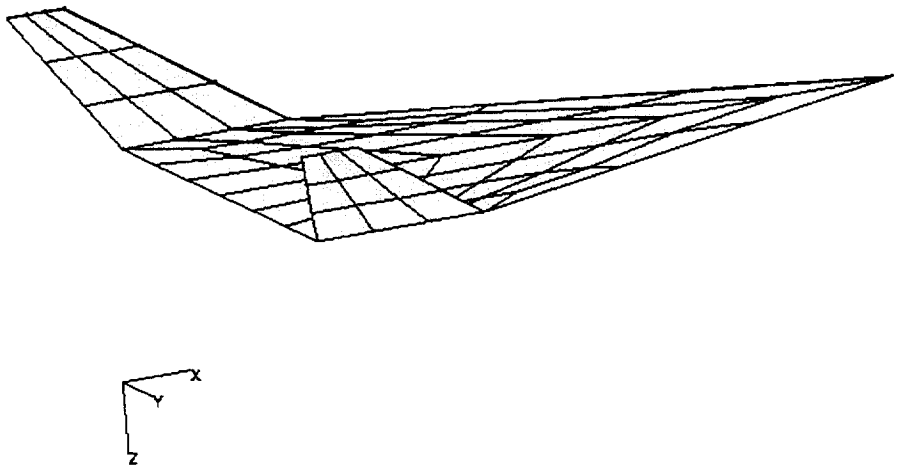

Figure 9: Undeformed generic hypersonic vehicle

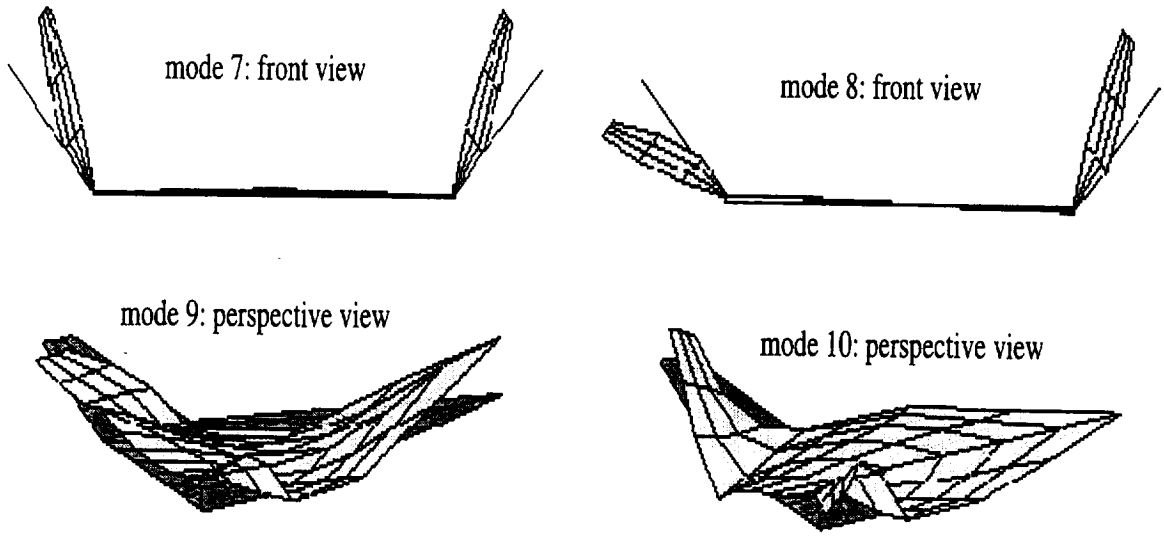

Figure 10: First four flexible modes of vehicle

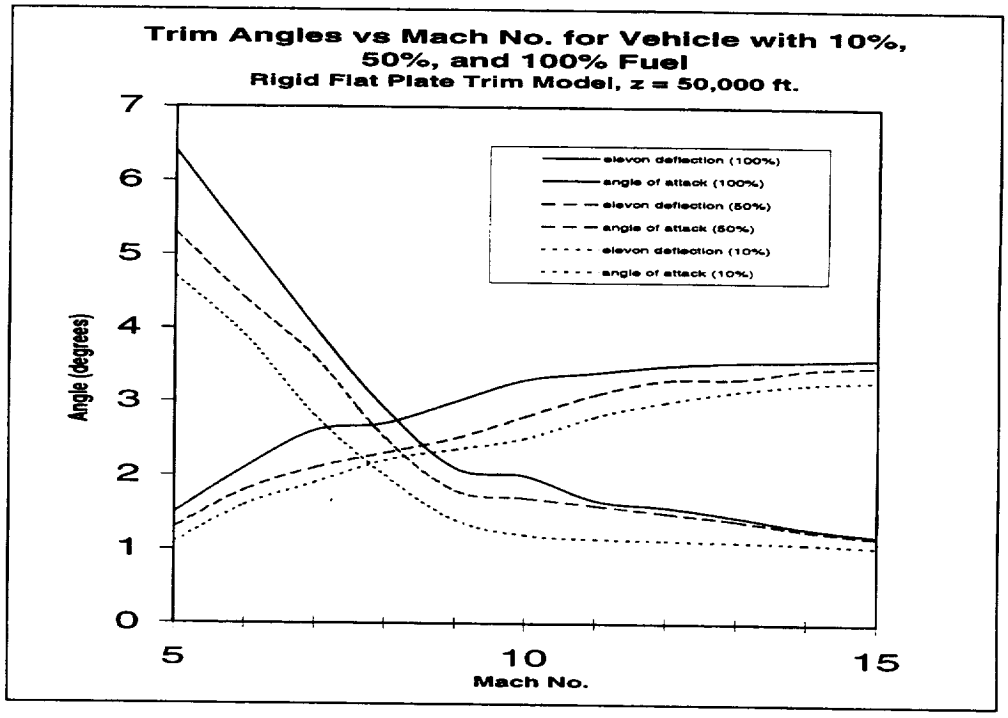

Figure 11: Trim curves for fueled vehicle

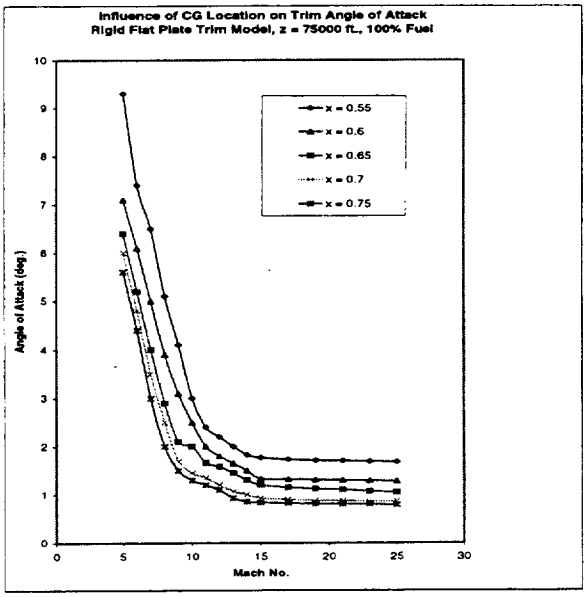

Figure 12: Influence of vehicle c.g. placement on trim angle of attack

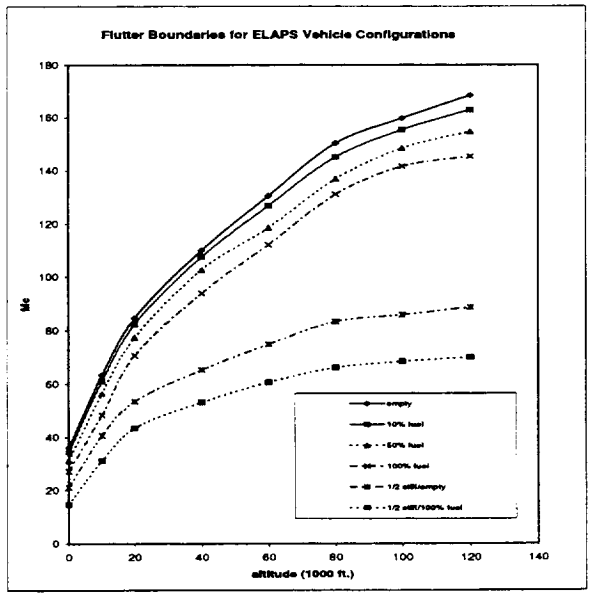

Figure 14: Flutter boundaries for generic hypersonic vehicle

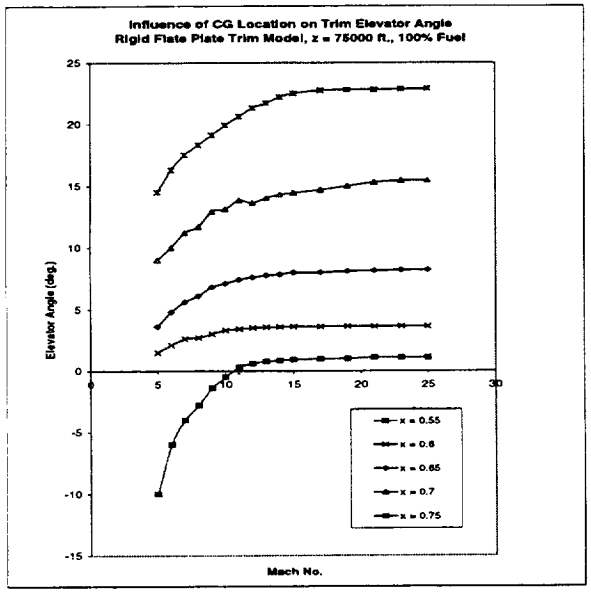

Figure 13: Influence of vehicle c.g. placement on trim elevon angle

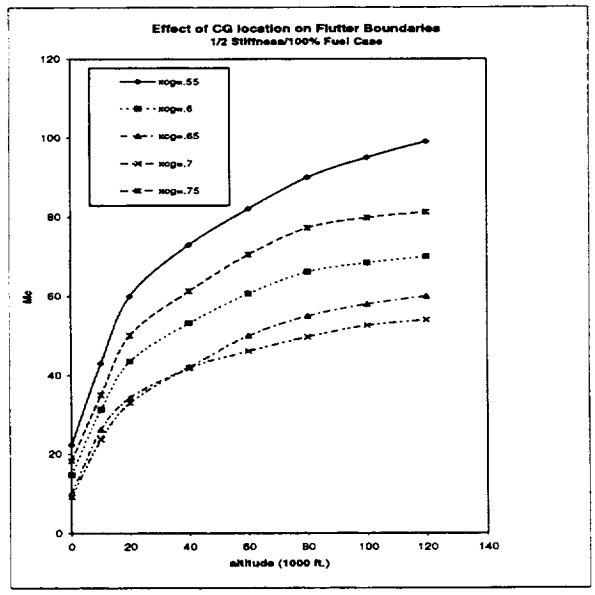

Figure 15: Effect of vehicle c.g. location on flutter boundaries

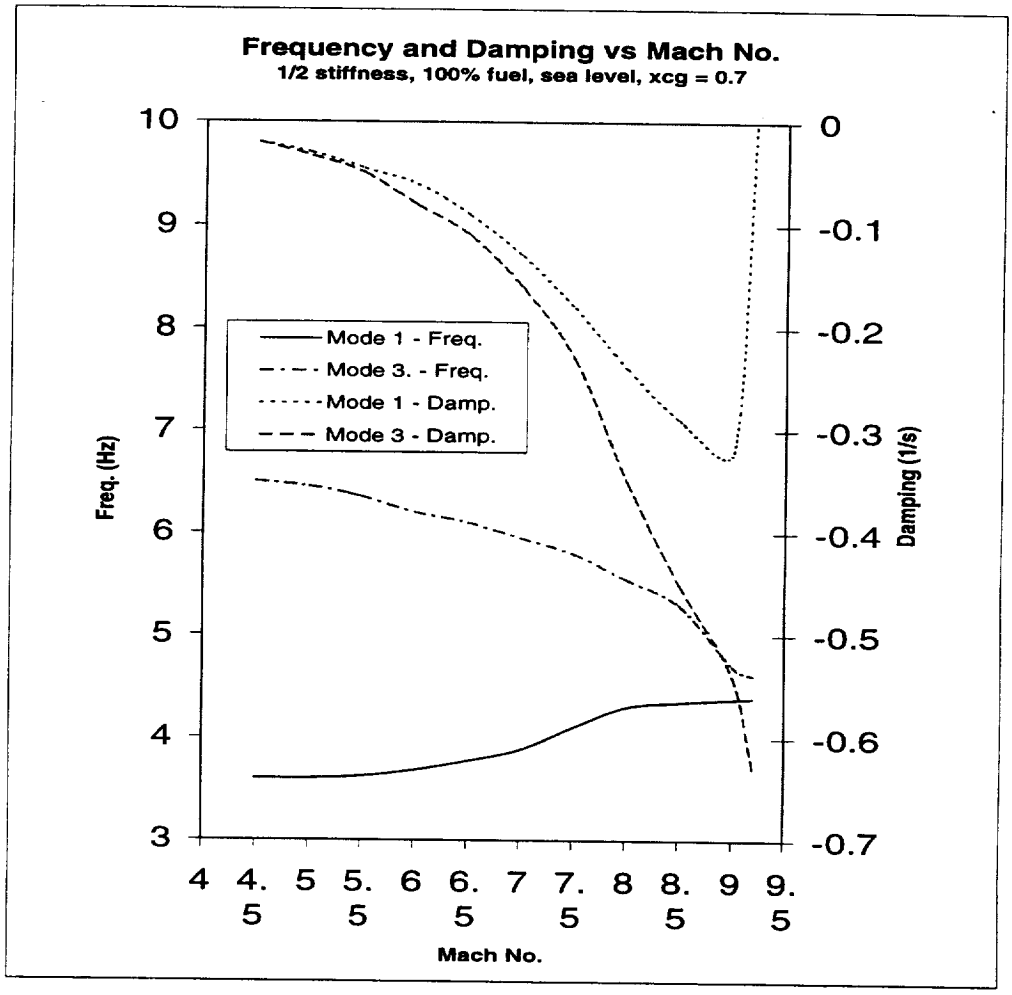

Figure 16: Dependence of modal frequency and damping on Mach No.

STIFFNESS AND DAMPING EFFECTS OF LAUNCH VEHICLE AEROELASTIC COUPLING

K. W. Dotson, R. L. Baker and B. H. Sako
The Aerospace Corporation, Los Angeles, California 90009-2957, USA

Abstract

The self-sustained coupling of structural responses with transonic flow state transitions at the nose of launch vehicle payload fairings can be analyzed by solving the nonlinear system equation of motion based on the force-response relationship and the periodicity condition. The traditional analysis approach for this phenomenon, however, linearizes the equation of motion by converting the alternating flow forces into an aerodynamic damping term and defines a stability criterion as the response amplitude that yields zero net system damping. This work clarifies the relationship between the new and traditional methods, and compares results and conclusions. The feasibility of modifying a launch vehicle buffet analysis (of random fluctuations caused by turbulent flow) to include aeroelastic coupling effects is also explored. The aerodynamic stiffness and damping terms formulated are consistent with trends observed in wind tunnel test data. It is shown, however, that the modified buffet analysis approach can be inaccurate, particularly when the aeroelastic coupling contribution does not dominate the system response.

Nomenclature

AF = dynamic amplification factor, dimensionless
$[C^*]$ = modal damping matrix, N-s/m
F = external force, N
$\{F(t)\}$ = vector of system external forces, N
$[I]$ = modal mass matrix (identity matrix), kg
M = Mach number, dimensionless
n = normalized aerodynamic stiffness (single mode), dimensionless
$\dot{n}$ = normalized aerodynamic damping (single mode, dimensionless
$q(t)$ = generalized displacement (single mode), m
$\{q(t)\}$ = vector of generalized displacements, m
$\Re$ = relative measure of aeroelastic coupling contribution to total response, dimensionless
s = signal strength, dimensionless
T = period, s
$\{x(t)\}$ = vector of physical displacements, m
z = generalized translation normalized with respect to a static value, dimensionless
Δt = time required for flow state change, s
ζ = structural damping, dimensionless
η = aerodynamic stiffness (single mode), rad^2/s^2
$\dot{\eta}$ = aerodynamic damping (single mode), rad/s
θ = rotation, deg
ξ = force variation, dimensionless
ϕ = modal value (single mode), 1/kg
$[\phi]$ = modes matrix, dimensionless
ω = undamped circular natural frequency, rad/s
$[\omega^2]$ = modal stiffness matrix, N/m

Subscripts

a = aeroelastic coupling
b = buffeting
cr = critical
e = excitation
f = physical force application points
i = bending mode number
n = nose
r = rotation
rms = root mean square
st = static
t = total (or effective)
∞ = freestream state

Introduction

During transonic flight the flow at the cone cylinder junction of launch vehicle payload fairings can alternate between separated and attached states (Chevalier & Robertson 1963; Robertson & Chevalier 1963). Schlieren photographs from Robertson & Chevalier (1963) are reproduced in Figure 1. A flow state change on the leeward side of the payload fairing model (with a 25-deg nose cone angle) is evident when the angle of attack equals two degrees. Because the pressure profiles for the separated and attached states are different, the flow state changes impose an exciting force on the launch vehicle.

Investigations of self-sustained coupling of this force with launch vehicle elastic responses have been conducted using three different approaches. Computational fluid dynamics has been used in conjunction with structural dynamic models to predict the launch vehicle behavior (Chen & Dotson 1999). This approach is purely analytic but is computationally intensive and limited by the accuracy of the transonic aerodynamic formulation.

The other two methods are more tractable for analysis of this phenomenon and use experimental data to quantify the pressure distributions on the payload fairing.

The force variation is idealized, and the flow alternations are triggered when the deflection angle reaches a critical value. Ericsson (1967), in the first of these two semiempirical methods, assumed that the flow state changes instantaneously after an implicit time lag and that the alternations occur on only one side of the payload fairing. More recently, Dotson *et al.* (1998a) assumed that the flow state changes linearly during an explicit time lag, as shown in Fig. 2, and that the alternations occur on both sides of the payload fairing. One-sided and instantaneous flow state changes can also be analyzed using the techniques employed by Dotson *et al.* (1998a).

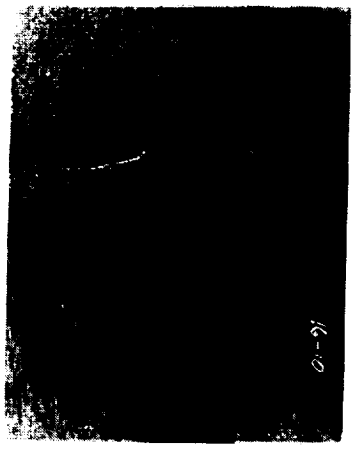

a) zero-deg angle of attack

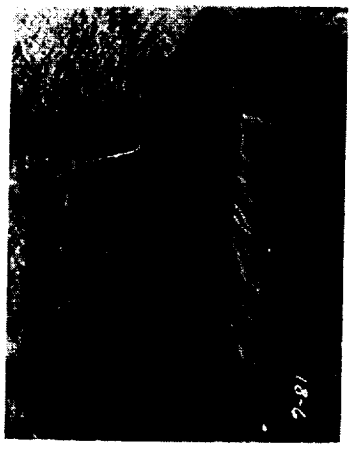

b) two-deg angle of attack

Fig. 1 Schlieren photographs of flow state changes observed in wind tunnel tests for $M_\infty = 0.89$. Reproduced with permission of Arnold Engineering Development Center.

Ericsson (1967) linearized the equation of motion by converting the forces resulting from the flow alternations into an assumed equivalent aerodynamic damping term, corresponding to harmonic response at the vehicle bending mode frequency. The limit cycle amplitude for bounded system responses was then defined as the value that corresponds to zero net system damping. Dotson *et al.* (1998a) established the steady-state behavior of the launch vehicle using analysis techniques for nonharmonic periodic excitation. The amplitude of the limit cycle oscillation and the response frequency were predicted directly without deriving an aerodynamic damping term.

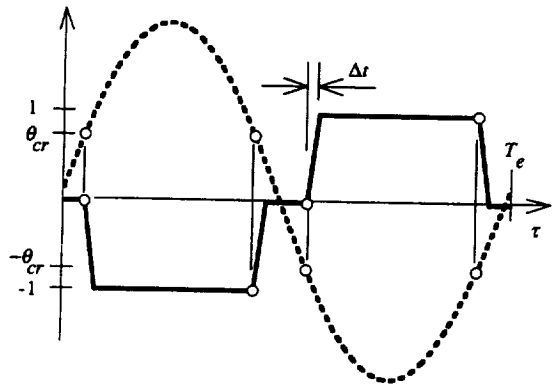

Fig. 2 Schematic of one cycle of steady-state coupled force and response in present theory. (—) normalized force variation ξ_w ; (- - -) payload fairing rotation.

Self-sustained oscillations for the Titan IV launch vehicle were evaluated by Dotson *et al.* (1998b), and it was shown that the responses and loads can be more than an order of magnitude smaller than those predicted by the Ericsson (1967) stability criterion. It was, furthermore, shown that the differences in predicted results between the two methodologies can be traced to the value of the time lag defined explicitly by Dotson *et al.* (1998a) and implicitly by Ericsson (1967). There are two major implications of this finding: first, Ericsson's (1967) stability criterion is misleading because a finite limit cycle amplitude always exists for structurally-damped launch vehicles; second, a reasonable estimate of the magnitude of the time lag is critical to prevent overprediction of the launch vehicle responses and corresponding loads. This overprediction can have highly undesirable programmatic impacts, such as vehicle redesign and launch "no-go" decisions due to low thresholds on measured winds.

Even though it is unnecessary to define an aerodynamic damping term to determine the limit cycle amplitude for launch vehicle aeroelastic coupling, it is common in a variety of flow-induced vibration problems to equate self-sustained oscillation with a change in the

system damping for one or more of the system modes. For example, the "galloping" of ice-laden cables and the vortex-induced oscillation of stacks are civil engineering problems that have been thus analyzed (Dowell 1995). In aeronautical engineering, the torsional response of wings in transonic flow has been expressed as a reduction in net system damping flow (Mabey 1989). Indeed, launch vehicle aeroelastic coupling belongs, along with transonic wing torsion and aircraft control surface "buzz," in the class of single degree-of-freedom problems involving feedback between transonic shock-wave motion and structural responses. Experimental and empirical solutions are typically used for these problems because the aerodynamic nonlinearities are significant (Dowell 1995).

Equations of motion presented by Ericsson (1967) imply that an extended analysis of launch vehicle responses caused by buffeting (i.e., by random fluctuations associated with turbulent flow) can be conducted using modified bending mode stiffness and damping values to account for aeroelastic coupling effects. Buffet forcing functions have broad-band spectra, and buffeting analyses include numerous system modes for accurate response and load predictions. Hence, in a modified buffet approach, the stiffness and damping values would be altered for the bending mode speculated to experience aeroelastic coupling, and the response analysis would be conducted for the linear multi degree-of-freedom system. Application of this analysis approach does not appear to have been demonstrated for launch vehicle aeroelastic coupling. It is interesting to note, however, that procedures have been developed for the prediction of bridge flutter including buffeting effects (Dowell 1995).

The feasibility of a modified launch vehicle buffet analysis is investigated herein. It is shown that a buffet analysis without aeroelastic coupling effects must be conducted prior to calculating the modified stiffness and damping values, and that the bending mode response from a modified buffet analysis can be inaccurate. The derivations of the system damping (and ancillary stiffness) effects nevertheless place launch vehicle aeroelastic coupling in the context of other flow-induced vibration problems. Analytical results are provided using Titan IV system parameters.

Analysis Approach

The equations of motion for the coupled system are

$$[I]\{\ddot{q}(t)\}+[C^*]\{\dot{q}(t)\}+[\omega^2]\{q(t)\} = [\phi]_f^T\{F(t)\} \quad (1)$$

in which

$$\{x(t)\} = [\phi]\{q(t)\} \quad (2)$$

In a rigorous treatment of the transonic system responses, the vector $\{F(t)\}$ would include time-consistent forces induced by buffeting, gusts, control system parameters, static aeroelasticity, and maneuvering, as well as those caused by aeroelastic coupling (Fleming 1994). However, because it is impossible to predict the amplitudes and phasing of the forces that will occur during the actual flight, a rigorous prelaunch analytical treatment is untenable (Kabe 1998). In practice, equation (1) is broken up into constituent airloads events that are analyzed separately and treated statistically (Fleming 1994). The mean and dispersed values for each of the dynamic load components are predicted, and total loads are computed using a combination equation that yields values for a specified probability of nonexceedance during flight (Macheske *et al.* 1993). In the present analysis, the vector $\{F(t)\}$ includes predictions of external forces induced by aeroelastic coupling and buffeting but, for the sake of simplicity, neglects those caused by other transonic loads phenomena.

Equation (1) can be simplified if it assumed that the alternating flow forces couple with a single bending mode, and that aeroelastic coupling for each of the lower bending modes can be analyzed independently. Dotson *et al.* (1998b) investigated this assumption through transient analysis of a fully coupled launch vehicle dynamic model and showed it to be acceptable, provided that the frequencies of the higher-order components in the Fourier series expansion of the alternating flow forces are not very close to the frequencies of system modes in the plane of the excitation. Extracting from equation (1) the modal equation that best represents the ith system bending mode yields

$$\ddot{q}_{t,i}(t)+2\zeta_i\omega_i\dot{q}_{t,i}(t)+\omega_i^2 q_{t,i}(t) = \sum_{j=1}^{2}\phi_{i,j}F_{a,j}(q_{t,i}) + \sum_{k=1}^{m}\phi_{i,k}F_{b,k}(t) \quad (3)$$

The modal values in equation (3) correspond to the points in the launch vehicle model at which the discrete force histories are applied. The first term on the right hand side of equation (3) represents the generalized force history for aeroelastic coupling. The two force resultants in this summation are defined by pressure profiles for the alternating flow states and are described in further detail by Dotson *et al.* (1998a). The alternating flow forces are a function of the generalized displacement $q_{t,i}$ because the changes in flow state occur when the deflection angle of the payload fairing nose cone equals a critical value, as shown in Figure 2. Dotson *et al.* (1998a) proved using energy principles that the generalized aeroelastic coupling force must be out of phase

with the vehicle response to induce limit cycle oscillation.

For the Titan IV at Mach 0.8, the amplitudes $F_{a,1}$ and $F_{a,2}$ equal 6.7 and 26.2 kN, respectively (Dotson *et al.* 1998a). The corresponding generalized force history is in phase with the vehicle response, such that the flow state changes cannot induce limit cycle oscillation for this vehicle. Herein, the signs of the force resultants are artificially reversed so that the generalized force history is out of phase with the vehicle response, and Titan IV modal data can be used to analyze aeroelastic coupling with buffeting. The fundamental pitch bending mode for a Titan IV mission with a 26.2 m-long payload fairing was selected for the present study. The frequency and damping of this mode equal 1.27 Hz and 0.71 percent, respectively.

The maximum static value of the generalized response for aeroelastic coupling is defined by

$$q_{st} = \omega^{-2} \left| \phi_1 F_{a,1} + \phi_2 F_{a,2} \right| \tag{4}$$

The value from equation (4) is not constant because the magnitude and location of the force resultants vary with respect to Mach number. If the maximum value of equation (4) during the transonic region is used, normalization of equation (3) with respect to equation (4) yields

$$\ddot{z}_i(t) + 2\zeta\omega\, \dot{z}_i(t) + \omega^2 z_i(t) = \omega^2\, \xi_i(z_i, t) \tag{5}$$

in which

$$\xi_i(z_i, t) = s\, \xi_a(z_i) + \xi_b(t) \tag{6}$$

The subscript i has been dropped for convenience. The flow state changes initiate when the response equals

$$z_{cr} = \theta_{cr} / \left| \phi_{r,n} \right| q_{st} \tag{7}$$

The range of the scalar s in equation (6) is $0 \le s \le 1$, such that $s = 0$ corresponds to the absence of flow state transitions, and $s = 1$ corresponds to the maximum contribution of aeroelastic coupling to the total system response. When buffeting is ignored, equation (5) reduces to the nonlinear equation analyzed by Dotson *et al.* (1998a). The buffeting term, therefore, acts as noise superimposed on the force variation shown in Figure 2.

The value of s changes as the vehicle flies through the early transonic regime; it begins with $s=0$, increases to $s=1$ at the maximum aeroelastic coupling time, and finally returns to $s=0$ near Mach 1. Therefore, the signal-to-noise ratio generally increases, then decreases, with respect to Mach number and time. In the Titan IV analyses to be presented it is (justifiably) assumed that maximum aeroelastic coupling occurs at Mach 0.8.

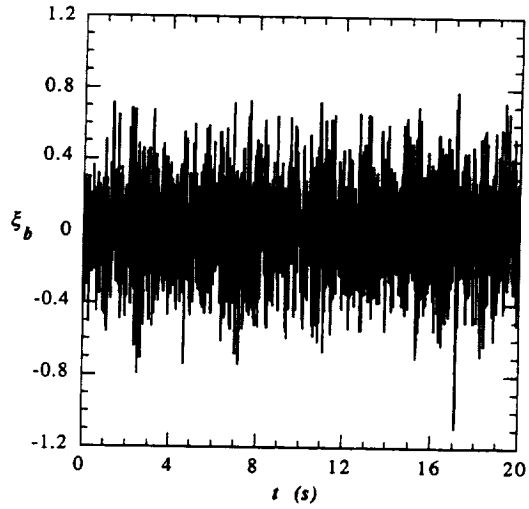

Fig. 3 Time history of normalized Titan IV buffet generalized force for fundamental pitch bending mode.

The Titan IV buffet generalized force during transonic flight is shown in Figure 3. Ninety eight [m in equation (3)] buffet forcing functions with frequency content up to 50 Hz are applied to all components of the Titan IV vehicle. These buffet forces are based on wind tunnel test data but include modifications to ensure conservative response predictions relative to observed flight data. The maximum value of the buffeting noise in Figure 3 exceeds unity, the amplitude of the aeroelastic coupling force variation shown in Figure 2. However, the time history is dominated by frequency components in the 10-20 Hz range, and the amplitude of the content around the frequency of the vehicle fundamental bending mode is relatively low. Indeed, it will be shown that aeroelastic coupling dominates the Titan IV bending response at Mach 0.8 and 0.9.

Aeroelastic Coupling Response

Before developing the modified buffet analysis approach, it is necessary to summarize some key results from Dotson *et al.* (1998a). The characteristic equation for the period of the aeroelastic coupling response based on a nonharmonic trial function is given by

$$\left(T_e/T_i\right)\csc\left(\omega T_e/2\right) - 1/\pi = \Delta t/\zeta T_i \tag{8}$$

The steady-state response can be approximated by a harmonic solution that yields the relationship

$$T_e/T_i = \left(1 + 4\zeta/\omega\Delta t\right)^{-1/2} \tag{9}$$

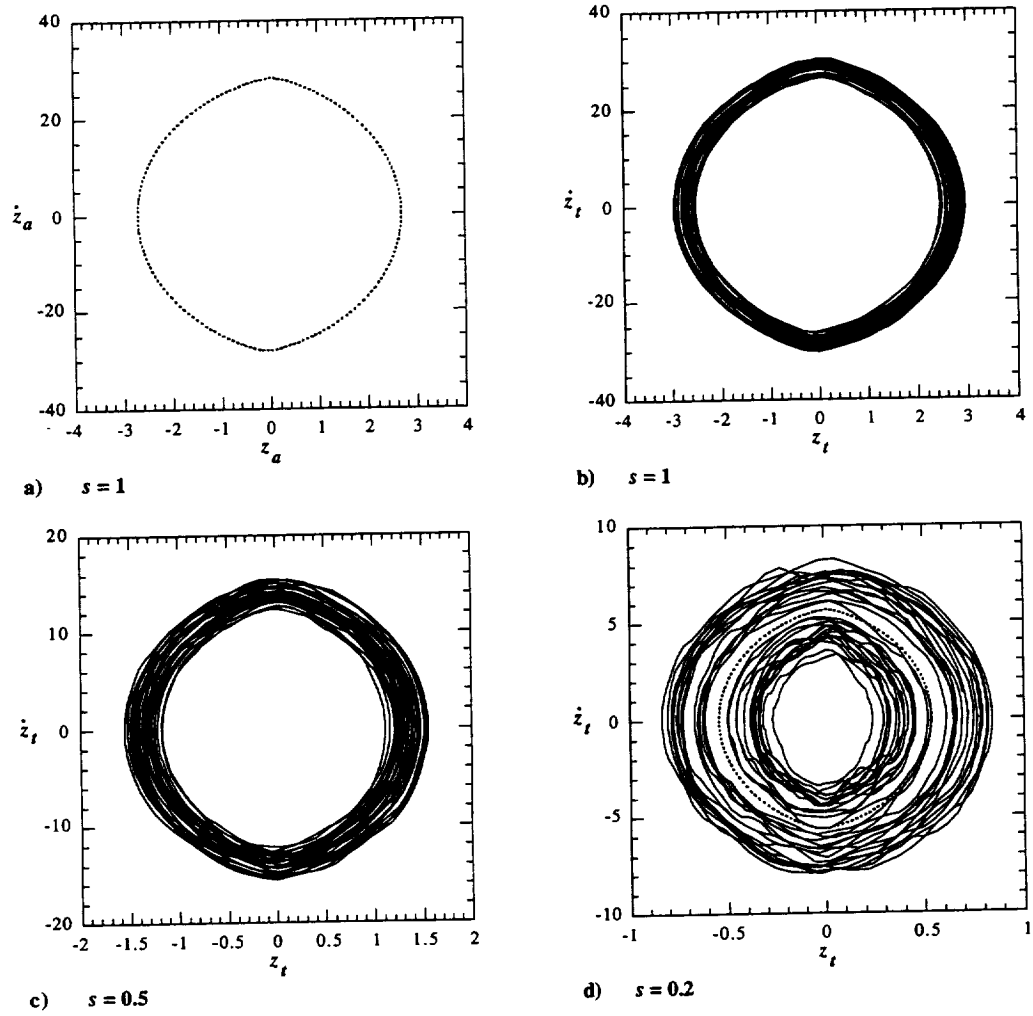

Fig. 4 Phase plane diagram from simulation with f = 1.27 Hz, ζ = 0.71%, and Δt = 7 ms. (——) with buffeting; (- - - -) without buffeting.

It can be shown that equation (9) is valid for all critical nose deflection angles. The harmonic approximation leads to the dynamic amplification factor

$$AF = 2\left(\Delta t/\zeta T_i\right)\cos\left[\sin^{-1}\left(z_{cr}\left(\zeta T_i/\Delta t\right)\right)/2\right] \quad (10)$$

For zero critical deflection, equation (10) reduces to

$$AF = 2\left(\Delta t/\zeta T_i\right) \quad (11)$$

By comparison, for $\Delta t << T_e$ the nonharmonic trial function leads to

$$AF = \sec(\omega T_e/4) - 1 \quad (12)$$

in which the ratio T_e/T_i is established from equation (8). The harmonic approximation always underestimates the response amplitude, and its accuracy depends on the salient ratio $\Delta t/\zeta T_i$ (Dotson *et al.* 1998a).

Numerical Simulations

It is assumed that the buffeting noise plotted in Figure 3 is valid for all transonic Mach numbers and is unaffected by local angle of attack changes caused by the vehicle bending mode response. The buffeting event, therefore, is treated strictly as a function of time. This is the approach used by the launch vehicle community for dynamic analysis of launch vehicle loads induced by buffeting.

The simulation computer algorithm presented by Dotson *et al.* (1998a) was modified to include buffeting noise. The modified code is used herein to assess the effect of buffeting on the aeroelastic coupling response and to validate equations for the effective system frequency and damping. At each time step, the buffet force

ξ_b is added to the aeroelastic coupling force $s\xi_a$ [see equation (6)]. Because buffeting affects the system response, the function ξ_a differs from that without buffeting. The aeroelastic coupling force is taken to be out-of-phase with the response as required for self-sustained oscillation. The computer code solves equation (5) given initial displacement and velocity values. Convergence of the solution is verified by reducing the integration time step and repeating the analysis.

Figure 4a shows the phase plane diagram for the Titan IV parameters without buffeting noise. The initial conditions for this simulation are given by zero velocity and displacement equal to the limit cycle amplitude without buffeting, 2.7. Figure 4b shows the effect of buffeting when $s=1$, i.e., when the aeroelastic coupling contribution is a maximum. It can be concluded from Figures 4a and 4b that the inclusion of buffeting noise prevents the system response from attaining a true limit cycle. However, the aeroelastic coupling contribution is large enough for this example that the deviations from the limit cycle state are small and the response is quasiperiodic.

The phase plane diagrams for numerical simulation with $s=0.5$ and $s=0.2$ are shown in Figures 4c and 4d, respectively. Because the system displacement is normalized with respect to the maximum aeroelastic contribution, the initial condition $z(0)$ and critical deflection z_{cr} are scaled by s. Figure 4c shows that $s<1$ increases the relative deviation from the aeroelastic coupling contribution. Figure 4d shows that when the value of s is small enough, the system response cannot be described as a simple deviation from the aeroelastic coupling limit cycle state.

Modified Buffet Analysis

Separation of Response Contributions

To assess the effects of aeroelastic coupling in combination with buffeting, it is assumed that equation (5) can be split into constituents such that

$$\ddot{z}_a(t) + 2\zeta\omega\,\dot{z}_a(t) + \omega^2 z_a(t) \;=\; \omega^2\,\xi_a(z_a) \qquad (13)$$

$$\ddot{z}_b(t) + 2\zeta\omega\,\dot{z}_b(t) + \omega^2 z_b(t) \;=\; \omega^2\,\xi_b(t) \qquad (14)$$

in which

$$z_t(t) \;=\; sz_a(t) + z_b(t) \qquad (15a)$$

$$\dot{z}_t(t) \;=\; s\dot{z}_a(t) + \dot{z}_b(t) \qquad (15b)$$

$$\ddot{z}_t(t) \;=\; s\ddot{z}_a(t) + \ddot{z}_b(t) \qquad (15c)$$

The subscript-a terms are defined by aeroelastic coupling without buffeting, while the subscript-b terms are defined by buffeting without aeroelastic coupling.

Equation (15) is approximate because response superposition is valid only for linear systems. But the approximation is acceptable if the buffet contribution does not significantly alter the time points at which the system response reaches the critical value for changes in the alternating flow forces. In this case, the aeroelastic coupling contribution is close to that without buffeting. Equation (15), therefore, is most useful when the signal strength s is large. As the value of s decreases, the aeroelastic coupling force variation becomes affected by the buffeting noise and the accuracy of the approximation diminishes.

Conversion of Alternating Flow Forces

Converting the aeroelastic coupling force variation in equation (13) into equivalent aerodynamic stiffness and damping terms yields

$$\ddot{z}_a(t) + \left(2\zeta\omega + \dot{\eta}\right)\dot{z}_a(t) + \left(\omega^2 + \eta\right) z_a(t) \;=\; 0 \qquad (16)$$

Equation (16) can also be expressed as

$$\ddot{z}_a(t) + 2\omega\left(\zeta + \dot{n}\right)\dot{z}_a(t) + \omega^2(1+n)\,z_a(t) \;=\; 0 \qquad (17)$$

The terms n and $\dot{n}$ modify the system stiffness and damping, respectively. Equation (17) yields the conventional differential equation for a single degree-of-freedom linear system

$$\ddot{z}_a(t) + 2\zeta_a\omega_a\dot{z}_a(t) + \omega_a^2 z_a(t) \;=\; 0 \qquad (18)$$

when the effective frequency and damping are defined by

$$\omega_a \;=\; \omega\sqrt{1+n} \qquad (19a)$$

$$\zeta_a \;=\; \left(\zeta + \dot{n}\right)/\sqrt{1+n} \qquad (19b)$$

and the aerodynamic stiffness and damping terms n and $\dot{n}$ are assumed to be constant. The aeroelastic coupling response must now originate from specified initial conditions because the forcing function no longer appears in the equation of motion.

Dotson *et al.* (1998a) used energy principles to prove, and numerical simulations to validate, that when the force caused by the alternating flow states opposes the response and the initial conditions are larger than known critical values, structurally-damped systems always attain a stable limit cycle. Only for the unrealistic case in which $\zeta \equiv 0$ will the system response diverge, i.e., be-

come unbounded and fail to attain a limiting amplitude. The effective damping constant ζ_a, therefore, ultimately equals zero, which leads to the identity

$$\dot{n} \equiv -\zeta \tag{20}$$

Dotson *et al.* (1998a) further showed that if the initial conditions in the phase plane lie outside of the limit cycle, the transient response diminishes, implying that the net system damping is *initially* positive. Similarly, if the initial conditions lie inside of the limit cycle but are larger than known critical values, the transient response increases, implying that the net system damping is *initially* negative.

A single value of the effective damping constant ζ_a, therefore, cannot model the nonlinear response for all time t, unless the initial conditions conform exactly to the limit cycle state. This case is assumed herein for the modified buffet analysis. Fortunately, the limit cycle state is of most interest: if the initial conditions lie outside of the limit cycle, the final response state is more benign than the initial one; similarly, if the initial conditions lie inside of the limit cycle, the final amplitude is greater and is given by the limit cycle response.

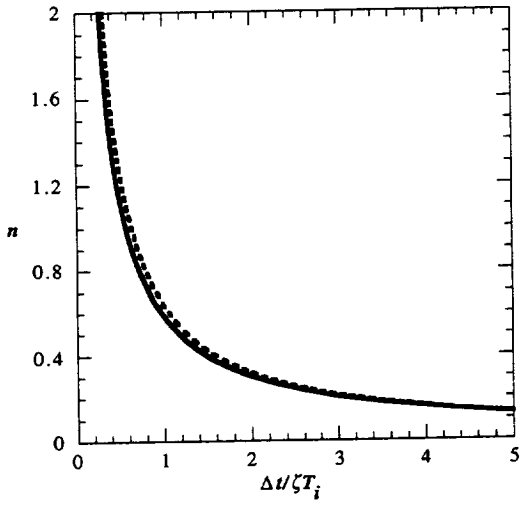

Fig. 5 Normalized aerodynamic stiffness. (——) nonharmonic solution; (- - - -) harmonic approximation.

The conversion of the periodic alternating flow forces into an aerodynamic damping term for the limit cycle state is constrained by equation (20). It is evident from equation (19a) that the aerodynamic stiffness term is similarly constrained by

$$n \equiv \left(\omega_a/\omega\right)^2 - 1 \tag{21}$$

Figure 5 illustrates equation (21) with values of T_e/T_i that satisfy equation (8). As the salient ratio $\Delta t/\zeta T_i$ increases, the modification introduced by the stiffness term n diminishes to zero, and the system frequency tends to that of the bending mode.

Using equations (9) and (21), it can be shown that the harmonic approximation yields

$$n = \frac{2}{\pi}\left(\Delta t/\zeta T_i\right)^{-1} \tag{22}$$

This expression is compared in Figure 5 with the nonharmonic solution. The agreement is reasonable, particularly for the higher values of $\Delta t/\zeta T_i$.

For $\zeta_a \equiv 0$, equation (18) has a steady-state harmonic as its solution. The aeroelastic coupling response then is implicitly harmonic when the step-like forcing functions are converted into constant aerodynamic stiffness and damping terms. It can be shown that when the alternating flow forces are converted formally, the aerodynamic stiffness and damping terms are time dependent. It can be concluded that conversion of the forces into constant values is inherently less accurate than nonharmonic analysis. The magnitude of the discrepancy depends on the value of $\Delta t/\zeta T_i$.

Combination of Response Contributions

The equation of motion for the total system response can now be reformulated by summing equations (14) and (18) with the scalar s and $\zeta_a \equiv 0$, such that

$$\ddot{z}_t(t) + 2\zeta\omega\left[\dot{z}_t(t) - s\,\dot{z}_a(t)\right] + \omega^2\left[z_t(t) + ns\,z_a(t)\right] = \omega^2\,\xi_b(t) \tag{23}$$

Equation (23) is still unsuitable because it requires aeroelastic coupling displacement and velocity histories. Unless the time dependence of the aeroelastic coupling contribution is removed, there is no benefit in using equation (23), which is approximate, rather than the exact formulation given by equation (5). In other words, constant stiffness and damping coefficients that account for the aeroelastic coupling effects are required if a modified buffet analysis is sought. To this end, a relative measure $\Re$ of the aeroelastic coupling and total responses must be introduced such that

$$\ddot{z}_t(t) + 2\zeta\omega\left[1 - s\,\Re\left(\dot{z}_a/\dot{z}_t\right)\right]\dot{z}_t(t) + \omega^2\left[1 + ns\,\Re\left(z_a/z_t\right)\right]z_t(t) = \omega^2\,\xi_b(t) \tag{24}$$

The computation of $\Re$ is subjective. One possible method uses the root-mean-square (rms) values of the aeroelastic coupling and buffet time histories such that

$$\ddot{z}_t(t) + 2\zeta\omega\left(1 - s\,\dot{z}_{a,\mathrm{rms}}/\dot{z}_{t,\mathrm{rms}}\right)\dot{z}_t(t) + \omega^2\left(1 + ns\,z_{a,\mathrm{rms}}/z_{t,\mathrm{rms}}\right)z_t(t) \;=\; \omega^2\,\xi_b(t) \tag{25}$$

Equation (25) can be written in the conventional form for a single degree-of-freedom linear system

$$\ddot{z}_t(t) + 2\zeta_t\omega_t\dot{z}_t(t) + \omega_t^2 z_t(t) \;=\; \omega_t^2\,\xi_b'(t) \tag{26}$$

in which

$$\zeta_t \;=\; \zeta\left(\frac{1 - s\,\dot{z}_{a,\mathrm{rms}}/\dot{z}_{t,\mathrm{rms}}}{\sqrt{1 + ns\;z_{a,\mathrm{rms}}/z_{t,\mathrm{rms}}}}\right) \tag{27a}$$

$$\omega_t \;=\; \omega\sqrt{1 + ns\,z_{a,\mathrm{rms}}/z_{t,\mathrm{rms}}} \tag{27b}$$

$$\xi_b'(t) \;=\; \frac{\xi_b(t)}{1 + ns\,z_{a,\mathrm{rms}}/z_{t,\mathrm{rms}}} \tag{27c}$$

Aeroelastic coupling modifies the system stiffness and damping terms but the solution of equation (26) will, nevertheless, fail to account for the limit cycle oscillation unless appropriate initial conditions are specified.

Recall that buffeting noise is assumed to be independent of the system response and, hence, strictly a function of time. In this case, the aeroelastic coupling and buffeting responses are uncorrelated, and the rms value of the total response can be approximated by

$$z_{t,\mathrm{rms}} \;=\; \sqrt{\left(sz_{a,\mathrm{rms}}\right)^2 + z_{b,\mathrm{rms}}^2} \tag{28a}$$

$$\dot{z}_{t,\mathrm{rms}} \;=\; \sqrt{\left(s\dot{z}_{a,\mathrm{rms}}\right)^2 + \dot{z}_{b,\mathrm{rms}}^2} \tag{28b}$$

In order to implement equation (26), it is necessary to: 1) define rms values of the steady-state aeroelastic coupling displacement and velocity; 2) conduct a transient buffet analysis without aeroelastic coupling effects; 3) compute the rms value of the buffet displacement and velocity; 4) calculate the stiffness, damping, and force modifications using equation (27); and finally, 5) repeat the buffet transient analysis with the modified parameters.

Several features of equation (26) should be noted. First, as the aeroelastic coupling or buffet responses diminish, equation (26) reduces to equations (14) and (18) with $\zeta_a \equiv 0$, respectively. Second, the modified damping value defined by equation (27a) is always nonnegative and has the range $0 \le \zeta_t \le \zeta$. Third, as a consequence, the aeroelastic coupling component, introduced through the initial conditions, generally decreases over the analysis duration. And finally, the value s first increases, then decreases, as the launch vehicle flies through the transonic region such that the effective frequency and damping vary with Mach number.

Time histories computed using the Titan IV parameters and the modified buffet approach show that the single degree-of-freedom linear response is in good agreement with the nonlinear simulated response when the value of s is large but tends to overpredict the response amplitude for small s values.

General Assessment of Aeroelastic Coupling Effects

Trends in the effective frequency and damping are best illustrated using the harmonic approximation of the aeroelastic coupling response given by equations (9) and (10). In this case, the aeroelastic coupling rms values can be expressed in closed form as

$$z_{a,\mathrm{rms}} = \sqrt{2}\,\left(\Delta t/\zeta\,T_i\right)\,\cos\left[\sin^{-1}\left(z_{cr}\left(\zeta\,T_i/\Delta t\right)\right)/2\right] \tag{29a}$$

$$\dot{z}_{a,\mathrm{rms}} = \sqrt{2}\;\omega\left(\Delta t/\zeta\,T_i\right)\sqrt{1 + \frac{2}{\pi}\left(\zeta\,T_i/\Delta t\right)}\;\cos\left[\sin^{-1}\left(z_{cr}\left(\zeta\,T_i/\Delta t\right)\right)/2\right] \tag{29b}$$

The operand of the arcsine function in equation (29) cannot exceed unity. A limit cycle, therefore, exists in the harmonic approximation only for $0 \le z_{cr} \le \Delta t/\zeta\,T_i$. Dotson *et al.* (1998a) showed that this limiting value is in reasonable agreement with that for the nonharmonic solution and that the response spirals in the phase plane to a state of rest for larger values of z_{cr}.

The curves of frequency as a function of s shown in Figure 6a were constructed using the modified buffet analysis with the Titan IV parameters and the harmonic approximation for aeroelastic coupling. Three values of $\Delta t/\zeta\,T_i$ and the range of z_{cr} for limit cycle oscillation are illustrated. Since the values of ζ and T_i are known for the Titan IV (0.71 percent and 0.79 s, respectively), the curves actually reflect variations in the time lag. For example, $\Delta t/\zeta T_i = 1$ corresponds to $\Delta t = 5.5$ ms. Similarly, z_{cr} can be explicitly evaluated, and $\Delta t/\zeta T_i = 1$ corresponds to $\theta_{cr} = 0.05°$. Figure 6a indicates that aeroelastic coupling only modestly increases the effective system frequency, particularly for large values of $\Delta t/\zeta\,T_i$. As aeroelastic coupling decreases relative to buffeting (i.e., as the value of s decreases), the system frequency tends to the natural frequency of the bending mode.

Corresponding curves of effective system damping are shown in Figure 6b. In contrast to the effective system frequency, the effective system damping depends strongly on the aeroelastic coupling signal strength. A modest contribution from aeroelastic coupling (i.e., small value of s) can lead to a significant drop in the total system damping, even for relatively small values of the time lag. This large reduction in system damping is supported by wind tunnel test data (Ericsson & Reding 1986). Figures 6a and 6b, furthermore, show that increasing the size of the time lag reduces the effect on system frequency, but exacerbates the effect on system damping. Finally, provided aeroelastic coupling occurs (i.e., $0 \le z_{cr} \le \Delta t/\zeta T_i$), the value of the normalized critical nose cone deflection for the flow state changes [equation (7)] has a minor effect on frequency and damping, particularly for large values of $\Delta t/\zeta T_i$.

Dotson *et al.* (1998a) computed force resultants $F_{a,1}$ and $F_{a,2}$ for the Titan IV when $M_\infty = 0.8$ and 0.9. The hypothetical limit cycle amplitude for Mach 0.8 is larger because the force resultants for Mach 0.9 shift further aft from the payload fairing nose, and the magnitude of their summation decreases. It is assumed herein that $s = 1$ at $M_\infty = 0.8$, i.e., that limit cycle oscillation during the transonic regime is maximized at Mach 0.8. It can be shown that the force resultants for $M_\infty = 0.9$ then lead to $s = 0.7$. These s values and Figure 6 indicate that there is little change in effective system frequency or damping over the range $0.8 < M_\infty < 0.9$.

Random Decrement Stiffness and Damping Values

Predicted effective system stiffness and damping values are shown in Figure 7 for the Titan IV example with $\Delta t = 7$ ms and no dead zones in the force variation (see Figure 2). Values from application of the Random Decrement technique (Ibrahim 1977) to the simulation time histories are included in Figure 7 for comparison. Random Decrement averages the random excitation (induced, in this case, by buffeting) out of the total system response, yielding the homogeneous response from which effective stiffness and damping values can be estimated. The bars in Figure 7 represent uncertainty in the Random Decrement estimates and were established by conducting sensitivity studies with the technique's parameters. Random Decrement is relatively insensitive to these parameters for large values of s. However, the amplitude of the aeroelastic coupling response is roughly equal to that for buffeting when $0.2 \le s \le 0.4$, and the Random Decrement result varies significantly in this range depending on the parameters chosen.

Figure 7 shows that the trends in the stiffness and damping estimates from the modified buffet analysis and Random Decrement are similar. The effective system damping from equation (27a), however, is lower than that estimated by Random Decrement.

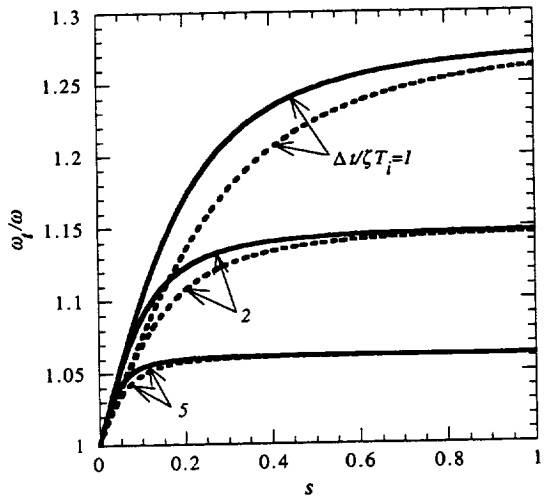

a) System frequency

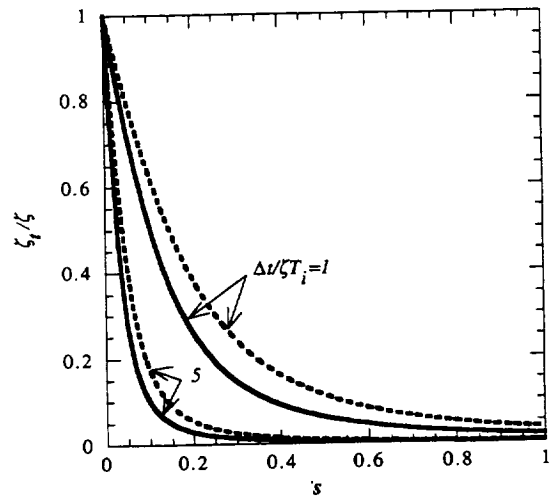

b) System damping

Fig. 6 Aeroelastic coupling effects as a function of signal strength. (——) $z_{cr} = 0$; (- - - -) $z_{cr} = \Delta t/\zeta T_i$.

The accuracy of the Random Decrement results can be assessed because the buffeting force is known. Time histories computed using the Random Decrement stiffness and damping estimates show that the single degree-of-freedom linear response is correctly phased but that the nonlinear response amplitude is significantly underpredicted. Recall that the modified buffet analysis tends to overpredict the response amplitude for small s values. Responses computed by trial-and-error variation of the constant damping value generally yield the best agreement when ζ_r/ζ is between the modified buffet and Random Decrement values shown in Figure 7b. For example, $\zeta_r/\zeta = 0.11\%$ yields agreement when $s = 0.5$. It

can be concluded that schemes that use averaged stiffness and damping values to model the nonlinear equation of motion may be heuristic but inaccurate.

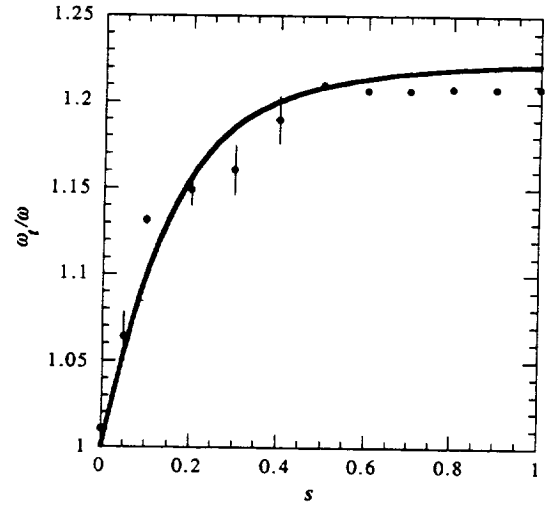

a) System frequency

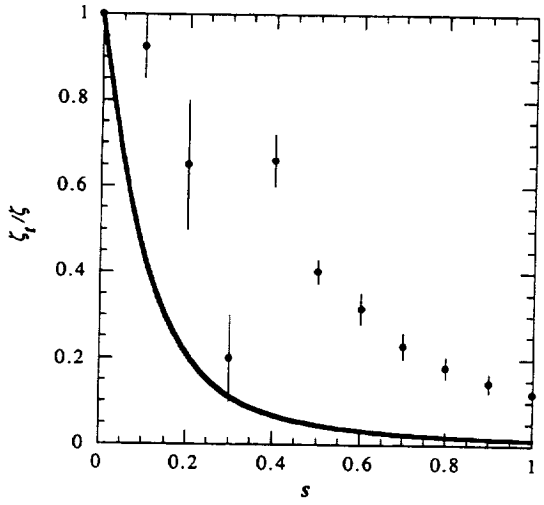

b) System damping

Fig. 7 Comparison of analytic and derived estimates. (—) modified buffet analysis; (|) range of Random Decrement estimates; (•) midpoint of range.

Conclusions

The theory presented by Dotson *et al.* (1998a) provides straightforward closed-form equations for the prediction of limit cycle oscillation from aeroelastic coupling, based strictly on the idealized force-response coupling relationship and periodicity condition. This theory can be used to derive constant aerodynamic stiffness and damping values in the system equation of motion, and the characteristics of these derived values are consistent with trends observed in transonic wind tunnel test data. The conversion of alternating flow forces into aerodynamic stiffness and damping terms, however, introduces a harmonic approximation that underestimates the response amplitude. More important, the use of similar terms, modified to include buffet effects, in an analysis intended to account comprehensively for aeroelastic coupling and buffeting can lead to errors in response phasing and amplitude. The largest errors occur when the aeroelastic coupling contribution to the total system response is not dominant.

References

CHEN, S.-H. & DOTSON, K. W. 1999 A Time-Marching Aeroelastic Analysis of Launch Vehicles in Transonic Flow. *CEAS/AIAA/ICASE/NASA Langley International Forum on Aeroelasticity and Structural Dynamics.*

CHEVALIER, H. L. & ROBERTSON, J. E. 1963 Pressure Fluctuations Resulting from an Alternating Flow Separation and Attachment at Transonic Speeds. TDR-63-204, Tullahoma, Tennessee, U.S.A.: Arnold Engineering Development Center.

DOTSON, K. W., BAKER, R. L. & SAKO, B. H. 1998a Launch Vehicle Self-Sustained Oscillation from Aeroelastic Coupling Part 1: Theory. *Journal of Spacecraft and Rockets* **35,** 365-373.

DOTSON, K. W., BAKER, R. L. & BYWATER, R. J. 1998b Launch Vehicle Self-Sustained Oscillation from Aeroelastic Coupling Part 2: Analysis. *Journal of Spacecraft and Rockets* **35,** 374-379.

DOWELL, E. H. (ed.) 1995 *A Modern Course in Aeroelasticity*, 3rd edn., pp. 119-128, 297-369. Dordrecht, The Netherlands: Kluwer.

ERICSSON, L. E. 1967 Aeroelastic Instability Caused by Slender Payloads. *Journal of Spacecraft and Rockets* **4,** 65-73.

ERICSSON, L. E. & READING, J. P. 1986 Fluid Dynamics of Unsteady Separated Flow. Part I. Bodies of Revolution. *Progress in Aerospace Sciences* **23,** 1-84.

FLEMING, E. R. 1994 Launch Vehicle Loads. *Flight-Vehicle Materials, Structures, and Dynamics - Assessment and Future Directions. Vol. 1 - New and Projected Aeronautical and Space Systems, Design Concepts, and Loads*, A95-24426, pp. 530-541. New York: ASME.

IBRAHIM, S. R. 1977 Random Decrement Technique for Modal Identification of Structures. *Journal of Spacecraft and Rockets* **14,** 696-700.

KABE, A. M. 1998 Design and Verification of Launch and Space Vehicle Structures. AIAA Paper 98-1718.

MABEY, D. G. 1989 Physical Phenomena Associated with Unsteady Transonic Flows. *Unsteady Transonic Aerodynamics. Progress in Astronautics and Aeronautics* **120,** 1-55, Washington, D.C.: AIAA.

MACHESKE, V. M., WOMACK, J. M. & BINKLEY, J. F. 1993 A Statistical Technique for Combining Launch Vehicle Loads During Atmospheric Flight. AIAA Paper 93-0755.

ROBERTSON, J. E. & CHEVALIER, H. L. 1963 Characteristics of Steady-State Pressures on the Cylindrical Portion of Cone-Cylinder Bodies at Transonic Speeds. TDR-63-104, Tullahoma, Tennessee, U.S.A.: Arnold Engineering Development Center.

Finite Element Model Updating using Experimental Vibration Data: Parameterisation and Regularisation

Michael I Friswell
Department of Mechanical Engineering, University of Wales Swansea, Swansea SA2 8PP, UK.

John E Mottershead
Department of Engineering, Liverpool University, Liverpool L69 3BX, UK.

Abstract

Two critical issues in model updating are deciding how a finite element model should be parameterised and estimating the unknown parameters from the resulting ill-conditioned equations. A lack of understanding of these issues will lead to updated models without physical meaning. This paper outlines the authors' approach to parameterisation, using physical, geometric and generic element parameters. It also applies useful methods of regularisation, namely parameter constraints, the singular value decomposition, 'L' curves and cross validation to model updating.

1. Introduction

Finite element model updating has become a viable approach to increase the correlation between the dynamic response of a structure and the predictions from a model. In model updating parameters of the model are adjusted to reduce a penalty function based on residuals between a measurement set and the corresponding model predictions. Typical measurements include the modal model (natural frequencies and mode shapes) and the frequency response functions. The choice of penalty function, and also the optimisation approach, has been the subject of much research and are well covered by the authors' survey paper (Mottershead and Friswell 1993), book (Friswell and Mottershead 1995) and special issue of Mechanical Systems and Signal Processing (Mottershead and Friswell 1998). This paper considers the issues of how to parameterise a finite element model and how to regularise the resulting estimation equations to obtain a well-conditioned solution. These are critical issues in model updating.

2. Parameterisation of the Finite Element Model

Parameterisation is a key issue in finite element model updating. It is important that the chosen parameters should be able to clarify the ambiguity of the model, and in that case it is necessary for the model output to be sensitive to the parameters. Usually elements in the mass and stiffness matrices perform very poorly as candidate parameters, and this is one reason why the direct methods of model updating are not favoured (Friswell and Mottershead 1995). One reason for this poor performance is that the stiffness matrix element values are dominated by the high frequency modes, whereas the low frequency modes are measured. Element parameters, such as the flexural rigidity of a beam element, may be used provided there is some justification as to why the element properties should be in error. Mottershead *et al.* (1996) used geometric parameters, such as beam offsets, for the updating of mechanical joints and boundary conditions. Gladwell and Ahmadian (1995) and Ahmadian, Gladwell and Ismail (1997) demonstrated the effectiveness of parameterising the modes at the element level, and used both geometric parameters and element-modal parameters (i.e. the so-called generic element method) to update mechanical joints. The following subsections will concentrate on the modelling of joints, since these are often the most difficult areas of a structure to model.

2.1. Physical and Geometric Parameters

There are a number of physical parameters of a joint that could be updated. A beam with a flange welded as a 'T' joint, shown in figure 1, will be taken as an example. The beam part was of length 0.4 m and cross-section 70 mm × 12 mm. The flange area was 110 mm × 70 and the thickness of the flange was 6 mm. Pairs of bolt holes, of diameter 12 mm and 40 mm apart, were drilled 25 mm from the edge of the longer part of the flange and 15 mm from the edge of the longer part of the flange, as shown in figure 1. Only vibration in a single plane was considered. The resonances of the structure are lightly damped and well separated, making natural frequency identification and mode shape pairing straightforward.

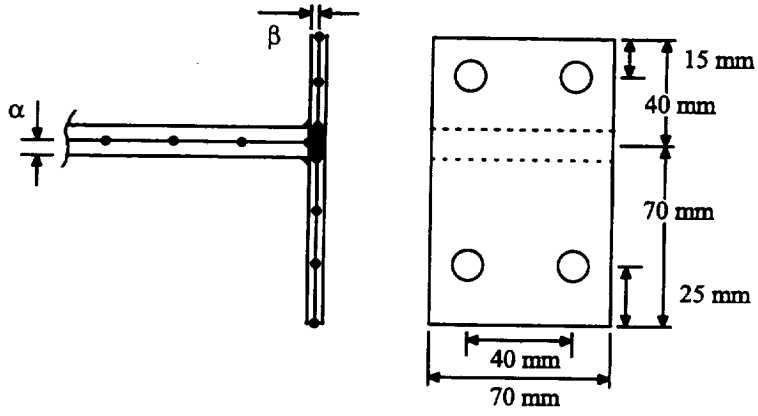

Figure 1. Modelling of the welded joint

The beam structure was modelled with cubic beam elements for the transverse motion and linear bar extension elements. The nodes possess axial and transverse translation degrees of freedom together with a rotation in the same plane. The beam was represented by eight elements, each of the flanges was represented by five elements, and nodes were located to coincide with the bolt holes. The shaded area is considered rigid and is enforced by a constraint matrix linking nodes a, b and c. Only the degrees of freedom corresponding to node c are independent and included in the model. The mass and inertia of the rigid area were lumped at node c.

One approach to updating this joint is to alter the beam stiffness of the elements closest to the joint. Although this often gives good results, the model error is not localised at the joint, but spread through the updated elements. Flexibility may be introduced into the rigid area by using discrete translational and rotary springs between nodes a, b and c. Mottershead *et al.* (1996) showed that for typical joints the structure's response is insensitive to the stiffness of these discrete springs, and such insensitivity causes great problems for the updating algorithms. A powerful alternative is to update geometric parameters, for example the offset of nodes b and c from node a, denoted by α and β in figure 1. The offset parameters have a physical meaning with regard to stiffness updating: the shaded (rigid) region in figure 1 can be considered to expand or contract depending upon whether the offset dimensions are extended or reduced by updating. The offset dimensions are assumed to only affect the stiffness matrix and the mass matrix is unaffected. A third parameter, the variation in the thickness of the beam and flange was used to allow for a global shift in all the modelled natural frequencies. The beam was tested twice: under free-free conditions

	Natural Frequencies (Hz)									
	Free-Free						Clamped-Free			
Measured	324	823	1243	1975	3022	3898	56	354	986	1523
Initial	318	813	1212	1940	2976	3833	55	349	972	1504
Updated	325	827	1235	1978	3023	3897	56	356	989	1525

Table 1. Natural frequencies for the welded joint in the beam

	α (mm)	β (mm)	Thickness Change (%)
Initial	6.0	3.0	
Updated	6.4	3.0	-3.2

Table 2. Updated parameters for the welded joint in the beam

and clamped at the flanges. Updating was carried out using both sets of natural frequency data, using a sensitivity based approach (Mottershead *et al.* 1996). Table 1 shows the measured, and the initial and updated analytical natural frequencies, and table 2 shows the initial and updated parameter values. The natural frequencies are much improved after updating. The beam thickness only changes by about 3%, which is within the tolerance that the thickness of the beams was measured.

2.2. Generic Parameters

Gladwell and Ahmadian (1995) and Ahmadian, Gladwell and Ismail (1997) introduced the generic element approach. The method depends on the eigenvalue decomposition of stiffness and mass matrices at the element level, or substructure masses and stiffnesses typically at a joint. The joint would then be updated by adjusting a set of parameters related to its own eigenvalues and eigenvectors. It would be possible for example to update parameters related to the bending behaviour in a particular mode of a joint whilst retaining the original stiffness of the other modes. Model correction using submodel coefficients or physical parameters (such as Young's modulus or the thickness of a beam) can be restrictive and may lead to converged models whose physical interpretation does not match the real structure. The generic element approach is equivalent to modifying the coefficients in the element shape-function equations but not the order of the shape functions. Generic elements are based on the element (or substructure) free-free modes but other co-ordinate systems are possible of course, and might have advantages for particular updating problems.

The mass matrix of a substructure, such as a joint, is assumed to be correct. The substructure stiffness matrix may be decomposed as

$$\mathbf{K}^s = \mathbf{V}_0 \Lambda_0 \mathbf{V}_0^T \tag{1}$$

where Λ_0 and $\mathbf{V}_0$ are the eigenvalues and unit normalised eigenvectors (mode shapes) of the stiffness matrix. The corrected eigenvectors are assumed to be obtained by a transformation of these eigenvectors and the eigenvalues are also varied. With 3 strain modes, for example, the substructure stiffness matrix is

$$\mathbf{K}^{su} = \mathbf{V}_0 \begin{bmatrix} \kappa_{11} & \kappa_{12} & \kappa_{13} \\ & \kappa_{22} & \kappa_{23} \\ \text{sym} & & \kappa_{33} \end{bmatrix} \mathbf{V}_0^T . \tag{2}$$

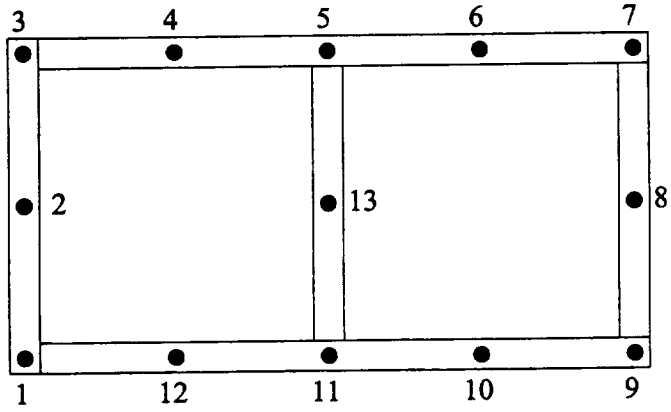

Figure 2. The frame structure. Out of plane vibration is considered

The six terms $\kappa_{11},\ldots,\kappa_{33}$ are available for updating. If only the diagonal terms, namely $\kappa_{11},\kappa_{22},\kappa_{33}$, are changed then this amounts to changing the natural frequencies of the substructure strain modes, while keeping the mode shapes unaltered. These generic parameters have a meaning in terms of the interaction between the physical modes, which is especially important if substructures are related through constraints.

As an example, consider the out of plane vibration of the frame structure shown in figure 2.

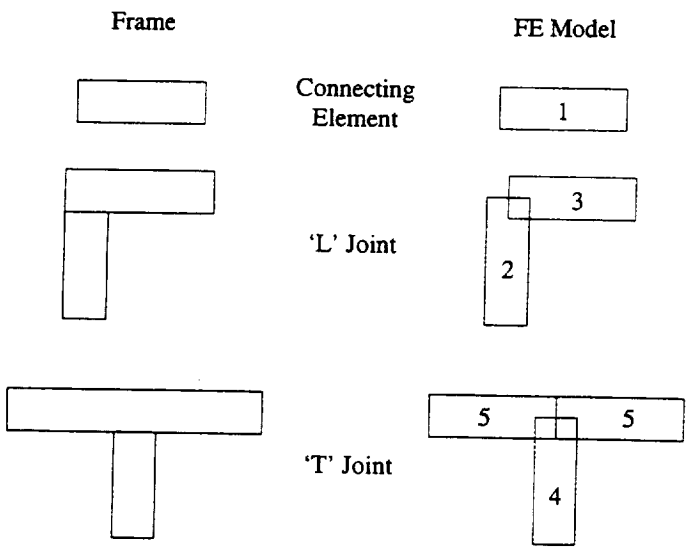

Figure 3. Element types for the frame example

Figure 3 shows the substructure types for the frame, namely a connecting element and the 'L' and 'T' shaped joints. Although each of these substructures could be updated using generic parameters, generic parameters relating to elements will be updated here. Figure 3 also shows the 5 elements that will be used in the updating. Each of the beam/bar elements has 3 rigid body modes and 3 strain modes. The number of parameters in the frame example is large. Just considering elements adjacent to the joints gives 14 elements, each with 6 generic parameters. Updating these 72 parameters produces ill-conditioned equations that require regularisation. Hence this example will be used later to demonstrate the regularisation methods.

2.3. Equivalent Models

Occasionally part of the structure is so ill-defined that no finite element model can be constructed with confidence. A common example are welded joints in frames and in structures such as automobile bodies. The example considered here is the rubber seal which provides the connection between a vehicle window and the car-body structure. The seal has a complicated cross-sectional shape into which the window glass and the steel sheet are pressed to form the joint. Furthermore it is important to model the seal accurately because vibration of the window has a strong influence on the acoustics of the passenger compartment. In such cases there seems to be no reasonable alternative to *direct* parameter estimation.

The glass and the body panels are regularly modelled with plate elements having 3 degrees-of-freedom at each node. Thus, the equivalent rubber seal (ERS) element should have the same degrees-of-freedom at each node. In its most general form the element is chosen to have 4 nodes and 12 degrees of freedom. The tests on the seal were performed with a very stiff foundation that was assumed to be rigid in the model. Although this is not the configuration in which the seal operates in the vehicle, Ahmadian, Mottershead and Friswell (1997) showed that by using the various physical constraints and the symmetry of the element, the model of the seal may be derived from measurements on the rigid foundation.

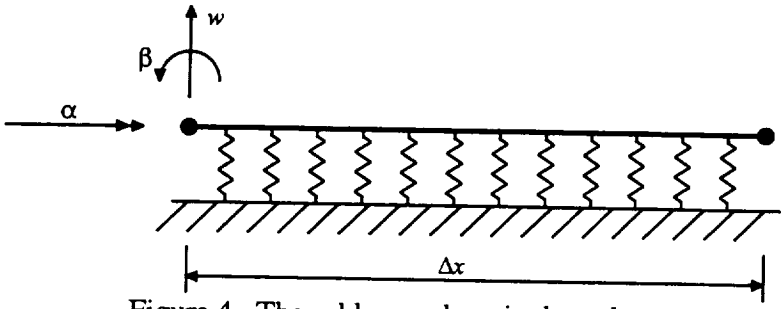

Figure 4. The rubber seal equivalent element

Figure 4 shows the model of seal in the experimental configuration. Essentially there are two unknown parameters, denoted k_w and k_α, that relate to a distributed bending and torsional stiffness per unit length. By ensuring that the displacement function within the seal matches the cubic displacement function along the edge of the plate, and assuming that the torsional and bending motions decouple, enables the stiffness matrix of the seal to be

calculated. The bending stiffness matrix has the same form as the mass matrix of the standard Euler-Bernoulli beam element because the stiffness is assumed to be distributed.

In the experiment the glass was rectangular (which is not typical of a car window) but the rubber seal was of the type used in modern vehicles. The seal was mounted in a rigid frame. The glass plate (of dimension 0.5 m × 0.8 m × 0.0025 m) was modelled with a mesh of 5 × 8 plate elements, which was sufficient to eliminate the discretisation error in the first 10 modes of vibration. The rubber seal was modelled by using 26 elastic support elements. The parameters k_w and k_α were obtained by minimising the error between the measured natural frequencies and the finite element prediction and the results are given in Table 3. The greatest error occurs in the first natural frequency and has been attributed to the dynamics of the experimental rig which is supposed to provide a rigid boundary constraint but behaves like a rigid body mode at very low frequencies because of its large mass. Almost identical results were obtained when the mesh was refined to 10 × 16, as shown in Table 3.

Mode	Measured	Predicted 5×8 mesh	Predicted 10×16 mesh
1	30.39	33.79	33.76
2	65.17	65.54	65.49
3	111.21	112.14	112.01
4	118.84	114.98	114.92
5	139.94	140.39	140.28
6	181.27	183.63	183.52
7	184.23	187.30	187.38
8	229.91	236.25	235.70
9	234.91	252.61	252.94
10	263.68	262.55	261.95

Table 3. Measured and identified natural frequencies (Hz) for the equivalent rubber seal

When the glass was replaced by a steel plate new measurements were obtained, and these were compared to predictions from the previously identified models, but with the plate elements given the properties of steel. The results, shown in Table 4, indicate that the identified seal parameters have physical meaning, otherwise the excellent agreement between the measured and predicted results is unlikely to have been achieved. The agreement shows that the discretisation error in the rubber seal model has the same order or is smaller than that in the plate element.

Mode	Measured	Predicted 5×8 mesh	Predicted 10×16 mesh
1	29.61	32.71	32.69
2	60.42	59.63	59.62
3	98.89	101.69	101.61
4	106.23	104.19	104.23
5	120.14	126.34	126.38
6	155.39	165.56	165.65
7	164.13	167.22	167.61
8	209.26	211.14	210.64
9	228.44	223.94	224.77
10	233.90	232.87	232.50

Table 4. Measured and predicted natural frequencies (Hz) for the equivalent rubber seal with a steel plate

3. Regularisation

The treatment of ill-conditioned, noisy systems of equations is a problem central to finite element model updating (Ahmadian *et al.*, 1998, gave further details). Such equations often arise in the correction of finite element models by using vibration measurements. The regularisation problem centres around the linear equation,

$$\mathbf{A}\,\theta = \mathbf{b} \tag{3}$$

where θ is a vector of the m parameter changes we wish to determine, and $\mathbf{b}$ is a vector of n residual quantities derived from the measured data and the current estimate of the model. In model updating the relationship

between the measured output (for example, natural frequencies, mode shapes, or the frequency response function) is generally non-linear. In this case the problem is linearised using a Taylor series expansion and iteration performed until convergence. When **b** is contaminated with additive, independent random noise with zero mean, it is well known that the least-squares solution, θ_{LS}, is unique and unbiased provided that $\text{rank}(\mathbf{A}) = m$. When **A** is close to being rank deficient then small levels of noise may lead to a large deviation in the estimated parameters from its exact value. The solution is said to be unstable and (3) is ill-conditioned

A different problem occurs when $m > n$ so that (3) is under-determined and there are an infinite number of solutions. The Moore-Penrose pseudo-inverse provides the solution of minimum norm, as does singular value decomposition (SVD). For the case when $\text{rank}(\mathbf{A}) = r < \min(m,n)$, the SVD will again result in the minimum norm solution. This is a form of regularisation which has been widely applied in the model updating community. Unfortunately minimum norm solutions rarely lead to physically meaningful updated parameters.

3.1. Side Constraints

Model updating often leads to an ill-conditioned parameter estimation problem, and an effective form of regularisation is to place constraints on the parameters. This could be that the deviation between the parameters of the updated and the initial model are minimised, or differences between parameters could be minimised. For example, in a frame structure a number of 'T' joints may exist that are nominally identical. Due to manufacturing tolerances the parameters of these joints will be slightly different, although these differences should be small. Therefore a side constraint is placed on the parameters, so that both the residual and the differences between nominally identical parameters are minimised. Thus if (3) generates the residual, the parameter is sought which minimises the quadratic cost function,

$$J(\theta) = \|\mathbf{A}\theta - \mathbf{b}\|^2 + \lambda^2 \|\mathbf{C}\theta - \mathbf{d}\|^2 \tag{4}$$

for some matrix **C**, vector **d** and regularisation parameter λ. The regularisation parameter is chosen to give a suitable balance between the residual and the side constraint. For example, if there were only two parameters, which were nominally equal, then

$$\mathbf{C} = [\,1 \quad -1\,] \qquad\qquad \mathbf{d} = \{0\} \tag{5}$$

Minimising (4) is equivalent to minimising the residual of

$$\begin{bmatrix} \mathbf{A} \\ \lambda\mathbf{C} \end{bmatrix} \theta = \begin{Bmatrix} \mathbf{b} \\ \lambda\mathbf{d} \end{Bmatrix} \tag{6}$$

Equation (6) then replaces (3), although with the significant difference that (6) is generally over-determined, whereas (3) if often under-determined. The constraints should be chosen to satisfy Morozov's complementation condition, $\text{rank}\begin{bmatrix} \mathbf{A} \\ \mathbf{C} \end{bmatrix} = m$.

3.2. The Singular Value Decomposition

The singular value decomposition (SVD) of **A** may be written in the form,

$$\mathbf{A} = \mathbf{U}\Sigma\mathbf{V}^T = \sum_{i=1}^{m} \sigma_i \mathbf{u}_i \mathbf{v}_i^T \tag{7}$$

where $\mathbf{U}=[\mathbf{u}_1\ \mathbf{u}_2 \ldots \mathbf{u}_n]$ and $\mathbf{V}=[\mathbf{v}_1\ \mathbf{v}_2 \ldots \mathbf{v}_m]$ are $n\times n$ and $m\times m$ orthogonal matrices and $\Sigma=\mathrm{diag}(\sigma_1,\sigma_2,\ldots,\sigma_m)$, where the singular values, σ_i, are arranged in descending order $(\sigma_1 \geq \sigma_2 \geq \ldots \geq \sigma_m)$. In ill-posed problems two commonly occurring characteristics of the singular values have been observed; the singular values decay steadily to zero with no particular gap in the spectrum, and the left and right singular vectors $\mathbf{u}_i$ and $\mathbf{v}_i$ tend to have more sign changes in their elements as the index i increases.

The solution for the parameters using the SVD is

$$\theta=\sum_{i=1}^{m}\frac{\mathbf{u}_i^T\mathbf{b}}{\sigma_i}\mathbf{v}_i. \tag{8}$$

Thus the high frequency components (corresponding to low singular values) have only a small contribution to **A** but a large contribution to the estimated parameters. Equation (8) shows the noise will be amplified when $\sigma_i < \mathbf{u}_i^T\mathbf{b}$, and this may be used to decide where to truncate the singular values. If **A** does not contain noise then the singular values will decay to zero whereas the $\mathbf{u}_i^T\mathbf{b}$ terms will decay to the noise level.

The standard SVD is incapable of taking account of the side constraint, as this requires the generalised SVD. Thus, in (6) **A** and **C** are decomposed simultaneously. The regularisation parameter, λ, has the effect of damping the effect of the lower singular values (lower than about λ) and thus smoothing the solution. It is also possible for the generalised SVD to truncate the solution and retain only a limited number of singular values, equivalent to truncating the series in (8) (Ahmadian *et al.*, 1998).

3.3. 'L' Curves

One way of obtaining the optimum value of the regularisation parameter in the presence of correlated noise is to define an upper bound for the side constraint and minimise the residue, or alternatively to set a limit for the residue and minimise the deviation from the side constraint. Of course the success of this approach is highly dependent on the physical insight of the analyst in determining the allowable constraint violation or measurement error (residue magnitude).

A different approach is to plot the norm of the side constraint, $\|\mathbf{C}\theta-\mathbf{d}\|$, against the norm of the residue, $\|\mathbf{A}\theta-\mathbf{b}\|$, obtained by minimising the penalty function (4) for different values of λ. Hansen (1992) showed that the norm of the side constraint is a monotonically decreasing function of the norm of the residue. He pointed out that for a reasonable signal-to-noise ratio and the satisfaction of the Picard condition, the curve is approximately vertical for $\lambda<\lambda_{opt}$, and soon becomes a horizontal line when $\lambda>\lambda_{opt}$, with a corner near the optimal regularisation parameter λ_{opt}. The curve is called the 'L'-curve because of this behaviour. The optimum value of the regularisation parameter, λ_{opt}, corresponds to the point with maximum curvature at the corner of the log-log plot of the 'L'-curve. This point represents a balance between confidence in the measurements and the analyst's intuition.

3.4. Cross-Validation

The idea of cross-validation is to maximise the predictability of the model by choice of the regularisation parameter λ. A predictability test can be arranged by omitting one data point, b_k, at a time and determining the

best parameter estimate using the other data points, by minimising (4). Then for each of the estimates, predict the missing data and find the value of λ that on average predicts the b_k best, in the sense of minimising the cross-validation function

$$V_0(\lambda) = \frac{1}{n} \sum_{k=1}^{n} \left(b_k - \tilde{b}_k(\lambda)\right)^2 \tag{9}$$

where $\tilde{b}_k(\lambda)$ is the estimate of b_k obtained from the remaining data. This is the method of cross-validation.

A rotational invariant version of ordinary cross validation, called generalised cross-validation (GCV), has been developed which is essentially a weighted version of the ordinary cross validation. Ahmadian *et al.* 1998 give the background and further details. The GCV function may be conveniently computed via the generalised SVD. Furthermore, the GCV based on the solution from the truncated generalised SVD may be computed.

3.5. An Example of Regularisation

The regularisation methods were tested on the frame shown in figure 2. The frame was made from 25.4 mm square section aluminium tubing with 2.38 mm wall thickness. The frame was 584 mm long and 279 mm wide, and contained 4 'L' shaped welded joints and 2 'T' joints that are difficult to model. Experimental data was obtained using standard hammer impact testing procedures on the freely suspended frame. The natural frequencies for the first 5 out-of-plane bending modes were identified, together with the corresponding mode shapes at the 13 locations shown in figure 2. Table 5 lists the measured natural frequencies.

	Natural Frequency (Hz)		
Mode	Measured	Initial	Updated
1	226.8	269.5	221.0
2	275.2	287.7	270.8
3	537.4	615.0	536.6
4	861.5	928.7	861.8
5	974.8	1071.3	972.9

Table 5. Natural frequencies for the frame example

A finite element model was constructed to model the out-of-plane bending vibration of the frame. Each short beam was split into 4 elements and the longer beams split into 8 elements, giving a total of 28 beam/bar elements. Each of the 27 nodes had 3 degrees of freedom, producing a finite element model with 81 degrees of freedom. The beam parts of the elements were Euler-Bernoulli beams, and the torsional contribution to the dynamics was also modelled. Table 5 lists the first 5 natural frequencies obtained from this model. Although there is some error in the natural frequencies, the mode shape correlation (determined by the Modal Assurance Criterion) was very good. The measured modes were expanded using dynamic expansion to the full set of degrees of freedom of the finite element model.

The model of the frame was updated using generic parameters, described earlier. The elements were split into 5 types shown in figure 3; namely, connecting elements, 2 types relating to each side of the 'L' joint, and 2 elements of the 'T' joints. Each element group has an associated set of 6 parameters per element, giving a total of 168 parameter in 30 groups. Parameters within each group are assumed to be nominally equal, and this gives the contraint matrix, **C**. The values within two of the parameter groups are not changed since these parameters would make the stiffness matrices of connecting elements different if the elements were rotated by 180°. Many models of the structure may be created, and this model is not necessarily optimum, but it will serve to demonstrate the methods outlined in this paper.

The residual minimised in this example is given by

$$J(\theta)=\sum_{i=1}^{n_{mode}} \left\| \left[-\omega_i^2\mathbf{M}+\mathbf{K}(\theta)\right]\phi_i \right\|^2 + W_{orthog}^2 \left| \phi_i^T \mathbf{K}(\theta)\phi_i - \omega_i^2 \right|^2 \qquad (10)$$

where ω_i and ϕ_i are the i th measured natural frequency and expanded mode shape (normalised with respect to the analytical mass matrix), n_{mode} is the number of modes measured, and only the stiffness matrix is a function of the vector of generic parameters θ. The first term minimises the error in the eigenvalue equation. W_{orthog} is a weighting factor for the error in the stiffness orthogonality, and essentially weights the natural frequency error. In this example, there are 405 equations (81 degrees of freedom for 5 modes) from the error in the eigenvalue equation, and a further 5 equations from the stiffness orthogonality. Thus n=410, and m=140. The orthogonality weighting factor, W_{orthog}, together with the regulation parameter, λ, may both be changed and the norms of the residual and constraint plotted to give a surface rather than the standard 'L' curve. Instead, for this example, a number of 'L' curves were plotted for different values of W_{orthog}, and engineering judgement used to assess when the natural frequencies were given sufficient weight.

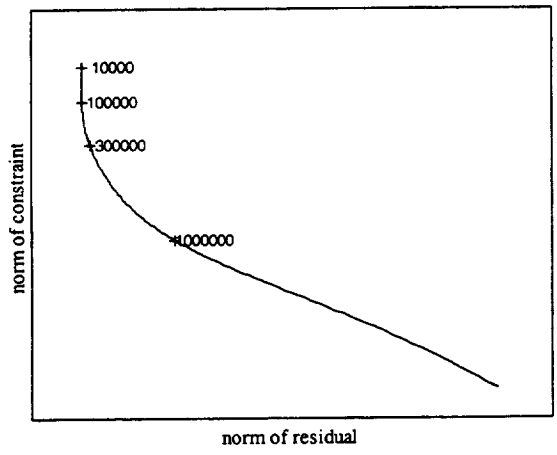

Figure 5. The 'L' curve for the frame example

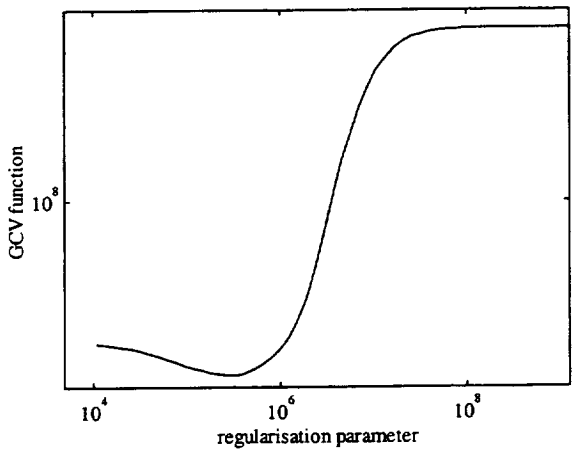

Figure 7. The generalised cross validation function for the frame example

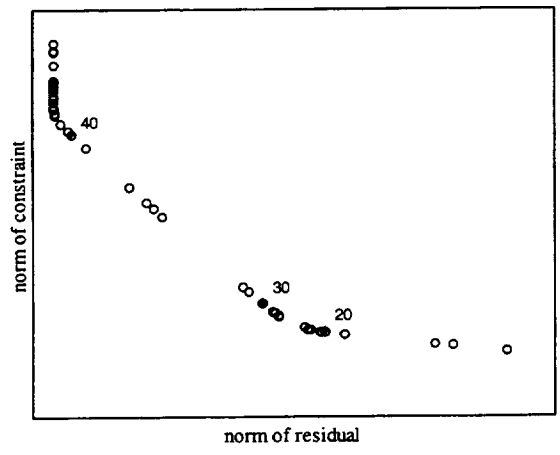

Figure 6. The 'L' curve for the frame example based on the truncated SVD

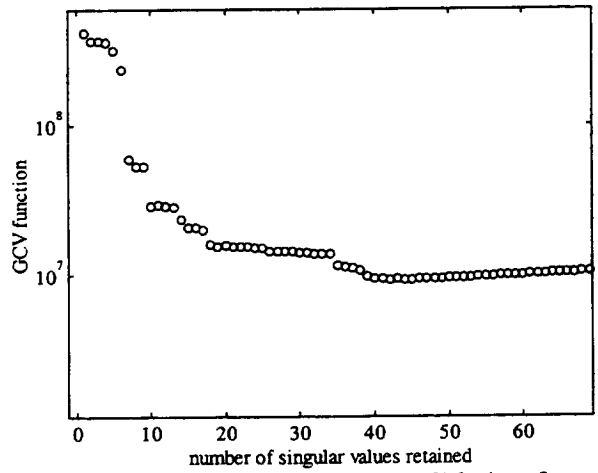

Figure 8. The generalised cross validation function for the frame example based on the truncated SVD

Figures 5 shows the 'L' curve as the regularisation parameter, λ, is changed. There is a corner at a value of λ of approximately $3x10^5$. Using the truncated SVD approach gives a similar 'L' curve, shown in figure 6, and shows that approximately 30 singular values should be retained. Using the generalised cross validation function gives a defined minimum at $2.8x10^5$ (figure 7), which is close to the value given by the 'L' curve. The updated natural frequencies based on the value for the regularisation parameter are shown in table 5. Finally figure 8 shows the generalised cross validation based on the truncated SVD, having a minimum at 44 singular values, although this minimum is not particularly marked.

5. Conclusion

This paper has outlined the authors' philosophy in dealing with two of the major issues in model updating, namely how to parameterise a structure and how to regularise the equations required to estimate the parameter values. Parameters should be chosen which have physical meaning, but are also able to model the errors in the finite element model. Geometric parameters, generic elements and equivalent models were shown to have good features for model updating. Regularisation based on physical considerations lead to updated models with physical meaning. Constraints on the parameters, such as minimising the difference between nominally identical parameters, works very well. One difficulty with this approach is determining the relative weight given to the constraints, and this paper proposed a number of approaches to determine this regularisation parameter. A number of physical examples using experimental data have been described to show the effectiveness of the proposed approaches.

Acknowledgement

Dr. Friswell gratefully acknowledges the support of the EPSRC through the award of an Advanced Fellowship.

References

Ahmadian, H., Mottershead, J.E. and Friswell, M.I., 1998, Regularisation Methods for Finite Element Model Updating. Mechanical Systems and Signal Processing **12**(1), 47-64.

Ahmadian, H., Mottershead, J.E. and Friswell, M.I., 1997, Parameterisation and identification of a rubber seal. *15th International Modal Analysis Conference,* Orlando, Florida, USA, 142-146.

Ahmadian, H., Gladwell, G.M.L. and Ismail, F., 1997, Parameter selection strategies in finite element model updating. Journal of Vibration and Acoustics 119, 37-45.

Friswell, M.I. and Mottershead, J.E., 1995, Finite Element Model Updating in Structural Dynamics. Kluwer Academic Publishers, Dordrecht.

Friswell, M.I., Mottershead, J.E. and Ahmadian, H., 1998, Combining subset selection and parameter constraints in model updating. *Journal of Vibration and Acoustics* **120**(4), 854-859.

Gladwell, G.M.L. and Ahmadian, H., 1995, Generic element matrices suitable for finite element model updating. Mechanical Systems and Signal Processing 9, 601-614.

Hansen, P.C., 1992, Analysis of discrete ill-posed problems by means of the L-curve. SIAM Review **34**(4), 561-580.

Mottershead, J.E. and Friswell, M.I., 1993, Model updating in structural dynamics: a survey. Journal of Sound Vibration **162**, 347-375.

Mottershead, JE., Friswell, M.I., Ng, G.H.T. and Brandon, J.A., 1996, Geometric Parameters for Finite Element Model Updating of Joints and Constraints. *Mechanical Systems and Signal Processing* **10**, 171-182.

Mottershead, J.E. and Friswell, M.I., (Guest Eds.), 1998, Model Updating, Special Issue of Mechanical Systems and Signal Processing, **12**(1), January 1998.

Optimal System Realization in Frequency Domain

Jer-Nan Juang *and Peiman G. Maghami †
NASA Langley Research Center
Hampton, VA 23681

Abstract

Several approaches are presented to identify an experimental system model directly from frequency response data. The formulation begins with a matrix-fraction description as the model structure. Frequency weighting such as exponential weighting is introduced to solve a weighted least-squares problem to obtain the coefficient matrices for the matrix-fraction description. A multi-variable state-space model can then be formed using the coefficient matrices of the matrix-fraction description. An approach is introduced to fine-tune the model using nonlinear programming methods to minimize the desired cost function. The method deals with the model in the real Schur or modal form and reassigns a subset of system poles using a nonlinear optimizer. At every optimization step, the input and output influence matrices are refined through least-squares procedures. The proposed approaches are used to identify an analytical model for a NASA testbed from experimental data.

1 Introduction

One major objective of system identification is to provide mathematical models for dynamics and control analysis and designs. However, models of systems can have various forms, such as transfer functions, differential or difference equations, and state-space equations. A frequency-domain state-space identification method [1 – 5] provides a state-space model of a linear system from frequency response data.

The method called the State-Space Frequency Domain (SSFD) identification algorithm [2] can estimate Markov parameters (pulse response) from the frequency response function (FRF) without window distortion when an arbitrary frequency weighting is used to shape the estimation error. The method uses a rational matrix fraction description (the ratio of a matrix polynomial and a monic scalar polynomial denominator) to curve-fit the frequency data and compute the Markov parameters from FRF. The curve-fitting problem must be solved either by nonlinear optimization techniques or by linear approximate algorithms with several iterations. To obtain the state-space models from the Markov parameters, the Eigensystem Realization Algorithm (ERA) or its variant ERA/DC is used [5].

Frequency domain methods presented in Refs. [3, 4, 5] start with identifying a left matrix-fraction description (LMFD) of the transfer function matrix. The advantage of using the LMFD, as an intermediate model between the data and the desired final state-space model, is that from frequency response data to the LMFD is a linear least-squares problem, which is easy to solve.

*Principal Scientist, Structural Dynamics Branch, (j.juang@larc.nasa.gov)
†Senior Aerospace Engineer, Guidance and Control Branch, (p.g.maghami@larc.nasa.gov)

This method works quite well when the frequency response data are fairly accurate; however, it might yield unstable, erroneous models if the data contains too much distortion and/or error. Data distortion in the frequency domain is caused by a number of factors; limited sampling frequency, filters to remove noise, and lack of periodicity. This data distortion often causes unstable modes to be present in the identified system model. An improved method was introduced in Ref. [6] to deal with the problem when data distortion is present. The idea is to stabilize or remove the unstable modes before expanding the matrix-fraction description (MFD) into the Markov parameters (pulse responses). This approach avoids introducing unstable modes while still maintaining the frequency response close to the data.

In this paper, exponential frequency weighting [2, 7] is used to solve a weighted least-squares problem for the LMFD coefficient matrices. A multi-variable state-space model is then realized from the LMFD coefficient matrices. To improve the identified model, nonlinear programming methods [8] are used to fine-tune the model parameters. A formulation is introduced in this paper for parameter optimization. This formulation deals with system realizations in the real Schur or modal forms, and uses a subset of system poles for parameter optimization. At every optimization step, the input and output influence matrices are refined through least-squares procedures. Two additional formulations for parameter optimization have also been developed. The first formulation uses a general system realization, and utilizes nonlinear programming along with an eigenvalue assignment [9 – 11] technique to adjust a subset of system poles. The second formulation deals with system realizations in the real Schur or modal forms, and uses a subset of system poles, as well as some coefficients to adjust the columns (rows) of the input (output) influence matrix for parameter optimization. These formulations are not presented here due to space limitations, however, full details on the two approaches is provided in Ref. [12]. Experimental data from a NASA testbed with fifteen inputs and fourteen outputs are used with a total of two hundreds and ten transfer functions to demonstrate the concepts proposed in this paper.

2 Weighted Least-Squares Method

Given the system frequency response function $G(z_k)$ at the frequency point z_k, consider the left matrix-fraction

$$G(z_k) = \alpha^{-1}(z_k)\beta(z_k) \tag{1}$$

where

$$\alpha(z_k) = I_m + \alpha_1 z_k^{-1} + \cdots + \alpha_p z_k^{-p} \tag{2}$$

$$\beta(z_k) = \beta_0 + \beta_1 z_k^{-1} + \cdots + \beta_p z_k^{-p} \tag{3}$$

are matrix polynomials with I_m being an identity matrix of order m. The matrix α_i is an $m \times m$ real square matrix and each β_i is an $m \times r$ real rectangular matrix. The factorization in Eq. (1) is not unique. For convenience and simplicity, one can choose the order of both polynomials to be equal to p.

Pre-multiplying Eq. (1) by $\alpha(z_k)$ produces

$$\alpha(z_k)G(z_k) = \beta(z_k) \tag{4}$$

which can be rearranged into

$$\begin{aligned} G(z_k) &= -\alpha_1 G(z_k) z_k^{-1} - \cdots - \alpha_p G(z_k) z_k^{-p} \\ &\quad + \beta_0 + \beta_1 z_k^{-1} + \cdots + \beta_p z_k^{-p} \end{aligned} \tag{5}$$

or

$$G(z_k) = \Theta \mathcal{G}_k \tag{6}$$

where the matrix Θ, of dimension $m \times [p(m+r)+r]$, and the matrix $\mathcal{G}_k$, of dimension $[p(m+r)+r] \times r$, are defined as

$$\Theta = \left[\begin{array}{cccccccc} \alpha_1 & \cdots & \alpha_p & \beta_0 & \beta_1 & \beta_2 & \cdots & \beta_p \end{array} \right] \tag{7}$$

$$\mathcal{G}_k = \left[\begin{array}{c} G(z_k) z_k^{-1} \\ \vdots \\ G(z_k) z_k^{-p} \\ I_r \\ I_r z_k^{-1} \\ \cdots \\ I_r z_k^{-p} \end{array} \right] \tag{8}$$

Here, I_r is an $r \times r$ identity matrix. With $G(z_k)$ and z_k^{-1} known, Eq. (5) or (6) is a linear equation. Because $G(z_k)$ is known at $z_k = e^{j\frac{2\pi(k-1)}{\ell}}$ $(k = 1, \ldots, \ell)$, there are ℓ equations available.

The parameter matrix Θ in Eq. (6) is a real matrix whereas $G(z_k)$ and $\mathcal{G}_k$ are both complex matrices. Thus Eq. (6) is a complex matrix equation with a total of ℓ complex equations . Let us define

$$\tilde{G}_k = [\text{Real}(G(z_k)) \;\; \text{Imag}(G(z_k))] \qquad \text{and} \qquad \tilde{\mathcal{G}}_k = [\text{Real}(\mathcal{G}_k) \;\; \text{Imag}(\mathcal{G}_k)] \tag{9}$$

Equation (6) may be rewritten as

$$\tilde{G}_k = \Theta \tilde{\mathcal{G}}_k \tag{10}$$

Equation (10) is a real matrix equation consisting of 2ℓ linear equations for computing the parameter matrix Θ. The matrix $\tilde{G}_k$ at the frequency point k is an $m \times 2r$ matrix, whereas $\tilde{\mathcal{G}}_k$ is a $[p(m + r) + r] \times 2r$ matrix.

Often, experimental data from a completed test is available which allows all calculations to be performed at once. A batch version is presented in this section. Stacking the 2ℓ equations in Eq. (10) yields

$$\tilde{G} = \Theta \tilde{\mathcal{G}} \tag{11}$$

where

$$\begin{aligned} \tilde{G} &= \left[\begin{array}{cccc} \tilde{G}_0 & \tilde{G}_1 & \cdots & \tilde{G}_\ell \end{array} \right] \\ \tilde{\mathcal{G}} &= \left[\begin{array}{cccc} \tilde{\mathcal{G}}_0 & \tilde{\mathcal{G}}_1 & \cdots & \tilde{\mathcal{G}}_\ell \end{array} \right] \end{aligned} \tag{12}$$

To solve Eq. (11), let us first define a weighted cost function to be minimized as

$$J(\Theta, \ell) = \sum_{i=1}^{\ell} w^{\ell-i} \parallel \Theta \tilde{\mathcal{G}}_{\ell-i} - \tilde{G}_{\ell-i} \parallel_2^2 \tag{13}$$

where $0 < w \leq 1$ is a forgetting factor weighting the frequency data. The data at the lowest frequency point is given unit weight, but data that is k frequency points higher is weighted by w^k. The method is commonly called exponential forgetting. The cost function defined in Eq. (13) is motivated by the fact that accelerometers are commonly used as the measurement device in structural testing. The corresponding frequency response functions have better response levels in the high frequency range. Identifying lower frequency information in the presence of measurement noise becomes a problem. One way to solve this problem is to weight more the lower frequency region. On the other hand, displacement sensors have better response capability for the low frequency region.

For this case, the forgetting factor may be switched to weight the high frequency region more than the lower frequency region. The form of Eq. (13) is unchanged except for the index $\ell - i$ is replaced by i. The least-squares solution for Θ, from Eq. (13), is given by

$$\Theta = \tilde{G}\tilde{\mathcal{G}}_w^T[\tilde{\mathcal{G}}\tilde{\mathcal{G}}_w^T]^{-1} \tag{14}$$

where

$$\tilde{\mathcal{G}}_w = \left[\begin{array}{cccc} \tilde{\mathcal{G}}_0 & w\tilde{\mathcal{G}}_1 & \cdots & w^\ell\tilde{\mathcal{G}}_\ell \end{array} \right] \tag{15}$$

The subscript w associated with $\tilde{\mathcal{G}}_w$ indicates that the forgetting factor w is inserted into $\tilde{\mathcal{G}}$ with an appropriate power at each frequency point.

The weighting w^ℓ at the frequency point ℓ can be quite small depending on the length ℓ of the data and the choice of the forgetting factor w. Fox example, $w^\ell \approx 4.3 \times 10^{-5}$ with $\ell = 1000$ and $w = 0.99$. Unless the amplitudes of those frequencies near the highest frequency are in the order of 10^{-5}, their contribution to the identification process may become negligible. Using accelerometers, the ratio of the highest frequency to the lowest frequency can be as high as 10^3 to 10^5. For this case, the forgetting factor used in Eq. (15) is indeed a good weighting technique to perform a better low-frequency identification.

On the other hand, one may prefer to have freedom of choosing a weighting factor. A slight modification of Eq. (15) will provide such freedom, i.e.,

$$\tilde{\mathcal{G}}_w = \left[\begin{array}{cccc} \tilde{\mathcal{G}}_0 & w_1\tilde{\mathcal{G}}_1 & \cdots & w_\ell\tilde{\mathcal{G}}_\ell \end{array} \right] \tag{16}$$

The quantities $w_1, w_2, \ldots, w_\ell$, can be all independent. They may be randomly or specifically chosen. Some obvious choices include

$$w_k = e^{-10(1-k)/\ell}, \quad w_k = \frac{1}{k}, \quad w_k = \frac{1}{k^2}; \quad k = 1, 2, \ldots, \ell$$

For the case where the low frequency resolution is better than the high frequency resolution, the weighting must be reversed.

Substituting Eq. (16) in Eq. (11) and solving for the parameter Θ that minimizes the following cost function,

$$J(\Theta, \ell) = \sum_{i=1}^{\ell} w_i \parallel \Theta\tilde{\mathcal{G}}_i - \tilde{G}_i \parallel_2^2 \tag{17}$$

yields results similar to Eq. (14) except for the weighting factor.

In the next section, optimization-based approaches to further improve the least-square solution are discussed.

3 Nonlinear Optimization

Another approach to enhance the identified model is to use nonlinear programming to tune the model parameters obtained from the solution to Eq. (11). Once the solution, represented by the parameter matrix Θ, is computed using Eq. (14), a state-space realization is determined. The state-space realization can be in any canonical form such as Schur form, modal form, Jordan form, observable form, etc. A formulation is introduced in this paper for parameter optimization. This formulation deals with system realizations in the real Schur or modal forms, and uses a subset of system poles for parameter optimization. The input and output influence matrices are refined through least-squares procedures at every optimization step.

As mentioned earlier, two additional formulations for parameter optimization have also been developed. The first formulation uses a general system realization, and utilizes nonlinear programming along with an eigenvalue assignment technique to adjust a subset of system poles. The second

formulation deals with system realizations in the real Schur or modal forms, and uses a subset of system poles, as well as some coefficients to adjust the columns (rows) of the input (output) influence matrix for parameter optimization. These formulations are not presented here due to space limitations, however, full details on the two approaches is provided in Ref. [12].

The details of the proposed parameter optimization approach for least-squares solution refinement is presented next. This method starts with selecting a subset of system poles as optimization parameters to minimize the error between the experimental and the identified transfer functions over a frequency range of interest. The optimizer reassigns the system poles, which reside on the diagonal elements or 2×2 block diagonal partitions of the state matrix. At each optimization step, corrections are made to the input matrix B, the output matrix C, and the direct transmission matrix D, through two least-squares solutions.

An optimization problem is presented below for improving the match between identified and experimental transfer functions. Let (A, B_0, C_0, D_0) represent an initial realization for the identified system, and parameterize the input and output influence matrices as follows,

$$B = B_0 S_b + N_{B_0} R_B = [\, B_0 \quad N_B \,] \begin{pmatrix} S_B \\ R_B \end{pmatrix} \equiv \overline{B} Q_B \tag{18}$$

$$C = S_C C_0 + R_C N_{C_0} = (\, S_C \quad R_C \,) \begin{bmatrix} C_0 \\ N_{C_0} \end{bmatrix} \equiv Q_C \overline{C} \tag{19}$$

where the columns of N_{B_0} represent a set of basis vectors in the null space of B_0, the rows of N_{C_0} represent a set of basis vectors in the null space of C_0, and Q_B, defined in terms of S_B and R_B, and Q_C, defined in terms of S_C and R_C, are the appropriate coefficient matrices. These coefficients are determined, at each optimization step, by solving least-squares-based corrections of the absolute error norm. The optimization problem is given as:

Minimize J_1:

$$J_1 = ||G(z_k) - \hat{G}(z_k)||_F \tag{20}$$

over

$$\text{blkdiag}(A)$$

subject to

$$|\lambda(\text{blkdiag}(A))| < 1$$

The complex matrix $\hat{G}(z_k)$ represents a system realization given by

$$\hat{G}(z_k) = C(z_k I_n - A)^{-1} B + D \tag{21}$$

The constraint on the modulus of $\lambda(\text{blkdiag}(A))$ guarantees the stability of the identified system, and can be omitted if stability is not of concern. At each optimization step, as a new state matrix A is defined, corrections are performed to the B and D matrices via a least-squares solution, followed by corrections to the C and D matrices. These solutions are defined as follows.

First, let $\overline{G}(z_k) = G(z_k) - D$, and repartition the $n_d \times (m \times r)$ transfer function matrix, $\overline{G}(z_k)$, columnwise, such that each column of the repartitioned $(n_d \times m) \times r$ matrix, $\overline{G}_{col}$, is associated with an input. Define $\hat{\overline{G}}(z_k) = C_0(z_k I_n - A)^{-1}\overline{B}$, repartition $\hat{\overline{G}}(z_k)$ similar to $\overline{G}_{col}$ to obtain $\hat{\overline{G}}_{col}$, and define the absolute error function as

$$e = \overline{G}_{col} - \hat{\overline{G}}_{col} Q_B \tag{22}$$

Now, solve for Q_B, in a least-squares sense, to obtain

$$Q_B = (\hat{\overline{G}}_{col}^T \hat{\overline{G}}_{col})^{-1} \hat{\overline{G}}_{col}^T \overline{G}_{col} \tag{23}$$

Once, Q_B is computed, then D is computed as

$$D = \mu\left(G(z_k) - C_0(z_k I_n - A)^{-1}B\right) \tag{24}$$

where $\mu(\ )$ denotes the mean over frequency points.

To compute Q_C, first define $\overline{G}(z_k) = G(z_k) - D$, and repartition the $n_d \times (m \times r)$ transfer function matrix, $\overline{G}(z_k)$, rowwise, such that each row of the repartitioned $m \times (n_d \times r)$ matrix, $\overline{G}_{row}$, is associated with an output. Define $\hat{\overline{G}}(z_k) = \overline{C}(z_k I_n - A)^{-1}B$, repartition $\hat{\overline{G}}(z_k)$ similar to $\overline{G}_{row}$ to obtain $\hat{\overline{G}}_{row}$, and define the error function as

$$e = \overline{G}_{row} - Q_C \hat{\overline{G}}_{row} \tag{25}$$

Now, solve for Q_C, in a least-squares sense, to obtain

$$Q_C = \overline{G}_{row}\hat{\overline{G}}_{row}^T(\hat{\overline{G}}_{row}\hat{\overline{G}}_{row}^T)^{-1} \tag{26}$$

Once, Q_C is computed, then D is recomputed as

$$D = \mu\left(G(z_k) - C(z_k I_n - A)^{-1}B\right) \tag{27}$$

The number of poles that can be used as design parameters in the optimization is arbitrary. One can use all the poles in the system, or just a few, for example, the real poles of the system. If one starts the optimization with a system realization from the least-squares solution of Eq. (14), then it is very likely that the complex poles of the identified system, representing resonant peaks in the frequency response plots, match the experimental results well, and hence need not be manipulated any further. In such a case, real poles of the system and unstable poles, real or complex, are the best candidates for design optimization. However, one could conceivably use the modulus of all complex poles, which determine the damping associated with each mode, as design parameters as well.

One of the problems with nonlinear programming is the tendency of the solution to converge to a local minimum. The problem becomes more aggravated as the number of design parameters increases. One way to deal with this problem is to restart the optimization from another set of design points in the neighborhood of the last optimal design. Another way of avoiding this problem is to introduce an additional constraint requiring that the cost function be less than a desired value, i.e.,

$$J \leq J_d \tag{28}$$

This constraint would move many of the local minima to the infeasible region, thereby avoiding them.

The cost function in Eq. (20), which is the Frobenius norm of the error in the transfer functions (experimental and identified), is dominated by the peaks (resonants) of the transfer functions. Hence, optimization with Eq. (20) works well in reducing the errors at or around those peaks, or wherever the transfer function magnitude is significant, but it may not do much in reducing the errors elsewhere, e.g., zeros. In fact, the errors around the valleys might become worst. A more equitable trade between the errors for peaks and valleys can be obtained by considering a complementary optimization problem, wherein a norm of the relative error is optimized instead of the absolute error given in Eq. (20). Details of this optimization problem are provided in Ref. [12].

4 Applications

This section describes the application of the proposed techniques to the system identification for the PARTI wind-tunnel model [13], a laboratory test structure at NASA Langley. The model is

a five-foot long, high aspect ratio wing designed to flutter at low speeds to simplify aerodynamic analyses and wind-tunnel testing. The fully assembled semi-span model is shown in Fig. 1. The model has a total of 72 actuators bonded to both sides of the plate. Each actuator contains two stacks of two 0.01 inch piezoelectric patches. The 72 actuators are hardwired to actuate in 15 different groups. The 15 groupings were chosen such that each group primarily affects one of the first three natural modes. Each group can be considered as one input, because all the actuators in the group use the same signal. The piezoelectric patches were only used for actuation; ten strain gages and four accelerometers were used as sensors. As a result, there are a total of 15 inputs and 14 outputs. Due to space limitations, only a few of the results are presented here. A full presentation and discussion of the results are given in Ref. [12].

4.1 Weighted Least-Squares Solution

In the first application, the transfer function from input No. 1 to all outputs is considered for identification. With signals from 14 sensor outputs ($m = 14$), input No. 1 ($r = 1$), and 10th order polynomials ($p = 10$) used in the matrix-fraction expansion (see Eqs. (1)-(3)), a weighted least-squares solution was first obtained from Eq. (14), using an exponential weighting function, given as

$$w^k \; ; \quad k = 0, 1, \ldots, \ell$$

Here, $k = 0$ refers to the zero frequency component of the FRF often known as the direct current (DC) term in electrical engineering, and w was chosen at 0.98. By adjusting the value of w one may emphasize the low frequencies or the higher frequencies. Values of w less than 1 would emphasize the lower end of the frequency spectrum. Here, w was set to 0.98, to emphasize the range of frequency from 0 to 25 Hz. The weighted least-squares solution resulted in an identified model of order 140, which included 4 unstable poles. However, since the actual testbed is stable, it is desired to obtain a stable identified model. Truncating the unstable states yielded a 136-order state-space realization of the system. Magnitude and phase FRF plots for output No. 7 are shown in Fig.2.

Comparison of the plots indicates an excellent agreement between the experimental FRF (solid line) and the identified FRF (dashed line), particularly around the peaks of the FRF or where the gain values are significant. However, discrepancies can be observed around some of the zeros as well as where the gain values are small. This should be expected because the least-squares problem is dominated by the peaks and large gain values. Further inspection of these plots also indicates that the agreement between the experimental and identified results is better in the 0-25 Hz range. The Frobenius norm of the error between the experimental and identified transfer functions was computed at 90.128, the majority of which is due to the differences between two FRFs at DC frequency. In fact, since the DC gain values are quite large, particularly in some output channels, they tend to dominate the rest of the FRF in a least-squares solution. Keep in mind that the DC gain values may not be accurate due to the use of accelerometers and their insensitivity at very low frequencies, drift problems that hampers accurate measurements, and lack of sufficient data. Therefore, in this case, it is reasonable to de-emphasize the DC values by assigning a zero value to the corresponding weighting function, such that the DC weight is set to zero. The FRF plots, using the *modified weighting function*, are shown in Fig. 2 as dashed-dotted lines. This figure indicates moderate improvements in various frequency ranges. The Frobenius norm of the error between the experimental and identified transfer functions was computed to be 90.134, a very minor change from the previous results. Comparing, the norm of the error for all frequency points except DC, shows that the error went down from 0.241 to 0.223, which quantifies the better match by using the modified weighting function. In order to show the effectiveness of the modified exponential weighting, a polynomial with $p = 3$ is used in the matrix-fraction description. The weighted least-squares solution resulted in a stable identified model of order 40. Figure 3 illustrate the stable least-squares solutions for the nominal and modified exponential weightings for output No. 7. These figures clearly demonstrate the advantage of modified exponential weighting for this problem. In fact, the Frobenius norm of the error between the experimental and identified transfer functions dropped from 12.035 to 0.3021, a significant improvement.

4.2 Further Enhancements: Nonlinear Programming

To demonstrate the potential of the nonlinear programming approaches to further enhance the least-squares solution, the parameter optimization approach, posed in Eq. (20), is applied to an identified model for the PARTI testbed, obtained from a least-squares solution. In this optimization, the Frobenius norm of the absolute error is minimized while adjusting the eigenvalues of the state matrix, subject to stability constraints. Moreover, the optimization included corrections to the B and D matrices, followed by corrections to the C and D matrices, at each functional evaluation (see Eq. (23)-(24) and (26)-(27)). The 6 design variables used in the optimization were the values of the real poles of the system. The optimization included 7 constraints, the first six to guarantee the stability of the systems as the poles were reassigned, and a constraint on the value of the error norm to avoid undesirable local minima. The initial design used in the optimization was taken from a stable least-squares solution with modified exponential weighting, i.e., zero DC weighting. The optimization reduced the norm of the absolute error from the initial value of 0.250 to 0.197, which is over 20% reduction. Plots, comparing the FRF matrices for the experimental, nominal, and optimal results are provided in Fig. 4, for output No. 7. The identified model (via optimization) agrees very well with the experimental data.

All the identification results obtained so far were based on the 14 FRFs from the first input to all 14 outputs. Now, let us consider the FRFs from all 15 inputs to all 14 outputs for identification. With the signals from all 14 sensor outputs ($m = 14$) and all 15 inputs ($r = 15$), and 3rd order polynomials ($p = 3$) used in the matrix-fraction expansion(see Eqs. (1)-(3)), a weighted least square solution was first obtained from Eq. (14). Similar to the previous cases, an exponential weighting function was used, with parameter w chosen at 0.98 to emphasize the range of low frequencies. In addition, the DC weight was set to zero. The Frobenius norm of the error between the experimental and identified FRFs was computed at 246.855, the majority of which is due to a discrepancy between two FRFs at the DC frequency, i.e., zero frequency. The Frobenius norm of the absolute error, for all frequency points except the DC, was computed to be 1.721. For the purpose of illustration, plots for the experimental and realized FRFs are depicted in Fig. 5, for output No. 7 with input No. 1, and in Fig.6, for the same output with input No. 8. The experimental transfer functions are shown as solid lines and the transfer functions, obtained via direct least square, as dashed lines. These figures indicate moderate to good agreement between the transfer functions in low frequencies ranges, particularly, around the peaks or high gain areas of the transfer functions.

Now consider the least-squares optimization approach presented in Eq. (20) for the 15 inputs and 14 output case. The initial design used in the optimization was the stable least-squares solution with modified exponential weighting. This realization had 14 real poles, whose locations were used as design variables in the optimization, i.e., there were 14 design variables. The optimization included 15 constraints, the first 14 to guarantee the stability of the systems as the poles were reassigned, and the last constraint on the value of the error norm to avoid convergence to undesirable local minima. The optimization reduced the norm of the error from the initial value of 1.165 to 1.090, about a 6.5% reduction. Plots, comparing for the experimental (solid line), nominal (dashed line), and optimal transfer function (dashed-dotted line) are provided in Figs. 5 and 6. It is observed that the identified model (obtained via optimization) performs well, although only 3rd order polynomials were used in the matrix fraction description to match a 15 input by 14 output transfer function. Comparing Fig. 5 and Fig. 4, which correspond to the same input and output channels, confirms the good level of correlation obtained following the optimization-based approach.

5 Concluding Remarks

Several techniques have been presented to identify an experimental system model directly from frequency response data. The techniques used a matrix-fraction description (MFD) to describe the identified system. The MFD coefficients were obtained from the solution of a weighted least-squares problem. Frequency weighting concepts were introduced in order to emphasize a frequency range of interest. An optimization-based method was introduced to fine-tune the experimentally realized

models. The method adjusts a subset of the system poles to improve the identified model. The input and output influence matrices are computed at every optimization step through least-squares procedure. These techniques were applied to data from PARTI wind tunnel model, a laboratory testbed at NASA Langley Research Center. The benefits of the optimization-based refinement technique as well as frequency weighting techniques were demonstrated. It was shown that with optimal fine-tuning and proper choice of frequency weighting a 40th order system realization could provide almost the same level of model fit as a full-order 136th order model. The numerical computation of the gradients may require a large number of functional evaluation, which would be costly in a computational sense. Alternatively, one may attempt to obtain analytical expressions for the gradients, and perhaps second-order partial derivatives, to improve computational efficiency and accuracy.

References

[1] Juang, J.-N. and Suzuki, H., "An Eigensystem Realization in Frequency Domain for Modal Parameter Identification," *Journal of Vibration, Acoustics, Stress and Reliability in Design,* Vol. 110, No. 1, January 1988, pp. 24-29.

[2] Bayard, D. S., "An Algorithm for State Space Frequency Domain Identification without Windowing Distortions," *Proceedings of the Control and Decision Conference*, December 1992.

[3] Chen, C. W., Juang, J.-N., and Lee, G., "Frequency Domain State-Space System Identification," *Transactions of the ASME, Journal of Vibration and Acoustics*, Vol. 116, No. 4, Oct. 1994, pp. 523-528

[4] Horta, L. G., Juang, J.-N., and Chen, C.-W., "Frequency Domain Identification Toolbox," *NASA Technical Memorandum 109039*, September 1996, pp. 1-28.

[5] Juang, J.-N., *Applied System Identification*, Prentice Hall, Inc., Englewood Cliffs, New Jersey 07632, 1994, ISBN 0-13-079211-X.

[6] Chen, C.-W., Juang, J.-N., and Lee, G., "Stable State Space System Identification from Frequency Domain Data," *Proceedings of the first IEEE Regional Conference on Aerospace Control Systems*, CA., May 25-27, 1993.

[7] Astrom, K.J., and Witenmark, B., *Adaptive Control,* Addison-Wesley Publishing Company, 1995.

[8] Gill, P. E., Murray, W., and Wright, M. H., *Practical Optimization*, John Academic Press, London, 1981.

[9] Juang, J. N., Lim, K. B., and Junkins, J. L., "Robust Eigensystem Assignment for Flexible Structures," *Journal of Guidance, Control and Dynamics,* Vol. 12, No. 3, May-June 1989, pp. 381-387.

[10] Maghami, P. G., and Juang, J. N., "Efficient Eigenvalue Assignment for Large Space Structures," *Journal of Guidance, Control and Dynamics,* Vol. 13, No. 6, Nov.-Dec. 1990, pp. 1033-1039.

[11] Juang, J. N., and Maghami, P. G., "Robust Eigensystem Assignment for Second Order Dynamics System," *Mechanics and Control of Large Space Structures* edited by John L. Junkins, AIAA Monograph on Progress in Astronautics and Aeronautics, Vol 29, 1990, pp. 373-387.

[12] Juang, J. N., and Maghami, P., "Optimal Frequency-Domain System Realization with Weighting" to be published as *NASA TM,* 1999.

[13] McGowan, A. R., Heeg, J., and Lake, R. C., "Results of Wind-Tunnel Testing from the Piezoelectric Aeroelastic Response Tailoring Investigation," 1996 Structures, Structural Dynamics, and Materials Conference.

Figure 1: PARTI Model

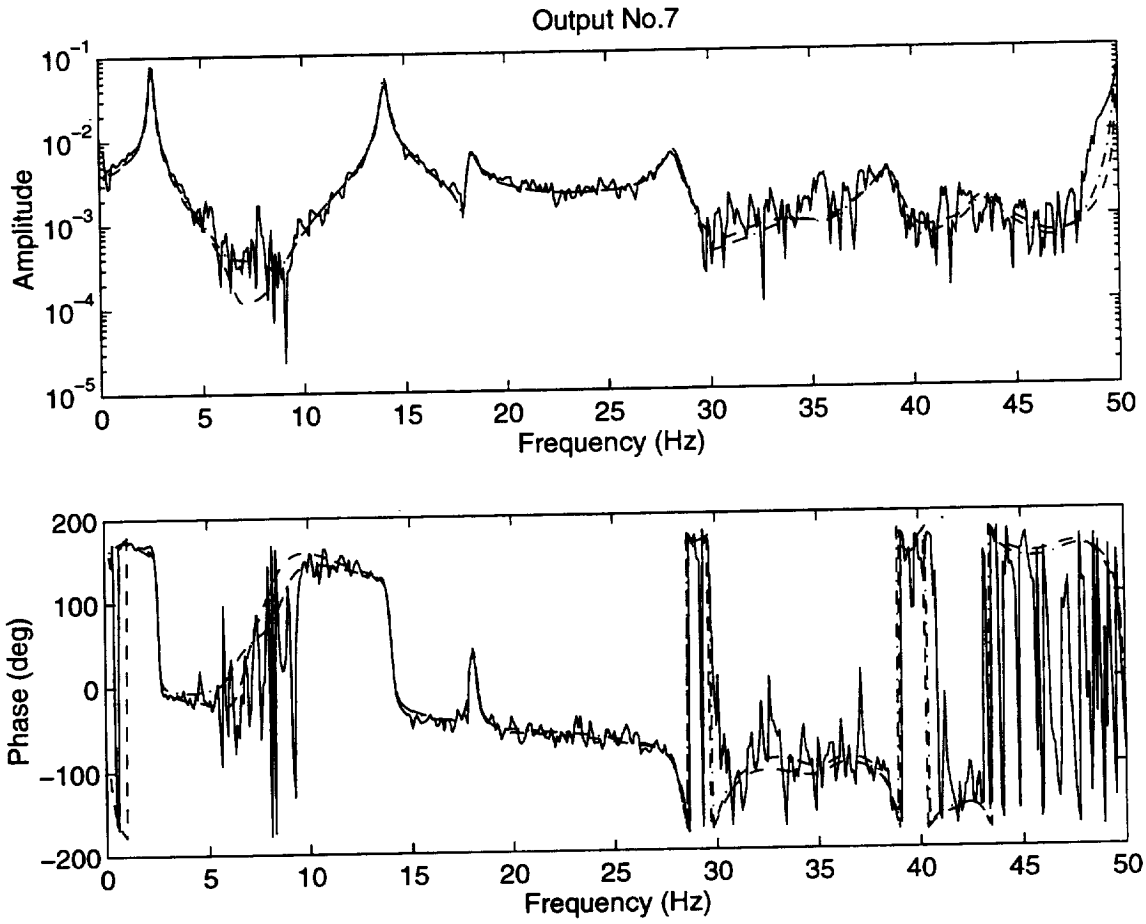

Figure 2: Comparison of FRFs for Output No. 7 with exponential weighting and 136-order system: experimental FRF (solid line), identified FRF (dashed line), identified FRF with zero DC weighting (dashed-dotted line).

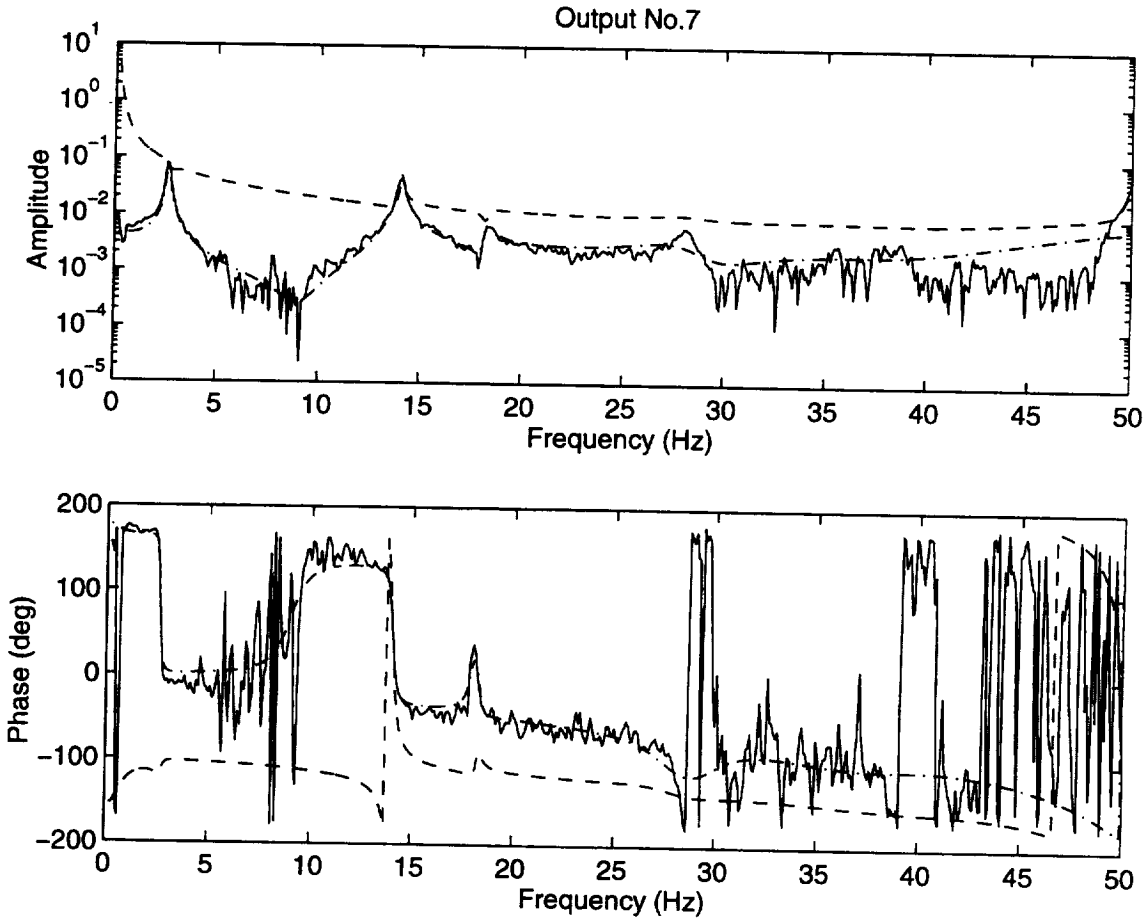

Figure 3: Comparison of FRFs for Output No. 7 with exponential weighting and 40-order of system: experimental FRF (solid line), identified FRF (dashed line), identified FRF with zero DC weighting (dashed-dotted line)

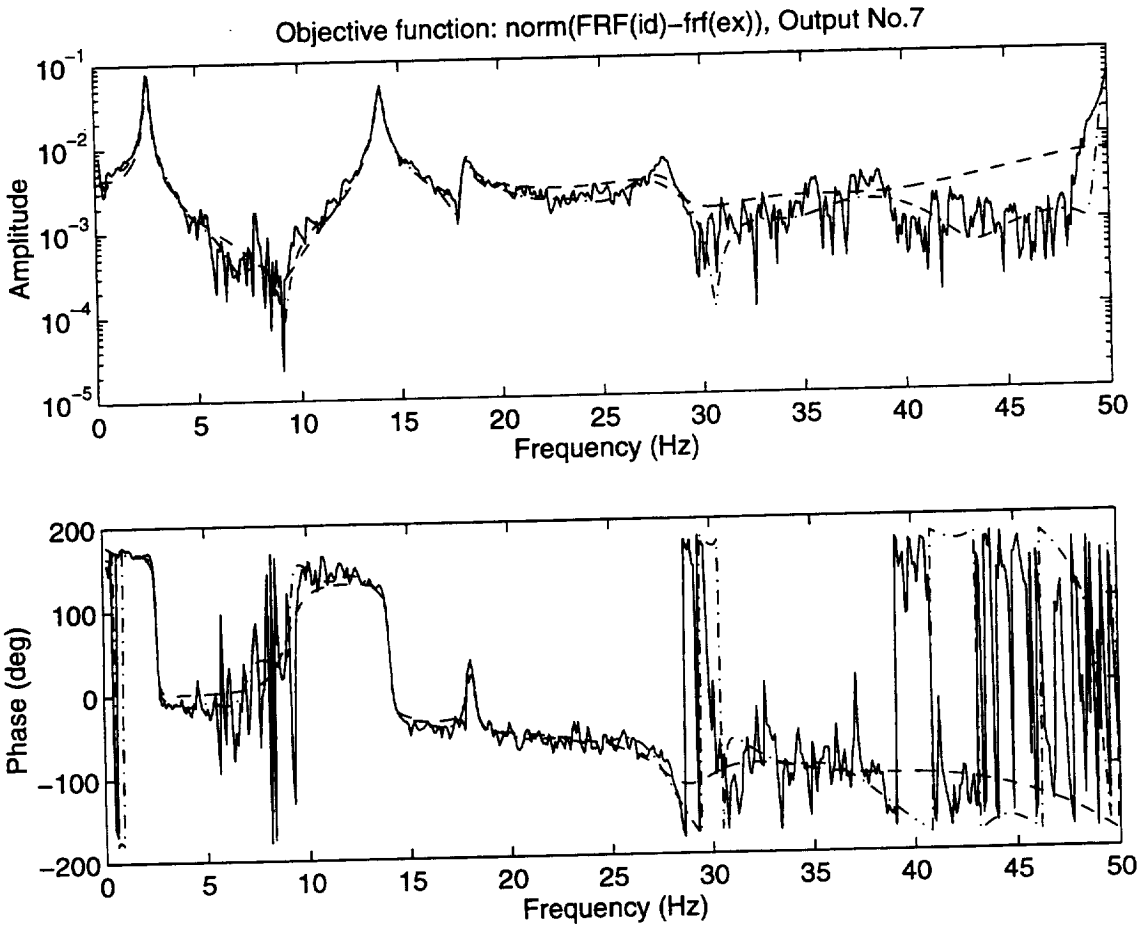

Figure 4: Comparison of FRFs for Output No. 7 with least-squares optimization approach and 40-order system: experimental FRF (solid line), identified FRF (dashed line) with zero DC weighting, enhanced FRF with absolute-error optimization (dashed-dotted line)

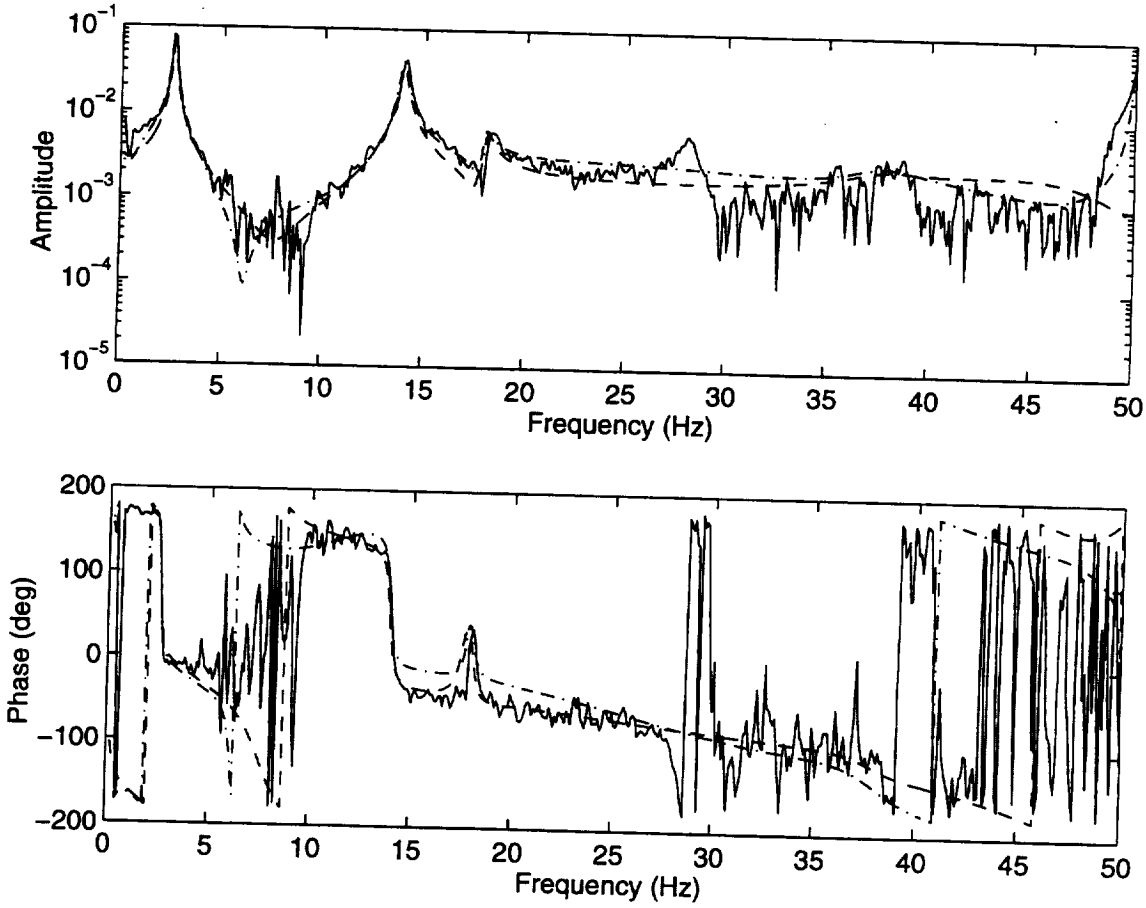

Figure 5: Comparison of FRFs for Output No. 7 and Input No. 1 with least-squares optimization approach and 42-order system: experimental FRF (solid line), identified FRF (dashed line) with zero DC weighting, enhanced FRF with absolute-error optimization (dashed-dotted line)

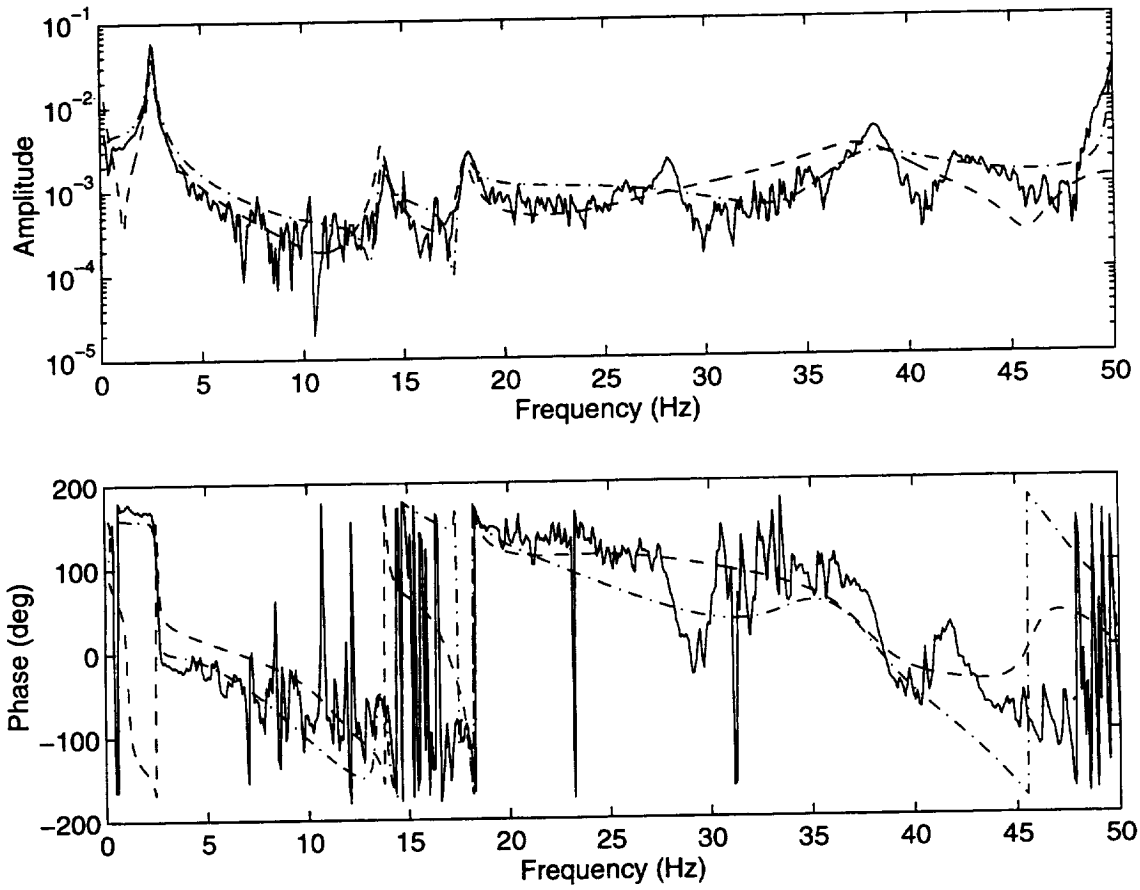

Figure 6: Comparison of FRFs for Output No. 7 and Input No. 8 with least-squares optimization approach and 42-order system: experimental FRF (solid line), identified FRF (dashed line) with zero DC weighting, enhanced FRF with absolute-error optimization (dashed-dotted line)

IDENTIFICATION OF A NON-PROPORTIONALLY DAMPED TRUSS STRUCTURE

Steven Naylor[1], Jan R. Wright and Jonathan E. Cooper[2].

ABSTRACT

In this paper, an extension of the force appropriation approach used for identifying the dynamic characteristics of non-proportionally damped structures is applied to a 3 bay cantilevered truss structure with damped struts. The Resonant Decay method involves exciting each mode of a structure using an appropriated excitation vector and then removing the excitation such that any modes coupled by damping forces will respond. A Least Squares curve fit is employed in modal space in order to identify the modal damping matrix. Three configurations are considered.

1. INTRODUCTION

The identification of accurate dynamic models of structures from experimental data is of considerable importance in predicting the response to forcing functions and in permitting damage to be detected. In particular, there is a growing interest in identifying damping models for non-proportionally damped structures (i.e. where damping is not proportional to a linear combination of mass and stiffness). Identification of damping is notoriously inaccurate.

The normal mode testing approach has a number of advantages (Cooper and Wright, 1997) and permits undamped normal modes of a structure to be excited directly using a vector of appropriated forces, determined using some force appropriation method (Nash, 1991). Undamped normal modes for a non-proportionally damped structure may also be identified, whereas nearly all classical curve fitting methods yield damped (complex) modes of vibration for such systems. One approach to estimating the modal damping matrix (Rades, 1981) uses complex energy but damping estimates are inaccurate when modes are not well tuned (Naylor, 1998). An alternative Resonant Decay method (Naylor et al, 1998) uses a short "burst" excitation of each mode of interest with the appropriated force vector applied at the undamped natural frequency. This burst will cause a response in other modes, significantly coupled by damping forces, as the mode of interest decays. A curve fit is then performed in modal space to yield the modal damping matrix.

One motivation for identification of damping is that it is a parameter that is very sensitive to changes occurring in a structure due to damage of any sort and also the parameter that has a major influence on dynamic response. In this paper, the application of the Resonant Decay method to a 3 bay truss structure will be evaluated experimentally. This structure was the subject of a study (Smith et al, 1997) into the identification of damage. Whilst the identification of the modal damping matrix does not lead directly to identification of individual damping elements in a structure, a Genetic Algorithm approach may be used to seek discrete damping values that match the modal damping matrix identified (Naylor, 1998). The RD method is arguably powerful for continuous type structures where damping is distributed and a modal model is more appropriate.

2. THEORY

2.1 *Force Appropriation*

[1] Arvin Cheswick Research and Development, Preston, Lancs, UK (ex University of Manchester)
[2] Dynamics and Aeroelasticity Research Group, Manchester School of Engineering, University of Manchester, Manchester UK

Force Appropriation is the name given to the process of determining, from a measured Frequency Response Function (FRF) matrix, the undamped natural frequency and monophase force vector for excitation of each normal mode of a structure. The "phase resonance" condition is sought, such that all responses are in monophase and in quadrature with the excitation. The Modified MMIF (Multivariate Mode Indicator Function) method (Nash, 1991) was used for this work and is based upon an eigenvalue formulation involving the FRF matrix. Once the frequency and force vector are obtained, the mode can be "tuned", i.e. it is excited and measured in isolation of all other modes. This force appropriation approach is quite different to the phase separation philosophy in which a model is typically fitted to the FRF matrix in order to obtain the damped (complex) modes of the structure.

For *proportionally* damped structures, the mode of interest may be excited over a band of frequencies because here the force vector is chosen to excite only the mode of interest and to do no work in the other modes. However, for *non-proportionally* damped structures, the excitation force vector is chosen so as to counteract any damping coupling forces and a single mode may still be excited at, but only at, the undamped natural frequency.

2.2 *Identification of Non-Proportionally Damped Systems using the Resonant Decay (RD) method*

Consider the equations of motion expressed in modal space

$$[M]\{\ddot{p}\} + [C]\{\dot{p}\} + [K]\{p\} = \{Q\} \qquad (1)$$

where [M], [C] and [K] are the modal mass, damping and stiffness matrices, {Q} is the modal force vector and {p} is the modal displacement vector. It is well known that $\{Q\} = [\phi]^T \{f\}$ and $\{y\} = [\phi]\{p\}$, where {y} and {f} are the physical response and force vectors and [ϕ] is the modal matrix.

The modal mass and stiffness matrices are diagonal. The modal damping matrix is only diagonal if the damping is proportional but in the general case of non-proportional damping, there will be non-zero off-diagonal terms where two or more modes are coupled by damping forces. In practice, only a subset of the off-diagonal terms will be significant in magnitude and most are likely to be negligible. The critical coupling terms tend to be those between modes which are close in frequency.

The idea of the Resonant Decay method (Naylor et al, 1998) is to excite a mode of interest via the force appropriation process and then to remove the excitation. The mode of interest will then obviously decay but any other modes that are significantly coupled to it by damping forces will respond during this decay because the force vector counteracting the coupling terms will have disappeared. The damping coupling terms may then be estimated by fitting a modal model to the response. This process has also been referred to as "burst appropriation" because the excitation is applied in a burst.

Consider as an example the burst excitation of the jth mode, coupled to, typically, the kth mode by damping forces. The modal equation for the jth mode will then be

$$M_{jj}\,\ddot{p}_j + C_{jj}\,\dot{p}_j + C_{jk}\,p_k + K_{jj}\,p_j = Q_j \qquad (2)$$

where the subscripts refer to elements in the relevant modal vectors or matrices. If it is assumed that the modal matrix [ϕ] is known from the initial force appropriation process, then the modal force Q_j may be estimated from {f} and the modal responses p_j and p_k estimated from {y}. Provided the modal velocities and accelerations may also be estimated, then a Least Squares fit may be performed on equation (2) using excitation and response sampled values. This will lead to an estimate of the unknown modal mass, stiffness and damping terms for the jth mode, as well as the cross coupling term C_{jk}. This procedure is

then repeated for each mode of interest, so yielding a full set of modal parameters including the modal damping matrix. Some coupling criterion (Naylor et al, 1998) can be employed in order to indicate which cross coupling terms should be included in the curve fit. It may also be assumed that the damping matrix is symmetric (i.e. reciprocity holds) and this modifies the curve fit. The identification may be viewed as an extension of the basic force appropriation process used in normal mode tuning.

It should be noted that, even though the voltage applied to the exciters may be switched off after the burst, the actual applied force will not immediately become zero and needs to be included in the fit. In practice, only the acceleration is measured so that integration will be required to yield velocity and displacement. By choosing the burst excitation and acquisition window length carefully, the excitation and response signals will start and end at a zero value so that there will be no leakage if the integration is performed in the frequency domain.

3. TRUSS STRUCTURE

In this paper, the identification approach is applied to a 3 bay truss structure, previously used for damage location studies (Smith et al, 1997) and loaned by McDonnell Douglas Aerospace and the University of Kentucky. The basic truss is shown in Figure 1, having basic struts and 4 visco-elastically damped struts that allow the damping configuration to be controlled. The truss is cantilevered vertically upwards from its base (nodes 1,2,3 and 4), supported on a bed-plate, and exhibits beam-like behaviour for the first three modes, two bending and one torsional; higher bending modes are obscured by local strut modes. Accelerometers (PCB336A) were positioned in the x and y directions at nodes 5-16. The three exciters were attached to the structure at node 9 in the x direction and nodes 11 and 12 in the –y direction via stinger rods and force gauges (PCB208B). A separate frame was used to support each exciter in a pendulum arrangement, so that the only coupling between the exciters and the truss was via the stingers. The excitation and data acquisition were controlled by an HP700 computer and LMS-DIFA SCADAS front end with LMS software. The program for performing the burst excitation was written in LMS-UPA, a user programming language. MATLAB was used to perform the curve fits in modal space.

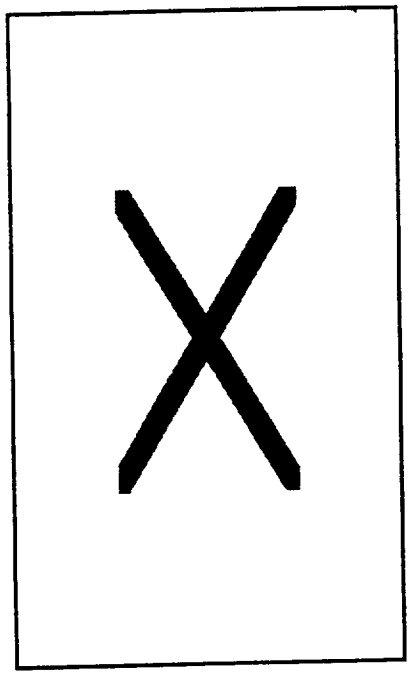

Figure 1 Truss Configuration

4. RESULTS

4.1 *Original Build – No Damped Strut*

As an initial check, the basic structure with no damped struts (assumed to be proportionally damped) was tested and compared to results obtained earlier (Smith et al, 1997). Linearity and reciprocity checks were performed and indicated linear behaviour over the frequency range of interest (20-150 Hz). A 24 by 3 FRF matrix was estimated, the MMIF method applied to obtain force vectors and natural frequencies and the modes tuned. The first three tuned modes were of high quality, with little phase scatter (indicator function >0.99, where pure phase resonance has a value of 1.00). The mode shapes were used to construct the modal matrix. A curve fit was carried out using the Frequency Domain Direct Parameter Identification (FDPI) method, though results from the Polyreference method were very similar. The frequencies agreed well with previous results as shown in Table 1 below. Damping results differed somewhat, probably due to different boundary conditions and identification approaches; an impact test was used previously and this is not usually as reliable an approach for damping estimation.

The Resonant Decay method was then applied using the force vectors and frequencies obtained from the MMIF method. The acquisition time was 2.048 s and the sampling rate was 2000 Hz (i.e. 4096 points and at least 16 points per cycle on the sine wave). The burst occupied 50% of the acquisition window. Note that the start and end of the burst sine wave were tapered in order to minimise transients. The modal forces and velocity responses for Mode 1 are shown in Figure 2. A modal force is present in all three modes which is rather surprising for a proportionally damped structure where modal force would be expected to exist only in mode 1. This occurs because there is in fact an inadequate number of exciters present for perfect force appropriation (Naylor, 1998). Had 4 exciters been used then this would not have occurred. However, the tuning is obviously effective as there is no significant response in modes 2 and 3 during the near steady-state "tuned" portion of the response (around 0.75 s). This is because, even with fewer exciters than is ideal, the modes are well enough separated for this not to matter. During the decay part of the burst, there is no significant response in modes 2 and 3, as expected for a proportionally damped structure. The process was repeated for the other two modes. A curve fit in modal space was performed for each of modes 1-3, with no cross coupling terms included. Using the diagonal modal damping matrix identified, the corresponding modal damping values were obtained. These are presented in Table 1. The results are very similar to those obtained from the classical FDPI curve fit which was encouraging.

	Smith et al		**FDPI**		**RD method**	
	Frequency (Hz)	Damping (%)	Frequency (Hz)	Damping (%)	Frequency (Hz)	Damping (%)
Mode 1	62.81	0.87	62.27	1.51	62.26	1.57
Mode 2	73.50	1.31	73.81	2.69	73.49	2.73
Mode 3	121.80	0.36	119.15	0.11	118.87	0.15

Table 1 Comparison of Frequencies and Damping Values for Original Build

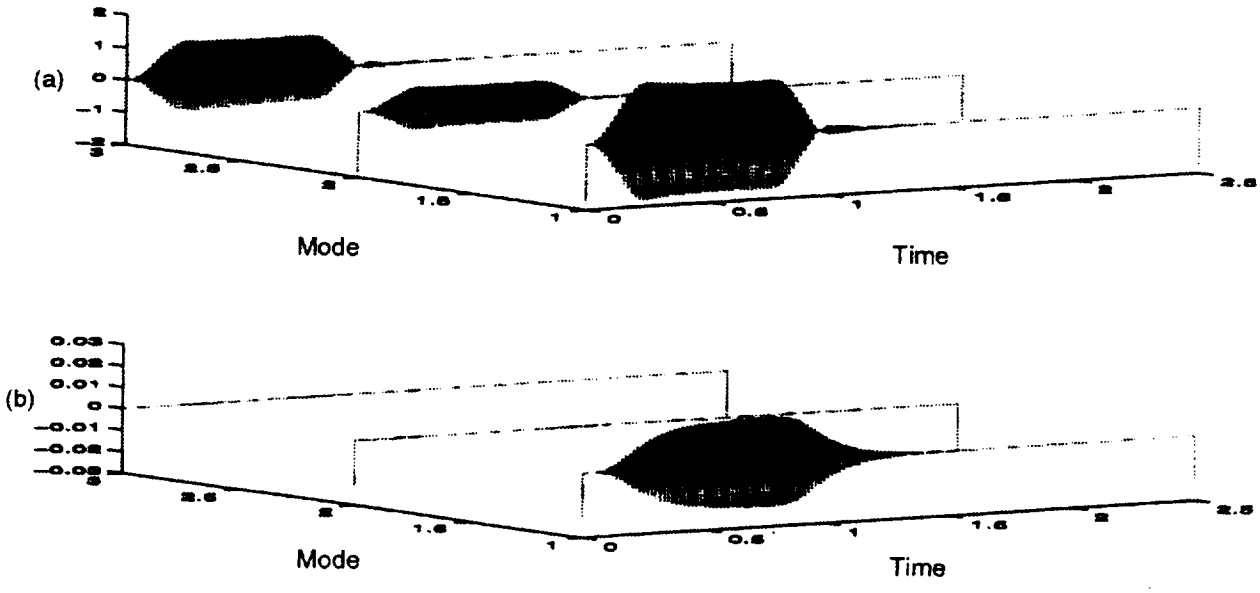

Figure 2 Modal Forces and Velocities for Excitation of Mode 1 – Original Build

4.2 *Original Build – Localised Damping*

In the earlier study of the truss (Smith et al, 1997), vertical struts in the first (root) or second bay were replaced with 1, 2 or 4 damped struts to affect mode 1 alone, mode 2 alone or both modes 1 and 2. This was possible because the first two bending mode shapes were spatially orthogonal, i.e. bending occurred along the directions of the diagonals of the truss footprint (nodes 1-4 for mode 1 and 2-3 for mode 2). Tests were then performed for these nominal test cases and also for damage configurations simulated by removing a particular strut (not a damped one).

Whether any of these configurations are actually non-proportionally damped is an interesting question. Consider the case where damped struts are inserted between nodes 1-5 and 4-8, so affecting mode 1 alone. When the truss vibrates in mode 2, then the spatial orthogonality of this mode means that there will be zero or very small strains (and hence forces) in the dampers because they lie essentially on the neutral axis of bending in mode 2. Thus, by definition, there is little or no damping coupling. The same argument occurs for the other 2 strut, and indeed for the 4 strut, configuration. Even when a vertical strut is removed, there will be no damping coupling because the orthogonal nature of the two modes will not change. Only removal of a horizontal strut will affect the orthogonality and introduce small couplings. Thus it is considered that the previous configurations are essentially proportionally damped. This feature would not be the case for a more advanced truss structure where the basic mode shapes would be more complicated.

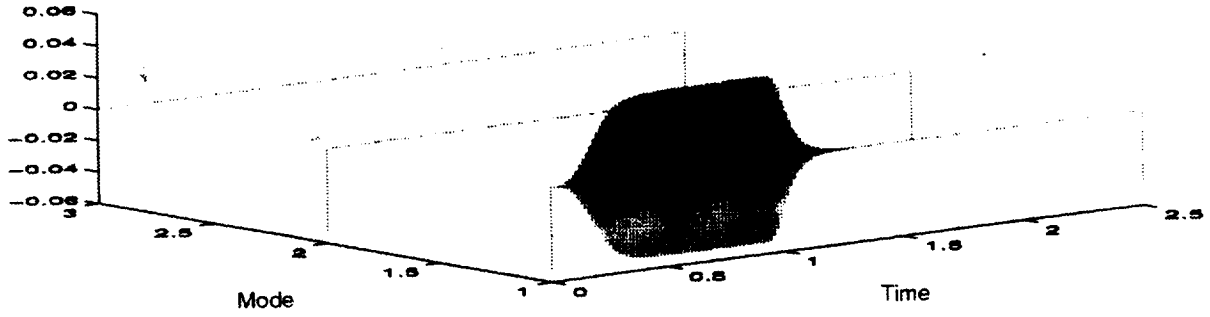

Figure 3 Modal Velocities for Excitation of Mode 1 – Original Build + Localised Damping

	Smith et al		FDPI		RD method	
	Frequency (Hz)	Damping (%)	Frequency (Hz)	Damping (%)	Frequency (Hz)	Damping (%)
Mode 1	69.37	3.12	67.77	4.07	67.74	3.97
Mode 2	76.94	2.16	77.93	4.53	77.44	4.41
Mode 3	121.80	0.39	119.37	0.14	119.17	0.14

Table 2 Comparison of Frequencies and Damping Values for Original Build + Localised Damping

In order to illustrate this point, a configuration where all the vertical struts in the first bay were replaced with damped struts was tested in the same way as for the original build. The modes were again tuned to a high quality (indicator function >0.99). The RD approach gave similar quality results and a sample set of

modal velocity responses for mode 1 are shown in Figure 3; it is clear that there is no damping coupling, confirming that this structure configuration is proportionally damped. The frequency and damping results are shown in Table 2 and show similar levels of agreement to those obtained earlier. The frequencies for modes 1 and 2 are higher, because of the increased stiffness of the damped struts whereas the torsion mode frequency is essentially unchanged because the vertical struts have little effect on this mode. As expected, the damping values are also higher but again there is good agreement between the FDPI and RD approaches.

4.3 *Modified Build*

In order to test the ability of the RD method to identify a non-proportionally damped structure, a modified configuration was sought. Removal of a vertical strut will affect one of the bending modes, but not introduce damping non-proportionality, whereas a horizontal strut will mainly influence the torsional mode, though this effect is small. However, removal of a *diagonal* strut should have a significant effect on the modal characteristics of the whole structure. After some initial trials, a modified build was chosen, with diagonal struts removed between nodes 3-8, 11-13 and 6-10; damped struts were inserted between nodes 1-5, 3-7, 4-8 and 7-11. The idea was to destroy the regularity of the structure so as to introduce non-proportional damping.

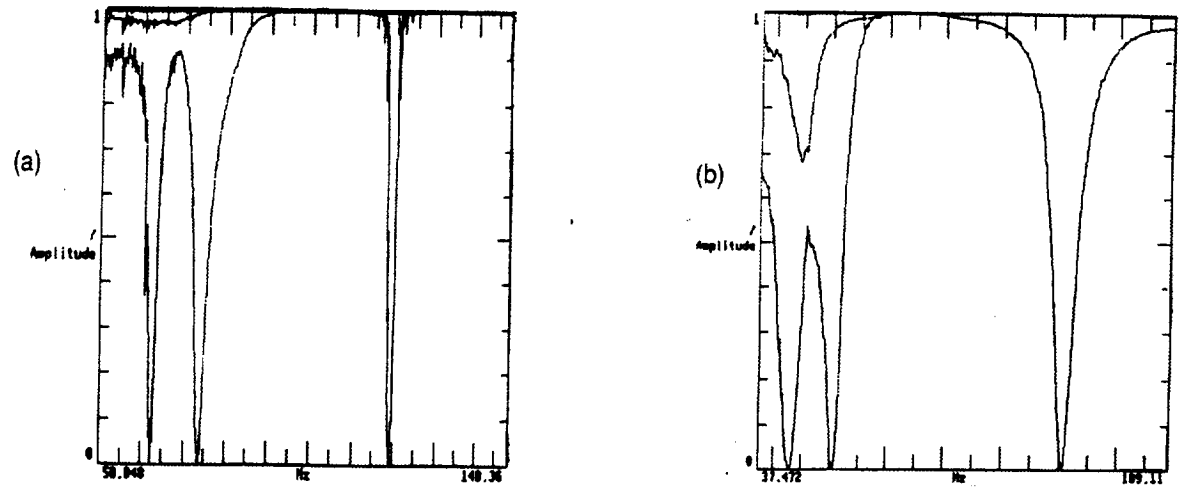

Figure 4 Variation of MMIF Eigenvalues with Frequency (a) Original and (b) Modified Build

The modified build case was tested as before. The use of the MMIF method for obtaining force vectors indicated that some damping non-proportionality was present by observing the variation of the MMIF eigenvalues with frequency. Figures 4a and b show the eigenvalues for the original build (with dampers) and the modified build. In both cases, the primary eigenvalues drop to very near zero at each undamped natural frequency. However, the secondary eigenvalue drops noticeably in between the first two modes for the modified build and this is a characteristic of non-proportional damping (Holmes, 1996). Once again, high quality normal modes were tuned (indicator function ≥ 0.99) and the first two mode shapes are shown in Figures 5a and b. These are no longer as simple as they were before and are not spatially orthogonal. The FDPI method was used to curve fit the FRF matrix and the resulting modes showed some degree of complexity as expected.

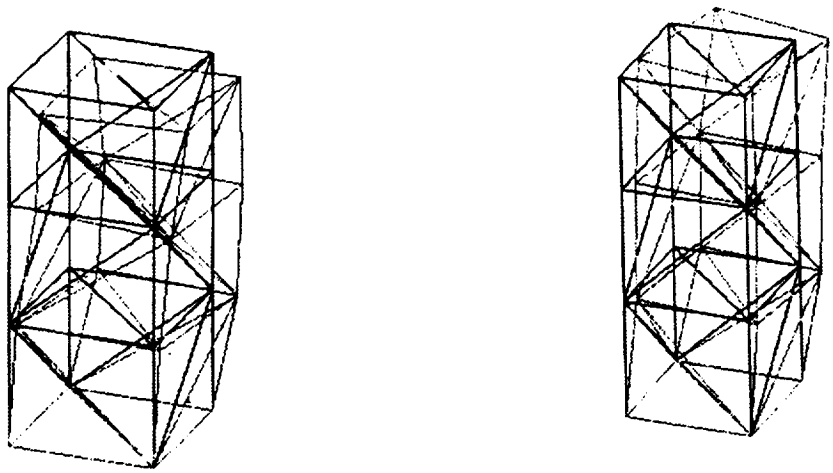

Figure 5 Mode Shapes for Modes 1 and 2 – Modified Build

The RD method was used as before. Figure 6 shows the modal velocity for the excitation of mode 1. It can now be seen that some responses in mode 2 are present away from the steady-state condition, because the modal coupling forces are not counteracted by the excitation vector. A similar result occurs for mode 2, with mode 1 responding. However, for mode 3, there are no cross couplings. Thus there is evidence of damping coupling between modes 1 and 2. A curve fit was performed with (i) no couplings allowed for and (ii) with mode 1/2 coupling terms included. The modal damping matrix for the second case is shown in Table 3. It may be seen that the two off diagonal terms are very similar in magnitude, which should be the case for a linear structure and is a good indicator of the quality of the identification since each value was obtained from a different test and analysis. These coupling terms are also of similar magnitude to the diagonal terms.

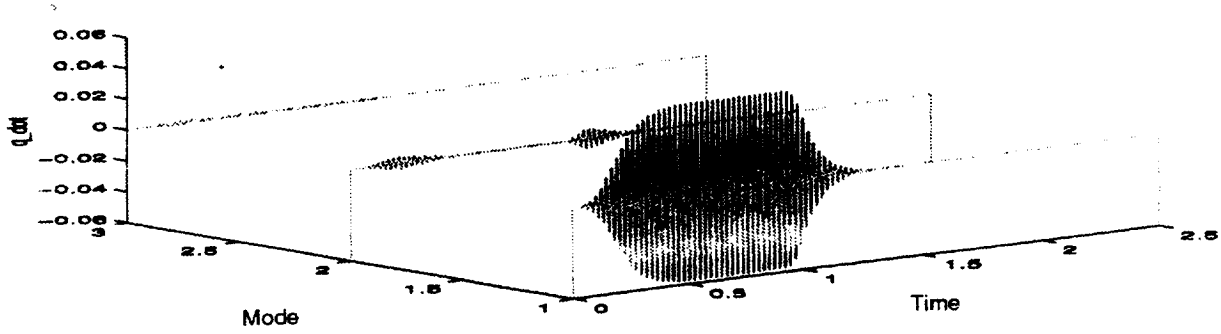

Figure 6 Modal Velocities for Excitation of Mode 1 – Modified Build

149.1	32.2	0
31.3	42.6	0
0	0	41.6

Table 3 Modal Damping Matrix for Modified Build

The frequency and damping results are shown in Table 4. The frequency values are much lower than before because of the struts removed. Where no coupling was included, modal damping values may be

deduced as before. However, when the cross coupling terms were estimated, a complex mode eigenvalue analysis was performed in order to obtain comparative damping values; these are the values quoted in the table. Damping values are of similar magnitude to those found earlier, except that the torsion mode damping is considerably larger.

	FDPI		RD method	No coupling	RD method	Coupling
	Frequency (Hz)	Damping (%)	Frequency (Hz)	Damping (%)	Frequency (Hz)	Damping (%)
Mode 1	43.83	4.68	43.19	3.18	43.19	4.21
Mode 2	54.23	4.08	53.73	5.54	53.73	4.39
Mode 3	91.19	2.67	90.98	2.88	90.98	2.88

Table 4 Comparison of Frequencies and Damping Values for Modified Build

In order to validate the coupled model, the response of the modal model to a chirp excitation applied at one position was obtained and compared to the equivalent response measured experimentally. The chirp was applied over the frequency range 35-60 Hz with a linear sweep rate. The range encompassed the first two modes. Figure 7 shows a sample comparison of acceleration responses at position 5 for the uncoupled and coupled models. It is clear that the inclusion of the mode 1/2 coupling term significantly improves the ability of the model to replicate the measured response. Ignoring the coupling introduces nearly a factor of 2 error.

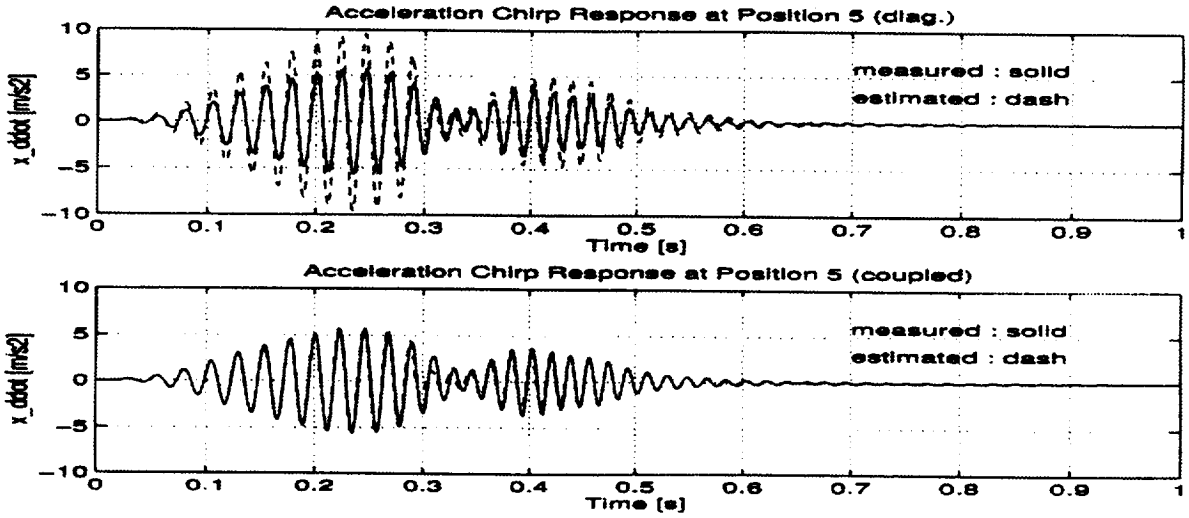

Figure 7 Comparison of Acceleration Responses to Chirp Excitation – Structure and Identified Model (a) Diagonal Modal Damping Matrix and (b) Coupled Modal Damping Matrix

5. CONCLUSION

The Resonance Decay Method has been applied to several configurations of a truss structure. The method uses an appropriated excitation vector applied in a burst to drive a mode of interest at resonance and then allow it to decay, so that any modes coupled to it by damping forces can respond. A curve fit of the response in modal space yields a modal model. Results compared well to those from a curve fit to the

FRF matrix and the method was able to identify a modal damping matrix for a non-proportionally damped configuration of the truss by including cross coupling terms in the identification.

ACKNOWLEDGEMENTS

The authors would like to acknowledge the support of the EPSRC, British Aerospace Airbus Ltd, Leuven Measurement Systems (LMS) and LMS-DIFA. They would also like to thank McDonnell Douglas Aerospace and the University of Kentucky for the loan of the damped struts and truss respectively.

REFERENCES

Cooper, J.E. and Wright, J.R. "To Fit or to Tune – That is the Question", Proc of 15th International Modal Analysis Conference, pp1353-1359, 1997.

Nash, M. "A Modification of the Multivariate Mode Indicator Function employing Principal Force Vectors", Proc 9th International Modal Analysis Conference, pp688-693, 1991.

Naylor, S. "Identification of Non-proportionally Damped Structures using Force Appropriation", PhD thesis, University of Manchester, 1998.

Naylor, S., Wright, J.R., Cooper, J.E. "Identification of Non-proportionally Damped Structures using a Force Appropriation Technique", Proc 23rd International Seminar on Modal Analysis, Leuven, 1998.

Holmes, P.S. "Advanced Applications of Normal Mode Testing", PhD Thesis, University of Manchester, 1996.

Rades, M. "On Modal Analysis of Structures with Non-proportional Damping", Revue Roumane des Sciences Techniques Serie Mechanique Applique, 26(4), pp605-622, 1981.

Smith, S.W., Zimmerman, D.C., Bartkowicz, T.J. and Kim, H.M. "Experiments for Damage Location in a Damped Structure", ASME Design Engineering Technical Conferences, Sacramento, 1997.

Nonlinear Aeroelastic System Identification via Wavelet Analysis in the Neighbourhood of a Limit Cycle

F. Mastroddi and A. Bettoli
Dipartimento Aerospaziale - Università degli Studi di Roma "La Sapienza"
via Eudossiana, 16 - 00184 Rome - Italy - E-mail franco@mastroddi.ing.uniroma1.it

Abstract

A wavelet analysis on the output signal of a nonlinear systems in the neighbourhood of a Hopf bifurcation (i.e., a limit-cycle oscillation) has been performed to point out the linear and nonlinear signatures of the system. Indeed, this kind of nonlinear behaviour is characterised not only by a simple harmonic oscillation in developed steady-state condition, but also by an initial transitory phase with a complex time evolution of the spectral signal content. Both of issues could be described in an analytical way via a singular perturbation analysis but they could be also directly analyzed by a signal-processing tool via wavelet analysis (Continuous Wavelet Transform, CWT): this is obtained using the wavelet capability in describing efficiently the time evolution of the spectrum of the signal (i.e., a nonlinear "signature" of a Hopf bifurcation). The novelty of the paper constists of applying the wavelet theoretical tool in the behavior description of a wing experiencing a limit cycle.

1 Introduction

The identification methods based on wavelet transforms have shown several advantages in the aeroelastic analysis with respect to the standard ones above all for the de-noising effects included to the method: in Refs. [1] and [2] an overview of flight-test data analysis using wavelets for aeroelastic system identification and de-noising was shown; the wavelet tools have been also used for the modal parameters identification of linear structural-dynamical systems in Refs. [3] and [4]; moreover, in reference to the class of aeroelastic problems, in Refs. [5] and [6] the evaluation of the stability margin with respect to a given parameter (*e.g.*, the flight speed) based on measured data was presented to be as a relevant issue. Nevertheless, for both system identification and stability-margins identification, the transient nature of the inflight aeroelastic dynamics (intermittency, modulation, nonperiodicity, nonstationariness, time-variance and nonlinearity in the data) seems to show the standard Fourier analysis to be inadeguate. Because of these reasons, time-scale analyses have recently been developed in this field, having these tools more suitable features to the mentioned problems with respect to the classical methods of signal processing analysis. Specifically, wavelets are waveforms that, once correlated to the signal, allow one to localize in time and frequency the signal energetic content with arbitrary high resolution in time at high frequencies and arbitrary high frequency resolution at low frequencies: in this way, one can identify the features of the signal localized or spread both in time and frequency. Assuming that the transient of the energetic content of the output signal is generally a very relevant signature of systems (*e.g.*, consider the impulse response for linear systems), one may realize the wavelet capabilities for the identification of the main features of linear and nonlinear systems and, in particular, their stability margins.
In Reference [7] the description offered by the wavelet analysis for system responses (used for the identification of linear mechanical systems and applied in Ref. [6] for the stability-margin estimate of nonlinear system) has been studied interpreting the obtained results via a singular perturbation analysis, Ref. [8]. To achieve this goal, a wavelet analysis of the response - to initial conditions - of nonlinear systems in the neighbourhood of a Hopf bifurcation (*i.e.*, limit cycle behaviour) will be examined with the support of the analytical predictions given by a singular perturbation method: one-parameter autonomous dynamical

systems, with algebraic nonlinearities and admitting trivial steady-state solution, will be considered. The parameter will be denoted by μ, and the analyses will be performed in the neighbourhood of its critical value μ_0, for which the linear analysis predicts the transition from stable to unstable behaviour. Then, it is assumed that for $\mu < \mu_0$, the steady-state solution $\mathbf{x} = 0$ is linearly stable, in the sense that all the eigenvalues of the perturbation matrix around $\mathbf{x} = 0$ have a negative real part; moreover, it is assumed that, at $\mu = \mu_0$, the system experiences a Hopf bifurcation in the sense that one (and only one) pair of complex conjugate eigenvalues crosses the imaginary axis (Ref. [9]). As emphasized in most of the paper in the field of nonlinear aeroelasticity (see Ref. [10] for a recent and rich review on the subject), this mathematical description is physically performed by most of the aeroelastic systems in the neighbourhood of their critical stability margin: in this case, μ is typically the flight speed U_∞, the instability connected with the Hopf bifurcation is flutter, and then μ_0 is referred to as the flutter speed (U_{∞_F}). The analytical solution for the transient and steady-state behaviour will be expressed by using an asymptotic-expansion obtained in Ref. [11] through a singular-perturbation method.

In the Section 2 we will analyze the general analytical solutions available by the singular perturbation analysis in the neighbourhood of a Hopf bifurcation and referring to Ref. [7] for the details. In the same Section we will give an outlook on the Continuous Wavelet Transforms (CWT) and we will establish a theoretical connection between the analytical predictions (by the singular perturbation analysis) and the results obtained by a CWT analysis of the time response. In the Section 3 we present an aeroelastic application to a six-mode wing experiencing a limit cycle (which is the novelty of this paper).

2 Theoretical basis

Let us consider a general nonlinear system represented in the state space by:

$$\dot{\mathbf{z}} = \mathbf{A}(\mu)\mathbf{z} + \mathbf{f}(\mathbf{z}, \mu) \tag{1}$$

where $\mathbf{z} \in \mathbf{R}^{N_s}$ (N_s is the state-space dimension) is the state-space vector, $\mathbf{A}$ represents the linear part of the system, $\mathbf{f}$ the nonlinear part (without loss of generality, we will consider algebraic nonlinearities only), and μ is a parameter. Let us suppose that if $\mu < \mu_0$, the trivial solution of the linear part of the system is stable (all of the eigenvalues of $\mathbf{A}$ have negative real part), while if $\mu > \mu_0$ the linear part of the system is unstable (there is at least one real eigenvalue or a complex coniugate pair of eigenvalues with positive real part). Considering, for the sake of simplicity, only cubic nonlinearities, one has:

$$\mathbf{f}(\mathbf{z}, \mu) = \left\{ \sum_{p,q,r=1}^{N_s} c_{npqr}(\mu) z_p z_q z_r \right\}. \tag{2}$$

where $c_{npqr}(\mu)$ is a $N_s \times N_s \times N_s \times N_s$ nonlinear-coefficient matrix. In the next Subsection, the general solution for the above system in the neighbourhood of a Hopf bifurcation has been presented in details in Ref. [7]; next, the basic concepts of the CWT analysis and the theoretical relationship between this two different point of views will be presented in Subsection 2.2.

2.1 Hopf Bifurcation via Singular Perturbation Analysis (SPA)

The system given by Equation 1 has been considered in the neighbourhood of a limit cycle solution (*i.e.*, for $\mu \simeq \mu_0$). Calling $\varepsilon = |\mu - \mu_0|$ a small-perturbation parameter, we have $\mu = \mu_0 \pm \varepsilon$, where the plus (minus) holds for post-critical (pre-critical) response. We will also suppose that for $\mu = \mu_0$ a couple (and only one) of eigenvalues of the matrix $\mathbf{A}$ have real part equal to zero (say $\lambda_{1,2} = \pm j\omega_0$) while the remaining eigenvalues are still stable. Calling $\mathbf{A}_0 = \mathbf{A}(\mu_0)$, $\mathbf{A}_1 = \partial\mathbf{A}/\partial\mu|_{\mu=\mu_0}$, one has, $\mathbf{A}(\mu) = \mathbf{A}_0 \pm \varepsilon\mathbf{A}_1 + \mathcal{O}(\varepsilon^2)$, while $c_{npqr}(\mu) = c_{npqr}(\mu_0) + \mathcal{O}(\varepsilon)$. Considering

$$\mathbf{z} = \sqrt{\varepsilon}\ \mathbf{U}\mathbf{x} \tag{3}$$

where $\mathbf{U}$ is the eigenvector matrix of $\mathbf{A_0}$ (we assume that in the first two columns of $\mathbf{U}$ there are the eigenvectors $\mathbf{u}^{(1)}, \mathbf{u}^{(2)}$ corresponding to the critical eigenvalues $\lambda_{1,2}$), Equation 1 becomes:

$$\dot{\mathbf{x}} = \mathbf{\Lambda_0 x} + \varepsilon \left\{ \pm \sum_{s=1}^{N_s} \alpha_{js} x_s + \sum_{p,q,r=1}^{N_s} \gamma_{jpqr} x_p x_q x_r \right\} \tag{4}$$

where $\mathbf{\Lambda_0}$ is the diagonal matrix containing the $\mathbf{A_0}$ eigenvalues and

$$\alpha_{js} := \sum_{l,m=1}^{N_s} U_{jl}^{-1} A_{1_{lm}} U_{ms} \quad \gamma_{jpqr} := \sum_{s,t,u,v=1}^{N_s} U_{js}^{-1} c_{stuv} U_{tp} U_{uq} U_{vr} \tag{5}$$

Thus, considering the above Equations, the SPA gives the solution ([14, 11, 9, 7])

$$\begin{aligned} \mathbf{z} = \sqrt{\varepsilon} \left(\mathbf{u}^{(1)} A_1 e^{j\varphi_1} + \mathbf{u}^{(2)} A_1 e^{-j\varphi_1} + \sum_{n=3}^{N_c} \mathbf{u}^{(n)} A_n e^{i\varphi_n} + \sum_{m=N_c+1}^{N_s} \mathbf{u}^{(m)} y_m \right) \\ + \varepsilon\sqrt{\varepsilon} \mathbf{U} \left\{ \sum_{s=1}^{N_s} \frac{\alpha_{js}^{\text{aus}}}{\lambda_s - \lambda_j} y_s + \sum_{p,q,r=1}^{N_s} \frac{\gamma_{jpqr}^{\text{aus}}}{\lambda_p + \lambda_q + \lambda_r - \lambda_j} y_p y_q y_r \right\} \end{aligned} \tag{6}$$

where

$$A_1 = \left[\frac{-\beta_R^{(1)}/\gamma_R^{(1)}}{1 + k\, e^{2\beta_R^{(1)} t}} \right]^{1/2} \qquad \varphi_1 = t(-\beta_I^{(1)} + \gamma_I^{(1)} \beta_R^{(1)}/\gamma_R^{(1)}) + (\gamma_I^{(1)}/\gamma_R^{(1)}) \ln(A_1) + \varphi_1^0 \tag{7}$$

where k, φ_1^0 depend on the initial conditions and:

$$\beta^{(1)} := \beta_R^{(1)} + j\beta_I^{(1)} = -j\omega_0 \mp \varepsilon\, \alpha_{11} = -j\omega_0 \mp \varepsilon \mathbf{v}^{(1)^{\mathrm{T}}} \mathbf{A}_1 \mathbf{u}^{(1)} \tag{8}$$

$$\begin{aligned} \gamma^{(1)} &:= \gamma_R^{(1)} + j\gamma_I^{(1)} = -\varepsilon\, (\gamma_{1211} + \gamma_{1121} + \gamma_{1112}) \\ &= -\varepsilon \mathbf{v}^{(1)^{\mathrm{T}}} \left\{ \sum_{p,q,r=1}^{N_s} c_{jpqr} \left(u_p^{(1)^*} u_q^{(1)} u_r^{(1)} + u_p^{(1)} u_q^{(1)^*} u_r^{(1)} + u_p^{(1)} u_q^{(1)} u_r^{(1)^*} \right) \right\} \end{aligned} \tag{9}$$

whereas α_{js}^{aus}, α_{js}^{ess}, $\gamma_{jpqr}^{\text{aus}}$, and $\gamma_{jpqr}^{\text{ess}}$ are suitable selections of α_{js} and γ_{jpqr}. Note that the contribution of the real (stable) eigenvalues has been also included (see Ref. [12]; for a higher order analysis considering only the critical mode of vibration but using higher order terms, see Ref. [13]). Note also that the limit-cycle solution may be stable if (see Ref. [14]), although the linear part of the system is unstable, $\beta_R^{(1)} < 0$ (*i.e.* $\mu > \mu_0$), the nonlinear part of the system is stable, $\gamma_R^{(1)} > 0$: *i.e.*, if $\beta_R^{(1)} < 0$ and $\gamma_R^{(1)} > 0$ are both satisfied, a stable limit cycle may be observed in the post-critical response of the system. This case is interesting in an aeroelastic point of view because it represents a benign (nonlinear) *flutter*, *i.e.*, a stable limit cycle oscillation.

2.2 Continuous Wavelet Transform *vs* SPA

In order to overcome Fourier transform limits (*e.g.*, the impossibility to analyze signals whose spectral characteristics are strongly time-dependent) (Refs. [15], [16]), in the last decade a new method, based on wavelets, has been developed. The wavelets are particular waveforms that, correlated to the signal, are able to show and identify its features with arbitrary frequency resolution at low frequencies and arbitrary time resolution at high frequencies (Ref. [17]). The Continous Wavelet Transform $T^{wav}x$ of the signal $x(t)$ is defined as (Ref. [17]):

$$(T^{wav}x)(a,\tau) := \frac{1}{\sqrt{a}} \int_{-\infty}^{+\infty} x(t) \psi\left(\frac{t-\tau}{a}\right) dt \tag{10}$$

where a is the so called *scaling parameter*, τ is the *localization parameter* and $\psi(t)$ is called *mother wavelet*. The previous transform has been performed for all the applications presented in this paper using the *MATLAB Wavelet Toolbox*, Ref. [16]. The set of wavelets $\psi^{a,\tau}$ is obtained by streching or compressing the mother wavelet by the scaling parameter and localizing it by the parameter τ. Then, one has:

$$\psi^{a,\tau}(t) = \frac{1}{\sqrt{a}}\psi\left(\frac{t-\tau}{a}\right) \tag{11}$$

The mother wavelet used in the present paper is the Morlet Wavelet (Ref. [17]) defined by:

$$\psi(t) = e^{-\frac{t^2}{2}}e^{j\omega_0 t} \tag{12}$$

Specifically, in order to obtain real CWT functions we consider only the real part of the Morlet mother wavelet, with Fourier Transform given by (note that as ψ is real and the considerd signal are also real; then the CWT function given by Equation 10 is real too):

$$\hat{\psi}(\omega) = \sqrt{\frac{\pi}{2}}\left(e^{-\frac{1}{2}(\omega-\omega_0)^2} + e^{-\frac{1}{2}(\omega+\omega_0)^2}\right) \tag{13}$$

where the symbol $\hat{}$ denotes the Fourier transform. This mother wavelet was chosen because it generates wavelets $\psi^{a,\tau}$ having sinusoidal waveforms with gaussian envelope in the time-domain and gaussian shape in the frequency-domain: therefore, these wavelets are similar, from a functional point of view, to vibration signals (and then, suitable to be correlated with these kind of signals) and in the meanwhile they are localized in time (see the gaussian time function in Equation 12) and frequency (see Equation 13). The Continuous Wavelet Transform (CWT) of a signal may be represented in a time-scale plane, but on a time-frequency plane as well. As a matter of fact, the relation between frequency f and scale a is:

$$a = \frac{\omega_0}{2\pi f} = \frac{\omega_0}{\omega} \tag{14}$$

where ω is the angular frequency corresponding to the scale a. The previous equation allows one to map the time-scale plane in a time-frequency plane.

It is necessary to find a formula able to reconstruct the time signal by its CWT because an inverse CWT may not exist for certain wavelet type (Ref. [17]): this reconstruction formula could also be used to find the Frequency Response Functions (FRF) of a linear system, or to identify the linear part of nonlinear systems. This can be carried out in a least-square sense because the wavelets set given by Equation 11 is not a set of orthogonal functions. In order to obtain that, one applies the Fourier transform to Equation 10 from the domain τ to the domain $\bar{\omega}$ obtaining:

$$\hat{T}^{wav}x(a,\bar{\omega}) = \sqrt{a}\,\hat{\psi}(a\bar{\omega})\hat{x}(\bar{\omega}) \tag{15}$$

where $\hat{x}(\bar{\omega})$ is the Fourier transform (from the time domain) of the signal and $\hat{T}^{wav}x(a,\bar{\omega})$ is the Fourier transform of the CWT of the signal performed in the domain of the localization parameter τ. Thus, as $\hat{T}^{wav}x(a,\bar{\omega})$ and $\hat{\psi}$ are known functions, one can obtain (in a least-square sense) $\hat{x}(\bar{\omega})$; then, applying the inverse of the Fourier transform (from the domain $\bar{\omega}$ to the domain t), one can find the reconstructed signal $x(t)$. Indeed, from a numerical point of view, the Equation 15 may be written for several values of the scaling parameter a, and the system of equation could then be solved in a least-square sense:

$$\hat{x}(\bar{\omega}) = \begin{bmatrix} \hat{\psi}_{a_1}(\bar{\omega}) \\ \hat{\psi}_{a_2}(\bar{\omega}) \\ \vdots \\ \hat{\psi}_{a_M}(\bar{\omega}) \end{bmatrix}^T \begin{bmatrix} \hat{T}^{wav}x(a_1,\bar{\omega}) \\ \hat{T}^{wav}x(a_2,\bar{\omega}) \\ \vdots \\ \hat{T}^{wav}x(a_M,\bar{\omega}) \end{bmatrix} / \begin{bmatrix} \hat{\psi}_{a_1}(\bar{\omega}) \\ \hat{\psi}_{a_2}(\bar{\omega}) \\ \vdots \\ \hat{\psi}_{a_M}(\bar{\omega}) \end{bmatrix}^T \begin{bmatrix} \hat{\psi}_{a_1}(\bar{\omega}) \\ \hat{\psi}_{a_2}(\bar{\omega}) \\ \vdots \\ \hat{\psi}_{a_M}(\bar{\omega}) \end{bmatrix} \tag{16}$$

where $\hat{\psi}_{a_i} = \sqrt{a_i}\hat{\psi}(a_i\omega)$ $(i = 1..M)$ and M the number of sampled values of a. Note that this least square procedure may be noise filtering (Ref. [7]): this is due to the fact that the system of Equations 16 was solved in a least-square sense, *i.e.*, averaging the equations corresponding to different values of a.

Next, we shall show how the Continuous Wavelet Transform (CWT) offers the possibility to identify the time-varying frequencies ω_i and the amplitudes A_i $(i = 1..N_c)$ of a nonlinear system in a Hopf bifurcation (see previous section). From Equation 6 we see that the terms of order $\sqrt{\varepsilon}$ oscillate with the frequencies:

$$\omega_1(t) := \frac{\partial\varphi_1}{\partial t} = -\beta_I^{(1)} + \gamma_I^{(1)}\frac{\frac{\beta_R^{(1)}}{\gamma_R^{(1)}}}{1 + ke^{2\beta_R^{(1)}t}} \tag{17}$$

$$\omega_n(t) := \frac{\partial\varphi_n}{\partial t} = -\beta_I^{(n)} + \gamma_I^{(n)}\frac{\frac{\beta_R^{(1)}}{\gamma_R^{(1)}}}{1 + ke^{2\beta_R^{(1)}t}} \qquad n = 3,..,N_c \tag{18}$$

$$\omega_m(t) := \frac{\partial\varphi_m}{\partial t} = 0 \qquad m = N_c + 1,..,N_s \tag{19}$$

From Equations 17 and 18 we observe that the frequencies in the neighbourhood of the eigenvalues with non-zero imaginary part vary during the transient response. Thus, it is necessary to consider both the time- and the frequency-information (*i.e.*, time-scale or time-frequency decompositions of the signal) if one wants to identify the nonlinear nature of these systems. Estending the result linear systems, in Ref. [7] it was shown the the relationship between $T^{wav}y_1(a_1,\tau)$ and the amplitude A_1 (see Eq. 6), when A_1, ω_1 are slowly varying functions, is

$$|T^{wav}y_1(a_1,\tau)| \simeq \sqrt{\frac{\pi\omega_0}{2\omega_1}}A_1(\tau) \tag{20}$$

where a_1 is the scale correspondent to ω_1. On the other hand, if A_n, ω_n and $\log A_1$ (see Eq. 18) are slowly varying:

$$|T^{wav}y_n(a_n,\tau)| \simeq \sqrt{\frac{\pi\omega_0}{2\omega_n}}A_n(\tau) \qquad n = 3,..,N_c \tag{21}$$

Thus, the envelopes of the CWT logarithmic cross sections, taken at the scales correspondent to the nonlinear-characteristic frequencies, are proportional to the energy associated to that particular frequency and predicted by using the singular perturbation method. Equations 20 and 21 hold both for the pre- and post-critical behaviour. Besides identifying the amplitude A_1, we may also identify the system's stability margins through pre-critical ($\mu < \mu_0$) simulations or tests. As a matter of fact, taking the logarithm of Equation 7, we have:

$$\log A_1 = \frac{1}{2}\log\left|\frac{\beta_R^{(1)}}{\gamma_R^{(1)}}\right| - \frac{1}{2}\log\left(1 + ke^{\beta_R^{(1)}t}\right) \tag{22}$$

In pre-critical conditions $\beta_R^{(1)} > 0$, then, if $ke^{\beta_R^{(1)}t} \gg 1$, we obtain:

$$\log|T^{wav}y_1(a_1,\tau)| \simeq \frac{1}{2}\log\frac{\pi\omega_0}{2\bar{\omega}} + \log A_1(t) \simeq K - \beta_R^{(1)}t \tag{23}$$

Thus, the slope ϕ of the logarithm plot of the CWT cross-sections is analytically given by the coefficient $\beta_R^{(1)}$ and then proportional to ε (from Equation 8). By identifying ϕ through several tests at different pre-critical values of μ, the CWT allows one to identify the system stability margin μ_0.

3 Application to a 3-D Aeroelastic System

In order to show the practical advantages given by the methods shown, a test on a real complex model has been performed. The model considered is a transport aircraft wing whose geometrical and structural characteristics for the linear part of the model are presented in Ref. [7]: the linear part of the model has been obtained using a modal description (6 modes) for the structural dynamics and the Finite-State Aerodynamics for the unsteady aerodynamics (see [18] for details): then, the model can be represented in the state space by

$$\dot{\mathbf{z}} = \mathbf{A}(U_\infty)\mathbf{z} + c\mathbf{f}(\mathbf{z}) \tag{24}$$

with $\mathbf{z}^T = \{\mathbf{q}^T|\dot{\mathbf{q}}|\mathbf{r}\}$ where $\mathbf{q}$ and $\dot{\mathbf{q}}$ are the Lagrangian variables and $\mathbf{r}$ the aerodynamic vector given by the FSA modeling; $\mathbf{f}(\mathbf{z})$ is given by $\mathbf{f}(\mathbf{z}) = \left\{\sum_{p,q,r=1}^{N_s} c_{npqr} z_p z_q z_r\right\}$., with $c_{7222} = c_{7333} = c_{10\,222} = c_{10\,333} = 0.5$, $c_{8222} = c_{8333} = 1$, $c_{11\,222} = c_{11\,333} = 0.1$, $c_{12\,222} = c_{12\,333} = 0.01$, and $c_{npqr} = 0$ in all the other cases.[1] The coefficients c_{npqr} where chosen in order to have structural stabilizing nonlinear terms, whose most important part was given by the weakly damped modes. By varying the coefficient c it is possible to obtain several models with weak (low values of c) or strong (high values of c) nonlinearities . In the following results three cases have been considered: the linear ($c = 0$), a weakly nonlinear ($c = 10$), and a strongly nonlinear ($c = 20$) one. The cases considered have been tested for different values of the flight speed and for different values of the Signal-to-Noise Ratio. The noise is introducted on the generic output signal $x(t)$ by considering $x_{noise}(t) = x(t)(1 + \delta_1 n(t)) + \delta_2 m(t)$, where $n(t)$, $m(t)$ are white noises with gaussian probability distribution and zero mean value; the SNR is regulated through the coefficients δ_1, δ_2. In Figures 1, 2 the systems responses are shown in the two cases of a pre-critical test and of a

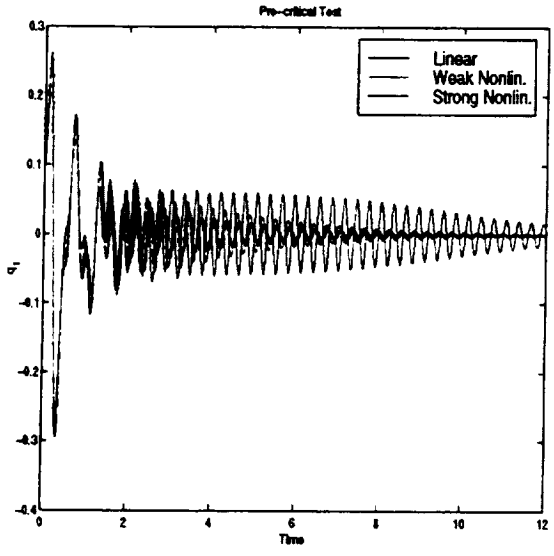

Figure 1: *Pre-critical response of the models considered.*

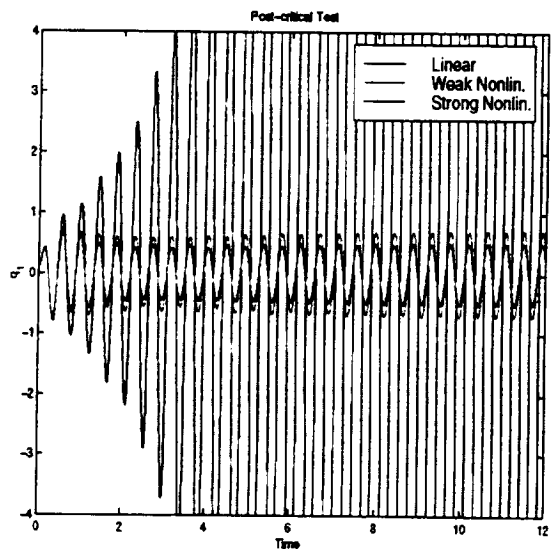

Figure 2: *Post-critical response of the models considered.*

post-critical test. As the figure shows, in post critical conditions after the transitory phase the systems performs a limit cycle solution whose amplitude is larger for the weakly nonlinear system (being the structural nonlinearities stabilizing). Figure 3 shows the pre-critical response of the weakly nonlinear system for two diffrent values of the SNR, then considered for the stability margin (U_{∞_F}) estimation. As already shown in the previous Section, after the signal has been recorded it is necessary to analyze the CWT sections to identify the natural frequencies and their time evolution. Figure 4 shows that, even if

[1] Note that the modeling of the nonlinear contribution does not correspond to any actual physical model; nevertheless any other arbitrary choice does not change the meaning of the obtained results.

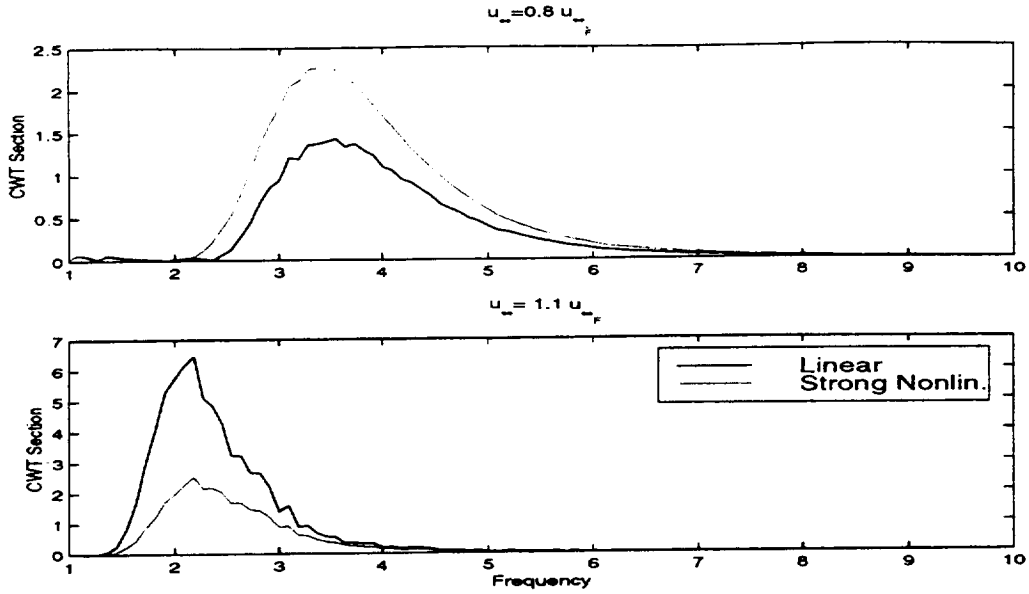

Figure 4: *CWT pre-critical ($\tau = 2s$) and post-critical ($\tau = 5s$) sections.*

Acknowledgements: This work has been supported by the University of Rome I *"La Sapienza,"* finanziamento progetti di ricerca afferenti la quota 60% (ricerche di Facoltà), grant 1996: *"Controllo Nonlineare della Stabilità di Sistemi Aeroelastici in Fase Pre- e Post-Critica."*

References

[1] M.J. BRENNER, R.C. LIND, AND D.F. VORACEK 1997 *NASA Technical Memorandum* 4792. Overview of Recent Flight Flutter Testing Research at NASA Dryden.

[2] M.J. BRENNER 1997 *NASA Technical Memorandum* 4793. Wavelet Analyses of F/A-18 Aeroelastic and Aeroservoelastic Flight Test Data.

[3] R. LIND, M. BRENNER, AND S. HALEY 1997 *AIAA Atmosferic Flight Mechanics Conference, New Orleans, California.* Estimation of modal parameters using a wavelet-based approach.

[4] L. FREUDINGER, R. LIND, AND M. BRENNER 1998 *16th IMAC, Santa Barbara, California.* Correlation Filtering of Modal Dynamics using the Laplace Wavelet.

[5] M. BRENNER 1998 *AIAA Structures, Structural Dynamics and Materials Conference paper 98-1896, Long Beach, California.* Wavelet Filtering to Reduce Conservatism in Aeroservoelastic Robust Stability Margin.

[6] R. LIND, K.SNYDER, AND M. BRENNER 1998 *AIAA Structures, Structural Dynamics and Materials Conference paper 98-1808, Long Beach, California.* Investigating Transient and Limit Cycle Behaviours of a Nonlinear Structure by Wavelet transforms.

[7] F. MASTRODDI, A. BETTOLI, 1999 accepted for publication on *Journal of Sound and Vibration.* Wavelet Analysis for Hopf Bifurcation with Aeroelastic Analysis.

[8] A.H. NAYFEH 1993 *The Method of Normal Forms.* New York: John Wiley & Sons.

[9] F. MASTRODDI AND L. MORINO 1996 *The Aeronautical Journal* 100(999), 389-396. Limit-Cycle Taming by Nonlinear Control with Application to Flutter.

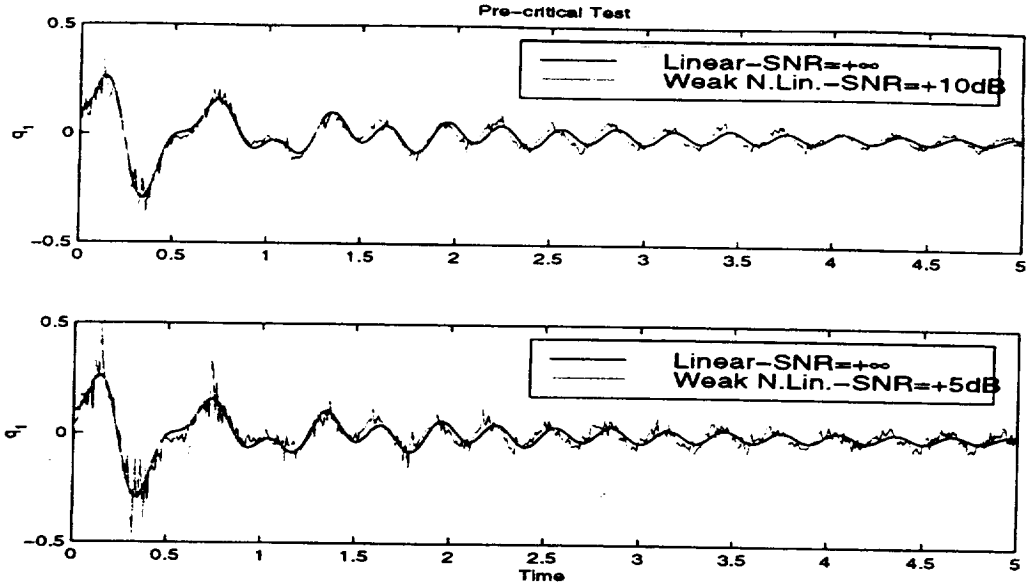

Figure 3: *Pre critical responses for several Signal to Noise Ratios.*

the initial conditions were chose such as to excite all the natural modes, after a short time the most part of the energy is obviously associated to the critical mode. From the figure it may be observed that while for pre crical conditions the frequency corresponding to the maximum energy is $f_{max} = 3.5Hz$, while for post critical conditions $f_{max} = 2.2Hz$. This was due to the behaviour of the linear model considered. As a matter of fact, it has been discovered that this model have, as U_∞ approaches U_{∞_F} two natural modes with a very low damping. The first corresponds to the critical mode, but the second one is already dominant at $U_\infty = 1.05U_{\infty_F}$. This causes the dynamic of the system to be similar to a 2 *DOF* system as shown in Fig. 5 that depicts the CWT of the response for pre-critical and post-critical conditions. Analyzing the evolution with time of the signal energetic content it is clearly apparent that while the mode at $f_n = 3.5Hz$ is dominant for $U_\infty < U_{\infty_F}$, for $U_\infty > U_{\infty_F}$ the mode at $f_n = 2.2Hz$ becomes dominant. Considering the CWT cross-sections (corresponding to th etwo frequencies identified) as shown in Figure 6, it is possible to evaluate the damping of the critical mode in pre-critical condition using the following robust estimate: in Figure 7 the semi-logarithmic envelopes of the CWT cross sections are shown for different SNR at several flight speds. As predicted by Eq.23, the slope ϕ decreases as U_∞ approaches U_{∞_F}. In Table 1 the estimate $\bar{U}_{\infty_F}$ of the system stability margin is shown. The

SNR	$\bar{U}_{\infty_F}$	$\varepsilon(\%)$
$+\infty$	243	1.1 %
10 *dB*	235	-1.9 %
5 *dB*	233	-3.1 %

SYSTEM	$\bar{U}_{\infty_F}$	$\varepsilon(\%)$
Linear	242	0.7 %
Weak Nonlin.	243	1.1 %
Strong Nonlin.	244	1.6 %

Table 1: *Stability margin estimates: SNR influence (on left) and nonlinearities influence (on right; $SNR = +\infty dB$).*

estimation has been performed by a linear interpolation of the values of ϕ for different speeds. Obviously, as the SNR decreases the estimation become worse, but remains acceptable even if for very low SNR for the reasons mentioned in the previous section. In Figure 8 the semi-logarithmic envelopes of the CWT cross sections are shown for the three model considered at several flight speds. In Table 1 the estimate $\bar{U}_{\infty_F}$ of the system stability margin is shown for different levels of nonlinearities.

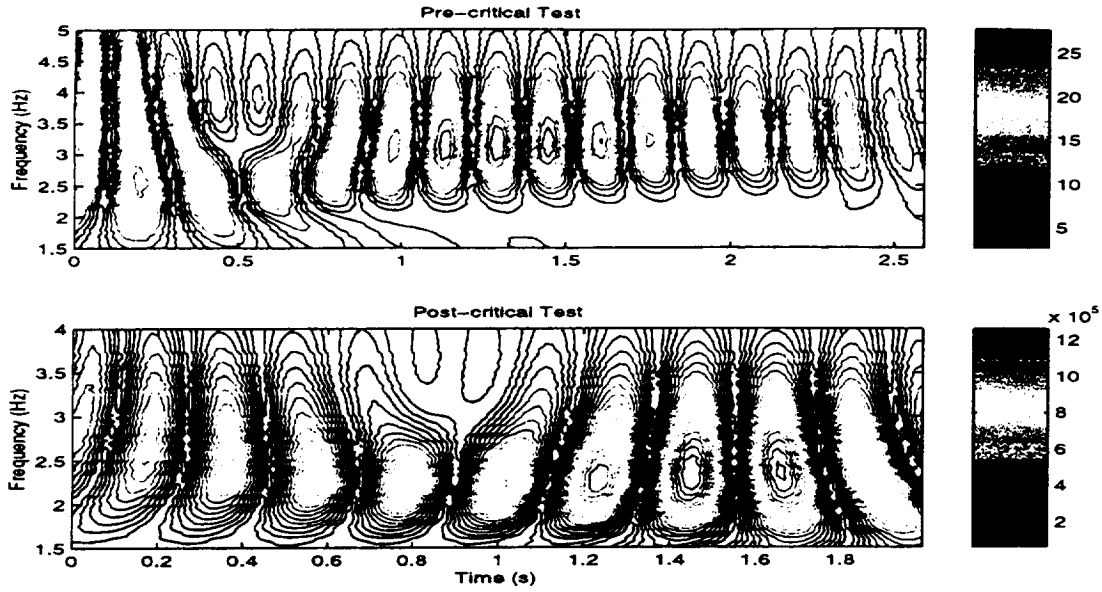

Figure 5: *Evolution of the signal energetic content of the response.*

[10] E.H. DOWELL, L.N. VIRGIN, D.M. TANG, AND M.D. CONNER 1997 *Proceedings of CEAS International Forum on Aeroelasticity and Structural Dynamics, Rome*, I, 79-91. Nonlinear Dynamics of Aeroelastic Systems.

[11] F. MASTRODDI 1994 *PhD thesis in Aerospace Engineering, University of Rome La Sapienza.* Aeroservoelasticità : Problematiche non Lineari.

[12] L. MORINO, F. MASTRODDI, AND M. CUTRONI 1995 *Nonlinear Dynamics* **7**, 403-428. Lie Transformation Method for Dynamical Systems Having Chaotic Behaviour.

[13] D. DESSI, L. MORINO, AND F. MASTRODDI 1997 *Proceedings of CEAS International Forum on Aeroelasticity and Structural Dynamics, Rome*, I, 79-91. A Fifth-Order No-Reconstruction Multiple-Scale Solution for Hopf-Bifurcations.

[14] L. SMITH AND L. MORINO 1976 *AIAA Journal*, **14**(3), 333-341. Stability Analysis of Nonlinear Differential Autonomous Systems with Applications to Flutter.

[15] T.P. KRAUSS, L. SHURE, AND J.N. LITTLE 1992 *Signal Processing Toolbox for Use with MATLAB©*. Massachussets: The Math Work Inc.

[16] M. MISITI, Y. MISITI, G. OPPENHEIM, AND J.M. POGGI 1996 *Wavelet Toolbox for Use with MATLAB©*. Massachussets: The Math Work Inc.

[17] I. DAUBECHIES 1992 *Ten Lectures on Wavelets.* Philadelphia: SIAM.

[18] F. MASTRODDI, E. CIANCALEONI, L. MORINO 1999 *Aeroelastic Constraints in MDO, CEAS Internation Forum on Aeroelasticity and Structural Dynamics*, Williamsburg, VA.

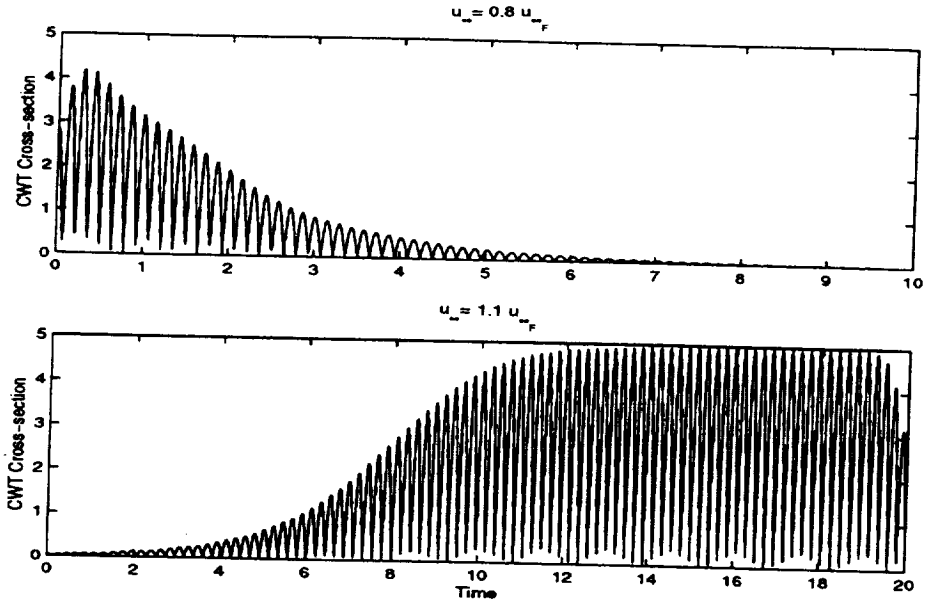

Figure 6: *CWT pre-critical ($f = 3.5Hz$) and post-critical ($f = 2.2Hz$) cross-sections.*

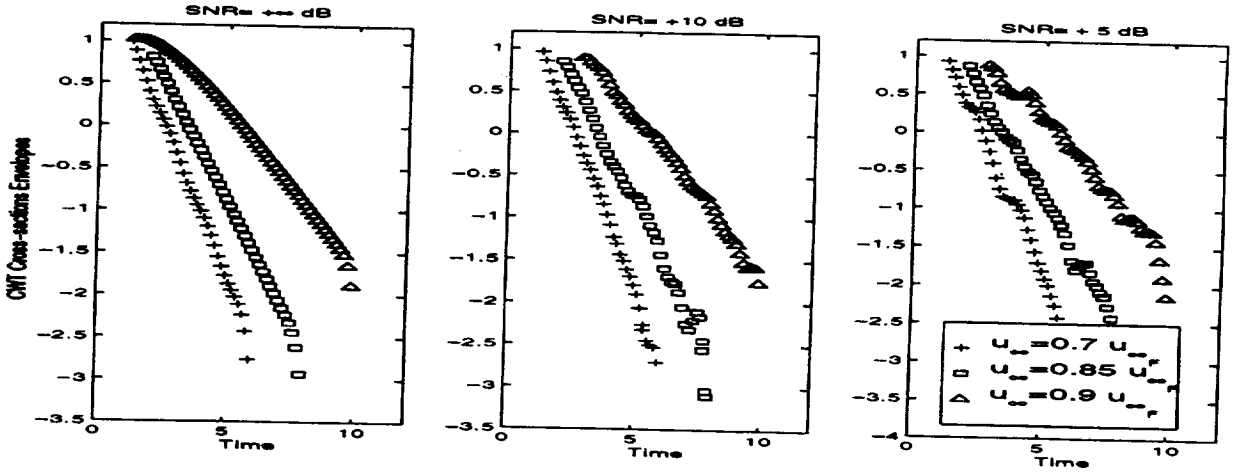

Figure 7: *CWT cross-sections envelopes for different SNR (weak nonlinearities).*

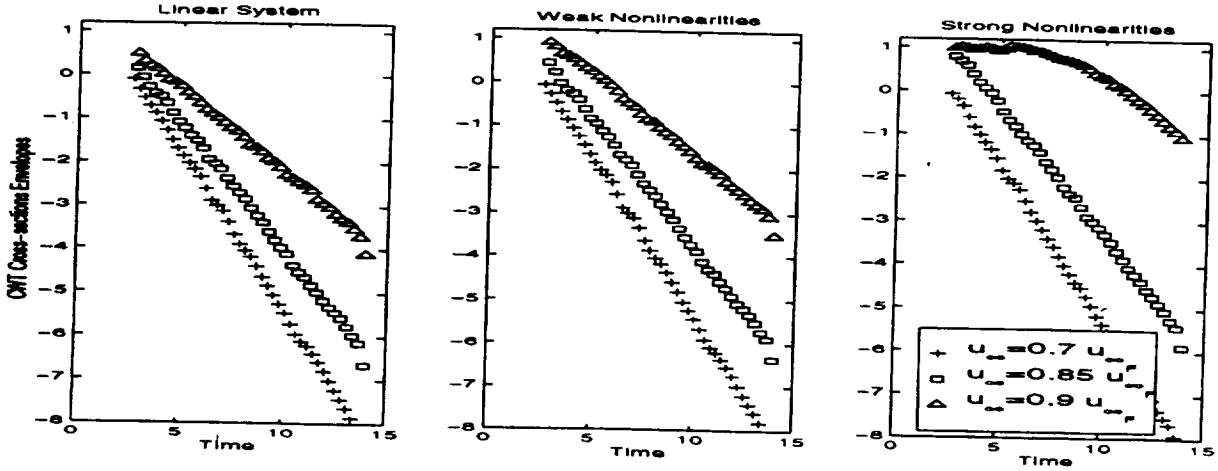

Figure 8: *CWT cross-sections envelopes for different models ($SNR = +\infty$).*

REPORT DOCUMENTATION PAGE

Form Approved
OMB No. 07704-0188

1. AGENCY USE ONLY *(Leave blank)*	2. REPORT DATE	3. REPORT TYPE AND DATES COVERED
	June 1999	Conference Publication

4. TITLE AND SUBTITLE
CEAS/AIAA/ICASE/NASA Langley International Forum on Aeroelasticity and Structural Dynamics 1999

5. FUNDING NUMBERS
505-90-52-01

6. AUTHOR(S)
Woodrow Whitlow, Jr., and Emily N. Todd

7. PERFORMING ORGANIZATION NAME(S) AND ADDRESS(ES)
NASA Langley Research Center
Hampton, VA 23681-2199

8. PERFORMING ORGANIZATION REPORT NUMBER
L-17863B

9. SPONSORING/MONITORING AGENCY NAME(S) AND ADDRESS(ES)
National Aeronautics and Space Administration
Washington, DC 20546-0001

10. SPONSORING/MONITORING AGENCY REPORT NUMBER
NASA/CP-1999-209136/PT 2

11. SUPPLEMENTARY NOTES
Whitlow: NASA John H. Glenn Research Center at Lewis Field, Cleveland, OH
Todd: Institute for Computer Applications in Science and Technology (ICASE), Hampton, VA

12a. DISTRIBUTION/AVAILABILITY STATEMENT
Unclassified–Unlimited
Subject Category 02 Distribution: Standard
Availability: NASA CASI (301) 621-0390

12b. DISTRIBUTION CODE

13. ABSTRACT ***(Maximum 200 words)***

These proceedings represent a collection of the latest advances in aeroelasticity and structural dynamics from the world community. Research in the areas of unsteady aerodynamics and aeroelasticity, structural modeling and optimization, active control and adaptive structures, landing dynamics, certification and qualification, and validation testing are highlighted in the collection of papers. The wide range of results will lead to advances in the prediction and control of the structural response of aircraft and spacecraft.

14. SUBJECT TERMS
Aeroelasticity; Unsteady aerodynamics; Computational fluid dynamics; Flutter; Multidisciplinary design optimization; Structural optimization; Structural dynamics; Smart materials; Active control

15. NUMBER OF PAGES
419

16. PRICE CODE
A18

17. SECURITY CLASSIFICATION OF REPORT	18. SECURITY CLASSIFICATION OF THIS PAGE	19. SECURITY CLASSIFICATION OF ABSTRACT	20. LIMITATION OF ABSTRACT
Unclassified	Unclassified	Unclassified	UL